Topics in Applied Physics 121

Nianjun Yang *Editor*

Novel Aspects of Diamond

From Growth to Applications

Springer

Topics in Applied Physics

Volume 121

Topics in Applied Physics is a well-established series of review books, each of which presents a comprehensive survey of a selected topic within the broad area of applied physics. Edited and written by leading research scientists in the field concerned, each volume contains review contributions covering the various aspects of the topic. Together these provide an overview of the state of the art in the respective field, extending from an introduction to the subject right up to the frontiers of contemporary research.

Topics in Applied Physics is addressed to all scientists at universities and in industry who wish to obtain an overview and to keep abreast of advances in applied physics. The series also provides easy but comprehensive access to the fields for newcomers starting research.

Contributions are specially commissioned. The Managing Editors are open to any suggestions for topics coming from the community of applied physicists no matter what the field and encourage prospective editors to approach them with ideas.

More information about this series at http://www.springer.com/series/560

Nianjun Yang
Editor

Novel Aspects of Diamond

From Growth to Applications

Springer

Editor
Nianjun Yang
University of Siegen
Siegen
Germany

ISSN 0303-4216 ISSN 1437-0859 (electronic)
ISBN 978-3-319-09833-3 ISBN 978-3-319-09834-0 (eBook)
DOI 10.1007/978-3-319-09834-0

Library of Congress Control Number: 2014951145

Springer Cham Heidelberg New York Dordrecht London

Printed on acid-free paper

Springer is part of Springer Science+Business Media (www.springer.com)

Preface

Diamond, as a wide bandgap semiconducting material, has been extensively studied for years. For more than 25 years, diamond has been known as a perfect material for mechanical, optical, thermal, and electronic applications due to its excellent physical and chemical properties. High temperature electronic devices, radiation detectors, high voltage switches, X-ray windows, audio speaker diaphragms, and protective coatings are examples of diamond-based devices. In the initial stage of diamond research, natural diamond crystals and single-crystalline diamond synthesized by the high-temperature/high-pressure (HPHT) were mostly utilized. About 30 years ago, the realization of the low-pressure chemical vapor deposition (CVD) of diamond triggered novel aspects of diamond research in laboratories and in industries all over the world. CVD-grown diamond films offer advantages for electronic applications with respect to crystal purification and doping for p-type or n-type conductivity. For example, the diamond films become electrically conductive when they are heavily doped with boron. Such boron-doped diamond films possess wide potential window, low background current, and long stability. They are, therefore, recognized as the perfect electrodes in the fields of electroanalysis, pollution degradation, electrosynthesis, electrochemical biosensing, and so on.

This book is dedicated to presenting reviews of novel aspects in diamond research and technology, which were realized and appeared very recently. These novel topics and technologies accelerate the breakthrough of diamond research in fundamental studies as well as in industrial applications. In this book, five aspects have been selected: CVD diamond growth (Chaps. 1 and 2), surface chemistry of diamond (Chaps. 3 and 4), surface nanostructuring of diamond (Chaps. 5 and 6), applications of diamond for energy and power devices (Chaps. 7 and 8), and diamond based electrochemical sensing devices (Chaps. 9 and 10).

Chapter 1 deals with the growth of diamond using chemical vapor deposition (CVD) techniques, emphasizing the technologies for the homoepitaxial growth of high-quality single-crystal diamond films with atomically flat surfaces. The growth mechanism and control of homoepitaxial diamond growth is discussed. Chapter 2 summarizes the preparation, properties, and applications of diamond composite films with β-SiC. Control of the crystallinity, orientation, and phase distribution of

diamond and SiC are shown. This composite film possesses advantages of both diamond and β-SiC. Their applications as a DNA biosensing platform are demonstrated.

Chapter 3 focuses on the effect of adsorbed species on the chemical and electronic properties of diamond. Theoretical modeling and mathematic simulation clarify the roles of surface terminations of diamond on its surface reactivity, surface processes including surface stability, modification, and functionalization. Growth mechanisms of thin diamond film and surface electrochemistry of diamond are discussed. Chapter 4 reviews surface chemistry of nanodiamonds, which is tunable via surface terminations and surface charges of diamond nanoparticles. The link between surface chemistry, surface charge, and colloidal properties of nanodiamonds is particularly emphasized. Developments of bio-applications of nanodiamonds are summarized. The challenges for nanodiamond-based biomedicine are discussed.

Chapter 5 summarizes various synthetic methods to prepare diamond nanowires. The mechanical, electron field emission, structural stability, electrochemical properties of such one-dimensional diamond nanowires are reviewed. Several physical and electrochemical applications of diamond nanowires have been demonstrated. Chapter 6 presents surface nanostructuring via depositing different nanoparticles. Two types of structured diamond electrodes are demonstrated: nanoparticle-modified diamond electrodes and detonation nanodiamond-based electrodes. Their construction, modification, and physical characteristics are reviewed. The discussion about the progress on the interactions between metals and diamond at nanoparticle-based electrodes is highlighted.

Chapter 7 summarizes the electrochemical applications of diamond films for energy storage and conversions. The techniques used for surface modification of diamond materials are summarized. The applications of such electrode systems for proton exchange membrane fuel cells (methanol and ethanol oxidation) are shown. The production of porous diamond films and their applications for electrochemical capacitors are described. Chapter 8 reviews the electron emission properties of hydrogen-terminated diamond surfaces with a negative electron affinity. The recent development of electron emitters based on diamond *PN* and *PIN* junctions and their application for a high voltage vacuum power switch are presented.

Chapter 9 overviews the technologies to fabricate and characterize diamond microelectrode, ultramicroelectrode, and nanoelectrode, and their arrays. The beneficial characteristics of individual micro-/nano-electrodes and arrays are discussed. Their applications such as sensitive detection of dopamine, surface sensitive detections are demonstrated. Chapter 10 takes the device of diamond microelectrode as an example to demonstrate diamond-based devices for in vivo biosensing applications. The development of boron-doped diamond as electrode material leads to significant improvement toward sensitivity, reproducibility, and stability during the in vivo monitoring of electroactive species. The most recent developments in monitoring of dopamine and glutathione using diamond microelectrodes are described.

It is hoped that these chapters present novel aspects of diamond researches achieved and appeared recently. We believe that this book will simulate more researchers from universities, research institutions, and industrials to contribute and promote diamond related researches in different fields.

Siegen, Germany Nianjun Yang

Contents

Contributors

J.C. Arnault CEA, LIST, Diamond Sensors Laboratory, Gif Sur Yvette, France

Patricia Rachel Fernandes da Costa Instituto de Química, Universidade Federal do Rio Grande do Norte, Natal, RN, Brazil

Djalma Ribeiro da Silva Instituto de Química, Universidade Federal do Rio Grande do Norte, Natal, RN, Brazil

Elisama Vieira dos Santos Instituto de Química, Universidade Federal do Rio Grande do Norte, Natal, RN, Brazil

Yasuaki Einaga Faculty of Science and Technology, Department of Chemistry, Keio University, Yokohama, Japan

Stéphane Fierro Faculty of Science and Technology, Department of Chemistry, Keio University, Yokohama, Japan

John S. Foord Department of Chemistry, Oxford University, Oxford, UK

Jakob Hees Fraunhofer-Institute for Applied Solid State Physics (IAF), Freiburg, Germany

Xin Jiang Department of Mechanical Engineering, Institute of Materials Engineering, University of Siegen, Siegen, Germany

Satoshi Koizumi Environment and Energy Materials Division, National Institute for Materials Science (NIMS), Tsukuba, Ibaraki, Japan

Karin Larsson Department of Materials Chemistry, Uppsala University, Uppsala, Sweden

Carlos A. Martínez-Huitle Instituto de Química, Universidade Federal do Rio Grande do Norte, Natal, RN, Brazil

Christoph E. Nebel Fraunhofer-Institute for Applied Solid State Physics (IAF), Freiburg, Germany

Geoffrey W. Nelson Department of Chemistry, Oxford University, Oxford, UK

Juan M. Peralta-Hernández Departamento de Investigación Ambiental Omega-201, Centro de Inovación Aplicada en Tecnologías Competitivas (CIATEC), Fraccionamiento Industrial Delta, Leon, Guanajuato, Mexico

Giancarlo R. Salazar-Banda Instituto de Tecnologia e Pesquisa e Programa de Pos-Graduacao em Engenharia de Processos, Universidade Tiradentes, Aracaju, SE, Brazil

Daisuke Takeuchi Energy Technology Research Institute, National Institute of Advanced Industrial Science and Technology (AIST), Tsukuba, Ibaraki, Japan

Norio Tokuda Faculty of Electrical and Computer Engineering, Institute of Science and Engineering, Kanazawa University, Kanazawa, Japan

Liangzhuan Wu Key Laboratory of Photochemical Conversion and Optoelectronic Materials, Technical Institute of Physics and Chemistry, Chinese Academy of Sciences, Beijing, People's Republic of China

Nianjun Yang Institute of Materials Engineering, University of Siegen, Siegen, Germany

Yuan Yu Key Laboratory of Photochemical Conversion and Optoelectronic Materials, Technical Institute of Physics and Chemistry, Chinese Academy of Sciences, Beijing, People's Republic of China

Jinfang Zhi Key Laboratory of Photochemical Conversion and Optoelectronic Materials, Technical Institute of Physics and Chemistry, Chinese Academy of Sciences, Beijing, People's Republic of China

Hao Zhuang Department of Mechanical Engineering, Institute of Materials Engineering, University of Siegen, Siegen, Germany

Chapter 1
Homoepitaxial Diamond Growth by Plasma-Enhanced Chemical Vapor Deposition

Norio Tokuda

Abstract Both carbon and silicon are group IV members, but carbon has the smaller atomic number. Diamond, with the same crystalline structure as that of silicon, is expected to act as the basic material for the next generation of high-power electronic, optoelectronic, bio/chemical electronic, quantum computing devices, etc. This is because diamond exhibits electrical properties similar to those of silicon, while having superior physical properties. In this chapter, the author reviewed and discussed the homoepitaxial growth of high-quality single-crystal diamond films with atomically flat surfaces, by using plasma-enhanced chemical vapor deposition (PECVD).

1.1 Introduction

Growth of diamond films by chemical vapor deposition (CVD), which has been studied since the 1950s, must be conducted under nonequilibrium conditions. This is because under normal conditions, graphite is a more stable phase of carbon than diamond. Furthermore, during the CVD process, hydrogen radicals (atomic hydrogen) must be present to remove nondiamond carbon, including graphite which is formed on the diamond surface. The hydrogen radicals are generated either by thermal dissociation on a hot filament of W or Ta, or in plasma by electron impact, collisional energy transfer, etc. In plasma, the external energy input couples directly to free electrons, producing hydrogen radicals via

$$H_2 + e^- \rightarrow 2H + e^-. \tag{1.1}$$

N. Tokuda (✉)
Faculty of Electrical and Computer Engineering, Institute of Science and Engineering, Kanazawa University, Kanazawa 920-1192, Japan
e-mail: tokuda@ec.t.kanazawa-u.ac.jp

N. Yang (ed.), *Novel Aspects of Diamond*, Topics in Applied Physics 121,
DOI 10.1007/978-3-319-09834-0_1

Methane is commonly used as the carbon source for CVD diamond growth. Activated CH_x (x = 0, 1, 2, 3) species are formed by hydrogen abstraction reactions; for example, hydrogen radicals may produce methyl radicals from methane:

$$H + CH_4 \rightarrow CH_3 + H_2. \tag{1.2}$$

Then, recombination of the methyl radicals induces to form activated C_2H_y (y = 0, 1, 2, 3, 4, 5, 6) species:

$$CH_3 + CH_3 + M \rightarrow C_2H_6 + M \tag{1.3}$$

$$C_2H_y + H + M \leftrightarrow C_2H_{y-1} + H_2 + M, \tag{1.4}$$

where M is a third body. The CH_x and C_2H_y radicals are regarded as precursors for diamond growth during the CVD process, as shown in Fig. 1.1 [1–8]. Thus, radicals play an important role in CVD diamond growth; this differs from the other semiconductor films' growth conducted by nonplasma processes such as thermal CVD and molecular beam epitaxy.

Hot-filament CVD has been applied to large-scale industrial processes because of its simple system configuration and ability to coat large areas and complex shapes. However, hot-filament CVD of diamond films must be carried out at lower gas temperatures and pressures than those of plasma CVD because of the upper temperature limit of the filament materials and the low production rate of hydrogen radicals. This leads to relatively low growth rates of diamond films compared to

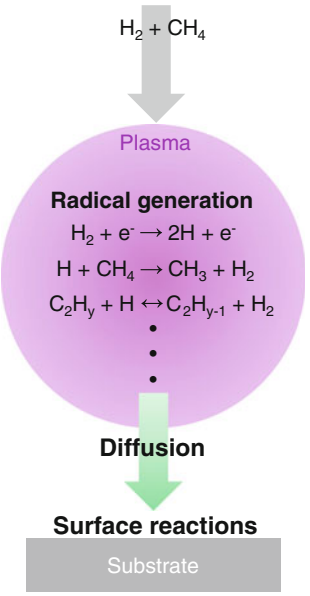

Fig. 1.1 Schematic of CVD diamond processes

diamond growth by plasma-enhanced CVD (PECVD). Recently, homoepitaxial diamond growth rates of >100 μm/h by PECVD have been reported [9–15]. Additionally, both *p*- and *n*-type diamond films have been reproducibly grown by PECVD [16–42]. Therefore, the diamond films used in diamond electronic devices were grown by PECVD [43–75].

In this chapter, recent studies on homoepitaxial diamond growth by PECVD are reviewed. Additionally, impurity doping into diamond and the growth of atomically flat diamond surfaces are described.

1.2 Growth Mechanism

More than a decade has passed since PECVD of diamonds was established. Since then, many experimental and theoretical studies have been reported. Diamond growth by PECVD is not driven by thermodynamics but by the chemistry and kinetics of vapor phase and surface reactions. To elucidate the diamond growth mechanism during PECVD, both vapor-phase and surface reactions need to be understood. Evaluations of the vapor phase have been based on optical emission spectroscopy (OES) and mass spectrometry (MS) [76–83]. Here, as described in Sect. 1.1, the production and diffusion of hydrogen, CH_x radicals, and C_2H_y radicals are key processes, as shown in Fig. 1.1. Recently, the distributions of the radical, gas, and electron temperatures in plasmas have been simulated [84–94]. The simulation results provide some information on vapor-phase reactions in the CVD diamond process, but microscopic experimental results are still needed. Those radicals that arrive at diamond surfaces migrate and react with hydrogen, terminating the surface and/or carbon. It is extremely challenging to identify the involved processes because of the difficulty of conducting in situ characterizations in plasma environments. In this section, the author reviewed only those aspects of diamond surface chemistry that pertain to chemical reactions of hydrogen radicals and diamond precursors (CH_x and C_2H_y radicals).

1.2.1 Hydrogen

During diamond growth by PECVD, the diamond surfaces are continuously bombarded with hydrogen radicals. While under typical growth conditions, the hydrogen concentration is 95 % or higher (the hydrogen concentration is defined as the ratio of hydrogen flow rate to total gas flow rate). Consequently, most diamond surfaces are terminated by hydrogen and cannot react with diamond precursors. However, hydrogen radicals abstract the hydrogen from terminated diamond surfaces, C_d–H, to form an active site, C_d•:

$$\text{(hydrogen abstraction)} \qquad C_d - H + H \rightarrow C_{d\bullet} + H_2. \tag{1.5}$$

Then, the active site contributes to the diamond growth, but there is also a large possibility that, the active site again reacts with a hydrogen radical and is terminated again with hydrogen.

$$\text{(hydrogen adsorption)} \qquad C_{d\bullet} + H \rightarrow C_d - H. \tag{1.6}$$

During diamond growth by PECVD, the fraction of active sites is determined by the dynamic equilibrium between chemical reactions (1.5) and (1.6). The diamond surfaces after the hydrogen plasma treatment and diamond growth by PECVD are terminated by hydrogen, as shown in Fig. 1.2.

Hydrogen radicals also play a role in the growth of high-quality diamond films by removing nondiamond carbon. Diamond is etched by reactions with hydrogen radicals, although the etching rate is lower than that of nondiamond carbon. The diamond etching rates by hydrogen radicals depend on the structures on the diamond surface: monohydride (CH), dihydride (CH_2), and trihydride (CH_3). Chen et al. proposed that the diamond etching rates, R, by hydrogen radicals are $R_{monohydride} < R_{dihydride} < R_{trihydride}$ [95]. They also reported that {111}-oriented facets form on both single-crystal diamond {110} and {100} surfaces by anisotropic etching. Thus, diamond growth by PECVD is accompanied by the reactions of hydrogen abstraction (1.5) and adsorption (1.6) and by anisotropic etching on diamond surfaces, which limits chemisorption of diamond precursors and diamond nucleation.

1.2.2 Carbon

As described in Sect. 1.2.1, diamond surfaces are nearly fully terminated by hydrogen during diamond growth by PECVD. Chemisorption by diamond precursors occurs not at hydrogen-terminated sites but at active sites, which are hydrogen-abstracted sites:

$$\text{(CH_3 radical chemisorption)} \quad C_{d\bullet} + CH_3 \rightarrow C_d - CH_3. \tag{1.7}$$

The chemisorbed structure is a trihydride, which is readily etched by hydrogen radicals. Structures composed of monohydrides and/or dihydrides may need to nucleate on diamond surfaces during PECVD. Observation of the growth surface is crucial for elucidation of the growth mechanism because the growth process influences the structure of the growth surface. Scanning probe microscopy (SPM), low-energy electron diffraction (LEED), Fourier transform-infrared spectroscopy (FT-IR), and electron energy loss spectroscopy (EELS) provides physical and chemical information on surfaces at the atomic level, and are powerful tools for the study of diamond CVD growth. Results from such techniques reveal that as-grown diamond {100} and {111} surfaces have 2 × 1:H reconstructed structures with

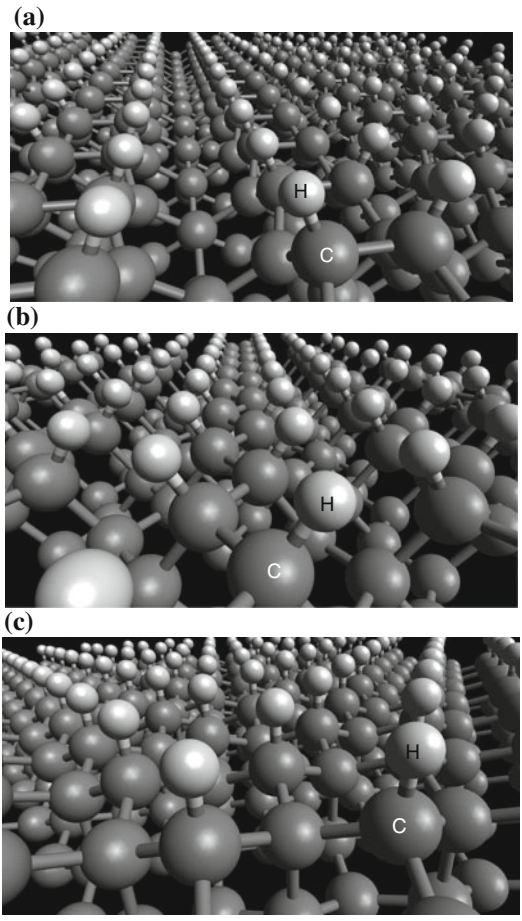

Fig. 1.2 Hydrogen-terminated diamond {100}, {110}, and {111} surfaces. **a** H-terminated diamond {100} surface. **b** H-terminated diamond {110} surface. **c** H-terminated diamond {111} surface

carbon dimer rows and 1 × 1:H structures, respectively [96–108]. Nevertheless, at present, the mechanism of diamond growth by PECVD is still not well-understood because of the difficulty of in situ observations.

1.3 Growth Modes

To realize diamond-based electronics, a growth technique is needed for producing device-grade diamond films. As described in Sect. 1.2, the growth mechanism of diamond films by PECVD remains poorly understood because of the difficulty of in situ characterization in plasma environments [109]. Additionally, the control of dynamic characterizations on well-defined surfaces, such as a scanning electron

or probe microscope-molecular beam epitaxy system used for Si [110], GaAs [111], and GaN [112], is needed to elucidate the growth mode of PECVD diamond films.

Figure 1.3 illustrates a simplified model for the determination of growth modes by an alternative to in situ characterizations [113, 114]. Figure 1.3 illustrates the surface steps present on an ideal surface of an as-received diamond substrate after the formation of a mesa structure due to a misoriented angle between the basal plane and polished surface. Then, homoepitaxial growth is carried out under a lateral growth mode without 2D nucleation on terraces, as described below. Each atomic step on the mesa surface grows laterally. Under ideal conditions in which 2D terrace nucleation is completely suppressed, there would be no further growth perpendicular to the basal plane. Finally, a step-free surface is formed over the mesa surface, leaving the basal plane surface. In 2D island growth, new steps are formed by nucleation on the terraces during lateral growth. Finally, a surface with single atomic steps and atomically flat terraces is formed on the mesa surface. The interval between the formed islands is wider than the terrace width estimated from the misoriented angle of the substrate. In 3D growth, the interval between the formed islands is narrower than the terrace width estimated from the misoriented angle. As a result, the surface is very rough. In addition, this mesa structure eliminates the influence of abnormal growth, such as spiral growth induced by screw dislocations from trench bottoms. Thus, diamond growth modes can be determined from ex situ surface observations of diamond films grown on mesa surfaces.

Figure 1.4 shows atomic force microscopy (AFM) images of diamond {111} mesa surfaces before and after homoepitaxial growth by PECVD. For diamond growth at low methane concentrations (0.005–0.025 % $CH_4/(H_2+CH_4)$ ratio), a step-free surface, that is, a perfectly flat surface without any atomic steps, was formed on the mesa. This result shows that the growth mode of the homoepitaxial diamond {111} films was an ideal lateral growth without 2D terrace nucleation. For diamond growth at middle methane concentrations (0.05–0.25 % $CH_4/(H_2+CH_4)$ ratio), equilateral-triangular islands and/or single bi-atomic layer step/terrace structures on atomically flat surfaces were formed on the mesa. This shows that the growth mode of the homoepitaxial diamond {111} films is 2D island growth with 2D terrace nucleation and lateral growth. Additionally, the formation of equilateral-triangular islands shows that the diamond growth had extremely high selectivity. For diamond growth at high methane concentrations (>0.25 % $CH_4/(H_2+CH_4)$ ratio), the film surface, whose RMS value was 0.84 nm, is much rougher than the initial surface before growth (RMS = 0.44 nm). This shows that the growth mode for the homoepitaxial diamond {111} films is 3D growth.

Variations in methane concentrations give rise to different fluxes of hydrocarbon precursors arriving at the surface. This is because growth rates increase with methane concentration. Since the substrates used for growth have the same misoriented angle, the concentrations of adatoms on terraces increase with higher methane concentrations. When the flux is low, adatoms on a terrace remain below the critical size for 2D terrace nucleation. Adatoms, which are adsorbed precursors on the diamond surface, arriving at steps crystallize, resulting in step-edge growth (no 2D terrace nucleation).

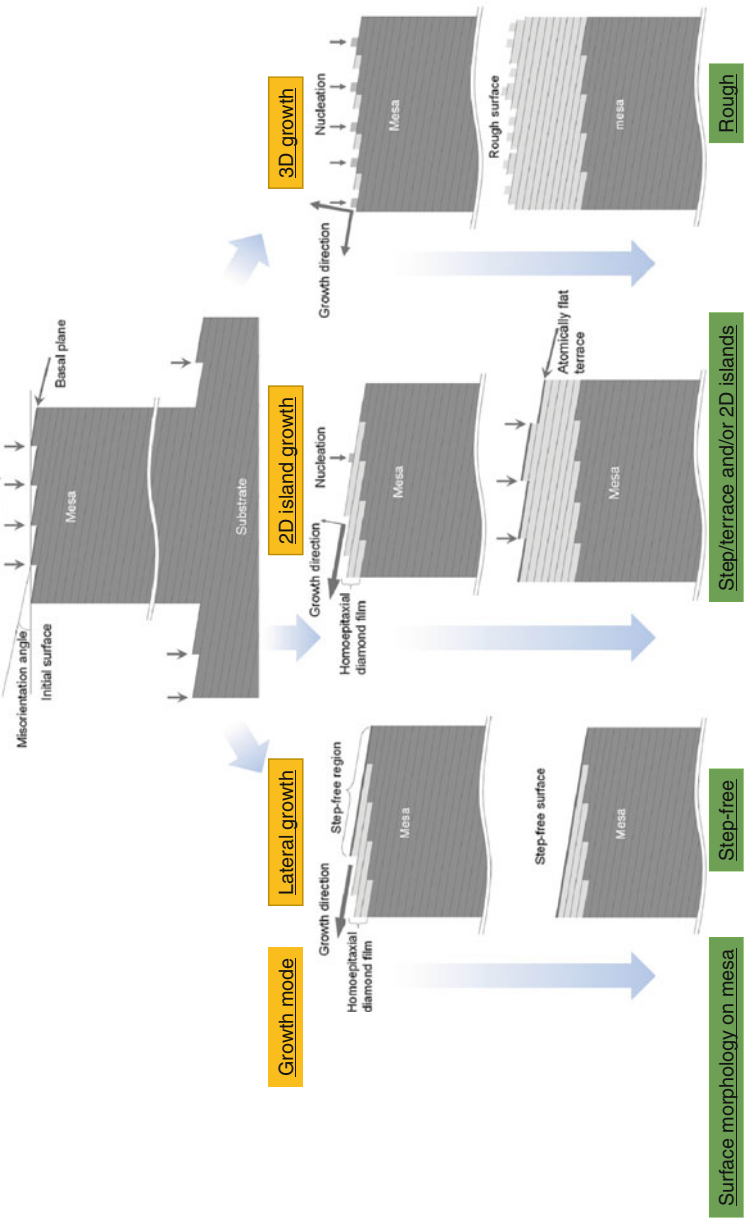

Fig. 1.3 Simplified models for the determination of growth modes by using mesa structures

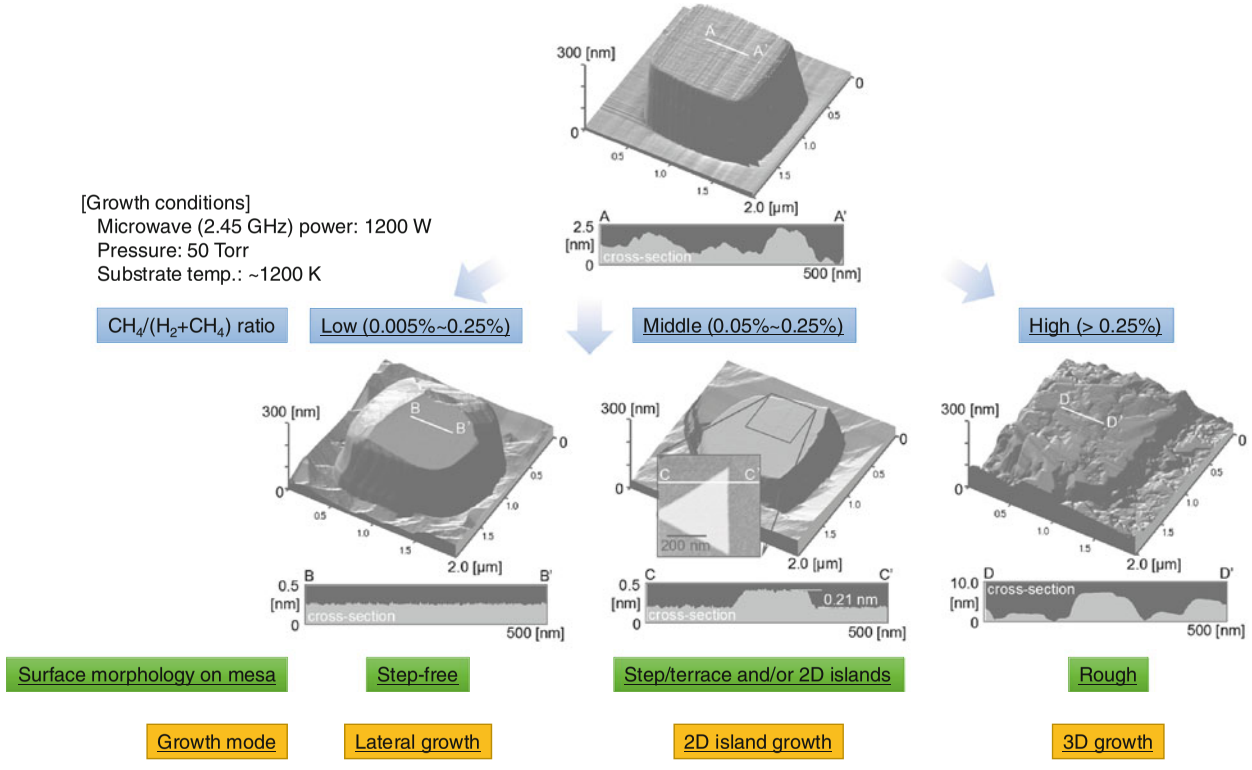

Fig. 1.4 AFM images of diamond {111} mesa surfaces before and after homoepitaxial growth by PECVD

In the middle methane concentration region, the adatom concentration increases and passes the critical value needed for 2D nucleation. Adatoms can cluster more easily on terraces because of their higher population. This causes 2D nucleation on terraces. As the methane concentration is increased further (into the high methane concentration region), adatoms form clusters as soon as they land on surfaces from the gas phase. This causes surface roughening because of 3D growth. This growth mechanism is a common process in thermal CVD and MBE. Despite the extremely short migration length, the common mechanism may also apply to PECVD diamond {111} growth because of the formation of atomically flat surfaces of diamond films.

1.4 Doping

For the realization of diamond-based electronic devices, doping acceptor and donor impurities into diamond is necessary to control the carrier type and concentration and to control the electrical resistivity of diamond semiconductors. Nitrogen is the most common impurity in diamond. Nitrogen is likely to form several types of complexes with vacancies. Recently, the nitrogen-vacancy (N–V) center in diamond has attracted much attention as a promising solid-state spin system for quantum information and sensing applications [71, 115–123]. However, as a donor, nitrogen in diamond has a high activation energy of 1.7 eV, which is higher than the bandgap of silicon (1.1 eV). The resistivity of nitrogen-doped diamond is extremely high at room temperature because of the extremely low concentration of thermally activated electrons. Generally, boron and phosphorus are used as *p*- and *n*-type dopants of diamond semiconductors, respectively. The activation energies of boron- and phosphorus-doped diamond are 0.37 and 0.57 eV, respectively, which are lower than that of nitrogen-doped diamond. However, compared with boron- and phosphorus-doped silicon, the resistivity of doped diamond is still too high, as shown in Fig. 1.5. Although other dopants with lower activation energies have been investigated, reproducibility has not yet been obtained.

Doping into diamond is carried out by HPHT, PECVD, and ion implantation [124–129]. Recently, Bormashov et al. reported that boron-doped {100} diamond without any extended defect. It was synthesized by HPHT and showed the high Hall hole mobility of 2,200 cm^2/V s at 300 K and 7,200 cm^2/V s at 180 K [130]. For device fabrication, doped diamond films are mostly grown on HPHT or CVD diamond substrates by PECVD because doping by PECVD provides both *p*- and *n*-type diamond with controlling concentrations of impurities. During homoepitaxial diamond growth by PECVD boron and phosphorus doping is carried out by introducing diborane (or trimethylboron) and phosphine (or tertiarybutylphosphine) gases, respectively. The highest Hall hole and electron mobility of PECVD diamond films are 1,860 cm^2/V s at 290 K [131] and 660 cm^2/V s at 300 K [34], respectively. Carrier mobility decreases with increasing boron or phosphorus concentrations in diamond films, reducing the resistivity of diamond. For $[B] < 10^{19}$ cm^{-3}, conduction

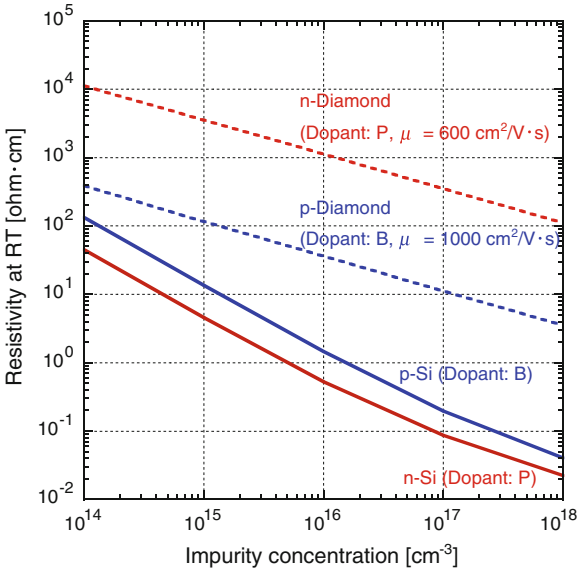

Fig. 1.5 Room-temperature resistivities of Si and diamond as functions of impurity concentration. The resistivities of *p*- and *n*-type diamond were calculated when the compensation ratio was zero and mobility was constant

is dominated by free holes in the valence band. At higher doping concentrations, variable-range hopping conduction appears, and then the metal-insulator transition and superconductivity arise around 3×10^{20} B atoms/cm^3 [132–138]. The resistivity of heavily boron-doped diamond {100} film with 3×10^{20} B atoms/cm^3 is 10 mΩ cm or less at room temperature [132, 139–141]. In contrast, the resistivity of heavily phosphorus-doped diamond {111} film with 10^{20} P atoms/cm^3 is around 70 Ω cm at room temperature [142]. These can lead to the fabrication of chemical/bio and electronic devices, such as Schottky barrier diodes, *pn*-junction diodes, Schottky *pn* diodes, JFETs, and bipolar transistors.

1.5 Growth of Atomically Flat Diamond

To realize electronic devices with proper performance characteristics, one of the most important issues is the roughness of surfaces and interfaces in semiconductor materials. Device applications of diamond semiconductors require sharp interfaces at diamond homo- and hetero-junctions. Generally, growth of *p*- and *n*-type diamond semiconductors for Schottky contacts and *pn* junctions, etc., is carried out by boron and phosphorus doping, respectively, during homoepitaxial diamond growth. However, growth hillocks, which are macroscopic defects, are often observed on as-grown diamond surfaces after homoepitaxial diamond growth by PECVD, as shown in Fig. 1.6. In most cases, even macroscopic flat surfaces excluding hillocks are not atomically flat, as shown in Fig. 1.7. Therefore, surface flattening of homoepitaxial diamond films is extremely important.

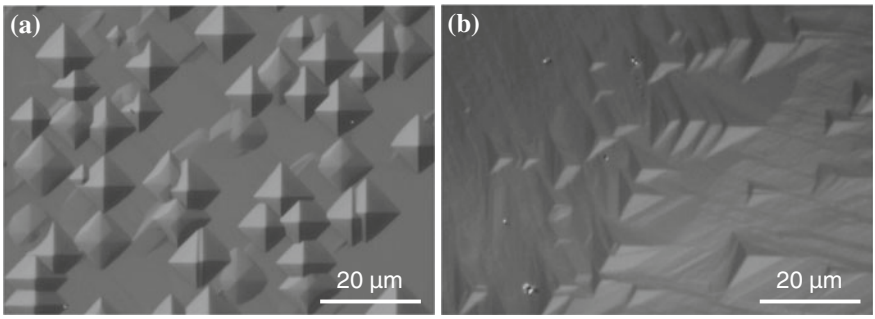

Fig. 1.6 OM images of hillocks formed on diamond surfaces after homoepitaxial growth by PECVD. **a** Quadrangular hillocks were observed on diamond {100} surfaces and **b** triangular hillocks on diamond {111} surfaces

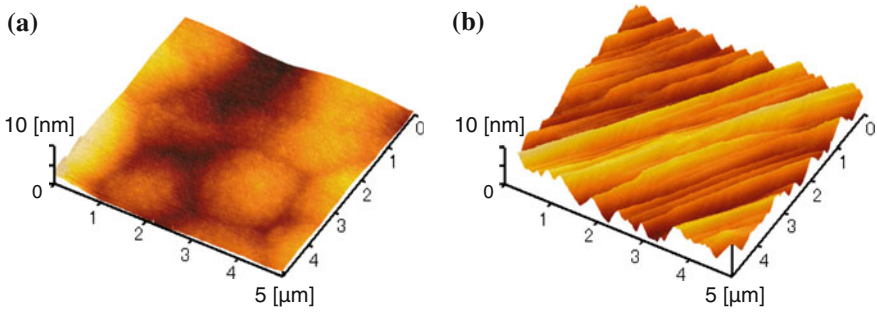

Fig. 1.7 3D AFM images of diamond surfaces, excluding hillocks, after homoepitaxial growth by PECVD. **a** The surface roughness (RMS) of the homoepitaxial diamond {100} film was 0.54 nm. **b** The surface roughness (RMS) of the homoepitaxial diamond {111} film was 1.68 nm

Surface flattening can be carried out by a polishing process. For example, defect-free Si wafers with surface flatness at the atomic level can be obtained by chemical–mechanical polishing. However, as-received diamond substrate surfaces are not atomically flat; instead, they have a roughness of several nanometers or more after mechanical polishing, as shown in Fig. 1.8. Compared with as-received Si wafer surfaces after chemical–mechanical polishing, as shown in Fig. 1.9, diamond surfaces are much rougher. Recently, a new technique for diamond surface polishing has been reported [143–145]. It is expected that surface roughness of diamond substrates will be reduced to that of Si wafers via some breakthrough diamond polishing technique. In this section, the author describe the growth of hillock-free, atomically step/terrace, and step-free diamond films.

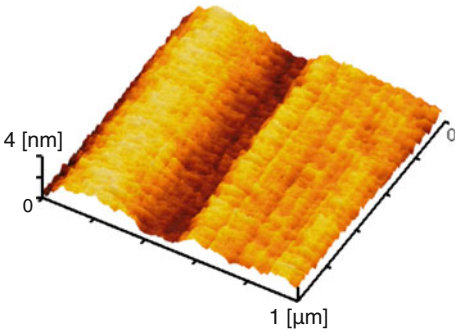

Fig. 1.8 3D AFM image of as-polished single-crystal diamond surface after acid treatment. The surface roughness (RMS) was 0.44 nm

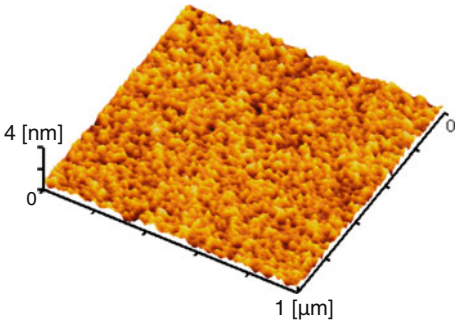

Fig. 1.9 3D AFM image of as-polished single-crystal Si surface after modified RCA cleaning. The surface roughness (RMS) was 0.16 nm

1.5.1 Hillock-Free Surfaces

Growth hillocks are often observed on homoepitaxial diamond {100} and {111} surfaces, as shown in Fig. 1.6. A growth hillock is formed by spiral growth centered on a screw dislocation core, as shown in Fig. 1.10 [114, 146], and the diamond surface is increasingly roughened by the growth of hillocks. The spiral growth rate at a screw dislocation is higher than the normal growth rate on the surface, excluding such crystal defects. Generally, growth hillocks make device fabrication difficult; hillocks are related to dielectric breakdown and current leakage in electronic devices such as *pn* junctions, Schottky contacts, and MIS structures. Therefore, it is extremely important to eliminate hillocks from epitaxial diamond films. The most effective method for achieving hillock-free diamond is to completely eliminate dislocations from single-crystal diamond. However, dislocation-free diamond substrates are very expensive compared to common single-crystal diamond substrates with dislocation densities of 10^4–10^5 cm^{-2}. Alternatively, it is

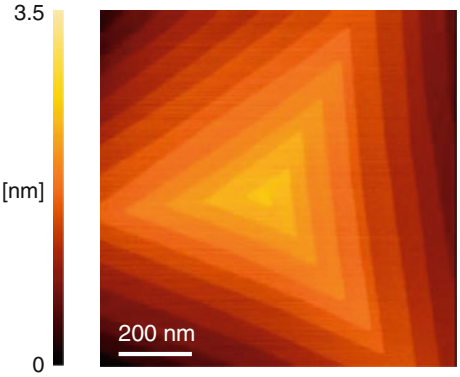

Fig. 1.10 AFM image of spirally grown diamond {111} film due to screw dislocation. Each step height was approximately 0.21 nm, which is consistent with the single BL step height of {111} diamond

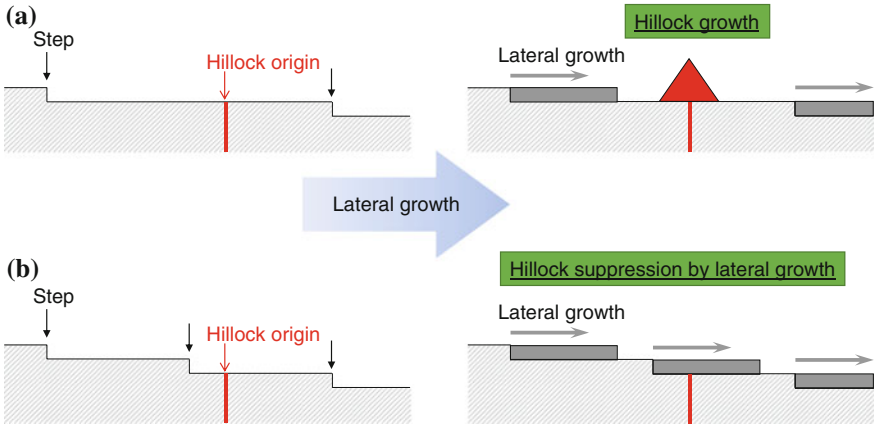

Fig. 1.11 Simplified models of hillock growth and suppression on samples having (**a**) low and (**b**) high misorientation angles θ by lateral growth

possible to eliminate hillocks by homoepitaxial lateral growth on highly misoriented diamond substrates. Figure 1.11 shows a simple model for suppressing the growth of hillocks [141]. The mechanism of hillock formation during diamond growth is considered to be as follows. The origins of hillocks have a growth rate higher than those of other areas. A local increase in growth rate due to the defects observed by transmission electron microscopy, which are dislocations [147] and twinning structures [148], has been reported. Hence, growth at the origins of hillocks could be suppressed when the growth rate of a normal epitaxial area exceeds that of hillocks, indicating an enhancement of lateral growth.

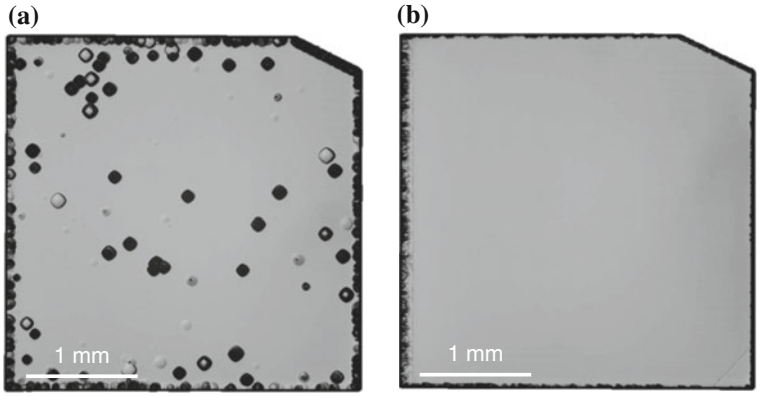

Fig. 1.12 OM images of homoepitaxial diamond film surfaces on single-crystal diamond {100} substrates with (**a**) low and (**b**) high misorientation angles, θ. The low and high values of θ were 0.2 and 2.2, respectively. The homoepitaxial diamond films were grown under the same conditions (1,200 W, 50 Torr, 0.6 % $CH_4/(H_2+CH_4)$ ratio, 1.6 % B/C ratio, 70 h) [141]

Figure 1.12 shows the optical microscopy (OM) images of homoepitaxial diamond films grown on diamond {001} substrates with (a) $\theta = 0.2°$ and (b) $\theta = 2.2°$. Hillocks were observed to spread over the entire surface of the low-θ sample, as shown in Fig. 1.12a. The density and size of the hillocks were 2×10^3 cm^{-2} and below 200 μm, respectively. The Hillock size increases with film thickness, and thus, the film surface becomes rough macroscopically. This roughening is a fatal issue for the additional growth of homoepitaxial diamond films intended for device fabrication. However, suppression of hillock growth can be achieved by increasing θ to above 2° [141]. The OM image of the high-θ sample is shown in Fig. 1.12b. Judging from this image, a hillock-free diamond film with a macroscopically flat surface was obtained over the entire surface by homoepitaxial lateral growth on highly misoriented substrates.

1.5.2 Step/Terrace Structures

As described in Sect. 1.5.1, it is possible to obtain a hillock-free diamond film with a macroscopically flat surface by homoepitaxial lateral growth on a highly misoriented substrate. In most cases, the homoepitaxial lateral growth of diamond films accompanies 2D terrace nucleation. Therefore, macroscopically flat diamond surfaces, excluding hillocks, after homoepitaxial growth are not atomically flat but roughened because of 2D terrace nucleation, as shown in Fig. 1.7. Therefore, it is necessary to suppress 2D terrace nucleation during homoepitaxial growth by PECVD.

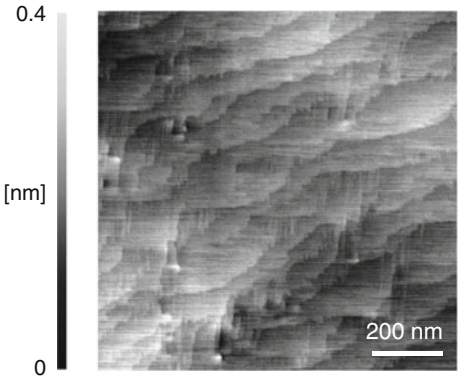

Fig. 1.13 AFM image of atomically flat diamond {100} surfaces after homoepitaxial lateral growth at a low methane concentration (0.05 %)

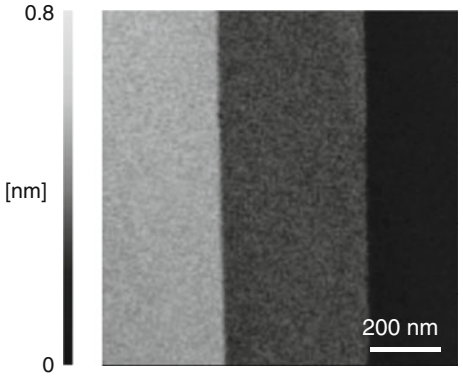

Fig. 1.14 AFM image of atomically flat diamond {111} surfaces after homoepitaxial lateral growth at a low methane concentration (0.05 %)

Watanabe et al. successfully formed an atomically flat diamond {100} film over the entire substrate by homoepitaxial lateral growth at extremely low CH_4/H_2 ratios [149]. Figure 1.13 shows an AFM image of an atomically flat diamond {100} surface by such a growth. The step heights were approximately 0.1 nm, which is consistent with the single atomic step of {100} diamond (0.089 nm), or 0.2 nm, which is consistent with the bi-atomic step of {100} diamond (2×0.089 nm). The average interval between steps (66 nm) is consistent with the estimated terrace width from the misorientation angle of the diamond {100} substrate (65 nm).

Atomically flat diamond {111} surfaces were also formed by homoepitaxial lateral growth, as shown in Fig. 1.14. The step height was approximately 0.2 nm, which is consistent with the single atomic step of {111} diamond (0.206 nm). The atomically flat diamond {111} surfaces with step/terrace structures were selectively formed by lateral growth on a diamond {111} substrate with mesa structures [150, 151].

1.5.3 Atomically Step-Free Surfaces

Much effort has been expended on flattening the surfaces of Si, GaAs, SiC, and GaN at the atomic level; those efforts have led to the achievement of perfectly flat surfaces without any atomic steps (atomically *step-free* surfaces) through step-flow growth without 2D nucleation on terraces [152–156]. The aluminum nitride (AlN)/diamond heterostructure is expected to combine the features of both wide-bandgap materials, thereby providing a new scheme for both nitride and diamond devices because they have opposite tendencies in doping characteristics [157–161]. Hirama et al. reported that single-crystal AlN {0001} growth on a diamond {111} surface was achieved [160], but the AlN layer on a diamond {100} surface had a multidomain structure consisting of tilted and rotated domains [162]. To realize useful devices, high-quality AlN films on {111} diamond and sharp AlN/diamond {111} interfaces are essential. For GaN/SiC heterostructures, previous studies have revealed that surface steps promote extended crystal defects in heteroepitaxial films grown on SiC [163–165]. Bassim et al. reported that very low dislocation densities were achieved in GaN films on step-free SiC mesa surfaces [166], and ultraviolet luminescence of GaN *pn*-junction diodes fabricated on the step-free SiC {0001} surfaces was improved relative to that on atomically flat SiC surfaces with atomic steps [167]. Thus, the formation of step-free diamond surfaces is a promising technique for improving the performance of devices that use diamond heterostructures.

Two methods for the formation of *step-free* surfaces have been proposed, as shown in Fig. 1.15. Both methods utilize an ideal lateral growth mode without 2D terrace nucleation. In method I, a mask, which is not etched and on which no nucleation occurs in the growth environment, is used for selective growth. Method II,

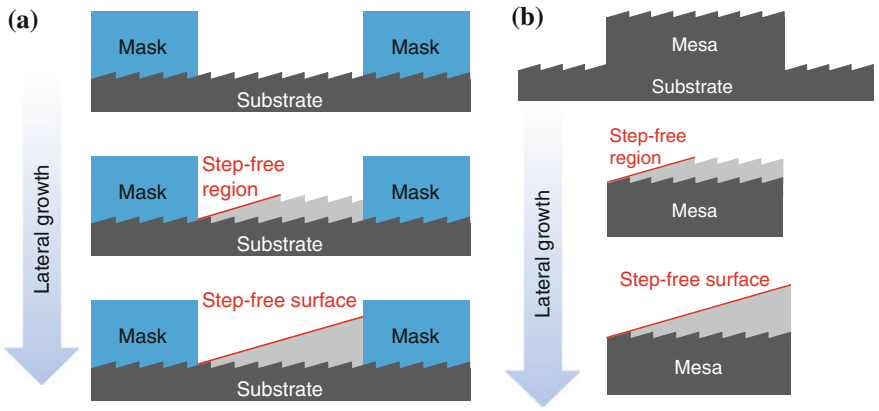

Fig. 1.15 Simplified models of step-free surface growth using **a** mask and **b** maskless processes. The step-free surfaces of GaAs and GaN were grown using the mask process, while Si, SiC, and diamond were grown using the maskless process

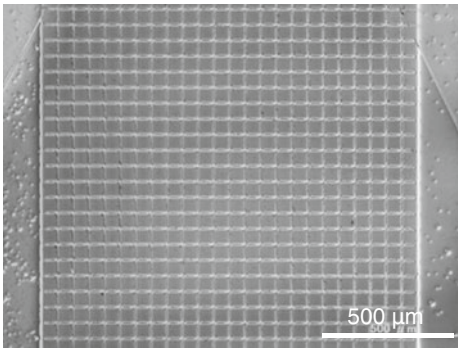

Fig. 1.16 OM image of single-crystal diamond substrates with 50 × 50 μm^2 mesas

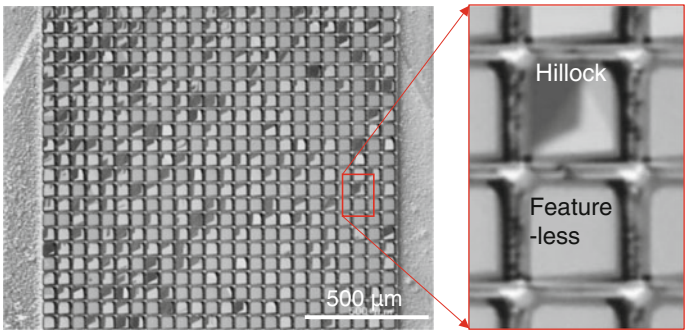

Fig. 1.17 OM image of diamond {111} films on single-crystal diamond substrates with 50 × 50 μm^2 mesas after homoepitaxial lateral growth

in which a mesa structure is used, is a maskless process. Method II should be utilized for diamond growth by PECVD because, in plasma environments, most materials do not meet the conditions necessary for the mask. Figure 1.16 shows an OM image of a {111} diamond substrate surface after mesa fabrication. The array formation of 50 × 50 μm^2 mesas on single-crystal diamond substrates was carried out through a conventional lithographic technique. Figure 1.17 shows an OM image of a diamond {111} surface after homoepitaxial lateral growth by MPCVD. The mesas exhibit one of the following two characteristics in the OM observations shown in Fig. 1.17: (1) the surface was featureless; or (2) the surface contained at least one hillock, which grew spirally on the substrate, as shown in Fig. 1.10. The hillock was induced by a screw dislocation, as shown in Fig. 1.18 [114, 146]. The featureless mesa surface is an atomically step-free surface, as shown in Fig. 1.19a. Additionally, the diamond {111} films with step-free surfaces contained no dislocations, as shown in Fig. 1.20. Recently, the growth of a 100 × 100 μm^2 step-free diamond {111} surface has been

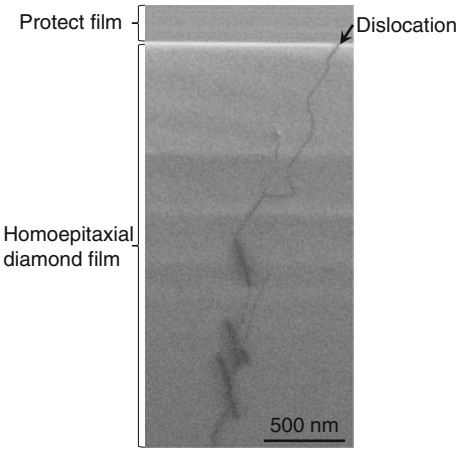

Fig. 1.18 Cross-sectional transmission electron microscope (XTEM) image of homoepitaxial diamond {111} film obtained from the mesa with hillock

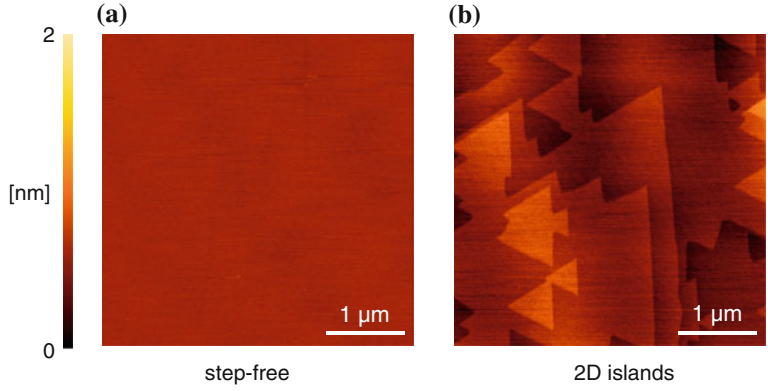

Fig. 1.19 AFM images of **a** atomically step-free diamond {111} surface and **b** atomically flat diamond {111} surface with 2D islands. The 2D islands were composed of atomically flat surfaces and a single BL step

reported [113, 114]. This indicates the possibility of forming a step-free diamond surface over a substrate if the substrate contains no dislocation. The author is also sure that this growth technique will be a key to realize high-quality diamond wafers which will allow manufacturing high quality interfaces and devices, e.g. high power devices, deep ultra-violet light-emitting diodes, bio/chemical sensors, quantum devices, etc.

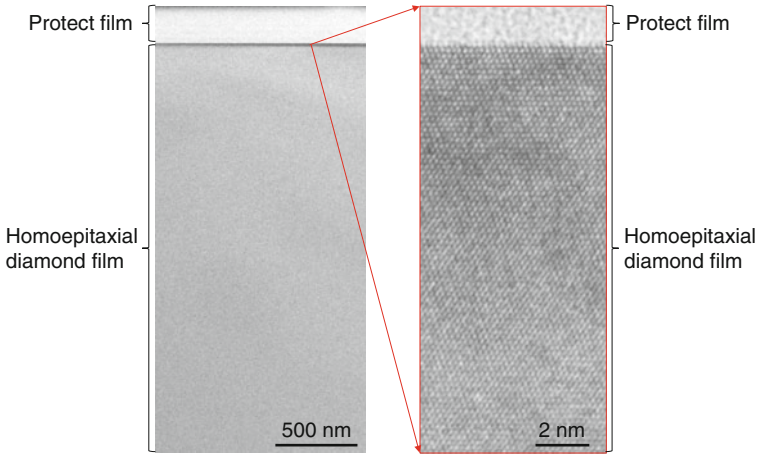

Fig. 1.20 XTEM images of homoepitaxial diamond {111} film obtained from featureless mesas

1.6 Conclusions

In this paper, the mechanism and control of homoepitaxial diamond growth by PECVD was reviewed. Recently, homoepitaxial diamond films have been used to fabricate many diamond devices. Judging from the reported performance of such devices, the technology of homoepitaxial diamond growth seems to have reached a certain level. However, because of the difficulty of in situ characterization in plasma environments, the growth mechanism remains unclear at present, especially regarding formation of precursors and their surface reactions. In the future, further developments of epitaxial diamond growth technology, including impurity doping and defect control, will be necessary to realize diamond-based electronics.

Acknowledgments The author sincerely thanks Prof. Satoshi Yamasaki, Dr. Hideyo Okushi, Dr. Daisuke Takeuchi, Dr. Masahiko Ogura, Dr. Toshiharu Makino, Dr. Hiromitsu Kato, Dr. Hitoshi Umezawa, Dr. Takehide Miyazaki of the National Institute of Advanced Industrial Science and Technology; Dr. Sung-Gi Ri of the National Institute for Materials Science; and Professor Takao Inokuma of Kanazawa University for fruitful discussions. This study was partly supported by a Grant-in-Aid for Young Scientists (A) (No. 24686074) from the Japan Society for the Promotion of Science, and Adaptable and Seamless Technology Transfer Program (A-STEP) and Core Research for Evolutional Science and Technology (CREST) from the Japan Science and Technology Agency.

References

1. B.V. Spitsyn, L.L. Bouilov, B.V. Derjaguin, Vapor growth of diamond on diamond and other surfaces. J. Cryst. Growth **52**(Part 1), 219–226 (1981). doi:10.1016/0022-0248(81)90197-4
2. S. Matsumoto, Y. Sato, M. Kamo, N. Setaka, Vapor deposition of diamond particles from methane. Jpn. J. Appl. Phys. **21**(4, Part 2), L183–L185 (1982). doi:10.1143/JJAP.21.L183

3. M. Kamo, Y. Sato, S. Matsumoto, N. Setaka, Diamond synthesis from gas phase in microwave plasma. J. Cryst. Growth **62**(3), 642–644 (1983). doi:10.1016/0022-0248(83)90411-6
4. M. Kamo, H. Yurimoto, Epitaxial growth of diamond on diamond substrate by plasma assisted CVD. Appl. Surf. Sci. **33–34**, 553–560 (1988). doi:10.1016/0169-4332(88)90352-2
5. D.G. Goodwin, J.E. Butler, in *Handbook of Industrial Diamond and Diamond Films*, ed. by M.A. Prelas, G. Popovici, L.K. Biglow (Marcel Dekker, Inc., NY, 1997), p. 527
6. T. Teraji, in *Physics and Applications of CVD Diamond,* ed. by S. Koizumi, C.E. Nebel, M. Nesladek (Wiley-VCH Verlag GmbH & Co. KGaA, Weinheim, 2008), p. 29
7. J.E. Butler, A. Cheesman, M.N.R. Ashfold, in *CVD Diamond for Electronic Devices and Sensors,* ed. by R.S. Sussmann (Wiley, UK, 2009), p. 103
8. J.E. Butler, Y.A. Mankelevich, A. Cheesman, J. Ma, M.N.R. Ashfold, Understanding the chemical vapor deposition of diamond: recent progress. J. Phys.: Cond. Mat. **21**(5), 364201 (2009). doi:10.1002/pssa.200777501
9. O.A. Williams, R.B. Jackman, High growth rate MWPECVD of single crystal diamond. Diam. Relat. Mater. **13**(4–8), 557–560 (2004). doi:10.1016/j.diamond.2004.01.023
10. J. Achard, F. Silva, O. Brinza, A. Tallaire, A. Gicquel, Coupled effect of nitrogen addition and surface temperature on the morphology and the kinetics of thick CVD diamond single crystals. Diam. Relat. Mater. **16**(4–7), 685–689 (2007). doi:10.1016/j.diamond.2006.09.012
11. H. Yamada, A. Chayahara, Y. Mokuno, S. Shikata, Numerical and experimental studies of high growth-rate over area with 1-inch in diameter under moderate input-power by using MWPCVD. Diam. Relat. Mater. **17**(7–10), 1062 (2008). doi:10.1016/j.diamond.2008.01.045
12. Q. Liang, C.Y. Chin, J. Lai, C. Yan, Y. Meng, H. Mao, R.J. Hemley, Enhanced growth of high quality single crystal diamond by microwave plasma assisted chemical vapor deposition at high gas pressures. Appl. Phys. Lett. **94**(2), 024103 (2009). doi:10.1063/1.3072352
13. Y. Gu, J. Lu, T. Grotjohn, T. Schuelke, J. Asmussen, Microwave plasma reactor design for high pressure and high power density diamond synthesis. Diam. Relat. Mater. **24**, 210–214 (2012). doi:10.1016/j.diamond.2012.01.026
14. Y. Su, H.D. Li, S.H. Cheng, Q. Zhang, Q.L. Wang, X.Y. Lv, G.T. Zou, X.Q. Pei, J.G. Xie, Effect of N_2O on high-rate homoepitaxial growth of CVD single crystal diamonds. J. Cryst. Growth **351**(1), 51–55 (2012). doi:10.1016/j.jcrysgro.2012.03.041
15. J. Lu, Y. Gu, T.A. Grotjohn, T. Schuelke, J. Asmussen, Experimentally defining the safe and efficient, high pressure microwave plasma assisted CVD operating regime for single crystal diamond synthesis. Diam. Relat. Mater. **37**, 17–28 (2013). doi:10.1016/j.diamond.2013.04.007
16. N. Fujimori, T. Imai, A. Doi, Characterization of conducting diamond films. Vacuum **36** (1–3), 99–102 (1986). doi:10.1016/0042-207X(86)90279-4
17. N. Fujimori, H. Nakahata, T. Imai, Properties of boron-doped epitaxial diamond films. Jpn. J. Appl. Phys. **29**(5, Part 1), 824–827 (1990). doi:10.1143/JJAP.29.824
18. S. Yamanaka, D. Takeuchi, H. Watanabe, H. Okushi, K. Kajimura, Low-compensated boron-doped homoepitaxial diamond films using trimethylboron. Phys. Stat. Sol. A **174**(1), 59–64 (1999). doi:10.1002/(SICI)1521-396X(199907)174:1<59::AID-PSSA59>3.0.CO;2-A
19. T. Tsubota, T. Fukui, M. Kameta, T. Saito, K. Kusakabe, S. Morooka, H. Maeda, Effect of total reaction pressure on electrical properties of boron doped homoepitaxial (100) diamond films formed by microwave plasma-assisted chemical vapor deposition using trimethylboron. Diam. Relat. Mater. **8**(6), 1079–1082 (1999). doi:10.1016/S0925-9635(99)00096-5
20. S. Ri, H. Kato, M. Ogura, H. Watanabe, T. Makino, S. Yamasaki, H. Okushi, Electrical and optical characterization of boron-doped (111) homoepitaxial diamond films. Diam. Relat. Mater. **14**(11–12), 1964–1968 (2005). doi:10.1016/j.diamond.2005.06.032
21. C. Baron, M. Wade, A. Deneuville, F. Jomard, J. Chevallier, Cathodoluminescence of highly and heavily boron doped (100) homoepitaxial diamond films. Diam. Relat. Mater. **15**(4–8), 597–601 (2006). doi:10.1016/j.diamond.2006.01.015
22. T. Teraji, H. Wada, M. Yamamoto, K. Arima, T. Ito, Highly efficient doping of boron into high-quality homoepitaxial diamond films. Diam. Relat. Mater. **15**(4–8), 602–606 (2006). doi:10.1016/j.diamond.2006.01.011

23. T. Teraji, Chemical vapor deposition of homoepitaxial diamond films. Phys. Stat. Sol. A **203** (13), 3324–3357 (2006). doi:10.1002/pssa.200671408
24. V. Mortet, M. Daenen, T. Teraji, A. Lazea, V. Vorlicek, J. D'Haen, K. Haenen, M. D'Olieslaeger, Characterization of boron doped diamond epilayers grown in a NIRIM type reactor. Diam. Relat. Mater. **17**(7–10), 1330–1334 (2008). doi:10.1016/j.diamond.2008.01.087
25. J. Barjon, N. Habka, C. Mer, F. Jormard, J. Chevallier, P. Bergonzo, Resistivity of boron doped diamond. Phys. Stat. Sol. RRL **3**(6), 202–204 (2009). doi:10.1002/pssr.200903097
26. J. Pernot, P.N. Volpe, F. Omnès, P. Muret, Hall hole mobility in boron-doped homoepitaxial diamond. Phys. Rev. B **81**(20), 205203 (2010). doi:10.1103/PhysRevB.81.205203
27. F. Omnès, P. Muret, P.N. Volpe, M. Wade, J. Pernot, F. Jomard, Study of boron doping in MPCVD grown homoepitaxial diamond layers based on cathodoluminescence spectroscopy, secondary ion mass spectroscopy and capacitance–voltage measurements. Diam. Relat. Mater. **20**(7), 912–916 (2011). doi:10.1016/j.diamond.2011.05.010
28. M. Ogura, H. Kato, T. Makino, H. Okushi, S. Yamasaki, Misorientation-angle dependence of boron incorporation into (0 0 1)-oriented chemical-vapor-deposited (CVD) diamond. J. Cryst. Growth **317**(1), 60–63 (2011). doi:10.1016/j.jcrysgro.2011.01.010
29. M.E. Belousov, Y.A. Mankelevich, P.V. Minakov, A.T. Rakhimov, N.V. Suetin, R.A. Khmelnitskiy, A.A. Tal, A.V. Khomich, Boron-doped homoepitaxial diamond CVD from microwave plasma-activated ethanol/trimethyl borate/hydrogen mixtures. Chem. Vap. Depos. **18**(10–12), 302–306 (2012). doi:10.1002/cvde.201206993
30. J. Achard, R. Issaoui, A. Tallaire, F. Silva, J. Barjon, F. Jomard, A. Gicquel, Freestanding CVD boron doped diamond single crystals: a substrate for vertical power electronic devices? Phys. Stat. Sol. A **209**(9), 1651–1658 (2012). doi:10.1002/pssa.201200045
31. A. Lazea, Y. Garino, T. Teraji, S. Koizumi, High quality p-type chemical vapor deposited {111}-oriented diamonds: growth and fabrication of related electrical devices. Phys. Stat. Sol. A **209**(10), 1978–1981 (2012). doi:10.1002/pssa.201228162
32. S. Koizumi, M. Kamo, Y. Sato, H. Ozaki, T. Inuzuka, Growth and characterization of phosphorous doped {111} homoepitaxial diamond thin films. Appl. Phys. Lett. **71**(8), 1065–1067 (1997). doi:10.1063/1.119729
33. S. Koizumi, T. Teraji, H. Kanda, Phosphorus-doped chemical vapor deposition of diamond. Diam. Relat. Mater. **9**(3–6), 935–940 (2000). doi:10.1016/S0925-9635(00)00217-X
34. M. Katagiri, J. Isoya, S. Koizumi, H. Kanda, Lightly phosphorus-doped homoepitaxial diamond films grown by chemical vapor deposition. Appl. Phys. Lett. **85**(26), 6365–6367 (2004). doi:10.1063/1.1840119
35. M. Suzuki, H. Yoshida, N. Sakuma, T. Ono, T. Sakai, S. Koizumi, Electrical characterization of phosphorus-doped n-type homoepitaxial diamond layers by Schottky barrier diodes. Appl. Phys. Lett. **84**(13), 2349–2351 (2004). doi:10.1063/1.1695206
36. M. Suzuki, S. Koizumi, M. Katagiri, H. Yoshida, N. Sakuma, T. Ono, T. Sakai, Electrical characterization of phosphorus-doped n-type homoepitaxial diamond layers. Diam. Relat. Mater. **13**(11–12), 2037–2040 (2004). doi:10.1016/j.diamond.2004.06.022
37. H. Kato, S. Yamasaki, H. Okushi, n-Type doping of (001)-oriented single-crystalline diamond by phosphorus. Appl. Phys. Lett. **86**(22), 222111 (2005). doi:10.1063/1.1944228
38. S. Koizumi, M. Suzuki, n-Type doping of diamond. Phys. Stat. Sol. A **203**(13), 3358–3366 (2006). doi:10.1002/pssa.200671407
39. H. Kato, T. Makino, S. Yamasaki, H. Okushi, n-Type diamond growth by phosphorus doping on (001)-oriented surface. J. Phys. D Appl. Phys. **40**(20), 6189–6200 (2007). doi:10.1088/0022-3727/40/20/s05
40. J. Perot, S. Koizumi, Electron mobility in phosphorous doped {111} homoepitaxial diamond. Appl. Phys. Lett. **93**(5), 052105 (2008). doi:10.1063/1.2969066
41. H. Kato, D. Takeuchi, N. Tokuda, H. Umezawa, S. Yamasaki, H. Okushi, Electrical activity of doped phosphorus atoms in (001) n-type diamond. Phys. Stat. Sol. A **205**(9), 2195–2199 (2008). doi:10.1002/pssa.200879722

42. M.-A. Pinault-Thaury, B. Berini, I. Sternger, E. Chikoidze, A. Lusson, F. Jomard, J. Chevallier, J. Barjon, High fraction of substitutional phosphorus in a (100) diamond epilayer with low surface roughness. Appl. Phys. Lett. **100**(19), 192109 (2012). doi:10.1063/1.4712617
43. S. Koizumi, K. Watanabe, M. Hasegawa, H. Kanda, Ultraviolet emission from a diamond pn junction. Science **292**(5523), 1899–1901 (2001). doi:10.1126/science.1060258
44. H. Okushi, High quality homoepitaxial CVD diamond for electronic devices. Diam. Relat. Mater. **10**(3–7), 281–288 (2001). doi:10.1016/S0925-9635(00)00399-X
45. T. Makino, N. Tokuda, H. Kato, M. Ogura, H. Watanabe, S. Ri, S. Yamasaki, H. Okushi, High-efficiency excitonic emission with deep-ultraviolet light from (001)-oriented diamond p-i-n junction. Jpn. J. Appl. Phys. **45**(37–41, Part 2), L1042–L1044 (2006). doi:10.1143/jjap.45.l1042
46. D. Shin, N. Tokuda, B. Rezek, C.E. Nebel, Periodically arranged benzene-linker molecules on boron-doped single-crystalline diamond films for DNA sensing. Electrochem. Commun. **8**(5), 844–850 (2006). doi:10.1016/j.elecom.2006.03.014
47. D. Shin, B. Rezek, N. Tokuda, D. Takeuchi, H. Watanabe, T. Nakamura, T. Yamamoto, C.E. Nebel, Photo- and electrochemical bonding of DNA to single crystalline CVD diamond. Phys. Stat. Sol. A **203**(13), 3245–3272 (2006). doi:10.1002/pssa.200671402
48. H. Umezawa, N. Tokuda, M. Ogura, S. Ri, S. Shikata, Characterization of leakage current on diamond Schottky barrier diodes using thermionic-field emission modeling. Diam. Relat. Mater. **15**(11–12), 1949–1953 (2006). doi:10.1016/j.diamond.2006.08.030
49. K.-S. Song, T. Hiraki, H. Umezawa, H. Kawarada, Miniaturized diamond field-effect transistors for application in biosensors in electrolyte solution. Appl. Phys. Lett. **90**(6), 063901 (2007). doi:10.1063/1.2454390
50. E. Kohn, A. Denisenko, Concepts for diamond electronics. Thin Solid Films **515**(10), 4333–4339 (2007). doi:10.1016/j.tsf.2006.07.179
51. M. Liao, Y. Koide, J. Alvarez, Single Schottky-barrier photodiode with interdigitated-finger geometry: application to diamond. Appl. Phys. Lett. **90**(12), 123507 (2007). doi:10.1063/1.2715440
52. T. Makino, N. Tokuda, H. Kato, M. Ogura, H. Watanabe, S. Ri, S. Yamasaki, H. Okushi, Electrical and light-emitting properties of (001)-oriented homoepitaxial diamond p–i–n junction. Diam. Relat. Mater. **16**(4–7), 1025–1028 (2007). doi:10.1016/j.diamond.2007.01.024
53. C.E. Nebel, D. Shin, B. Rezek, N. Tokuda, H. Uetsuka, H. Watanabe, Diamond and biology. J. R. Soc. Interface **4**(14), 439–461 (2007). doi:10.1098/rsif.2006.0196
54. H. Umezawa, T. Saito, N. Tokuda, M. Ogura, S. Ri, H. Yoshikawa, S. Shikata, Leakage current analysis of diamond Schottky barrier diode. Appl. Phys. Lett. **90**(7), 073506 (2007). doi:10.1063/1.2643374
55. T. Makino, N. Tokuda, H. Kato, S. Kanno, S. Yamasaki, H. Okushi, Electrical and light-emitting properties of homoepitaxial diamond p-i-n junction. Phys. Stat. Sol. A **205**(9), 2200–2206 (2008). doi:10.1002/pssa.200879717
56. T. Makino, S. Tanimoto, Y. Hayashi, H. Kato, N. Tokuda, M. Ogura, D. Takeuchi, K. Oyama, H. Ohashi, H. Okushi, S. Yamasaki, Diamond Schottky-pn diode with high forward current density and fast switching operation. Appl. Phys. Lett. **94**(26), 262101 (2009). doi:10.1063/1.3159837
57. T. Makino, S. Ri, N. Tokuda, H. Kato, S. Yamasaki, H. Okushi, Electrical and light-emitting properties from (111)-oriented homoepitaxial diamond p–i–n junctions. Diam. Relat. Mater. **18**(5–8), 764–767 (2009). doi:10.1016/j.diamond.2009.01.016
58. K. Oyama, S. Ri, H. Kato, M. Ogura, T. Makino, D. Takeuchi, N. Tokuda, H. Okushi, S. Yamasaki, High performance of diamond p[sup +]-i-n[sup +] junction diode fabricated using heavily doped p+ and n+ layers. Appl. Phys. Lett. **94**(15), 152109 (2009). doi:10.1063/1.3120560
59. P.-N. Volpe, P. Muret, J. Pernot, F. Omnès, T. Teraji, Y. Koide, F. Jomard, D. Planson, P. Brosselard, N. Dheilly, B. Vergne, S. Scharnholz, Extreme dielectric strength in boron doped homoepitaxial diamond. Appl. Phys. Lett. **97**(22), 223501 (2010). doi:10.1063/1.3520140

60. R. Hoffmann, A. Kriele, H. Obloh, N. Tokuda, W. Smirnov, N. Yang, C.E. Nebel, The creation of a biomimetic interface between boron-doped diamond and immobilized proteins. Biomaterials **32**(30), 7325–7332 (2011). doi:10.1016/j.biomaterials.2011.06.052
61. T. Kawae, Y. Hori, T. Nakajima, H. Kawasaki, N. Tokuda, S. Okamura, Y. Takano, A. Morimoto, Structure and electrical properties of (Pr, Mn)-codoped $BiFeO_3$/B-doped diamond layered structure. Electrochem. Solid-State Lett. **14**(6), G31–G34 (2011). doi:10.1149/1.3568838
62. H. Kawarada, A.R. Ruslinda, Diamond electrolyte solution gate FETs for DNA and protein sensors using DNA/RNA aptamers. Phys. Stat. Sol. A **208**(9), 2005–2016 (2011). doi:10.1002/pssa.201100503
63. R. Hoffmann, H. Obloh, N. Tokuda, N. Yang, C.E. Nebel, Fractional surface termination of diamond by electrochemical oxidation. Langmuir **28**(1), 47–50 (2012). doi:10.1021/la2039366
64. T. Iwasaki, Y. Hoshino, K. Tsuzuki, H. Kato, T. Makino, M. Ogura, D. Takeuchi, T. Matsumoto, H. Okushi, S. Yamasaki, M. Hatano, Diamond junction field-effect transistors with selectively grown n+-side gates. Appl. Phys. Express **5**(9), 091301 (2012). doi:10.1143/apex.5.091301
65. H. Kato, K. Oyama, T. Makino, M. Ogura, D. Takeuchi, S. Yamasaki, Diamond bipolar junction transistor device with phosphorus-doped diamond base layer. Diam. Relat. Mater. **27–28**, 19–22 (2012). doi:10.1016/j.diamond.2012.05.004
66. T. Kawae, H. Kawasaki, T. Nakajima, N. Tokuda, S. Okamura, A. Morimoto, Y. Takano, A. Morimoto, Y. Takano, Fabrication of (Bi,Pr)(Fe,Mn)O3 thin films on polycrystalline diamond substrates by chemical solution deposition and their properties. Jpn. J. Appl. Phys. **51**(9 S1), 09LA08 (2012). doi:10.1143/jjap.51.09la08
67. R. Edgington, A.R. Ruslinda, S. Sato, Y. Ishiyama, K. Tsuge, T. Ono, H. Kawarada, R.B. Jackman, Boron delta-doped (111) diamond solution gate field effect transistors. Biosens. Bioelectron. **33**(1), 152–157 (2012). doi:10.1016/j.bios.2011.12.044
68. H. Kawarada, High-current metal oxide semiconductor field-effect transistors on H-terminated diamond surfaces and their high-frequency operation. Jpn. J. Appl. Phys. **51**(9R), 090111 (2012). doi:10.1143/jjap.51.090111
69. T. Makino, H. Kato, D. Takeuchi, M. Ogura, H. Okushi, S. Yamasaki, Device design of diamond Schottky-pn diode for low-loss power electronics. Jpn. J. Appl. Phys. **51**(9R), 090116 (2012). doi:10.1143/jjap.51.090116
70. S. Cheng, L. Sang, M. Liao, J. Liu, M. Imura, H. Li, Y. Koide, Integration of high-dielectric constant Ta2O5 oxides on diamond for power devices. Appl. Phys. Lett. **101**(23), 232907 (2012). doi:10.1063/1.4770059
71. N. Mizuochi, T. Makino, H. Kato, D. Takeuchi, M. Ogura, H. Okushi, M. Nothaft, P. Neumann, A. Gali, F. Jelezko, J. Wrachtrup, S. Yamasaki, Electrically driven single-photon source at room temperature in diamond. Nat. Photon. **6**, 299–303 (2012). doi:10.1038/nphoton.2012.75
72. M. Liao, L. Sang, T. Teraji, M. Imura, J. Alvarez, Y. Koide, Comprehensive investigation of single crystal diamond deep-ultraviolet detectors. Jpn. J. Appl. Phys. **51**(9R), 090115 (2012). doi:10.1143/jjap.51.090115
73. D. Takeuchi, T. Makino, H. Kato, M. Ogura, H. Okushi, H. Ohashi, S. Yamasaki, High-voltage vacuum switch with a diamond p–i–n diode using negative electron affinity. Jpn. J. Appl. Phys. **51**(9R), 090113 (2012). doi:10.1143/jjap.51.090113
74. H. Umezawa, M. Nagase, Y. Kato, S. Shikata, High temperature application of diamond power device. Diam. Relat. Mater. **24**, 201–205 (2012). doi:10.1016/j.diamond.2012.01.011
75. G. Chicot, A. Marèchal, R. Motte, P. Muret, E. Gheeraert, J. Pernot, Metal oxide semiconductor structure using oxygen-terminated diamond. Appl. Phys. Lett. **102**(24), 242108 (2013). doi:10.1063/1.4811668
76. A. Gicquel, K. Hassouni, S. Farhat, Y. Breton, C.D. Scott, M. Lefebvre, M. Pealat, Spectroscopic analysis and chemical kinetics modeling of a diamond deposition plasma reactor. Diam. Relat. Mater. **3**(4–6), 581–586 (1994). doi:10.1016/0925-9635(94)90229-1

77. C. Benndorf, P. Joeris, R. Kröger, Mass and optical emission spectroscopy of plasmas for diamond synthesis. Pure Appl. Chem. **66**(6), 1195–1205 (1994). doi:10.1351/pac199466061195
78. T. Fujii, M. Kareev, Mass spectrometric studies of a CH_4/H_2 microwave plasma under diamond deposition conditions. J. Appl. Phys. **89**(5), 2543–2546 (2001). doi:10.1063/1.1346655
79. P. Deák, A. Kováts, P. Csíkváry, I. Maros, G. Hárs, Ethynyl (C_2H): a major player in the chemical vapor deposition of diamond. Appl. Phys. Lett. **90**(5), 051503 (2007). doi:10.1063/1.2437718
80. H. Zhou, J. Watanabe, M. Miyake, A. Ogino, M. Nagatsu, R. Zhan, Optical and mass spectroscopy measurements of $Ar/CH_4/H_2$ microwave plasma for nano-crystalline diamond film deposition. Diam. Relat. Mater. **16**(4–7), 675–678 (2007). doi:10.1016/j.diamond.2006.11.074
81. J. Ma, M.N.R. Ashfold, Y.A. Mankelevich, Validating optical emission spectroscopy as a diagnostic of microwave activated $CH_4/Ar/H_2$ plasmas used for diamond chemical vapor deposition. J. Appl. Phys. **105**(4), 043302 (2009). doi:10.1063/1.3078032
82. A. Gicquel, N. Derkaoui, C. Rond, F. Benedic, G. Cicala, D. Moneger, K. Hassouni, Quantitative analysis of diamond deposition reactor efficiency. Chem. Phys. **398**, 239–247 (2012). doi:10.1016/j.chemphys.2011.08.022
83. J.C. Richley, M.W. Kelly, M.N.R. Ashfold, Y.A. Mankelevich, Optical emission from microwave activated C/H/O gas mixtures for diamond chemical vapor deposition. J. Phys. Chem. A **116**(38), 9447–9458 (2012). doi:10.1021/jp306191y
84. P. Bou, J.C. Boettner, L. Vandenbulcke, Kinetic calculations in plasmas used for diamond deposition. Jpn. J. Appl. Phys. **31**(5A, Part 1), 1505–1513 (1992). doi:10.1143/JJAP.31.1505
85. M.C. McMaster, W.L. Hsu, M.E. Coltrin, D.S. Dandy, C. Fox, Dependence of the gas composition in a microwave plasma-assisted diamond chemical vapor deposition reactor on the inlet carbon source: CH_4 versus C_2H_2. Diam. Relat. Mater. **4**(7), 1000–1008 (1995). doi:10.1016/0925-9635(95)00270-7
86. J.M. Larson, M.T. Swihart, S.L. Girshick, Characterization of the near-surface gas-phase chemical environment in atmospheric-pressure plasma chemical vapor deposition of diamond. Diam. Relat. Mater. **8**(10), 1863–1874 (1999). doi:10.1016/S0925-9635(99)00143-0
87. O. Aubry, J.-L. Delfau, C. Met, L. Vandenbulcke, C. Vovelle, Precursors of diamond films analysed by molecular beam mass spectrometry of microwave plasmas. Diam. Relat. Mater. **13**(1), 116–124 (2004). doi:10.1016/j.diamond.2003.09.009
88. J. Achard, F. Silva, A. Tallaire, X. Bonnin, G. Lomvardi, K. Hassouni, A. Gicquel, High quality MPACVD diamond single crystal growth: high microwave power density regime. J. Phys. D **40**(20), 6175–6188 (2007). doi:10.1088/0022-3727/40/20/S04
89. H. Yamada, A. Chayahara, Y. Mokuno, Simplified description of microwave plasma discharge for chemical vapor deposition of diamond. J. Appl. Phys. **101**(6), 063302 (2007). doi:10.1063/1.2711811
90. J. Ma, J.C. Richley, M.N.R. Ashfold, Y.A. Mankelevich, Probing the plasma chemistry in a microwave reactor used for diamond chemical vapor deposition by cavity ring down spectroscopy. J. Appl. Phys. **104**(10), 103305 (2008). doi:10.1063/1.3021095
91. F. Silva, J. Achard, O. Brinza, X. Bonnin, K. Hassouni, A. Anthonis, K.D. Corte, J. Barjon, High quality, large surface area, homoepitaxial MPACVD diamond growth. Diam. Relat. Mater. **18**(5–8), 683–697 (2009). doi:10.1016/j.diamond.2009.01.038
92. K. Hassouni, F. Silva, A. Gicquel, Modelling of diamond deposition microwave cavity generated plasmas. J. Phys. D **43**(15), 153001 (2010). doi:10.1088/0022-3727/43/15/153001
93. H. Yamada, A. Chayahara, Y. Mokuno, S. Shikata, Model of reactive microwave plasma discharge for growth of single-crystal diamond. Jpn. J. Appl. Phys. **50**(1S1), 01AB02 (2011). doi:10.1143/jjap.50.01ab02
94. H. Yamada, Numerical simulations to study growth of single-crystal diamond by using microwave plasma chemical vapor deposition with reactive (H, C, N) species. Jpn. J. Appl. Phys. **51**(9R), 090105 (2012). doi:10.1143/jjap.51.090105

95. C.-L. Cheng, H.-C. Chang, J.-C. Lin, K.-J. Song, J.-K. Wang, Direct observation of hydrogen etching anisotropy on diamond single crystal surfaces. Phys. Rev. Lett. **78**(19), 3713–3716 (1997). doi:10.1103/PhysRevLett.78.3713
96. T. Tsuno, T. Imai, Y. Nishibayashi, K. Hamada, N. Fujimori, Epitaxially grown diamond (001) 2×1/1×2 surface investigated by scanning tunneling microscopy in air. Jpn. J. Appl. Phys. **30**(5, Part 1), 1063–1066 (1991). doi:10.1143/JJAP.30.1063
97. H. Sasaki, H. Kawarada, Structure of chemical vapor deposited diamond (111) surfaces by scanning tunneling microscopy. Jpn. J. Appl. Phys. **32**(12A, Part 2), L1771–L1774 (1993). doi:10.1143/JJAP.32.L1771
98. L.F. Sutcu, C.J. Chu, M.S. Thompson, R.H. Hauge, J.L. Margrave, M.P. D'Evelyn, Atomic force microscopy of (100), (110), and (111) homoepitaxial diamond films. J. Appl. Phys. **71** (12), 5930–5940 (1992). doi:10.1063/1.350443
99. T. Tsuno, T. Tomikawa, S. Shikata, T. Imai, N. Fujirmori, Diamond(001) single-domain 2×1 surface grown by chemical vapor deposition. Appl. Phys. Lett. **64**(5), 572–574 (1994). doi:10.1063/1.111107
100. T. Tsuno, T. Tomikawa, S. Shikata, N. Fujimori, Diamond homoepitaxial growth on (111) substrate investigated by scanning tunneling microscope. J. Appl. Phys. **75**(3), 1526–1529 (1994). doi:10.1063/1.356389
101. M. McGonigal, J.N. Russell Jr., P.E. Pehrsson, H.G. Maguire, J.E. Butler, Multiple internal reflection infrared spectroscopy of hydrogen adsorbed on diamond(110). J. Appl. Phys. **77** (8), 4049–4053 (1995). doi:10.1063/1.359487
102. H. Kawarada, H. Ssaki, A. Sato, Scanning-tunneling-microscope observation of the homoepitaxial diamond (001) 2×1 reconstruction observed under atmospheric pressure. Phys. Rev. B **52**(15), 11351–11358 (1995). doi:10.1103/PhysRevB.52.11351
103. Y. Kuang, Y. Wang, N. Lee, A. Badzian, T. Badzian, T.T. Tsong, Surface structure of homoepitaxial diamond (001) films, a scanning tunneling microscopy study. Appl. Phys. Lett. **67**(25), 3721–3723 (1995). doi:10.1063/1.115361
104. C.-L. Cheng, J.-C. Lin, H.-C. Chang, J.-K. Wang, Characterization of CH stretches on diamond C(111) single and nanocrystal surfaces by infrared absorption spectroscopy. J. Chem. Phys. **105**(19), 8977–8978 (1996). doi:10.1063/1.472938
105. T. Takami, K. Suzuki, I. Kusunoki, I. Sakaguchi, M. Nishitani-Gamo, T. Ando, RHEED and AFM studies of homoepitaxial diamond thin film on C(001) substrate produced by microwave plasma CVD. Diam. Relat. Mater. **8**(2–5), 701–704 (1999). doi:10.1016/S0925-9635(98)00391-4
106. T. Takami, I. Kusunoki, M. Nishitani-Gamo, T. Ando, Homoepitaxial diamond (001) thin film studied by reflection high-energy electron diffraction, contact atomic force microscopy, and scanning tunneling microscopy. J. Vac. Sci. Technol. B **18**(3), 1198–1202 (2000). doi:10.1116/1.591360
107. A. Heerwagen, M. Strobel, M. Himmelhaus, M. Buck, Chemical vapor deposition of diamond: an in situ study by vibrational spectroscopy. J. Am. Chem. Soc. **123**(27), 6732–6733 (2001). doi:10.1021/ja016056q
108. L.K. Bigelow, M.P. D'Evelyn, Role of surface and interface science in chemical vapor deposition diamond technology. Surf. Sci. **500**(1–3), 986–1004 (2002). doi:10.1016/S0039-6028(01)01545-X
109. L. Ackermann, W. Kulisch, Investigation of diamond etching and growth by in situ scanning tunneling microscopy. Diam. Relat. Mater. **8**(7), 1256–1260 (1999). doi:10.1016/S0925-9635(99)00119-3
110. B. Voigtländer, M. Kästner, P. Šmilauer, Magic islands in Si/Si(111) homoepitaxy. Phys. Rev. Lett. **81**(4), 858–861 (1998). doi:10.1103/PhysRevLett.81.858
111. H. Yamaguchi, Y. Homma, Imaging of layer by layer growth processes during molecular beam epitaxy of GaAs on (111)A substrates by scanning electron microscopy. Appl. Phys. Lett. **73**(21), 3079–3081 (1998). doi:10.1063/1.122678

112. M.H. Xie, S.M. Seutter, W.K. Zhu, L.X. Zheng, H. Wu, S.Y. Tong, Anisotropic step-flow growth and island growth of GaN(0001) by molecular beam epitaxy. Phys. Rev. Lett. **82**(13), 2749–2752 (1999). doi:10.1103/PhysRevLett.82.2749
113. N. Tokuda, T. Makino, T. Inokuma, S. Yamasaki, Formation of step-free surfaces on diamond (111) mesas by homoepitaxial lateral growth. Jpn. J. Appl. Phys. **51**(9R), 090107 (2012). doi:10.1143/JJAP.51.090107
114. N. Tokuda, T. Makino, T. Inokuma, S. Yamasaki, Formation of step-free diamond (111) surfaces by plasma-enhanced CVD. J. Jpn. Assoc. Cryst. Growth **39**(4), 185–189 (2012) (in Japanese)
115. F. Jelezko, T. Gaebel, I. Popa, A. Gruber, J. Wrachtrup, Observation of coherent oscillations in a single electron spin. Phys. Rev. Lett. **92**(7), 076401 (2004). doi:10.1103/PhysRevLett.92.076401
116. L. Childress, M.V. Gurudev Dutt, J.M. Taylor, A.S. Zibrov, F. Jelezko, J. Wrachtrup, P.R. Hemmer, M.D. Lukin, Coherent dynamics of coupled electron and nuclear spin qubits in diamond. Science **314**(5797), 281–285 (2006). doi:10.1126/science.1131871
117. M.V. Gurudev Dutt, L. Childress, L. Jiang, E. Togan, J. Maze, F. Jelezko, A.S. Zibrov, P.R. Hemmer, M.D. Lukin, Quantum register based on individual electronic and nuclear spin qubits in diamond. Science **316**(5829), 1312–1316 (2007). doi:10.1126/science.1139831
118. J.R. Maze, J.M. Taylor, M.D. Lukin, Electron spin decoherence of single nitrogen-vacancy defects in diamond. Phys. Rev. B **78**(9), 094303 (2008). doi:10.1103/PhysRevB.78.094303
119. P. Neumann, N. Mizuochi, F. Rempp, P. Hemmer, H. Watanabe, S. Yamasaki, V. Jacques, T. Gaebel, F. Jelezko, J. Wrachtrup, Multipartite entanglement among single spins in diamond. Scinece **320**(5881), 1326–1329 (2008). doi:10.1126/science.1157233
120. G. Balasubramanian, P. Neumann, D. Twitchen, M. Markham, R. Kolesov, N. Mizuochi, J. Isoya, J. Achard, J. Beck, J. Tissler, V. Jacques, P.R. Hemmer, F. Jelezko, J. Wrachtrup, Ultralong spin coherence time in isotopically engineered diamond. Nat. Mater. **8**, 383–387 (2009). doi:10.1038/nmat2420
121. B.B. Buckley, G.D. Fuchs, L.C. Bassett, D.D. Awschalom, Spin-light coherence for single-spin measurement and control in diamond. Science **330**(6008), 1212–1215 (2010). doi:10.1126/science.1196436
122. X. Zhu, S. Saito, A. Kemp, K. Kakuyanagi, S. Karimoto, H. Nakano, W.J. Munro, Y. Tokura, M.S. Everitt, K. Nemoto, M. Kasu, N. Mizuochi, K. Semba, Coherent coupling of a superconducting flux qubit to an electron spin ensemble in diamond. Nature **478**(7368), 221–224 (2011). doi:10.1038/nature10462
123. K.C. Lee, M.R. Sprague, B.J. Sussman, J. Nunn, N.K. Langford, X.-M. Jin, T. Champion, P. Michelberger, K.F. Reim, D. England, D. Jaksch, I.A. Walmsley, Entangling macroscopic diamonds at room temperature. Science **334**(6060), 1253–1256 (2011). doi:10.1126/science.1211914
124. J.F. Prings, Activation of boron-dopant atoms in ion-implanted diamonds. Phys. Rev. B **38**(8), 5576–5584 (1988). doi:10.1103/PhysRevB.38.5576
125. C. Uzan-Saguy, R. Kalish, R. Walker, D.N. Jamieson, S. Prawer, Formation of delta-doped, buried conducting layers in diamond, by high-energy, B-ion implantation. Diam. Relat. Mater. **7**(10), 1429–1432 (1998). doi:10.1016/S0925-9635(98)00231-3
126. K. Ueda, M. Kasu, T. Makimoto, High-pressure and high-temperature annealing as an activation method for ion-implanted dopants in diamond. Appl. Phys. Lett. **90**(12), 122102 (2007). doi:10.1063/1.2715034
127. N. Tsubouchi, M. Ogura, Enhancement of dopant activation in B-implanted diamond by high-temperature annealing. Jpn. J. Appl. Phys. **47**(9R), 7047–7051 (2008). doi:10.1143/JJAP.47.7047
128. N. Tsubouchi, M. Ogura, N. Mizuochi, H. Watanabe, Electrical properties of a B doped layer in diamond formed by hot B implantation and high-temperature annealing. Diam. Relat. Mater. **18**(2–3), 128–131 (2009). doi:10.1016/j.diamond.2008.09.013

129. A.K. Ratnikova, M.P. Dukhnovsky, Y.Y. Fedorov, V.E. Zemlyakov, A.B. Muchnikov, A.L. Vikharev, A.M. Gorbachev, D.B. Radishev, A.A. Altukhov, A.V. Mitenkin, Homoepitaxial single crystal diamond grown on natural diamond seeds (type IIa) with boron-implanted layer demonstrating the highest mobility of 1150 cm^2/V s at 300 K for ion-implanted diamond. Diam. Relat. Mater. **20**(8), 1243–1245 (2011). doi:10.1016/j.diamond.2011.07.007
130. V.S. Bormashov, S.A. Tarelkin, S.G. Buga, M.S. Kuznetsov, S.A. Terentiev, A.N. Semenov, V.D. Blank, Electrical properties of the high quality boron-doped synthetic single-crystal diamonds grown by the temperature gradient method. Diam. Relat. Mater. **35**, 19–23 (2013). doi:10.1016/j.diamond.2013.02.011
131. S. Yamanaka, H. Watanabe, S. Masai, D. Takeuchi, H. Okushi, K. Kajimura, High-quality B-doped homoepitaxial diamond films using trimethylboron. Jpn. J. Appl. Phys. **37**(10A, Part 2), L1129–L1131 (1998). doi:10.1143/JJAP.37.L1129
132. J.-P. Lagrange, A. Deneuville, E. Gheeraert, Activation energy in low compensated homoepitaxial boron-doped diamond films. Diam. Relat. Mater. **7**(9), 1390–1393 (1998). doi:10.1016/S0925-9635(98)00225-8
133. E.A. Ekimov, V.A. Sidrov, E.D. Bauer, N.N. Mel'nki, N.J. Curro, J.D. Thompson, S.M. Stishov, Superconductivity in diamond. Nature **428**(6982), 542–545 (2004). doi:10.1038/nature02449
134. Y. Takano, M. Nagao, I. Sakaguchi, M. Tachiki, T. Hatano, K. Kobayashi, H. Umezawa, H. Kawarada, Superconductivity in diamond thin films well above liquid helium temperature. Appl. Phys. Lett. **85**(14), 2851–2853 (2004). doi:10.1063/1.1802389
135. T. Yokoya, T. Nakamura, T. Matsushita, T. Muro, Y. Takano, M. Nagao, T. Takenouchi, H. Kawarada, T. Oguchi, Origin of the metallic properties of heavily boron-doped superconducting diamond. Nature **438**(7068), 647–650 (2005). doi:10.1038/nature04278
136. E. Bustarret, Superconducting diamond: an introduction. Phys. Stat. Sol. A **205**(5), 997–1008 (2008). doi:10.1002/pssa.200777501
137. T. Klein, P. Achatz, J. Kacmarcik, C. Marcenat, F. Gustafsson, J. Marcus, E. Bustarret, J. Pernot, F. Omnes, B.E. Sernelius, C. Persson, A. Silva, C. Cytermann, Metal-insulator transition and superconductivity in boron-doped diamond. Phys. Rev. B **75**(16), 165313 (2007). doi:10.1103/PhysRevB.75.165313
138. A. Kawano, H. Ishiwata, S. Iriyama, R. Okada, T. Yamaguchi, Y. Takano, H. Kawarada, Superconductor-to-insulator transition in boron-doped diamond films grown using chemical vapor deposition. Phys. Rev. B **82**(8), 085318 (2010). doi:10.1103/PhysRevB.82.085318
139. N. Tokuda, T. Saito, H. Umezawa, H. Okushi, S. Yamasaki, The role of boron atoms in heavily boron-doped semiconducting homoepitaxial diamond growth—study of surface morphology. Diam. Relat. Mater. **16**(2), 409–411 (2007). doi:10.1016/j.diamond.2006.08.013
140. N. Tokuda, H. Umezawa, T. Saito, K. Yamabe, H. Okushi, S. Yamasaki, Surface roughening of diamond (001) films during homoepitaxial growth in heavy boron doping. Diam. Relat. Mater. **16**(4–7), 767–770 (2007). doi:10.1016/j.diamond.2006.12.024
141. N. Tokuda, H. Umezawa, K. Yamabe, H. Okushi, S. Yamasaki, Hillock-free heavily boron-doped homoepitaxial diamond films on misoriented (001) substrates. Jpn. J. Appl. Phys. **46**(4A, Part 1), 1469–1470 (2007). doi:10.1143/JJAP.46.1469
142. H. Kato, D. Takeuchi, N. Tokuda, H. Umezawa, H. Okushi, S. Yamasaki, Characterization of specific contact resistance on heavily phosphorus-doped diamond films. Diam. Relat. Mater. **18**(5–8), 782–785 (2009). doi:10.1016/j.diamond.2009.01.033
143. T. Yatsui, W. Nomura, M. Naruse, M. Ohtsu, Realization of an atomically flat surface of diamond using dressed photon-phonon etching. J. Phys. D **45**(47), 475302 (2012). doi:10.1088/0022-3727/45/47/475302
144. A. Kubota, S. Fukuyama, Y. Ichimori, M. Touge, Surface smoothing of single-crystal diamond (100) substrate by polishing technique. Diam. Relat. Mater. **24**, 59–62 (2012). doi:10.1016/j.diamond.2011.10.022

145. Y. Kato, H. Umezawa, S. Shikata, M. Touge, Effect of an ultraflat substrate on the epitaxial growth of chemical-vapor-deposited diamond. Appl. Phys. Express **6**(2), 025506 (2013). doi:10.7567/APEX.6.025506
146. N. Tokuda, H. Umezawa, K. Yamabe, H. Okushi, S. Yamasaki, Growth of atomically step-free surface on diamond {111} mesas. Diam. Relat. Mater. **19**(4), 288–290 (2010). doi:10.1016/j.diamond.2009.11.015
147. H. Sawada, H. Ichinose, H. Watanabe, D. Takeuchi, H. Okushi, Cross-sectional TEM study of unepitaxial crystallites in a homoepitaxial diamond film. Diam. Relat. Mater. **10**(11), 2030–2034 (2001). doi:10.1016/S0925-9635(01)00477-0
148. T. Tsuno, T. Imai, N. Fujimori, Twinning structure and growth hillock on diamond (001) epitaxial film. Jpn. J. Appl. Phys. **33**(7A, Part 1), 4039–4043 (1994). doi:10.1143/JJAP.33.4039
149. H. Wanatanbe, D. Takeuchi, S. Yamanaka, H. Okushi, K. Kajimura, T. Sekiguchi, Homoepitaxial diamond film with an atomically flat surface over a large area. Diam. Relat. Mater. **8**(7), 1272 (1999). doi:10.1016/S0925-9635(99)00126-0
150. N. Tokuda, H. Umezawa, S. Ri, M. Ogura, K. Yamabe, H. Okushi, S. Yamasaki, Atomically flat diamond (111) surface formation by homoepitaxial lateral growth. Diam. Relat. Mater. **17**(7–10), 1051–1054 (2008). doi:10.1016/j.diamond.2008.01.089
151. N. Tokuda, H. Umezawa, H. Kato, M. Ogura, S. Gonda, K. Yamabe, H. Okushi, S. Yamasaki, Nanometer scale height standard using atomically controlled diamond surface. Appl. Phys. Express **2**(5), 055001 (2009). doi:10.1143/APEX.2.055001
152. D. Lee, J.M. Blakely, T.W. Schroeder, J.R. Engstrom, A growth method for creating arrays of atomically flat mesas on silicon. Appl. Phys. Lett. **78**(10), 1349–1351 (2001). doi:10.1063/1.1352656
153. T. Nishida, N. Kobayashi, Step-free surface grown on GaAs (111) B substrate by selective area metalorganic vapor phase epitaxy. Appl. Phys. Lett. **69**(17), 2549–2550 (1996). doi:10.1063/1.117735
154. T. Nishida, N. Kobayashi, Formation of a 100-μm-wide stepfree GaAs (111)B surface obtained by finite area metalorganic vapor phase epitaxy. Jpn. J. Appl. Phys. **37**(1A/B, Part 2), L13–L14 (1998). doi:10.1143/JJAP.37.L13
155. J.A. Powell, P.G. Neudeck, A.J. Trunek, G.M. Beheim, L.G. Matus, R.W. Hoffman Jr., L.J. Keys, Growth of step-free surfaces on device-size (0001)SiC mesas. Appl. Phys. Lett. **77**(10), 1449–1451 (2000). doi:10.1063/1.1290717
156. T. Akasaka, Y. Kobayashi, M. Kasu, Step-free GaN hexagons grown by selective-area metalorganic vapor phase epitaxy. Appl. Phys. Express **2**(9), 091002 (2009). doi:10.1143/APEX.2.091002
157. C.E. Nebel, C.R. Miskys, J.A. Garrido, M. Hermann, O. Ambacher, M. Eickoff, M. Stutzmann, AlN/diamond np-junctions. Diam. Relat. Mater. **12**(10–11), 1873–1876 (2003). doi:10.1016/S0925-9635(03)00313-3
158. C.R. Miskys, J.A. Garrido, C.E. Nebel, M. Hermann, O. Ambacher, M. Eickhoff, M. Stutzmann, AlN/diamond heterojunction diodes. Appl. Phys. Lett. **82**(2), 290–292 (2003). doi:10.1063/1.1532545
159. Y. Taniyasu, M. Kasu, MOVPE growth of single-crystal hexagonal AlN on cubic diamond. J. Cryst. Growth **311**(10), 2828–2830 (2009). doi:10.1016/j.jcrysgro.2009.01.021
160. K. Hirama, Y. Taniyasu, M. Kasu, Heterostructure growth of a single-crystal hexagonal AlN (0001) layer on cubic diamond (111) surface. J. Appl. Phys. **108**(1), 013528 (2010). doi:10.1063/1.3452362
161. M. Imura, K. Nakajima, M. Liao, Y. Koide, Growth mechanism of c-axis-oriented AlN on (111) diamond substrates by metal-organic vapor phase epitaxy. J. Cryst. Growth **312**(8), 1325–1328 (2010). doi:10.1016/j.jcrysgro.2009.09.020
162. K. Hirama, Y. Taniyasu, M. Kasu, Hexagonal AlN(0001) heteroepitaxial growth on cubic diamond (001). Jpn. J. Appl. Phys. **49**(4s), 04DH01 (2010). doi:10.1143/JJAP.49.04DH01
163. S. Tanaka, R.S. Kern, R.F. Davis, Initial stage of aluminum nitride film growth on 6H-silicon carbide by plasma-assisted, gas-source molecular beam epitaxy. Appl. Phys. Lett. **66**(1), 37 (1995). doi:10.1063/1.114173

164. J.A. Powell, J.B. Petit, J.H. Edgar, I.G. Jenkins, L.G. Matus, J.W. Yang, P. Pirouz, W.J. Choyke, L. Cleman, M. Yoganathan, Controlled growth of 3C-SiC and 6H-SiC films on low-tilt-angle vicinal (0001) 6H-SiC wafers. Appl. Phys. Lett. **59**(3), 333–335 (1991). doi:10.1063/1.105587
165. T. Ouisse, Electron transport at the SiC/SiO2 interface. Phys. Status Solidi A **162**(1), 339–368 (1997). doi:10.1002/1521-396X(199707)162:1<339::AID-PSSA339>3.0.CO;2-G
166. N.D. Bassim, M.E. Twigg, C.R. Eddy Jr., J.C. Culbertson, M.A. Mastro, R.L. Henry, R.T. Holm, P.G. Neudeck, A.J. Trunek, J.A. Powell, Lowered dislocation densities in uniform GaN layers grown on step-free (0001) 4H-SiC mesa surfaces. Appl. Phys. Lett. **86**(2), 021902 (2005). doi:10.1063/1.1849834
167. J.D. Caldwll, M.A. Mastro, K.D. Hobart, O.J. Glembocki, C.R. Eddy Jr., N.D. Bassim, R.T. Holm, R.L. Henry, M.E. Twigg, F. Kub, P.G. Neudeck, A.J. Trunek, J.A. Powell, Improved ultraviolet emission from reduced defect gallium nitride homojunctions grown on step-free 4H-SiC mesas. Appl. Phys. Lett. **88**(26), 263509 (2006). doi:10.1063/1.2218045

Chapter 2
Diamond/β-SiC Composite Thin Films: Preparation, Properties and Applications

Xin Jiang and Hao Zhuang

Abstract Diamond/β-SiC composite films have been fabricated using chemical vapor deposition techniques. The ultimate goal is to create a superior material with combined advantages of both diamond and β-SiC for a wide range of applications, such as tribological and biological coatings, sensors, windows for harsh environment, and electronic devices etc. In this chapter, the recent processes made in the synthesis, characterization and applications of the diamond/β-SiC composite films are reviewed.

2.1 Introduction

Driven by the ambition to technologically harness both diamond and β-SiC's numerous outstanding properties, the fabrication of diamond/β-SiC composite films was firstly launched using chemical vapor deposition technique in 1992 [1]. The ultimate goal of this activity is to create a superior material with combined advantages of both diamond and β-SiC for a wide range of applications. During the course of the time, good control over the crystallinity, phase distribution and orientation of both diamond and β-SiC phases have been achieved. The composite films have been applied to enhance the adhesion of diamond film on various technologically important substrates, as well as for the fabrication of DNA biosensors. This chapter will start from the basic knowledge of synthesizing diamond/β-SiC composite films, and then move on to present the main approaches in controlling their orientation, phase distribution and crystallinity. In the end of this chapter, the application of the composite film as coating for cutting tools and biosensors will be introduced.

X. Jiang (✉) · H. Zhuang
Institute of Materials Engineering Department of Mechanical Engineering, University of Siegen, 57076 Siegen, Germany
e-mail: jiang@lot.mb.uni-siegen.de

N. Yang (ed.), *Novel Aspects of Diamond*, Topics in Applied Physics 121,
DOI 10.1007/978-3-319-09834-0_2

2.2 Basics of Synthesizing Composite Films

The feasibility of the fabrication of diamond/β-SiC composite films was revealed via a simple thermal dynamic calculation [2]. The co-deposition of diamond and β-SiC phases was predicted to be possible by the addition of tetramethylsilane (TMS) during the diamond growth [2]. However, it is only possible in a narrow temperature region. Too high or too low substrate temperatures result in the growth of only pure β-SiC films. Under this guidance, the diamond/β-SiC composite films have been successfully synthesized by microwave plasma chemical vapor deposition (MWCVD) and hot filament chemical vapor deposition (HFCVD) techniques. Similar to the pure diamond thin film deposition, a surface pretreatment process, which is normally done by bias enhanced nucleation [3], abrasion of the substrate surface using diamond powder [4] or ultrasonic seeding [5] etc., is required to enhance the diamond nucleation density on the target substrates prior to the deposition. The pretreated substrates are then transferred to the reactor chamber for deposition. The deposition conditions of composite film are similar to those of the diamond deposition (substrate temperature of 700–1,000 °C, $CH_4/H_2 = 0.5–2$ %). The main differences lay in the gas phase composition: a very low concentration of TMS (125–500 ppm) is added into the gas phase for the co-deposition of β-SiC phase along with diamond. To achieve such low concentration, diluted TMS (1 % in H_2) is supplied. In this context, if the total gas flow rate is fixed at 400 sccm, the supply of 5 sccm TMS corresponds to a TMS concentration of 125 ppm in the gas mixture.

Figure 2.1 shows the typical SEM in-lens mode images of the nanocrystalline diamond/β-SiC composite films deposited in MWCVD reactor with a microwave power of 700 W [6]. The films consist of brighter and darker regions corresponding to the diamond and β-SiC phases, respectively. The observation of such phase

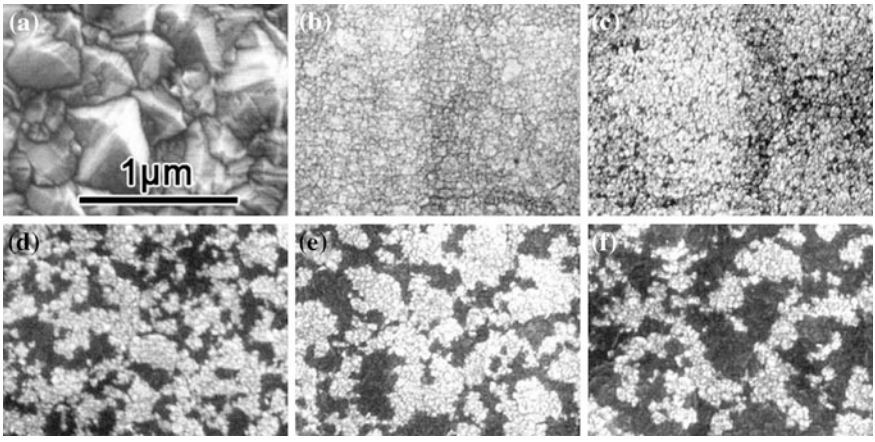

Fig. 2.1 "In-lens" mode SEM morphology of nanocrystalline diamond/β-SiC composite films deposited with **a** 0, **b** 2.5, **c** 5, **d** 10, **e** 15, and **f** 20 sccm TMS gas flow rates, respectively [6]

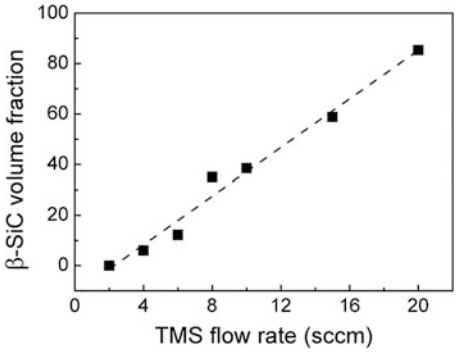

Fig. 2.2 Variation of β-SiC volume fraction (%) with TMS flow rate [6]

contrast is not surprising. The in-lens SEM mode detects the secondary electrons directly produced by the primary electrons, which is, therefore, very sensitive to the surface conditions of the films. Since H-terminated diamond surface has very high secondary electron yield [7] compared with β-SiC, the diamond phase is much brighter in the "in-lens" mode SEM images. With increasing TMS flow rate, it is easy to observe that the β-SiC/diamond ratio in the composite film increases. A quantitative determination of the volume fraction of β-SiC phase in the film with different TMS flow rates has been done through the calculation based on the electron probe microanalysis (EPMA) of the composite film. As shown in Fig. 2.2 [6], a linear relationship is clearly observed, showing the composition of the film is determined by the TMS flow rate when the other parameters (substrate temperature, microwave power, gas phase pressure, total gas flow rate, methane concentration) are kept constant. Almost 100 % volume fraction of β-SiC can be achieved with a TMS flow rate of 20 sccm.

To understand the growth mechanism of the composite films, the growth process of the films has been carefully monitored by observing their cross-section. It reveals that there exists a space competition between diamond and β-SiC to occupy the spaces available on the substrate during growth [8]. Figure 2.3a shows the cross-sectional SEM images of one composite film. The schematic illustration of the initial nucleation and growth process is shown in Fig. 2.3b [8]. At the initial growth stage, islandlike diamond and layerlike β-SiC crystals grow. This is because, at this stage, diamond can only grow on the sites where there are diamond seeds or surface defects, and form three dimensional (3D) clusters; whereas β-SiC prefers to grow on virgin Si surface by a layered growth, even though it can also grow on diamond seeds, defects etc. [8]. With increasing growth time, the diamond clusters expand and the layered β-SiC region becomes narrower and narrower. This process continues until the diamond/β-SiC surface ratio reaches certain critical value at the given methane/TMS ratio. β-SiC then starts to nucleate and grow on some of the diamond clusters. At this point, an equilibrium in the diamond/β-SiC ratio in the composite film is reached, which continues till the TMS gas supply is changed [8]. Finally, the films exhibit structures shown in Fig. 2.1. Therefore, the volume ratios of β-SiC in the composite films are determined by the different TMS/CH_4 ratios in the gas mixture.

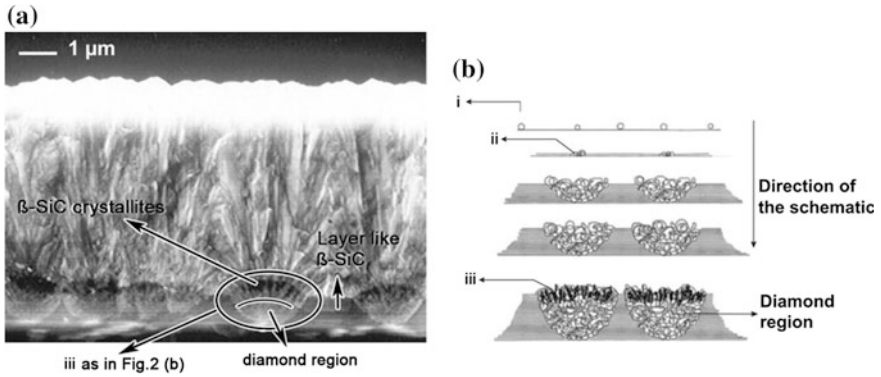

Fig. 2.3 **a** SEM cross-sectional structure of a diamond/β-SiC composite film deposited with a constant TMS content of 0.025 % in the gas phase. TMS supply was cut off after 6 h followed by the deposition of pure diamond top layer. **b** Schematic of the initial nucleation and growth process during the deposition of diamond/β-SiC composite film: i. The Si substrate is uniform seeded by diamond seeds after pretreatment process; ii. Beginning of the nucleation and growth of diamond on the diamond seeds via adsorption of diamond growth precursors from the activated gas phase and simultaneous nucleation and growth of β-SiC on "blank"Si surfaces; iii. Nucleation of β-SiC crystallites on diamond surfaces in the diamond rich regions and a equilibrium of the diamond/β-SiC raio in the composite film is reached. Reprinted with permission from [8]. Copyright (2006) American Institute of Physics

While talking about the TMS/CH_4 ratio, it is interesting to notice that, the volume of CH_4 and TMS is at a great disparity in the feed gas even at high TMS flow rate (for TMS flow rate of 20 sccm, the TMS/CH_4 ratio is only 0.08). To achieve further control of the synthesis, a microscopic level understanding on the gas phase reaction is required. In this context, theoretical calculations were carried out at the CCSD(T)/6-311 + G**//MP2/6-31 + G** level of theory [9]. It reveals that in the plasma environment, the Si–C bond in TMS breaks by atomic hydrogen (H), described by the following reactions [9]:

$$(CH_3)_nSiH_{(4-n)} + H \rightarrow (CH_3)_{n-1}SiH_{(4-n)} + CH_4 \quad (n = 1-4) \tag{2.1}$$

Si sources like SiH_{n-1} (n = 1−4) are produced by breaking the Si–H bond of TMS with the assistance of H radicals, described by the following reactions:

$$SiH_n + H \rightarrow SiH_{n-1} + H_2 \quad (n = 1-4) \tag{2.2}$$

CH_4 can also go through a similar process to produce CH_{n-1} (n = 1−4), as shown in the following:

$$CH_n + H \rightarrow CH_{n-1} + H_2 \quad (n = 1-4) \tag{2.3}$$

Among the various CH_n and SiH_n (n = 1−4) radicals, CH_3 and SiH_3 are the main ones contributing to the growth of both diamond and β-SiC crystals [9].

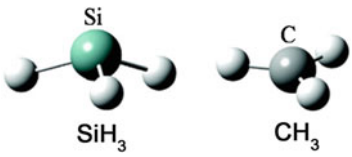

Fig. 2.4 Geometrical structures of SiH_3 and CH_3 [9]

Nevertheless, they have slight differences in their structures which results in their different reactivities: the SiH_3 radicals remain as a good sp^3 hybridized structure, whereas the CH_3 radical change to an sp^2 planar structure, as shown in Fig. 2.4. When these species contribute to the growth of diamond and β-SiC composed by sp^3 carbon and Si atoms, such differences in the ion structure lead to different attaching rates of the species, which, in turn, results in the different growth rates of diamond and β-SiC. Moreover, the activation energies (ΔE_a) of Reaction (2.2) are much lower than those of Reaction (2.3); and reaction heats (ΔH_f) of Reaction (2.2) are more negative than those of Reaction (2.3). Such a result indicates that the occurrence of Reaction (2.2) is much easier than that of Reaction (2.3). In combination with the good sp^3 hybridized structure of SiH_3, a much higher concentration of methane than that of TMS in the gas phase is required to obtain comparable diamond content in the final composite film.

2.3 Controlling the Orientation, Crystallinity, and Phase Distribution

In the composite films shown in Fig. 2.1, only nanocrystalline diamond and nanocrystalline β-SiC phases are observed. This is due to the random reaction of Si- or C-containing species with diamond or β-SiC surfaces, which interrupts the growth of both phases, resulting in nanocrystalline composite films. This argument is supported by the detection of trace Si content in the diamond region by EDX measurement [8]. Nevertheless, owning to the different surface properties, the reactivities of CH_3 and SiH_3 species with different diamond facets are different. Using frontier orbital theory, the reaction occurrence of CH_3 and SiH_3 species with different facets of diamond can be analyzed. The analysis is done by judging the energy differences between the frontier molecular orbitals (FMOs) of the reactants diamond and CH_3/SiH_3 [10]. Figure 2.5 shows the energy levels of FMOs and other nearby orbitals of CH_3, diamond nanoparticle ($C_{54}H_{56}$), and SiH_3, determined at HF/6-31G** level of theory. The diamond nanoparticle, expressed by the fomular $C_{54}H_{56}$, has a tetragonal pyramid shape with its four (111) facets on the side and one (100) facet at the bottom. Owning to the H-rich atmosphere during the diamond growth, its surface dangling bonds are saturated by H. It can be observed from Fig. 2.5 that the highest occupied molecular orbitals (HOMO) of diamond is closer to that of SiH_3 than CH_3, implying the higher probability of the reaction occurrence

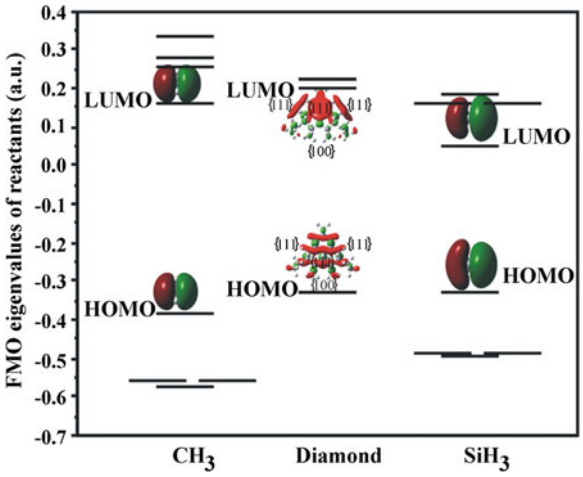

Fig. 2.5 The energy levels of FMOs and other nearby orbitals of the reactants of CH_3, diamond nanoparticle ($C_{54}H_{56}$), and SiH_3. Reprinted with permission from [10]. Copyright (2008) American Institute of Physics

between diamond and SiH_3. Moreover, {111} diamond facets show denser isosurface compared with the {100} facets. In this regard, the {111} facets are easier to react with the SiH_3 species in the gas phase than {100} facets. This leads to the conclusion that, the secondary nucleation is easier to occur on the {111} diamond facets. Such a result provides us a possibility to obtain a (100)-textured growth of diamond phase in the composite film, which is then realized experimentally (Fig. 2.6).

Figure 2.6 shows the SEM and TEM surface images of the composite film with large (100) oriented diamond crystals deposited at relatively low substrate temperature (600–700 °C). The film is deposited with the TMS addition of 0.05 % to

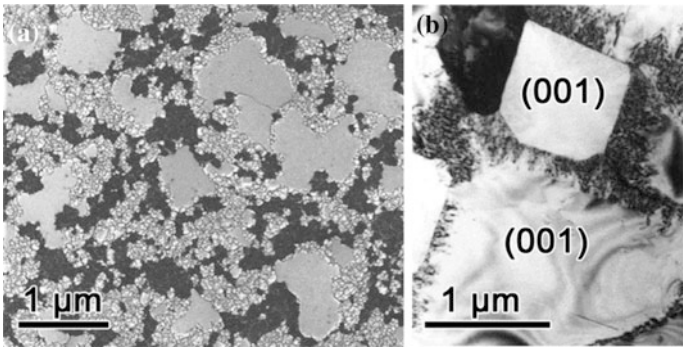

Fig. 2.6 **a** SEM and **b** TEM surface images of the composite film with (100) diamond crystals. Reprinted with permission from [10]. Copyright (2008) American Institute of Physics

H_2 and CH_4 (corresponding to a TMS flow rate of 20 sccm). It exhibits significant [001] texture of the diamond grains. The {100} facets of the crystals are restrictively parallel to each other and to the substrate surface. The TEM image shown in Fig. 2.6b depicts that, most of the grain boundaries of the diamond crystals are parallel to the {110} planes, even though some of them are parallel to the {100} planes. In the {111} growth zone along the grain boundaries, defects, such as dislocations, twins and stacking faults, exist. Nevertheless, the dark β-SiC phase domains composed by nanocrystals are formed between the (001) diamond facets and/or cover the (111) diamond facets. On the surface ({100} facets) of the diamond crystals, no obvious defects are observed. In this regard, the growth of (100) orientated diamond crystals in the composite film by the selective deposition of Si containing species on the non-{100} facet has been achieved.

Even though the growth of large (100) orientated diamond crystals is possible from the above, it only happens locally and the rest of the diamond phase as well as the β-SiC are still nanocrystalline. It is well understood that, there exists amorphous carbon phase in the grain boundaries of both diamond and β-SiC crystals, which deteriorates the intrinsic properties of both diamond and β-SiC phases, i.e. thermal conductivity, electrical resistivity, transparency, etc. In order to minimize such negative effects, it is essential to obtain high quality microcrystalline diamond and β-SiC phases in the whole composite film. The main factor that hinders us to achieve this goal is the high density of defect sites induced by the random reaction of Si or carbon containing species on diamond and β-SiC crystals. These defect sites act as secondary nucleation sites and limit the size of the crystals. Therefore, in order to obtain high quality composite films, it is essential to minimize the occurrence of the secondary nucleation process. For the growth of pure diamond films, the concentration of atomic hydrogen ([H]) is believed to be a crucial factor in the determination of its phase quality. An increasing [H] will increase the etching rate of graphite and other defect centers on diamond, and hence impede secondary nucleation of diamond, resulting in an increased film quality and growth rate [12, 13]. Therefore, a similar effect was also expected in the context of composite film

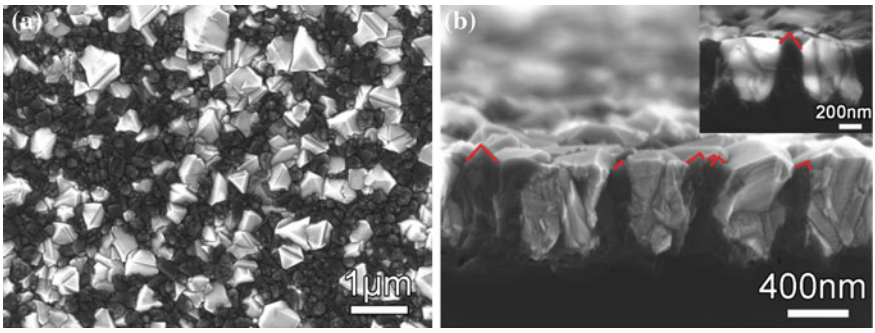

Fig. 2.7 **a** Surface and **b** cross-sectional SEM images of the composite film deposited at high [H]. The film is deposited at TMS flow rate of 5 sccm, methane flow rate of 4 sccm and substrate temperature of 800 °C. Reprinted with permission from [11]. Copyright (2011) Pergamon

deposition. In order to obtain a high [H], a high microwave power density (MWPD) was applied. Figure 2.7 shows the SEM images of the composite film deposited at MWPD of 33 W/cm^3 (2,250 W, 55 Torr), which is more than 3 times higher than the MWPD used to deposit the composite films shown in Figs. 2.1 and 2.6 (10 W/cm^3 at microwave power of 700 W with a gas phase pressure of 25 Torr). According to Gicquel et al.'s theoretical calculation, the [H] increases by a factor of more than 10 for an increase in the MWPD by a factor of 3 [14]. Micrometer sized diamond ($\sim$1 μm) and β-SiC ($\sim$0.5 μm) grains are clearly observable, indicating an improved quality of the film. As for the β-SiC phase, it even shows a highly (100) orientated characteristics: a pyramidal shape with (111) side planes meeting at a common point. The cross-sectional image (Fig. 2.7b) of the film depicts a columnar structures of diamond and β-SiC crystals, connoting the independent growth of the diamond and the β-SiC phases. Furthermore, the textured growth characteristics of the β-SiC phase can also be seen in the image (marked in red for indication). Since the deposition conditions of this film, i.e. gas phase composition, substrate temperature, gas flow rate etc., are identical to those of the nanocrystalline composite films shown in Fig. 2.1, the high [H] generated by the high MWPD is believed to be the main reason for the improved film crystallinity: at high [H], the defects sites formed on diamond and β-SiC crystals by the random reaction of SiH_3 and CH_3 radicals can be very efficiently etched away, and the surface dangling bonds are then saturated with hydrogen for further reaction until they bond with the "correct" radicals. As a result, the secondary nucleation rate becomes slow on both diamond and β-SiC crystals, and micrometer sized diamond and β-SiC grow. In this context, a "hydrogen induced selective growth model" was proposed to elucidate the mechanism, as shown in Fig. 2.8 [11].

(1) The excited plasma contains several reactive species, namely, H_2, H, CH_3, and SiH_3, which are responsible for the etching the defects, diamond growth and β-SiC growth. The diamond and β-SiC surfaces at any stage are terminated by H. Certain surface is activated by surface abstraction by the impingement of the plasma species, thus providing free unsaturated sites for further growth (Fig. 2.8a). Subsequently, the SiH_3 and CH_3 species bond with the activated surface sites by incorporation of SiH_3 and CH_3, respectively (Fig. 2.8b).
(2) The bonded SiH_3/excess CH_3 is not that stable on the diamond/β-SiC surface. At high [H], the high energy atomic H will immediately etch defect sites away and saturate the surface again with H bonds (Fig. 2.8c). At the same time, more surfaces are activated and bonds with correct species.
(3) The above two processes continuously take place and result in a layer-by-layer growth of the diamond and β-SiC crystals (Fig. 2.8d).

Following this growth model, it can be easily inferred that it is difficult for the SiC phase to form on pure diamond at high [H] during the composite film growth. In other words, a composite film will not even grow on a pure diamond area at relative high TMS flow rates. This offers the opportunity to control the lateral distribution of diamond and β-SiC phases to obtain patterned diamond/β-SiC composite films. It can be achieved by the deposition of composite film on patterned diamond

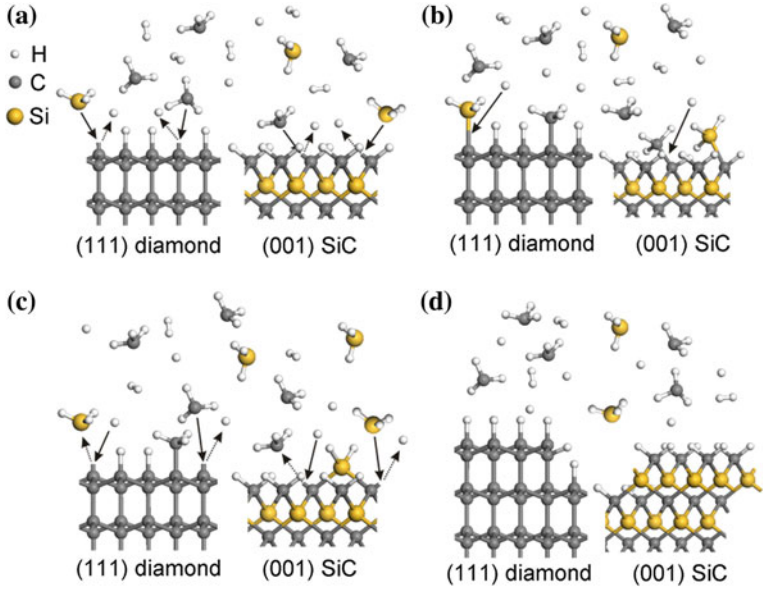

Fig. 2.8 Hydrogen induced selective growth model for the deposition of high quality diamond/β-SiC composite films at high [H]. The growth is illustrated on a (111) diamond and (111) β-SiC surfaces (see text for details)

substrates, as illustrated in Fig. 2.9. In this context, a thin patterned diamond film is essentially required, which can be done by either dry etching [15, 16] or selective area deposition techniques [17–26]. Figure 2.10 shows two patterned diamond thin films deposited using a micro-contact-printing of nano-diamond particles followed by diamond growth in MWCVD [26]. On these two samples, the growth of patterned composite film has been achieved, which is depicted in Fig. 2.11. The boundaries of two phases are well defined by the previous selective area deposition, which leads to the conclusion that no β-SiC was able to grow on the already existing diamond

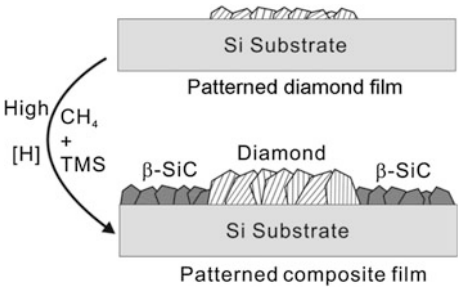

Fig. 2.9 Schematic illustration of the growth of patterned diamond/β-SiC composite film. Reprinted with permission from [11]. Copyright (2011) Pergamon

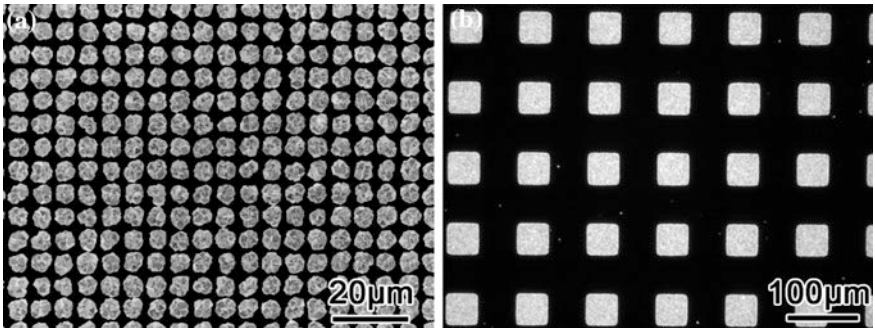

Fig. 2.10 Diamond film with different pattern sizes. **a** ~5 μm; **b** ~50 μm [26]

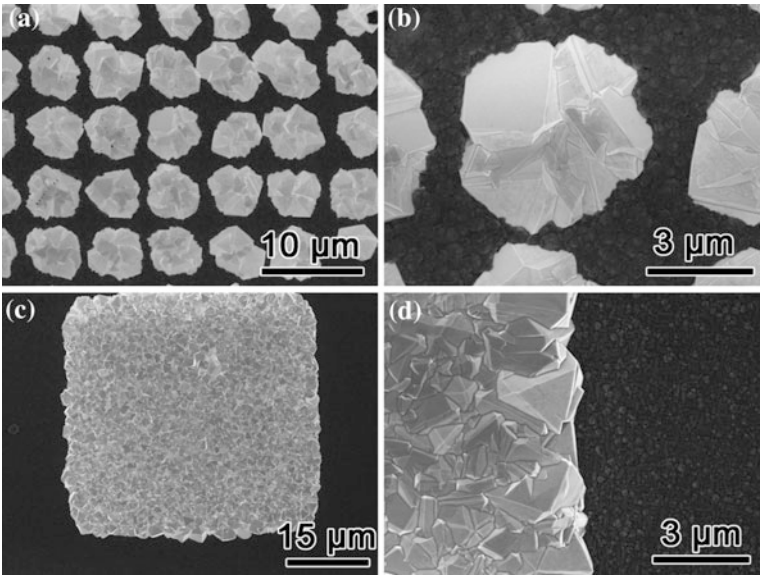

Fig. 2.11 Patterned diamond/β-SiC composite films deposited on the samples shown in Fig. 2.9. **a** ~5 μm pattern. **b** Magnified image of (**a**). **c** ~50 μm pattern. **d** Magnified image of (**c**)

phase. Due to the prolonged growth time, the over growth of the diamond phase is clearly observed. The edges of the diamond pattern become not as sharp as the original printed pattern (see Fig. 2.10). Moreover, the thickness of diamond phase is a little bit higher than that of the β-SiC phase, which might be due to the pre-growth of diamond phase and the differences in the growth rate of both phases. Nevertheless, the successful deposition of the patterned composite film not only proves the validity of the "hydrogen induced selective growth" model, but also opens the door to numerous appealing electrical and mechanical based applications of the composite film owning to the excellent electric and mechanic properties of diamond and β-SiC.

2.4 Properties and Applications of the Composite Films

2.4.1 Improvement of the Film Adhesion

Even though diamond thin films possess excellent mechanical properties, their application as protection layer has been hampered by the poor adhesion on the technologically important materials. The main obstacle is the large residual stress at the film/substrate interface, which is caused by the significant differences in the thermal expansion coefficient and hardness between the coating and the substrates. Take the widely used cutting tool material—WC-6 % Co—for example. Its thermal expansion coefficient and hardness are 4.6×10^{-6} K^{-1} and 17 Gpa, respectively, which are significantly different from those of the diamond films (thermal expansion coefficient and hardness are 1×10^{-6} K^{-1} and 60–100 GPa), making it difficult to directly obtain well-adhesive diamond coatings on it. In this context, a graded interlayer with its properties vary smoothly from the substrate material to top diamond layer presents an excellent candidate in solving the above problem. Diamond/β-SiC composite film fulfills the above requirements: (1) its properties are dependent on the composition (see Fig. 2.12 for the hardness change of the composite film with increasing β-SiC content); (2) its composition can be tuned in situ by controlling the gas phase composition and can range from β-SiC rich to diamond rich; (3) the thermal expansion coefficient (4×10^{-6} K^{-1}) and the hardness (30 GPa) of the β-SiC rich composite film are closer to those of WC-6 % Co. While applying such graded composite film as interlayer, the residual stress in the composite film as well as in the top pure diamond layer is expected to be drastically reduced [27], resulting in the improved adhesion of the film. Nevertheless, a basic understanding of the influence of composite interlayer on the overall film properties is required before applying it onto the cutting tools. Therefore, researches have been firstly carried out to apply the gradient composite interlayer on the standard substrates, i.e. Si, W, and Mo.

The deposition of the gradient composite interlayer is straightforward. It can be obtained by continuously reducing the TMS flow rate from a high value

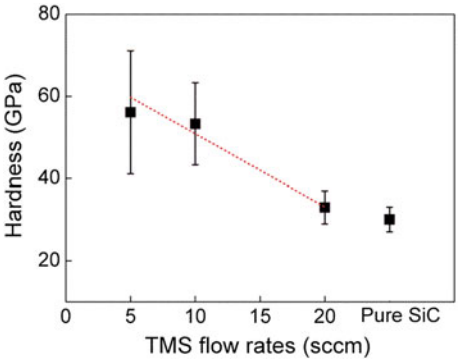

Fig. 2.12 Berkovich hardness of the composite film with different TMS flow rates (different diamond/β-SiC ratio)

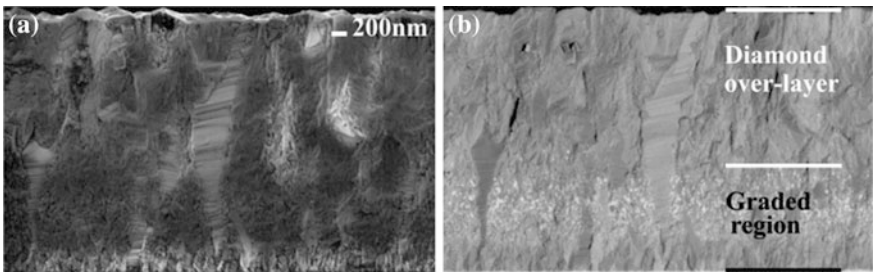

Fig. 2.13 **a** SEM cross-sectional morphology of the gradient composite film deposited on Si and **b** the corresponding backscattered electron image. The brighter spot like regions in (**b**) represent β-SiC phase. Reprinted with permission from [27]. Copyright (2009) Elsevier S.A

(i.e. 20 sccm) to 0 sccm during deposition. Continuing the process when the TMS flow rate reaches 0, a pure diamond top layer forms. Therefore, the growth of pure diamond top layer and the gradient composite interlayer can be done in just one process. Figure 2.13 shows the cross-sectional image of one gradient composite film with pure diamond top layer on Si substrate. Owning to gradual release of residual stress in the gradient layer, the top diamond layer is nearly stress-free, as characterized by Raman spectroscopy [27]. Similar results have also been observed on metallic substrates. The stress test shows that the diamond films grown on gradient composite layers on W and Mo substrates exhibit 25 % less residual biaxial stress than those without an interlayer [28]. The reduced residual stress implies the improve film adhesion. To confirm this, the Brinell indentation test has been carried out and the results are shown in Fig. 2.14 [28]. In the case of the pure diamond film direct coated on W and Mo, an indentation load of 62.5 kgf is sufficient to induce a significant film delamination. When a gradient interlayer was introduced, the film

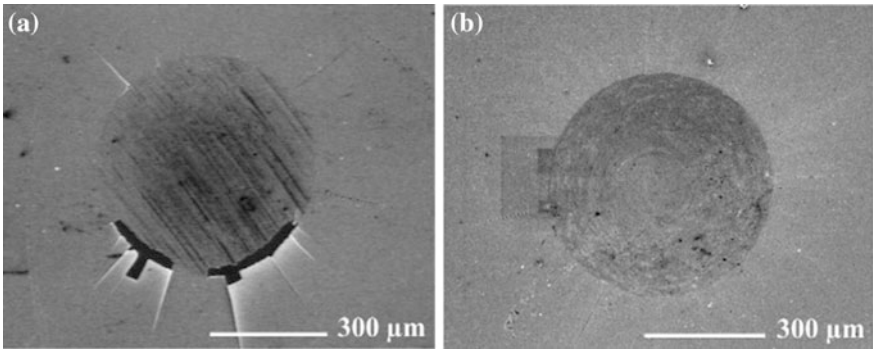

Fig. 2.14 SEM images of the indentations zones that resulted by applying an indentation load of 125 kgf on different films. **a** Delamination of a diamond film directly coated on the substrate. **b** Crater with lateral cracks of a diamond top layer on a gradient composite film. Reprinted with permission from [28]. Copyright (2007) Elsevier S.A

delamination didn't occur up to a normal load of 100 kgf. Even though a load larger than 100 kgf initiate the formation of crack, the film remained attached to substrate. These results strongly indicate that the gradient composite film interlayer can be a very promising candidate in improving the adhesion of diamond film on technologically important substrates.

After the above basic understanding, the gradient composite interlayer is then applied to improve the adhesion of diamond film on the WC-6 % Co cutting inserts. A successful improvement of the lifetime of the cutting inserts is observed by cutting AlSi20 material. For the uncoated tool, it can only machine an area of 75 cm^2 before failure. Coating of the tool with pure diamond (without interlayer) can improve its machining area to 300 cm^2. When a gradient composite interlayer is introduced between the diamond layer and the cutting tool, the machining area can be further improved to 400 cm^2 before failure, indicating the improved adhesion of the film in the existence of the gradient interlayer [29, 30].

2.4.2 Biosensor Application

The good biocompatibilities and diverse sensing abilities of diamond and β-SiC [31–35], make the diamond/β-SiC composite film also qualify as a good candidate for biosensor applications. However, while fabricating thin film based biosensors, the surfaces are more than often chemically or physically treated to make them clean and highly active [36–38], aiming at enhancing the adhesion of the chemical or biochemical species on the solid surface while minimizing the nonspecific adsorption of those species which disturbs the sensing process [39, 40]. In this context, the wettability of the thin film surface is important to explain its interactions with chemicals or biological species. It has been illustrated that different bio-technological applications require different surface hydrophilicities or hydrophobicities [41–46]. Therefore, to fabricate the composite films based biosensors, it is essential to firstly understand and modify the surface status of the films. For the diamond/β-SiC composite films produced above, a tunable surface wettability has been observed by varying its composition, making them suitable for diverse biotechnological activities which require different surface wettability [47]. This is achieved by selective H-termination of diamond phase and OH-termination of β-SiC phase in the composite film. It is well known that diamond can be easily H-terminated in the H_2 plasma treatment, while the β-SiC surface is known for its difficult H-termination. The conventional methods used for diamond (H_2 plasma) and Si (HF etching) H-termination don't work on SiC surface, leaving OH-terminated surface. Therefore, the simultaneous H-termination of diamond and OH-termination of β-SiC in the composite films can be easily done by oxidizing the whole composite film (i.e. treated in oxidizing mixture of boiling H_2SO_4 and KNO_3) followed by H_2 plasma treatment.

Figure 2.15a shows the water contact angle variation on the composite film surfaces before and after chemical treatment. Because of the H_2 rich atmosphere during deposition, the "as deposited" composite films are all H-terminated with

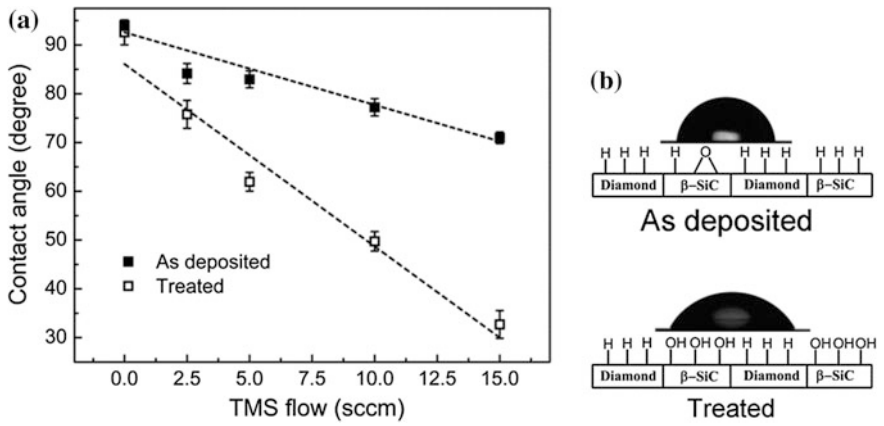

Fig. 2.15 **a** Water contact angle variation on the composite films surfaces. **b** Contact angle photo illustration along with the surface termination schematic of the as deposited and chemically treated composite films. Reprinted with permission from [47]. Copyright (2010) American Chemical Society

water contact angle higher than 70°. Nevertheless, a slight decrease of the contact angle is also observed, which is due to the slight oxidation of the β-SiC phase in the air. After chemical treatment, the water contact angle drastically decreases from 92.6 ± 2.5° to 32.7 ± 2.8° with increasing TMS flow rate indicating an increase in hydrophilicities. The surface status of the composite films was elucidated by SIMS measurement [47], which shows the oxygen content on the surface increases drastically with increasing β-SiC content. Since the diamond phase can be easily H-terminated under H_2 plasma, the increasing oxygen content on the surface is attributed to the increasing OH-terminated β-SiC phase after the chemical treatment. The surface termination status of the composite film before and after chemical treatment is shown schematically in Fig. 2.15b along with the photo illustration of the water contact angle.

Based on the above discussions, if the diamond/β-SiC ratio on the same surface can be controlled, a thin film surface with gradient wettability and thereby the surface energy can be fabricated. Such kind of surface is highly desired in the application of bio-microfluid devices. To obtain such kind of surface, a good control in the growth process is required. It is previously discussed that a space competition exists between diamond and β-SiC phases during the composite film growth which leads to the formation of composite films with different diamond/β-SiC ratios. Therefore, by controlling the lateral diamond nucleation density over the substrate surface, a gradient diamond/β-SiC composite film can be obtained. Figures 2.16a–e show the SEM plane view images of the composite film surface with a gradient nature from the left edge to the right edge over a length of 15 mm. The left part of the film is dominated by diamond phase (see Fig. 2.16a), while the right edge of the film is dominated by β-SiC phase (see Fig. 2.16e). The variation of water contact angle on this surface is shown in Fig. 2.16f. A decrease in the water

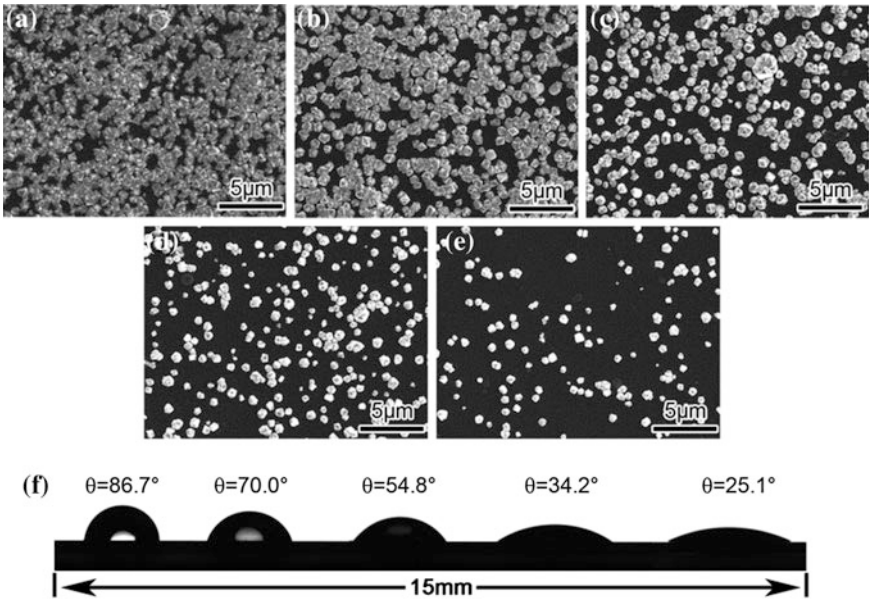

Fig. 2.16 A surface with gradient hydrophilicities. **a–e** SEM images of the composite film, the surface morphologies of the gradient film from the left edge (high diamond nucleation density) to the right edge (low diamond nucleation density). **f** The contact angle change. Reprinted with permission from [47]. Copyright (2010) American Chemical Society

CA from 86.7° to 25.1° is clearly observed. Such a surface has comparable contact angle values as the self-assembled-monolayer (SAM) modified surfaces [48–50]. However, its much higher stability in electrolyte solution makes it more promising for biological applications.

Because of the OH-terminated β-SiC phase, the surface of the chemically treated composite films is charged in solutions with different pH values [40, 42]. While considering a modified thin film surface for the biosensoric applications, this implication is very important, since the biomolecules are also charged in the solutions. If the charge of the surface is of the opposite sign with respect to that of the biomolecules to be sensed, non-specific adsorption of the biomolecules onto the substrate surface will take place. This will drastically reduce the specificity and sensitivity of the sensor [40]. On the OH-terminated β-SiC phase in the composite films, the ionized bonds are present as C–O^-, Si–O^- or C$-OH_2^+$ Si$-OH_2^+$ in solution, as shown in the following equation [40, 42]:

$$C-OH_2^+ + Si-OH_2^+ \leftrightarrow C-O^- + Si-O^- + 4H^+ \tag{2.4}$$

Therefore, the surface will be negatively charged at high pH (majority of the hydroxyl groups exist as C–O and Si–O^-) and positively charged at low pH (majority of the hydroxyl groups exist as C$-OH_2^+$ and Si$-OH_2^+$). In this context,

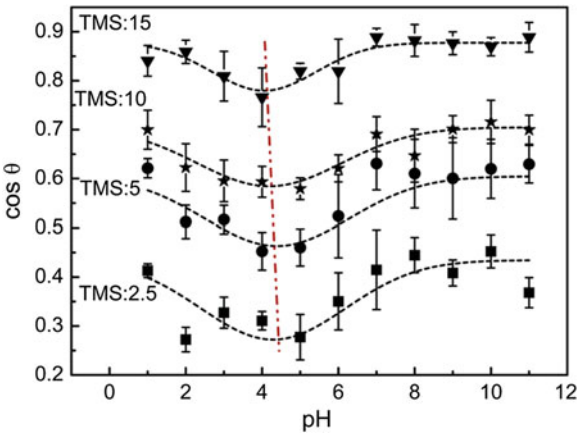

Fig. 2.17 Plots of cosine of the contact angle on the 'treated' composite film surfaces versus pH. The PZCs of the films were pH ~ 4. Reprinted with permission from [47]. Copyright (2010) American Chemical Society

the surface charge status of the film at given pH can be determined by the determination of its pH of the point of zero charge (PZC). According to Cerivic et al., the surface charge density σ can be expressed as [40, 51]:

$$\sigma/F = \frac{\gamma_L}{2.303\ RT} \bullet \frac{d(\cos\theta)}{d(\mathrm{pH})} \tag{2.5}$$

where F is the Faraday constant, γ_L is the surface tension of probe solution, R and T are the gas constant and absolute temperature, respectively; and θ is the contact angle. By plotting cosine of the contact angle versus pH, the pH of PZC can be obtained. Figure 2.17 shows the plot of cosθ versus pH for the 'treated' samples. It can be observed that for all the 'treated' surfaces, the PZC is at pH ~ 4. This is not surprising because only the OH-terminated β-SiC phase will be influenced by the pH change, and the PZC of the composite films are determined by the PZC of β-SiC. At pH = 7.5–8.5, which is most suitable pH for DNA hybridization activities [52], the composite surfaces will be negatively charged enhancing the sensitivity of the DNA sensor [40].

The advantages mentioned above motivated the fabrication of the composite films as DNA biosensors. Since both diamond and β-SiC phases in the film are chemically inert, surface functionalization is essentially required to make the film bio-active prior to the attachment of biomolecules. In this context, photochemical method was used to link allylamine—a three carbon chain unsaturated amine—onto the composite film surface. Figure 2.18 shows the schematic illustration of the main procedures in the functionalization process. To prevent the oxidation of the amine group under UV illumination, it is protected by trifluoroacetic acid group before functionalization. After the attachment, the sample is washed to remove any non-specifically attached allylamine. Then the amine group is deprotected and linked to a single stranded DNA for further detection of the DNA in the solution which contains fluorescence dye for the indication of successful hybridization process.

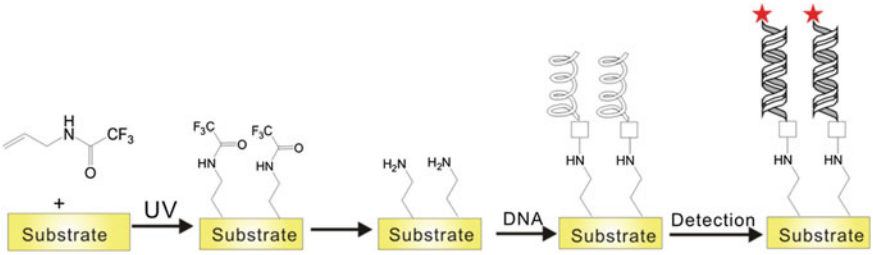

Fig. 2.18 Schematic illustration of the main procedure in the photochemical functionalization of diamond/β-SiC composite films for DNA biosensor applications

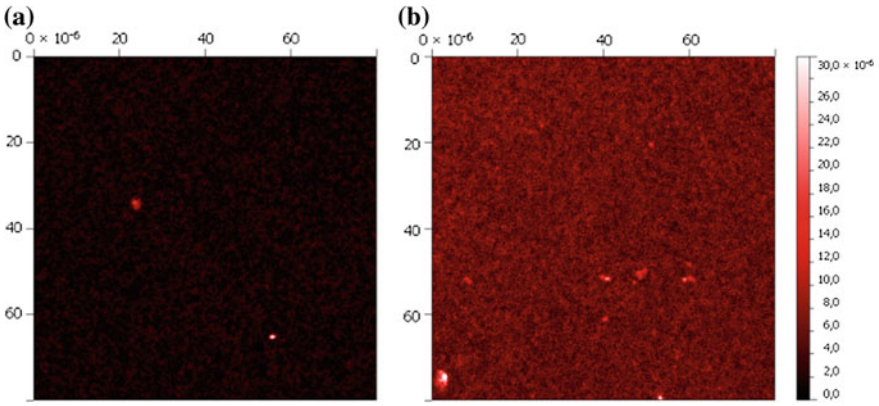

Fig. 2.19 Fluorescence microscopic images of DNA functionalized composite film surface: **a** unfunctionalized area; **b** functionalized area

Figure 2.19 shows the fluorescence microscopy images of the functionalized and unfunctionalized areas on the same sample. Clear contrast on the fluorescence signal can be observed: high intensity fluorescence signal is observed in the functionalized area. The above observation indicates that DNA has been attached onto the composite film surface through the allylamine linkage and it is still bioactive. Such an observation not only shows the suitability and possibility of the bio-surface functionalization of the composite film, but also opens the application of composite film as DNA biosensors.

2.5 Conclusions and Feature Aspects

Diamond/β-SiC composite films have been successfully synthesized via MWCVD and HFCVD processes. Till date, good control in the crystallinity, orientation and phase distribution have been achieved. The films show good adhesion to the cutting

tool materials and have drastically improved their life time. The surface status of the composite film has been systematically studied, which shows high potential in biological applications. In this context, a composite film based DNA sensor is fabricated. However, to fully explore the potential of the composite films, it would be helpful to address the following aspects of diamond/β-SiC composite film systems in future studies.

The achievement in the controlled synthesis of composite films offers us the possibility in designing the growth of composite films with complex 3D structures to improve the toughness and wear resistance of diamond films on various substrates. However, to obtain these structures, a high resolution in the selective growth of diamond or likewise β-SiC on a surface along with (ii) the ability to process-wise define and steer the structural properties like grain size and possibly crystallographic orientation of the phase(s) growing at the selected spot(s) and throughout the deposition process is needed. This requires a deep understanding in the growth process, especially at high microwave power densities which induce the selective growth of the composite films. At the same time, a systematic analysis at film/substrate interface and diamond/β-SiC boundary etc. under different loadings or environments is also of great importance.

The successful growth of patterned composite films opens the door to numerous composite films based electronic device applications. In this regard, doping of the composite film is essential. Boron is expected to be a good dopant, as diamond and β-SiC can be both easily doped by boron to a high level. Nitrogen would be another promising candidate: β-SiC can be easily doped with nitrogen, whereas the nitrogen doping in diamond is known to be difficult. By employing nitrogen as the dopant, the selective doping of β-SiC in the composite film, leaving the diamond phase undoped, will be possible. This produces the conductive β-SiC electrode embedded in insulating diamond films. Combined with the good stability of both diamond and β-SiC, such kind of electrode would be very suitable for harsh environment applications as well as biosensor applications. Nevertheless, the influence of the addition of boron or nitrogen containing species on the co-deposition of diamond and β-SiC is still unknown and requires systematic study. For example, it will affect the growth rates and defects evolution of diamond and β-SiC crystals, which might result in the disappearance of either phase in the composite film. Moreover, when boron is employed, owning the great disparity of the volume of methane and TMS in the gas phase, the doping level of diamond and β-SiC phases would also be different in the composite films.

The composite films have been successfully applied for the fabrication of DNA biosensor via the linkage of allylamine. However, the linkage of allylamine onto diamond and β-SiC is expected to have different reaction rates, owning to its different reactivities with diamond and β-SiC. Therefore, it is reasonable to expect that before allylamine fully covers one phase, its full coverage on the other phase has been already achieved and the cross-polymerization of allylamine has already started. As a result, inhomogeneity of the surface amine layer exists, and this will have a strong impact on the electrical detection of biomolecules. If the amine layer coverage is low, the signal from the DNA hybridization will possibly be too low for

detection. If the amine layer coverage, on the other hand, is too high or even cross-polymerized, the electric response of the DNA hybridization event will be blocked. Therefore, special attention will have to be given to achieve a relatively homogeneous amine layer on the composite film surface. The surface wettability studies of the composite films show that the H-termination of the diamond surface and the OH-termination of the SiC surface are possible simultaneously. Different surface termination allows for selective surface reactivity with respect to the diamond and SiC phases. For example, the OH-terminated SiC surface reacts with organosilanes while the H-terminated diamond is not able to do so. Consequently, it is possible to exploit the selective functionalization of diamond and SiC by utilizing two different functional groups (i.e. diamond-NH_2, SiC–COOH), respectively. These functional groups are, in turn, able to react and link with two different kinds of DNAs featuring different end groups, respectively. Due to the homogeneous distribution of diamond and SiC phases in the composite film, the detection range of the biosensor chip would be doubled. In order to achieve this, a strategy will have to be evaluated which allows to functionalize one phase while leaving the other phase unaffected. However, this still requires additional dedicated research.

References

1. X. Jiang, C.P. Klages, Synthesis of diamond β-SiC composite films by microwave plasma assisted chemical vapor. Appl. Phys. Lett. **61**(14), 1629–1631 (1992). doi:10.1063/1.108458
2. V.V.S.S. Srikanth, V.B. Trindade, T. Staedler, X. Jiang, Thermodynamic aspects of diamond/β-SiC composite films. Chem. Vapor Deposit. **14**(3–4), 78–84 (2008). doi:10.1002/cvde.200706673
3. X. Jiang, C.P. Klages, R. Zachai, M. Hartweg, H.J. Fusser, Epitaxial diamond thin-films on (001) silicon substrates. Appl. Phys. Lett. **62**(26), 3438–3440 (1993). doi:10.1063/1.109041
4. C. Niu, G. Tsagaropoulos, J. Baglio, K. Dwight, A. Wold, Nucleation and growth of diamond on Si, Cu and Au. J. Solid State Chem. **91**(1), 47–56 (1991). doi:10.1016/0022-4596(91)90056-N
5. O.A. Williams, O. Douheret, M. Daenen, K. Haenen, E. Osawa, M. Takahashi, Enhanced diamond nucleation on monodispersed nanocrystalline diamond. Chem. Phys. Lett. **445**(4–6), 255–258 (2007). doi:10.1016/j.cplett.2007.07.091
6. V. Srikanth, T. Staedler, X. Jiang, Structural and compositional analyses of nanocrystalline diamond/beta-SiC composite films. Appl. Phys. Mater. Sci. Process. **91**(1), 149–155 (2008). doi:10.1007/s00339-007-4388-8
7. D.P. Malta, J.B. Posthill, T.P. Humphreys, R.E. Thomas, G.G. Fountain, R.A. Rudder, G.C. Hudson, M.J. Mantini, R.J. Markunas, Secondary electron emission enhancement and defect contrast from diamond following exposure to atomic hydrogen. Appl. Phys. Lett. **64**(15), 1929–1931 (1994). doi:10.1063/1.111745
8. V. Srikanth, M.H. Tan, X. Jiang, Initial growth of nanocrystalline diamond/β-SiC composite films: a competitive deposition process. Appl. Phys. Lett. **88**(7), 073109 (2006). doi:10.1063/1.2175478
9. Y.L. Zhao, R.Q. Zhang, V. Srikanth, X. Jiang, Possible gas-phase reactions of H_2/CH_4/tetramethylsilane in diamond/β-SiC nanocomposite film deposition: an ab-initio study. J. Phys. Chem. A **111**(18), 3554–3559 (2007). doi:10.1021/jp070014s

10. X. Jiang, V.V.S.S. Srikanth, Y.L. Zhao, R.Q. Zhang, Facet dependent reactivity and selective deposition of nanometer sized β-SiC on diamond surfaces. Appl. Phys. Lett. **92**(24), 243107 (2008). doi:10.1063/1.2944143
11. H. Zhuang, L. Zhang, T. Staedler, X. Jiang, Highly selective diamond and β-SiC crystal formation at increased atomic hydrogen concentration: a route for synthesis of high-quality and patterned hybrid diamond/β-SiC composite film. Scr. Mater. **65**(6), 548–551 (2011). doi:10.1016/j.scriptamat.2011.06.023
12. D.G. Goodwin, Simulations of high rate diamond synthesis—methyl as growth species. Appl. Phys. Lett. **59**(3), 277–279 (1991). doi:10.1063/1.105620
13. S.J. Harris, Mechanism for diamond growth from methyl radicals. Appl. Phys. Lett. **56**(23), 2298–2300 (1990). doi:10.1063/1.102946
14. F. Silva, A. Gicquel, A. Tardieu, P. Cledat, T. Chauveau, Control of an MPACVD reactor for polycrystalline textured diamond films synthesis: role of microwave power density. Diam. Relat. Mater. **5**(3–5), 338–344 (1996). doi:10.1016/0925-9635(95)00428-9
15. Y. Kawabata, J. Taniguchi, I. Miyamoto, XPS studies on damage evaluation of single-crystal diamond chips processed with ion beam etching and reactive ion beam assisted chemical etching. Diam. Relat. Mater. **13**(1), 93–98 (2004). doi:10.1016/j.diamond.2003.09.005
16. S. Kiyohara, Y. Yagi, K. Mori, Plasma etching of CVD diamond films using an ECR-type oxygen source. Nanotechnology **10**(4), 385–388 (1999). doi:10.1088/0957-4484/10/4/304
17. X. Jiang, E. Boettger, M. Paul, C.P. Klages, Approach of selective nucleation and epitaxy of diamond films on Si(100). Appl. Phys. Lett. **65**(12), 1519–1521 (1994). doi:10.1063/1.112030
18. Y.C. Chen, Y. Tzeng, A.J. Cheng, R. Dean, M. Park, B.M. Wilamowski, Inkjet printing of nanodiamond suspensions in ethylene glycol for CVD growth of patterned diamond structures and practical applications. Diam. Relat. Mater. **18**(2–3), 146–150 (2009). doi:10.1016/j.diamond.2008.10.004
19. A. Kromka, O. Babchenko, B. Rezek, M. Ledinsky, K. Hruska, J. Potmesil, M. Vanecek, Simplified procedure for patterned growth of nanocrystalline diamond micro-structures. Thin Solid Films **518**(1), 343–347 (2009). doi:10.1016/j.tsf.2009.06.014
20. O. Babchenko, T. Izak, E. Ukraintsev, K. Hruska, B. Rezek, A. Kromka, Toward surface-friendly treatment of seeding layer and selected-area diamond growth. Phys. Status Solidi B **247**(11–12), 3026–3029 (2010). doi:10.1002/pssb.201000124
21. S.K. Lee, J.H. Kim, M.G. Jeong, M.J. Song, D.S. Lim, Direct deposition of patterned nanocrystalline CVD diamond using an electrostatic self-assembly method with nanodiamond particles. Nanotechnology **21**(50), 505302 (2010). doi:10.1088/0957-4484/21/50/505302
22. N.A. Fox, M.J. Youh, J.W. Steeds, W.N. Wang, Patterned diamond particle films. J. Appl. Phys. **87**(11), 8187–8191 (2000). doi:10.1063/1.373516
23. J.L. Davidson, C. Ellis, R. Ramesham, Selective deposition of diamond films. J. Electron. Mater. **18**(6), 711–715 (1989). doi:10.1007/BF02657523
24. S. Mirzakuchaki, M. Hajsaid, H. Golestanian, R. Roychoudhury, E.J. Charlson, E.M. Charlson, T. Stacy, Selective area deposition of diamond thin films on patterns of porous silicon by hot filament chemical vapor deposition. Appl. Phys. Lett. **67**(24), 3557–3559 (1995). doi:10.1063/1.114920
25. Y. Sakamoto, M. Takaya, H. Sugimura, O. Takai, N. Nakagiri, Fabrication of a micro-patterned diamond film by site-selective plasma chemical vapor deposition. Thin Solid Films **334**(1–2), 161–164 (1998). doi:10.1016/S0040-6090(98)01136-5
26. H. Zhuang, B. Song, T. Staedler, X. Jiang, Microcontact printing of mono-diamond nanoparticles: an effective route towards patterned diamond structure fabrication. Langmuir **27**(19), 11981–11989 (2011). doi:10.1021/la2024428
27. V.V.S.S. Srikanth, T. Staedler, X. Jiang, Deposition of stress-free diamond films on Si by diamond/beta-SiC nanocomposite intermediate layers. Diam. Relat. Mater. **18**(10), 1326–1331 (2009). doi:10.1016/j.diamond.2009.07.007

28. V.S.S. Srikanth Vadali, H.A. Samra, T. Staedler, X. Jiang, Nanocrystalline diamond/β-SiC composite interlayers for the deposition of continuous diamond films on W and Mo substrate materials. Surf. Coat. Technol. **201**(22–23), 8981–8985 (2007). doi:10.1016/j.surfcoat.2007.04.018
29. V.V.S.S. Srikanth, X. Jiang, A. Koepf, Deposition of diamond/beta-SiC nanocomposite films onto a cutting tool material. Surf. Coat. Technol. **204**(15), 2362–2367 (2010). doi:10.1016/j.surfcoat.2010.01.008
30. V. Srikanth, *Deposition and Characterization of Nanocrystalline Diamond/β-SiC Composite Film System* (Shaker Verlag, Aachen, 2008)
31. N. Yang, H. Zhuang, R. Hoffmann, W. Smirnov, J. Hees, X. Jiang, C.E. Nebel, Nanocrystalline 3C-SiC electrode for biosensing applications. Anal. Chem. **83**(15), 5827–5830 (2011). doi:10.1021/ac201315q
32. S. Santavirta, M. Takagi, L. Nordsletten, A. Anttila, R. Lappalainen, Y.T. Konttinen, Biocompatibility of silicon carbide in colony formation test in vitro—a promising new ceramic THR implant coating material. Arch. Orthop. Trauma Surg. **118**(1–2), 89–91 (1998). doi:10.1007/s004020050319
33. C.M. Zettetling (ed.), *Process Technology for Silicon Carbide Device* (Institution of Electrical Engineers, London, 2002)
34. R.S. Sussmann (ed.), *CVD Diamond for Electronic Devices and Sensors* (Wiley-VCH, Weinheim, 2009)
35. L. Tang, C. Tsai, W.W. Gerberich, L. Kruckeberg, D.R. Kania, Biocompatibility of chemical vapor deposited diamond. Biomaterials **16**(6), 483–488 (1995). doi:10.1016/0142-9612(95)98822-V
36. R.T.W. Popoff, H. Asanuma, H.Z. Yu, Long-term stability and electrical performance of organic mono layers on hydrogen-terminated silicon. J. Phys. Chem. C **114**(24), 10866–10872 (2010). doi:10.1021/jp101595w
37. W.S. Yang, O. Auciello, J.E. Butler, W. Cai, J.A. Carlisle, J. Gerbi, D.M. Gruen, T. Knickerbocker, T.L. Lasseter, J.N. Russell, L.M. Smith, R.J. Hamers, DNA-modified nanocrystalline diamond thin-films as stable, biologically active substrates. Nat. Mater. **1**(4), 253–257 (2002). doi:10.1038/nmat779
38. B. Sun, P.E. Colavita, H. Kim, M. Lockett, M.S. Marcus, L.M. Smith, R.J. Hamers, Covalent photochemical functionalization of amorphous carbon thin films for integrated real-time biosensing. Langmuir **22**(23), 9598–9605 (2006). doi:10.1021/la061749b
39. V. Vermeeren, S. Wenmackers, M. Daenen, K. Haenen, O.A. Williams, M. Ameloot, M. Vandeven, P. Wagner, L. Michiels, Topographical and functional characterization of the ssDNA probe layer generated through EDC-mediated covalent attachment to nanocrystalline diamond using fluorescence microscopy. Langmuir **24**(16), 9125–9134 (2008). doi:10.1021/la800946v
40. S. Kuga, J.H. Yang, H. Takahashi, K. Hiirama, T. Iwasaki, H. Kawarada, Detection of mismatched DNA on partially negatively charged diamond surfaces by optical and potentiometric methods. J. Am. Chem. Soc. **130**(40), 13251–13263 (2008). doi:10.1021/ja710167z
41. S.A. Hanifah, L.Y. Heng, M. Ahmad, Biosensors for phenolic compounds by immobilization of tyrosinase in photocurable methacrylic-acrylic membranes of varying hydrophilicities. Anal. Sci. **25**(6), 779–784 (2009). doi:10.2116/analsci.25.779
42. H. Barhoumi, A. Maaref, N. Jaffrezic-Renault, Experimental study of thermodynamic surface characteristics and pH sensitivity of silicon dioxide and silicon nitride. Langmuir **26**(10), 7165–7173 (2010). doi:10.1021/la904251m
43. S. Zhang, H.J. Du, S.E. Ong, K.N. Aung, H.C. Too, X.G. Miao, Bonding structure and haemocompatibility of silicon-incorporated amorphous carbon. Thin Solid Films **515**(1), 66–72 (2006). doi:10.1016/j.tsf.2005.12.037
44. B. Janczuk, A. Zdziennicka, A study on the components of surface free-energy of quartz from contact-angle measurements. J. Mater. Sci. **29**(13), 3559–3564 (1994). doi:10.1007/BF00352063

45. S.C.H. Kwok, W. Jin, P.K. Chu, Surface energy, wettability, and blood compatibility phosphorus doped diamond-like carbon films. Diam. Relat. Mater. **14**(1), 78–85 (2005). doi:10.1016/j.diamond.2004.07.019
46. B. Menaa, M. Herrero, V. Rives, M. Lavrenko, D.K. Eggers, Favourable influence of hydrophobic surfaces on protein structure in porous organically-modified silica glasses. Biomaterials **29**(18), 2710–2718 (2008). doi:10.1016/j.biomaterials.2008.02.026
47. H. Zhuang, B. Song, V.V.S.S. Srikanth, X. Jiang, H. Schönherr, Controlled wettability of diamond/β-SiC composite thin films for biosensoric applications. J. Phys. Chem. C **114**(47), 20207–20212 (2010). doi:10.1021/jp109093h
48. Y. Ito, M. Heydari, A. Hashimoto, T. Konno, A. Hirasawa, S. Hori, K. Kurita, A. Nakajima, The movement of a water droplet on a gradient surface prepared by photodegradation. Langmuir **23**(4), 1845–1850 (2007). doi:10.1021/la0624992
49. A. Shovsky, H. Schonherr, New combinatorial approach for the investigation of kinetics and temperature dependence of surface reactions in thin organic films. Langmuir **21**(10), 4393–4399 (2005). doi:10.1021/la046967o
50. S.V. Roberson, A.J. Fahey, A. Sehgal, A. Karim, Multifunctional ToF-SIMS: combinatorial mapping of gradient energy substrates. Appl. Surf. Sci. **200**, 150–164 (2002). doi:10.1016/S0169-4332(02)00887-5
51. L.S. Cerivic, S.K. Milonjic, M.B. Todorovic, M.I. Trtanj, Y.S. Pogozhev, Y. Blagoveschenskii, E.A. Levashov, Point of zero charge of different carbides. Colloids Surf. A **297**(1–3), 1–6 (2007). doi:10.1016/j.colsurfa.2006.10.012
52. J. Zhang, H.P. Lang, G. Yoshikawa, C. Gerber, Optimization of DNA hybridization efficiency by pH-driven nanomechanical bending. Langmuir **28**(15), 6494–6501 (2012). doi:10.1021/la205066h

Chapter 3
Surface Chemistry of Diamond

Karin Larsson

Abstract The diamond material possesses very attractive properties, such as superior electronic properties (when doped), in addition to a controllable surface termination. During the process of diamond synthesis, the resulting chemical properties will mainly depend on the adsorbed species. These species will have the ability to influence both the chemical and electronic properties of diamond. All resulting (and interesting) properties of a terminated diamond surface, make it clear that surface termination is very important for especially those applications in which diamond can function as an electrode material. Theoretical modeling has during the last decades been proven to become highly valuable in the explanation and prediction of experimental results. Simulation of the dependence of various factors influencing the surface reactivity, will aid important information about surface processes including surface stability, modification and functionalization. Other examples include thin film growth mechanisms and surface electrochemistry.

3.1 Introduction

The diamond material possesses very attractive properties, such as high transparency, high thermal conductivity at room temperature, radiation hardness, as well as an extreme mechanical hardness. In addition, diamond also exhibits superior electronic properties (including high carrier mobility), large electrochemical potential window, low dielectric constant, controllable surface termination, and a high breakdown voltage. Furthermore, when considering the well-known combination of chemical inertness and high degree of biocompatibility [1], diamond became recently a promising candidate for applications like artificial photosynthetic

K. Larsson (✉)
Department of Materials Chemistry, Uppsala University, 75121 Uppsala, Sweden
e-mail: karin.larsson@kemi.uu.se

N. Yang (ed.), *Novel Aspects of Diamond*, Topics in Applied Physics 121,
DOI 10.1007/978-3-319-09834-0_3

water-splitting, where interfaces between a photo-electrode surface and a redox protein is of utterly importance [2]. Boron-doped diamond surfaces, with attached Pt nanoparticles as the catalytic surface, are nowadays working as a new class of electrode materials. The boron-doped diamond electrode is a semiconducting material with very promising properties like (i) a wider potential window in aqueous solution (approximately −1.35 to +2.3 V versus the normal hydrogen electrode), (ii) low background current, and (iii) corrosion stability in aggressive environments [3].

More generally, the intrinsic reactivity of a surface atom (for a solid material) depends of various factors, such as (i) number of binding atoms, (ii) surface reconstructing, (iii) type and degree of chemisorption to the surface, and (iv) elemental doping into the upper surface region. The number of bonding atoms to a surface atom (factor i) is always smaller than the binding situation for a bulk atom. Moreover, a surface atom has the driving force to become more bulk-like (i.e., the more preferred surrounding electron density is the one for a bulk atom). This is one explanation to the larger surface reactivity relative the bulk. Factors (ii)–(iv) do all represent changes in the surrounding electron density for the surface atoms, of which all are different from the situations for the bulk atoms.

It must here be stressed that the solid surface reactivity is not identical to the surface energy. When creating a surface by, for example, breaking the bonds along a specific crystallographic orientation (e.g., when breaking a thin Si substrate into smaller pieces by exerting a force onto the substrate), a certain number of Si–Si bonds (N) have to be broken in the formation of two surfaces. Let us now assume that the bond density is ρ_N Si–Si/cm^2. The energy/cm^2 that is needed for this Si wafer to be cracked into two pieces is thereby $\rho_N \times (\text{Si–Si})_{\text{bond energy}}$, with a corresponding surface energy (γ) of $\rho_N \times (\text{Si–Si})_{\text{bond energy}}/2$ kJ/mol for the surface of one of the resulting pieces. The $(\text{Si–Si})_{\text{bond energy}}$ is a direct measure of the surface reactivity. Hence, the surface energy considers both the reactivity and density of the surface atoms, whilst the surface reactivity only takes into consideration the atomic reactivity.

Theoretical modeling based predominantly on Density Functional Theory (DFT) has during the last decades proven to become highly valuable in the explanation and prediction of experimental results. The simulation and theoretical analysis of surface reactivity has been shown to aid important information about thin film growth mechanisms, as well as about surface reconstruction, modification and functionalization.

3.2 Methods and Methodologies

Theoretical modeling and simulations are tools that are often necessary in (i) the interpretation of experimental results, (ii) within precursor design of interface materials (i.e. the prediction of experimental parameters), and (iii) for theoretical

"experiments" where it is not possible to perform practical experiments. First-principle DFT calculations have become a useful tool for many inorganic materials of practical importance. It is well known that electronic structures and, especially, band gaps are sensitive to choice of theoretical method.

Moreover, chemical reactions where bonds are formed and/or broken need methods that consider the electrons in the system. Hence, the quantum mechanical DFT method is very useful for studies of e.g. surface stability, termination, functionalization and other types of surface (or interfacial) chemical processes.

The DFT calculations done for solid surfaces are most often performed under periodic boundary conditions. More specifically, ultrasoft pseudopotential [4] plane-wave approaches are most often used, based on the Perdew-Wang (PW91) generalized gradient approximation (GGA) [5] for the exchange-correlation functional. The GGA method usually gives a better overall description of the electronic subsystem, compared to the more simple LDA (local density approximation) corrections. The reason is that LDA, which is based on the known exchange-correlation energy of a uniform electron gas, is inclined to overbind atoms and to overestimate the cohesive energy in the system under study. On the contrary, GGA takes into account the gradient of the electron density, which gives a much better energy evaluation [6]. The total energy obtained from a DFT-calculation, and for a specific model, can further on be used in e.g. the calculations of reaction energies.

The atomic charges and bond electron populations (i.e. electron densities within the bond), might be estimated by using the methods of Mulliken analysis, which can be performed by using a projection of the plane wave states onto the localized basis by a technique described by Sanchez-Portal et al. [7]. The calculated atomic charges, electron density (ρ), Fukui function and information about bond electron populations are important tools in the interpretation of the underlying causes to the observed surface reactivities, and the resulting surface properties.

The Fukui functions of the surface area generally used in visualizing the surface reactivity. Parr and Yang [8, 9] improved the frontier orbital theory introduced by Fukui [10, 11], whereby it became possible to calculate the so-called Fukui functions:

$$f(r) = \left(\frac{\delta\rho(r)}{\delta N}\right)_V \tag{3.1}$$

where N is the total number of electrons in the system, and ρ(r) is the electron density at a certain position and at a fixed external potential, V. There is three Fukui functions defined as f^0, f^+, and f^-, which correspond to a surface reactivity towards radical, electrophilic and nucleophilic attack, respectively. Previous work has shown that this f^0 function can be very useful in studying the surface reactivity of diamond [12]. The atomic charges can also be carefully estimated to give information about degree of ionic bond strengths, whilst the bond populations contribute with covalent bond strength information.

3.3 Reactivity of Different Diamond Surface Planes

One of the factors that are decisive for the surface reactivity of diamond is the number of binding atoms for a surface atom. The resulting chemical properties will mainly depend on the number of unpaired electrons at the surface (i.e., dangling bonds). A bulk diamond C atom has four covalently binding C neighbors in sp^3 hybridization. For the most commonly observed diamond facets, the (111) surface atoms will only have three binding neighbors whilst the (100) atoms have two (Fig. 3.1a, b). When instead describing the situation in terms of dangling bonds, a (111) surface atom has only 1 dangling bond whilst the (100) counterpart has 2.

Hence, the (100) surface should be more reactive. However, the presence of dangling bonds will also most often result in surface reconstruction, solely with the purpose to lower the surface energy. Therefore, the diamond (100) surface will most often undergo a surface reconstruction forming a 2 × 1 surface structure (Fig. 3.1c). As a matter of fact, also the more ideal (111) surface will at higher temperatures be transferred to a 2 × 1 reconstruction, called the Pandey chain structure (Fig. 3.1d).

The relative energies for these surface structures have earlier been calculated theoretically using careful DFT methods [13]. It was shown that the 2 × 1 reconstruction of the bare diamond (100) surface will result in a stabilization of the total energy by 1.85 eV per surface C. The corresponding energy stabilization for the bare diamond (111) surface (i.e. to the Pandey chain structure) was 0.54 eV per

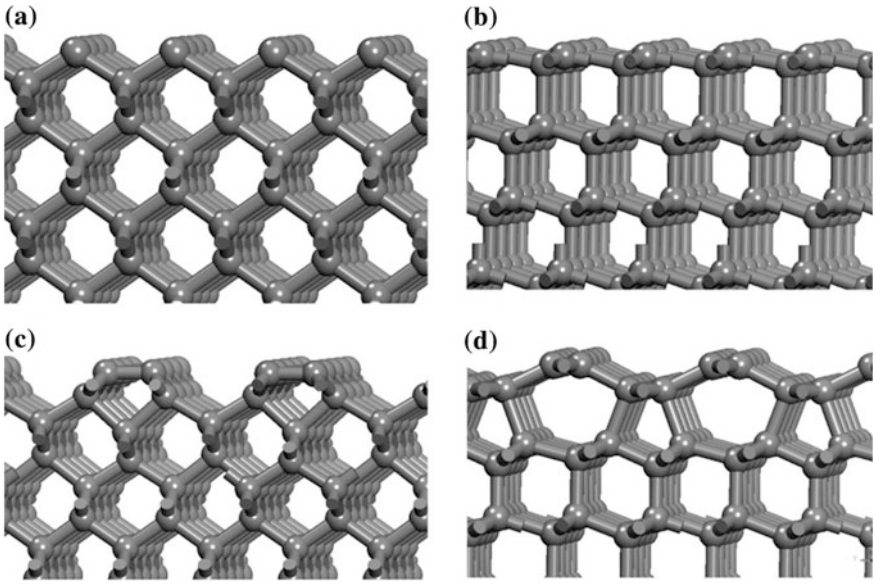

Fig. 3.1 Final structures of 1 × 1-reconstructed diamond (111) and (100) surfaces (**a**, **b**), in addition to bare 2 × 1-reconstructed diamond (111) and (100) surfaces (**c**, **d**)

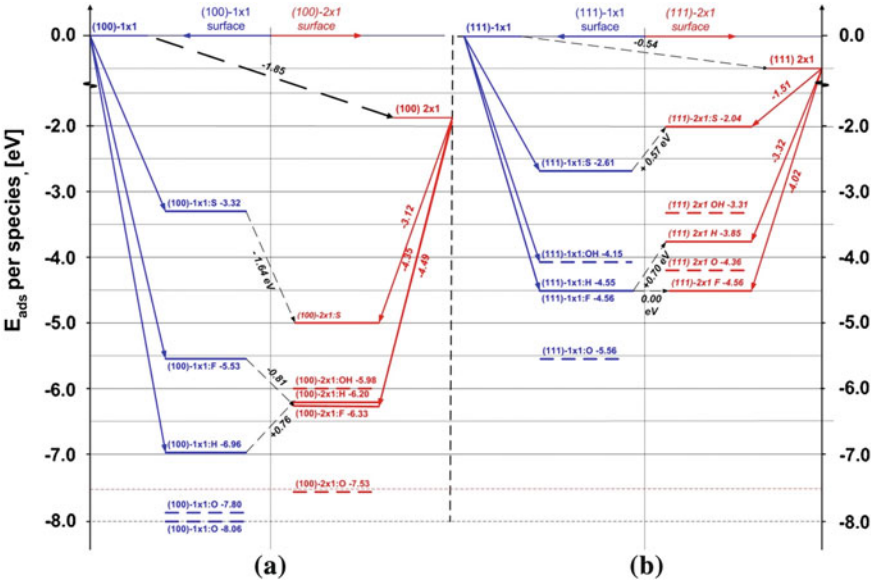

Fig. 3.2 Adsorption energies for various terminating species (H, OH, O, F and S) onto (1 × 1)- and (2 × 1)-reconstructed diamond (100) (**a**) and (111) (**b**) surfaces [13]. Reprinted with permission from Journal of Physical Chemistry C. Copyright 2008, American Chemical Society

surface C (see Fig. 3.2). These stabilization energies will not, however, say anything about the kinetics of the transfer from, e.g., the ideal diamond (100)−1 × 1 structure to diamond (100)−2 × 1. However, the barrier of energy for the transfer between these phases has also been calculated earlier, using very careful DFT calculations.

As can be seen in Fig. 3.3, a very small barrier of energy (of 0.32 eV) was found for the transfer from a bare (111)−1 × 1 surface to the slightly more stable Pandey chain structure—(111)−2 × 1. This tiny activation energy has recently been justified by the usage of ab initio molecular dynamic (MD) simulations in heating up the diamond (111)−1 × 1 surface to a temperature of about 500 K [14].

3.4 Effect of Co-adsorption on Diamond Surface Reactivity

3.4.1 General

Generally, the chemisorption of atoms (or molecules) to the diamond surface will lower the surface energy values. The reactivity of the remaining surface radical C sites will decrease, which most probably will have an effect on both chemical surface processes, as well as on the properties of the surface. Chemical surface

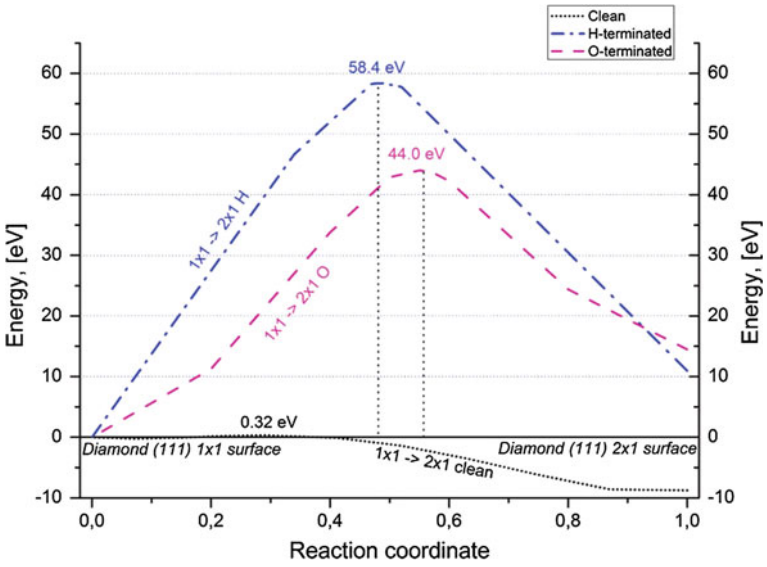

Fig. 3.3 Calculated activation energies for transformation between diamond (111) (1 × 1) and (2 × 1) structures as a function of surface termination with H and O, respectively [13]. Reprinted with permission from Journal of Physical Chemistry C. Copyright 2008, American Chemical Society

processes is a very broad term that include processes like growth, functionalisation and anchoring to larger molecules (just to mention a few).

Despite the efficiency in upholding the cubic structure of the diamond surface, different types of surface termination species have been shown to change the properties of the diamond surface region (e.g., by inducing surface electronic conductivity and interfacial charge transfer properties). Another example of properties that may be affected by chemisorption is the field emission characteristics. The electronegativity of the chemisorbed species will thereby influence the emission current and threshold voltage [15]. The phenomena of diamond surface termination have experimentally also been observed to significantly influence the broad-band infrared reflectivity [16]. Hydrogen-terminated diamond surfaces have been found to be hydrophobic [17], and to show unique p-type surface electronic conductivity [18]. On the other hand, oxygen-terminated diamond surfaces generally show hydrophilic properties [17], and exhibit positive electron affinity [19]. In addition, OH-terminated surfaces can be formed during etching in a mixture of oxygen and water vapor [20]. Fluorine-termination will, compared to H-termination, result in even more strongly hydrophobic diamond surfaces, and have also recently been found to enhance the sp^3 characteristics of the diamond upper C layer (thereby improving the geometrical structure of this surface [21]). All these interesting properties of terminated diamond surfaces make it clear that surface termination is very important for especially those applications were diamond can function as an electrode material.

3.4.2 Energetic Stability of Surface Termination

3.4.2.1 General

The adsorption energies for gaseous species, chemisorbed onto the diamond (111) and (100) surfaces at different surface coverage, are presented in different plots where the adsorption and stabilization energies are shown over the whole range (0–100 %) of surface coverage (see Figs. 3.4, 3.5 and 3.6). Starting from 100 % hydrogen coverage, these plots show the successive adsorption energies as hydrogen are replaced with oxygen, or hydroxyl groups.

The stabilization energy is defined as the adsorption energy for all species on the diamond surface compared to the total adsorption energy for a 100 % H-terminated surface. A surface configuration with negative relative stabilization energy is hence more favorable than the situation with a 100 % H-terminated surface.

3.4.2.2 Hydrogen-Termination

A clean surface was the starting point for the hydrogen adsorption studies. As can be seen in Fig. 3.4, the clean (111)−2 × 1 surface is energetically more favorable than the corresponding 1 × 1 reconstruction. However, when 5/16 of the surface

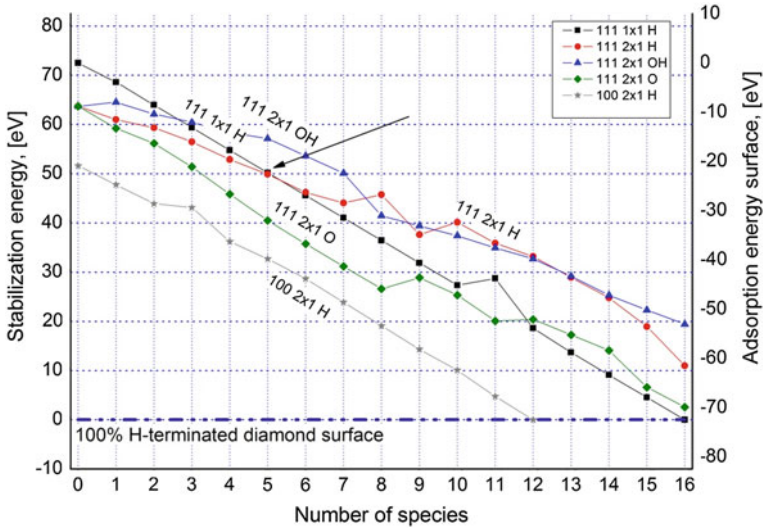

Fig. 3.4 The adsorption profiles for the (i) successive hydrogen chemisorption to bare diamond (111) and (100) surfaces, and the (ii) successive hydrogen replacements by oxygen (both bridged and on-top positioned) and OH groups. *Left axis* is the stabilization energy that relates the adsorption energy (*right axis*) to a 100 % H-terminated surface [13]. Reprinted with permission from Journal of Physical Chemistry C. Copyright 2008, American Chemical Society

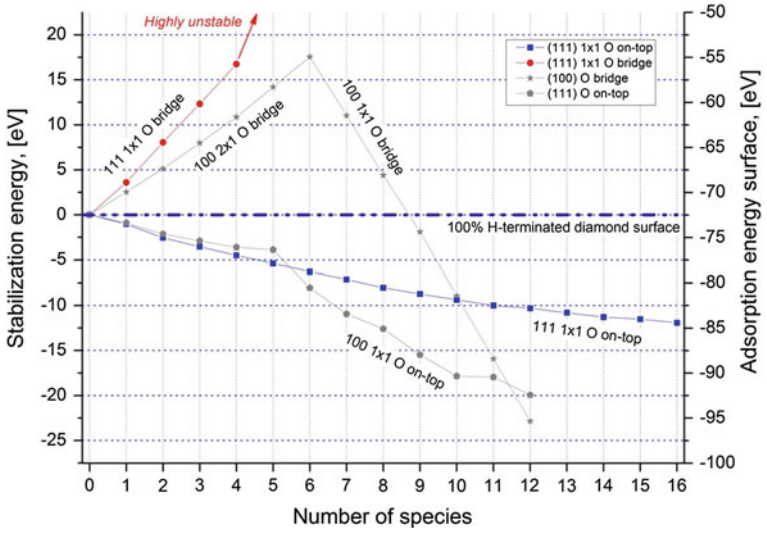

Fig. 3.5 The adsorption profiles for the successive hydrogen replacements by oxygen (both bridged and on-top positioned) and OH groups. *Left axis* is the stabilization energy that relates the adsorption energy (*right axis*) to a 100 % H-terminated surface [13]. Reprinted with permission from Journal of Physical Chemistry C. Copyright 2008, American Chemical Society

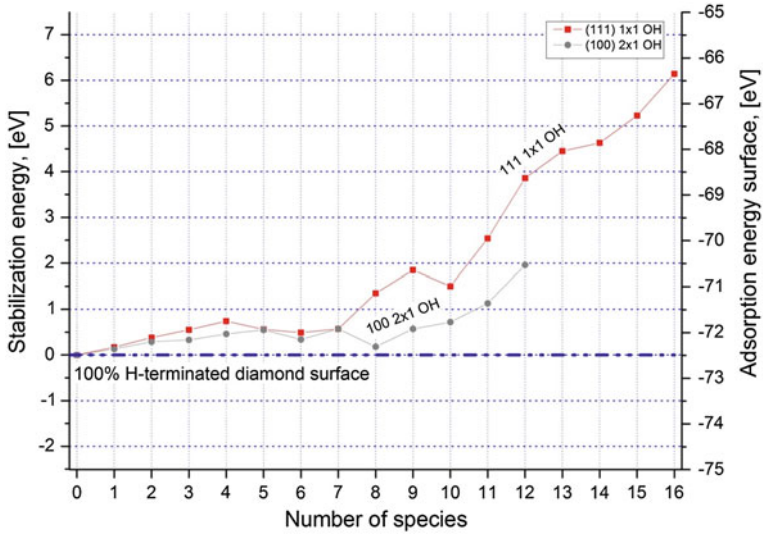

Fig. 3.6 Calculated stabilization and adsorption energies, for both diamond (111) and (100) surface, for the situation when surface-terminating H species are successively replaced with O in either on top or bridge positions [13]. Reprinted with permission from Journal of Physical Chemistry C. Copyright 2008, American Chemical Society

becomes H-terminated, both the partially H-terminated 1 × 1 and 2 × 1 surfaces show identical energies. The (111)−1 × 1 is more favorable for hydrogen coverage above 30 %. In fact, a small number of hydrogen atoms on the diamond surface may reconstruct the (111)−2 × 1 to the 1 × 1 configuration [22]. A LEED pattern showed that 0.05 ML would effectively reconstruct the (111)−2 × 1 surface to the 1 × 1 reconstruction. The unfavorable adsorption energy for a 100 % H-terminated (111) −2 × 1 is coherent with other DFT studies [23, 24]. A 100 % hydrogen-terminated (111)−2 × 1 surface was shown to be stable towards reconstruction, but with lower adsorption energies compared to the 1 × 1 surface (+0.69 eV per H). Hence, hydrogen stabilizes the carbon atoms of the Pandey chain less compared to the 1 × 1 surface. A plausible explanation may be that the delocalized π-bonds of the Pandey chain are weakened. Hence, the electron configuration that stabilized the clean Pandey chain becomes perturbed. However, the value of the adsorption energy for hydrogen on the diamond (100) 1 × 1 surface is surprisingly high (−6.96 eV). Two hydrogens per carbon atom, were chemisorbed onto the surface to saturate the two dangling bonds per surface carbon atom. Hence, hydrogen must be present on the (100)−1 × 1 surface to uphold the sp^3 configuration and to prevent the 2 × 1 reconstruction.

This dihydride configuration has been under much speculation [25–29], but it is generally accepted [30] that it does not occur during CVD growth conditions. Nevertheless, a very successful model attempting to describe growth mechanisms has been based on this dihydride configuration [31]. The very favorable adsorption energy for the dihydride surface configuration is probably not seen experimentally due to the favorable (and spontaneous) 2 × 1 reconstruction. Hence, two hydrogen atoms, per surface carbon, adsorbed onto the diamond (100)−1 × 1 surface are not realistic due to the faster reconstruction to the 2 × 1 surface. The adsorption energy for hydrogen on the (100)−2 × 1 surface (−4.30 eV) is in excellent agreement with experimental investigations [32]. The adsorption energy for H on an otherwise 100 % H-terminated (111)−1 × 1 (and 2 × 1) surface has in two different studies been calculated to −4.15 (−3.45) [24] and −4.98 (−4.34) [23] eV, respectively. The results obtained in the former study (using molecular dynamics based on LDA) are more in agreement with these observations; −4.53 (−3.29) eV.

3.4.2.3 Oxygen-Termination

Oxygen atoms often stabilize a hydrogen-terminated surface. In addition, due to the divalent nature of oxygen and its strong electronegativity value, it may break the C–C double bonds and induce a surface reconstruction. As presented in Fig. 3.5, a high coverage of oxygen (in both the on-top and bridge positions) yielded a reconstruction of the (100)−2 × 1 surface into a bulk-equivalent 1 × 1 configuration. The most favorable position for oxygen on the (100) surface seems to be the bridge position which is supported by other experimental and theoretical studies [32–34]. In addition, the surface morphology will change and yield more oxygen in the on-top positions at elevated temperatures. An initial H–C–O–C–H surface configuration has been proposed as a plausible oxidation mechanism [35]. However, other

studies have shown that the on-top position is more likely to occur, but with a rather small difference in adsorption energy [36].

The spontaneous reconstruction from (100)−2 × 1 to (100)−1 × 1 was observed in Fig. 3.4. This implies that no activation barrier can be present, since DFT is a 0 K method. Conversely, no surface reconstruction was observed because of oxygen adsorption on the (111)−2 × 1 surface. Hence, the fully oxygen-terminated (111) −2 × 1 to (111)−1 × 1 reconstruction is associated with an activation energy. Furthermore, the on-top and bridge oxygen atoms were not stable for the 2 × 1 and 1 × 1 reconstruction, respectively. An oxygen coverage above 50 % on the (111) −2 × 1 surface resulted in a removal of the ether configuration and an introduction of rather strong O–O bonds. Although the total adsorption energy continued to decrease, the adsorption energy per species increased (i.e., became unfavorable) from −5.74 to −4.37 eV. In fact the adsorption energy per species of the eight oxygen atoms on the Pandey chain was found to be more favorable than for the situation with the 1 × 1 surface (−5.74 vs. −5.68 eV), even though the resulting order of energies became reversed at 100 % coverage (−4.37 vs. −6.21 eV) [13]. In addition, experimental results have shown that CO desorption from the (111)−2 × 1 surface involves 50 % of the surface carbon, i.e., a 50 % oxygen coverage was expected [23].

3.4.2.4 Hydroxyl-Adsorption

The adsorbed OH-groups showed both adsorbate-adsorbate interactions through hydrogen bonding (energy stabilization) and steric repulsion (energy de-stabilization). The hydrogen bonding is noticeable at low OH coverage, whereas steric-repulsion dominates at higher coverage. However, OH-groups may not induce a surface reconstruction due to the mono-valent character of the oxygen atom in the hydroxyl species. The amount of electrons that may be withdrawn, and reallocated, is larger for oxygen atoms compared to hydroxyl groups. The destabilization of hydrogen- terminated surfaces due to hydroxyl group adsorption, is supported by an experimental study that reports small number of hydroxyl groups present on an oxygenated (100) surface [32]. Hydrogen bonding enthalpies of −0.15 eV were reported. The adsorption energies for the hydroxyl groups on the Pandey chain are unfavorable up to a 30 % coverage (see Fig. 3.6). A severe weakening of the π-bond chain, as well as absence of hydrogen bonding, is probably responsible for this effect. A nine carbon cluster MP2-calculation on OH-terminated diamond (100) surfaces resulted in an adsorption energy of −3.3 eV per OH for a 100 % surface coverage. This value is somewhat higher compared to −4.1 eV found in this work [37]. Another DFT study for the diamond (111) surface has reported on OH adsorption energies of −4.2 (−4.0) eV for the 1 × 1 (and 2 × 1) reconstruction. Hence, the adsorption energies are in good agreement for the 1 × 1 surface (0.1 eV difference), but the 2 × 1 Pandey chain shows much larger adsorption energies compared to the results presented herein [23].

3.4.2.5 Fluorine-, Sulfur- and Chlorine-Adsorption

The adsorption of hydrogen, fluorine, sulfur and chlorine onto diamond (100) and (111) in their most common surface reconstructions, 1 × 1 and 2 × 1, was studied in [13]. Only 100 % terminated surfaces were considered, and the resulting adsorption energies are shown in Fig. 3.2. Fluorine is the termination species that most resembles hydrogen; mono-valent with a rather small covalent radius. Moreover, due to the strong anti-bonding occupancy of the electrons within the fluorine molecule, the F–F bond enthalpy is very low compared to Cl–Cl; 159 versus 243 kJ/mol. Conversely, the bond enthalpy of HF is greater than for HCl (574 vs. 431 kJ/mol). Hence, fluorine molecules may more readily dissociate into atoms than chlorine molecules. The large HF bond enthalpy may induce a fluorine desorption process and, hence, yield additional radical sites for diamond growth precursors. Hence, fluorine may be involved both in the gas phase and on the surface in diamond growth. Fluorine has been found to be strongly adsorbed to all of the studied diamond surfaces (−5.53, −6.33, −4.56 and −4.56 eV for the (100)−1 × 1, (100)−2 × 1, (111)−1 × 1 and (111)−2 × 1 surfaces, respectively). Although the diamond (100)−1 × 1 surface has two unpaired electrons, two fluorine atoms per carbon (difluoride configuration) atom was in [13] found to be highly unstable. Half of the fluorine-carbon bonds were severely weakened with C–F bond-lengths of more than 2 Å. The diamond (100)−1 × 1 surface reconstructs to a 2 × 4 pattern due to the mono-valent F, i.e., C–C bonds formed and F atoms were aligned in a perfect, bulk diamond equivalent, 1 × 1 pattern. Sterical repulsions between the adsorbed fluorine atoms as well as the electron withdrawal power of fluorine, rendering underlying C–C bonds less rigid compared to e.g., monohydride (100)−2 × 1 surface, are plausible reasons for this reconstruction.

Sulfur atoms could be adsorbed onto the surface, but showed small adsorption energies despite the divalent character of sulfur. Sulfur is probably too large for strong C–S bonds to occur and steric S–S repulsions became pronounced. Noteworthy, the most favorable sulfur adsorption energies are observed at the (100) surface, and especially for the 2 × 1 surface reconstruction. This is expected due to the larger intrinsic reactivity of the (100) surface compared to the (111) surface. The larger adsorption energy for the (100)−2 × 1 surface reconstruction is probably influenced by the formation of sulfur-sulfur bonds on this surface. The geometry of the (100)−2 × 1 surface will probably allow a better orbital overlap compared to other surfaces, except for the Pandey chain, where comparable S–S bond lengths were found. However, the S–C bonds lengths present on the Pandey chain surface were found to be very long, and, thus, weak. Conversely, a stable 100 % coverage of chlorine could only be found for the Pandey chain. However, the adsorption energy is very weak (−0.18 eV) and desorption is expected at higher temperatures. Some chlorine was desorbed for the (100)−1 × 1 and (111)−1 × 1 surface as a result of geometry optimization. Hence, no adsorption energy for a full coverage could be obtained.

As seen in Fig. 3.2, the general trend in adsorption energy strength is S < Cl < OH < H < F < O. Oxygen and fluorine atoms form very strong bonds with

the carbon atoms on the diamond surfaces. However, fluorine does not induce any larger reconstructions, except for the (100)−1 × 1 surface as described above. The adsorption energies for the OH-groups indicate that C–O bonds are more favorable than C–O–H bonds, despite potential hydrogen bonding. Sulfur atoms at 100 % coverage generally bind very weakly to the (111) surfaces (−2.61 eV and −1.54 eV), compared to the (100) surfaces (−3.32 eV and −3.12 eV). As described above, chlorine shows no, or very little, tendency to cover the surface totally due to the size of the chlorine.

3.5 Size Effects

It is a well-known effect that surface chemical properties will be affected by the combination of surface plane and termination (e.g. H-termination gives surface conductivity). Nano-crystalline diamond has a large amount of (111) and (100) morphologies (i.e. terraces). Hence, the size effect of adsorption energies of H has just recently been calculated for various diamond planes, and various nano-crystalline particle sizes [38]. It was shown the DFT and the semi-empirical VAMP methods are most successful in modeling the H adsorption energy (as compared to Tight-binding DFT (DFTB+)). For a diamond particle diameter of 7 Å, the adsorption energies for the adsorption of H are −390, −438, and 658 kJ/mol for VAMP, DMol3 and DFTB, respectively. The experimental value is −413 kJ/mol. Hence, it is here assume that the DFT method is accurate enough to be used in the present type of investigation.

In studying the size effect for one-dimensional confinement (i.e., in studying thin films of various thicknesses), it was shown that a thickness greater than approximately 7 Å will give a constant surface reactivity towards chemisorption of H onto diamond (111) or (100) (see Fig. 3.7 for diamond (100)).

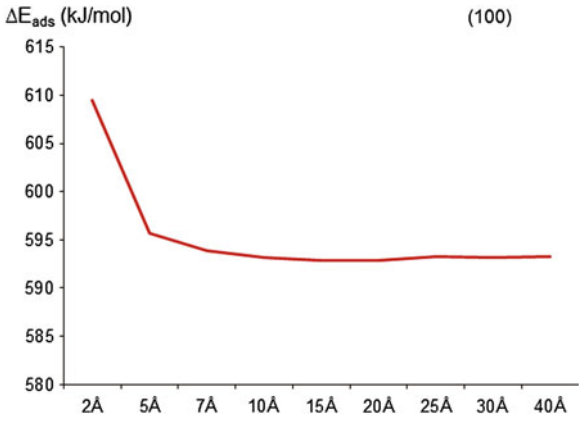

Fig. 3.7 Effect of film thickness, on the absolute H adsorption energy, for the diamond (100) surface. The (111) surface show an almost identical trend

Three-dimensional confinement has shown that the adsorption energy of H will decrease with size, reaching a more or less constant value at a particle diameter of 7–10 Å. Hence, diamond particle sizes of more than 1 nm in diameter, will not show any size dependency when it comes to chemical adsorption of species to the surface. In other words, it is possible to model these larger particle sizes by using periodic modeling of terraces.

3.6 Doping Effects

3.6.1 General

Although diamond has been proven to be a genuine multifunctional material, thereby useful for quite many applications, it is still quite expensive to grow it using vapor phase methods like CVD. However, it has been experimental proven that e.g. N doping will enhance the diamond growth rate, and thereby reduce the production costs. The influence of nitrogen on the deposition rate has already been reported for both poly- and mono-crystalline diamond [39–42]. Recently, the catalytic effect by N on the CVD diamond growth rate enhancement has been studied using laser reflection interferometry [43]. In addition, gaseous N concentrations as low as a few ppm, were found to strongly boost up the crystal growth rate in the (100) orientation. As an explanation to this observation, Bar-Yam and Moustakas proposed a defect-induced stabilization of diamond [44]. However, this model does not explain the crystal orientation dependence of the increase in growth rates. More recently, Frauenheim et al. suggested an alternative model, in which donor electrons originating from sub-surface N will lead to a lengthening of the (100) surface reconstruction bond [45].

Nitrogen (with its extra electron compared to C) is a well-known n-type dopant, with a very deep donor level in diamond (1.7 eV below the lower edge of the conduction band) [46]. In choosing a suitable donor for diamond one has, however, not only to consider its donor level but also its solubility and mode of incorporation (e.g., incorporation during growth by in-diffusion or by ion implantation). Impurities have been shown to become introduced into diamond during CVD or HPHT growth [47]. Several reviews have, in addition, been reporting doping by implantation [48]. A substitutional n-type doping of diamond *during growth* has been of a special interest to study in the present investigation. The resulting substitutional doping will, hence, depend not only on the solubility of the impurity, but will also depend on the kinetics of the growth. Kinetic trapping may then be possible although the final n-type doped product is thermodynamically somewhat unfavorable.

The Chemical Vapor Deposition (CVD) of diamond is a very complex and dynamic process. The growing surface has to be terminated with e.g. H atoms, since it will otherwise collapse to the graphitic phase. However, these terminating species

must be abstracted away from the surface to leave room for a growth species (e.g. CH_3). However, in the initial part of the diamond growth process, the abstraction of two surface H (terminating the surface and one of the H ligands on CH_3) has to take place before any surface migrating can take place, ending with a final incorporation at a step edge. Hence, the process of H abstraction is a very important reaction step during the overall diamond growth mechanism. Since it is an endothermic reaction (or close to), whilst the adsorption of e.g. CH_3 highly exothermic (−40 to +17 vs. −348 kJ/mol), it is here assumed that the H abstraction is one of the rate-limiting steps for the diamond growth process.

It is experimentally very difficult to determine in which form N will be efficient in the diamond growth process. To be more specific, it is experimentally not possible to discriminate between the effect of nitrogen in the form of an N-containing species adsorbed on the surface, or as N substitutionally positioned within the upper part of the diamond surface. For this purpose, high-level DFT calculations have been proven to be most useful. In addition to the growth enhancement effect of the N doping, it has also been shown possible to steer towards the growth of diamond (100) [49].

3.6.2 H-Abstraction Rates for Growth of Non-doped Diamond

The H abstraction process has been found to take place in two steps; (1) adsorption of H to a surface-terminating H species, and (2) desorption of molecular H_2 [50]. The energy barriers for these steps were thereby calculated for three different H-terminated diamond planes; (100)−2 × 1, (110) and (111). When studying step 1 in the abstraction process, the numerical values of the respective energy barriers became quite different for the various surface planes (12, 6 vs. 5 kJ/mol). Despite of the variations in energy evolution for the incoming H radical to the surfaces, each of these three planes showed a final energy minimum at a distance of 1.2–1.4 Å from the surface-binding H species. At this distance, the H radical is interacting with the H adsorbate, but to various extents depending on surface plane (as can be seen in Fig. 3.8).

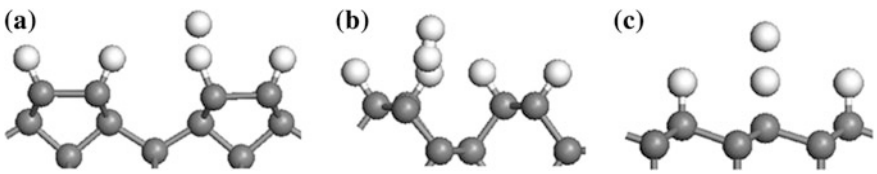

Fig. 3.8 Structural geometries at the energy minima for an approaching H radical to a surface-terminating H species, on the following different diamond planes; (100)−2 × 1, (110) and (111)

When the approaching H comes close enough to the adsorbed H, an electron population will be observed between the approaching H and the terminating one, being a strong indication of an H–H interaction in the form of bond covalency. For the (110) surface, this bond population will continue to increase as the H–H distance becomes smaller (with a simultaneous decrease in bond population for the C–H bond), with the final formation of gaseous H_2 (see Fig. 3.8b). The resulting value of bond population for H–H in H_2 is much larger than the electron bond population for the final C–H entity (0.73 vs. −0.04), indicating the C–H bond has been broken completely. However, it is only the approach of a radical H to the diamond (110) surface that will immediately result in the release of H_2. For the other two planes, the energy minima correspond to electron populations in both the H–H and C–H "bonds". As will be discussed below, an energy barrier has to be overcome for the H_2 molecule to be able to leave the diamond (111) and (100)−2 × 1 surfaces.

Step 2 in the abstraction process, which involve the removal (i.e. desorption) of H_2 from the surface, was found to take place with either zero energy barrier (for diamond (110) since the approaching H radical will directly induce the removal of H_2 from the surface), or with a smaller energy barrier as compared with step 1; (111)—3 versus 5 kJ/mol, and (100)−2 × 1—6 versus 12 kJ/mol. It is thereby obvious that the barrier energies for desorption of H_2 (step 2 in the desorption process) are smaller than for the adsorption of the approaching radical H (step 1). Hence, it is only the adsorption part of the abstraction process which will be the dominating one in determining the H abstraction reaction rate.

In addition to the barrier energies for the different H abstraction processes, Table 3.1 gives information about the relative growth rates (with respect to the slowest one) under the assumption that H abstraction is a rate limiting growth step. It is thereby only the barrier for the approaching H radical that has been used for the rate estimations. The Arrhenius relation has been used in order to make a careful estimation of the growth rate ($v = v_0 \cdot e^{-\Delta E/RT}$), under the assumption that the pre-exponential factor, v_0, is almost identical for the different surface planes. T is the temperature during diamond growth; R is the universal gas constant, and ΔE is the barrier of energy for the abstraction process. The relative H abstraction rate, and thereby relative diamond growth rate, can be rewritten as $v_1/v_2 = e^{(\Delta E2 - \Delta E1)/(RT)}$.

In addition to calculated values, also experimentally determined growth rates for the various diamond planes are presented in Table 3.1. Chu et al. investigated the growth of different diamond planes, and also presented different kinetic curves for

Table 3.1 Comparison between experimental and theoretical growth rates for the surface planes (110), (111) and (100), respectively

Plane	Growth rate (μm/h)	Relative growth rate (experimental)	Energy barrier (kJ/mol)	Relative growth rate (theoretical)
110	0.24	1.9	4.73	2.4
111	0.19	1.4	6.06	2.0
100	0.13	1.0	11.83	1.0

All values are related to the smallest growth rate (i.e. for (100))

each plane [51]. For this purpose, they used a hot-filament CVD technique at a substrate temperature of 600–1,000 K, together with a methane mole fraction of 0.4 %. Chu et al. used surface kinetic control during CVD growth of diamond, which means that the diamond growth rate will be determined by the activation energy of the rate determining step. This circumstance makes it ideal to add theoretical modeling and simulations for support and explanations. As can be seen in Table 3.1, the experimental diamond growth rates at 700 °C were found to be 0.13, 0.19 and 0.24 μm/h for diamond (100), (111) and (110), respectively. These absolute values correspond to the relative numbers 1.0, 1.4 versus 1.9.

As can be seen in Table 3.1, the experimentally observed trend in diamond growth rate is identical to the order of H abstraction rates, as carefully estimated from our theoretical calculations; (100) < (111) < (110). There are though some minor differences when comparing the experimental and theoretical relative rates strictly numerically. However, considering the large number of parameters that may influence the growth rate experimentally, these small differences are acceptable. Moreover, the large similarity in relative H abstraction rates with relative experimental growth rates, will strongly support the conclusion that H abstraction is indeed a rate-determining step in the growth mechanism of diamond (111), (100) and (110). When comparing experimental results with calculated ones, the identity in trends and large similarity in numerical values will furthermore justify the theoretical method and methodology used.

3.6.3 H-Abstraction Rates for Growth of N-Doped Diamond

3.6.3.1 General

As was presented above, the introduction of nitrogen into the CVD reaction chamber has been found to induce an increased diamond growth rate. For instance, Dunst et al. was studying the effect of diamond growth by introducing nitrogen into a microwave plasma-activated CVD reactor in depositing single crystalline diamond (100) at 800 °C [40]. The results of that study as that the introduction of N_2 will improve the diamond growth rate with a factor of approximately 2.5 at a CH_4 concentration of 2 %. However, the underlying cause to this growth improvement was not clear; Did N has this effect when incorporated into the diamond lattice, or was the effect induced by chemisorbed N-containing species? The main advantage with theoretical DFT calculations is that surface processes, including the breakage and formation of bonds, will be most carefully simulated. A deeper level of knowledge, about the influence by nitrogen onto the diamond growth rate, can thereby be obtained. The nitrogen dopant was, in [50], either substitutionally positioned into the upper diamond lattice, or chemisorbed onto the surface in the form of NH or NH_2 (the former being a radical).

3.6.3.2 N Substitutionally Positioned into Various C Atomic Layers

The effect by substitutionally positioning N within different C atomic layers close to the surface, were also evaluated in [50]. For this purpose, both the H adsorption energy and surface H abstraction energy were calculated for both diamond (111) and (100)−2 × 1 surface planes. As can be seen in Fig. 3.9, these two surfaces show completely different behavior. However, the trends for H adsorption energy (Fig. 3.9a) and H abstraction energy (Fig. 3.9b) show, as expected, similar, but mirrored, results. For the (100)−2 × 1 surface, there are peaks in the adsorption curves for the position of N within C layers 2 and 3 in the upper diamond surface. Hence, the H adsorption process becomes less energetic feasible, whilst the H abstraction becomes much more exothermic.

Two different factors have in the present study been found to be responsible for this effect. When positioning N within the second, or third, atomic C layer in an otherwise completely H-terminated diamond (100)−2 × 1 surface, the extra electron in N will occupy the anti-bonding state within one N–C bond. This will result in the breakage of the N–C bond, which, however, will re-bind again after the H abstraction from the surface (with the formation of an electron pair at the vacant surface position). This rather severe surface reconstruction is not possible to take place when positioning N further down in the diamond surface (from the fourth atomic layer, and deeper below). From this explanation it is clear that N naturally will improve the abstraction process, and to show a negative effect on the adsorption process. For the H adsorption process, the values are the following; −458 (non-doped) to −319 (N in 2nd layer) kJ/mol. The corresponding values for the surface H abstraction process are −41 (non-doped) to −138 (N in 2nd layer) kJ/mol.

For the diamond (111) surface, it is obvious that the N element will have a strong effect for the C surface layers 2–5. Numerically, these dopant effects are of the same size for all layers. For the H adsorption process, the values are the following; −434 (non-doped) to −349 (N in 2nd layer) kJ/mol. The corresponding values for the surface H abstraction process are 19 (non-doped) to −165 (N in 2nd layer) kJ/mol. For this specific diamond surface, the only dopant effect is the electron transfer towards the C(surface)–H bond, thereby weakening it. As was also the situation with the (100)−2 × 1 surface, an electron pair will be formed on the radical C atom as a result of the H abstraction process. There is a clear indication that this effect also will become less pronounced with an increase in distance from the surface.

3.6.3.3 N Substitutionally Positioned Within the C Atomic Layer 2

Nitrogen, substitutionally positioned within the second C layer of various diamond surface planes, was in [50] chosen since it was found that this is a position that has a large effect on the H abstraction reaction, and hence on the surface reactivity in general. To analyze this effect on the surface reactivity, Fukui function calculations were performed with the intention to localize the surface sites that are most susceptible towards a radical attack. As can be seen in Fig. 3.10, there is a major effect

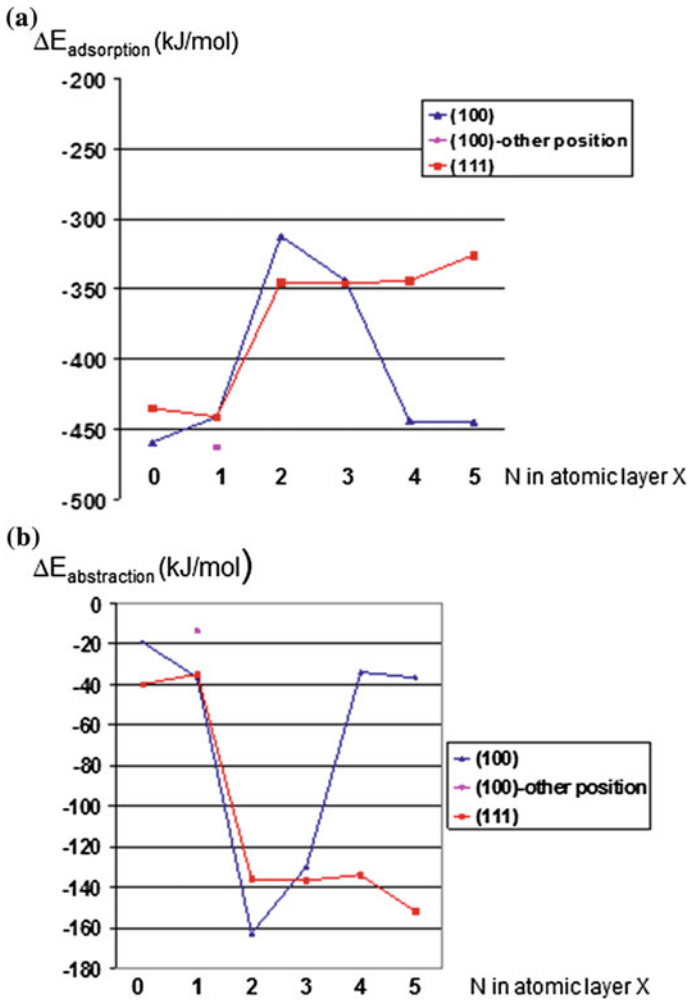

Fig. 3.9 Variation in H adsorption energy (**a**), and surface H abstraction energy (**b**), when positioning N in different atomic C layers. The zero value represents a non-doped diamond surface

by the substitutionally positioned N dopant on the radical susceptibility of the surfaces (100)−2 × 1, (110) and (111), respectively. This effect is more delocalized for the (110) surface, whilst the others show a more local, but still very strong, effect (local means close the N dopant).

Based on the Fukui function calculations, the position of H radical attack onto the H-terminated diamond surfaces, were determined from Fig. 3.11. An identical methodology, as for the non-doped diamond surfaces, was followed in trying to estimate the energy barriers for the H abstraction processes. The values of H abstraction energy barrier for the different diamond surface planes, and for different

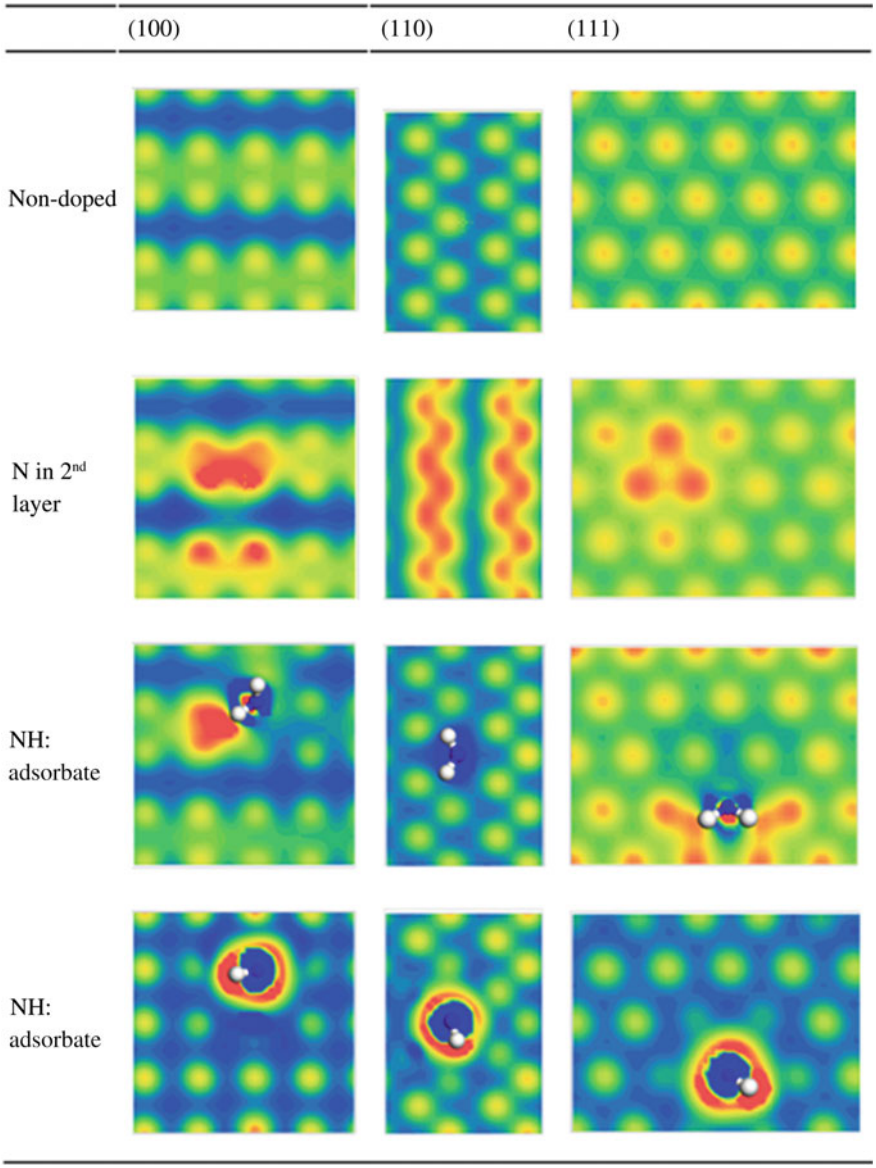

Fig. 3.10 Isosurface maps, showing the Fukuji functions for the distribution of radical susceptibility on the diamond surfaces [(100), (110), (100)−2 × 1], and for various dopant situations

kinds of nitrogen-doping, are shown in Table 3.2. The most interesting result is obtained for substitutionally nitrogen doping in the second C atomic layer, for which there is no energy barrier (for the approaching H radical) for any of the surface planes investigated.

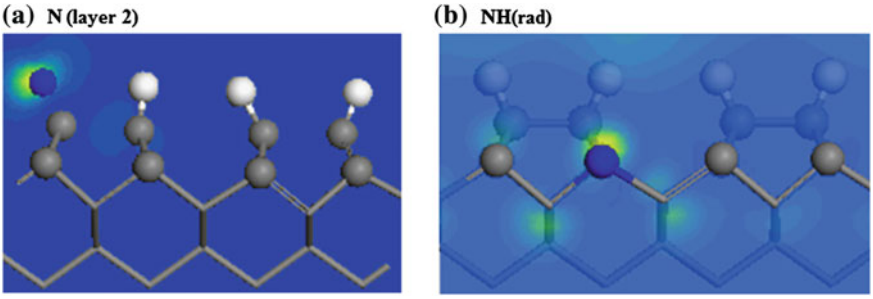

Fig. 3.11 Demonstration of the electron spin density for diamond (100)−2 × 1, with N substitutional positioned within the 2nd C atomic layer (**a**), or chemisorbed in the form of a radical NH species (**b**)

Table 3.2 Effect of N on the surface H abstraction energy and relative growth rate (in relation to the respective non-doped surface planes); (110), (111) versus (100)−2 × 1

		Energy barrier (kJ/mol)	Relative growth rate
110	Non-doped	4.7	1.0
	N in 2nd layer	0	1.7
	NH_2 adsorbate	5.7	0.9
111	Non-doped	6.1	1.0
	N in 2nd layer	0	1.9
	NH_2 adsorbate	6.0	1.1
100	Non-doped	11.8	1.0
	N in 2nd layer	0	3.7
	NH_2 adsorbate	8.2	1.5

The question is now to explain this theoretical observation. Nitrogen has an extra valence electron compared to carbon, and it is at first very important to get information about where this extra electron density will be positioned. Spin electron density calculations have shown that the density from this extra electron will be more globally distributed amongst the bonds in the vicinity to N for the diamond (100)−2 × 1 surface (see Fig. 3.11a).

Electron deformation densities have also been calculated with the purpose to investigate the effect of N dopants on the individual bonds within the H-terminated diamond surface (i.e., atom-atomic interactions) within the systems. As can be seen in Fig. 3.12a, the bond population analysis supports these results, showing that the extra spin will cause a weakening of both the N–C(layer 1) (0.55) and C–H (0.63) bonds. The former one is to be compared with the N–C(layer 3) bonds: 0.60 versus 0.65. And the later with the C–H bonds for non-doped diamond: 0.88. It is thereby obvious that the extra electron in the N dopant (positioned in the 2nd C atomic layer) will weaken the absolute upper surface part of the diamond (100) surface, and it is assumed that this is also the case for diamond (111) and (110).

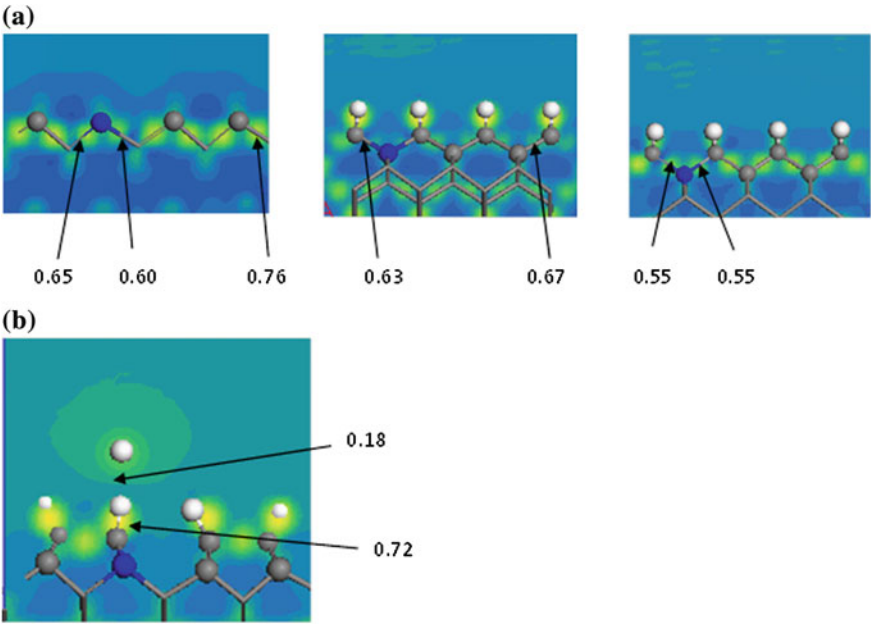

Fig. 3.12 Electron density difference maps, showing the induced weakening by the N dopant in the lattice (**a**), and the interaction between the approaching H and the surface H atom (**b**)

The electron deformation densities were also calculated for the approaching H radical at a so called transitions state (TS) distance from the diamond (100)−2 × 1 surface (i.e., identical to the TS distance for non-doped diamond). As can be seen in Fig. 3.12b, there is a strong interaction between the incoming H and the surface H. There is an electron density between these two atoms (0.18), indicating an electron orbital overlap. In addition, there has been a partial electron transfer to the approaching H radical, and there is a weakening of the C–H bond (from 0.90 to 0.72). All of these values do strongly support the zero-level barrier energy value for abstraction of H from the three different diamond surfaces.

3.6.3.4 N Chemisorbed onto the Surface in the Form NH or NH_2

Since it was not experimentally clear in what form nitrogen will aid for the improved diamond growth rate, nitrogen was attached to the surface in the form of a radical NH group (i.e., chemisorbed onto the diamond surface). As can be seen in Fig. 3.11b, the non-paired electron will stay locally at the adsorbate NH place. This local position of the extra electron is further supported by the deformation density results in Fig. 3.12b. The extra electron in NH does not show any tendency to

interact with the surface in weakening bonds by filling anti-bonding orbitals. Due to this reason, the barrier energy for the H abstraction is expected to be very similar as for the non-doped diamond surfaces, and these calculations have hence no been included in the present study.

However, when nitrogen is chemisorbed in the form of NH_2 onto the diamond surface, the situation becomes more complex (even though NH_2 is not a radical species when adsorbed to the diamond surface). For the (100)−2 × 1 surface plane, the reactivity of the surface hydrogen in the vicinity to one of the hydrogen atoms within the NH_2 group is enhanced. The situation with the (110) plane is quite different in that the reactivity close to NH_2 becomes weakened. For the situation with the (111) plane, it will be similar to the situation for the (100)−2 × 1 plane. The reactivity of the surface hydrogen closest to the hydrogen atom in the NH_2 group will be reinforced while the one closest to the nitrogen atom will decrease in reactivity. However, these changes in surface reactivity are apparently not large enough to affect the H abstraction barrier energy (see Fig. 3.10 and Table 3.2). The usefulness with these Fukui maps is that they are visualizing the most reactive surface H atoms, whereto the gaseous H shall be approached.

Similar to the situation with NH adsorbates, the nitrogen doping in the form of NH_2 adsorbed do not show any larger effect as compared to the non-doped scenario. To be more specific, the H abstraction energy barriers for the diamond (100)−2 × 1 and (111) planes were observed to decrease, whilst the barrier for the (110) plane increased; NH_2-doping (8, 6, 6) versus non-doping (12, 6. 5 (see Table 3.2). However, it must be stressed that these difference are marginal for diamond (111) and (110). There is also a correlation observed between these changes in activation energy and the effect by NH_2 doping on the surface reactivates. The Fukui function maps for the diamond (100)−2 × 1 and (111) planes show a slight improvement in surface reactivity, whilst the corresponding one for the (110) plane show a decrease in reactivity (see Fig. 3.10). However, as stated above, these effects are relatively.

3.6.3.5 Theoretical Versus Experimental Results Regarding Growth Improvement by N Doping

As was the situation in Table 3.1 for non-doped diamond, the energy barrier values for the various N doping situations can be used in forming ratios of diamond growth for the various diamond surface planes (see Table 3.2). In the Arrhenius relation used for this purpose, the temperature, T, was set to 1,073 K since this is the substrate temperature that was used in the experimental work that the present study is referring to [21]. Moreover, that experimental work did only consider the effect by N-doping on the diamond (100)−2 × 1 growth. A comparison with experimental results for the situation with N doping can, hence, only be done for this specific surface. It is also in Table 3.2 assumed that the H abstraction step is the rate determining one in the growth of diamond, which in [50] has been shown to be a very realistic conclusion.

As is quite clear from Table 3.2, there is a remarkable increase in growth rate when introducing N within the 2nd C atomic. This is especially the situation for the diamond (100)−2 × 1 surface, where a growth enhancement has been calculated with a factor of 3.7, compared to the non-doped scenario. The experimental growth rate enhancement for diamond (100)−2 × 1 was found to depend on the combination of N_2 and CH_4 concentration in the MWPA-CVD reaction chamber, with a maximum value of 3.5 [21]. Hence, there is an almost perfect resemblance between the here calculated factor and the experimentally observed one. This result is first of all a justification of the theoretical methods and methodology used in the present study. Secondly, it also strongly supports the general assumption that the H abstraction process from the diamond surface is the rate limiting step in the complete diamond growth mechanism. At last, the very good correspondence between theory and experiments confirm the experimental observation, and takes a step further in making the assumption that it is most probably N, incorporated in the lattice, that is responsible for the observed growth rate enhancement.

An issue that has to be high-lighted is the catalytic effect by the N dopant. The problem is that a very low concentration of N dopants shall be able to give a more pronounced effect on the overall diamond growth rate. However, it has earlier been shown that the surface hydrogens are very mobile on the diamond surface [52]. Hence, the desorption of an H species nearby the N dopant, will immediately be replaced by a neighboring H species on the surface, causing radical surface C sites at longer distances from the N dopant.

3.7 Surface Electrochemistry

3.7.1 General

Even though diamond is a wide band gap material, the material can get different energy states by using selective doping and/or by modifying the surface (e.g., by terminating the surface). Thin film diamond has shown to have prominent possibilities as an electrode material for environmental and energy applications, as well as for sensor application and for quantitative analysis of various compounds [3, 53]. The high sensitivity of diamond towards red/ox reactions, together with its exceptional large potential window, will increase its potential for pH sensor applications [54].

Intrinsic diamond is an insulator, whereas B-doped (of p-type) and N-doped (of n-type) diamond gives surface states in the band gap which increases the electronic conductivity within the bulk material. Different types of surface termination species has been shown to change the properties of the diamond surface region (e.g., by inducing surface electronic conductivity and interfacial charge transfer properties). It has already shown possible to use diamond thin films in high power and high frequency field-effect transistors (FETs) applications [55]. The induced surface

conductivity by specific surface termination of the diamond film, is basically an induced surface doping phenomenon. Landstrass and Ravi showed that both natural diamond and CVD grown diamond films show an increase in charge conductivity of several orders of magnitude when subjected to hydrogen plasma [54]. This observation has later on been verified by other groups [55]. The explanation to this enhanced conductivity was not clear in the beginning. A hypothetical acceptor-like surface state was proposed by Kawarada et al. [56], whereas Hayasi et al. [57] proposed very shallow hydrogen induced subsurface acceptor state inside diamond. Later, Takeuchi et al. [58] and Ristein et al. [59] continued to investigate the location of the acceptors. Though their result could be explained by assuming acceptor-states on the surface, their results showed a very unrealistic high surface defect density and a very sharp subsurface acceptor level.

Another mechanism, including an atmospheric environment, was proposed by Maier et al. [60] Supporting result were shown by Ri et al. [61], which were later confirmed by Foord et al. [62], and Vittone et al. [63]. According to this proposed mechanism, an H-terminated diamond surface requires an atmospheric adlayer for p-type surface conductivity to occur. Foord et al. [62] proposed that electron transfer takes place from the upper part of the valence band to an oxidative species in the physisorbed adsorbate. This type of charge transfer can be regarded as an electrochemical process where the upper diamond will be oxidized and the adlayer species reduced. This mechanism has recently been supported and further explained in some theoretical investigations by Larsson et al. [64–66]. The effect of both various surface termination species (H, O_{ontop}, O_{bridge}, OH and NH_2), as well as of various oxidative species in the adlayer (water, water + oxygen, water + H_3O^+ + oxygen, water + ozone, water + H_3O^+ + ozone), were then focused upon.

3.7.2 *Electronic Transfer Over the Diamond//Atmospheric Adlayer Interface*

The combination of (i) diamond surface termination, (ii) atmospheric adlayer chemical composition, and (iii) geometrical structures, are decisive for the surface electronic states, as well as for the molecular orbitals states of the adlayer. In turn, these parameters will strongly affect the tendency for chemical interactions and electron transfer across the diamond//adlayer interface. The degree of electron transfer over the interface can be identified by performing various theoretical analysis calculations. In [66], electron population analyses were made by projecting the electron density on atomic orbitals in a Mulliken atomic approach [7]. The individual atomic charges could thereby be estimated from which information about eventual partial electron transfer over the interfaces could be obtained.

The degree of electron transfer over the diamond (100)//atmospheric adlayer interface, was in [66] calculated for various surface termination species (H, O_{ontop}, O_{bridge}, OH and NH_2), as well as for various oxidative species in a very thin

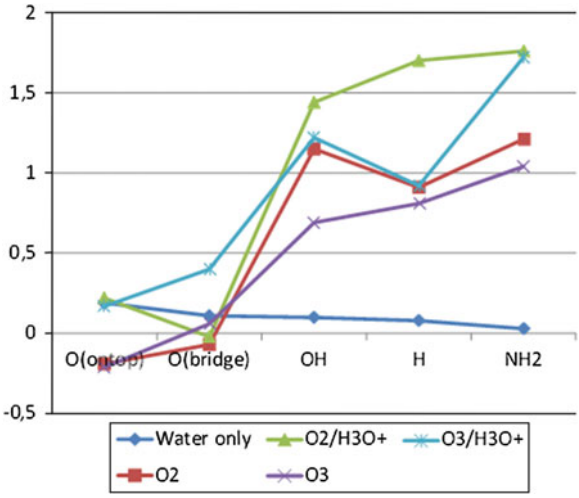

Fig. 3.13 Degree of electron transfer (in unit e) from an x-terminated (x = O_{ontop}, O_{bridge}, OH, H or NH_2) diamond (100)−2 × 1 surface, to an atmospheric water adlayer containing different types of oxidative species

atmospheric adlayer (water, water + oxygen, water + H_3O^+ + oxygen, water + ozone, water + H_3O^+ + ozone). As can be seen in Fig. 3.13, the presence of oxidative species in the adlayer is of utterly importance for an electron transfer to take place. Hence, a neutral water adlayer give no observable degree of charge transfer. In addition, O-terminated surfaces, in the form of O_{ontop} and O_{bridge}, showed very similar results in that an insignificant degree of electron transfer was observed to occur between the surface and the adlayer. When adding O_3 and H_3O^+ to the water adlayer (resulting in a very oxidative environment), it is though only the O_{bridge} scenario that show any appreciable degree of electron transfer over the interface; 0.40.

For the H-, NH_2- and OH-terminated diamond surfaces, the degree of electron transfer from the diamond (100) surface to the adlayer was, with an exception for a neutral water adlayer, found to be much more pronounced (see Fig. 3.13). The presence of adlayer oxidizing agents like O_2 and O_3 was found to increase the degree of electron transfer (from the surface to the adlayer). The addition of H_3O^+ ions in the adlayer was found to enhance the electron transfer even more. The degree of electron transfer increased from 0.08 to 0.95 e in the presence of O_2 within the adlayer. Extra addition of H_3O^+ was found to enhance the charge transfer even more (to 1.70 e). As was the situation with O_2 in the adlayer, the addition of O_3 resulted in a partial electron transfer of 0.81 e, which was further enhanced to 0.92 e when adding H_3O^+ to the same system.

The NH_2-terminated diamond (100) surface showed a similar trend. However, the degree of electron transfer over the surface//adlayer interface was here found to be much larger (as compared with H-termination). The only exception is for a neutral water adlayer, which still will not induce any electron transfer from the surface: 0.03 e (NH_3) versus 0.08 e (H). The presence of O_2 in the water adlayer was found to increase the charge transfer to 1.21 e (NH_3) versus 0.21 e (H). The relative increase

with O_3 in the adlayer was though not that high; 1.04 e (NH_3) versus 0.81 e (H). When adding hydronium to the systems, the following results were obtained: 1.76 e (NH_3) versus 1.70 e (H); Type v: 1.72 e (NH_3) versus 0.92 e (H).

For the situation with an OH-terminated diamond (100) surface, all adlayers containing species other than water were found to give a significant degree of electron transfer from the surface to the adlayer. There is an extra feature observed for this type of termination. In the presence of H_3O^+ ions within the adlayer, there will be a transfer of H^+ from the surface OH groups to the adlayer hydronium ions, forming water and hydrogen molecules. As can be seen in Fig. 3.12, for the situation with O_2 and H_3O^+ in the water adlayer, the numerical value of the partial electron transfer was 1.44 e. However, as there will also be a proton transfer occurring in the same direction, the resulting negative charge transfer was found to be 0.90 e from the diamond surface to the water-based adlayer. The situation is identical for a water adlayer containing O_3 and H_3O^+. The numerical value of the partial electron transfer is 1.22 e, whilst the overall charge transfer will be 0.22 e. The result for the OH-termination was otherwise being very similar to the NH_2 scenario. There was a minor partial electron transfer for neutral water (0.10 e vs. 0.3 e). Moreover, O_2 or O_3 in the water adlayer were found to induce a larger degree of electron transfer, being unexpectedly somewhat lower for the more oxidative O_3 species; 1.15 e versus 1.21 e (O_2), and 1.04 e versus 0.69 e (O_3). However, as expected, H_3O^+ ions in the adlayer were observed to increase the degree of electron transfer; from 1.15 e to 1.44 e (O_2), and from 0.69 e to 1.22 e (O_3).

In summary, is it apparent from Fig. 3.13, that O_{ontop}- and O_{bridge}-termination will not render any measurable electron transfer from the diamond (100) surface to the water-based adlayer. This is also the situation for the neutral water adlayers, attached to H-, OH- and NH_2-terminated diamond (100) surfaces. However, the presence of the oxidative species O_2, O_3, and H_3O^+, are proven to induce measurable partial electron transfer from the diamond surface to the atmospheric adlayer.

3.7.3 Adhesion Energies for the Attachment of Atmospheric Adlayers

The calculations of the adhesion processes for the attached atmospheric adlayer to the diamond surfaces will generally give an indication of the bond strengths, and eventual also of the type of interactions between the surface and the adlayer. Those systems that show a significant amount of electron transfer are expected to experience a stronger interaction of an electrostatic type. On the other hand, a smaller (or insignificant) degree of electron transfer over the interface must have a weak electrostatic binding across the interface. The adhesion energies between the surface and the respective adlayers have in [66] been calculated as the difference of the total energy of the interfacial system and the individual energies of the adlayer and the surface, respectively.

The adsorption energies for various terminations, and adlayer situations, are shown in Fig. 3.14. It is clear that only H- and NH_2-termination show a more pronounced interfacial bond, and hence a larger degree of hydrophilicity (the OH-termination situation has been excluded in these calculations since there are situation where the OH adsorbate will donate an H species to the adlayer). The lower adhesion energies for the O_{ontop}- and O_{bridge}-terminations are well correlated with the loss of electron transfer over the interface (see Fig. 3.13). For the H-termination, pure water will give bonding, with an adhesion energy of −95.6 kJ/mol, even though it is well known that an H-terminated diamond surface is hydrophobic. However, this is the situation for liquid water. The situation here is that we use a very thin atmospheric adlayer which behaves completely different in contact with a surface. The presence of an oxidative agent in the water adlayer will, though, change the situation completely. The adhesion processes are exothermic, and the numerical values are between −138.8 and −215.9 kJ/mol for the super cell. These larger adhesion energies are very well correlated with larger degrees of electron transfer; from 0.81 to 1.70 electrons over the super cell (see Fig. 3.13).

The NH_2-terminated surfaces results in rather strong bonding situations over the diamond-adlayer interface, and for all investigated adlayer types. As was the situation with the H-terminated surface, there is a correlation with the adhesion energies and the degree of electron transfer for all adlayer situations, except for pure water. The exothermicity for this type of surface termination is most probably caused by the probability to form hydrogen bonds between the NH_2-adsorbates and the adlayer molecules (e.g. H_2O molecules). In summary, a clear correlation between type of surface termination and degree of electron transfer was observed in [66].

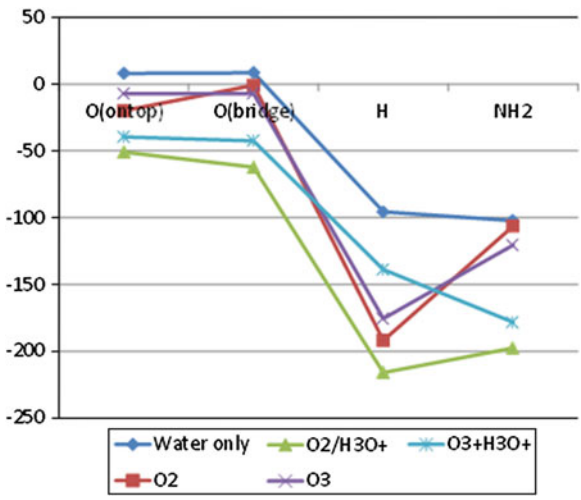

Fig. 3.14 Adhesion energy for an attached atmospheric water adlayer (containing various oxidative species) and x-terminated diamond (100) −2 × 1 surfaces (x = O_{ontop}, O_{bridge}, OH, H or NH_2)

References

1. M. Amaral, A.G. Dias, P.S. Gomes, M.A. Lopes, R.F. Silva, J.D. Santos, M.H. Fernandes, Nanocrystalline diamond: *in vitro* biocompatibility assessment by MG63 and human bone marrow cells cultures. J. Biomed. Mater. Res. A **87**(1), 91–99 (2008). doi:10.1002/jbm.a.31742
2. J.P. McEvoy, G.W. Brudvig, Water-splitting chemistry of photosystem II. Chem. Rev. **106** (11), 4455–4483 (2006). doi:10.1021/cr0204294
3. M. Panizza, G. Cerisola, Application of diamond electrodes to electrochemical processes. Electrochim. Acta **51**(2), 191–199 (2005). doi:10.1016/j.electacta.2005.04.023
4. D. Vanderbilt, Soft self-consistent pseudopotentials in a generalized eigenvalue formalism. Phys. Rev. B **41**(11), 7892–7895 (1990). doi:10.1103/PhysRevB.41.7892
5. J.P. Perdew, K. Burke, Ernzerhof M generalized gradient approximation made simple. Phys. Rev. Lett. **77**(18), 3865–3868 (1996). doi:10.1103/PhysRevLett.77.3865
6. D. Petrini, K. Larsson, Origin of the reactivity on the nonterminated (100), (110), and (111) diamond surfaces: an electronic structure DFT study. J. Phys. Chem. C **112**(37), 14367–14376 (2008). doi:10.1021/jp711190r
7. H.J. Monkhorst, J.D. Pack, Special points for Brillouin-zone integrations. Phys. Rev. B **13** (12), 5188–5192 (1976). doi:10.1103/PhysRevB.13.5188
8. R.G. Parr, W.T. Yang, Density functional approach to the frontier-electron theory of chemical reactivity. J. Am. Chem. Soc. **106**(14), 4049–4050 (1984). doi:10.1021/ja00326a036
9. W. Yang, R.G. Parr, R. Pucci, Electron density, Kohn-Sham frontier orbitals, and Fukui functions. J. Chem. Phys. **81**(6), 2862–2863 (1984). doi:10.1063/1.447964
10. K. Fukui, T. Yonezawa, H. Shingu, A molecular orbital theory of reactivity in aromatic hydrocarbons. J. Chem. Phys. **20**(4), 722–725 (1952). doi:10.1063/1.1700523
11. K. Fukui, Role of frontier orbitals in chemical reactions. Science **218**(4574), 747–754 (1982). doi:10.1126/science.218.4574.747
12. B. Delley, An all-electron numerical method for solving the local density functional for polyatomic molecules. J. Chem. Phys. **92**(1), 508–517 (1990). doi:10.1063/1.458452
13. D. Petrini, K. Larsson, Theoretical study of the thermodynamic and kinetic aspects of terminated (111). J. Phys. Chem. C **112**(8), 3018–3026 (2008). doi:10.1021/jp709625a
14. Y. Song, N. Yang, C.E. Nebel, K. Larsson, Formation conditions for epitaxial graphene on diamond (111) surfaces. (Submitted)
15. P.W. May, J.C. Stone, M.N.R. Ashfold, K.R. Hallam, W.N. Wang, N.A. Fox, The effect of diamond surface termination species upon field emission properties. Dia. Rel. Mater. **7**(2–5), 671–676 (1998). doi:10.1016/S0925-9635(97)00181-7
16. B.L. Mackey, J.N. Russell, J.E. Crowell, J.E. Butler, Effect of surface termination on the electrical conductivity and broad-band internal infrared reflectance of a diamond (110) surface. Phys. Rev. B **52**(24), R17009–R17012 (1995). doi:10.1103/PhysRevB.52.R17009
17. H.B. Martin, A. Argoitia, U. Landau, A.B. Anderson, J.C. Angus, Hydrogen and oxygen evolution on boron-doped diamond electrodes. J. Electrochem. Soc. **143**(6), L133–L136 (1996). doi:10.1149/1.1836901
18. C.E. Nebel, F. Ertl, C. Saurer, M. Stutzmann, C.F.O. Graeff, P. Bergonzo, O.A. Williams, R.B. Jackman, Low temperature properties of the p-type surface conductivity of diamond. Dia. Rel. Mater. **11**(3–6), 351–354 (2002). doi:10.1016/S0925-9635(01)00586
19. F. Maier, J. Ristein, L. Ley, Electron affinity of plasma-hydrogenated and chemically oxidized diamond (100) surfaces. Phys. Rev. B. **64**(16), 165411 (2001). doi:10.1103/PhysRevB.64.165411
20. F. De Theije, O. Roy, N.J. van der Laag, W.J.P. van Enckevort, Oxidative etching of diamond. Dia. Rel. Mater. **9**(3–6), 929–934 (2000). doi:10.1016/S0925-9635(99)00239-3
21. H. Touhara, F. Okino, Property control of carbon materials by fluorination. Carbon **38**(2), 241–267 (2000). doi:10.1016/S0008-6223(99)00140-2

22. T. Yamada, T.J. Chuang, H. Seki, Y. Mitsuda, Chemisorption of fluorine, hydrogen and hydrocarbon species on the diamond C(111) surface. Mol. Phys. **76**(4), 887–908 (1992). doi:10.1080/00268979200101741
23. L. Kian Ping, X.N. Xie, S.W. Yang, J.C. Zheng, Oxygen adsorption on (111)-oriented diamond: a study with ultraviolet photoelectron spectroscopy, temperature-programmed desorption, and periodic density functional theory. J. Phys. Chem. B **106**(20), 5230–5240 (2002). doi:10.1021/jp0139437
24. G. Kern, J. Hafner, J. Furthmueller, G. Kresse, (2x1) reconstruction and hydrogen-induced de-reconstruction of the diamond (100) and (111) surfaces. Surf. Sci. **352–354**, 745–749 (1996). doi:10.1016/0039-6028(95)01244-3
25. S.H. Yang, D.A. Drabold, J.B. Adams, Ab initio study of diamond C(100) surfaces. Phys. Rev. B **48**(8), 5261–5264 (1993). doi:10.1103/PhysRevB.48.5261
26. Y.L. Yang, M.P. D'Evelyn, in *38th National Symposium of the American Vacuum Society*, 11–15 Nov 1991, AVS, Seattle, Washington (USA)
27. X.M. Zheng, P.V. Smith, The topologies of the clean and hydrogen-terminated C(100) surfaces. Surf. Sci. **256**(1–2), 1–8 (1991). doi:10.1016/0039-6028(91)91194-3
28. G.D. Kubiak, A.V. Hamza, R.H. Stulen, E.G. Sowa, K.W. Kolasinski, Hydrogen desorption and subsequent reconstruction on natural diamond surfaces. Carbon **28**(6), 751–752 (1990). doi:10.1016/0008-6223(90)90268-4
29. A.V. Hamza, G.D. Kubiak, R.H. Stulen, Hydrogen chemisorption and the structure of the diamond C(100)-(2x1) surface. Surf. Sci. **237**(1–3), 35–52 (1990). doi:10.1016/0039-6028(90)90517-C
30. B.D. Thoms, J.E. Butler, HREELS and LEED of H/C(100): the 2x1 monohydride dimer row reconstruction. Surf. Sci. **328**(3), 291–301 (1995). doi:10.1016/00396028(95)00039-9
31. J.E. Butler, R.L. Woodin, L.M. Brown, P. Fallon, Thin film diamond growth mechanisms. Phil. Trans. R. Soc. A **342**(1664), 209–224 (1993). doi:10.1098/rsta.1993.0015
32. P.E. Pehrsson, T.W. Mercer, Oxidation of the hydrogenated diamond (100) surface. Surf. Sci. **460**(1–3), 49–66 (2000). doi:10.1016/S0039-6028(00)00494-5
33. M. Frenklach, D. Huang, R.E. Thomas, R.A. Rudder, R.J. Markunas, Activation energy and mechanism of CO desorption from (100) diamond surface. Appl. Phys. Lett. **63**(22), 3090 (1993). doi:10.1063/1.110217
34. P. Badziag, W.S. Verwoerd, MNDO analysis of the oxidised diamond (100) surface. Surf. Sci. **183**(3), 469–483 (1987). doi:10.1016/S0039-6028(87)80222-4
35. J. Nakamura, T. Ito, *Oxidization Process of CVD Diamond (1 0 0): H2x1 Surfaces* (Hammatsu, Japan; Elsevier, Amsterdam, 2005)
36. X.M. Zheng, P.V. Smith, The stable configurations for oxygen chemisorption on the diamond (100) and (111) surfaces. Surf. Sci. **262**(1–2), 219–234 (1992). doi:10.1016/0039-6028(92)90473-J
37. S. Skokov, B. Weiner, M. Frenklach, Theoretical study of oxygenated diamond (100) surfaces in the presence of hydrogen. Phys. Rev. B (Cond. Matter.) **55**(3), 1895–1902 (1997). doi:10.1103/PhysRevB.55.1895
38. Non-published results
39. G.Z. Cao, J.J. Schermer, W.J.P. van Enckewort, W.A. Elst, L.J. Giling, Growth of 100 textured diamond films by the addition of nitrogen. J. Appl. Phys. **79**(3), 1357–1364 (1996). doi:10.1063/1.361033
40. W. Muller-Sebert, E. Wörner, F. Fuchs, C. Wild, P. Koidl, Nitrogen induced increase of growth rate in chemical vapor deposition of diamond. Appl. Phys. Lett. **68**(6), 759–760 (1996). doi:10.1063/1.116733
41. C.S. Yan, Y.K. Vohra, Multiple twinning and nitrogen defect center in chemical vapor deposited homoepitaxial diamond. Dia. Rel. Mater. **8**(11), 2022–2031 (1999). doi:10.1016/S0925-9635(99)99148-X

42. T. Liu, D. Raabe, Influence of nitrogen doping on growth rate and texture evolution of chemical vapor deposition diamond films. Appl. Phys. Lett. **94**(2), 21119 (2009). doi:10.1063/1.3072601
43. S. Dunst, H. Sternschulte, M. Schreck, Growth rate enhancement by nitrogen in diamond chemical vapor deposition—a catalytic effect. Appl. Phys. Lett. **94**(22), 224101 (2009). doi:10.1063/1.3143631
44. Y. Bar-Yam, T.D. Moustakas, Defect-induced stabilization of diamond films. Nature **342**, 786 (1989). doi:10.1038/342786a0
45. T. Frauenheim, G. Jungnickel, P. Sitch, M. Kaukonen, F. Weich, J. Widany, D. Porezag, A molecular dynamics study of N-incorporation into carbon systems: doping, diamond growth and nitride formation. Diam. Relat. Mater. **7**(2–5), 348–355 (1998). doi:10.1016/S0925-9635(97)00186-6
46. G.B. Bachelet, D.R. Hamann, M. Scluter, Pseudopotentials that works: from H to Pu. Phys. Rev. B **26**(8), 4199–4228 (1982). doi:10.1103/PhysRevB.26.4199
47. R. Kalish, The search for donors in diamond. Diam. Relat. Mater. **10**(9–10), 1749–1755 (2001). doi:10.1016/S0925-9635(01)00426-5
48. S.A. Kajihara, A. Antonelli, J. Bernholz, R. Car, Nitrogen and potential n-type dopants in diamond. Phys. Rev. Lett. **66**(15), 2010–2013 (1991). doi:10.1103/PhysRevLett.66.2010
49. A. Tallaire, J. Achard, F. Silva, O. Brinza, A. Gicquel, Growth of large size diamond single crystals by plasma assisted chemical vapour deposition: recent achievements and remaining challenges. C.R. Phys. **14**(2–3), 169–184 (2013). doi:10.1016/j.crhy.2012.10.008
50. Z. Yiming, F. Larsson, K. Larsson, Effect of CVD diamond growth by doping with nitrogen. Theor. Chem. Acc. **133**(2), 1432 (2014). doi:10.1007/s00214-013-1432-y
51. C.J. Chu, B.J. Bai, N.J. Komplin, D.E. Patterson, M.P. D'evelyn, R.H. Hauge, J.L. Margrave, Homoepitaxial growth rate studies on diamond (110), (111), and (100) surfaces in a hot-filament reactor. Novel Forms Carbon **270**, 341–346 (1992). doi:10.1557/PROC-270-341
52. K. Larsson, J.-O. Carlsson, Surface migration during diamond growth studied by molecular orbital calculations. Phys. Rev. B **59**(12), 8315–8322 (1999). doi:10.1103/PhysRevB.59.8315
53. H. Martin, P. Morrison, Application of a diamond thin film as a transparent electrode for in situ infrared spectroelectrochemistry. J. Electrochem. Solid-State Lett. **4**(4), E17–E20 (2001). doi:10.1149/1.13531621
54. M. Landstrass, K. Ravi, Resistivity of chemical vapor deposited diamond films. Appl. Phys. Lett. **55**(10), 975–977 (1989). doi:10.1063/1.101694
55. H. Kawarada, A. Ruslinda, Diamond electrolyte solution gate FETs for DNA and protein sensors using DNA/RNA aptamers. Phys. Stat. Sol. A **208**(9), 2005–2016 (2011). doi:10.1002/pssa.201100503
56. H. Kawarada, M. Aoki, K. Sasaki, K. Tsugawa, Characterization of hydrogen-terminated CVD diamond surfaces and their contact properties. Diam. Relat. Mater. **3**(4–6), 961–965 (1994). doi:10.1016/0965-9635(94)90309-3
57. K. Hayashi, S. Yamanaka, H. Okushi, K. Kajimura, Study of the effect of hydrogen on transport properties in chemical vapor deposited diamond films by Hall measurements. Appl. Phys. Lett. **68**(3), 376783 (1996). doi:10.1063/1.116690
58. D. Takeuchi, M. Riedel, J. Ristein, L. Ley, Surface band bending and surface conductivity of hydrogenated diamond. Phys. Rev. B **68**(4), 41304(R) (2003). doi:10.1103/PhysRevB.68.041304
59. J. Ristein, M. Riedel, L. Ley, D. Takeuchi, H. Okushi, Band diagrams of intrinsic and p-type diamond with hydrogenated surfaces. Phys. Stat. Sol. A **199**(1), 64–70 (2003). doi:10.1002/pssa.200303814
60. F. Maier, M. Riedel, B. Mantel, J. Ristein, L. Ley, Origin of surface conductivity in diamond. Phys. Rev. Lett. **85**(16), 3472–3475 (2000). doi:10.1103/PhysRevLett.85.3472
61. S. Ri, T. Kazuhiro, T. Seiichi, F. Takao, K. Hideki, K. Tateki, I. Masamori, Hall effect measurements of surface conductive layer on undoped diamond films in NO_2 and NH_3 atmospheres. Jpn. J. Appl. Phys. **38**(6A), 3492–3496 (1999). doi:10.1143/JJAP.38.3492

62. J. Foord, C.H. Lau, M. Hiramatsu, R. Jackman, C. Nebel, P. Bergonzo, Influence of the environment on the surface conductivity of chemical vapor deposition diamond. Diam. Relat. Mater. **118**(3–6), 856–860 (2002). doi:10.1016/S0925-9635(01)00689-6
63. E. Vittone, E. Ravizza, F. Fizotti, C. Paolini, C. Manfredotti, *Presented at the VIIIth International Workshop on Surface and Bulk Defects*, Diepenbeek, Feb (2003)
64. K. Larsson, J. Ristein, Diamond surface conductivity under atmospheric conditions: theoretical approach. J. Phys. Chem. B **109**(20), 10304–10311 (2005). doi:10.1021/jp050419h
65. D. Petrini, K. Larsson, Electron transfer from a diamond (100) surface to an atmospheric water adlayer: a quantum mechanical study. J. Phys. Chem. C **111**(37), 13804–13812 (2007). doi:10.1021/jp070565i
66. M.M. Hassan, K. Larsson, J. Phys. Chem (submitted)

Chapter 4
Surface Modifications of Nanodiamonds and Current Issues for Their Biomedical Applications

J.C. Arnault

Abstract Combining numerous unique assets, nanodiamonds are promising nanoparticles for biomedical applications. The present chapter focuses on the current knowledge of their properties. It shows how the control of their surface chemistry governs their colloidal behavior. This allows a fine tuning of their surface charge. Developments of bioapplications using nanodiamonds are summarized and further promising challenges for biomedicine are discussed.

4.1 Introduction

Nanoparticles (NPs) are currently designed and developed for nanomedecine applications which constitute an emerging research field [1]. Among the main stakes, cancer therapy expands with three main paradigms: drug delivery, biomarkers for diagnosis and therapeutics.

The main interest to use NPs for drug delivery is the ability to target cancer cells. Indeed, some tumors present a higher vascularisation which could favor a passive targeting of NPs via the EPR effect (Enhanced Permeability and Retention) [2]. The targeting can also be active when a specific grafting of NPs with specific markers is performed [3]. The use of NPs can enhance the treatment efficiency allowing the delivery of higher doses while it reduces significantly side effects. Polymeric NPs [4] and liposomes are currently the most used NPs to encapsulate drugs. The polymer degradation permits their progressive delivery.

Second, NPs can also act as biomarkers for tumor imaging or tracking via their optical properties as quantum dots [5] or gold NPs via surface plasmon resonance [6]. However, some of these luminescent probes are limited either by their photostability or their cytotoxicity. Inorganic NPs can be used as contrast agents for magnetic resonance imaging [7, 8]. Lastly, C^{14} grafting on carbon nanotubes was

J.C. Arnault (✉)
CEA, LIST, Diamond Sensors Laboratory, 91191 Gif Sur Yvette, France
e-mail: jean-charles.arnault@cea.fr

N. Yang (ed.), *Novel Aspects of Diamond*, Topics in Applied Physics 121,
DOI 10.1007/978-3-319-09834-0_4

reported conferring radiolabeling properties for exploration of the in vivo biodistribution and pharmacokinetics [9].

Third, NPs can have therapeutic roles if they could be activated by an external stimulus. For example, under an external magnetic field, metallic NPs can generate temperature elevation called hyperthermia leading to cell death [10]. This activation can also be performed thanks to optical properties i.e. phototherapy for graphene oxide nanosheets [11, 12] or metallic NPs [13]. Efficiency of radiotherapy treatments can be enhanced by coupling with NPs. This constitutes a promising way to treat resistant tumors. Such approach may permit the delivery of lower doses for the same efficacy. A radiosensitization effect can be obtained under irradiation producing Reactive Oxygen Species (ROS) in cells. For this application, gold [14], platinum [15] or rare earths [16] NPs are used due to their high ratio of Auger electrons generated under irradiation.

The current trend which associates therapeutic and diagnostic properties is called theranostics [17, 18]. For this purpose, hybrid nanoparticles are designed combining properties of their core and shell: for example, superparamagnetic NPs embedded in mesoporous silica [19] or gold NPs in liposomes [20].

Nanodiamonds (NDs) constitute promising NPs for biomedicine applications. They possess many unique assets. They are scalable with sizes ranging from 100 nm down to 5 nm. One can expect the elimination by kidney for the smaller NDs (diameter lower than 6 nm) [21]. Nanodiamonds are also available in large quantities at reasonable prices (< \$1/g). Several studies reported their very low toxicity related to the high chemical inertia of diamond [22–25]. Recent research demonstrates they are even biocompatible with advantages for drug delivery or fluorescence labels [26, 27]. NDs enable covalent grafting of various chemical moieties on their surfaces [28] resulting in stable colloidal aqueous solutions. Covalent chemistry works similar way on NDs as for organics.

Their surface charge can be tuned allowing the electrostatic adsorption of biomolecules such as siRNA [27, 29]. They have been used for drug delivery applications [30–32].

Moreover, NDs can act as biomarkers for diagnosis. Indeed, color centers can be generated from nitrogen present in the diamond core by electron or helium irradiation [33] followed by a thermal annealing. Under green illumination, produced nitrogen-vacancy (NV) centers emits in the red wavelength region, they are highly photostable presenting neither photoblinking nor photobleaching [34].

Potential therapeutic behaviors of NDs related to their specific surface properties are currently under investigation.

Investigations of nanodiamonds for biomedical applications started quite recently. Numerous parameters remain partially controlled such as their different surface chemistry, their surface charge, their colloidal stability and the role of facets in their surface properties. The present chapter summarizes the current knowledge and the assets of NDs for nanomedecine. First, the different ways to produce nanodiamonds will be briefly presented (Part 4.2). Then, the characterization tools of their core and surface will be detailed focusing on the most relevant characterization methods (Part 4.3). The main surface modifications performed using different approaches

(chemical, physical or plasma treatments) will be reviewed (Part 4.4). Electronic properties of modified nanodiamonds will be presented as well as their colloidal behaviors in water (Part 4.5). Finally, main assets of NDs for biomedical applications will be discussed before giving some future promising challenges (Part 4.6).

4.2 Production of Nanodiamonds

According to thermodynamics, graphite is the stable carbon form at ambient conditions while diamond is metastable [35, 36]. Since 1950s, synthetic diamond can be obtained by high pressure high temperature (HPHT) method using hydraulic press which reproduces the conditions of natural diamond formation [37]. In 1980s, chemical vapor deposition (CVD) diamond was discovered and developed [38]. Different techniques are presently used to fabricate nanodiamonds: either NDs could be obtained by milling of HPHT/CVD diamond or NDs could be synthetized using explosives or laser ablation of graphite precursors [39, 40].

Monocrystalline nanodiamonds with size down to 20 nm can be obtained by ball milling of micron-sized HPHT diamonds. High Resolution Transmission Electron Microscopy (HRTEM) revealed faceted shapes with sharp edges corresponding to fractured crystallographic planes. In few cases, quasi spherical nanodiamonds smaller than 10 nm were obtained by HPHT milling [41, 42]. More recently, 70–80 nm nanodiamonds were also produced from polycrystalline CVD diamond by bead assisted sonic disintegration (BASD) [43].

Alternatively, nanodiamonds could be synthetized by several dynamic processes from molecules of explosives and different carbon precursors [44] (Fig. 4.1). Three methods could be distinguished: the direct transformation of graphite by an external shock wave, the detonation of graphite mixed with explosives (hexogen/RDX) or the detonation of high energy explosives (TNT/hexogen/RDX). For detonation synthesis, the key parameters governing the yield of nanodiamonds are the heat capacity, the content and the reactivity of the medium, the cooling of detonation products [45]. Nanodiamonds produced by detonation usually exhibit smaller diameters ranging typically from 2 to 20 nm. Several models were proposed to explain their formation by detonation synthesis [45]. More details about ND synthesis by detonation methods could be found in previous reports [45, 46].

After detonation, the collected soot contains metals, metal oxides and carbides. In addition to carbon, its elemental composition reveals hydrogen, nitrogen and oxygen species. Indeed, nitrogen is initially present in HPHT diamond and in explosives used in the detonation synthesis. In most cases, a-C and/or sp^2 carbon are surrounding the diamond core. Detonation NDs are extracted after purification procedures using liquid oxidants to remove non-diamond carbon. Indeed, diamond and non-diamond carbon have different stability to oxidants. The efficiency of an ozone treatment was also reported to eliminate the non-diamond carbon [46]. Then, liquid-phase oxidation using HCl or other high boiling acids is applied to eliminate

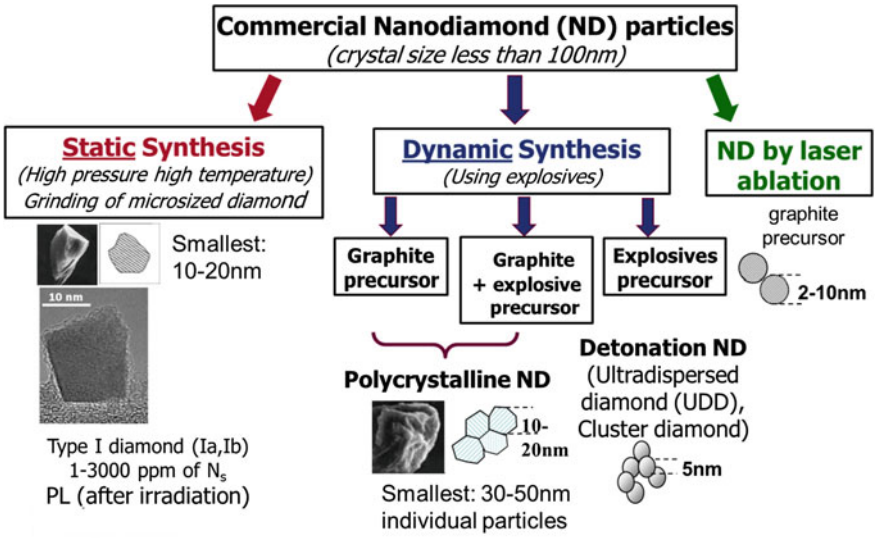

Fig. 4.1 The different natures of NDs [44] courtesy of O. Shenderova, International Technology Center, USA

the non-carbon impurities. The resulting surface chemistry of detonation nanodiamonds will be described in the next paragraph (Part 4.3).

Diamond nanoparticles have been classified according to their size [44]. Nanocrystalline particles (10–100 nm) could be either monocrystalline (HPHT milling) or polycrystalline after shock-wave compression of graphite or detonation of carbon/explosives mixture. Ultrananocrystalline NDs (2–10 nm) are mainly produced by detonation or laser ablation. Smallest particles behave to the family of diamondoids. Higher diamondoids (1–2 nm) are extracted from petroleum with hydrogen termination [47]. The smallest specie of cubic diamond, the adamantane, contains 10 carbon atoms ($C_{10}H_{16}$).

4.3 Characterization Tools

Depending on their synthesis methods (Part 4.2), nanodiamonds can behave different core-shell structures, morphologies and surface chemistry. Experimental and theoretical works reported multi-shell structures based on a diamond core which could be surrounded by defective diamond, amorphous carbon and/or several onion like outer-shells [48, 49]. According to calculations, this structure constitutes the most stable energetic form for sp^3 nanometric clusters [50]. Characterization methods were developed to specifically probe the crystalline structure as well as the chemical composition of diamond core, outer shells and surface of nanodiamonds. The most relevant techniques to assess these characteristics are presented in Table 4.1.

Table 4.1 Characterization tools of nanodiamonds

Diamond core	
Particle size, crystalline structure	HRTEM, XRD, SAXS
Morphology and shape	HRTEM
Structural defects	HRTEM
Chemical impurities	XPS, EELS/STEM
Local environment	NEXAFS, ESR, NMR, ELNES
NV centers	Time resolved PL, confocal PL
Outer shells and surface	
a–C, sp^2 carbon	Raman, HRTEM, XRD, XPS
Surface chemistry and grafting	FTIR, XPS, TDMS

4.3.1 Diamond Core

Its crystalline structure can be accurately investigated by high resolution transmission electron microscopy (HRTEM) in bright field mode. The signature of diamond lattice is also confirmed in the diffraction mode. Moreover, structural defects as twins or dislocations within diamond lattice can be resolved especially for nanodiamonds produced by detonation method [51]. The spherical or faceted shape of nanodiamonds which could greatly influence their reactivity could be characterized at the nanoscale using HRTEM. As an illustration, (111) facets with (100)-type truncations were identified even for detonation NDs of 2 nm [51] (Fig. 4.2). More recently, modern HRTEM instruments were developed to operate at low electron energy down to 40 keV. Lens aberrations are reduced allowing image resolution down to 50 pm [52]. In these experimental conditions, the graphitization of NDs which may occur under electron beam is completely avoided. Diamond core structure and size of nanodiamonds can be also investigated by X-ray Diffraction (XRD) [53] or Small Angle X-ray Scattering (SAXS) [54]. Contrary to XRD which is limited by diffraction effects leading to physical broadening, SAXS give access to sizes very close to HRTEM. Size distributions can even be extracted from SAXS data assuming a shape for NDs.

The concentration of chemical impurities (N, O, H, metals remaining from synthesis) within diamond core and their location in the diamond lattice is another important issue. For example, the nitrogen presence could confer optical properties to nanodiamonds via the formation of luminescent nitrogen vacancy (NV) centers. Atomic concentrations of impurities (excepted hydrogen) could be assessed from X-ray Photoemission Spectroscopy (XPS). Typically, the detection limit for oxygen and nitrogen is close to 0.5 at% [55]. Very few techniques such as SIMS or NMR are sensitive to hydrogen. During synthesis of nanodiamonds, hydrogen is likely to be inserted into diamond core. Indeed, hydrogen diffusion was previously reported in bulk diamond [56]. There is a crucial need to probe hydrogen into diamond core because it could confer new properties to nanodiamonds.

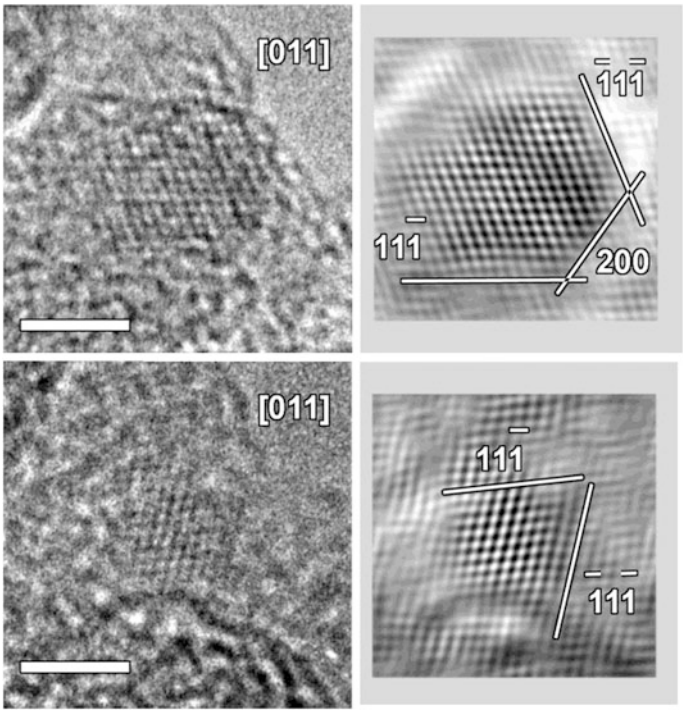

Fig. 4.2 HRTEM pictures of detonation nanodiamonds, scale bar 2 nm [51] courtesy of S. Turner, University of Antwerp

Electron spin resonance (ESR) is the most sensitive method to detect nitrogen (10^{12} spins) [57, 58]. Indeed, single nitrogen in substitution in diamond lattice is paramagnetic [59]. Core loss electron energy loss spectroscopy (EELS) profiles can also probe light elements as nitrogen, oxygen, boron or carbon. Energy loss near edge structures (ELNES) technique provides a signature of the local binding of impurities. For example, the tetrahedral configuration can be deduced from the nitrogen K edge structure [51, 60]. Recent work shows this technique permits to confirm the tetrahedral insertion of boron atoms in diamond leading to p-doping [61, 62]. EELS combined with scanning TEM (STEM) can even provide mapping or profiles of impurities with an atomic resolution [63–65]. Near-edge X-ray absorption fine structure (NEXAFS) technique could probe the local bonding environment [66]. Nuclear Magnetic Resonance permits to probe hydrogen (^{1}H), nitrogen (^{15}N) and carbon (^{13}C) spins [67].

Photoluminescence (PL) spectroscopy can reveal signature of structural imperfection of diamond lattice (defects, impurities). Luminescent NV centers composed by a nitrogen atom in substitution combined with a neighbouring vacancy are characterized by PL. Under excitation at 531 nm, emission wavelengths at 575 and 638 nm are detected corresponding to different charge states NV^0 and NV^-,

respectively [57]. NV centers exhibit a high stability without any photo-blinking or photo-bleaching. Recently, the influence of NDs surface chemistry on NV luminescence was shown, especially a quenching of the NV^- luminescence when nanodiamond surface is hydrogenated [68].

4.3.2 Outer Shells and Surface Chemistry

Surface chemistry of nanodiamonds is strongly dependent on their synthesis method and the purification treatments (Part 4.2). For pristine NDs, the diamond core is usually coated with non sp^3 carbon. These carbon outer-shells could be structured as onion-like shells [69] or could exhibit an amorphous structure (a–C) [70]. The nature of outer shells must be well characterized because it strongly affects the surface reactivity of nanodiamonds. Raman spectroscopy gives access to composition and structure for bulk carbon phases [71]. A signature at 1332 cm^{-1} is obtained for diamond while D and G bands at 1410 and 1590 cm^{-1} originate from amorphous and graphitic carbon, respectively. Nevertheless, a specific Raman interpretation is needed for detonation nanodiamonds (size lower than 6 nm) taking into account a phonon confinement leading to a downshift and an asymmetry of the diamond Raman peak [72, 73]. Some features like the one located at 1640 cm^{-1} are still a matter of debate [36]. XPS is also sensitive to sp^2 and sp^3 hybridization of carbon, it was recently used to monitor the surface graphitization of nanodiamonds [55]. However, artefacts due to nanomaterials especially the high fraction of surface versus bulk must be taken into account in the data interpretation [74, 75]. Auger Electron Spectroscopy (AES) is even more sensitive to carbon hybridization because two valence electrons are involved in the C KVV transition [70]. Using low loss EELS, a–C or graphite could also be discriminated [76]. HRTEM imaging provides the structure of the outer-shells at atomic scale [51, 75].

After their synthesis, nanodiamonds underwent oxidizing treatments to clean metallic impurities (Part 4.2). This leads to a heterogeneous surface chemistry involving different carbon-oxygen groups. To investigate the surface chemistry of nanodiamonds after purification or functionalization, Fourier Transformed Infra-Red (FTIR) Spectroscopy is a powerful technique as diamond core is transparent to IR. It is sensitive to the vibrations of carbon-hydrogen ($C–H_x$) [77] and the different carbon-oxygen bonds (O–H, C–O, C–O–C, C=O). Moreover, it could detect C–N or N–H vibrations [78]. Although FTIR is usually done in transmission mode, a diamond-coated ATR prism for infrared absorption spectroscopy was recently used to characterize surface-modified diamond nanoparticles [79]. Raman spectroscopy performed under UV light could provide signature of C–H surface bonds for hydrogenated diamond surface [80, 81]. High resolution electron energy loss spectroscopy (HREELS) can probe the surface bonds of the first atomic plane with a resolution of 5 meV. It was recently used to characterize the surface chemistry of hydrogenated nanodiamonds [76]. NMR experiments are sensitive to ozone-treated or hydroxylated nanodiamonds as well as functionalization with fluorine (^{19}F) [67].

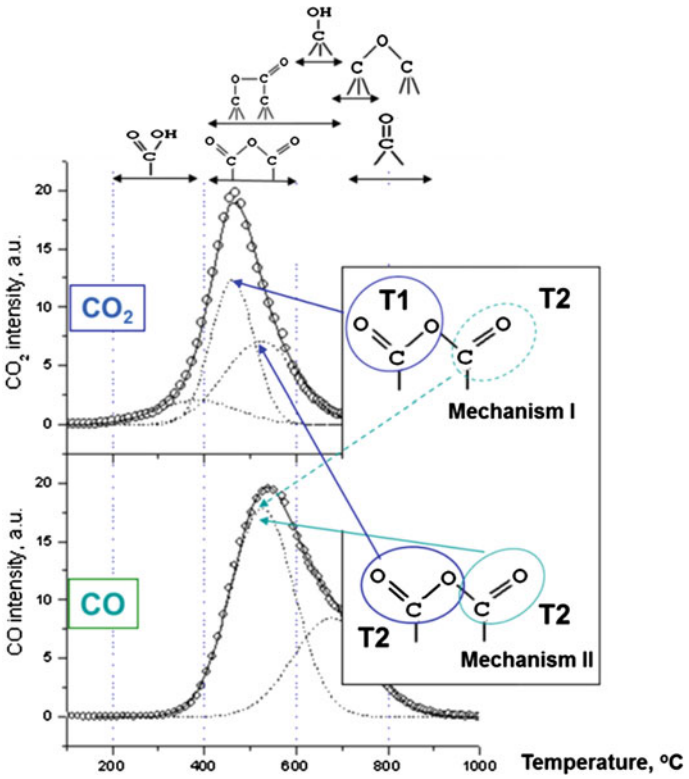

Fig. 4.3 Two possible desorption mechanisms of anhydrides on ozone treated NDs for two temperatures from TDMS [46] courtesy of O. Shenderova, International Technology Center, USA

Finally, as an indirect surface chemistry probe, let cite the thermal desorption mass spectrometry (TDMS) analysis which is a continuous measurement of the mass spectra of gases released from a sample under programmed heating [82, 83]. This technique permits a fine identification of functional groups according to their specific desorption temperature and gives information concerning their thermal stability. As an illustration, TDMS spectra can help to understand the anhydrides desorption from ozone purified NDs [46] (Fig. 4.3).

4.4 Surface Modifications of Nanodiamonds

Nanodiamond surface appears highly heterogeneous exhibiting different carbon-oxygen functional groups (ether, hydroxyl, carbonyl, carboxyl,…), a–C and/or sp^2 carbon. This scattered surface chemistry is mainly related to purification steps (Part 4.3). Surface treatments were developed to get homogeneous chemistry allowing

Table 4.2 Surface terminations of NDs vs treatments

Surface terminations		Treatments	Objectives
Hydrogenated		H_2 plasma [70, 87]	positive ZP with SCL grafting
		annealing at 500 °C under H_2 [88]	
Oxidized	*Carboxylated*	different acid treatments [28]	negative ZP disaggregation grafting of peptides
		air annealing at 400–430 °C [89]	
		ozone treatment at 150–200 °C [46]	
	Hydroxylated	borane reduction [90]	grafting silanization
		Fenton reagent [91]	
		milling with beads [69, 92]	
		photochemistry [93]	
Fluorinated		F_2/H_2 exposure at 150–470 °C [94]	grafting
		CF_4 plasma [95]	
Aminated		Cl-term NDs in gaseous ammonia [96]	positive ZP grafting
		covalent grafting of amine derivative [84, 97, 98]	
Surface graphitised		annealing at 750 °C under vacuum [55, 99, 100]	positive ZP by oxygen hole doping hybrid properties
		long beads milling [101]	

more efficient further graftings [28] either by chemical, thermal or plasma approaches. In addition, these controlled surface chemistries help to stabilize ND_S in aqueous suspension limiting aggregation (Part 4.5). Indeed, detonation NDs tend to aggregate while many applications require isolated primary NDs [36]. Milling or BASD procedures [84] were successfully applied for deaggregation. Nevertheless, these treatments can induce either chemical contaminations or surface graphitization. The efficiency of surface treatments such as oxidation in air [85] or plasma hydrogenation [86] was reported. Indeed, tuning the surface chemistry can confer intrinsic electronic properties to NDs surface having consequences on their aggregation and colloidal behavior (Part 4.5). Thermal treatments permit to create hybrid nanoparticles constituted by a diamond core surrounded by sp^2 reconstructions [75]. Table 4.2 presents the major reported terminations and their uses.

4.4.1 Surface Hydrogenation of Nanodiamonds

The aim is to generate homogeneous C–H bonds at nanodiamond surface. Hydrogenated intrinsic diamond surface behave specific electronic properties characterized by a negative electron affinity (NEA) [102]. After air exposure, it presents a surface conductivity by a transfer doping involving adsorbed species [103]. Hydrogen atoms

may also diffuse into the diamond lattice where they are preferentially trapped on structural defects or chemical impurities [56].

Annealing treatments under H_2 flow at 850–900 °C were reported for diamond particles bigger than 100 nm [104, 105]. Nevertheless, this temperature range is very close to the one leading to graphitization for smaller nanodiamonds. Recent reports demonstrated that surface graphitization started at 750 °C for 5 nm detonation NDs [55, 99]. Similar treatments performed at lower temperature (typically 500 °C) seem to produce an efficient deaggregation of detonation NDs after centrifugation. Nevertheless, HRTEM reveals that onion like shells are still present after the annealing [88]. FTIR shows a partial coverage by C–H bonds conferring a hydrophobic behavior to treated nanodiamonds [88, 106]. These results suggest hydrogen is more likely bonded to sp^2 carbon. Another method for hydrogenation would use organic chemistry with metal catalyst such as Pd, Pt or Ni [107, 108]. However, in that case, catalysts must be further eliminated.

An interesting alternative consists to expose NDs to H_2 CVD plasma. Under microwave field or thermal cracking [97, 109], dihydrogen molecules are efficiently dissociated into atomic hydrogen. This specie has a high reactivity towards carbon and etches sp^2 carbon easier than sp^3 carbon [110]. Thus, its interaction with nanodiamonds may allow the loss of non-diamond carbon, the reduction of oxygen species at the surface and the formation of C sp^3-H bonds. This surface hydrogenation by CVD plasma is widely used for diamond layers to get hydrogen-terminated boron doped diamond for electrochemistry [111, 112]. Optimized CVD conditions for hydrogenation were determined for detonation nanodiamonds using a Microwave Plasma Chemical vapor Deposition (MPCVD) reactor connected to a UHV set-up [70]. Nanodiamonds were deposited on multilayer Silicon On Insulator (SOI) substrates by drop-casting and samples were analyzed without air exposure. A XPS sequential study allows the monitoring of the oxygen removal after MPCVD exposure. A temperature threshold of 700 °C is needed to fully remove oxygen from detonation NDs. The hydrogenation efficiency is closely related to the concentration of atomic hydrogen produced in the MPCVD plasma [70].

Proper conditions were then used in a home-made set-up allowing plasma hydrogenation of NDs in powder (Fig. 4.4). Nanodiamonds located in a quartz tube are directly treated in the gas phase [87]. A rotation of this tube allows the exposure of their whole surface to atomic hydrogen. This method is able to treat simultaneously a large amount of NDs (hundreds mg) which is a prerequisite to a meaningful surface functionalization. Both HPHT and detonation nanodiamonds which differ by their size and the graphitic shells surrounding the sp^3 core, have been hydrogenated.

The surface chemistry of hydrogenated nanodiamonds (H-NDs) was then characterized using XPS and FTIR (Fig. 4.4b). For dried H-NDs, FTIR spectra well exhibit signals located around 2900 cm^{-1} [87]. These bands have been previously assigned to C–H stretching on hydrogenated NDs surfaces [77].

The surface reactivity of HPHT H-NDs (50 nm) was investigated applying several surface modifications [93]: a selective oxidation under UV exposure and functionalization with alkenes and diazonium moieties. These reactions are common

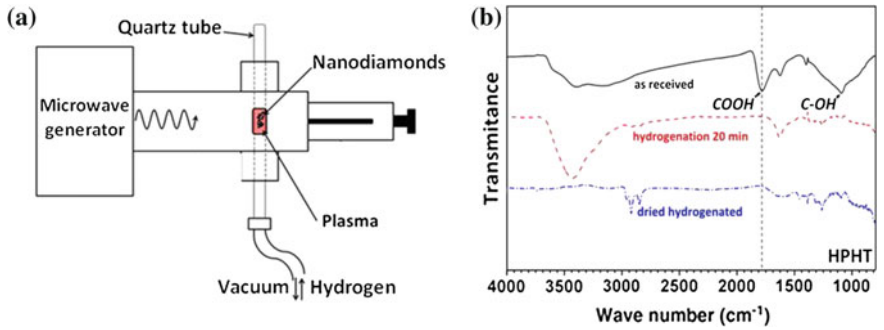

Fig. 4.4 **a** Set-up for plasma hydrogenation; **b** FTIR spectra of hydrogenated HPHT NDs [87]

on hydrogenated diamond films towards efficient biological functionalizations (DNA, proteins grafting) [113–115] so their use on NDs may also lead to promising developments. However, the chemical mechanisms involved in these grafting routes require specific surface properties, involving charge transfer, which is only provided to the diamond surface by C–H hydrogen terminations [116].

On H-NDs, the oxidation procedure under UV gives rise to a surface hydroxylation as shown by the FTIR bands at 1050 and 3300 cm^{-1}. In addition, a new component appears in the XPS C1s core level [93]. A similar modification of the C1s peak was reported for a diamond surface after UV oxidation [117]. This oxidation treatment appears selective on H-NDs as neither carboxyl nor carbonyl groups were evidenced by XPS or FTIR. An inversion of the Zeta potential was measured after UV oxidation +30 mV compared to −45 mV for as received NDs. The origin of this positive Zeta potential will be discussed in the Part 4.5.

HPHT NDs were also reacted with pure undecylenic acid under 254 nm UV irradiation. This alkene was chosen for its long alkyl chain and its acid group, both functionalities easily identifiable by FTIR analysis with characteristic structures at 2800 cm^{-1} and 1700 cm^{-1} respectively (Fig. 4.5). Furthermore, the vinyl function is evidenced by a peak located around 900 cm^{-1}. For comparison, the same reaction was also conducted on as-received NDs.

The different signatures of undecylenic acid are observed only on the FTIR spectra for hydrogenated HPHT NDs (Fig. 4.5). Moreover, the essential role of UV light in the mechanisms of grafting was demonstrated. On diamond layers, numerous studies report that C–H strongly enhances chemical reaction [116] leading to the formation of covalent C–C bonds between the diamond surface and the grafted moiety. Indeed, hydrogenated terminations confer to the diamond layers specific electronic surface properties, such as a superficial conductive layer (SCL) [118] and a negative electron affinity (NEA) [102, 119]. The latter is usually highlighted to explain the reactivity of hydrogenated diamond layers towards alkenes, by the mean of photo-excited electrons allowed to propagate out of the diamond into the nearby liquid phase, even with sub-bandgap excitation [120, 121]. Authors agree that hydrogen terminations are required for this reaction, and that

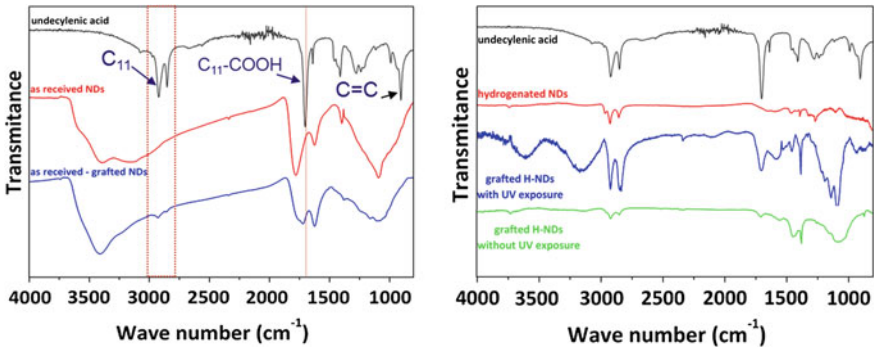

Fig. 4.5 FTIR spectra on (*left*) as received HPHT NDs (*right*) HPHT H-NDs [93]

electron transfer arises from sp^3 surfaces and not from grain boundaries and/or sp^2 species at the interface. This constitutes a strong indirect proof of the efficiency of hydrogen plasma on NDs.

The spontaneous grafting of a diazonium salt on hydrogenated HPHT NDs was also demonstrated [93]. On a diamond surface, this arises from specific electronic properties conferred by C–H terminations [122]. The covalent bonding goes through the creation of a phenyl radical by the mean of an electron transfer from the diamond surface to the aryldiazonium salt. This electron transfer is related to the presence of a superficial conductive p-type layer. The commonly accepted mechanism, so-called transfer doping [118] describes an accumulation of holes due to an electron transfer from the valence band and a redox couple adsorbed on the surface when the diamond surface is exposed to wet atmosphere or immersed in an electrolyte. This phenomenon is only possible on hydrogenated layers which exhibit a low ionization potential, matching with the chemical potentials of the adsorbates.

These different surface modifications of hydrogenated HPHT NDs suggest their chemical reactivity is very similar to the one of hydrogenated diamond surfaces. In the Part 4.5, surface properties of hydrogenated nanodiamonds will be discussed.

4.4.2 Oxidation of Nanodiamonds

The surface chemistry of pristine nanodiamonds is highly heterogeneous (Part 4.3). The selective formation of C–O bonds at the surface by applying specific treatments is a major challenge to obtain more efficient graftings.

Among C–O groups, carboxylic acid termination has a specific interest. Indeed, its basic form (COO^-) confers a negative charge to the NDs over a wide pH range in water [75]. This ensures stable colloidal suspensions (Part 4.5). Surface of NDs could be saturated with carboxyl functions using nitric (HNO_3), sulfuric (H_2SO_4) or perchloric (HCl) acids. A mixture of these acids in equal amounts reveals powerful

[45, 89, 123]. "Piranha" water (sulfuric acid and hydrogen peroxide) constitutes an efficient alternative [124]. Air annealing of NDs at 400–450 °C leads to the formation of acid functions mainly carboxylic and to the etching of non-diamond carbon [89, 125, 126]. A quantitative analysis of COOH groups was performed using Boehm titration after acid treatment [127]. The mean amount corresponds to 0.85 COOH groups par nm^2 of ND surface. Recently, ozone purification treatment was reported leading to the formation of anhydrides [46].

Starting from pristine nanodiamonds, several procedures inducing hydroxyl terminations were reported. First, chemical reduction can be performed with borane (BH_3) or hydrides ($LiAlH_4$) starting from COOH [128, 129]. Second, C-OH bonds can also be formed using the "Fenton reaction" which takes place in a mixture of hydrogen peroxide and iron sulfate in strong acid solution [91, 130]. Third, a significant amount of hydroxyl groups can be generated during milling [69] or BASD [84] of NDs in water. More recently, a photochemical oxidation under UV was performed on NDs previously hydrogenated [93].

A recent review provides more details on the different oxidation procedures [28].

4.4.3 Amination, Fluorination or Chlorination of Nanodiamonds

Several attempts to generate fluorine, amine or chlorine terminations at NDs surface by annealing under controlled atmosphere were reported [36, 94, 131, 132]. Nevertheless, annealing temperatures are usually limited to avoid surface graphitization (Part 4.4.4). As a consequence, some oxidized groups and non-diamond carbon may remain at the surface. The selectivity of these gaseous treatments is often limited: after heating in ammonia flow, aminogroups, C≡N and C=N-containing groups were identified at ND surface [132, 133]. In order to create more reactive species, a CF_4 atmospheric pressure plasma was used [95]. Chlorination of NDs was also successfully achieved by photochemical reaction of gaseous chlorine with NDs previously hydrogenated [96]. The interaction of these chlorinated NDs with ammonia led to the formation of NH_2 groups.

4.4.4 Surface Graphitization of Nanodiamonds

Diamond graphitization can be induced by different mechanisms: via thermal treatment under vacuum [134, 135] or exposure to reactive gas under ambient atmosphere [136–138]. It can be also obtained by beam irradiation (electron, ion, laser, gamma-ray) [139–141]. Finally, the graphitization could be catalyzed by metals as Fe or Co [142–144].

A recent review was devoted to diamond phase transitions at nanoscale [145]. For nanodiamond, the graphitization process can lead to a full transformation into onion

like carbon (OLC) structures formed by concentric closed graphitic shells. Corresponding kinetics were extensively studied experimentally by annealing at temperatures included between 1100 and 1900 °C in different atmospheres (vacuum, oxygen, argon, hydrogen) [100, 111, 146–150]. Formations of curved graphite like structures and concentric-shells fullerenes on nanodiamonds were theoretically investigated [151–153]. For nanodiamonds 4–5 nm in size, the evolution of carbon bulk density measured by a gamma-ray attenuation method drops from 3.1 to 2.2 g cm^{-3} in the 900–1300 °C temperature range [154]. By comparison, the diamond/graphite transition occurs above 1600 °C for bulk diamond [154, 155]. Starting from detonation nanodiamonds, HRTEM revealed the formation of fullerene like shells after an annealing at 1100–1300 °C [146]. At 1500 °C, nanodiamonds are completely converted into OLC structures while polygonal hollow onions are formed at temperatures higher than 1870 °C (Fig. 4.6). OLC have promising properties for energy storage, catalysis or composites [147–149, 156].

The graphitization mechanism is strongly sensitive to the presence of non-diamond carbon at the NDs surface [145]. Indeed, detonation NDs underwent purification procedures which can differ from a supplier to another (Part 4.2). This can explain the wide dispersion for the onset temperature of nanodiamonds graphitization reported in the literature, it varies from 670 to 1000 °C [157, 158]. The selective desorption of oxygen groups has also a significant effect on the graphitization onset. For HPHT NDs, a size effect is expected with a higher temperature suitable to initiate graphitization. Graphitization kinetics for submicron diamond and NDs were compared, different graphitization rates were determined [154].

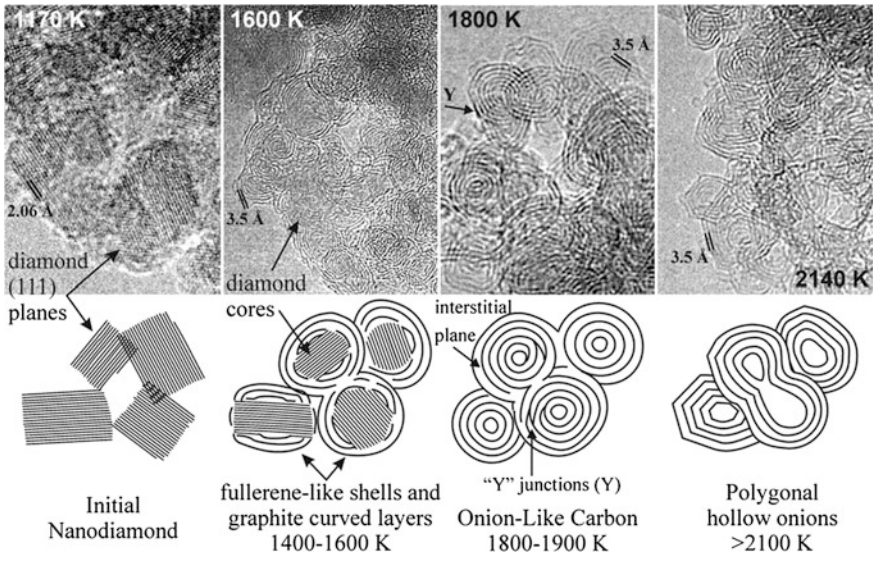

Fig. 4.6 Transformation of NDs into onion like carbon [146] courtesy of Y.V. Butenko, ESTEC, The Netherlands

Moreover, the previous report demonstrates that activation energies differ for {110} and {111} crystallographic facets [145, 159].

Recently, several groups focused on the early stages of surface graphitization of detonation NDs using XPS, HRTEM, Raman or NMR characterizations [55, 75, 99, 160, 161]. The aim is to control the formation of hybrid nanoparticles with a sp^2 organized surface covering a sp^3 core, thus avoiding the graphitization of the diamond core. Such hybrid NPs may have promising properties linked to fullerene or graphene assets as radiosensitization or photothermal therapy [162, 163]. In addition, surface graphitized nanodiamonds exhibit electrical conductivity sufficient for electrochemical applications [164, 165].

Surface graphitization of detonation NDs by annealing under UHV was monitored using XPS [55]. The evolution of the carbon core level (C1s) shows the existence of two regimes according to annealing temperature T (Fig. 4.7). For T included between 700 and 900 °C, surface graphitization is initiated from non-diamond carbon present at ND surface. Fullerene like reconstructions (FLRs) are formed as shown by HRTEM [75]. On the other hand, for T > 900 °C, the diamond core starts to graphitize leading to the formation of bucky diamond. It is thus possible to generate FLRs at the surface without altering the diamond core. The stability of FLRs at the NDs surface was previously demonstrated by ab initio calculations confirmed by x-ray absorption and emission [152]. The selective synthesis of a thin graphitic layer on the ND surface by annealing under vacuum at temperature lower than 900 °C gives rise to hybrid nanocarbons combining the intrinsic core properties of diamond with the surface reactivity of sp^2-based nanomaterials. These results were recently confirmed by a Raman study of the sp^3 to sp^2 conversion for detonation NDs [160]. NMR and EPR investigations detect the early stages of graphitization for annealing temperatures included between 600 and 800 °C [161].

Proper conditions determined for surface graphitization were then reported in a set-up where nanodiamonds are annealed under vacuum in a crucible. Annealed NDs are dispersable in water, their colloidal properties will be discussed in the Part 4.5. HRTEM observations confirm the structure modifications previously described showing FLRs formation [75]. A specific chemical reactivity was reported for detonation NDs after annealing at 750 °C exhibiting FLRs structures allowing arylation reactions [99].

In conclusion, surface chemistry of nanodiamonds can be tuned by thermal annealing, plasma exposure or chemical reactions. Hydrogenated and carboxylated NDs are currently well controlled whereas hydroxylation remains more difficult to achieve. These terminations are particularly suitable for the grafting of biomolecules or drugs on NDs [28, 36]. Sp^2 reconstructions can be generated at detonation NDs surface without altering the diamond core [55]. Arylation reactions allow their functionalization with complex organic moieties for bioapplications [99]. On the other hand, further progresses are needed to control the selectivity of amination, fluorination and chlorination of NDs.

The control of NDs surface charge is essential for electrostatic loading of drugs [27, 31]. Moreover, it greatly influences the interaction with cell membrane and the

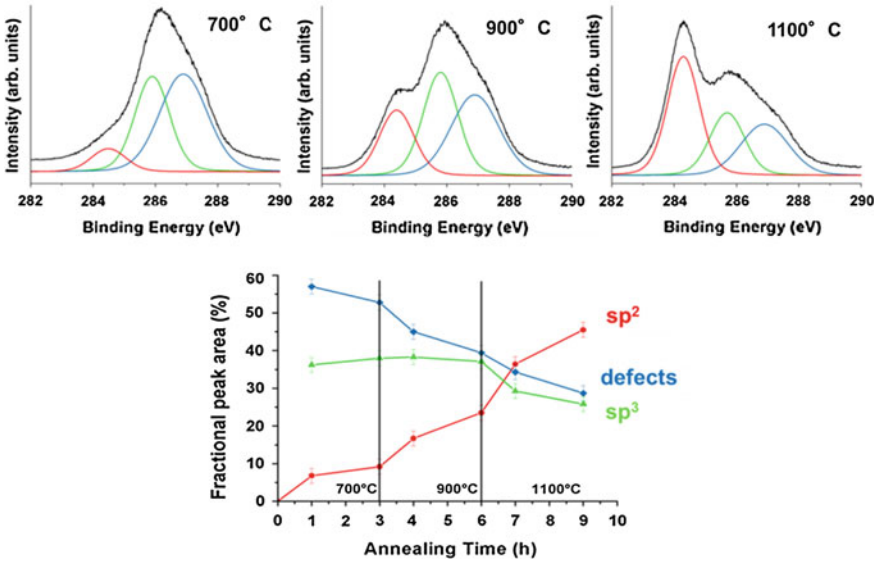

Fig. 4.7 C1s XPS spectra of NDs after sequential annealing treatments of 3 h at 700, 900, 1100 °C. Fitting components CI (*red*), CII (*green*), CIII (*blue*), related to sp^2 carbon-carbon bonds, sp^3 carbon-carbon bonds, and defects, respectively, are plotted under the experimental curves. Evolution of the fractional peak areas versus annealing time [55]

internalization pathways of NDs into cells [166]. The control of surface terminations allows a tuning of NDs surface charge in suspension from negative to positive versus pH. Colloidal properties of modified nanodiamonds in water will be now presented (Part 4.5). The link between their Zeta potential and their surface electronic properties will be investigated in details.

4.5 Colloidal Properties of Modified Nanodiamonds

The colloidal stability of nanodiamonds in biologic media is of major interest for their biomedical applications. It strongly depends on their surface charge which controls hydrophilic/hydrophobic interactions with other NDs and moieties. Moreover, in the biological media, proteins adsorption leads to the formation of a corona [167] surrounding nanoparticles. The nature of proteins forming the corona is a key parameter for cell internalization pathways which occur by their specific recognition. In liquid media, nanodiamonds tend to form aggregates, this may be favored by opposite charged facets [168] or by graphitic carbon present at NDs surface [69, 128]. Several experimental methods were developed to reduce aggregation and obtain monodisperse colloidal suspensions. Bead assisted sonic disintegration (BASD) was performed using ceramic microbeads, nevertheless, it can produce

chemical contaminations or surface graphitization [84, 169, 170]. Dry milling using salts and sugars avoiding contamination was also reported [171]. Modifications in NDs surface chemistry like plasma hydrogenation [86], surface graphitization [99], oxidation in air [85] or borane reduction [128] have also proved their efficiency for de-aggregation.

The behavior of nanoparticles in liquid media could be investigated by Dynamic Light Scattering (DLS). From diffused intensity signal, this technique provides the measurement of the hydrodynamic diameter of stable NPs. This diameter is higher than the real one because it includes the solvated layer of adsorbed ions which is solvent and ionic force dependent [172]. The Zeta Potential (ZP) is defined from the double layer model (Stern and Gouy-Chapman layers) which describes the counter-ions adsorption. ZP is the potential at the surface of the electrical double layer called slipping plane. It is obviously related to the surface charge of NDs, very different values are obtained versus surface chemistry and size [24]. Zeta Potential is calculated from the electrophoretic mobility measured in DLS. Its evolution versus pH must be investigated. Indeed, functional groups present at NDs surface can switch from protonated to deprotonated states according to their pKa value. The colloidal stability will be then dependent on pH value. Indeed, the ZP governs the electrostatic repulsive interactions in liquid medium. Stable NPs in colloids usually exhibit ZP potential absolute value higher than 30 mV [173, 174].

The control of ND surface charge is essential for drug or biological moieties adsorption [27, 29, 31] it can also play a major role in internalization pathways and interactions with negatively charged cell membrane [166]. In this part, the surface reactivity of modified NDs will be discussed. Especially, stable NDs in aqueous suspensions exhibiting positive or negative ZP will be considered, mechanisms such as charge transfer leading to these specific charges will be also discussed.

4.5.1 Surface Reactivity of Modified NDs

The hydrophilicity of detonation nanodiamonds from the same origin was investigated versus their surface chemistry after plasma hydrogenation, air oxidation and surface graphitization [86]. Water adsorption isotherms measured by BET revealed a significantly higher hydrophilicity for H-NDs and sp^2-NDs compared to COOH-NDs. Taking into account the specific surface area and assuming a monomolecular adsorption, hydrophilic sites were estimated to 2.2, 1.7 and 1.4 sites/nm^2 for sp^2-NDs, H-NDs and COOH-NDs, respectively. These hydrophilic sites on H-NDs and sp^2-NDs are likely to facilitate the dispersion in water of otherwise hydrophobic NDs (Part 4.5.2).

This high affinity of hydrogenated and surface graphitized NDs with oxygen is supported by XPS analysis performed after air exposure. Oxygen atomic concentrations of 6.5 at% and 4.0 at% were measured for sp^2-NDs and H-NDs after air exposure [86] while it was completely removed after plasma hydrogenation or annealing under vacuum (Part 4.4) [55, 70].

4.5.2 Solubility, Stability in Colloids

Stable suspensions of individual detonation NDs in water were achieved by successive sonication and centrifugation [88, 92]. Sonication allows the breaking of Van der Waals interactions between aggregated NDs. This is an important issue for biomedical applications because detonation nanodiamonds (<10 nm) are expected to be easily eliminated by kidney (Part 4.6) [21]. The colloidal stability is closely related to surface charge of NDs because of electrostatic repulsive interactions. Indeed, these interactions can also promote aggregation as discussed previously. Among the literature, positive [129, 98] or negative [45, 88, 175–177] ZP were reported for nanodiamonds in suspension depending on their surface chemistry. These colloidal properties constitute an important asset for nanodiamonds compared to other carbon nanomaterials. Fullerenes or carbon nanotubes exhibit hydrophobic behavior and their stability in water suspension can only be obtained after their functionalization [178–180]. These colloids of NDs in water were also used to obtain homogeneous seeding of substrates for CVD growth of thin diamond films [181, 182]. Some groups used surfactants like sodium oleate [98] or oleylamine [183] to improve the colloidal stability of NDs. Nevertheless, aqueous suspensions are more suitable for bioapplications such as drug delivery.

4.5.3 Negatively Charged NDs

Carboxylated nanodiamonds obtained after annealing in air (Part 4.4.2) exhibit a strong negative Zeta potential included between −30 and −50 mV when dispersed in water for pH > 5 [45, 75]. The origin of this negative potential is related to the presence at the surface of carboxylate groups (COO^-) the basic form of COOH. Below pH = 5, the formation of mainly carboxylic groups (COOH) leads to a drop of Zeta potential. This threshold pH value is close to the pKa of COOH/COO^- couple [184].

Several studies [69, 88, 185] reported a similar behavior i.e. negative ZP for pristine NDs. This has been explained by the presence of carboxylate groups at the NDs surface formed during purification treatments (Part 4.4).

4.5.4 Positively Charged NDs

Other “as received” nanodiamonds from different suppliers were stabilized in water suspensions exhibiting a positive Zeta potential (> + 30 mV) [45, 175]. The origin of this positive ZP is not yet clearly understood. In the literature, colloidal aqueous suspensions of positively charged NDs (ZP > 30 mV) were also reported after different surface modifications: reduction with borane or $LiAlH_4$ [18, 129], UV

hydroxylation [93], annealing under hydrogen flow [88], plasma hydrogenation [86] or surface graphitization [75]. These charge modifications may be related to graphitic carbon surrounding NDs core or to protonation of some chemical functional groups or lastly to intrinsic properties of hydrogenated diamond surface. Different likely mechanisms have been previously proposed in the literature and will be now discussed.

4.5.5 Presence of Graphitic Carbon at the NDs Surface

Gibson et al. reported positive Zeta potential for detonation nanodiamonds after two oxidization treatments CrO_2/H_2SO_4 followed by $NaOH/H_2O_2$ [177]. Authors attributed this positive ZP to electrostatic interactions between pyrone groups and π-electrons from sp^2-carbon present at NDs surface corresponding to protonation of pyrone structures. Theoretical investigations supported this effect leading to carbon basicity [186, 187].

Williams et al. obtained a positive Zeta potential for detonation NDs exposed to hydrogen flow at 500 °C then dispersed into water solution [88]. Authors claimed it originates from the interaction of OLC structures (π bonding) remaining at NDs surface with oxonium ions (H_3O^+) present in water suspension at acidic pH. Their HRTEM pictures support the presence of OLC on hydrogen treated NDs. By analogy with carbon black, authors proposed an electron-donor-acceptor complex may be formed [188]. In both previous studies, a charge exchange between species from aqueous solution and sp^2 carbon remaining at NDs surface is involved.

More recently, positive Zeta potential was measured at pH < 8 on detonation NDs on which FLRs were intentionally generated by annealing under vacuum before their dispersion into water (Fig. 4.8) [75]. The origin of the positive charge was linked to the formation of endoperoxide groups by cycloaddition of O_2 molecules on FLRs. BET and XPS measurements well emphasize the high reactivity of sp^2-NDs toward oxygen species after air exposure [86]. In situ XPS analysis after UHV annealing suggests a reversible oxidation similar to the one observed on graphene [189]. Moreover, after in situ desorption, the FTIR spectrum exhibits an intense band at 1100 cm^{-1} well corresponding to C–O stretching of ether or epoxy groups [190]. This last result supports the formation of endoperoxide groups on FLRs structures. The protonation of these endoperoxides may be the explanation for oxygen hole doping [75].

4.5.5.1 Chemically Induced Positive ZP

Ozawa et al. reported on a positive Zeta potential switching after hydroxylation of carboxylated detonation NDs by a borane reduction [191]. Hydroxyl groups probed on their NDs by FTIR measurements, allowed further silanization coupling. Shenderova et al. obtained positive ZP for detonation NDs initially carboxylated

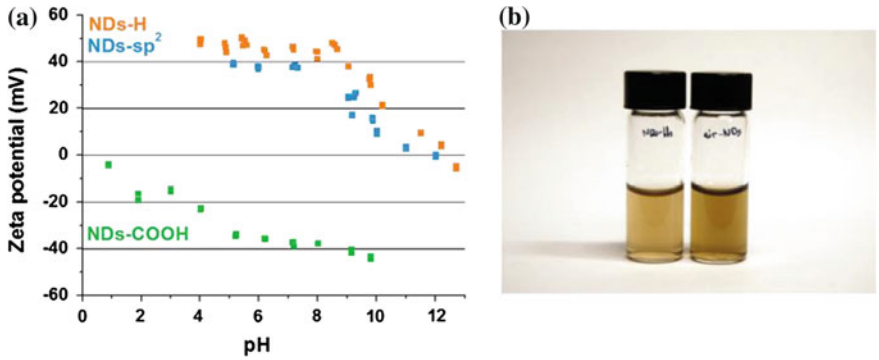

Fig. 4.8 **a** Zeta potential of H-NDs, COOH-NDs and sp^2-NDs dispersed in water versus pH **b** Colloidal suspensions of sp^2-NDs and COOH-NDs in water

after $LiAlH_4$ reduction [129]. Girard et al. also observed a ZP inversion (+30 mV at pH = 7 compared to −45 mV initially) after UV photochemical treatment of HPHT nanodiamonds [93]. Hydroxyl groups were identified from FTIR and XPS investigations. Nevertheless, any previous work provides an explanation for this positive charge and no link between positive ZP and hydroxylation has been currently established.

Finally, positive ZP potential (25 mV for pH between 2 and 3) was measured for nanodiamonds grafted with ethylenediamine (EDA) [176]. According to authors, protonation of amino groups may explain the basic properties in acidic environment.

4.5.5.2 Specific Surface Properties of Hydrogenated Nanodiamonds

Stable aqueous suspensions of detonation nanodiamonds previously plasma hydrogenated were recently reported [86]. Measured ZP is included between +45 and −50 mV for pH values in the range of 4–9 (Fig. 4.8). The experiment was carried out on initially negatively or positively charged NDs. According to authors, a transfer doping occurs onto 5 nm diamond nanoparticles suspended in water based on the semi-conductive behavior of the NDs core. These experiments show that an electrochemical exchange between residual CO_2 takes place between aqueous solution and hydrogenated diamond surface leading to holes accumulation similarly to the one observed for micro-sized diamond particles [192]. The key role played by oxygen was underlined by nitrogen flushing which provokes flocculation of H-NDs. A transfer doping similar to the one occurring on diamond surfaces also occurs onto 5 nm NDs suspended in water [86]. This effect was not obvious at nanoscale. Indeed, the band bending inducing the hole accumulation layer is of the same order of magnitude than the particle diameter. This transfer doping at the hydrogenated ND surface was recently confirmed by resistivity measurements [193]. Resistivity drops from 10^7 to 10^5 $\Omega \cdot$ cm for detonation nanodiamonds heated in hydrogen gas

(600–900 °C). Oxidation of the hydrogenated sample at 300 °C recovers resistivity to its original value.

To conclude, Zeta potential of nanodiamonds can be tuned over a wide pH range applying different surface modifications. This behaviour is highly suitable for bio-applications. According to the literature, ZP switching can be explained by charge exchanges between NDs surface and species from aqueous suspensions. Some works emphasized the role played by sp^2 carbon at NDs surface. Other studies were performed using surface cleaned nanodiamonds i.e. Fenton reaction which clearly consumes a part of NDs or plasma hydrogenation. In the latter case, positive Zeta potential of H-NDs is due to specific surface properties of hydrogenated diamond surface. Neither chemical functional groups nor graphitic structures seem to be involved. This suggests mechanisms of different natures could explain this positive surface charge.

4.6 Nanodiamonds and Biomedical Applications

4.6.1 NDs Assets

Nanodiamonds (NDs) combined many required assets for biomedical applications: extremely low cytoxicity and genotoxicity, carbon chemistry allowing covalent grafting, photoluminescent color centers, tunable size (down to 5 nm). Let us discuss these advantages.

4.6.1.1 NDs Toxicity and Biodistribution

Several long-term in vitro [22, 194] and in vivo [195–197] previous studies demonstrated that NDs are non-cytotoxic, better tolerated by cells than other nanocarbon materials [198]. NDs introduced into *Caenorhabditis elegans* worm did not cause any detectable stress to worms [198]. In mice, intravenous injection of 50 nm NDs led to long-term entrapment in the liver and the lung [195], but no mice showed any abnormal symptoms. Similarly, subcutaneous and intraperitoneal injection of 100 nm NDs in rats led to accumulation of NDs in retention organs over 1 month with no impact on the rats' viability [197]. However, a slight surface-dependent genotoxicity of NDs was recently reported on embryonic stem cells [199].

Until now, no extensive study combining cytotoxicity and genotoxicity of NDs was reported. A recent study [25] focuses on in vitro cytotoxicity and genotoxicity of HPHT NDs perfectly characterized in terms of size (20 nm and 100 nm) and surface chemistry. The cellular induced effects of two sets of NDs were investigated in six human cell lines: HepG2 and Hep3B (liver), Caki-1 and Hek-293 (kidney), HT29 (intestine) and A549 (lung). The screening of ND cytotoxicity was carried out by measuring cell impedance (xCELLigence). This technique permits real-time

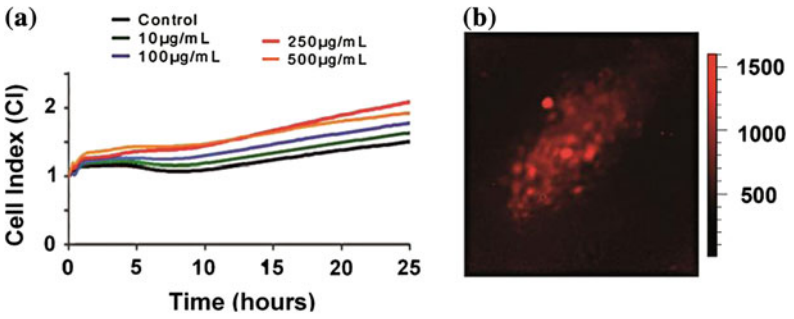

Fig. 4.9 **a** Cell index real-time monitoring of HepG2 cells exposed 24 h to 20 nm NDs; **b** Raman/photoluminescence image on a HepG2 cell [25]

monitoring of NPs effects on cell morphology, proliferation, adhesion and membrane potential [200]. Flow cytometry allowed the discrimination of viable cells, containing or not NDs, and dead cells. Finally, using immunofluorescence detection of nuclear γ-H2Ax foci, considered the most sensitive method for detecting DNA double-strand breaks [201], genotoxicity was also analyzed. According to the results, NDs do not induce any significant toxic effect on the six cell lines up to an exposure dose of 250 mg/mL (Fig. 4.9). As a comparison, 25 nm SiO_2 NPs are 9 times more genotoxic at a 10 times lower concentration [25].

4.6.1.2 Grafting of Biological Moieties

We have previously underlined surface charge of NDs suspended in aqueous solution can be tuned over a wide pH range (Part 4.5) thanks to specific surface modifications (Part 4.4). Efficient surface treatments also permit to conjugate ND surfaces with fluorescent molecules [202–205], with DNA [206], siRNA [27], proteins [207, 208], lysozymes [208], growth hormones [209], antibodies [210, 211], anti-cancer drugs [30–32], as well as with dopamine derivatives [212].

Either covalent or non-covalent graftings were performed depending on expected bio-applications. These attempts have been recently reviewed in details [28]. The non-covalent grafting of large biomolecules based on electrostatic interactions was performed from well controlled NDs surface charge (Part 4.5). Cytochrome c [98] and bovine insulin [213] were immobilized on nanodiamonds. Furthermore, lysozymes [34, 214, 215] and apoobelin [216] were attached. Anticancer drugs like doxorubicine [217, 218], paclitaxel [30] or HCPT [32] were non-covalently adsorbed and then delivered. Some polymer coatings like polyethylenimine (PEI) have been also carried out on NDs to confer cationic surface charge for siRNA adsorption and delivery for gene therapy (Ewing's sarcoma) [27, 29, 206, 219]. In most cases, the functionality of biomolecules is preserved [214, 220] although significantly less efficiency has sometimes been observed. Cumulative effects were even obtained as lysozyme adsorption is combined with cytochrome c [215]. Depending on the

functionality of the biologic unit, covalent grafting via organic chemistry could be suitable to get a specific binding site on the ND or to avoid modifications of the biomolecule conformation. Grafting routes which may involve a linker molecule could be performed from different surface terminations of NDs [28].

4.6.1.3 Photoluminescent NV Centers

Color centers could be efficiently generated in HPHT nanodiamonds by high-energy particle beam irradiation (He^+ or electrons) leading to vacancy creation [124, 203]. During annealing, vacancies combined with nitrogen atoms to form NV centers which could be characterized by Photoluminescence (Part 4.3). HPHT NDs exhibited stable photoluminescence without bleaching or blinking in the red and near-infrared region corresponding to transmission window of tissues for size down to 7 nm [221]. These properties allowed the long-term tracking of fluorescent NDs into cells localized at subcellular scale by fluorescence and TEM microscopies. Expected applications concern biomedical imaging [203] and fluorescence energy transfer (FRET) with other fluorophores [222]. For detonation NDs, the limited nitrogen amount, the nanometric size (<5 nm) and structural defects present at the surface and in the diamond core prevent the observation of stable photoluminescence [65, 68].

4.6.1.4 Tunable Size

Nanodiamonds are scalable nanoparticles down to few nanometers [92]. For smallest NDs, in vivo clearance or kidney elimination could be expected according to the size of kidney capillarities. This constitutes an essential advantage for drug delivery or biomarkers applications. In addition, size effects on photoluminescence were reported which tune the wavelength of emitted photons [223].

4.6.2 Some Current Challenges

According to the previous assets, several challenges appear highly relevant and promising for the development of future bio-applications involving nanodiamonds: their labeling, their use for safer by design or their developments as a multifunctional platform for drug delivery.

4.6.2.1 Labeling

Labeling is inescapable for biodistribution and pharmacokinetics studies, for development of biomarkers or targeted drug delivery. Although NV centers are promising for in vitro imaging applications [203, 224, 225], their limited photoluminescence

intensity is an obstacle to their detection in the body. In the literature, several groups reported the efficient tracking of NDs into cells by grafting of fluorophores [24, 98, 202, 226]. Bright blue luminescence was even obtained by octadecylamine covalently attached to NDs-COOH [227]. The main stake concerns the stability of fluorophores in cellular environment. An interesting alternative for tracking consists to combine NDs with contrast agents currently used for magnetic resonance imaging (MRI). The rich surface chemistry of NDs (Part 4.4) allows the covalent grafting of amine-functionalized Gd(III). Gd(III)-NDs conjugates exhibited ten times higher relaxivity and can be well detected by MRI [228]. Finally, contrary to carbon nanotubes [9], any radioactive labeling has been yet reported for nanodiamonds. This constitutes a major challenge because radioactive imaging is ordinarily used for biodistribution and pharmacokinetics studies of NPs.

4.6.2.2 Safer by Design

An important issue for drug delivery concerns the conception of safer nanoparticles [229, 230]. For this purpose, NPs physicochemical determinants such as size, shape, composition, surface chemistry or coating nature which may be critical for cytotoxic and genotoxic effects must be investigated. In vitro screening for assessing the possible reactivity, biomarkers of inflammation and cellular uptake can provide precious indications to chemists and physicists to design "safe" nanomaterials. According to their extremely weak in vitro toxicity [25], nanodiamonds constitute excellent candidates to study the specific effects of physical and chemical parameters on toxicity.

4.6.2.3 Multifunctional Platform for Drug Delivery

Nanodiamonds combine biocompatibility, scalability and stability in aqueous solution (Part 4.5). Moreover, several studies reported their ability to carry and deliver different classes of drugs [30–32] or nucleic acids like siRNA [26, 27, 29, 219]. To build such platform, a stable labeling is required to allow tracking of NDs. Another important issue is related to the specific targeting of proteins or DNA. A recent study [184] reports on 20 nm HPHT NDs covalently grafted with peptide nucleic acids (PNA). The original functionalization route is based on an optimized amidation of ND carboxylic acids groups. ND-PNA conjugates were validated through a successful recognition of complementary DNA in a mixture, showing their efficiency toward nucleic acid detection (Fig. 4.10). Such nucleic acid functionalized NDs open the way to a wide range of biomedical applications towards genetic diseases, genomic research or early cancer diagnosis.

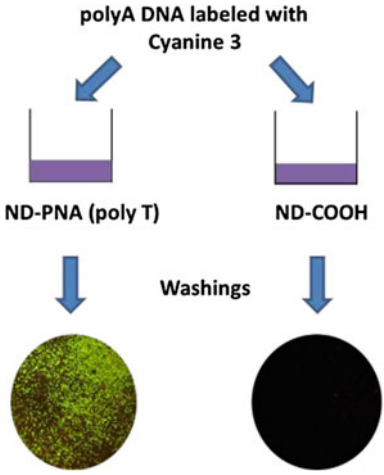

Fig. 4.10 Fluorescence of ND-PNA conjugates compared to ND-COOH after DNA hybridization observed at λ_{exc} = 550 nm and λ_{em} = 570 nm [184]

4.7 Conclusion

Nanodiamonds can behave very different surface properties according to their tunable surface chemistry. The current state of art of controlled surface terminations was summarized in this chapter. The link between surface chemistry, surface charge and colloidal properties of NDs was particularly emphasized. Indeed, it appears highly relevant for biomedical applications because it is a key parameter for drug adsorption or interactions with cell membrane. Among the potential surface chemistries, hydroxyl and halogen terminations (F, Cl, Br) offer specific reactivity. However, experimental protocols must be further improved to reach a higher selectivity.

Some NDs characteristics related to the diamond core remain also partially understood at the present state. In particular, it is essential to further investigate the impact of structural defects or chemical impurities on NDs properties. The presence of different crystallographic facets on HPHT and some detonation NDs should also significantly influence their surface reactivity. Moreover, consequences of hydrogen incorporated in nanodiamonds especially during detonation synthesis (Part 4.2) must be better understood. According to previous works performed on bulk diamond, hydrogen should be trapped by structural defects or chemical impurities [56].

Among further main challenges for biomedecine, the radioactive labeling appears as a priority to investigate in vivo the biodistribution and pharmacokinetics on NDs. Such achievement has not been yet reported. Mechanisms of drug adsorption/desorption on NDs must be deeper understood to achieve a controlled release. These phenomena are highly sensitive to size and surface chemistry. The combination of NDs with NV centers can permit novel developments in biology like the probing of ion channels in cells or the neuron imaging. Finally, the synthesis of hybrid NDs is also an essential challenge. For example, surface graphitized NDs may possess surface properties linked to fullerene or graphene assets required

for radiosensitization or photothermal therapy. In conclusion, according to their multiple assets, nanodiamonds constitute excellent candidates to be used as active NPs with therapeutic behaviors for biomedical applications.

Acknowledgments J.C. Arnault would like to thank H.A. Girard and T. Petit for fruitful discussions. He also acknowledges the different coworkers which contribute to studies dealing with surface modified nanodiamonds. The author also thanks Professor E. Osawa for providing detonation nanodiamonds.

References

1. M.L. Etheridge, S.A. Campbell, A.G. Erdman, C.L. Haynes, S.M. Wolf, J. McCullough, The big picture on nanomedicine: the state of investigational and approved nanomedicine products. Nanomed. Nanotechnol. Biol. Med. **9**(1), 1–14 (2013). doi:10.1016/j.nano.2012.05.013
2. Y. Matsumura, H. Maeda, A new concept for macromolecular therapeutics in cancer chemotherapy: mechanism of tumoritropic accumulation of proteins and the antitumor agent smancs. Cancer Res. **46**(12_Part 1), 6387–6392 (1986)
3. J.D. Byrne, T. Betancourt, L. Brannon-Peppas, Active targeting schemes for nanoparticle systems in cancer therapeutics. Adv. Drug Deliv. Rev. **60**(15), 1615–1626 (2008). doi:10.1016/j.addr.2008.08.005
4. E.V. Batrakova, A.V. Kabanov, Pluronic block copolymers: evolution of drug delivery concept from inert nanocarriers to biological response modifiers. J. Control. Release **130**(2), 98–106 (2008). doi:10.1016/j.jconrel.2008.04.013
5. X. Michalet, F.F. Pinaud, L.A. Bentolila, J.M. Tsay, S. Doose, J.J. Li, G. Sundaresan, A.M. Wu, S.S. Gambhir, S. Weiss, Quantum dots for live cells, in vivo imaging, and diagnostics. Science **307**(5709), 538–544 (2005). doi:10.1126/science.1104274
6. T.A. Taton, C.A. Mirkin, R.L. Letsinger, Scanometric DNA array detection with nanoparticle probes. Science **289**(5485), 1757–1760 (2000). doi:10.1126/science.289.5485.1757
7. H.B. Na, I.C. Song, T. Hyeon, Inorganic nanoparticles for MRI contrast agents. Adv. Mater. **21**(21), 2133–2148 (2009). doi:10.1002/adma.200802366
8. D. Yoo, J.H. Lee, T.H. Shin, J. Cheon, Theranostic magnetic nanoparticles. Acc. Chem. Res. **44**(10), 863–874 (2011). doi:10.1021/ar200085c
9. D. Georgin, B. Czarny, M. Botquin, M. Mayne-L'hermite, M. Pinault, B. Bouchet- Fabre, M. Carriere, J.L. Poncy, Q. Chau, R. Maximilien, V. Dive, F. Taran, Preparation of (14) C-labeled multiwalled carbon nanotubes for biodistribution investigations. J. Am. Chem. Soc. **131**(41), 14658–14659 (2009). doi:10.1021/ja906319z
10. C.S.S.R. Kumar, F. Mohammad, Magnetic nanomaterials for hyperthermia based therapy and controlled drug delivery. Adv. Drug Deliv. Rev. **63**(9), 789–808 (2011). doi:10.1016/j.addr.2011.03.008
11. K. Yang, S. Zhang, G. Zhang, X. Sun, S.T. Lee, Z. Liu, Graphene in mice: ultrahigh in vivo tumor uptake and efficient photothermal therapy. Nano Lett. **10**(9), 3318–3323 (2010). doi:10.1021/nl100996u
12. K. Yang, J. Wan, S. Zhang, B. Tian, Y. Zhang, Z. Liu, The influence of surface chemistry and size of nanoscale graphene oxide on photothermal therapy of cancer using ultra-low laser power. Biomaterials **33**(7), 2206–2214 (2012). doi:10.1016/j.biomaterials.2011.11.064
13. P. Cherukuri, E.S. Glazer, S.A. Curley, Targeted hyperthermia using metal nanoparticles. Adv. Drug Deliv. Rev. **62**(3), 339–345 (2010). doi:10.1016/j.addr.2009.11.006
14. J.F. Hainfeld, D.N. Slatkin, H.M. Smilowitz, The use of gold nanoparticles to enhance radiotherapy in mice. Phys. Med. Biol. **49**(18), N309–N315 (2004). doi:10.1088/0031-9155/49/18/N03

15. E. Porcel, S. Liehn, H. Remita, N. Usami, K. Kobayashi, Y. Furusawa, C. Le Sech, S. Lacombe, Platinum nanoparticles: a promising material for future cancer therapy? Nanotechnology **21**(8), 85103 (2010). doi:10.1088/0957-4484/21/8/085103
16. L. Maggiorella, G. Barouch, C. Devaux, A. Pottier, E. Deutsch, J. Bourhis, E. Borghi, L. Levy, Nanoscale radiotherapy with hafnium oxide nanoparticles. Future Oncol **8**(9), 1167–1181 (2012). doi:10.2217/FON.12.96
17. M.J. Sailor, J.H. Park, Hybrid nanoparticles for detection and treatment of cancer. Adv. Mater. **24**(28), 3779–3802 (2012). doi:10.1002/adma.201200653
18. W.T. Al-Jamal, K. Kostarelos, Liposomes: from a clinically established drug delivery system to a nanoparticle platform for theranostic nanomedicine. Acc. Chem. Res. **44**(10), 1094–10104 (2011). doi:10.1021/ar200105p
19. M. Liong, J. Lu, M. Kovochich, T. Xia, S.G. Ruehm, A.E. Nel, F. Tamanoi, J.I. Zink, Multifunctional inorganic nanoparticles for imaging, targeting, and drug delivery. ACS Nano **2**(5), 889–896 (2008). doi:10.1021/nn800072t
20. G. Wu, A. Mikhailovsky, H.A. Khant, C. Fu, W. Chiu, J.A. Zasadzinski, Remotely triggered liposome release by near-infrared light absorption via hollow gold nanoshells. J. Am. Chem. Soc. **130**(36), 8175–8177 (2008). doi:10.1021/ja802656d
21. H.S. Choi, W. Liu, P. Misra, E. Tanaka, J.P. Zimmer, B. Itty Ipe, M.G. Bawendi, J.V. Frangioni, Renal clearance of quantum dots. Nat. Biotechnol. **25**(10), 1165–1170 (2007). doi:10.1038/nbt1340
22. V. Vaijayanthimala, Y.K. Tzeng, H.C. Chang, C.L. Li, The biocompatibility of fluorescent nanodiamonds and their mechanism of cellular uptake. Nanotechnology **20**(42), 425103 (2009). doi:10.1088/0957-4484/20/42/425103
23. Y. Yuan, X. Wang, G. Jia, J.H. Liu, T. Wang, Y. Gu, S.T. Yang, S. Zhen, H. Wang, Y. Liu, Pulmonary toxicity and translocation of nanodiamonds in mice. Diam. Relat. Mater. **19**(4), 291–299 (2010). doi:10.1016/j.diamond.2009.11.022
24. A.M. Schrand, S.A.C. Hens, O.A. Shenderova, Nanodiamond particles: properties and perspectives for bioapplications. Crit. Rev. Solid State Mater. Sci. **34**(1-2), 18–74 (2009). doi:10.1080/10408430902831987
25. V. Paget, J.A. Sergent, R. Grall, S. Altmeyer-Morel, H.A. Girard, T. Petit, G. Gesset, M. Mermoux, P. Bergonzo, J.C. Arnault, S. Chevillard, Carboxylated nanodiamonds are neither cytotoxic nor genotoxic on kidney, intestine, lung and liver human cell lines. Nanotoxicology. **8**(S1), 46–56 (2014). doi:10.3109/17435390.2013.855828
26. B. Zhang, Y. Li, C.Y. Fang, C.C. Chang, C.S. Chen, Y.Y. Chen, H.C. Chang, Receptor-mediated cellular uptake of folate-conjugated fluorescent nanodiamonds: a combined ensemble and single-particle study. Small **5**(23), 2716–2721 (2009). doi:10.1002/smll.200900725
27. A. Alhaddad, M.P. Adam, J. Botsoa, G. Dantelle, S. Perruchas, T. Gacoin, C. Mansuy, S. Lavielle, C. Malvy, F. Treussart, J.R. Bertrand, Nanodiamond as a vector for siRNA delivery to Ewing sarcoma cells. Small **7**(21), 3087–3095 (2011). doi:10.1002/smll.201101193
28. A. Krueger, D. Lang, Functionality is key: recent progress in the surface modification of nanodiamond. Adv. Funct. Mater. **22**(5), 890–906 (2012). doi:10.1002/adfm.201102670
29. A. Alhaddad, C. Durieu, G. Dantelle, E. Le Cam, C. Malvy et al., Influence of the internalization pathway on the efficacy of siRNA delivery by cationic fluorescent nanodiamonds in the Ewing sarcoma cell model. PLoS ONE **7**(12), e52207 (2012). doi:10.1371/journal.pone.0052207
30. K.K. Liu, W.W. Zheng, C.C. Wang, Y.C. Chiu, C.L. Cheng, Y.S. Lo, C. Chen, J.I. Chao, Covalent linkage of nanodiamond-paclitaxel for drug delivery and cancer therapy. Nanotechnology **21**(31), 315106 (2010). doi:10.1088/0957-4484/21/31/315106
31. E.K. Chow, X.Q. Zhang, M. Chen, R. Lam, E. Robinson, H. Huang, D. Schaffer, E. Osawa, A. Goga, D. Ho, Nanodiamond therapeutic delivery agents mediate enhanced chemoresistant tumor treatment. Sci. Transl. Med. **3**(73), 73ra21 (2011). doi:10.1126/scitranslmed.3001713

32. J. Li, Y. Zhu, W. Li, X. Zhang, P. Peng, Q. Huang, Nanodiamonds as intracellular transporters of chemotherapeutic drug. Biomaterials **31**(32), 8410–8418 (2010). doi:10.1016/j.biomaterials.2010.07.058
33. Y.R. Chang, H.Y. Lee, K. Chen, C.C. Chang, D.S. Tsai, C.C. Fu, T.S. Lim, Y.K. Tzeng, C.Y. Fang, C.C. Han, H.C. Chang, W. Fann, Mass production and dynamic imaging of fluorescent nanodiamonds. Nat. Nanotech. **3**, 284–288 (2008). doi:10.1038/nnano.2008.99
34. J.I. Chao, E. Perevedentseva, P.H. Chung, K.K. Liu, C.Y. Cheng, C.C. Chang, C.L. Cheng, Nanometer-sized diamond particle as a probe for biolabeling. Biophys. J. **93**(6), 2199–2208 (2007). doi:10.1529/biophysj.107.108134
35. F.P. Bundy, W.A. Bassett, M.S. Weathers, R.J. Hemley, H.K. Mao, A.F. Goncharov, The pressure-temperature phase and transformation diagram for carbon; updated through 1994. Carbon **34**(2), 141–153 (1996). doi:10.1016/0008-6223(96)00170-4
36. V.N. Mochalin, O. Shenderova, D. Ho, Y. Gogotsi, The properties and applications of nanodiamonds. Nat. Nanotech. **7**, 11–23 (2012). doi:10.1038/NNANO.2011.209
37. F.P. Bundy, H.T. Hall, H.M. Strong, R.H. Wentorf, Man-made diamonds. Nature **176**(4471), 51–55 (1955). doi:10.1038/176051a0
38. J.C. Angus, C.C. Hayman, Low-pressure, metastable growth of diamond and "diamondlike" phases. Science **241**(4868), 913–921 (1988). doi:10.1126/science.241.4868.913
39. G.W. Yang, J.B. Wang, Q.X. Liu, Preparation of nano-crystalline diamonds using pulsed laser induced reactive quenching. J. Phys.: Condens. Matter **10**(35), 7923–7928 (1998). doi:10.1088/0953-8984/10/35/024
40. J. Sun, S.L. Hu, X.W. Du, Y.W. Lei, Ultrafine diamond synthesized by long-pulse-width laser. Appl. Phys. Lett. **89**(18), 183115 (2006). doi:10.1063/1.2385210
41. J.P. Boudou, P.A. Curmi, F. Jelezko, J. Wrachtrup, P. Aubert, M. Sennour, G. Balasubramanian, R. Reuter, A. Thorel, E. Gaffet, High yield fabrication of fluorescent Nanodiamonds. Nanotechnology **20**(35), 235602 (2009). doi:10.1088/0957-4484/20/35/359801
42. J.P. Boudou, J. Tisler, R. Reuter, A. Thorel, P.A. Curmi, F. Jelezko, J. Wrachtrup, Fluorescent nanodiamonds derived from HPHT with a size of less than 10 nm. Diam. Relat. Mater. **37**, 80–86 (2013). doi:10.1016/j.diamond.2013.05.006
43. E. Neu, C. Arend, E. Gross, F. Guldner, C. Hepp, D. Steinmetz, E. Zscherpel, S. Ghodbane, H. Sternschulte, D. Steinmüller-Nethl, Y. Liang, A. Krueger, C. Becher, Narrowband fluorescent nanodiamonds produced from chemical vapor deposition films. Appl. Phys. Lett. **98**(24), 243107 (2011). doi:10.1063/1.3599608
44. V. Danilenko, O. Shenderova, Advances in synthesis of nanodiamond particles. in *Ultrananocrystalline Diamond: Synthesis, Properties and Applications*, 2nd edn. ed. by O. Shenderova, D.M. Gruen (Elsevier, 2012)
45. V.Y. Dolmatov, Detonation-synthesis nanodiamonds: synthesis, structure, properties and applications. Russ. Chem. Rev. **76**(4), 339–360 (2007). doi:10.1070/RC2007v076n04ABEH003643
46. O. Shenderova, A. Koscheev, N. Zaripov, I. Petrov, Y. Skryabin, P. Detkov, T. Turner, G. Van Tendeloo, Surface chemistry and properties of ozone-purified detonation nanodiamonds. J. Phys. Chem. C **115**(20), 9827–9837 (2011). doi:10.1021/jp1102466
47. J.E. Dahl, S.G. Liu, R.M.K. Carlson, Isolation and structure of higher diamondoids, nanometer-sized diamond molecules. Science **299**(5603), 96–102 (2003). doi:10.1126/science.1078239
48. O.O. Mykhaylyk, Y.M. Solonin, D.N. Batchelder, R. Brydson, Transformation of nanodiamond into carbon onions: a comparative study by high-resolution transmission electron microscopy, electron energy-loss spectroscopy, x-ray diffraction, small-angle x-ray scattering, and ultraviolet Raman spectroscopy. J. Appl. Phys. **97**(7), 074302 (2005). doi:10.1063/1.1868054
49. E. Osawa, D. Ho, Nanodiamond and its application to drug delivery. J. Med. Allied Sci. **2**(2), 31–40 (2012)
50. A.S. Barnard, M. Sternberg, Crystallinity and surface electrostatics of diamond nanocrystals. J. Mater. Chem. **17**(45), 4811–4819 (2007). doi:10.1039/b710189a

51. S. Turner, O.I. Lebedev, O. Shenderova, I.I. Vlasov, J. Verbeeck, G. Van Tendeloo, Determination of size, morphology, and nitrogen impurity location in treated detonation nanodiamond by transmission electron microscopy. Adv. Funct. Mater. **19**(13), 2116–2124 (2009). doi:10.1002/adfm.200801872
52. D.C. Bell, C.J. Russo, D.V. Kolmykov, 40 keV atomic resolution TEM. Ultramicroscopy **114**, 38–45 (2012). doi:10.1016/j.ultramic.2011.12.001
53. B. Palosz, S. Stelmakh, E. Grzanka, S. Gierlotka, W. Palosz, Application of apparent lattice parameter to determination of core-shell structure of nanocrystals. Z. Kristallogr. **222**(11), 580–594 (2007). doi:10.1524/zkri.2007.222.11.580
54. V.L. Kuznetsov, M.N. Aleksandrov, I.V. Zagoruiko, A.L. Chuvilin, E.M. Moroz, V.N. Kolomiichuk, V.A. Lizholobov, P.M. Brylyakov, G.V. Sakovitch, Study of ultradispersed diamond powders obtained using explosion energy. Carbon **29**(4-5), 665–668 (1991). doi:10.1016/0008-6223(91)90135-6
55. T. Petit, J.C. Arnault, H.A. Girard, M. Sennour, P. Bergonzo, Early stages of surface graphitization on nanodiamond probed by x-ray photoelectron spectroscopy. Phys. Rev. B **84** (23), 233407 (2011). doi:10.1103/PhysRevB.84.233407
56. D. Ballutaud, F. Jomard, T. Kociniewski, E. Rzepka, H.A. Girard, S. Saada, Sp(3)/sp(2) character of the carbon and hydrogen configuration in micro- and nanocrystalline diamond. Diam. Relat. Mater. **17**(4-5), 451–456 (2008). doi:10.1016/j.diamond.2007.10.004
57. B.R. Smith, D. Inglis, B. Sandnes, J. Rabeau, A.V. Zvyagin, D. Gruber, C.J. Noble, R. Vogel, E. Osawa, T. Plakhotnik, Five-nanometer diamond with luminescent nitrogen-vacancy defect centers. Small **5**(14), 1649–1653 (2009). doi:10.1002/smll.200801802
58. V. Fionov, A. Lund, W.M. Chen, N.N. Rozhkova, I.A. Buyanova, G.I. Emel'yanova, L.E. Gorlenko, E.V. Golubina, E.S. Lokteva, E. Osawa, V.V. Lunin, Paramagnetic centers in detonation nanodiamonds studied by CW and pulse EPR. Chem. Phys. Lett. **493**(4-6), 319–322 (2010). doi:10.1016/j.cplett.2010.05.050
59. J.H.N. Loubser, J.A. Van Wyk, Electron spin resonance in the study of diamond. Rep. Progr. Phys. **41**(8), 1201–1248 (1978). doi:10.1088/0034-4885/41/8/002
60. V. Pichot, O. Stephan, M. Comet, E. Fousson, J. Mory, K. March, D. Spitzer, High nitrogen doping of detonation nanodiamonds. J. Phys. Chem. C **114**(22), 10082–10087 (2010). doi:10.1021/jp9121485
61. Y.G. Lu, S. Turner, J. Verbeeck, S.D. Janssens, P. Wagner, K. Haenen, G. Van Tendeloo, Direct visualization of boron dopant distribution and coordination in individual chemical vapor deposition nanocrystalline B-doped diamond grains. Appl. Phys. Lett. **101**(4), 041907 (2012). doi:10.1063/1.4738885
62. S. Turner, Y.G. Lu, S.D. Janssens, F. Da Pieve, D. Lamoen, J. Verbeeck, K. Haenen, P. Wagner, G. Van Tendeloo, Local boron environment in B-doped nanocrystalline diamond films. Nanoscale **4**(19), 5960–5964 (2012). doi:10.1039/c2nr31530k
63. A.V. Kvit, V.V. Zhirnov, T. Tyler, J.J. Hren, Aging effect and nitrogen distribution in diamond nanoparticles. Comp. Part B Eng. **35**(2), 163–166 (2004). doi:10.1016/j.compositesb.2003.08.003
64. I.I. Vlasov, Hydrid diamond-graphite nanowires produced by microwave plasma chemical vapor deposition. Adv. Mater. **19**(22), 4058–4062 (2007). doi:10.1002/adma.200700442
65. O.A. Shenderova, I.I. Vlasov, S. Turner, G. Van Tendeloo, S.B. Orlinskii, A.A. Shiryaev, A.A. Khomich, S.N. Sulyanov, F. Jelezko, J. Wrachtrup, Nitrogen control in nanodiamond produced by detonation shock-wave-assisted synthesis. J. Phys. Chem. C **115**(29), 14014–14024 (2011). doi:10.1021/jp202057q
66. T. Berg, E. Marosits, J. Maul, P. Nagel, U. Ott, F. Schertz, S. Schuppler, C. Sudek, G. Schonhense, Quantum confinement observed in the x-ray absorption spectrum of size distributed meteoritic nanodiamonds. J. Appl. Phys. **104**(6), 064303 (2008). doi:10.1063/1.2978217
67. A.M. Panich, Nuclear magnetic resonance studies of nanodiamonds. Crit. Rev. Solid State Mater. Sci. **37**(4), 276–303 (2012). doi:10.1080/10408436.2011.606930

68. C. Bradac, T. Gaebel, N. Naidoo, M.J. Sellars, J. Twamley, L.J. Brown, A.S. Barnard, T. Plakhotnik, A.V. Zvyagin, J.R. Rabeau, Observation and control of blinking nitrogen-vacancy centres in discrete nanodiamonds. Nat. Nanotech. **5**, 345–349 (2010). doi:10.1038/NNANO.2010.56
69. A. Krüger, F. Kataoka, M. Ozawa, T. Fujino, Y. Suzuki, A.E. Aleksenskii, A. Ya, A. Vul, E. Osawa, Unusually tight aggregation in detonation nanodiamond: identification and disintegration. Carbon **43**(8), 1722–1730 (2005). doi:10.1016/j.carbon.2005.02.020
70. J.C. Arnault, T. Petit, H.A. Girard, A. Chavanne, C. Gesset, M. Sennour, M. Chaigneau, Surface chemical modifications and surface reactivity of nanodiamonds hydrogenated by CVD plasma. Phys. Chem. Chem. Phys. **13**(6), 11481 (2011). doi:10.1039/c1cp20109c
71. M. Mermoux, B. Marcus, G.M. Swain, J.E. Butler, A confocal raman imaging study of an optically transparent boron-doped diamond electrode. J. Phys. Chem. B **106**(42), 10816–10827 (2002). doi:10.1021/jp0202946
72. S. Osswald, V.N. Mochalin, M. Havel, G. Yushin, Y. Gogotsi, Phonon confinement effects in the Raman spectrum of nanodiamond. Phys. Rev. B **80**(7), 075419 (2009). doi:10.1103/PhysRevB.80.075419
73. M. Chaigneau, G. Piccardi, H.A. Girard, J.C. Arnault, R. Ossikovski, Laser heating versus phonon confinement effect in the Raman spectra of diamond nanoparticles. J. Nanopart. Res. **14**(6), 955 (2012). doi:10.1007/s11051-012-0955-9
74. D.R. Baer, M.H. Engelhard, XPS analysis of nanostructured materials and biological surfaces. J. Electron Spectrosc. Relat. Phenom. **178–179**, 415–432 (2010). doi:10.1016/j.elspec.2009.09.003
75. T. Petit, J.C. Arnault, H.A. Girard, M. Sennour, T.Y. Kang, C.L. Cheng, P. Bergonzo, Oxygen hole doping of nanodiamond. Nanoscale **4**(21), 6792 (2012). doi:10.1039/c2nr31655b
76. S. Michaelson, A. Stacey, R. Akhvlediani, S. Prawer, A. Hoffman, High resolution electron energy loss spectroscopy surface studies of hydrogenated detonation nano-diamond spray-deposited films. Surf. Sci. **604**(15-16), 1326–1330 (2010). doi:10.1016/j.susc.2010.04.022
77. C.L. Cheng, C.F. Chen, W.C. Shaio, D.S. Tsai, K.H. Chen, The CH stretching features on diamonds of different origins. Diam. Relat. Mater. **14**(9), 1455–1462 (2005). doi:10.1016/j.diamond.2005.03.003
78. P.H. Chung, E. Perevedentseva, J.S. Tu, C.C. Chang, C.L. Cheng, Spectroscopic study of bio-functionalized nanodiamonds. Diam. Relat. Mater. **15**(4-8), 622–625 (2006). doi:10.1016/j.diamond.2005.11.019
79. Z. Remes, H. Kozak, B. Rezek, E. Ukraintsev, O. Babchenko, A. Kromka, H.A. Girard, J.C. Arnault, P. Bergonzo, Diamond-coated ATR prism for infrared absorption spectroscopy of surface-modified diamond nanoparticles. Appl. Surf. Sci. **270**, 411–417 (2013). doi:10.1016/j.apsusc.2013.01.039
80. S. Ghodbane, A. Deneuville, D. Tromson, P. Bergonzo, E. Bustarret, D. Ballutaud, Sensitivity of Raman spectra excited at 325 nm to surface treatments of undoped polycrystalline diamond films. Phys. Stat. Sol. A **203**(10), 2397–2402 (2006). doi:10.1002/pssa.200521462
81. A. Crisci, M. Mermoux, B. Saubat-Marcus, Deep ultra-violet Raman imaging of CVD boron-doped and non-doped diamond films. Diam. Relat. Mater. **17**(7-10), 1207–1211 (2008). doi:10.1016/j.diamond.2008.01.025
82. F. Cataldo, A. Koscheev, A study of the action of ozone and on the thermal stability of nanodiamond. Fuller. Nanotub. Carbon Nanostruct. **11**(3), 201 (2003). doi:10.1081/FST-120024039
83. A. Koshcheev, Thermodesorption mass spectrometry in the light of solution of the problem of certification and unification of the surface properties of detonation nano-diamonds. Russ. J. Gener. Chem. **79**(9), 2033–2044 (2009). doi:10.1134/S1070363209090357
84. A. Krueger, M. Ozawa, G. Jarre, Y. Liang, J. Stegk, L. Lu, Deagglomeration and functionalisation of detonation diamond. Physica Status Solidi A **204**(9), 2881–2887 (2007). doi:10.1002/pssa.200776330

85. A.E. Aleksenskiy, E.D. Eydelman, A.Y. Vul, Deagglomeration of detonation nanodiamonds. Nanosci. Nanotechnol. Lett. **3**(1), 68–74 (2011). doi:10.1166/nnl.2011.1122
86. T. Petit, H.A. Girard, A. Trouve, I. Batonneau-Genner, P. Bergonzo, J.C. Arnault, Surface transfer doping can mediate both colloidal stability and self-assembly of nanodiamonds. Nanoscale **5**(19), 8958–8962 (2013). doi:10.1039/c3nr02492j
87. H.A. Girard, J.C. Arnault, S. Perruchas, S. Saada, T. Gacoin, J.P. Boilot, P. Bergonzo, Hydrogenation of nanodiamonds using MPCVD: a new route toward organic functionalization. Diam. Relat. Mater. **19**(7–9), 1117–1123 (2010). doi:10.1016/j.diamond.2010.03.019
88. O.A. Williams, J. Hees, C. Dieker, W. Jäger, L. Kirste, C.E. Nebel, Size-dependent reactivity of diamond nanoparticles. ACS Nano **4**(8), 4824–4830 (2010). doi:10.1021/nn100748k
89. S. Osswald, G. Yushin, V. Mochalin, S.O. Kucheyev, Y. Gogotsi, Control of sp^2/sp^3 carbon ratio and surface chemistry of nanodiamond powders by selective oxidation in air. J. Am. Chem. Soc. **128**(36), 11635–11642 (2006). doi:10.1021/ja063303n
90. A. Krüger, Y. Liang, G. Jarre, J. Stegk, Surface functionalisation of detonation diamond suitable for biological applications. J. Mater. Chem. **16**(24), 2322–2328 (2006). doi:10.1039/b601325b
91. R. Martín, M. Álvaro, J.R. Herance, H. García, Fenton-treated functionalized diamond nanoparticles as gene delivery system. ACS Nano **4**(1), 65–74 (2010). doi:10.1021/nn901616c
92. Y. Morita, T. Takimoto, H. Yamanaka, K. Kumekawa, S. Morino, S. Aonuma, T. Kimura, N. Komatsu, A facile and scalable process for size-controllable separation of nanodiamond particles as small as 4 nm. Small **4**(12), 2154–2157 (2008). doi:10.1002/smll.200800944
93. H.A. Girard, T. Petit, S. Perruchas, J.C. Arnault, P. Bergonzo, Surface properties of hydrogenated nanodiamonds: a chemical investigation. Phys. Chem. Chem. Phys. **13**(32), 11511–11516 (2011). doi:10.1039/c1cp20424f
94. Y. Liu, Z. Gu, J.L. Margrave, V.N. Khabashesku, Functionalization of nanoscale diamond powder: fluoro-, alkyl-, amino-, and amino acid-nanodiamond derivatives. Chem. Mater. **16**(20), 3924–3930 (2004). doi:10.1021/cm048875q
95. M.A. Ray, T. Tyler, B. Hook, A. Martin, G. Cunningham, O. Shenderova, J.L. Davidson, M. Howell, W.P. Kang, G. McGuire, Cool plasma functionalization of nano-crystalline diamond films. Diam. Relat. Mater. **16**(12), 2087–2089 (2007). doi:10.1016/j.diamond.2007.07.016
96. K.I. Sotowa, T. Amamoto, A. Sobana, K. Kusakabe, T. Imato, Effect of treatment temperature on the amination of chlorinated diamond. Diam. Relat. Mater. **13**(1), 145–150 (2004). doi:10.1016/j.diamond.2003.10.029
97. W.S. Yeap, S. Chen, K.P. Loh, Detonation nanodiamond: an organic platform for the Suzuki coupling of organic molecules. Langmuir **25**(1), 185–191 (2009). doi:10.1021/la8029787
98. C.L. Huang, H.C. Chang, Adsorption and immobilization of cytochrome c on nanodiamonds. Langmuir **20**(14), 5879–5884 (2004). doi:10.1021/la0495736
99. Y. Liang, T. Meinhardt, G. Jarre, M. Ozawa, P. Vrdoljak, A. Schöll, F. Reinert, A. Krueger, Deagglomeration and surface modification of thermally annealed nanoscale diamond. J. Colloid Interface Sci. **354**(1), 23–30 (2011). doi:10.1016/j.jcis.2010.10.044
100. J. Chen, S.Z. Deng, J. Chen, Z.X. Yu, N.S. Xu, Graphitization of nanodiamond powder annealed in argon ambient. Appl. Phys. Lett. **74**(24), 3651 (1999). doi:10.1063/1.123211
101. Y. Liang, M. Ozawa, A. Krueger, A general procedure to functionalize agglomerating nanoparticles demonstrated on nanodiamond. ACS Nano **3**(8), 2288–2296 (2009). doi:10.1021/nn900339s
102. J.B. Cui, J. Ristein, L. Ley, Electron affinity of the bare and hydrogen covered single crystal diamond (111) surface. Phys. Rev. Lett. **81**(2), 429–432 (1998). doi:10.1103/PhysRevLett.81.429
103. L. Ley, J. Ristein, F. Meier, M. Riedel, P. Strobel, Surface conductivity of the diamond: a novel transfer doping mechanism. Phys. B **376-377**, 262–267 (2006). doi:10.1016/j.physb.2005.12.068

104. B.V. Spitsyn, S.A. Denisov, N.A. Skorik, A.G. Chopurova, S.A. Parkaeva, L.D. Belyakova, O.G. Larionov, The physical-chemical study of detonation nanodiamond application in adsorption and chromatography. Diam. Relat. Mater. **19**(2-3), 123–127 (2010). doi:10.1016/j.diamond.2009.10.020
105. S. Ida, T. Tsubota, O. Hirabayashi, M. Nagata, Y. Matsumoto, A. Fujishima, Chemical reaction of hydrogenated diamond surface with peroxide radical initiators. Diam. Relat. Mater. **12**(3-7), 601–605 (2003). doi:10.1016/S0925-9635(02)00334-5
106. I.I. Obraztsova, N.K. Eremenko, Physicochemical modification of nanodiamonds. Russ. J. Appl. Chem. **81**(4), 603–608 (2008). doi:10.1134/S107042720804006X
107. M.B. Smith, J. March, *March's Advanced Organic Chemistry*, 6th edn. (Wiley, Hoboken, 2007)
108. D. Ager, Hydrogenation of carbon-carbon double bonds, in *Science of Synthesis, Stereoselective Synthesis*, 1st edn. ed. by J.G. De Vries, G.A. Molander, P.A. Evans (2011), pp. 185–256
109. M. Yeganeh, P. Coxon, A. Brieva, V. Dhanak, L. Šiller, Y. Butenko, Atomic hydrogen treatment of nanodiamond powder studied with photoemission spectroscopy. Phys. Rev. B **75**(15), 1–8 (2007). doi:10.1103/PhysRevB.75.155404
110. J. Angus, H.A. Will, W.S. Stanko, Growth of diamond seed crystals by vapor deposition. J. Appl. Phys. **39**(6), 2915–2922 (1968). doi:10.1063/1.1656693
111. E. Van Hove, J. De Sanoit, J.C. Arnault, S. Saada, C. Mer, P. Mailley, P. Bergonzo, M. Nesladek, Stability of H-terminated BDD electrodes: an insight into the influence of the surface preparation. Phys. Stat. Solid. A **204**(9), 2931–2939 (2007). doi:10.1002/pssa.200776340
112. R. Kiran, E. Scorsone, J. De Sanoit, J.C. Arnault, P. Mailley, P. Bergonzo, Boron doped diamond electrodes for direct measurement in biological fluids: an in situ regeneration approach. J. Electrochem. Soc. **160**(1), H67–H73 (2013). doi:10.1149/2.014302jes
113. W.S. Yang, O. Auciello, J.E. Butler, W. Cai, J.A. Carlisle, J. Gerbi, D.M. Gruen, T. Knickerbocker, T.L. Lasseter, J.N. Russell, L.M. Smith, R.J. Hamers, DNA-modified nanocrystalline diamond thin-films as stable, biologically active substrates. Nat. Mater. **1**, 253–257 (2002). doi:10.1038/nmat779
114. T. Strother, T. Knickerbocker, J. Russell, J. Butler, L. Smith, R. Hamers, Photochemical functionalization of diamond films. Langmuir **18**(4), 968–971 (2002). doi:10.1021/la0112561
115. A. Hartl, E. Schmich, J.A. Garrido, J. Hernando, S.C.R. Catharino, S. Walter, P. Feulner, A. Kromka, D. Steinmuller, M. Stutzmann, Protein-modified nanocrystalline diamond thin films for biosensor applications. Nat. Mater. **3**, 736–742 (2004). doi:10.1038/nmat1204
116. Y. Zhong, K. Loh, The chemistry of C–H bond activation on diamond. Chem. Asian J. **5**(7), 1532–1540 (2010). doi:10.1002/asia.201000027
117. S. Szunerits, R. Boukherroub, Different strategies for functionalization of diamond surfaces. J. Solid State Electrochem. **12**(10), 1205–1218 (2008). doi:10.1007/s10008-007-0473-3
118. F. Maier, M. Riedel, B. Mantel, J. Ristein, L. Ley, Origin of surface conductivity in diamond. Phys. Rev. Lett. **85**(16), 3472–3475 (2000). doi:10.1103/PhysRevLett.85.3472
119. C. Bandis, B.B. Pate, Electron-emission due to exciton breakup from negative electron-affinity diamond. Phys. Rev. Lett. **74**(5), 777–780 (1995). doi:10.1103/PhysRevLett.74.777
120. B.M. Nichols, J.E. Butler, J.N. Russell, R.J. Hamers, Photochemical functionalization of hydrogen-terminated diamond surfaces: a structural and mechanistic study. J. Phys. Chem. B **109**(44), 20938–20947 (2005). doi:10.1021/jp0545389
121. D. Shin, B. Rezek, N. Tokuda, D. Takeuchi, H. Watanabe, T. Nakamura, T. Yamamoto, C.E. Nebel, Photo- and electrochemical bonding of DNA to single crystalline CVD diamond. Phys. Status Solidi A **203**(13), 3245–3272 (2006). doi:10.1002/pssa.200671402
122. S. Lud, M. Steenackers, R. Jordan, P. Bruno, D. Gruen, P. Feulner, J. Garrido, M. Stutzmann, Chemical grafting of biphenyl self-assembled monolayers on ultrananocrystalline diamond. J. Am. Chem. Soc. **128**(51), 16884–16891 (2006). doi:10.1021/ja0657049

123. Y.V. Butenko, V.L. Kuznetsov, E.A. Paukshtis, A.I. Stadnichenko, I.N. Mazov, S.I. Moseenkov, A.I. Boronin, S.V. Kosheev, The thermal stability of nanodiamond surface groups and onset of nanodiamond graphitization. Fullerenes, Nanotubes, Carbon Nanostruct. **14**(2-3), 557–564 (2006). doi:10.1080/15363830600666779
124. L. Rondin, G. Dantelle, A. Slablab, F. Grosshans, F. Treussart, P. Bergonzo, S. Perruchas, T. Gacoin, M. Chaigneau, H.C. Chang, V. Jacques, J.F. Roch, Surface-induced charge state conversion of nitrogen-vacancy defects in nanodiamonds. Phys. Rev. B **82**(11), 115449 (2010). doi:10.1103/PhysRevB.82.115449
125. O. Shenderova, I. Petrov, J. Walsh, V. Grichko, T. Tyler, G. Cunningham, Modification of detonation nanodiamonds by heat treatment in air. Diam. Relat. Mater. **15**(11-12), 1799–1803 (2006). doi:10.1016/j.diamond.2006.08.032
126. D. Mitev, R. Dimitrova, M. Spassova, C. Minchev, S. Stavrev, Surface peculiarities of detonation nanodiamonds in dependence of fabrication and purification methods. Diam. Relat. Mater. **16**(4-7), 776–780 (2007). doi:10.1016/j.diamond.2007.01.005
127. M. Comet, V. Pichot, B. Siegert, F. Britz, D. Spitzer, Detonation nanodiamonds for Doping Kevlar. J Nanosci. Nanotechnol. **10**(7), 4286–4292 (2010). doi:10.1166/jnn.2010.2186
128. A. Krueger, The structure and reactivity of nanoscale diamond. J. Mater. Chem. **18**(13), 1485–1492 (2008). doi:10.1039/b716673g
129. O. Shenderova, A.M. Panich, S. Moseenkov, S.C. Hens, V. Kuznetsov, H.M. Vieth, Hydroxylated detonation nanodiamond: FTIR, XPS, and NMR studies. J. Phys. Chem. C **115** (39), 19005–19011 (2011). doi:10.1021/jp205389m
130. R. Martin, P.C. Heydorn, M. Alvaro, H. Garcia, General strategy for high-density covalent functionalization of diamond nanoparticles using Fenton chemistry. Chem. Mater. **21**(19), 4505–4514 (2009). doi:10.1021/cm9012602
131. G. Lisichkin, V. Korol'kov, B. Tarasevic, I. Kulakova, A. Karpukhin, Photochemical chlorination of nanodiamond and interaction of its modified surface with C-nucleophiles. Russ. Chem. Bull. **55**(12), 2212–2219 (2006). doi:10.1007/s11172-006-0574-7
132. B.V. Spitsyn, J.L. Davidson, M.N. Graboboev, T.B. Galushko, N.V. Serebryakova, T.A. Karpukhina, I.I. Kulakova, N.N. Melnik, In road to modifications of detonation nanodiamond. Diam. Relat. Mater. **15**(2-3), 296–299 (2006). doi:10.1016/j.diamond.2005.07.033
133. V.N. Mochalin, S. Osswald, C. Portet, G. Yushin, C. Hobson, M. Havel, Y. Gogotsi, High temperature functionalization and surface modification of nanodiamond powders. MRS Proc. **1039**, 201–211 (2007). doi:10.1557/PROC-1039-P11-03
134. V. Ralchenko, L. Nistor, E. Pleuler, A. Khomich, I. Vlasov, R. Khmelnitskii, Structure and properties of high-temperature annealed CVD diamond. Diam. Relat. Mater. **12**(10-11), 1964–1970 (2003). doi:10.1016/S0925-9635(03)00214-0
135. S. Ogawa, T. Yamada, S. Ishizduka, A. Yoshigoe, M. Hasegawa, Y. Teraoka, Y. Takakuwa, Vacuum annealing formation of graphene on diamond C(111) surfaces studied by real-time photoelectron spectroscopy. Jpn. J. Appl. Phys. **51**(11s), 11PF02 (2012). doi:10.1143/JJAP.51.11PF02
136. T. Evans, Changes produced by high temperature treatment of diamond, in *The Properties of Natural and Synthetic Diamonds*, ed. by J.E. Field (Academic Press, London, 1979), pp. 403–425
137. K.S. Uspenskaya, Y.N. Tolmachev, D.V. Fedoseev, Oxidation and graphitization of diamond at low pressures. Zh. Fiz. Khim. **56**, 495 (1982) (in Russian)
138. D.V. Fedoseev, S.P. Vnusov, V.L. Bukhovets, B.A. Anikin, Surface graphitization of diamond at high temperatures. Surf. Coat. Technol. **28**(2), 207–214 (1986). doi:10.1016/0257-8972(86)90059-9
139. G. Davies, *Properties and Gowth of Diamond* (INSPEC, London, 1994)
140. J.F. Prins, Ion implantation of diamond for electronics applications. Semicond. Sci. Technol. **18**(3), S27 (2003). doi:10.1088/0268-1242/18/3/304
141. F. Banhart, Irradiation effects in carbon nanostructures. Rep. Prog. Phys. **62**(8), 1181 (1999). doi:10.1088/0034-4885/62/8/201

142. J.E. Field (ed.), *The Properties of Natural and Synthetic Diamonds* (Academic Press, London, 1977)
143. O.P. Krivoruchko, V.I. Zaikovski, K.I. Zamaraev, Formation of unsual liquid-like FeC particles and dynamics of their nehavior on amorphous carbon surface at 920–1170 K. Dkl. Akad. Nauk. **329**, 744 (1993)
144. M.S. Dresselhaus, G. Dresselhaus, P.C. Eklund, *Science of Fullerenes and Carbon Nanotubes* (Academic Press, San Diego, 1996)
145. V.L. Kutnetsov, Y.V. Butenko, Diamond phase transitions at nanoscale, in *Ultrananocrystalline Diamond: Synthesis, Properties and Applications*, 2nd edn. ed. by O. Shenderova, D.M. Gruen (Elsevier, 2012)
146. Y.V. Butenko, S. Krishnamurthy, A.K. Chakraborty, V.L. Kuznetsov, V.R. Dhanak, M.R.C. Hunt, L. Scaroniller, L. Šiller, Photoemission study of onionlike carbons produced by annealing nanodiamonds. Phys. Rev. B **71**(7), 75420 (2005). doi:10.1103/PhysRevB.71.075420
147. D. Pech, M. Brunet, H. Durou, P.H. Huang, V. Mochalin, Y. Gogotsi, Ultra-high-power micrometre-sized supercapacitors based on onion-like carbon. Nat. Nanotechnol. **5**, 651–654 (2010). doi:10.1038/NNANO.2010.162
148. O. Shenderova, C. Jones, V. Borjanovic, S. Hens, G. Cunningham, S. Moseenkov, Detonation nanodiamond and onion-like carbon: applications in composites. Phys. Stat. Sol. A **205**(9), 2245–2251 (2008). doi:10.1002/pssa.200879706
149. O. Shenderova, T. Tyler, V. Borjanovic, G. Cunningham, M. Ray, J. Walsh, M. Casulli, Nanodiamond and onion-like carbon polymer nanocomposites. Diam. Relat. Mater. **16**(9), 1213–1217 (2007). doi:10.1016/S0925-9635(07)00337-8
150. V.L. Kutnetsov, A.L. Chuvilin, Y.V. Butenko, I.L. Malkov, V.M. Titov, Onion-like carbon from ultradisperse diamond. Chem. Phys. Lett. **222**(4), 343–348 (1994). doi:10.1016/0009-2614(94)87072-1
151. F. Fugaciu, H. Hermann, G. Seifert, Concentric-shell fullerenes and diamond particles: a molecular-dynamics study. Phys. Rev. B **60**(15), 10711–10714 (1999). doi:10.1103/PhysRevB.60.10711
152. J.Y. Raty, G. Galli, C. Bostedt, T.W. van Buuren, L.J. Terminello, Quantum confinement and fullerenelike surface reconstructions in nanodiamonds. Phys. Rev. Lett. **90**(3), 37401 (2003). doi:10.1103/PhysRevLett.90.037401
153. V.L. Kuznetsov, I.L. Zilberberg, Y.V. Butenko, A.L. Chuvilin, B. Segall, Theoretical study of the formation of closed curved graphite-like structures during annealing of diamond surface. J. Appl. Phys. **86**(2), 863 (1999). doi:10.1063/1.370816
154. Y.V. Butenko, V.L. Kuznetsov, A.L. Chuvilin, V.N. Kolomiichuk, S.V. Stankus, R.A. Khairulin, The kinetics of the graphitization of dispersed diamonds at low temperatures. J. Appl. Phys. **88**(7), 4380–4388 (2000). doi:10.1063/1.1289791
155. G. Davies, T. Evans, Graphitization of diamond at zero temperature and a high pressure. Proc. R. Soc. **328**(1574), 413–427 (1972). doi:10.1098/rspa.1972.0086
156. D.S. Su, N.I. Maksimova, G. Mestl, V.L. Kuznetsov, V. Keller, R. Schlogl, N. Keller, Oxidative dehydrogenation of ethylbenzene to styrene over ultra-dispersed diamond and onion-like carbon. Carbon **45**(11), 2145–2151 (2007). doi:10.1016/j.carbon.2007.07.005
157. K. Xu, Q. Xue, A new method for deaggregation of nanodiamond from explosive detonation: graphitization-oxidation method. Phys. Solid State **46**(4), 649–650 (2004). doi:10.1134/1.1711442
158. O.E. Anderson, B.L.V. Prasad, H. Sato, T. Enoki, Y. Hishiyama, Y. Kaburagi, M. Yoshikawa, S. Bandow, Structure and electronic properties of graphite nanoparticles. Phys. Rev. B **58**(24), 16387–16395 (1998)
159. J. Qian, C. Pantea, J. Huang, T.W. Zerda, Y. Zhao, Graphitization of diamond powders of different sizes at high pressure-high temperature. Carbon **42**(12-13), 2691–2697 (2004). doi:10.1016/j.carbon.2004.06.017
160. J. Cebik, J.K. McDonough, F. Peerally, R. Medrano, I. Neitzel, Y. Gogotsi, S. Osswald, Raman spectroscopy study of the nanodiamond-to-carbon onion transformation. Nanotechnology **24**(20), 205703 (2013). doi:10.1088/0957-4484/24/20/205703

161. A. Panich, A.I. Shames, N.A. Sergeev, M. Olszewski, J.K. McDonough, V.N. Mochalin, Y. Gogotsi, Nanodiamond graphitization: a magnetic resonance study. J. Phys. Cond. Matter **25** (24), 245303 (2013). doi:10.1088/0953-8984/25/24/245303
162. Z. Markovic, V. Trajkovic, Biomedical potential of the reactive oxygen species generation and quenching by fullerenes (C60). Biomaterials **29**(26), 3561–3573 (2008). doi:10.1016/j.biomaterials.2008.05.005
163. K. Yang, J. Wan, S. Zhang, B. Tian, Y. Zhang, Z. Liu, The influence of surface chemistry and size of nanoscale graphene oxide on photothermal therapy of cancer using ultra-low laser power. Biomaterials **33**(7), 2206–2214 (2012). doi:10.1016/j.biomaterials.2011.11.064
164. C. Portet, G. Yushin, Y. Gogotsi, Electrochemical performance of carbon onions, nanodiamonds, carbon black and multiwalled nanotubes in electrical double layer capacitors. Carbon **45**(13), 2511–2518 (2007). doi:10.1016/j.carbon.2007.08.024
165. J. Zang, Y. Wang, L. Bian, J. Zhang, F. Meng, Y. Zhao, S. Ren, X. Qu, Surface modification and electrochemical behaviour of undoped Nanodiamonds. Electrochem. Acta **72**, 68–73 (2012). doi:10.1016/j.electacta.2012.03.169
166. G. Su, H. Zhou, Q. Mu, Y. Zhang, L. Li, P. Jiao, G. Jiang, B. Yan, Effective surface charge density determines the electrostatic attraction between nanoparticles and cells. J. Phys. Chem. C **116**(8), 4993–4998 (2012). doi:10.1021/jp211041m
167. Y.Y. Liu, H. Miyoshi, M. Nakamura, Nanomedicine for drug delivery and imaging: a promising avenue for cancer therapy and diagnosis using targeted functional nanoparticles. Int. J. Cancer **120**(12), 2527–2537 (2007). doi:10.1002/ijc.22709
168. A.S. Barnard, Self-assembly in nanodiamond agglutinates. J. Mater. Chem. **18**(34), 4038–4041 (2008). doi:10.1039/b809188a
169. E.D. Eidelman, V.I. Siklitsky, L.V. Sharonova, A stable suspension of single ultrananocrystalline diamond particles. Diam. Relat. Mater. **14**(11-12), 1765–1769 (2005). doi:10.1016/j.diamond.2005.08.057
170. E. Osawa, Recent progress and perspectives in single-digit nanodiamond. Diam. Relat. Mater. **16**(12), 2018–2022 (2007). doi:10.1016/j.diamond.2007.08.008
171. A. Pentecost, S. Gour, V. Mochalin, I. Knoke, Y. Gogotsi, Deaggregation of nanodiamond powders using salt- and sugar-assisted milling. ACS Appl. Mater. Interfaces **2**(11), 3289–3294 (2010). doi:10.1021/am100720n
172. R.J. Hunter, *Zeta Potential in Colloids Science* (Academic Press, New York, 1981)
173. T.M. Riddick, *Zeta-Meter Operating Manual ZM-75* (Zeta-Meter Inc, New York, 1968).
174. A.V. Delgado, F. González-Caballero, R.J. Hunter, L.K. Koopal, J. Lyklema, Measurement and interpretation of electrokinetic phenomena (IUPAC technical report). Pure Appl. Chem. **77**(10), 1753–1805 (2005). doi:10.1351/pac200577101753
175. M. Ozawa, M. Inakuma, M. Takahashi, F. Kataoka, A. Krueger, E. Osawa, Preparation and behavior of brownish, clear nanodiamond colloids. Adv. Mater. **19**(9), 1201–1206 (2007). doi:10.1002/adma.200601452
176. V.N. Mochalin, I. Neitzel, B. Etzold, A.M. Peterson, G. Palmese, Y. Gogotsi, Covalent incorporation of aminated nanodiamond into an epoxy polymer network. ACS Nano **5**(9), 7494–7502 (2011). doi:10.1021/nn2024539
177. N. Gibson, O. Shenderova, T.J.M. Luo, S. Moseenkov, V. Bondar, A. Puzyr, K. Purtov, Z. Fitzgerald, D.W. Brenner, Colloidal stability of modified nanodiamond particles. Diam. Relat. Mater. **18**(4), 620–626 (2009). doi:10.1016/j.diamond.2008.10.049
178. K. Kokubo, K. Matsubayashi, H. Tategaki, H. Takada, T. Oshima, Facile synthesis of highly water-soluble fullerenes more than half-covered by hydroxyl groups. ACS Nano **2**(2), 327–333 (2008). doi:10.1021/nn700151z
179. Y.F. Li, C.I. Hung, C.C. Li, W. Chin, B.Y. Wei, W.K. Hsu, A gas-phase hydrophilization of carbon nanotubes by xenon excimer ultraviolet irradiation. J. Mater. Chem. **19**(37), 6761–6765 (2009). doi:10.1039/b905995d
180. L. Pospíšil, M. Gál, M. Hromadová, J. Bulícková, V. Kolivoška, J. Cvacka, K. Nováková, L. Kavan, M. Zukalová, L. Dunsch, Search for the form of fullerene C(60) in aqueous medium. Phys. Chem. Chem. Phys. **12**(42), 14095–14101 (2010). doi:10.1039/c0cp00986e

181. H.A. Girard, S. Perruchas, C. Gesset, M. Chaigneau, L. Vieille, J.C. Arnault, P. Bergonzo, J. P. Boilot, T. Gacoin, Electrostatic grafting of diamond nanoparticles: a versatile route to nanocrystalline diamond thin films. ACS Appl. Mater. Interfaces **1**(12), 2738–2746 (2009). doi:10.1021/am900458g
182. J. Hees, A. Kriele, O.A. Williams, Electrostatic self-assembly of diamond nanoparticles. Chem. Phys. Lett. **509**(1-3), 12–15 (2011). doi:10.1016/j.cplett.2011.04.083
183. C.C. Li, C.L. Huang, Preparation of clear colloidal solutions of detonation nanodiamond in organic solvents. Colloids Surf. A Physicochem. Eng. Asp. **353**(1), 52–56 (2010). doi:10.1016/j.colsurfa.2009.10.019
184. A.I. Shames, A.M. Panich, V.Y. Osipov, A.E. Aleksenskiy, A.Y. Vul', T. Enoki, K. Takai, Structure and magnetic properties of detonation nanodiamond chemically modified by copper. J. Appl. Phys. **107**(1), 014318 (2010). doi:10.1063/1.3273486
185. C. Gaillard, H.A. Girard, C. Falck, V. Paget, V. Simic, N. Ugolin, P. Bergonzo, S. Chevillard, J.C. Arnault, Peptide nucleic acid–nanodiamonds: covalent and stable conjugates for DNA targeting. RSC Adv. **4**(7), 3566–3572 (2014). doi:10.1039/C3RA45158E
186. E. Fuente, J.A. Menendez, D. Suarez, M.A. Montes-Moran, Basic surface oxides on carbon materials: a global view. Langmuir **19**(8), 3505–3511 (2003). doi:10.1021/la026778a
187. M.A. Montes-Moran, D. Suarez, J.A. Menendez, E. Fuente, On the nature of basic sites on carbon surfaces: an overview. Carbon **42**(7), 1219–1225 (2004). doi:10.1016/j.carbon.2004.01.023
188. C. Leon, J.M. Solar, V. Calemma, L.R. Radovic, Evidence for the protonation of basal-plane sites on carbon. Carbon **30**(5), 797–811 (1992). doi:10.1016/0008-6223(92)90164-R
189. V.L. Kuznetsov, Y.V. Butenko, A.L. Chuvilin, A.I. Romanenko, A.V. Okotrub, Electrical resistivity of graphitized ultra-disperse diamond and onion-like carbon. Chem. Phys. Lett. **336**(5-6), 397–404 (2001). doi:10.1016/S0009-2614(01)00135-X
190. S. Biniak, G. Szymanski, J. Siedlewskia, A. Swiatkowskib, The characterization of activated carbons with oxygen and nitrogen surface groups. Carbon **35**(12), 1799–1810 (1997). doi:10.1016/S0008-6223(97)00096-1
191. A. Krueger, J. Stegk, Y.J. Liang, L. Lu, G. Jarre, Biotinylated nanodiamond: simple and efficient functionalization of detonation diamond. Langmuir **24**(8), 4200–4204 (2008). doi:10.1021/la703482v
192. V. Chakrapani, J.C. Angus, A.B. Anderson, S.D. Wolter, B.R. Stoner, G.U. Sumanasekera, Charge transfer equilibria between diamond and an aqueous oxygen electrochemical redox couple. Science **318**(5855), 1424–1430 (2007). doi:10.1126/science.1148841
193. T. Kondo, I. Neitzel, V.N. Mochalin, J. Urai, M. Yuasa, Y. Gogotsi, Electrical conductivity of thermally hydrogenated nanodiamond powders. J. Appl. Phys. **113**(21), 214307 (2013). doi:10.1063/1.4809549
194. K.K. Liu, C.C. Wang, C.L. Cheng, J.I. Chao, Endocytic carboxylated nanodiamond for the labeling and tracking of cell division and differentiation in cancer and stem cells. Biomaterials **30**(26), 4249–4259 (2009). doi:10.1016/j.biomaterials.2009.04.056
195. Y. Yuan, X. Wang, G. Jia, J.H. Liu, T. Wang, Y. Gu, S.T. Yang, S. Zhen, H. Wang, Y. Liu, Pulmonary toxicity and translocation of nanodiamonds in mice. Diam. Relat. Mater. **19**(4), 291–299 (2009). doi:10.1016/j.diamond.2009.11.022
196. N. Mohan, C.S. Chen, H.H. Hsieh, Y.C. Wu, H.C. Chang, In vivo imaging and toxicity assessments of fluorescent nanodiamonds in Caenorhabditis elegans. Nano Lett. **10**(9), 3692–3699 (2010). doi:10.1021/nl1021909
197. V. Vaijayanthimala, P.Y. Cheng, S.H. Yeh, K.K. Liu, C.H. Hsiao, J.I. Chao, H.C. Chang, The long-term stability and biocompatibility of fluorescent nanodiamond as an in vivo contrast agent. Biomaterials **33**(31), 7794–7802 (2012). doi:10.1016/j.biomaterials.2012.06.084
198. S.J. Yu, M.W. Kang, H.C. Chang, K.M. Chen, Y.C. Yu, Bright fluorescent nanodiamonds: no photobleaching and low cytotoxicity. J. Am. Chem. Soc. **127**(50), 17604–17605 (2005). doi:10.1021/ja0567081
199. Y. Xing, W. Xiong, L. Zhu, E. Osawa, S. Hussin, L. Dai, DNA damage in embryonic stem cells caused by nanodiamonds. ACS Nano **5**(3), 2376–2384 (2011). doi:10.1021/nn200279k

200. J.A. Sergent, V. Paget, S. Chevillard, Toxicity and genotoxicity of nano-SiO2 on human epithelial intestinal HT-29 cell line. Ann. Occup. Hyg. **56**(5), 622–630 (2012). doi:10.1093/annhyg/mes005
201. L.J. Mah, A. El-Osta, T.C. Karagiannis, gammaH2AX: a sensitive molecular marker of DNA damage and repair. Leukemia **24**(4), 679–686 (2010). doi: 10.1038/leu.2010.6
202. A.M. Schrand, J.B. Lin, S.C. Hens, S.M. Hussain, Temporal and mechanistic tracking of cellular uptake dynamics with novel surface fluorophore-bound nanodiamonds. Nanoscale **3** (2), 435–445 (2011). doi:10.1039/c0nr00408a
203. I.P. Chang, K.C. Hwang, C.S. Chiang, Preparation of fluorescent magnetic nanodiamonds and cellular imaging. J. Am. Chem. Soc. **130**(46), 15476–15481 (2008). doi:10.1021/ja804253y
204. U. Maitra, A. Jain, S.J. George, C.N. Rao, Tunable fluorescence in chromophore-functionalized nanodiamond induced by energy transfer. Nanoscale **3**(8), 3192–3197 (2011). doi:10.1039/c1nr10295h
205. Q. Zhang, V.N. Mochalin, I. Neitzel, I.Y. Knoke, J. Han, C.A. Klug, J.G. Zhou, P.I. Lelkes, Y. Gogotsi, Fluorescent PLLA-nanodiamond composites for bone tissue engineering. Biomaterials **32**(1), 87–94 (2011). doi:10.1016/j.biomaterials.2010.08.090
206. X.Q. Zhang, M. Chen, R. Lam, X.Y. Xu, E. Osawa, D. Ho, Polymer-functionalized nanodiamond platforms as vehicles for gene delivery. ACS Nano **3**(9), 2609–2616 (2009). doi:10.1021/nn900865g
207. H.D. Wang, Q. Yang, C.H. Niu, I. Badea, Protein-modified nanodiamond particles for layer-by-layer assembly. Diam. Relat. Mater. **20**(8), 1193–1198 (2011). doi:10.1016/j.diamond.2011.06.015
208. Y.K. Tzeng, O. Faklaris, B.M. Chang, Y. Kuo, J.H. Hsu, H.C. Chang, Superresolution imaging of albumin-conjugated fluorescent nanodiamonds in cells by stimulated emission depletion. Angew Chem. Int. Ed Eng. **50**(10), 2262–2265 (2011). doi:10.1002/anie.201007215
209. C.Y. Cheng, E. Perevedentseva, J.S. Tu, P.H. Chung, C.L. Cheng, K.K. Liu, J.I. Chao, P.H. Chen, C.C. Chang, Direct and in vitro observation of growth hormone receptor molecules in A549 human lung epithelial cells by nanodiamond labeling. Appl. Phys. Lett. **90**(16), 163903 (2007). doi:10.1063/1.2727557
210. D.T. Tran, V. Vermeeren, L. Grieten, S. Wenmackers, P. Wagner, J. Pollet, K.P. Janssen, L. Michiels, J. Lammertyn, Nanocrystalline diamond impedimetric aptasensor for the label-free detection of human IgE. Biosens. Bioelectron. **26**(6), 2987–2993 (2011). doi:10.1016/j.bios.2010.11.053
211. A.H. Smith, E.M. Robinson, X.Q. Zhang, E.K. Chow, Y. Lin, E. Osawa, J. Xi, D. Ho, Triggered release of therapeutic antibodies from nanodiamond complexes. Nanoscale **3**(7), 2844 (2011). doi:10.1039/c1nr10278h
212. A. Barras, J. Lyskawa, S. Szunerits, P. Woisel, R. Boukherroub, Direct functionalization of nanodiamond particles using dopamine derivatives. Langmuir **27**, 12451–12457 (2011). doi:10.1021/la202571d
213. R.A. Shimkunas, E. Robinson, R. Lam, S. Lu, X. Xu, X.Q. Zhang, H. Huang, E. Osawa, D. Ho, Nanodiamond-insulin complexes as pH-dependent protein delivery vehicles. Biomaterials **30**(29), 5720–5728 (2009). doi:10.1016/j.biomaterials.2009.07.004
214. E. Perevedentseva, P.J. Cai, Y.C. Chiu, C.L. Cheng, Characterizing protein activities on the lysozyme and nanodiamond complex prepared for bio applications. Langmuir **27**(3), 1085–1091 (2011). doi:10.1021/la103155c
215. T.T.B. Nguyen, H.C. Chang, V.W.K. Wu, Adsorption and hydrolytic activity of lysozyme on diamond nanocrystallites. Diam. Relat. Mater. **16**(4-7), 872–876 (2007). doi:10.1016/j.diamond.2007.01.030
216. V.S. Bondar, I.O. Pozdnyakova, A.P. Puzyr, Applications of nanodiamonds for separation and purification of proteins. Phys. Solid State **46**(4), 758–760 (2004). doi:10.1134/1.1711468
217. R. Lam, M. Chen, E. Pierstorff, H. Huang, E. Osawa, D. Ho, Nanodiamond-embedded microfilm devices for localized chemotherapeutic elution. ACS Nano **2**(10), 2095–2102 (2008). doi:10.1021/nn800465x

218. H. Huang, E. Pierstorff, E. Osawa, D. Ho, Active nanodiamond hydrogels for chemotherapeutic delivery. Nano Lett. **7**(11), 3305–3314 (2007). doi:10.1021/nl071521o
219. M. Chen, X.Q. Zhang, H.B. Man, R. Lam, E.K. Chow, D. Ho, Nanodiamond vectors functionalized with polyethylenimine for siRNA delivery. J. Phys. Chem. Lett. **1**(21), 3087–3095 (2010). doi:10.1021/jz1013278
220. H. Huang, E. Pierstorff, E. Osawa, D. Ho, Protein-mediated assembly of nanodiamond hydrogels into a biocompatible and biofunctional multilayer nanofilm. ACS Nano **2**(2), 203–212 (2008). doi:10.1021/nn7000867
221. J. Tisler, R. Reuter, A. Lammle, F. JElezko, G. Balasubramanian, P.R. Hemmer, F. Reinhard, J. Wrachtrup, Highly efficient FRET from single NV center in nanodiamonds to single organic molecule. ACS Nano **5**(10), 7893–7898 (2011). doi:10.1021/nn2021259
222. N. Mohan, Y.K. Tzeng, L. Yang, Y.Y. Chen, Y.Y. Hui, C.Y. Fang, H.C. Chang, Sub-20-nm fluorescent nanodiamonds as photostable biolabels and fluorescence resonance energy transfer donors. Adv. Mater. **22**(7), 843–847 (2010). doi:10.1002/adma.200901596
223. V. Grichko, T. Tyler, V.I. Grishko, O. Shenderova, Nanodiamond particles forming photonic structures. Nanotechnology **19**(22), 225201 (2008). doi:10.1088/0957-4484/19/22/225201
224. O. Faklaris, V. Joshi, T. Irinopoulou, P. Tauc, M. Sennour, H. Girard, C. Gesset, J.C. Arnault, A. Thorel, J.P. Boudou, P.A. Curmi, F. Treussart, Photoluminescent diamond nanoparticles for cell labeling: study of the uptake mechanism in mammalian cells. ACS Nano **3**(12), 3955–3962 (2009). doi:10.1021/nn901014j
225. L.P. McGuinness, Y. Yan, A. Stacey, D.A. Simpson, L.T. Hall, D. Maclaurin, S. Prawer, P. Milvaney, J. Wrachtrup, F. Caruso, R.E. Scholten, L.C.L. Hollenberg, Quantum measurement and orientation tracking of fluorescent nanodiamonds inside living cells. Nat. Nanotech. **6**, 358–363 (2011). doi:10.1038/nnano.2011.64
226. S.C. Hens, G. Cunningham, T. Tyler, S. Moseenkov, V. Kuznetsov, O. Shenderova, Nanodiamond bioconjugate probes and their collection by electrophoresis. Diam. Relat. Mater. **17**(11), 1858–1866 (2008). doi:10.1016/j.diamond.2008.03.020
227. V.N. Mochalin, Y. Gogotsi, Wet chemistry route to hydrophobic blue fluorescent nanodiamond. J. Am. Chem. Soc. **131**(13), 4594–4595 (2009). doi:10.1021/ja9004514
228. L.M. Manus, D.J. Mastarone, E.A. Waters, X.Q. Zhang, E.A. Schultz-Sikma, K.W. MacRenaris, D. Ho, T.J. Meade, Gd(III)-nanodiamond conjugates for MRI contrast enhancement. Nano Lett. **10**(2), 484–489 (2010). doi:10.1021/nl903264h
229. S.S. Tinkle, Maximizing safe design of engineered nanomaterials: the NIH and NIEHS research perspective. Wiley Interdiscip Rev Nanomed Nanobiotechnol **2**(1), 88–98 (2010). doi:10.1002/wnan.63
230. D.B. Warheit, P.J.A. Borm, C. Hennes, J. Lademann, Testing strategies to establish the safety of nanomaterials: conclusions of an ECETOC workshop. Inhal Toxicol. **19**(8), 631–643 (2007). doi:10.1080/08958370701353080

Chapter 5
Diamond Nanowires: Fabrication, Structure, Properties and Applications

Yuan Yu, Liangzhuan Wu and Jinfang Zhi

Abstract Diamond is a wide band gap semiconductor exhibiting a combination of superior properties, such as negative electron affinity, chemical inertness, high Young's modulus, the highest hardness and room-temperature thermal conductivity, etc. It is possible to control and enhance the fundamental properties of diamond by fabricating 1D diamond nanowires, due to the giant surface-to-volume ratio enhancements of 1D nanowires. Although theoretical comparisons with carbon nanotubes have shown that diamond nanowires are energetically and mechanically viable structures, reproducibly synthesizing the crystalline diamond nanowires has remained challenging. In this chapter, we present a comprehensive, up-to-date review for the diamond nanowires, wherein we will give a discussing for their synthesis along with their structures, properties and applications.

5.1 Introduction

Nanowires fabricated from metals, polymers, and semiconductors using top-down and/or bottom-up procedures are new kind of nanostructured materials. They have characteristics of low weight with sometimes extraordinary mechanical, electrical, thermal, and multifunctional properties [1, 2]. Nanowires can be used for tunable transport of electrons with electronic properties strongly influenced by little perturbations on the surface, for giant surface-to-volume ratio enhancements.

Diamond is a material of extremes. It is the hardest, the most conductive thermally, the highest hardness, the greatest in atomic density of any known material and stable in single-photon emission even at room temperature [3, 4]. Diamond can

Y. Yu · L. Wu · J. Zhi (✉)
Key Laboratory of Photochemical Conversion and Optoelectronic Materials, Technical Institute of Physics and Chemistry, Chinese Academy of Sciences, Beijing 100190, People's Republic of China
e-mail: zhi-mail@mail.ipc.ac.cn

N. Yang (ed.), *Novel Aspects of Diamond*, Topics in Applied Physics 121,
DOI 10.1007/978-3-319-09834-0_5

be doped n- and p-type, from insulating, semiconducting, to metallic, respectively. The electrochemical background current of BDD in phosphate buffer is ten times lower than that of gold electrode and 400 times lower than that of glassy carbon electrode. In addition, diamond shows strongest bonding stability to deoxyribonucleic acid (DNA) [5]. Applications of diamond electrodes in electrochemistry [6–8] and in biosensors [9–11] have been well demonstrated.

The synthesis of diamond nanowires (DNWs) is an interesting research since new approaches pave the way to nanoscale and atomic precision of material growth as well as to the search of new forms of carbon. The DNWs precursor of porous diamond films was successfully fabricated by reactive ion etching in O_2 and CF_4 plasma [12], thereafter, nanostructured diamond honeycomb films were prepared by oxygen plasma etching with porous anodic alumina mask [13]. Very recently, DNWs of 80–100 nm in length were synthesized in ultra-nanocrystalline diamond (UNCD) films which was deposited by microwave plasma enhanced chemical-vapor deposition (MPECVD) system with an introduction of nitrogen in the mixture gas [14, 15].

As a result of the numerous efforts, many synthetic methods of diamond nanowires have been developed. However, the synthesis of these diamond nanowires has proven to be a low probability event and very difficult to reproduce, despite the many attempts we and others have put in, and despite the their potential applications, such as its high efficiency single-photon emission at room temperature and high-brightness low-threshold electron field-emission as well as high-performance nano-electromechanical switches and biosensors, etc. This challenge is an attractive one although reproducibly synthesizing the crystalline diamond nanowires has remained challenging,

This review is presented in the hope that it will help generate more interest and more effort to address this challenge. We will present a comprehensive, up-to-date review of the diamond nanowires, wherein we discuss their synthesis along with their structures, properties and applications. We highlight some of the most important synthetic routes that underpin the synthesis of diamond nanowires, then discuss the structures and properties of the diamond nanowires from the reported theoretical and experimental results, finally, summarize the applications of the diamond nanowires [16, 17].

5.2 Synthetic Strategies of Diamond Nanowires

Numerous efforts have been directed to develop the synthetic methods of diamond nanowires, such as reactive-ion-etching (RIE) [18–23], plasma post-treatment carbon nanotubes [24, 25], transfer fullerene to diamond nanowires at high temperature and high pressure [26], template or catalyst assisted CVD method [26, 27], etc.

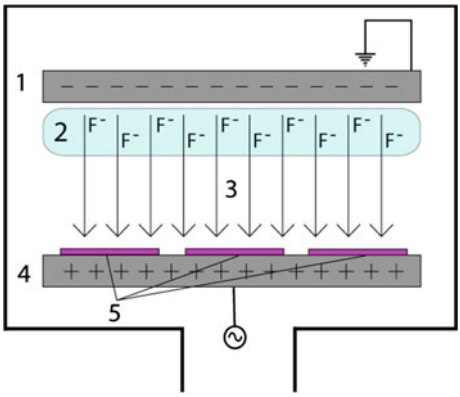

Fig. 5.1 A diagram of a common RIE setup. An RIE consists of two electrodes (*1* and *4*) that create an electric field (*3*) which can accelerate the ions (*2*) toward the surface of the samples (*5*)

5.2.1 Plasma-Assisted Reactive Ion Etching (RIE) Route

Reactive-ion etching (RIE) is an etching technology used in top-down micro- and nanofabrication. As shown in Fig. 5.1, it uses chemically reactive plasma to remove material deposited on wafers. High-energy ions from plasma attack the surface of the sample and react with it forming desired nanostructures [28]. The first realization of diamond nanowires by RIE was performed by Shiomi [12], who demonstrated the formation of porous diamond film through oxygen plasma RIE. Later, the plasma-assisted RIE technologies have been widely developing for the top-down fabrication of diamond nanowires. In the process, a planar nanocrystalline or microcrystalline diamond film was first deposited, and then nanowires or nanorods arrays film was fabricated by the etching of planar film. Depending on whether the mask is used, the plasma-assisted RIE technologies for diamond nanowires consist of two types, mask-need and maskless ones.

5.2.1.1 Mask-Needed Plasma-Assisted RIE Technology

Diamond nanowires are generally obtained by etching of various planar diamond films through various masks including metal nanoparticles, oxides nanoparticles, and diamond nanoparticles. These nanoparticles used as masks were a few nanometers in diameter, and the density of the as-prepared diamond nanowires was depended on the size of the masks.

Metal-Masked Plasma-Assisted RIE Technology

The first realization of diamond nanowires was performed in 1997 by Shiomi [12], who demonstrated the formation of porous diamond film through oxygen plasma RIE by using Al as mask. Numerous columnar diamond nanowires of approximately

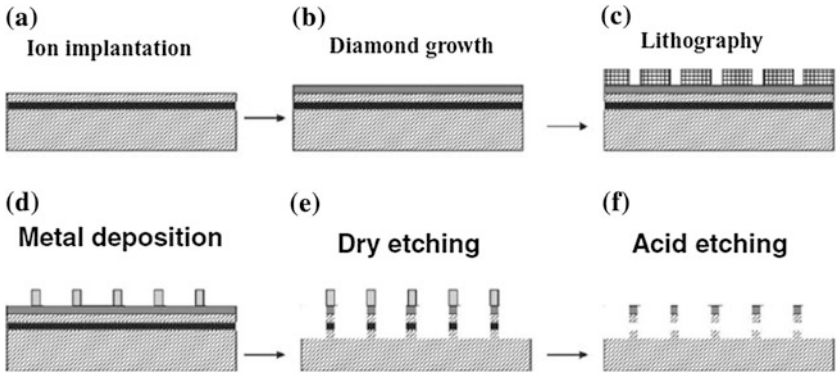

Fig. 5.2 Fabrication of single-crystal diamond nanowires. **a** Ion implantation into tybe-Ib diamond substrate by carbon ions at an energy of 180 keV and a dose of 10^{16} cm^{-2}. **b** Microwave plasma chemical vapor deposition growth with boron doping (concentration of 10^{18} cm^{-3}). During the chemical vapor deposition growth, a graphite-like layer with a thickness around 200 nm was formed below the diamond surface, which acted as the sacrificial layer. **c** E-beam lithography of the diamond. **d** Aluminum deposition and lift-off. **e** Nanowires formation by RIE. **f** Finally, removal of the Al and graphite by boiling in an acid solution. Reproduced from [30]. Copyright 2010 John Wiley

300 nm in length and 10 nm in width have been made by etching CVD polycrystalline diamond films in O_2 plasma. Subsequently, Hatta [29] and Ando [20] achieved aligned polycrystalline diamond nanowires through radio frequency (RF) RIE of planar diamond film (obtained from CVD) in Ar/O_2 or CF_4/O_2 plasma by the assistance of the patterned Al mask. The patterned Al masks were formed on diamonds by conventional photolithography. The as-prepared polycrystalline diamond nanowires have the disadvantages of the existence of grain boundaries, impurities, and large stress in the films. Recently, Liao [30] had successfully fabricated single-crystal diamond nanowires through Al-masked RIE method, and the fabrication process was shown in Fig. 5.2.

The fabrication of single-crystal diamond nanowires began from the high-pressure high-temperature (HPHT) type Ib-diamond substrate, which was implanted with carbon ions [31]. A homoepitaxial boron-doped p-type diamond was grown on the substrate by a microwave plasma chemical vapor deposition (MPCVD) apparatus at 930 °C. After growth, the diamond epilayer was annealed at 900 °C for 3 h in a UHV chamber (base pressure 10^{-7} Pa). A graphite layer with thickness of 200 nm was formed after the high-temperature processing. Conventional photolithographic and electron beam (e-beam) lithographic processes were employed to define the cantilevers or bridge structures. An aluminum layer with a thickness of 150 nm was deposited on the patterned diamond epilayer as a mask for reactive ion etching. After that, the sample was treated in a boiling HNO_3/H_2SO_4 acid solution to remove the Al and graphite, and single-crystal diamond nanowires were obtained. Besides Al, other metals, such as Mo [21, 32], Ni [22, 23], Au [33, 34],

have been successfully used as masks to oxygen plasma etch undoped or boron-doped diamond (BBD) nanowires. Recently, through de-wetting various metal films, i.e., Al, Ti, Co, Ni, Cu, Pd, Pt and Au film, metal masks of 5–50 nm in diameter were obtained. Gheeraert [35] systematically investigated the effect of metal film types and thicknesses on surface density, shape and size of the resulting metal masks.

Oxides-Masked Plasma-Assisted RIE Technology

Fujishima et al. reported a technique for the preparation of periodic diamond nanowires arrays by means of reactive ion etching with oxygen plasma using two-dimensional (2D) arrays and monodisperse solid SiO_2 particles as masks [36, 37]. In the planar diamond surface, fine SiO_2 particles [38] are packed in high-density, highly oriented layers over a wide surface area by water evaporation and lateral capillary forces [39]. After preparation of the 2D array, reactive ion etching (RIE) was carried out with oxygen plasma through the SiO_2 arrays in a plasma etching apparatus. Finally, the SiO_2 particles were removed from the diamond with the HF-HNO_3 solution, and the periodic diamond nanowires arrays was obtained. Afterward, some oxides nanoparticles, such as SiO_2 and Al_2O_3, have been successfully used as mask for realizing synthesis of diamond nanowires in both single crystal and polycrystalline diamond by Hausmann [40]. Drop-casted nanoparticles (Au, SiO_2 and Al_2O_3) as well as electron beam lithography defined spin-on glass and evaporated Au have been used as an etch mask. Al_2O_3 nanoparticles were found to be the most etch resistant. At the same time, the flowable oxides (FOx) e-beam resist (spin-on glass) proved to be a suitable etching mask for fabrication of ordered arrays of diamond nanowires.

Diamond Nanoparticles-Masked Plasma-Assisted RIE Technology

Yang et al. realized vertically aligned diamond nanowires from metallically boron doped single crystalline CVD diamond film by using of diamond nanoparticles as mask [19, 41–43]. The fabrication process of vertically aligned diamond nanowires was illustrated in Fig. 5.3. First, metallically boron-doped (p-type) diamonds with atomically smooth surfaces are grown by homoepitaxy on Ib diamond substrates [44]. Then, an etching mask from diamond nanoparticles is deposited. The diamond nanoparticles of about 8–10 nm in diameter are dissolved in water by ultrasonification to form a pseudo-stable suspension [45–47]. Then the planar diamond film is immersed into the suspension and sonificated to seed diamond nanoparticles on the diamond surface. The diamond nanoparticle layer is dense and depends on suspension quality and time of sonification. After deposition of diamond nanoparticles, reactive ion etching (RIE) in an O_2 (97 %)/CF_4 (3 %) gas mixture is applied. Vertically aligned diamond nanowires arise where diamond nanoparticles have been deposited.

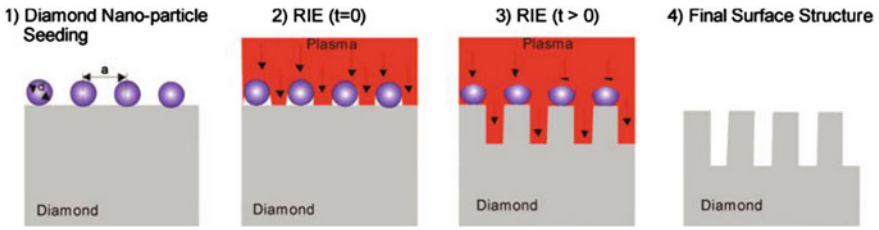

Fig. 5.3 Schematic plots of fabrication of diamond nanowires. Here d is the diameter of nanodiamond particles, and a is the distance between particles. Reproduced from [19]. Copyright 2008 John Wiley

5.2.1.2 Maskless Plasma-Assisted RIE Technology for Highly Doped Diamond Nanowires

As mentioned above, 1D nanostructured diamonds are generally fabricated by etching through various masks such as anodic alumina, SiO_2 ordered arrays, Au nanodots, molybdenum, nanodiamond particles, and other materials. However, these methods suffer from certain limitations and are unfavorable for large-scale fabrication. For example, some masks need be removed by additional chemical or physical processes, or an etching mask needs be intentionally deposited by pre-preparation processes. Fujishima et al. reported a RIE technology for heavily B-doped diamond (the boron doping level is 2.1×10^{21} B cm^{-3}) nanowires using oxygen plasma without any additional mask assistance [48]. It is assumed that boron oxides form on the surface at boron-rich nanometer-scale locations, and they are less volatile than the reaction products, i.e., CO and CO_2. In the initial stage of etching, the boron dopant atoms at the diamond surface contribute to the small, nanometer-scale structures. As the etching progressed, the boron species, including oxides, are removed together with carbon atoms, and then they appear to redeposit near the tops of the nanowires and continue to serve as an etching mask. The boron dopant atoms in the diamond act as the mask during plasma etching, so avoiding the complicated pre-preparation processes involved in using an intentional mask or removal of the template by using additional processes. The formation sites of the nanowire array depend greatly on the boron distribution. Figure 5.4 shows the SEM images of the microstructure of a BDD nanowire arrays. This straightforward method displays several advantages as it does not require any complicated processing steps such as mask deposition and removal. Until now, this maskless RIE method has been widely used to realize diamond nanowires [18, 49–53].

5.2.2 Chemical Vapor Deposition Method (CVD)

Vapor phase growth is extensively useful bottom-up method to produce nanowires. Starting with the simple evaporation technique in an appropriate atmosphere to

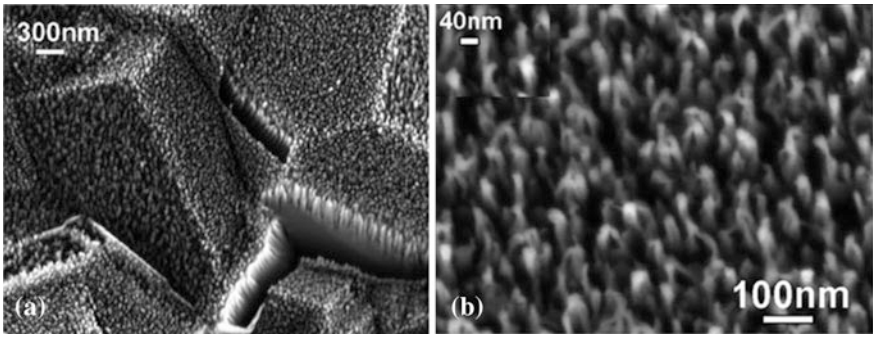

Fig. 5.4 SEM images of a BDD nanowire arrays at **a** low resolution and **b** high resolution. Reproduced from [48]. Copyright 2009, Royal Society of Chemistry

produce elemental or oxide nanowires, vapour–liquid–solid, vapour–solid and other processes are also used [54–57]. Depending on whether the template is used, the CVD technologies for diamond nanowires consist of two types, template-assisted and template-free ones.

5.2.2.1 Template-Assisted CVD Method

Template-assisted CVD synthesis is a convenient and versatile method for generating 1D nanostructures [58–61]. The template serves as a scaffold against which other materials with similar morphologies are synthesized. The in situ generated material is shaped into a nanostructure with a morphology complementary to that of the template. Templates could be nanoscale channels within mesoporous materials, such as porous alumina or polycarbonate membranes, etc.

Nanowires-Templated CVD for Diamond Nanowires

One of the most important methods for inorganic nanowire synthesis is template-assisted CVD. The semiconductor nanowires derived from non-colloidal synthesis makes them convenient templates for gas phase synthesis including both physical coating as well as chemical transformation. Nanowires-templated CVD method for diamond nanowires usually consists of two steps. One is the synthesis of various nanowires templates, and the other is conformal coating of the nanowires templates with nanodiamond forming polycrystalline diamond nanowires by CVD method. The size of the as-prepared diamond nanowires is dependent on the size of the nanowires templates. The possibility of deposition of layered microdiamond coatings onto tungsten wires by the CVD method was demonstrated for the first time by May et al. [62]. Afterward, many others reported successful the coating of microdiamond onto a variety of substrate wires including silicon carbide, copper,

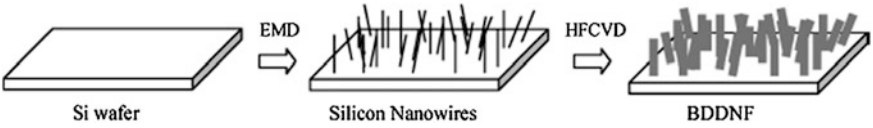

Fig. 5.5 Plots of fabrication of the boron-doped diamond nanowires arrays. Reproduced from [69]. Copyright 2009, American Chemical Society

tungsten, and titanium [63–65]. Singh et al. reported two-step method for synthesis of high-density nanocrystalline diamond fibers (nanowires). This method includes the synthesis of templates (silica (α-SiO_2) nanofibers) by a conventional vapor–liquid–solid method and the conformal coating of the nanofibers with 15–20 nm sized NCD grains by a microwave plasma enhanced chemical vapor deposition technique in hydrogen-deficient conditions [66–68]. The as-prepared diamond nanowires showed good electron field emission properties [67, 68]. Furthermore, our group also reported a Si nanowires-templated hot filament chemical vapor deposition method for fabrication boron-doped diamond nanowires arrays and 2D diamond nanowires network [69, 70]. The synthesis process of boron-doped diamond nanowires arrays is illustrated in Fig. 5.5. First, silicon nanowires were synthesized using the electroless metal deposition (EMD) method [71] on a p-type silicon wafer substrate. The substrate was then pretreated ultrasonically in a suspension of diamond nanoparticles for 20 min. Finally, the BDD nanowires arrays film was prepared by depositing a boron-doped diamond nanocrystals onto the as-fabricated Si nanowires (SiNWs) by HFCVD technology. A large amount of boron-doped diamond nanorods standing vertically on a silicon wafer can be observed. These nanowires possess rough and irregular surface and present polycrystalline morphology.

AAO-Templated CVD

Porous anodic aluminum oxide templates played a dominant role in the preparation of highly ordered nanowires [72, 73] with controllable size. Masuda et al. reported the preparation of well-aligned polycrystalline diamond nanocylinders (nanowires) and diamond-like carbon (DLC) nanotubes on anodic aluminum oxide templates by microwave plasma-assisted chemical vapor deposition (CVD) [74]. The alumina templates [75, 76] for diamond deposition were prepared by electrochemical anodization of aluminum sheet. As shown in Fig. 5.6, prior to deposition, the alumina templates were nucleated with 50 and 5 nm diamond particles for the deposition of diamond nanocylinders and diamond-like nanotubes, respectively. For the growth of nanowires arrays, the 50 nm particles were nucleated at the bottom of the alumina membrane pores possessing the same diameter (Fig. 5.6a). This enables the growth of diamond cylinders along the length of the pores. For the growth of nanotubes, smaller diamond nanoparticles (5 nm) were ultrasonically

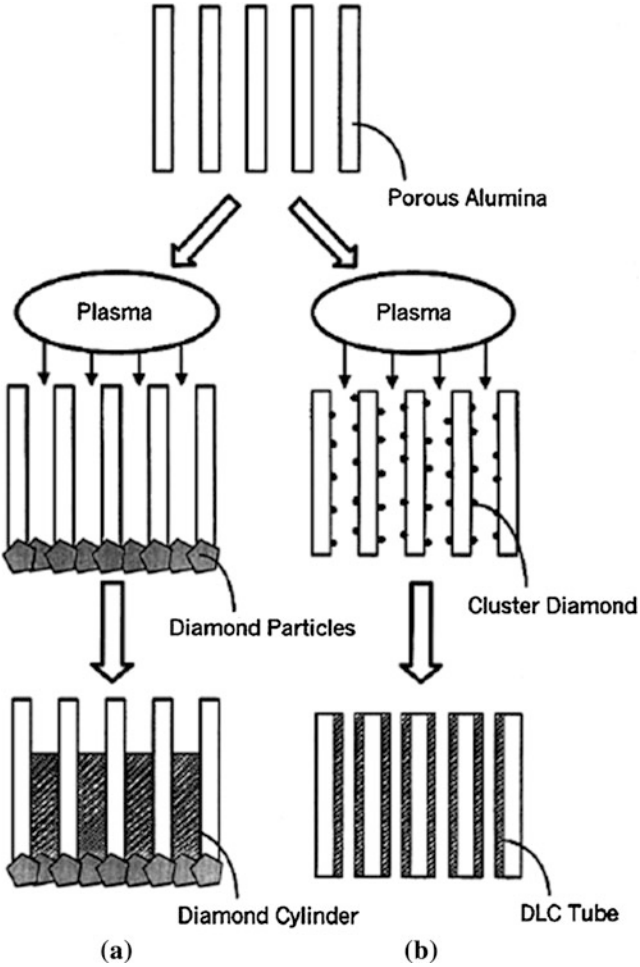

Fig. 5.6 Schematic diagram of fabrication process for cylindrical diamond and tubular structures. **a** The cylindrical structures were prepared by nucleating with 50 nm diamond particles at the bottom of the membrane holes, followed by microwave plasma CVD for 3 ± 4 h using acetone as the carbon source. **b** Tubular structures were fabricated by nucleating with 5 nm particles on the pore walls of the membrane followed by microwave plasma CVD. Reproduced from [74]. Copyright 2001, John Wiley

dispersed on the pore walls by keeping the templates in particle suspensions (Fig. 5.6b). The growth of diamond nanowires or nanotubes was carried out by plasma-assisted CVD. The deposition of diamond initially proceeds along the alumina pores and continues to grow on the membrane to yield a continuous film, which acts as a support for the nanostructures. The resulting nano-fibers were released from the alumina membrane by immersion in concentrated phosphoric acid at 250 °C.

5.2.2.2 Template-Free CVD for Diamond Nanowires

The growth of nanowires via a gas phase reaction involving the vapor–liquid–solid (VLS) and vapor–solid (VS) processes has been widely studied. The experimental observations suggest that there are three growth stages: metal alloying, crystal nucleation and axial growth in the CVD growth of a nanowire. More recently, the enhanced CVD methods, such as microwave or plasma enhanced CVD methods for diamond nanowires were widely investigated.

Microwave Plasma Enhanced CVD (MPCVD) Method

Valsov et al. reported on the MPCVD synthesis and characterization of new hybrid diamond-graphite nanowires, formed via ultra-nanocrystalline diamond (UNCD) film deposited with adding nitrogen gas [77]. The UNCD films were deposited on Si substrates in a microwave plasma CVD reactor in $Ar/CH_4/H_2/N_2$ mixtures [78]. Scanning electron microscopy (SEM) images show that the morphology of the UNCD film surface undergoes essential changes when 25 % of nitrogen is added in the gas mixture: wire-like structures appear along with diamond nano-grains. The Raman spectra show the as-prepared nanowires are hybrid diamond-graphite nanowires. The DNW cores are 5–6 nm in diameter and grow along the [110] direction. The experimental results showed that the N_2 play an important role on the growth of wire-like diamond grains, which is consistent with the results of Arenal's [14]. It is suggested that the low concentration of hydrogen and the introduction of nitrogen into the plasma are two favorable conditions for synthesis of one-dimensional diamond nanostructures by CVD [79]. According to theoretical models nanocrystalline diamond may be structurally stable both in quasi-zero dimension (nanograin) [80, 81] and in one dimension nanowires [82, 83]. However, in UNCD films grown without nitrogen only the diamond nanograins are observed. The high renucleation rate provided by the presence of C_2 dimers in the plasma suppresses the extension of the one-dimensional diamond nanostructures, this way limiting the grain size within the range of diamond phase stability, which is about 5 nm. The introduction of nitrogen in the plasma stimulates the formation of CN molecular species reducing the renucleation rate. This creates favorable conditions for an increase of the grain size and the formation of one-dimensional diamond nanostructures.

Shang et al. reported the growth of ultrathin diamond nanorods (UDNRs) by a MPCVD method (in N_2/CH_4 plasma) [84]. As-deposited UDNRs have a length of 50–300 nm and a thin diameter of 2.1 nm, less than the theoretical minimum value (2.7 nm) for energetically stable UDNRs [82, 83]. The growth of UDNRs is suggested to follow a heterogeneous self-catalytic vapor liquid mechanism. Recently, Sobia et al. reported the effect of nitrogen on hydrogen incorporation in diamond nanorods thin films obtained through MPCVD method (in $Ar/H_2/CH_4/N_2$ plasma).

The results showed that the addition of nitrogen in gas phase has been utilized to increase the nondiamond content in the films. The increase in incorporated amount of hydrogen is related to the low crystalline quality of the film due to increase in non-diamond content [85]. More recently, Shalini et al. reported the synthesis of diamond nanowires films using the MPCVD (in $Ar–N_2/CH_4$ plasma) [86, 87]. The experimental results showed that the electrical conductivity and the fraction of sp^2 bonding in the diamond nanowires film grain boundary (π states) increased proportionally with the amount of nitrogen incorporation [86].

In conclusion, during the DNW growth process of MPCVD, the N_2 play an important role on the growth of wire-like diamond grains. The introduction of nitrogen in the plasma stimulates the formation of CN molecular species reducing the renucleation rate provided by the presence of C_2 dimers in the plasma, which creates favorable conditions for an increase of the grain size and the formation of one-dimensional diamond nanostructures. In addition, the incorporation of hydrogen in the diamond nanowires was found to increase with increasing the addition of nitrogen in the feed gases in deposition chamber, which leads to the fraction of sp^2 bonding in the diamond nanowires film grain boundary (π states) increased proportionally with the amount of nitrogen incorporation, since the hydrogen incorporated in DNW can lower the crystalline quality of DNW. Therefore, MPCVD induced high N_2-incorporated DNW usually display good electrochemical properties, which is accounted for by increase in sp^2 content, new C–N bonds at the diamond grains, and increase in the electrical conductivity at the diamond grain boundary [87].

Hot Cathode Direct Current Plasma Chemical Vapor Deposition Method (HCDC-PCVD)

Nanocrystalline diamond films with different grain sizes, surface smoothness and quality have been prepared on Si substrate by changing the composition of $CH_4/Ar/H_2$ gas mixture using hot cathode direct current chemical vapor deposition (HCDC-PCVD) method [88]. HCDC-PCVD method is an effective method for the deposition of diamond films (including nanocrystalline, microcrystalline diamond films, etc.), and diamond films can be deposited uniformly with large area and high growth rate. Zeng et al. reported (111) diamond microcrystals and (100) diamond microcrystals and nanorods were synthesized on Si substrate by HCDC-PCVD method in CH_4/H_2 gas mixture [89]. The results showed that the high-temperature (1,223 K) and low CH_4 concentration led to the growth of (111) microcrystalline diamond films, but the low temperature (1,098 K) and high CH_4 concentration can lead to the growth of (100) diamond microcrystals and nanorods. Furthermore, the low reactor temperature and high CH_4 concentration decreased the grain sizes, purity, and quality of diamond films but increased the transmittance of diamond films.

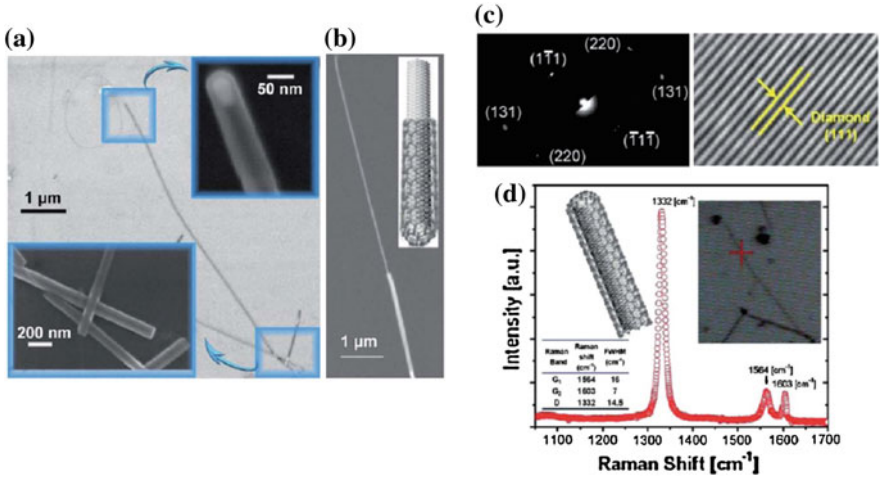

Fig. 5.7 **a** Electron microscopy of diamond nanowires encased within a carbon nanotube shell. Diamond core enclosed in a CNT sheath, typically tens of microns in length and 60–90 nm in exterior diameter. **b** An SEM micrograph showing laser-stripping of a portion of the graphitic shell of a CVD grown core-shell diamond nanowire. **c** High resolution transmission electron microscope (HRTEM) images and selective area electron diffraction (SAED) pattern of a single diamond nanowire indicating a crystalline cubic diamond (c-diamond) structure. **d** Raman spectroscopy of the diamond nanowire. Reproduced from [27]. Copyright 2010, American Chemical Society

Catalyst-Assisted Atmospheric-Pressure Chemical Vapor Deposition

As mentioned above, techniques for growing crystalline diamond have evolved from the high-temperature high-pressure (HTHP) method [90] to plasma enhanced chemical vapor deposition (PECVD) techniques [86, 87]. Diamond microwires with 25 μm diameter and 400 μm length were synthesized in 1968 using a radiation heating unit developed from a superhigh-pressure xenon tube [91]. However, the fabrication of long, single crystalline diamond nanowires using conventional thermal CVD methods has so far proven elusive, despite the potential benefits. Until to 2010, by chance, Hsu et al. synthesized diamond nanowires in an atmospheric pressure chemical vapor deposition method without plasma or energy radiation used during the CVD growth [26]. As shown in Fig. 5.7a, b, the as-prepared diamond were straight, thin and long, and longitudinally uniform in exterior diameter (60–90 nm) along the entire lengths of tens of micrometers and the structure of the nanowire indeed consists of a diamond core is encased within a graphitic shell. HRTEM image (Fig. 5.7c) of one of these nanowires reveals a crystalline diamond wire structure. Micro-Raman spectra (Fig. 5.7d) further verified the core-shell structure of the diamond nanowires. Hydrogen plays an important role in the formation of the diamond nanowires since it can facilitate the transformation of sp and sp^2 bonds into sp^3 bonds [92]. Meanwhile, transition metals (Fe in this experiment) are known to facilitate the dissociation of hydrogen molecules

into atomic hydrogen at significant low hydrogen dissociation barrier [93, 94]. The authors summarized their achievement in a mini-review, and gave a possible formation process of the diamond nanowires [95]. They rationalized that the diamond nanowire growth process begins with the conventional synthesis of either diamond stud or graphitic tubes with a vapor–liquid–solid (VLS) process and is then followed by *in situ* nucleation and growth of diamond wires, fuelled by the subsequent hydrogen flow in the presence of solid and vapor carbon feedstock.

5.2.3 *Diamond Nanowires Realized from sp^2 Carbon and sp^3 Diamondoid*

The transformation of graphite to diamond nanocrystals has been one of the most challenging problems of material science for many decades. Generally, high pressures and high temperatures are needed to induce this transformation, and catalysts are used to increase the yield of diamond. Research has revealed that carbon nanotubes could also transform to diamond nanocrystals under different processing conditions—laser induced transformation [96], chemical vapor deposition by nanotube coating [97], shock wave [98], and direct transformation under high pressures and high temperatures (HPHT) [99–101]. The mechanism of transformation from carbon nanotubes to diamond was proposed to be nanotubes–carbon onions–diamond [102]. The last step had been identified to be critical in the nucleation and growth of diamond nanocrystals in the centers of spherical carbon onions under intense electron irradiation at high temperatures. However, transferring sp^2 carbon to 1D diamond nanowires is still a challenging.

5.2.3.1 Hydrogen Plasma Post-treatment of Multiwalled Carbon Nanotubes (MWCNTs) for Diamond Nanowires

Sun et al. provided a simple way for the transformation from CNTs to nanocrystalline diamond, that is, hydrogen plasma induced structural transformation from CNTs to nanodiamond [103]. Only by prolonging the hydrogen plasma treatment time, diamond nanowires with diameters of 4–8 nm and with lengths up to several hundreds of nanometers were obtained [24, 25]. The nanowires form a core-sheath structure. Moreover, the vapor–liquid–solid (VLS) growth mechanism of 1D nanomaterials seems to be unlikely for the present diamond nanowires growth, since there is no metal catalysts used in the synthesis process. The author proposed a three-step process for diamond formation and growth under the hydrogen plasma treatment of MWCNTs, including clustering, crystallization, growth, and faceting, which is similar to that proposed by Singh [104] for diamond nucleation, crystallization, and growth from amorphous carbon precursors. Figure 5.8 shows the proposed model for the formation of nanodiamonds, and the growth of diamond

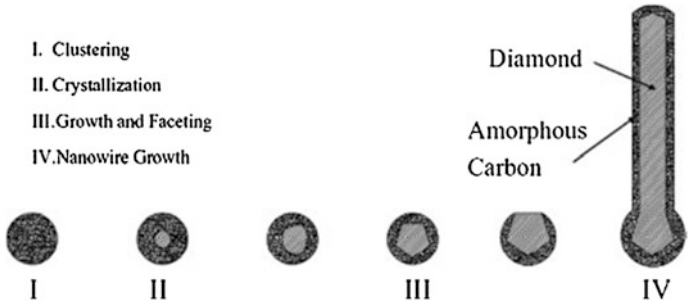

Fig. 5.8 The proposed model for the formation of nanodiamonds, and the growth of diamond nanowires under hydrogen plasma irradiation of multiwalled carbon nanotubes at high temperatures. Reproduced from [103]. Copyright 2004, American Physical Society

nanowires. Amorphous carbon clusters are formed in step I, the crystallization of diamond begins in the core of the carbon clusters(step II), followed by the diamond growth and faceting stage (step III), after the diamond nanocrystallites are faceted, diamond nanowires begin to grow at the nanowire tips (step IV). The amorphous carbon layers that sheathe both the diamond nanoparticles and nanowires are important for the 1D growth of diamond nanowires, by preventing the lateral growth of diamond and providing the carbon source for diamond nanowires growth.

5.2.3.2 Diamond Nanowires Grown from Fullerene (C_{60})

Dubrovinskaia et al. reported a bulk sample of nanocrystalline cubic diamond with crystallite sizes of 5–12 nm which was synthesized from fullerene C_{60} at 20 GPa and 2,000 °C using a multi-anvil apparatus [105]. The new material is at least as hard as single crystal diamond. It was found that nanocrystalline diamond at high temperature and ambient pressure kinetically is more stable with respect to graphitization than usual diamond. Almost at the same time, they synthesized aggregated diamond nanorods (ADNRs) from fullerene C_{60} at 20(1) GPa and 2,200 °C using a multi-anvil apparatus [26]. Individual diamond nanoroads are of 5–20 nm in diameter and longer than 1 μm. The measured density of ADNRs is about of 0.2–0.4 % higher than that of usual diamond.

5.2.3.3 Diamond Nanowires from Diamondoids

Diamondoids have been found to have strong affinity towards compatible host structures, such as cyclodextrins [106] and CNTs [107]. Analogous to the fabrication of 1D sp^2 CNTs from 0D sp^2 fullerenes [108, 109], the diamondoids may also fuse and transform into 1D sp^3 diamond nanowires. Templated growth of these

nanowires from 1D diamondoid assemblies confined in CNTs provides a probable pathway through a "face-fused" reaction. However, the fusion reaction of adamantane into diamond nanowires has been shown to be energetically unfavorable [107]. Zhang et al. presented theoretical and experimental evidence for the feasibility of a fusion reaction of diamondoid derivatives containing relatively reactive functional groups, diamantane-4,9-dicarboxylic acid to 1D diamond nanowires inside CNTs [110]. The bisapical diamondoid diacid is more reactive than the pristine diamondoid, requiring milder reaction conditions. Unlike in 3D space, the diamantine dicarboxylic acid molecules are pulled inside a CNT by an effective "capillary force" that originates in the stabilization of the molecule inside the surrounding nanotube. The fusion of diamantane-4,9-dicarboxylic acid under the confinement of CNTs may be a promising choice to yield diamond nanowires. The diamantane-4,9-dicarboxylic acid was sublimed and self-assembled into the quasi 1D space of double-wall CNTs (DWCNTs) by a vapor phase reaction. Since the sublimation temperature of diamantane-4,9-dicarboxylic acid was at 300 °C under air atmosphere, An encapsulation temperature of 280 °C was chosen for it at 10^{-6} Torr owing to its relatively low sublimation temperature in vacuo. Similar to adamantane, the encapsulation of diamantane-4,9-dicarboxylic acid is highly selective with respect to the CNT inner diameter (D_{inner}). There is no encapsulated diamantane-4,9-dicarboxylic acid in DWCNTs which have $D_{inner} < 0.8$ nm (Fig. 5.9a). However, the diamantane-4,9-dicarboxylic acid well aligned along the axis of DWCNTs with compatible $D_{inner} \approx 1.0$ nm (Fig. 5.9b), consistent with computational results for diamondoid encapsulation [111]. Multiple arrays of encapsulated molecules can often be found in CNTs with much wider D_{inner} (Fig. 5.9c). As demonstrated in the diamond formation by chemical vapor deposition (CVD) [112] and thermal annealing of adamantane inside CNTs [107], hydrogen plays a crucial role in retaining the sp^3 diamond cages. The as-produced diamondoid 1D assemblies in DWCNTs were annealed at 600 °C for 12 h under a flow of hydrogen. Diamond nanowires (CNWs) are then found inside DWCNTs with $D_{inner} \approx 1.3$ nm. The rod-shaped product has a diameter about 0.78 nm, and it is very stiff and straight. No nanowire structures have been observed in DWCNTs with a smaller D_{inner} of around 1.0 nm.

5.3 Structures and Properties: Simulation and Experiments

5.3.1 Structural Stability of Diamond Nanowires

Diamond-based materials have been suggested to be the optimal choice for nanomechanical designs because of their high elastic modulus and strength-to-weight ratio [113]. This has prompted a number of theoretical studies investigating various aspect of diamond on the nanoscale. Results of these investigations have shown that dehydrogenated C(111) octahedral nanodiamond surfaces are structurally unstable,

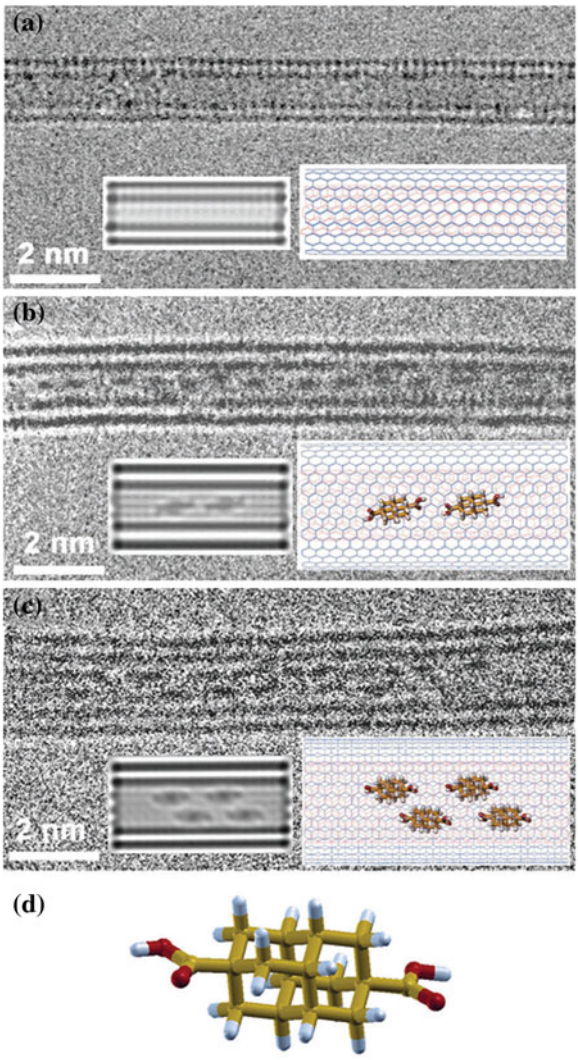

Fig. 5.9 HRTEM and simulated images, as well as model structures of **a** empty DWCNTs (Dinner < 0.8 nm), **b** linear diamondoid arrays inside DWCNTs (Dinner ≈ 1 nm), **c** multiple diamondoid arrays inside DWCNTs (Dinner ≈ 1.3 nm), and **d** optimized structure of the diamantane-4,9-dicarboxylic acid molecule; C yellow, O red, H white. Reproduced from [110]. Copyright 2013, John Wiley

with their presence inducing phase transitions from the sp^3 structure of nanodiamonds to the sp^2 structure of carbon onions. However, the presence of cubic surface facets has been found to promote stability. For example, whereas cuboctahedral nanodiamond structures have exhibited preferential exfoliation of C (111) surfaces over lower-index surfaces, increasing the C (100) surface area produces a more stable nanodiamond structure and reduced surface graphitization.

Attention is now turning to 1D diamond nanostructures. Barnard et al. studied the structural properties of dehydrogenated diamond nanowires using the Vienna ab initio simulation package (VASP) [83]. Three kinds of diamond wires, including dodecahedral, cubic and cylindrical nanowires have been considered. The dodecahedral

Table 5.1 Changes in energy per atom (ΔE), cross-sectional area (ΔA), and nanowire segment lengths (ΔL) resulting from the relaxation of each nanowire's morphology[a]

Morphology	Atoms	ΔE (eV)	ΔL (nm)	ΔA (nm^2)
Dodecahedral	75	−0.2271	+0.0883	−0.0428
Dodecahedral	144	−0.2150	+0.1051	−0.0578
Dodecahedral	196	−0.2057	+0.0722	−0.0586
Cubic[a]	84	−0 9812	−0.0222	
Cubic	132	−0.4847	−0.0034	−0.0265
Cubic	240	−0.4339	−00038	−0.0615
Cylindrical	63	−0.7063	+0.0199	−0.0336
Cylindrical	128	−0.5687	+0.0182	−0.0421
Cylindrical	228	0.2676	+0.0017	−0.0448

[a] Nonclassical nanotube

Reproduced from [83]. Copyright 2003, American Chemical Society

structures are bounded by (110) surfaces in all lateral directions, with a square cross section, and have a principal axis in the [100] direction. The cubic diamond nanowires are bounded by two C (100) surfaces and two C (110) surfaces in the lateral directions, with a rectangular cross section, and have a principal axis in the [110] direction. Finally, the three cylindrical nanowires considered here are bounded by two C (100) surfaces and two C (110) surfaces in the lateral directions, with a circular cross section, and have a principal axis in the [100] direction. Changes in energy per atom (ΔE), cross-sectional area (ΔA), and nanowire segment lengths (ΔL) resulted from the relaxation of each nanowire's morphology were shown in Table 5.1. It is apparent from Table 5.1 that the remaining cubic nanowires still exhibit unusual structural changes. t has been shown from the ab initio relaxation of diamond nanowires that nanocrystalline diamond may be structurally stable in one dimension. Diamond nanowires with dodecahedral and cubododecahedral morphology retained the diamond structure upon relaxation but did exhibit significant relaxation involving changes in the length and cross-sectional area. The stability, characterized by the variation in these structural properties from that of bulk diamond, has been found to be dependent on both the surface morphology and the crystallographic direction of the principal axis of the nanowire. For example, nanowires having a principal axis in the [110] direction do not represent an optimal choice for diamond nanowire structures.

Barnard et al. presented a theoretical investigation of the relative phase stability of 1D carbon nanostructures, including carbon nanotubes and diamond nanowires, using an atomic heat of formation model [82]. The results of this study indicate that carbon nanotubes represent the most energetically preferred form for fine 1D carbon nanostructures, and the diamond nanowires occupy a "window" of stability. This window ranges from approximately 2.7 nm to 3.7–9 nm in (lateral) diameter, beyond which graphite is energetically preferred. The limits of this range are

Table 5.2 Dimensions, strain energies, and HOMO–LUMO/band gaps of the icosahedral diamondoids and their 1D counterparts

Stoichiometry	No. of combined cages	Diameter (nm)	Length (nm)	ΔE	Gap (eV)
$C_{20}H_{20}$	1	0.66	0.66	14.6	8.49
$C_{35}H_{30}$	2	0.64	0.87	13.8	8.26
$C_{65}H_{50}$	4	0.64	1.56	13.2	8.14
$C_{125}H_{90}$	8	0.64	2.95	13	8.05
$C_{30}H_{20}$	∞	0.64	∞	12.8	8.01
$C_{20}@C_{30}H_{60}$	1	1.09	1.09	8.3	7.39
$C_{175}H_{90}$	2	1.09	1.59	8.7	7.26
$C_{325}H_{150}$	4	1.09	2.56	9	7.14
$C_{625}H_{270}$	8	1.09	5.04	9.1	7.11
$C_{150}H_{60}$	∞	1.09	∞	9.4	7.13
$C_{20}@C_{80}@C_{18O}H_{120}$	1	1.52	1.52	6.3	7.01
$C_{490}H_{180}$	2	1.53	2.31	7	6.81
$C_{910}H_{300}$	4	1.53	3.92	7.5	6.68
$C_{280}H_{120}$	∞	1.53	∞	8.2	6.65
$C_{80}H_{20}@C_{180}H_{120}$	1	1.52	1.52	7.9	6.43
$C_{450}H_{220}$	2	1.52	2.3	8.7	6.04
$C_{830}H_{380}$	4	1.52	3.89	9.2	5.87
$C_{380}H_{160}$	∞	1.53	∞	9.9	5.75

Reproduced from [114]. Copyright 2008, American Chemical Society

sensitive both to the nanowire morphology, and the method used to scale the graphite structures (required to ensure dimensional consistency). These results are considered to be useful in estimating the size range for which diamond nanowires may be expected during synthesis, and as a guide to the relative stability of some sp^2 and sp^3 carbon in 1D nanostructures.

Tanskanen et al. studied the structural stability of the polyicosahedral diamond nanowires obtained from icosahedral diamondoids and conventional diamond nanowires superimposable with bulk diamond [114]. Molecular structures of three icosahedral diamondoids, $C_{20}H_{20}$, $C_{20}@C_{80}H_{60}$, and $C_{20}@C_{80}@C_{180}H_{120}$, together with the corresponding polyicosahedral diamond nanowires are investigated. The B3LYP-calculated energetics, HOMO–LUMO gaps, and band gaps are summarized in Table 5.2. The strain energies suggest the 1D diamond nanowires (DNWs) to be favored over the dodecahedral $C_{20}H_{20}$. The low structural strain of the DNWs derived from the dodecahedrane is in agreement with previous studies on short oligomers of dodecahedrane [115, 116]. To take the effect of thermodynamics into account, the authors calculated the Gibbs corrected strain energies at T = 298.15 K for dodecahedrane and its 1D counterparts. The Gibbs corrections make the

dodecahedrane slightly favored over its 1D counterparts. The differences are small, however, suggesting the polyicosahedral DNWs to be thermodynamically viable. With the exclusion of dodecahedrane, the strain energies increase, while only slightly, as a function of length of the polyicosahedral diamondoid, suggesting the preference for icosahedral structures. Combining the icosahedral diamondoids to polyicosahedral DNRs reduces the number of strain-inducing pentagons. However, connecting the cages introduce additional strain to the interface region due to fused pentagons. Nevertheless, the strain energies are systematically lower for the polyicosahedral DNRs than for the experimentally known dodecahedrane. The relative proportion of the fused pentagons becomes reduced as a function of the diameter, decreasing the strain energies of the polyicosahedral DNRs derived from the larger icosahedral diamondoids [114]. Comparisons between the 1D diamond nanowires of $C_{20}@C_{80}@C180H_{120}$ and the corresponding hollow $C_{80}H_{20}@C_{180}H_{120}$ show the filled structures to be energetically favored.

Representative examples of the hydrogenated conventional DNWs, i.e., DNWs that are superimposable with bulk diamond, are investigated. The calculated strain energies are clearly the lowest for those conventional DNWs that are parallel to the [110] direction of bulk diamond. The highest stability of the [110] DNWs can be understood to originate from surface hydrogenation. The H–H distance between the surface hydrogen is around 2.5 Å for the [110] DNWs, while they are down to 2.0 Å for the [100] and [111] DNWs. The repulsion between the surface hydrogen thus somewhat destabilizes the [100] and [111] DNWs, whereas the repulsion is negligible for the [110] DNWs. The described preference for hydrogenated [110] DNWs also has been experimentally observed, DNRs synthesized by hydrogen plasma post-treatment of multi-walled CNTs preferring the [110] growth direction [32]. Previously, dehydrogenated DNWs have been shown to prefer structures with principal axis parallel to the [100] direction, while [110] DNWs have been reported unstable [117]. Due to the impact of H–H interactions at the surface, the presence (or absence) of hydrogen in the synthesis process of DNWs and DNRs may have an effect on the orientation of the products.

5.3.2 Mechanical Properties of Diamond Nanowires

Shenderova et al. compared the stiffness and fracture force of hydrogenated diamond nanorods with those of single-walled and multi-walled carbon nanotubes [118]. It was determined that the mechanical properties of the nanorods depend on both the diameter of the nanorod and the orientation of the principal axis. The results of their molecular models indicate that diamond nanorods are energetically competitive with nanotubes of a similar diameter and possess desirable mechanical properties, making them a viable target for synthesis. The mechanical properties of the polyicosahedral and the conventional DNWs, including Poisson's ratios, Young's moduli, and shear moduli, were investigated by Tanskanen et al. [114].

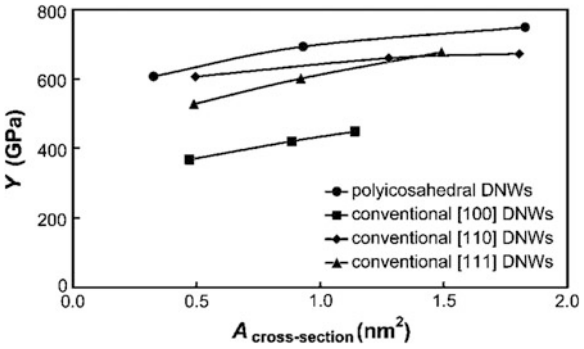

Fig. 5.10 Young's moduli (Y) of the hydrogenated conventional and the polyicosahedral DNWs as a function of the cross-sectional area of the structure. Reproduced from [114]. Copyright 2008, American Chemical Society

For a point of comparison, the elastic properties of a zigzag (22,0) CNT were determined by periodic calculations. The elastic moduli increases as a function of the length of the structure, as is clear from the calculated mechanical properties of $C_{20}H_{20}$ and $C_{20}@C_{80}H_{60}$ cages and their finite 1D counterparts. The Young's moduli increases because the stress caused by distortion from the equilibrium becomes distributed among a larger number of C–C bonds. The increase in shear moduli is due to larger shear surface.

In general, the Young's and shear moduli follow the same trends. The calculations give the highest Young's modulus for the CNT, included as a reference, a value of about 900 GPa being in agreement with previous theoretical and experimental work [119]. The studied conventional DNWs have Young's moduli around 360–680 GPa, the moduli increasing as a function of the wire diameter. For approximately the same cross-sectional area of the wire, the [100] DNWs have clearly lower moduli than the [110] and [111] DNWs. At a cross-sectional area of 1.4 nm^2 and beyond, the [111] DNWs have the highest Young's moduli of the studied conventional DNWs. This in agreement with previous calculations, suggesting the [111] direction having the highest Young's modulus for the low-index orientations of bulk diamond [26]. The Young's moduli of both hydrogenated conventional DNWs and the polyicosahedral DNWs are presented in Fig. 5.10. Similar to the conventional DNWs, the elastic moduli of the polyicosahedral DNWs increases as a function of the cross-sectional area. Furthermore, their Young's moduli are even higher than those of the conventional DNWs. Accordingly, the polyicosahedral DNWs, while being somewhat more strained than the conventional DNWs, could turn out to be valuable in nanomechanical designs.

Recently, strain rate, temperature and size dependent mechanical properties of [001] orientation diamond nanowires are investigated by Guo et al., using molecular dynamics simulations [120]. It is found that, for the same cross-sectional areas, strain rates have almost no effect on yield strength and Young's modulus, provided

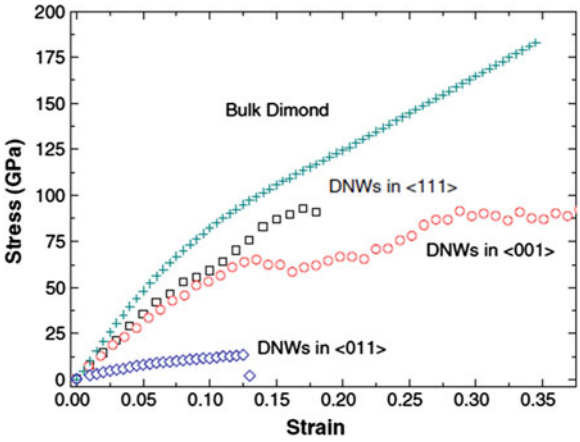

Fig. 5.11 Stress–strain curves with DNWs in [111], [001] and [011] crystal orientations at 300 K. Also shown are data of bulk diamond computed in this simulation. Reproduced from [120]. Copyright 2011, Elsevier

strain rates are within the range from 0.001 to 0.025 ps^{-1}. The calculated results have also indicated that, at the temperature ranging from 100 to 500 K, diamond nanowires' yield strength, Young's modulus, fracture strength and fracture strain are all decreasing with increasing temperature. Furthermore, at the temperature of 300 K, yield strength, Young's modulus, fracture strength and fracture strain increase dramatically with increasing cross sectional area. Finally, orientation dependent diamond nanowires mechanical properties are studied. Three crystal orientations DNWs have been considered, that is [111], [001] and [011] crystal orientations. All DNWs cross-sectional areas considered here are about 4.58 nm^2. The relationships between crystal orientations and stress–strain responses for these three crystal orientations DNWs are shown in Fig. 5.11. For [001] crystal orientation DNWs, the yield strength is 63 GPa and the Young's modulus is 688 GPa. However, for [011] crystal orientation DNWs, Young's modulus has a 74.7 % drop and the yield strength has a 77.8 % drop, respectively. For [111] crystal orientation DNWs, it will amount for 47.7 % in yield strength increase and 0.8 % in Young's modulus respectively. In particular, Young's modulus in [111] crystal orientation is significantly larger than in [001] and [011] crystal orientations. It has also indicated that Young's modulus in all DNWs considered here are lower than those of bulk diamond.

5.3.3 Density and Compressibility Properties of Diamond Nanowires

Dubrovinskaia et al., reported the synthesis of aggregated diamond nanorods (ADNRs) from fullerene C60 at 20(1) GPa and 2,200 °C using a multianvil apparatus [26]. Individual aggregated diamond nanorod is of 5–20 nm in diameter and longer than 1 μm. The X-ray density of diamonds with natural abundances of

isotopes is 3.515–3.519 g/cm^3. The lattice parameter of ADNRs obtained from X-ray powder diffraction is 3.5617(3) Å, and consequently, the X-ray density of the material is 3.528(1) g/cm^3, ~0.2–0.4 % higher than that of usual diamond [121, 122]. The samples synthesized in a multianvil apparatus have a cylindrical shape that allows us to determine their volumes. The measured density of the ADNRs bulk sample was found to be 3.532(5) g/cm^3 in good correspondence with X-ray data. This result is in agreement with theoretical calculations of the structural relaxations of the diamond nanowires [83]. Although exact crystallographic configuration realized for individual rods in ADNRs was not theoretically considered in [83], the main conclusion, that the outerlayer contraction, characteristic for diamond nanowires, causes shortening of the C–C bonds, may explain higher density of ADNRs. ADNRs are more than by 11 % less compressible than normal diamond that makes it, an incompressible form of carbon. It has also the lowest experimentally determined compressibility [123].

5.3.4 *Phonon Optical Mode and Electronic Structure of Diamond Nanowires*

The electronic structure of the polyicosahedral diamond nanowires and conventional diamond nanowires were determined by Tanskanen through quantum chemical calculations [114]. As shown in Table 5.2, comparing with the diamondoids, the HOMO–LUMO gaps of polyicosahedral diamond nanowires is smaller. The gaps are generally smaller for the polyicosahedral diamond nanowires with larger diameters and longer length. For conventional diamond nanowires, as shown in [114], the band gaps have the same trend as the band gaps calculated for the polyicosahedral DNWs.

It is well-known that phonon properties play an important role in the considered systems because of their significance for the analysis of various physical processes, such as, charge and thermal transport, and optical transitions, hence phonon band structures of Si and Ge nanowires have been investigated through DFPT (density functional perturbation theory) [124, 125]. Recently, A local bond-polarization model based on the displacement–displacement Green's function and the Born potential are applied to study the confined optical phonons and Raman scattering of diamond nanowires (DNWs) by Trejo et al. [126]. Also, the electronic band structure of DNWs are investigated by means of a semi-empirical tight binding (TB) approach and compared with density functional theory (DFT) within local density approximation (LDA). The results show that the highest-frequency Raman peak shifts to lower frequencies as the nanowire width increases, due to phonon confinement, in concordance with the experimental data [127]. The calculations of electronic band structure from TB for DNWs with d = 0.50, 0.37, and 0.25 nm have been solidly shifted by d = 4.58, 3.43, and 2.69 eV, respectively. It can be seen that the good agreement continues for the VBM but the LDA band gap

underestimation becomes greater when reducing size of DNWs. It is worth to observe that DFT–LDA band gap is always direct. Meanwhile, the TB one is indirect for all cases. The difference between the conduction bands could be due to that the s* orbital has non d-wave symmetry and additionally the geometry optimization is absent in the TB calculations. The calculation results also showed that the almost linear decrease in the band gap when the width of the diamond nanowires is increasing, and the important contribution of hydrogen atoms to the electronic states around the conduction band minimum (CBM).

5.3.5 Thermal Conductivity of Diamond Nanowires

On the basis of the high thermal conductivity of bulk diamond, DNWs may have thermal conductivities that rival CNTs. Moreover, the thermal conductivity of DNWs may be less sensitive to surface functionalization than modeling suggests for CNTs [128], thereby providing a potentially important mode for enhancing heat transfer within a nanocomposite via cross-linking. On the other hand, the nanometer-scale dimensions of DNWs may severely reduce their thermal conductivity compared to bulk diamond. Experiments and theoretical analysis by Novikov et al. [129], for example, show that thermal conductivity in polycrystalline diamond thin films is severely reduced as grain sizes approach the nanometer scale due to phonon scattering. Moreland et al., used simulations to characterize the thermal conductivity of a (10,10) CNT and a diamond nanowire [130]. They showed that the conductivity of the diamond nanowire is significantly less than that of the CNT but that the calculated values for the thermal conductivity for both structures depends on the choice of thermostat. Padgeet et al. reported thermal conductivity calculations using classical trajectories of hydrogen-terminated and functionalized DNRs with a [110] long axis, and cross sectional radii and lengths ranging from 0.578 to 1.606 nm and from 0.016 to 0.128 μm, respectively [131]. The simulations predict that thermal conductivities for DNRs with hydrogen surface termination are about a factor of 4 less than previously calculated values for pristine (10,10) CNTs. To study the effect of surface functionalization on thermal conductivity, structures on which attached phenyl groups replace surface hydrogen have been modeled. The simulations indicate that the thermal conductivities of DNRs are much less influenced by surface functionalization than are thermal conductivities of CNTs, suggesting that DNRs are a viable alternative to CNTs for thermal management in nanocomposites. The simulation results show a strong dependence of thermal conductivity on length and radius of the DNRs for both the hydrogen-terminated and surface functionalized structures. Guo et al. presented non-equilibrium molecular dynamics simulations on geometry and temperature dependent thermal conductivities of diamond nanowires [132]. The calculated results indicated that at temperature 300 K, diamond nanowire thermal conductivities increase with increase in length and cross-sectional areas. It is also found that at the same length,

temperature and cross-sectional area, thermal conductivities of the [011] crystal orientation DNWs are larger than those in the [001] and [111] crystal orientation DNWs. All diamond nanowires thermal conductivities considered in this work are smaller than those of the corresponding orientations bulk diamond. Additionally, in the temperature range 0–1,000 K, diamond nanowire's thermal conductivities initially increase with increasing temperature, and then decrease. Geometry and temperature effects on diamond nanowires thermal conductivities can be explained well by calculated densities of phonon states.

5.3.6 Electrochemical Properties of Diamond Nanowires

Planar boron-doped diamond (BDD) electrodes have been recognized as one of the most promising electrode materials and sensing platforms due to the unique physical properties of the diamond film. The diamond interface is chemically stable, exhibits favourable biocompatibility and shows an enlarged potential window together with a low background current, as compared to other electrode materials such as gold or glassy carbon [133]. Boron-doped diamond (BDD) has been recognized as the best electrode material for electrochemistry, since diamond electrodes have unique features like (a) high chemical stability, (b) no easy fouling, (c) good biocompatibility, (d) low background current, and (e) wide potential window [133], etc. The electrochemical background current of BDD in phosphate buffer is ten times lower than that of gold electrode and 400 times lower than that of glassy carbon electrode. In addition, diamond shows strongest bonding stability to deoxyribonucleic acid (DNA) [5]. Applications of diamond electrodes in electrochemistry [6–8] and in biosensors [9–11] have been well demonstrated. The electronic and chemical properties can be tuned by changing the surface termination of diamond [134]. BDD electrodes have been consequently used for a wide range of electrochemical applications [6, 133]. In the past years, diamond nanowires was motivated by increasing the surface area of the electrode to achieve higher sensitivity and selectivity, as compared to planar BDD interfaces [41, 42], for giant surface-to-volume ratio enhancements. For example, experimental results show that the good biocompatibility and electron transportation ability of nanograss array BDD greatly improve the direct electron transfer and can make it suitable for the anode of high performance MFC [135]. The nanograss array BDD showed higher electrocatalytic activity toward the catechol detection than did the as-grown BDD planar electrodes [136]. BDD nanograss array can enhance the chemiluminescence signals from the $Ru(bpy)_3^{2+}$/TPA system, due to the superior properties of the BDD nanograss array, such as improved electrocatalytic activity and accelerated electron transfer [137]. In addition, nanotextured diamond nanowire surfaces are promising to be applied as a novel platform to achieve direct electrochemistry of redox proteins and to construct novel biosensors [138].

5.4 Application of Diamond Nanowires

5.4.1 Field Emission from Diamond Nanowire

Diamond is a good candidate for solid-state electronics emitters because of its negative or very low electron affinity [139]. Electron emitters can be used in vacuum microelectronics such as Spindt-type emitters. Diamond has a negative electron affinity (NEA) when the diamond [111] surface is terminated by hydrogen [139, 140]. Nishimura et al. reported that the diamond [100] surface also exhibits the NEA property [141]. NEA permits diamond to be a superior field emitter [142]. Defects at the diamond tip may further assist the emission by providing a focal point for both field and current [143]. There are many reports concerning field emission from chemical vapor deposited (CVD) diamond nanocrystals or diamond-like carbon thin films. Up to now, a few examples on synthesis and field emission studies from 1D nanowire diamond-based systems have appeared.

5.4.1.1 Electron Field Emission (EFE) from Planar Diamond Nanowire Arrays Film

Electron field emission of nanodiamond emitter arrays was reported by Madaleno and his coworkers [68]. The EFE was measured using a parallel plate diode structure (Fig. 5.12). Emission starts abruptly when the applied field reaches 5.5 V/μm. This type of phenomenon was also reported by Jiang et al. [144] and Gupta et al. [145] in the case of NCD films. A small plateau can be observed in the current density, between 5.5 and 7 V/μm. The emission does not increase even with the increase of the applied field. A similar behavior was reported by Gan et al. [146] in the electron emission from hydrogenated natural diamond. A high emission current density of 10 mA cm^{-2} at 12 V/μm has been obtained from NCD microtip arrays. This value is comparable to those of high quality NCD diamond films deposited on silicon substrates. The field enhancement factor β can be taken from the slope of the FN plot if we assume a work function of 4.6 eV, typical for graphitic materials. The experimental field enhancement factor is $\beta = 2{,}000$. This value is extremely high. Shang et al. reported the growth of ultrathin diamond nanorods (DNRs) by a microwave plasma assisted chemical vapor deposition method, using a mixture gas of nitrogen and methane [84]. DNRs have a diameter as thin as 2.1 nm, which is not only smaller than reported one-dimensional diamond nanostructures (4–300 nm) but also smaller than the theoretical value for energetically stable DNRs. Together with diamond nanoclusters and multilayer graphene nanowires/nano-onions, DNRs are self-assembled into isolated electron emitting spherules and exhibit a low-threshold, high current-density (flat panel display threshold: 10 mA/cm^2 at 2.9 V/μm) field emission performance, better than that of all other conventional (Mo and Si tips, etc.) and popular nanostructural (ZnO nanostructure and nanodiamond, etc.) field emitters except for oriented CNTs. Very recently, Sankaran et al. reported the synthesis of

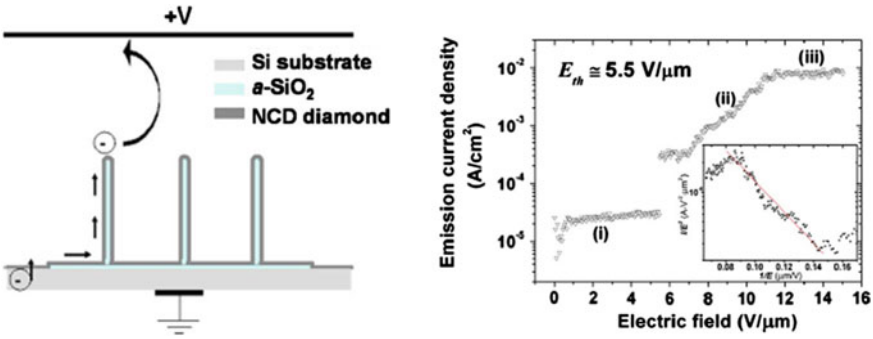

Fig. 5.12 Schematic diagram representing electron flow from Si substrate until emission at the fiber tip (*left*); and Plot of the emission current density versus external electric field of as-synthesized NCD microtip array (*right*). *Inset*: corresponding FN plot. Reproduced from [68]. Copyright 2008, American Physical Society

conducting diamond nanowires (DNWs) films by N_2-based microwave plasma enhanced chemical vapor deposition [147]. The EFE properties of the DNWs encased by the highly conducting graphite were tested. The results show emission current density, J, as a function of the applied electric field, E. It reveals a low turn-on field of 4.35 V/μm at a current density of 3 μA/cm^2. In addition, the current density increases rapidly and reaches the large magnitude of ~3.42 mA/cm^2 at the field of 9.1 V/μm. The DNWs film exhibits far more efficient EFE properties of lowest E_0 and highest J_e values than that of other diamond related materials reported previously [148–150]. This excellent EFE feature of DNWs films evidence a high potential for flat panel display applications [151].

5.4.1.2 Electron Field Emission from a Single Diamond Nanowire

Hsu and Xu reported for the first time the measurement of the field emission from a single diamond nanowire from the samples synthesized by catalyst-assisted atmospheric-pressure chemical vapor deposition method [95]. The result, shown in Fig. 5.13, is an I–V plot with a near-linear Fowler–Nordheim (F–N) relationship and reveals an ultra-low threshold electron field emission. When taking $\phi = 5$ eV for diamond as Shiraishi suggested [152], it was found that the field enhancement factor b reached $\sim$60,000. This is almost two orders of magnitude larger than the factor reported for carbon nanotube field emitters ($\sim$1,000) [153]. It is also worth noting the low threshold field (ETH). The threshold field is defined as the applied field required for an emission of a certain current, which was set to be 100 nA. The authors then compared their diamond nanowire to the field emission characteristic obtained by a single 80 nm diameter carbon nanotube reported by Smith and Silva [154]. The diamond nanowire's threshold field of 1.25 Vμm^{-1} is four times lower than the carbon nanotube's 5 Vμm^{-1}. The possible reasons for such a remarkable

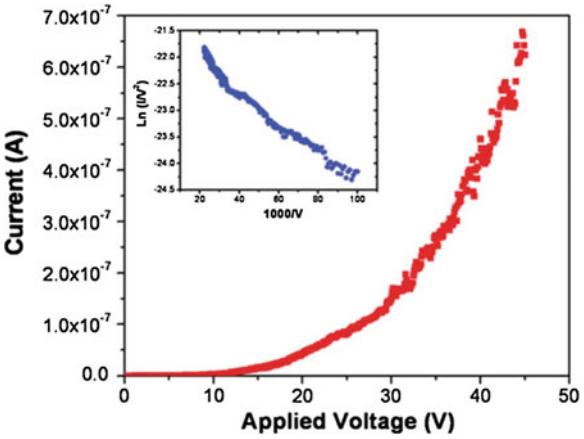

Fig. 5.13 Field emission data obtained from an individual diamond nanowire in an SEM by a nanomanipulator. The inset presents the emission current data plotted in Fowler–Nordheim coordinates, demonstrating the field emission behavior of the diamond nanowire. Reproduced from [95]. Copyright 2012, Royal Society of Chemical

high field enhancement factor (sixty times higher) and low threshold field (four times lower) of the diamond nanowire over carbon nanotubes are the negative electron affinity, the greatly intensified field at the tip of a large curvature and the possible defects at the nanowire tip, which itself is a "geometric singularity" [155]. Furthermore, the chemical inertness, high mechanical strength and high thermal conductivity of the diamond nanowires allow them to endure a longer and more intense emission. In addition, the wide band gap and the chemical inertness make diamond nanowires suitable for applications in high temperature and aggressive environments such as space or military applications.

5.4.2 *Diamond Nanowires for Highly Sensitive Matrix-Free Mass Spectrometry Analysis of Small Molecules*

Diamond-like carbon (DLC), an amorphous carbon with mixed levels of sp^3 and sp^2 hybridized carbons, has been successfully used for matrix-free laser desorption/ionization mass spectrometry (LDI-MS) particularly for the analysis of small metabolites such as carbohydrates, lipids, and low-molecular-weight peptides [156]. More recently, Coffinier et al. reported, for the first time, on the use of boron-doped diamond nanowires (BDD NWs) as an inorganic substrate for matrix-free LDI-MS analysis of small molecules [51]. The diamond nanowires are prepared by reactive ion etching (RIE) with oxygen plasma of highly boron-doped (the boron level is 10^{19} B cm^{-3}) or undoped nanocrystalline diamond substrates. The resulting diamond nanowires are coated with a thin silicon oxide layer that confers a

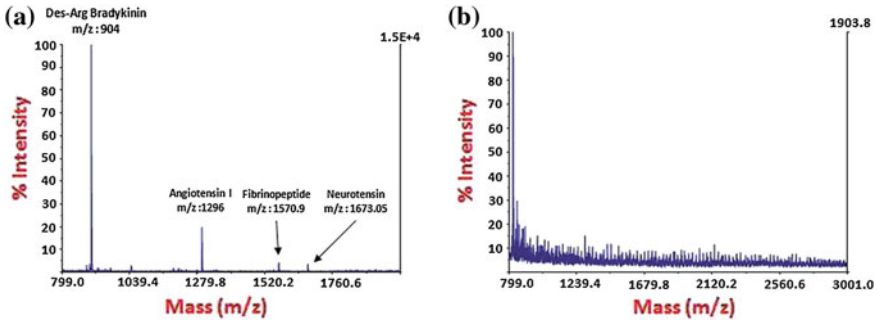

Fig. 5.14 MS spectra obtained for a peptide mixture (50 fmol uL^{-1}) on BDD NWs (**a**) and NcBDD starting material (**b**) substrates. Reproduced from [51]. Copyright 2012, Royal Society of Chemical. **a** Boron-depod diamond nanowires. **b** Boron-doped diamond

superhydrophilic character to the surface. To minimize droplet spreading, the nanowires were chemically functionalized with octadecyltrichlorosilane (OTS) and then UV/ozone treated to reach a final water contact angle of 120°. Figure 5.14a shows the mass spectrum of the peptide mixture obtained on BDD NWs interface. As it can be seen, all peptides have been detected with relatively high signal intensity. As a control, the same experiment was performed on a planar nanocrystalline BDD, i.e., the same interface without any RIE step process etching. The absence of peaks in the MS spectrum (Fig. 5.14b) clearly indicates that the presence of nanostructures on the BDD substrate is mandatory for achieving D/I of biomolecules. The signal to noise (S/N) ratio values obtained on BDD nanowires are 1,078, 431, 55 and 59.3 for [Des-Arg1]-bradykinin, angiotensin I, [Glu1]-fibrinopeptide B, and neurotensin, respectively, whereas those obtained on UDD nanowires are 115, 44, 8.3 and 4.3. We can notice that the S/N ratio values obtained using the UDD NWs are very low in comparison with those of BDD NWs, suggesting that to reach an efficient D/I on diamond, the surface should be nanostructured with a dense layer of wires and display antireflective properties. Boron-doped diamond nanowire substrate was successfully used as an energy absorbing material under UV laser irradiation, allowing D/I of small molecules and their mass spectrometry analysis.

5.4.3 Suspended Single-Crystal Diamond Nanowires (SCD) for High-performance Nano-electromechanical Switches

The current N/MEM switches based on silicon technologies are suffering from problems of stiction, abrasion, and poor mechanical and tribological properties, leading to the poor reliability of the electric contacts [134, 157]. In particular,

silicon-based switches are not able to work under extreme conditions such as high temperature, environments with corrosive chemicals, high-speed/high-power radiofrequency switches, etc. Diamond is the ideal material for high-performance N/MEMS devices due to its outstanding properties such as its extremely high Young's modulus, the highest hardness, hydrophobic surface, low mass density, the highest thermal conductivity, high corrosion resistance upon caustic chemicals, and biocompatibility. However, all the reported diamond N/MEMS devices are based on polycrystalline or nanocrystalline films, which have the disadvantages of the existence of grain boundaries, impurities, and large stress in the films; difficulty in electrical conductivity control; and poor reproducibility [158, 159]. Therefore, N/MEMS devices made from these diamonds suffer from degradation in performance and poor reproducibility.

Liao et al. demonstrate high-performance all-SCD NEM switches by developing a batch fabrication process for suspended SCD nanowires with well-controlled dimensions and by proposing a lateral device concept [30]. The SCD NEMS switches utilize a unique concept of diamond (conductor)-on-diamond (insulator), different from those of silicon-based technology. It is revealed that the SCD NEM switches exhibit no stiction, high controllability, high reproducibility, high-temperature stability above 500 K, and repeated switching. This work not only opens a novel class of NEM switches with all diamond, based on the concept of diamond-on-diamond, but also has an extensive impact on the field of NEMS. The NEM switching devices exhibit extremely low leakage current (<0.1 pA), which provides a high ON/OFF ratio of more than six orders of magnitude. The power consumption of this device in the OFF state is lower than 1 pW, which was calculated from the gate voltage and source leakage current. High Young's modulus of SCD nanowires provides a high lateral resonant frequency for high-speed switching. For example, the lateral fundamental resonant frequency for the cantilever with a width of 400 nm and a length of 5 μm reaches around 50 MHz, corresponding to a maximum switching speed of 20 ns. The speed could be as fast as 3 ns if the cantilever length is reduced to 2 μm. With the steady development of SCD wafer technology, accompanied by cost reduction, the diamond NEM switch may rival Si-NEMS structures. In particular, the resulting switches are powerful under harsh environments due to the all-SCD nature. On the other hand, since no p–n junction is required for NEM switches, the challenge of shallow doping in semiconductor diamond that has remained for decades can be circumvented by using the electromechanically switching approach [160, 161].

5.4.4 Diamond Nanowires for Electrochemical Sensor

BDD electrodes have been consequently used for a wide range of electrochemical applications [6, 133]. In the past years, diamond nanowires was motivated by increasing the surface area of the electrode to achieve higher sensitivity and selectivity, as compared to planar BDD interfaces [162–165].

5.4.4.1 Diamond Nanowires for DNA Sensing

Yang et al. introduced for the first time the electrochemical application of vertically aligned diamond nanowires for DNA sensing. Nanowires separated by approximately 11 nm were selected because anchoring DNA molecules onto these wires will result in a density of DNA of about 10^{12} cm^{-2}, which is promising for DNA sensing with high efficiency [19, 42, 43]. The tips of the nanowires were functionalized electrochemically with phenyl groups. Such functionalized nanowires are used to bond geometrically controlled oligonucleotide molecules to diamond. As DNA self-aligns with the phenyl linker groups, functionalization of the nanowire tips produces a pattern of dispersed DNA bonding governed by the nanowires' structure. Sensitivity curves for DNA hybridization were measured by varying the concentration of complementary target DNA from 1 to 10 pM. Sensing with diamond nanowires is about 100–1,000 times better than with smooth surfaces of Au or polycrystalline diamond. To identify the sensitivity limit exactly, experiments with between 0 and 10 pm of complementary DNA were performed, and the results indicate a sensitivity limit of around 2 pm. No degradation of the DNA on the nanowires was detected over 30 cycles of DNA hybridization/denaturation, which is comparable with the chemical stability of optical DNA biosensors from diamond [5].

5.4.4.2 Diamond Nanowires for Amperometric Glucose Biosensing

Our group [69] reported synthesis of boron-doped diamond nanowires arrays film by hot filament chemical vapor deposition (HFCVD) method using Si nanowires as template. This BDDNF electrode exhibits very attractive electrochemical performance compared to conventional planar boron-doped diamond (BDD) electrodes, notably improved sensitivity and selectivity for biomolecule detection. As shown in Fig. 5.15a, it is clear that the electrochemical response to glucose at the BDDNF electrode is very fast in reaching a dynamic equilibrium upon each addition of the sample solution, generating a steady-state current signal within a short time (less than 20 s). The calibration curve for the electrochemical responses of the BDDNF electrode to glucose at 0.7 V (vs SCE) in the concentration range between 0 and 15 mM is shown in Fig. 5.15b. The response to glucose displays a linear range from 0 to 7 mM with a correlation coefficient (R) of 0.993 and a sensitivity of 8.1 uA mM^{-1} cm^{-2} (slope). The limit of detection was estimated at a signal-to-noise ratio of 3 to be 0.2 ± 0.01 uM. The loss of the electrochemical activity was about 8 % after 150 repetitive cycles, suggesting that the BDDNF electrode is relatively stable owing to its inertness of the H-terminated diamond surface (Fig. 5.15c). Moreover, BDDNF electrode is very favorable for the selective determination of glucose in the presence of AA and UA.

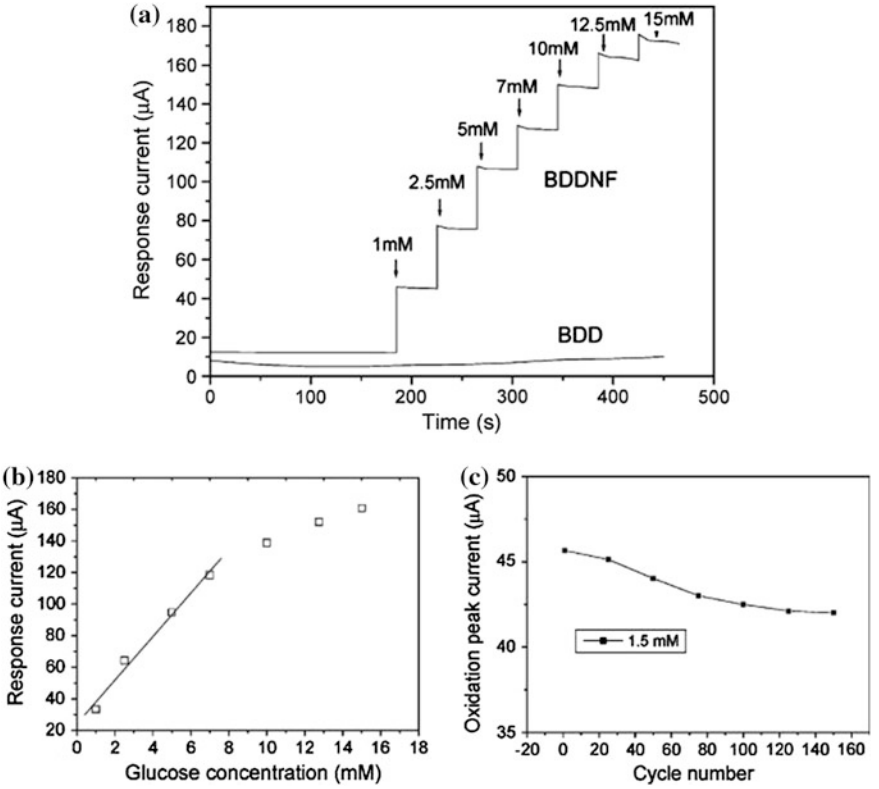

Fig. 5.15 **a** Current time responses of the BDDNF and BDD electrodes to a stirred solution containing 0.1 M NaOH at an applied potential of 0.7 V (vs SCE). **b** Calibration curve of the BDDNF electrode at a working potential of 0.7 V (vs SCE). **c** Long-term electrochemical cycling stability of the BDDNF electrode for 1.5 mM glucose. Reproduced from [69]. Copyright 2009, American Chemical Society

5.4.4.3 Diamond Nanowires for Tryptophan Sensing

Szunerits et al. reported on the fabrication and electrochemical investigation of boron-doped diamond nanowires (BDD NWs) electrodes [50]. The nanowires were obtained directly from highly doped polycrystalline diamond substrates using reactive ion etching (RIE) with oxygen plasma. The interface with the most favorable electrochemical response is investigated for the detection of tryptophan using differential pulse voltammetry. A direct detection of tryptophan using differential pulse voltammetry (DVP) was previously reported on polycrystalline BDD by Zhao et al. [166]. A linear relation between the oxidative peak at $E \approx 1.02$ V/SCE and the concentration of tryptophan was observed with a detection limit being 1×10^{-5} M. In this work, the authors used similar conditions for the

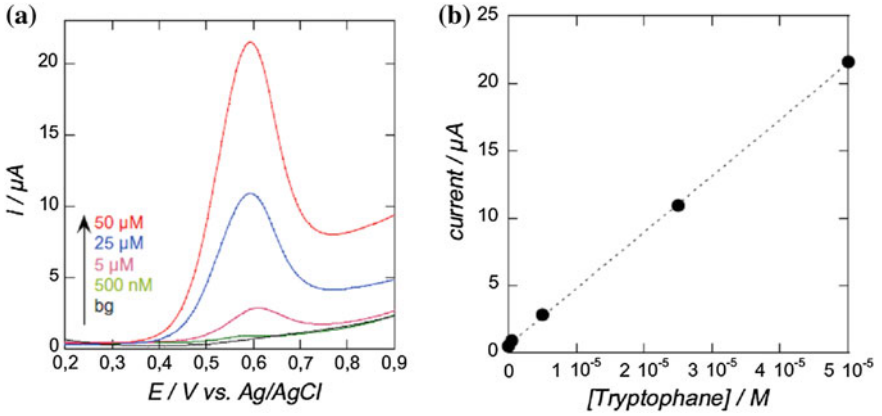

Fig. 5.16 **a** Differential pulse voltammograms of different concentrations of tryptophan (50, 25, 5, 0.5 uM) in Na_2PO_4/NaOH (pH 11) on oxidized BDD NWs; **b** calibration curve. Reproduced from [50]. Copyright 2010, Elsevier

electrochemical detection of tryptophan on oxidized BDD NWs interfaces. As shown in Fig. 5.16, A detection limit of 5×10^{-7} M was obtained on BDD NWs. This is significantly lower than on planar polycrystalline BDD [166], but an order of magnitude higher than reported on glassy carbon electrodes modified with single-walled carbon nanotube films [167].

5.4.4.4 Diamond Nanowires for Dopamine Sensing

Shalini et al. reported *in situ* detection of dopamine using nitrogen incorporated diamond nanowire electrode [87]. DNW films were grown on planar Si substrates using a microwave plasma enhanced chemical vapor deposition (MPECVD) method. The N_2-rich plasma lead to increase in sp^2 graphitic phase and the nanowire-like structure could be responsible for outstanding electrochemical properties, and exhibits a considerable degree of potential on the bio-sensing platform. The N_2-incorporated DNW film electrodes show excellent electrocatalytic activity towards the oxidation of small molecules, such as AA, DA, and UA. The electrochemical behavior of N_2-incorporated conducting DNW films has been studied by CV and DPV in both the absence and presence of AA and UA. The results of DPV show that N_2-incorporated DNW electrodes exhibit highly electro-catalytic activity to the oxidations of AA and UA. High selectivity and reliable antifouling ability may promote the DNW film electrodes to be an effective sensor for direct determination of AA, DA, and UA in a real sample.

5.5 Conclusions and Outlook

Numerous efforts have been directed to develop the various synthetic methods to prepare diamond nanowires, including reactive-ion-etching, plasma post-treatment carbon nanotubes, transfer fullerene to diamond nanowires at high temperature and high pressure, template or catalyst assisted CVD method, and so on. Template-assisted synthesis may be an effective approach for realization of reproducible diamond nanowires due to its unparalleled ability to produce highly controlled nanostructures.

On other hand, simulation and experiments have verified that 1D diamond nanowires possess excellent properties, including mechanical, electron field emission, structural stability, good electrochemical properties and so on. Many practical applications, such as EFE device, high-performance nano-electromechanical switches, and electrochemical biosensor etc., have been exploited. However, the promise of the application of the diamond nanowires has not been fulfilled. For example, despite the impressive progress in the development of BDD-based amperometric biosensors, the promise of the application of these biosensors in real biological systems has not been fulfilled, and there are still many challenges and obstacles related to the achievement of a highly stable and reliable continuous biomolecules monitoring.

Future developments will rely upon large-scale synthesis of diamond nanowires, and the close collaboration of analytical technology, electrochemistry, biological engineering, nanoelectronics and other relative technologies to ensure its effective application. Continued investigation into this area will likely yield many new synthetic approaches and open up larger application space of diamond nanowires.

Acknowledgments The authors appreciate the supports of the International Science and Technology Cooperation Program of China (no. 2013DFG50150), the Natural Foundation of Sciences of the People's Republic of China (Grant no. 21175144, and 20903111) and the Key Project of Beijing Natural Science Foundation (Grant No. 2120002).

References

1. G. Zheng, F. Patolsky, Y. Cui, W.U. Wang, C.M. Lieber, Multiplexed electrical detection of cancer markers with nanowire sensor arrays. Nat. Biotechnol. **23**, 1294–1301 (2005). doi:10.1038/nbt1138
2. Y. Cui, Q.Q. Wei, H. Park, C.M. Lieber, Nanowire nanosensors for highly sensitive and selective detection of biological and chemical species. Science **293**(5533), 1289–1292 (2001). doi:10.1126/science.1062711
3. V.V. Brazhkin, Interparticle interaction in condensed media: some elements are 'more equal than others'. Phys. Usp. **52**(4), 369–376 (2009). doi:10.3367/UFNe.0179.200904e.0393
4. R.F. Davis, *Diamond Films and Coatings* (Noyes Publications, New Jersey, 1992)
5. W. Yang, O. Auciello, J.E. Butler, W. Cai, J.A. Carlisle, J.E. Gerbi, D.M. Gruen, T. Knickerbocker, T.L. Lasseter, J.N. Russell, J. Smith, R.J. Hamers, DNA-modified nanocrystalline diamond thin-films as stable, biologically active substrates. Nat. Mater. **1**, 253–257 (2002). doi:10.1038/nmat779

6. Y. Zhou, J. Zhi, Y. Zou, W. Zhang, S.T. Lee, Direct electrochemistry and electrocatalytic activity of cytochrome c covalently immobilized on a boron-doped nanocrystalline diamond electrode. Anal. Chem. **80**(11), 4141–4146 (2008). doi:10.1021/ac702417x
7. T. Watanabe, T.A. Ivandini, Y. Makide, A. Fujishima, Y. Einaga, Selective detection method derived from a controlled diffusion process at metal-modified diamond electrodes. Anal. Chem. **78**(22), 7857–7860 (2006). doi:10.1021/ac060860j
8. A. Suzuki, T.A. Ivandini, K. Yoshimi, A. Fujishima, G. Oyama, T. Nakazato, N. Hattori, S. Kitazawa, Y. Einaga, Fabrication, characterization, and application of boron-doped diamond microelectrodes for in vivo dopamine detection. Anal. Chem. **79**(22), 8608–8615 (2007). doi:10.1021/ac071519h
9. H. Gu, X.D. Su, K.P. Loh, Electrochemical impedance sensing of DNA hybridization on conducting polymer film-modified diamond. J. Phys. Chem. B **109**(28), 13611–13618 (2005). doi:10.1021/jp050625p
10. W. Yang, J.E. Butler, J.N. Russell, R.J. Hamers, Interfacial electrical properties of DNA-modified diamond thin films: intrinsic response and hybridization-induced field effects. Langmuir **20**(16), 6778–6787 (2004). doi:10.1021/la036460y
11. B. Rezek, D. Shin, C.E. Nebel, Properties of hybridized DNA arrays on single-crystalline undoped and boron-doped (100) diamonds studied by atomic force microscopy in electrolytes. Langmuir **23**(14), 7626–7633 (2007). doi:10.1021/la0636661
12. H. Shiomi, Reactive ion etching of diamond in O-2 and CF4 plasma, and fabrication of porous diamond for field emitter cathodes. Jpn. J. Appl. Phys. **36**(12B, Part 1), 7745–7748 (1997). doi:10.1143/JJAP.36.7745
13. H. Masuda, M. Watanabe, K. Yasui, D. Tryk, T. Rao, A. Fujishima, Fabrication of a nanostructured diamond honeycomb film. Adv. Mater. **12**(6), 444–447 (2000). doi:10.1002/(SICI)1521-4095(200003)12:6<444::AID-ADMA444>3.0.CO;2-K
14. R. Arenal, P. Bruno, D.J. Miller, M. Bleuel, J. Lal, D.M. Gruen, Diamond nanowires and the insulator-metal transition in ultrananocrystalline diamond films. Phys. Rev. B **75**(19), 195431 (2007). doi:10.1103/PhysRevB.75.195431
15. R. Arenal, G. Montagnac, P. Bruno, D.M. Gruen, Multiwavelength Raman spectroscopy of diamond nanowires present in n-type ultrananocrystalline films. Phys. Rev. B **76**(24), 245316 (2007). doi:10.1103/PhysRevB.76.245316
16. Q.X. Liu, C.X. Wang, S.W. Li, J.X. Zhang, G.W. Yang, Nucleation stability of diamond nanowires inside carbon nanotubes: a thermodynamic approach. Carbon **42**(3), 629–633 (2004). doi:10.1016/j.carbon.2003.12.082
17. A.S. Barnard, S.P. Russo, I.K. Snook, Surface structure of cubic diamond nanowires. Surf. Sci. **538**(3), 204–210 (2003). doi:10.1016/S0039-6028(03)00733-7
18. C. Terashima, K. Arihara, S. Okazaki, T. Shichi, D.A. Tryk, T. Shirafuji, N. Saito, O. Takai, A. Fujisima, Fabrication of vertically aligned diamond whiskers from highly boron-doped diamond by oxygen etching. ACS Appl. Mater. Interfaces **3**(2), 177–182 (2011). doi:10.1021/am1007722
19. N. Yang, H. Uetsuka, E. Osawa, C.E. Nebel, Vertically aligned diamond nanowires for DNA sensing. Angew. Chem. Int. Ed. **47**(28), 5183–5185 (2008). doi:10.1002/anie.200801706
20. Y. Ando, Y. Nishibayashi, K. Kobashi, T. Hirao, K. Oura, Smooth and high-rate reactive ion etching of diamond. Diam. Relat. Mater. **11**(3–6), 824–827 (2002). doi:10.1016/S0925-9635(01)00617-3
21. E.S. Baik, Y.J. Baik, S.W. Lee, D. Jeon, Fabrication of diamond nano-whiskers. Thin Solid Films **377–378**, 295–298 (2000). doi:10.1016/S0040-6090(00)01431-0
22. W. Smirnov, A. Kriele, N. Yang, C.E. Nebel, Aligned diamond nano-wires: fabrication and characterisation for advanced applications in bio- and electrochemistry. Diam. Relat. Mater. **19**(2–3), 186–189 (2010). doi:10.1016/j.diamond.2009.09.001
23. N. Yang, W. Smirnov, C.E. Nebel, Three-dimensional electrochemical reactions on tip-coated diamond nanowires with nickel nanoparticles. Electrochem. Commun. **27**, 89–91 (2013). doi:10.1016/j.elecom.2012.10.044

24. L.T. Sun, J.L. Gong, Z.Y. Zhu, D.Z. Zhu, Z.X. Wang, W. Zhang, J.G. Hu, Q.T. Li, Synthesis and characterization of diamond nanowires from carbon nanotubes. Diam. Relat. Mater. **14** (3–7), 749–752 (2005). doi:10.1016/j.diamond.2005.01.025
25. L.T. Sun, J.L. Gong, D.Z. Zhu, Z.Y. Zhu, S.X. He, Diamond nanorods from carbon naotubes. Adv. Mater. **16**(20), 1849–1853 (2004). doi:10.1002/adma.200400429
26. N. Dubrovinskaia, L. Dubrovinsky, Aggregated diamond nanorods, the densest and least compressible form of carbon. Appl. Phys. Lett. **87**(8), 083106 (2005). doi:10.1063/1.2034101
27. C.H. Hsu, S.G. Cloutier, S. Palefsky, J. Xu, Synthesis of diamond nanowires using atmospheric-pressure chemical vapor deposition. Nano Lett. **10**(9), 3272–3276 (2010). doi:10.1021/nl100616x
28. G.S. Oehrlein, Reactive-ion etching. Phys. Today **39**(10), 26–33 (1986). doi:10.1063/1.881066
29. C.Y. Li, A. Hatta, Preparation of diamond whiskers using Ar/O_2 plasma etching. Diam. Relat. Mater. **14**(11–12), 1780–1783 (2005). doi:10.1016/j.diamond.2005.09.031
30. M.Y. Liao, S. Hishita, E. Watanabe, S. Koizumi, Y. Koide, Suspended single-crystal diamond nanowires for high-performance nanoelectromechanical switches. Adv. Mater. **22** (47), 5393–5397 (2010). doi:10.1002/adma.201003074
31. Y. Tzeng, J. Wei, J.T. Woo, W. Lanford, Free-standing single-crystalline chemical vapor deposited diamond films. Appl. Phys. Lett. **63**(16), 2216–2218 (1993). doi:10.1063/1.110531
32. E.S. Baik, Y.J. Baik, D. Jeon, Aligned diamond nanowhiskers. J. Mater. Res. **15**(4), 923–926 (2000). doi:10.1557/JMR.2000.0131
33. Y.S. Zou, T. Yang, W.J. Zhang, Y.M. Chong, B. He, I. Bello, S.T. Lee, Fabrication of diamond nanopillars and their arrays. Appl. Phys. Lett. **92**(5), 053105 (2008). doi:10.1063/1.2841822
34. W. Smirnov, A. Kriele, R. Hoffmann, E. Sillero, J. Hees, O.A. Williams, N. Yang, C. Kranz, C.E. Nebel, Diamond-modified AFM probes: from diamond nanowires to atomic force microscopy-integrated boron-doped diamond electrodes. Anal. Chem. **83**(12), 4936–4941 (2011). doi:10.1021/ac200659e
35. W. Janssen, E. Gheeraert, Dry etching of diamond nanowires using self-organized metal droplet masks. Diam. Relat. Mater. **20**(3), 389–394 (2011). doi:10.1016/j.diamond.2011.01.037
36. S. Okuyama, S.I. Matsushita, A. Fujishima, Preparation of periodic microstructured diamond surfaces. Chem. Lett. **20**(5), 534–535 (2000). doi:10.1246/cl.2000.534
37. S. Okuyama, S.I. Matsushita, A. Fujishima, Periodic submicrocylinder diamond surfaces using two-dimensional fine particle arrays. Langmuir **18**(22), 8282–8287 (2002). doi:10.1021/la011107i
38. M. Yamaki, J. Higo, K. Nagayama, Size-dependent separation of colloidal particles in 2-dimensional convective self-assembly. Langmuir **11**(8), 2975–2978 (1995). doi:10.1021/la00008a021
39. C.D. Dushkin, P.A. Kralchevsky, V.N. Paunov, H. Yoshimura, K. Nagayama, Torsion balance for measurement of capillary immersion forces. Langmuir **12**(3), 641–651 (1996). doi:10.1021/la950560p
40. B.J.M. Hausmann, M. Khan, Y. Zhang, T.M. Babinec, K. Martinick, M. McCutcheon, P.R. Hemmer, M. Loncar, Fabrication of diamond nanowires for quantum information processing applications. Diam. Relat. Mater. **19**(5–6), 621–629 (2010). doi:10.1016/j.diamond.2010.01.011
41. N. Yang, H. Uetsuka, E. Osawa, C.E. Nebel, Vertically aligned nanowires from boron-doped diamond. Nano Lett. **8**(11), 3572–3576 (2008). doi:10.1021/nl801136h
42. N. Yang, H. Uetsuka, C.E. Nebel, Biofunctionalization of vertically aligned diamond nanowires. Adv. Funct. Mater. **19**(6), 887–893 (2009). doi:10.1002/adfm.200801392
43. N. Yang, H. Uetsuka, O.A. Williams, E. Osawa, N. Tokuda, C.E. Nebel, Vertically aligned diamond nanowires: fabrication, characterization, and application for DNA sensing. Phys. Status Solidi A **206**(9), 2048–2056 (2009). doi:10.1002/pssa.200982222
44. N. Tokuda, H. Umezawa, T. Saito, K. Yamabe, H. Okushi, S. Yamasaki, Surface roughening of diamond (001) films during homoepitaxial growth in heavy boron doping. Diam. Relat. Mater. **16**(4–7), 767–770 (2007). doi:10.1016/j.diamond.2006.12.024

45. A. Kruger, F. Kataoka, M. Ozawa, T. Fujino, Y. Suzuki, A.E. Aleksenskii, A.Y. Vul, E. Osawa, Unusually tight aggregation in detonation nanodiamond: identification and disintegration. Carbon **43**(8), 1722–1730 (2005). doi:10.1016/j.carbon.2005.02.020
46. O.A. Williams, O. Douheret, M. Daenen, K. Haenen, E. Osawa, M. Takahashi, Enhanced diamond nucleation on monodispersed nanocrystalline diamond. Chem. Phys. Lett. **445** (4–6), 255–258 (2007). doi:10.1016/j.cplett.2007.07.091
47. O.A. Williams, M. Daenen, D.J. Haen, K. Haenen, J. Maes, V.V. Moshchalkov, M. Nesladek, D.M. Gruen, Comparison of the growth and properties of ultrananocrystalline diamond and nanocrystalline diamond. Diam. Relat. Mater. **15**(4–8), 654–658 (2006). doi:10.1016/j.diamond.2005.12.009
48. M. Wei, C. Terashima, M. Lv, A. Fujishima, Z.Z. Gu, Boron-doped diamond nanograss array for electrochemical sensors. Chem. Commun. **24**(24), 3624–3626 (2009). doi:10.1039/b903284c
49. P. Subramanian, Y. Coffinier, D. Steinmuller-Nethl, J. Foord, R. Boukherroub, S. Szunerits, Diamond nanowires decorated with metallic nanoparticles: a novel electrical interface for the immobilization of histidinylated biomolecules. Electrochim. Acta **110**, 4–8 (2013). doi:10.1016/j.electacta.2012.11.010
50. S. Szunerits, Y. Coffinier, E. Galopin, J. Brenner, R. Boukherroub, Preparation of boron-doped diamond nanowires and their application for sensitive electrochemical detection of tryptophan. Electrochem. Commun. **12**(3), 438–441 (2010). doi:10.1016/j.elecom.2010.01.014
51. Y. Coffinier, S. Szunerits, H. Drobecq, M. Oleg, R. Boukherroub, Diamond nanowires for highly sensitive matrix-free mass spectrometry analysis of small molecules. Nanoscale **4**(1), 231–238 (2012). doi:10.1039/c1nr11274k
52. L. Marcon, A. Addad, Y. Coffinier, R. Boukherroub, Cell micropatterning on superhydrophobic diamond nanowires. Acta Biomater. **9**(1), 4585–4591 (2013). doi:10.1016/j.actbio.2012.08.026
53. Y. Coffinier, E. Galopin, S. Szunerits, R. Boukherroub, Preparation of superhydrophobic and oleophobic diamond nanograss arrays. J. Mater. Chem. **20**(47), 10671–10675 (2010). doi:10.1039/c0jm01296c
54. P.S. Shah, T. Hanrath, K.P. Johnston, S.A. Korgel, Nanocrystal and nanowire synthesis and dispersibility in supercritical fluids. J. Phys. Chem. B **108**(28), 9574–9587 (2004). doi:10.1021/jp049827w
55. Y. Wu, P. Yang, Direct observation of vapor–liquid–solid nanowire growth. J. Am. Chem. Soc. **123**(13), 3165–3166 (2001). doi:10.1021/ja0059084
56. S. Kodambaka, J. Tersoff, M.C. Reuter, F.M. Ross, Germanium nanowire growth below the eutectic temperature. Science **316**(5825), 729–732 (2007). doi:10.1126/science.1139105
57. J.L. Lensch-Falk, E.R. Hemesath, D.E. Perea, L.J. Lauhon, Alternative catalysts for VSS growth of silicon and germanium nanowires. J. Mater. Chem. **19**(7), 849–857 (2009). doi:10.1039/b817391e
58. Y. Xia, P. Yang, Y. Sun, Y. Wu, B. Mayers, B. Gates, Y. Yin, F. Kim, H. Yan, One-dimensional nanostructures: synthesis, characterization, and applications. Adv. Mater. **15**(5), 353–389 (2003). doi:10.1002/adma.200390087
59. H. Ringsdorf, B. Schlarb, J. Verzmer, Molecular architecture and function of polymeric oriented systems-models for the study of organization, surface recognition, and dynamics of biomembranes. Angew. Chem. Int. Ed. **27**(1), 113–158 (1988). doi:10.1002/anie.198801131
60. C.N.R. Rao, A. Govindaraj, F.L. Deepak, N.A. Gunari, M. Nath, Surfactant-assisted synthesis of semiconductor nanotubes and nanowires. Appl. Phys. Lett. **78**(13), 1853–1855 (2001). doi:10.1063/1.1359145
61. Y. Yin, Y. Lu, Y. Sun, Y. Xia, Silver nanowires can be directly coated with amorphous silica to generate well-controlled coaxial nanocables of silver/silica. Nano Lett. **2**(4), 427–430 (2002). doi:10.1021/nl025508+
62. P.W. May, CVD diamond: a new technology for future. Endeavour **19**(3), 101–106 (1995). doi:10.1016/0160-9327(95)97494-S
63. S.S. Lee, O. Takai, H. Itoh, Uniform coating of CVD diamond on metallic wire substrates. J. Mater. Sci. **32**(9), 2417–2422 (1997). doi:10.1023/A:1018513425533

64. G. Chollon, R. Naslain, C. Prentice, R. Shatwell, P. May, High temperature properties of SiC and diamond CVD-monofilaments. J. Eur. Ceram. Soc. **25**(11), 1929–1942 (2005). doi:10.1016/j.jeurceramsoc.2004.06.013
65. V. Baranauskas, H.J. Ceragioli, A.C. Peterlevitz, A.F. Durrant, Development of tubes of micro-crystalline diamond and diamond-like carbon. Thin Solid Film **398**, 250–254 (2001). doi:10.1016/S0040-6090(01)01441-9
66. M.K. Singh, E. Titus, J.C. Madaleno, G. Cabral, J. Gracio, Novel two-step method for synthesis of high-density nanocrystalline diamond fibers. Chem. Mater. **20**(5), 1725–1732 (2008). doi:10.1021/cm0714741
67. M.K. Singh, E. Titus, M.G. Willinger, J.C. Madaleno, J. Gracio, Microstructure and electron field emission study of diamond nanorod decorated a-SiO_2 nanowires by microwave Ar–CH_4/H_2 plasma chemical vapor deposition with addition of N_2. Diam. Relat. Mater. **18** (5–8), 865–869 (2009). doi:10.1016/j.diamond.2009.02.021
68. J.C. Madaleno, M.K. Singh, E. Titus, G. Cabral, J. Gracio, Electron field emission from patterned nanocrystalline diamond coated a-SiO_2 micrometer-tip arrays. Appl. Phys. Lett. **92** (2), 023113 (2008). doi:10.1063/1.2835905
69. D. Luo, L. Wu, J. Zhi, Fabrication of boron-doped diamond nanorod forest electrodes and their application in nonenzymatic amperometric glucose biosensing. ACS Nano **8**(8), 2121–2128 (2009). doi:10.1021/nn9003154
70. D. Luo, L. Wu, J. Zhi, 2-D dimensional micro-network for boron-doped diamond film: fabrication and electrochemical sensing application. Chem. Commun. **46**(35), 6488–6490 (2010). doi:10.1039/c0cc01511c
71. K. Peng, Y.J. Yan, S.P. Gao, J. Zhu, Synthesis of large-area silicon nanowire arrays via self-assembling nanoelectrochemistry. Adv. Mater. **14**(16), 1164–1167 (2002). doi:10.1002/1521-4095(20020816)14:16<1164::AIDADMA1164>3.0.CO;2-E
72. C.G. Granqvist, A. Andersson, O. Hundri, Spectrally selective surfaces of Ni-pigmented anodic Al_2O_3. Appl. Phys. Lett. **35**(3), 268–270 (1979). doi:10.1063/1.91078
73. C.A. Huber, T.E. Huber, M. Sadoqi, J.A. Lubin, S. Mannlis, C.B. Prater, Nanowire array composites. Science **263**(5148), 800–802 (1994). doi:10.1126/science.263.5148.800
74. H. Masuda, T. Yanagishita, K. Yasui, K. Nishio, I. Yagi, T.N. Rao, A. Fujishima, Synthesis of well-aligned diamond nanocylinders. Adv. Mater. **13**(4), 247–249 (2001). doi:10.1002/1521-4095(200102)13:4<247::AIDADMA247>3.0.CO;2-H
75. F. Keller, M.S. Hunter, D.L. Robinson, Structural features of oxide coatings on aluminium. J. Electrochem. Soc. **100**(9), 411–419 (1953). doi:10.1149/1.2781142
76. H. Masuda, K. Fukuda, Ordered metal nanohole arrays made by a two-step replication of honeycomb structures of anodic alumina. Science **268**(5216), 1466–1468 (1995). doi:10.1126/science.268.5216.1466
77. I.I. Vlasov, O.I. Lebedev, V.G. Ralchenko, E. Goovaerts, G. Bertoni, G.V. Tendeloo, V.I. Konov, Hybrid diamond-graphite nanowires produced by microwave plasma chemical vapor deposition. Adv. Mater. **19**(22), 4058–4062 (2007). doi:10.1002/adma.200700442
78. I.I. Vlasov, V.G. Ralchenko, E. Goovaerts, A.V. Saveliev, M.V. Kanzyuba, Bulk and surface-enhanced Raman spectroscopy of nitrogen-doped ultrananocrystalline diamond films. Phys. Status Solidi A **203**(12), 3028–3035 (2006). doi:10.1002/pssa.200671119
79. D.M. Gruen, Nanocrystalline diamond films. Annu. Rev. Mater. Sci. **29**, 211–259 (1999). doi:10.1146/annurev.matsci.29.1.211
80. J.A. Nuth, Small-particle physics and interstellar diamonds. Nature **329**(6140), 589 (1987). doi:10.1038/329589b0
81. P. Badziag, W.S. Verwoerd, W.P. Ellis, N.R. Greiner, Nano-sized diamond are more stable than graphite. Nature **343**(6255), 244–245 (1990). doi:10.1038/343244a0
82. A.S. Barnard, I.K. Snook, Phase stability of nanocarbon in one dimension: nanotubes versus diamond nanowires. J. Chem. Phys. **120**(8), 3817–3821 (2004). doi:10.1063/1.1643354
83. A.S. Barnard, S.P. Russo, I.K. Snook, Ab initio modeling of diamond nanowire structures. Nano Lett. **3**(10), 1323–1328 (2003). doi:10.1021/nl034169x

84. N. Shang, P. Papakonstantinou, P. Wang, A. Zakharov, U. Palnitkar, I.N. Lin, M. Chu, A. Stamboulis, Self-assembled growth, microstructure, and field-emission high-performance of ultrathin diamond nanorods. ACS Nano **3**(4), 1032–1038 (2009). doi:10.1021/nn900167p
85. A.R. Sobia, S. Adnan, A. Mukhtiar, A.A. Khurram, A.A. Turab, A. Awais, A. Naveed, Q.J. Faisal, H. Javaid, G.J. Yu, Effect of nitrogen addition on hydrogen incorporation in diamond nanorod thin films. Curr. Appl. Phys. **12**(3), 712–717 (2012). doi:10.1016/j.cap.2011.10.008
86. J. Shalini, Y.C. Lin, T.H. Chang, K.J. Sankaran, H.C. Chen, C.Y. Lee, N.H. Tai, Ultra-nanocrystalline diamond nanowires with enhanced electrochemical properties. Electrochim. Acta **92**, 9–19 (2013). doi:10.1016/j.electacta.2012.12.078
87. J. Shalini, K.J. Sankaran, C.L. Dong, C.Y. Lee, N.H. Tai, I.N. Lin, In situ detection of dopamine using nitrogen incorporated diamond nanowire electrode. Nanoscale **5**(3), 1159–1167 (2013). doi:10.1039/c2nr32939e
88. L.Y. Zeng, H.Y. Peng, W.B. Wang, Y.Q. Chen, D. Lei, W. Qi, J.Q. Liang, J.L. Zhao, X.G. Kong, H. Zhang, Nanocrystalline diamond films deposited by the hot cathode direct current plasma chemical vapor deposition method with different compositions of CH4/Ar/H-2 gas mixture. J. Phys. Chem. C **112**(5), 1401–1406 (2008). doi:10.1021/jp710082n
89. L.Y. Zeng, H.Y. Peng, W.B. Wang, Y.Q. Chen, D. Lei, W. Qi, J.Q. Liang, J.L. Zhao, X.G. Kong, H. Zhang, Synthesis and characterization of diamond microcrystals and nanorods deposited by hot cathode direct current plasma chemical vapor deposition method. J. Phys. Chem. C **112**(15), 6160–6164 (2008). doi:10.1021/jp7109912
90. F.P. Bundy, H.T. Hall, H.M. Strong, R.H. Wentorf, Man-made diamonds. Nature **176**(4471), 51–55 (1955). doi:10.1038/176051a0
91. B.V. Derjaguin, D.V. Fedoseev, Synthetic diamond whiskers. Prog. Surf. Sci. **45**(1–4), 65–65 (1994). doi:10.1016/0079-6816(94)90033-7
92. W.R.L. Lambrecht, C.H. Lee, B. Segall, J.C. Angus, Z.D. Li, M. Sunkara, Diamond nucleation by hydrogenation of the edges of graphitic precursors. Nature **364**(6430), 607–610 (1993). doi:10.1038/364607a0
93. A. Gross, Hydrogen dissociation on metal surfaces—a model system for reactions on surfaces. Appl. Phys. A Mater. Sci. Process. **67**(6), 627–635 (1998). doi:10.1007/s003390050834
94. H.F. Berger, E. Grosslinger, K.D. Rendulic, Coupling of vibrational and translational energy in the adsorption of H2 on FE(100)—state-resolved sticking coefficients. Surf. Sci. **261**(1–3), 313–320 (1992). doi:10.1016/0039-6028(92)90242-X
95. C.H. Hsu, J. Xu, Diamond nanowire—a challenge from extremes. Nanoscale **4**(17), 5293–5299 (2012). doi:10.1039/c2nr31260c
96. J.H. Zhang, B.Q. Wei, J. Liang, Z.D. Gao, D.H. Wu, Synthesis of diamond from buckytubes by laser and quenching treatment. Mater. Lett. **31**(1–2), 79–82 (1997). doi:10.1016/S0167-577X(96)00239-X
97. Y.Q. Hou, D.M. Zhuang, G. Zhang, M.S. Wu, J.J. Liu, Preparation of diamond films by hot filament chemical vapor deposition and nucleation by carbon nanotubes. Appl. Surf. Sci. **185**(3–4), 303–308 (2002). doi:10.1016/S0169-4332(01)00988-6
98. Y.Q. Zhu, T. Sekine, T. Kobayashi, T. Takazawa, M. Terrones, H. Terrones, Collapsing carbon nanotubes and diamond formation under shock waves. Chem. Phys. Lett. **287**(5–6), 689–693 (1998). doi:10.1016/S0009-2614(98)00226-7
99. B.Q. Wei, J. Liang, Z.D. Gao, J.H. Zhang, Y.Q. Zhu, Y.B. Li, D.H. Wu, The transformation of fullerenes into diamond under different processing conditions. J. Mater. Process. Technol. **63**(1–3), 573–578 (1997). doi:10.1016/S0924-0136(96)02686-6
100. L.M. Cao, C.X. Gao, H.P. Sun, G.T. Zou, Z. Zhang, X.Y. Zhang, M. He, M. Zhang, Y.C. Li, J. Zhang, D.Y. Dai, L.L. Sun, W.K. Wang, Synthesis of diamond from carbon nanotubes under high pressure and high temperature. Carbon **39**(2), 311–314 (2001). doi:10.1016/S0008-6223(00)00243-8
101. H. Yusa, Nanocrystalline diamond directly transformed from carbon nanotubes under high pressure. Diam. Relat. Mater. **11**(1), 87–91 (2002). doi:10.1016/S0925-9635(01)00532-5
102. B. Wei, J. Zhang, J. Liang, D. Wu, The mechanism of phase transformation from carbon nanotube to diamond. Carbon **36**(7–8), 997–1001 (1998). doi:10.1016/S0008-6223(97)00232-7

103. L.T. Sun, J.L. Gong, Z.Y. Zhu, D.Z. Zhu, S.X. He, Nanocrystalline diamond from carbon nanotubes. Appl. Phys. Lett. **84**(15), 2901–2903 (2004). doi:10.1063/1.1704856
104. J. Singh, Nucleation and growth-mechanism of diamond during hot-filament chemical-vapor-deposition. J. Mater. Sci. **29**(10), 2761–2766 (1994). doi:10.1007/BF00356830
105. N. Dubrovinskaia, L. Dubrovinsky, F. Langenhorst, S. Jacobsen, C. Liebske, Nanocrystalline diamond synthesized from C_{60}. Diam. Relat. Mater. **14**(1), 16–22 (2005). doi:10.1016/j.diamond.2004.06.017
106. J. Voskuhl, M. Waller, S. Bandaru, B.A. Tkachenko, C. Fregonese, B. Wibbeling, P.R. Schreiner, B.J. Ravoo, Nanodiamonds in sugar rings: an experimental and theoretical investigation of cyclodextrin-nanodiamond inclusion complexes. Org. Biomol. Chem. **10** (23), 4524–4530 (2012). doi:10.1039/c2ob06915f
107. J. Zhang, Y. Feng, H. Ishiwata, Y. Miyata, R. Kitaura, J.E.P. Dahl, R.M.K. Carlson, H. Shinohara, D. Tomanek, Synthesis and transformation of linear adamantane assemblies inside carbon nanotubes. ACS Nano **6**(10), 8674–8683 (2012). doi:10.1021/nn303461q
108. D.A. Britz, A.N. Khlobystov, K. Porfyrakis, A. Ardavan, G.A.D. Briggs, Chemical reactions inside single-walled carbon nano test-tubes. Chem. Commun. **1**, 37–39 (2005). doi:10.1039/b414247k
109. J. Zhang, Y. Miyata, R. Kitaura, H. Shinohara, Preferential synthesis and isolation of (6,5) single-wall nanotubes from one-dimensional C-60 coalescence. Nanoscale **3**(10), 4190–4194 (2011). doi:10.1039/c1nr10602c
110. J. Zhang, Z. Zhu, Y.Q. Feng, H. Ishiwata, Y. Miyata, R. Kitaura, J.E.P. Dahl, R.M.K. Carlson, N.A. Fokina, P.R. Schreiner, Evidence of diamond nanowires formed inside carbon nanotubes from diamantine dicarboxylic acid. Angew. Chem. Int. Ed. **52**(13), 3717–3721 (2013). doi:10.1002/anie.201209192
111. G.C. McIntosh, M. Yoon, S. Berber, D. Tomanek, Diamond fragments as building blocks of functional nanostructures. Phys. Rev. B **70**(4), 045401 (2004). doi:10.1103/PhysRevB.70.045401
112. W. Piekarczyk, How and why CVD diamond is formed: a solution of the thermodynamic paradox. J. Mater. Sci. **33**(13), 3443–3453 (1998). doi:10.1023/A:1013214220026
113. O.A. Shenderova, V.V. Zhirnov, D.W. Brenner, Carbon nanostructures. Crit. Rev. Solid State Mater. Sci. **27**(3–4), 227–356 (2002). doi:10.1080/10408430208500497
114. J.T. Tanskanen, M. Linnolahti, A.J. Karttunen, T.A. Pakkanen, From fulleranes and icosahedral diamondoids to polyicosahedral nanowires: structural, electronic, and mechanical characteristics. J. Phys. Chem. C **112**(30), 11122–11129 (2008). doi:10.1021/jp7119262
115. F.L. Liu, Theoretical study on the coplanar double-cage dodecahedrane C35H30. Phys. Chem. Chem. Phys. **6**(5), 906–909 (2004). doi:10.1039/b312175e
116. F.L. Liu, L. Peng, J.X. Zhao, S.Q. Wang, Theoretical study of two C50H40 isomers with three dodecahedrane cages sharing two pentagons. Int. J. Quantum Chem. **103**(2), 167–175 (2005). doi:10.1002/qua.20499
117. A.S. Barnard, S.P. Russo, I.K. Snook, From nanodiamond to diamond nanowires: structural properties affected by dimension. Philos. Mag. **84**(9), 899–907 (2004). doi:10.1080/14786430310001627412
118. O.A. Shenderova, D.W. Brenner, R.S. Ruoff, Would diamond nanorods be stronger than fullerene nanotubes? Nano Lett. **3**(6), 805–809 (2003). doi:10.1021/nl025949t
119. J.N. Coleman, U. Khan, W.J. Blau, Y.K. Gun'ko, Small but strong: a review of the mechanical properties of carbon nanotube-polymer composites. Carbon **44**(9), 1624–1652 (2006). doi:10.1016/j.carbon.2006.02.038
120. J. Guo, B. Wen, R. Melnik, S. Yao, T. Li, Molecular dynamics study on diamond nanowires mechanical properties: strain rate, temperature and size dependent effects. Diam. Relat. Mater. **20**(4), 551–555 (2011). doi:10.1016/j.diamond.2011.02.016
121. F. Occelli, P. Loubeyre, R. Letoullec, Properties of diamond under hydrostatic pressures up to 140 GPa. Nat. Mater. **2**, 151–154 (2003). doi:10.1038/nmat831
122. T. Yamanaka, S. Morimoto, H. Kanda, Influence of the isotope ratio on the lattice-constant of diamond. Phys. Rev. B **49**(14), 9341–9343 (1994). doi:10.1103/PhysRevB.49.9341

123. H. Cynn, J.E. Klepeis, C.S. Yoo, D.A. Young, Osmium has the lowest experimentally determined compressibility. Phys. Rev. Lett. **88**(13), 135701 (2002). doi:10.1103/PhysRevLett.88.135701
124. H. Peelaers, B. Partoens, F.M. Peeters, Phonon band structure of Si nanowires: a stability analysis. Nano Lett. **9**(1), 107–111 (2009). doi:10.1021/nl802613p
125. H. Peelaers, B. Partoens, F.M. Peeters, Phonons in Ge nanowires. Appl. Phys. Lett. **95**(12), 122110 (2009). doi:10.1063/1.3236526
126. A. Trejo, A. Miranda, L. Rivera, A. Diaz-mendez, M. Cruz-Irisson, Phonon optical modes and electronic properties in diamond nanowires. Micoelectron. Eng. **90**, 92–95 (2012). doi:10.1016/j.mee.2011.04.052
127. K.W. Sun, J.Y. Wang, T.Y. Ko, Raman spectroscopy of single nanodiamond: phonon-confinement effects. Appl. Phys. Lett. **92**(15), 153115 (2008). doi:10.1063/1.2912029
128. C.W. Padgett, D.W. Brenner, Influence of chemisorption on the thermal conductivity of single-wall carbon nanotubes. Nano Lett. **4**(6), 1051–1053 (2004). DOI:10.1021/nl049645d
129. N.V. Novikov, A.P. Podoba, S.V. Shmegera, A. Witek, A.M. Zaitsev, A.B. Denisenko, W.R. Fahmer, M. Werner, Influence of isotopic content on diamond thermal conductivity. Diam. Relat. Mater. **8**(8–9), 1602–1606 (1999). doi:10.1016/S0925-9635(99)00040-0
130. J.F. Moreland, J.B. Freund, G. Chen, The disparate thermal conductivity of carbon nanotubes and diamond nanowires studied by atomistic simulation. Microscale Thermophys. Eng. **8**(1), 61–69 (2004). doi:10.1080/10893950490272939
131. C.W. Padgett, O. Shenderova, D.W. Brenner, Thermal conductivity of diamond nanorods: molecular simulation and scaling relations. Nano Lett. **6**(8), 1827–1831 (2006). doi:10.1021/nl060588t
132. J. Guo, B. Wen, R. Melnik, S. Yao, T. Li, Geometry and temperature dependent thermal conductivity of diamond nanowires: a non-equilibrium molecular dynamics study. Physica E **43**(1), 155–160 (2010). doi:10.1016/j.physe.2010.06.032
133. R.L. McCreery, Advanced carbon electrode materials for molecular electrochemistry. Chem. Rev. **108**(7), 2646–2687 (2008). doi:10.1021/cr068076m
134. A. Socoliuc, Atomic-scale control of friction by actuation of nanometer-sized contacts. Science **313**(5784), 207–210 (2006). doi:10.1126/science.1125874
135. W. Wu, L. Bai, X. Liu, Z. Tang, Z. Gu, Nanograss array boron-doped diamond electrode for enhanced electron transfer from *Shewanella loihica* PV-4. Electrochem. Commun. **13**(8), 872–874 (2011). doi:10.1016/j.elecom.2011.05.025
136. M. Lv, M. Wei, F. Rong, C. Terashima, A. Fujishima, Z. Gu, Electrochemical detection of catechol based on as-grown and nanograss array boron-doped diamond electrodes. Electroanalysis **22**(2), 199–203 (2010). doi:10.1002/elan.200900296
137. Y. Yang, J. Oh, Y. Kim, C. Terashima, A. Fujishima, J. Kim, H. Kim, Enhanced electrogenerated chemiluminescence of a rutheniumtris(2,2')bipyridyl/tripropylamine system on a boron-doped diamond nanograss array. Chem. Commun. **46**(31), 5793–5795 (2010). doi:10.1039/c0cc00773k
138. N. Yang, R. Hoffmann, W. Smirnov, A. Kriele, C.E. Nebel, Direct electrochemistry of cytochrome c on nanotextured diamond surface. Electrochem. Commun. **12**(9), 1218–1221 (2010). doi:10.1016/j.elecom.2010.06.023
139. F.J. Himpsel, J.A. Knapp, J.A. Vanvechten, D.E. Eastman, Quantum photoyield of diamond (111)—stable negative-affinity emitter. Phys. Rev. B **20**(2), 624–627 (1979). doi:10.1103/PhysRevB.20.624
140. B.J. Cui, J. Ristein, L. Ley, Electron affinity of the bare and hydrogen covered single crystal diamond (111) surface. Phys. Rev. Lett. **81**(2), 429–432 (1998). doi:10.1103/PhysRevLett.81.429
141. T. Ito, M. Nishimura, M. Yokoyama, M. Irie, C.L. Wang, Highly efficient electron emitting diode fabricated with single-crystalline diamond. Diam. Relat. Mater. **9**(9–10), 1561–1568 (2000). doi:10.1016/S0925-9635(00)00293-4
142. I.L. Krainsky, V.M. Asnin, G.T. Mearini, J.A. Dayton, Negative-electron-affinity effect on the surface of chemical-vapor-deposited diamond polycrystalline films. Phys. Rev. B **53**(12), R7650–R7653 (1996)

143. Y.K. Chang, H.H. Hsieh, W.F. Pong, M.H. Tsai, F.Z. Chien, P.K. Tseng, L.C. Chen, T.Y. Wang, K.H. Chen, D.M. Bhusari, J.R. Yang, S.T. Lin, Quantum confinement effect in diamond nanocrystals studied by X-ray-absorption spectroscopy. Phys. Rev. Lett. **82**(26), 5377–5380 (1999). doi:10.1103/PhysRevLett.82.5377
144. N. Jiang, K. Eguchi, S. Noguchi, T. Inaoka, Y. Shintani, Structural characteristics and field electron emission properties of nano-diamond/carbon films. J. Cryst. Growth **236**(4), 577–582 (2002). doi:10.1016/S0022-0248(01)02219-9
145. S. Gupta, B.L. Weiss, B.R. Weiner, G. Morell, Electron field emission from sulfur-incorporated nanocrystalline carbon thin films. Appl. Phys. Lett. **79**(21), 3446–3448 (2001). doi:10.1063/1.1411988
146. L. Gan, E. Baskin, C. Saguy, R. Kalish, Quantization of 2D hole gas in conductive hydrogenated diamond surfaces observed by electron field emission. Phys. Rev. Lett. **96**(19), 196808 (2006). doi:10.1103/PhysRevLett.96.196808
147. K.J. Sankaran, Y.F. Lin, W.B. Jian, H.C. Chen, K. Panda, B. Sundaravel, C.L. Dong, N.H. Tai, I.N. Lin, Structural and electrical properties of conducting diamond nanowires. ACS Appl. Mater. Interfaces **5**(4), 1294–1301 (2013). doi:10.1021/am302430p
148. W. Zhu, G.P. Kochanski, S. Jin, Low-field electron emission from undoped nanostructured diamond. Science **282**(5393), 1471–1473 (1998). doi:10.1126/science.282.5393.1471
149. D. Pradhan, I.N. Lin, Grain-size-dependent diamond-nondiamond composite films: characterization and field-emission properties. ACS Appl. Mater. Interfaces **1**(7), 1444–1450 (2009). doi:10.1021/am9001327
150. J.P. Thomas, H.C. Chen, N.H. Tai, I.N. Lin, Freestanding ultrananocrystalline diamond films with homojunction insulating layer on conducting layer and their high electron field emission properties. ACS Appl. Mater. Interfaces **3**(10), 4007–4013 (2011). doi:10.1021/am200867c
151. Q.H. Wang, A.A. Setlur, J.M. Lauerhaas, J.Y. Dai, E.W. Seeling, R.P.H. Chang, A nanotube-based field-emission flat panel display. Appl. Phys. Lett. **72**(22), 2912–2913 (1998). doi:10.1063/1.121493
152. M. Shiraishi, M. Ata, Work function of carbon nanotubes. Carbon **39**(12), 1913–1917 (2001). doi:10.1016/S0008-6223(00)00322-5
153. Z. Xu, X.D. Bai, E.G. Wang, Z.l Wang, Field emission of individual carbon nanotube with in situ tip image and real work function. Appl. Phys. Lett. **87**(16), 163106 (2005). doi:10.1063/1.2103420
154. R.C. Smith, S.R.P. Silva, Interpretation of the field enhancement factor for electron emission from carbon nanotubes. J. Appl. Phys. **106**(1), 014314 (2009). doi:10.1063/1.3149803
155. A. Mayer, N.M. Miskovsky, P.H. Cutler, Photon-stimulated field emission from semiconducting (10,0) and metallic (5,5) carbon nanotubes. Phys. Rev. B **65**(19), 195416 (2002). doi:10.1103/PhysRevB.65.195416
156. M. Najam-ul-Haq, M. Rainer, C.W. Huck, P. Hausberger, H. Kraushaar, G.K. Bonn, Nanostructured diamond-like carbon on digital versatile disc as a matrix-free target for laser desorption/ionization mass spectrometry. Anal. Chem. **80**(19), 7467–7472 (2008). doi:10.1021/ac801190e
157. J.M. Kim, J.H. Park, C.W. Baek, Y.K. Kim, The SiOG-based single-crystalline silicon (SCS) RF MEMS switch with uniform characteristics. J. Microelectromech. Syst. **13**(6), 1036–1042 (2004). doi:10.1109/JMEMS.2004.838365
158. M. Adamschik, J. Kuserer, P. Schmid, K.B. Schad, D. Grobe, E. Kohn, Diamond microwave micro relay. Diam. Relat. Mater. **11**(3–6), 672–676 (2002). doi:10.1016/S0925-9635(01)00619-7
159. V.P. Adiga, A.V. Sumant, S. Suresh, C. Gudeman, O. Auiello, J.A. Carlisle, R.W. Carpick, Mechanical stiffness and dissipation in ultrananocrystalline diamond microresonators. Phys. Rev. B **79**(24), 245403 (2009). doi:10.1103/PhysRevB.79.245403
160. S. Koizumi, K. Watanabe, M. Hasegawa, H. Kanda, Ultraviolet emission from a diamond pn junction. Science **292**(5523), 1899–1901 (2001). doi:10.1126/science.1060258

161. H. EI-Hajj, A. Denisenko, A. Kaiser, R.S. Balmer, E. Kohn, Diamond MISFET based on boron delta-doped channel. Diam. Relat. Mater. **17**(7–10), 1259–1263 (2008). doi:10.1016/j.diamond.2008.02.015
162. S. Szunerits, R. Boukherroub, Different strategies for functionalization of diamond surfaces. J. Solid State Electrochem. **12**(10), 1205–1218 (2008). doi:10.1007/s10008-007-0473-3
163. G. Carpini, F. Lucarelli, G. Marrazza, M. Mascini, Oligonucleotide-modified screen-printed gold electrodes for enzyme-amplified sensing of nucleic acids. Biosens. Bioelectron. **20**(2), 167–175 (2004). doi:10.1016/j.bios.2004.02.021
164. O. Paenke, A. Kirbs, F. Lisdat, Voltammetric detection of single base-pair mismatches and quantification of label-free target ssDNA using. Biosens. Bioelectron. **22**(11), 2656–2662 (2007). doi:10.1016/j.bios.2006.10.033
165. H. Aoki, H. Tao, Gene sensors based on peptide nucleic acid (PNA) probes: relationship between sensor sensitivity and probe/target duplex stability. Analyst **130**(11), 1478–1482 (2005). doi:10.1039/b507121f
166. G. Zhao, Y. Qi, Y. Tian, Simultaneous and direct determination of tryptophan and tyrosine at boron-doped diamond electrode. Electroanalysis **18**(8), 830–834 (2006). doi:10.1002/elan.200503455
167. W. Huang, G. Mai, Y. Liu, C. Yang, W. Qua, Voltammetric determination of tryptophan at a single-wall carbon nanotubes modified electrode. J. Nanosci. Nanotechnol. **4**(4), 423–427 (2004). doi:10.1166/jnn.2004.122

Chapter 6
Nanoparticle-Based Diamond Electrodes

Geoffrey W. Nelson and John S. Foord

Abstract This chapter reviews the construction, modification, and physical characteristics of two types of diamond electrodes: nanoparticle-modified diamond electrodes (NMDE) and detonation nanodiamond-based electrodes (DNDE). These particular types of diamond electrodes show great promise for improving the performance of diamond electrodes via the incorporation of nano-scale chemistry at their surfaces. The construction of both types of electrodes are reviewed, along with the resultant physical and electronic effects. The methods reviewed here are particularly applicable for electroanalytic and electrocatalytic applications of nanoparticle-based diamond electrodes. A brief review of progress on the interactions between metals and diamond at nanoparticle-based electrodes is also included. Finally, an outline of the present state-of-the art research in this field is presented.

6.1 Introduction

Carbon based materials have the potential to be an important class of materials for 21st century technologies. One particular carbon-based material has rather extreme properties—diamond. For several decades now, researchers have been excited by its transparency, extreme hardness, high thermal conductivity, bio-compatibility, and chemical resistance [1]. Examples of its utility abound. For instance, diamond is made conductive when doped, thus creating an useful electronic material. In this form, diamond can be used in biosensors, electroanalytical devices, and as a catalytic support in fuel cells [1–4]. At the cutting-edge of diamond research are efforts to investigate how nitrogen vacancies in diamond could be crucial to a functioning quantum computing device [5, 6]. The present interest in diamond remains high, as exemplified by the many reviews that describe the historical development, properties, and synthesis of this unique functional material [1, 7–12].

G.W. Nelson · J.S. Foord (✉)
Department of Chemistry, Oxford University, Oxford OX1 3TA, UK
e-mail: john.foord@chem.ox.ac.uk

N. Yang (ed.), *Novel Aspects of Diamond*, Topics in Applied Physics 121,
DOI 10.1007/978-3-319-09834-0_6

There exist many types of diamond, both natural and synthetic. However, it is the conductive forms of diamond which shows the most promise as a functional material. Conductive diamond is counter-intuitive, as diamond is usually considered an insulator. However, when doped to a 1:1,000 ratio of an intentionally added impurity (e.g. B or N), diamond can become a wide band-gap semiconductor [1]. In 1986, Fujimori et al. [13] were the first to develop a polycrystalline conductive diamond film using chemical vapour deposition (CVD) and boron-doping. Since then, boron-doped diamond (BDD) has become a commercially important material (i.e. Element Six, U.K.) and his heavily used for electrochemical applications.

The p-type semiconducting properties of BDD have desirable electrochemical properties, such as its low signal to background current ratio, wide potential window, robust nature, chemical resistance, and bio-compatibility [1]. BDD also does not suffer from extensive surface corrosion, oxide formation, or have unwanted electrical interactions with deposited catalyst, thus making it a useful substrate for fundamental chemical studies of electrocatalysis [10]. Its most unfavourable trait is its relative lack of electroactivity, compared to other carbon-based materials [14]. This is due to a reduced surface concentration of the following: sp^2 carbon, delocalised electrons, and oxygenated species. These characteristics reduce its electroactivity towards several chemical reactions of industrial and biological importance, such as the methanol oxidation reaction (MOR), oxygen reduction reaction (ORR), and neurotransmitter redox reactions. Thus, to make a practical diamond-based device, some modification of the diamond surface or structure is needed.

Many of the physical, wet chemical, and electrochemical routes leading to improved electrical properties are well-reviewed by others [4, 11, 14–16]. Of the many possible modifications, the incorporation of nano-scale chemistry to the surfaces and structure of diamond is of tremendous recent interest. The two most interesting research pathways are the nanoparticle modification of diamond, and the use of unmodified or modified diamond nanoparticles. An example of each type of substrate and their modification is shown in Figs. 6.1 and 6.2.

Diamond could be modified by a film of metal or metal oxide, but this is an expensive process. It is also a process which does not benefit from the well-known catalytic properties of nano-particulate metals and metal oxides. For instance, bulk gold is relatively inert, but in nanoparticle form it is highly catalytic towards certain redox reactions, such as the ORR [17]. The properties of BDE make it an effective and stable support for these NPs. The modification of BDE with metal and metal oxide NPs has been recently reviewed by Toghill and Compton [14]. In their review, they detail how BDE electrochemistry is enhanced by the high surface area, improved reactivity, and zero-overlap of diffusion zones, thereby ensuring maximum mass transfer of analytes or molecules to the surface [14]. The adsorption of reactants is different at nano-sized particles, compared to their macro-sized counterparts [18]. Also, the exploitation of quantum effects to enhance electrochemical reactions is possible on nanoparticles-based electrodes [18]. Consensus suggests that sub-monolayer coverage of nano-sized metals or metal oxides are effective catalysts for energy conversion and fuel cell applications.

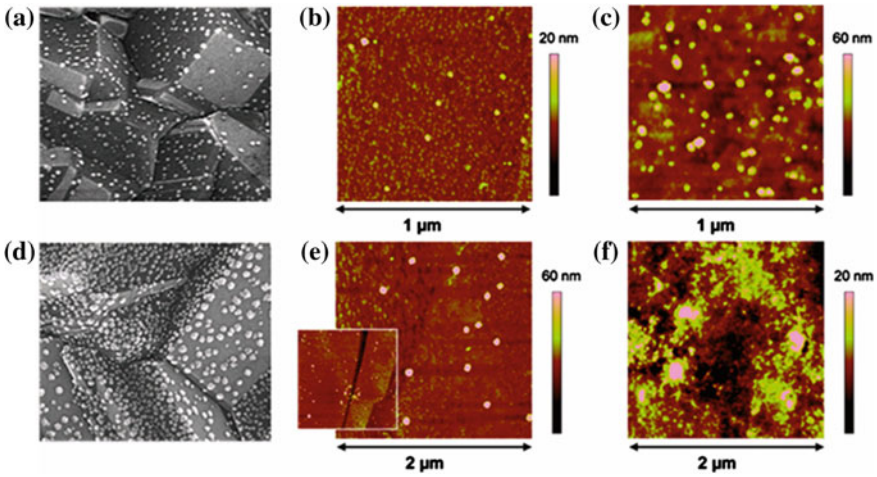

Fig. 6.1 SEM and AFM images of nanoparticles on boron-doped electrodes: SEM of BDD electrodes with Au nanoparticles after potentiostatic deposition at −0.4 V for **a** 10 s and **d** 60 s. AFM (tapping mode) of boron-doped diamond electrodes with $Ni(OH)_2$ after potentiostatic deposition in which $Ni(OH)_2$ was electro-precipitated onto polycrystalline boron-doped diamond electrode for **b** 1 s, **c** 15 s, **e** 30 s, and **f** 100 s. SEM images from Yamada et al. [218], with permission from Elsevier (Copyright © 2008); AFM images reprinted with permission from [56], Copyright (2011) American Chemical Society

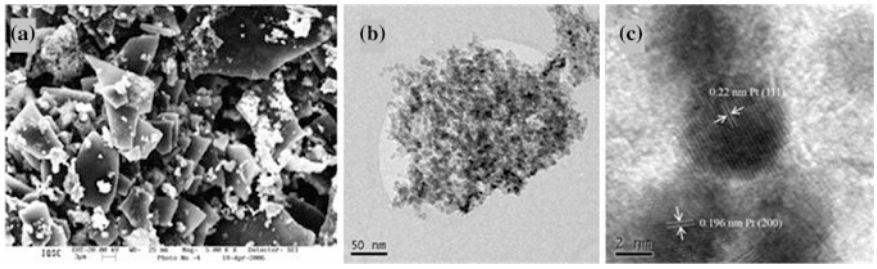

Fig. 6.2 Images of detonation nanodiamond particles decorated with nanoparticles: **a** SEM image of detonation nanodiamond powder surface decorated with Pt-RuO_x deposited by the sol-gel method; TEM (**b**) and HRTEM (**c**) images of DND powder decorated with Pt via microwave-heating of ethylene glycol solutions containing H_2PtCl_6 and the detonation nanodiamond particles. Figure adapted from Giancarlo et al. [67], with permission from Elsevier (Copyright © 2006) and from Bian et al. [150], with permission from the International Journal of Electrochemical Science (Copyright © 2012)

Alternatively, diamond can be made nano-sized via detonation of explosives in oxygen-rich environments. Unlike its bulk counterpart, detonation nanodiamond (DND) is electroactive in its undoped form. This remarkable property is due its "giant" surface area, coupled with a surface chemistry rich in reactive oxygen species, sp^2 carbon, unsaturated carbon bonds, and delocalised electrons [19]. The redox

behaviour of ND has been found to be "molecule-like", with the reduction and oxidation of the surface occurring at discrete electrochemical potentials [19]. This relatively novel material is now used in advanced sensor and catalytical technologies. Further information can be found in reviews by Holt [5] and others [20].

While there exist reviews on the topics of nanoparticle-modified diamond electrodes (NMDE) [14] and DND-based electrodes (DNDE) [5, 11, 20], there are no reviews detailing the progress made for their construction. If one wishes to optimize the effects of nano-scale chemistry at diamond-based devices, it is clear from the literature that the conditions of construction have a tremendous effect on their physical and electrical properties. Thus, a review of the key considerations required to create practical diamond electrodes is warranted.

Discussion will revolve around the use of these electrodes for electroanalysis and electrocatalysis. These are the two most popular applications for boron-doped diamond electrodes (BDE). Non-electronic or electrochemical applications will not be discussed here; however, the methods discussed are applicable to the creation of nano-composite materials in which diamond enhances their physical properties (e.g. improved durability, coating technologies).

Of the many means to modify BDE, only those concerning the construction of NMDE and DNDE will be discussed. These two types of modification have found wide application in the fields of electroanalysis and electrocatalysis. The methods used to construct them have a variety of chemical and physical consequences, which need to be discussed in detail. Finally, we will briefly outline the present state-of-the-art research concerning NMDE and DNDE.

6.2 Metal and Metal Oxide Nanoparticle Coated Diamond Electrodes

6.2.1 Choice of Material

Metals, metal alloys and metal oxides have all been used in electroanalytical and electrocatalytical applications [14], as summarized by Table 6.1 and seen in Fig. 6.1, in the case of $Ni(OH)_2$ and Pt deposition. Common reasons for choosing a particular material include: chemical aim, chemical environment, compatibility with deposition method, stability, and cost.

The chemical aim is the most important parameter. Metals, metal oxides, and alloys/composites are useful in a variety of chemical systems, as listed in Table 6.1. Notably, Au and Pt are popular materials due to their versatility and catalytic properties. Metal oxides are useful in photocatalytic applications and as alternatives to bimetallic alloys in direct methanol oxidation fuel cells [21]. Bimetallic alloys have advantages compared to their single metal counterparts, whereby metal-metal interactions (e.g. bifunctional mechanism, metal back-bonding) can increase reaction rates and decrease poisoning of reaction sites of a single metal catalyst (see Pt-based alloys in Table 6.1) [22–24]. Chemical aims may require other

Table 6.1 Materials, methods, and applications of nanoparticles on BDE

Material	Method	References	Applications
Metals			
Pt	Spontaneous wet chemical	[57]	H_2O_2 evolution, alcohol oxidation, electroanalysis (arsenite, enzymes), ORR. fuel cell technologies
	Wet chemical assisted	[35]	
	Potential step	[31, 105, 219]	
	CV/potential cycling	[36, 54, 76]	
	Multi-step electrodeposition	[76]	
	Potentiostatic	[31, 36, 43, 105]	
	Microemulsion	[101]	
	Sputtering/ion impact	[40, 63, 64]	
	Thermal salt decomposition	[105]	
	Electrochemical deposition		
	Linear potential sweep	[54]	
	Galvanostatic	[104]	
	Pulsed galvanostatic	[44]	
	Sol-Gel	[68, 69]	
Sb	Potentiostatic	[220]	Electroanalysis of heavy metals
Bi	Potentiostatic	[95]	Electroanalysis of heavy metals
Co	Potentiostatic	[79]	H_2O oxidation catalyst
	Photoreduction	[221]	
Ni	Potentiostatic	[110]	Alcohol oxidation, biosensing
	Metal implantation	[65, 66]	
Fe	Potentiostatic	[222]	H_2O_2 detection, electroanalysis
Pb	Potentiostatic	[83]	Electroanalysis of heavy metals
Ir	Metal implantation	[64]	Arsenic detection
Ag	Spontaneous deposition	[57]	Perchlorate oxidation, biosensing
Cu	Spontaneous deposition	[57]	Nitrate detection, biosensing, H_2O_2 detection, CO_2 reduction
	Potentiostatic Wet-chemical	[37] [181]	
	Potentiostatic cooulometry	[38]	
	Metal implantation	[65]	

(continued)

Table 6.1 (continued)

Material	Method	References	Applications
Au	Spontaneous deposition	[57]	Biosensing (proteins, neurotransmitters), ORR catalysis, arsenite detection
	Thermal salt decomposition	[219]	
	Sputtering	[61, 75]	
	Potentiostatic	[55]	
	Self-assembly	[27]	See end of first column
	Linear sweep voltammetry	[77]	
	Electro-aggregation	[223]	
Pd	Spontaneous deposition	[57]	Proton detection, hydrazine detection, ORR catalysis, neurotransmitter detection, C=C and C–C bond hydrogenation catalyst
	Potentiostatic	[50]	
Bimetallic			
Pt/Sn	Microemulsion	[74]	Alcohol oxidation, pollutant degradation
Pt-Ru	Microemulsion	[101, 102]	Alcohol oxidation for fuel cell technologies
	Potential cycling	[54]	
	Sequential and Simultaneous electro-deposition	[34]	
Pt–Au	Sputtering and potentiostatic	[60]	ORR
Metal Oxides			
Pt-RuO_x	Sol-gel	[33, 67]	MOR catalysis, fuel cell technologies
Pt-PrO_x	Multi-step potentiostatic with electrogeneration of oxide	[3]	MOR catalysis, fuel cell technologies
IrO_2	Thermal salt decomposition	[219]	H_2O_2 detection, pH sensors
	Potential pulsing	[58]	
	Potential cycling	[58]	
	Galvanostatic	[58]	
TiO_2	Wet chemical adsorption	[111]	Solar cell technologies, H_2 evolution, detection of maleic acid, Ni^{2+}, cytochrome c, drinking water purification

(continued)

Table 6.1 (continued)

Material	Method	References	Applications
RuO_x	Sol-gel /electrostatic	[88]	Cl evolution, H_2 evolution
FeO_x	Sol-gel	[88]	Oxidation of OH^- to O_2
$Ni(OH)_2$	Electrogeneration of OH at Ni particles	[56]	Glucose, MeOH and EtOH oxidation
PbO_x	Electro-deposition with power ultrasound	[107]	Ethylene glycol oxidation
Composites			
Pt-Nafion	Microemulsion with Nafion	[102]	Biosensing
Pt-Dendrimer	Dendrimer encapsulation	[219]	Biosensing
Pt-electropolymers	Electro-deposition/ polymerization	[28, 224]	Biosensing (proteins, neurotransmitters)

considerations. For instance, multi-step reactions may require more than one type of nanoparticle, or the presence of a specific facet, shape or set of interfaces to be present [25, 26]. The chemical effects or compatibility with stabilizers (e.g. Nafion), conductive, and bio-compatible coatings (e.g. SAMs on Au) also need to be considered [27–30].

The chemical environment to which the electrode is exposed will dictate the type of nanoparticles to be deposited. A crucial consideration is the use of toxic metals (e.g. Pb, Ag) on an electrode to be used in biological environments. It may be better to use a non-toxic metal, such as gold. The environment of fuel cells and batteries can be either acidic or alkaline. The dissolution of metal nanoparticles in acids makes their use in the former environment challenging. Metal oxides are an alternative material, due to their increased stability in those harsh environments. For biological applications, metal nanoparticles need to be modified with known organo-metallic chemistry to render it more bio-inert and/or stable at the surface (e.g. SAMs on Au, Ag).

The material must be compatible with the chosen deposition route. For instance, metal nanoparticles are easily deposited using various electrochemical methods. However, the deposition of metal oxides or alloys require more complex methods, such as: multi-step electrochemical routes and sol-gel based methods [14]. The deposition of metal oxides can occur by physical vapour deposition (PVD), with recent advances promising to enable the deposition of core-shell metal oxides onto surfaces (i.e. Mantis Deposition Ltd.).

Ideally, electrodes should be functional more than once. Therefore, the resultant NP-modification must be stable, both physically and chemically. Some nanoparticles, such as platinum, are known to have weak adhesion to diamond, thus motivating the search for their increased stability at BDE [31, 32]. Stability is of utmost

importance in biological environments, where NPs are known to have inflammatory properties in solution. The instability of metals can be resolved by using alternative metal oxides, as exemplified by the replacement of Ti, Ta, Ti-Pd alloys on carbon-based electrodes by RuO_2 for electrocatalysis and chlorine evolution [33].

The cost of materials can be high, particularly those with the best catalytic versatility and performance (e.g. Pt, Au). Although these materials have been shown to be electroactive at extremely low loading rates (i.e. sub-monolayer), any further reduction in cost, without sacrificing performance is attractive [14]. Many strategies are used, including the use of cheaper materials (e.g. Ni, Pb, Sn, Fe, Cu, Co) and the metal oxides [14], as outlined in Table 6.1. It is clear from this table that these alternatives can be used for the same reactions as those of Pt and Au. The use of an alternative material may offer superior performance, or reduce costs by increasing nanoparticle stability and longevity.

6.2.2 Methods of Deposition

Ideally, nanoparticles should be deposited in a chemically active form, having small size, uniform distribution, and low mass loading (<10 % of surface coverage); these characteristics are associated with the best performing electrochemical and catalytic diamond-based electrodes [14, 34]. The deposition method chosen is paramount to achieving these results. The deposition methods in Table 6.1 can be generally categorized by whether they utilise electrochemistry or not. These two general approaches are discussed in this section.

6.2.2.1 Electrochemical Methods

Electrodeposition, in its various forms, is the most popular route towards metal nanoparticle deposition. These methods share a common feature, with metal cations from the appropriate salt (e.g. H_2PtCl_6) being reduced at the diamond electrode by some applied potential (e.g. Fig. 6.1b) [14]. The deposition is further controlled by the choice of electrochemical method, the deposition time, deposition potential, metal ion concentration, scan rate, and number of deposition phases/stages [14]. The advantages and disadvantages of popular electro-deposition methods are described here.

The potentiostatic method is most popular technique. This is certainly clear from Table 6.1 and noted elsewhere [14]. Simply, it involves the exposure of the electrode to a metal salt solution, followed by deposition at a fixed potential [14]. The deposition conditions, such as applied potential, duration, and metal salt concentration are easily tuned. For instance, it is accepted that deposition time is proportional to mass loading for most nanoparticles [35–39]. An example of this phenomenon is demonstrated by comparing Fig. 6.1a, d in the case of Pt deposition on BDE. The method has disadvantages. As noted in several reports, potentiostatic deposition leads to poor

particle adhesion, large particle size (cf. Fig. 6.1a, d), low mass loading, and inhomogeneous distribution; all these characteristics could result in an impractical diamond electrode, despite decent electrocatalytic performance [32, 40–42].

Changing the electrochemical method is often a useful strategy. Potential step deposition methods, such as cyclic voltammetry (CV), linear sweep voltammetry (LSV), potentiostatic step deposition (PSD), chronoamperometry, and galvanostatic methods have all been used to control Pt deposition on diamond (see Table 6.1). The first three alternatives lead to more uniform size and distribution of Cu and Pt nanoparticles [35–39]. CV and LSV are slow techniques, but Welch et al. [38] have noted that slowly increasing or decreasing the potential during deposition offers better control over nanoparticle nucleation, growth, and mass loading. Chronoamperometry has the advantage of promoting high mass loading of Au particles via enhanced mass transfer effects initiated by its use [42, 43]. Galvanostatic and pulsed galvanostatic methods favour the growth of individual Pt particles, as these methods minimize the overlap of reactant depletion zones [44]; lower pulse times and higher applied currents lead to lower particle size and denser distribution [32, 44, 45].

Multi-step and/or multi-technique deposition is a successful means to minimizing the disadvantages of any single method. The Foord group has shown that the combination of potentiostatic and potentiostatic step deposition enables particles to grow by both instantaneous and progressive nucleation stages [3]. Also, potentiostatic deposition followed by LSV increases and homogenizes particle size [37]. Combining electrodeposition with electropolymerization of a polymeric stabilizer (e.g. Nafion) or conductive polymer (e.g. polyaniline) is an effective route towards stabilizing nanoparticles on the diamond surface [46–48].

Deposition Conditions

The conditions at which deposition occur are extremely important. The most important of which is that the potential applied to facilitate deposition must be sufficient to drive the reduction of metal cations at the electrode [14]. The most systematic studies have been conducted by the Compton group, notably their work on Cu [38, 49], Pt, Pd [50, 51], Ag [49], Au [49], Ir [52] and other metals, as reviewed here [14]. Vinokur et al. [53] demonstrated that the nucleation of Ag and Hg on BDE depends on overpotential. The appropriate applied potential(s) can provide a higher driving force for the deposition reaction, with the consequences of higher nanoparticle nucleation rates, higher nanoparticle densities, and smaller sizes [14, 41].

Caution and thought must be employed when choosing the applied potential(s). Depositing at potentials near that of H_2 or O_2 evolution is problematic, as gas bubbles can dislodge freshly deposited nanoparticles [41]. Also, the potential can have desirable or undesirable *chemical* effects, such as H_2 cleansing of Pt nanoparticles [41], the co-deposition of bimetallic alloys [54], the pre-concentration of other ions at the interface (e.g. OH^-, H^+) [3], or the stripping of nanoparticles from the electrode [38]. In addition, the choice of potential has been found to affect the

shape of Au [55], Cu [37], and Pt [34] nanoparticles. Examples of these effects can be seen by comparing Fig. 6.3a, c, as well as Fig. 6.3e, f pairwise. In the first pair, it is clear that applied potential can affect shape, while in the second pair shows that applied potential can affect particle size. For the deposition of metal oxides via an electrochemical route, the choice of deposition potential is essential for the deposition of the nanoparticle *and* the electro-precipitation of the oxide, due to local pH changes at the nanoparticle surface during deposition [3, 56]. This can result in the deposition of nanoparticles with controllable size and morphology compared to sol-gel routes. An example of this electro-deposition is shown in Fig. 6.1a, for the case of $Ni(OH)_2$.

Other controllable conditions include the length of deposition, the scan rate, the nature of the deposition solution. The length of deposition is generally proportional to mass loading [3, 32] and is known to influence the morphology of deposition, with longer times exploited to great larger particle sizes [32]. In the case of CV, multiple scans can homogenize the size of nanoparticles, but not the particle

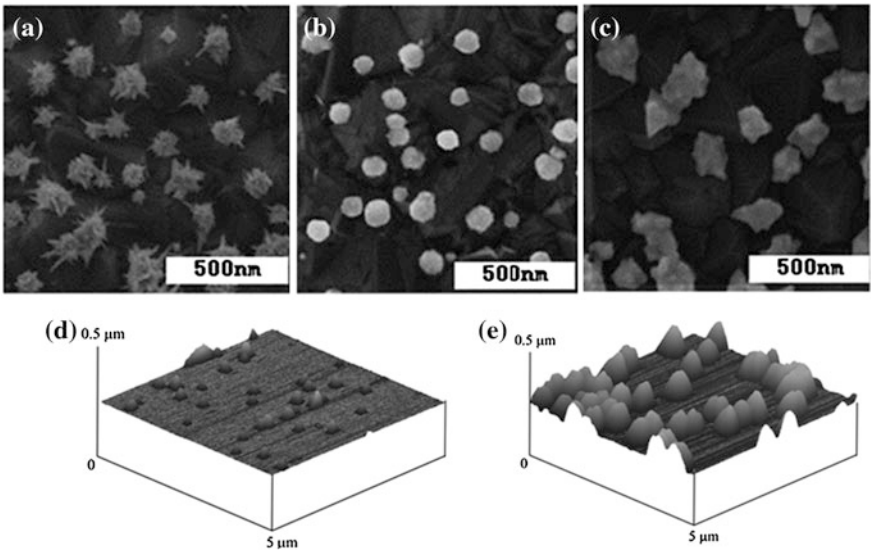

Fig. 6.3 Images of nanoparticles on diamond with electrodeposition influenced by applied potential or concentration of metal salt in solution. (*Top row*) SEM images of gold nanoparticles electrodeposited on boron-doped diamond surfaces: **a** Flower-like Au nanoparticles deposited at +0.5 V versus Ag/AgCl in 0.2 M H_2SO_4 solution containing 2 mM $HAuCl_4$; **b** Spherical nano-gold deposited at +0.5 V versus Ag/AgCl in 0.2 M H_2SO_4 solution containing 0.2 mM $HAuCl_4$; **c** Convex polyhedron nano-gold prepared in same conditions as A, except at an applied potential of −0.1 V versus Ag/AgCl. (*Bottom Row*) In situ tapping mode AFM images of cobalt grown on a BDD surface from 10 mm Co(II) at potentials of **e** −1.05 V and **f** −1.15 V. Reprinted from Li et al. [55] with permission from Elsevier (Copyright © 2006). Reprinted from Simm et al. [79] with permission from Wiely-VCH (Copyright © 2006 WILEY-VCH Verlag GmbH & Co. KGaA, Weinheim)

distribution [38]. Adjustment of the scan rate has been shown to promote facet selective deposition of Pt on polycrystalline diamond [39]. At higher sweep rates, particles preferred to deposit on the (111) facet, as dramatically shown in Fig. 6.4. The sweep rate also affected shape and distribution, with the (111) facet having more numerous and smaller particles than the (110) facet. Oxygenated surface moieties are thought to concentrate on (111) facets. As mentioned in other sections, the presence of oxygen functionality increases nanoparticle stability, nucleation, and diamond is more electroactive in such regions [39].

The nature of the solution in which electrodeposition occurs is an important consideration. The concentration of metal ions in solutions seems to affect the nucleation pathway of Ag and Hg deposition [53]. In addition, concentration affects nanoparticle shape. This is shown in Fig. 6.3, where a 10-fold dilution of $HAuCl_4$ leads to spherical deposition, compared to "flower-like" shape at higher concentrations (see Fig. 6.3a, b) [55]. Adjusting concentration can have unusual effects. For instance, the density of electrodeposited Ag nanoparticles is inversely proportional to size, except at very dilute concentrations of the metal salt [57]. Other adjustments to the type of solution and pH can be made. Additionally, the pH of the solution [27, 58] or local pH at the interface [3, 59] can affect electrodeposition. The latter has been discussed in the previous section for the case of metal oxide deposition.

6.2.2.2 Non-electrochemical Methods

Non-electrochemical methods are used less frequently. They are often complex and require advanced equipment, unavailable in most laboratories. Two of the more common techniques are briefly discussed here.

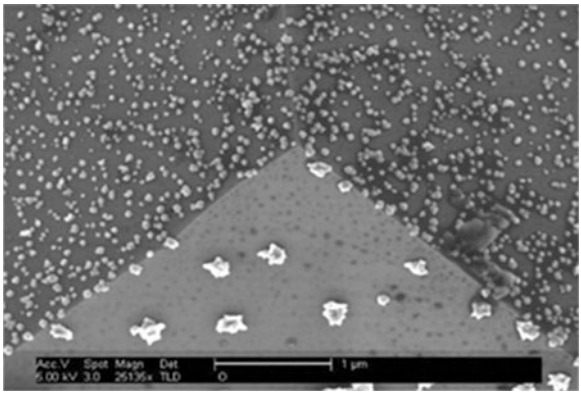

Fig. 6.4 Scanning electron microscopy image of Pt nanoparticles on boron-doped diamond deposited with potential cycling from −0.8 V to +1.6 versus Ag/AgCl in 0.5 M H_2SO_4 at a sweep rate of 500 mV/s. The (111) facet edge is clearly visible. Reprinted with permission from Gonzalez-Gonzalez et al. [21], Copyright (2009) American Chemical Society

Physical vapour deposition techniques, such as ion impact and sputtering depositions are effective in vacuo methods for depositing nanoparticles on diamond. Both techniques vaporise metal from a source, but the former accelerates the ions by 800 keV towards the sample, rather than merely coating the surface by physical deposition [14]. Often, these techniques are used to modify CVD diamond films during their creation. For instance, DC magnetron sputtering was used by the Swain group to create Pt-sandwich electrodes, in which a Pt layer was sputtered between two CVD grown layers, halfway through the CVD process [40]. Bimetallic deposition is possible if two or more metal sources are in the vacuum chamber. Uniform nanoparticle distribution is often the result of using a PVD method, as nanoparticle deposition is relatively unaffected by the inhomogeneous distribution of boron at BDE or by grain boundaries [42]. Heat treatment post-PVD deposition may be necessary, as in the case of Au nanoparticles [60–62]. When conducting ion implantation, the modified BDD must be heated by high temperature in the presence of ambient H_2 not necessarily to modify the structure of deposited nanoparticles, but to recover metastable diamond structures produced by the ion bombardment itself [63–66]. By far the greatest advantage of PVD methods is that the ultra-high vacuum conditions reduce unwanted physio-chemical effects (i.e. oxidation, water) on nanoparticles due to solution or ambient conditions. Widespread use of PVD techniques is not possible, due to the cost and complexity of the UHV systems required.

The sol gel method is a popular means to deposit metal oxide nanoparticles on a diamond surface [14, 67–69]. Generally, a metal precursor is stabilized as a colloid in ethanol, or 2 propanol, and then coated onto the electrode by dip-coating, spin-coating, or as a paste. Afterwards, a thermal heat treatment is sufficient to ensure nanoparticle formation having the proper structure. For example, anatase TiO_2 has been deposited onto diamond via this route at thermal heat treatment at 400 °C [70]. While the sol-gel method typically leads to random and uniform distribution of nanoparticles on diamond, it suffers from the disadvantages of large particle sizes and particle aggregation. This is exemplified by the image of Fig. 6.2a, in the case of nanoparticle deposition on diamond nanoparticles. A recently developed alternative to the sol-gel method is the aforementioned electro-precipitation of the oxide, either during a single step [56] or as a coating for pre-deposited nanoparticles [3]. Results suggest that this method offers better control of nanoparticle deposition via electrochemical parameters, the effects of which are discussed in some detail later. Some of the state-of-the-art wet-chemical deposition routes are discussed in Sect. 6.5.

6.2.2.3 Substrate

Thus far, conductive diamond has been referred to simply as BDE. In actual fact, BDE are categorized by the method of their creation and by their crystallinity. More detail than will be described here concerning the manufacturing of BDE can be found in several reviews [1, 4, 9, 71, 72]. The chemical vapour deposition (CVD)

method is most commonly used, and this has several consequences for the deposition of metal and metal oxide nanoparticles on diamond substrates.

CVD diamond is made by ionizing hydrogen and methane with a thermal or microwave source. The ions re-combine on a substrate—often silicon—to form a sp^3 carbon network. Boron doping can be introduced to the diamond film by having a source of boron in vapour form during the CVD process. This manufacture process can be adjusted to make a wide variety of diamond substrates, with different distributions of B doping and crystallinity. The substrate does not affect the nanoparticle growth or distribution tremendously when non-electrochemical methods are used to deposit nanoparticles. Therefore, subsequent discussion concerns itself with the affect substrate has on the electro-deposition of nanoparticles.

Metal nanoparticle nucleation occurs at the most electroactive sites on a diamond surface, such as boron centres, grain boundaries, and defects [14]. Thus, the distribution of B and the dimensions of surface crystals are important factors to be considered. The distribution of boron centres is inhomogeneous, thus partially explaining the non-uniformity of nanoparticle growth when using electrodeposition techniques [44, 45, 73]. This inhomogeneity can be seen in Fig. 6.5a–c. The grain boundaries have increased surface concentrations of electroactive sp^2 carbon and oxygen moieties; thus, denser concentrations of nanoparticles tend to found in these regions [64, 74, 75]. Further increases in nanoparticle density can be achieved by depositing onto BDE with smaller grain sizes (i.e. macro > micro > nano), due to their increased surface area [76]. This trend can be seen by comparing Fig. 6.5c, d. It is thought that this trend explains the effectiveness of lower nanoparticle loadings on micro-crystalline diamond electrode, compared to its macro counterpart [76]. Smaller grain sizes also help to reduce aggregation, reduce particle sizes, and make distribution more uniform, as seen in Fig. 6.5d. This distribution and morphology promotes hemispherical diffusion profiles, which are electrochemically favourable [14, 76]. There is some debate whether metal nanoparticles deposit randomly or non-randomly on polycrystalline diamond, with the work of the Macpherson group suggesting is both random and uniform [43].

Pre-treatment of BDE prior to deposition has been shown to lead to improved nanoparticle stability and electrode performance. Oxygen-terminated diamond stabilizes metal nanoparticles better than hydrogenated diamond [33, 43]. One can add oxygen functionality to the surface by a variety of means, including oxygen plasma and anodic electrochemical treatment [77, 78]. However, passivation of the diamond film by thick overlayers of oxygen is to be avoided. Pre-roughening of the BDE surface can increase surface area, thereby improving nanoparticle adhesion and uptake; this is shown to be effective by Hu et al. [32] who used nanodiamond powder suspensions as the roughening medium.

Interestingly, the diamond surface alone may not necessarily have an effect, but rather the material which supports it. Recently, Gao et al. [57] demonstrated that the spontaneous deposition of Ag, Cu, Au, Pd, and Pt on diamond could be achieved in HF, when the diamond surface was in ohmic contact with hydrogen-terminated silicon. It is thought that this type of contact increases the surface electron energy of diamond, thereby promoting the migration of excess electrons from the silicon/HF

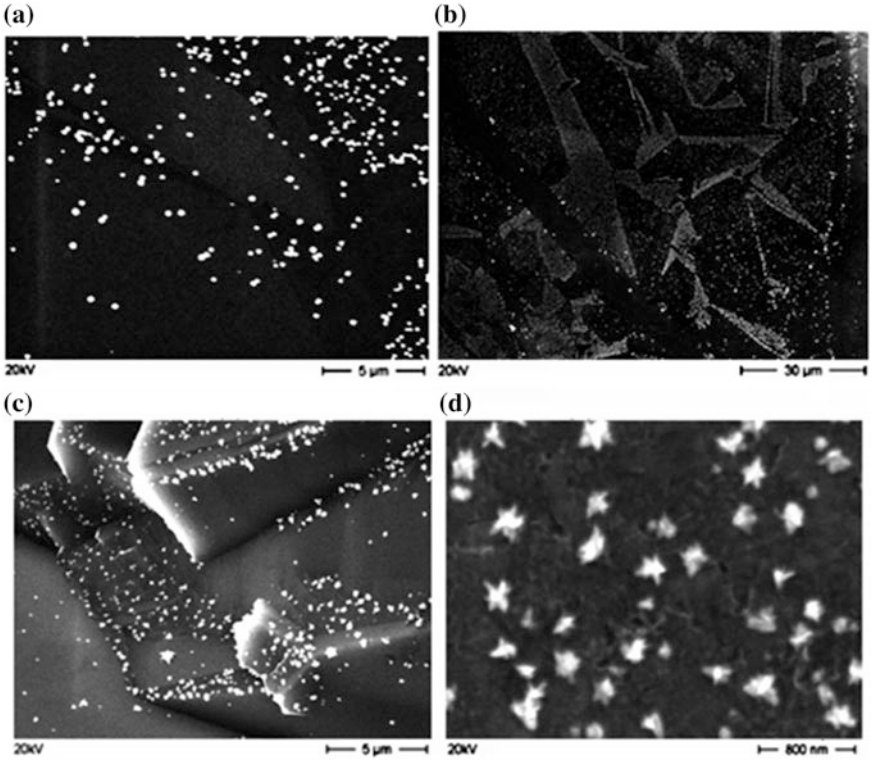

Fig. 6.5 SEM images of platinum deposited on (**a**, **b**) polished smooth boron-doped diamond electrode, **c** as-grown large grain, and **d** small grain diamond substrates. Reprinted from Hu et al. [31] with permission from Wiley-VCH, Copyright © 2009 WILEY-VCH Verlag GmbH & Co. KGaA, Weinheim

interface to the conductive diamond interface [57]. In this manner, the diamond surface is made more reductive, thereby leading to the spontaneous reduction of metal ions onto the diamond surface. Silicon dioxide was unable to achieve this same effect, thus highlighting the importance of substrate choice to deposition chemistry.

6.2.3 Surface Characteristics

6.2.3.1 Characterization Techniques

Surface characterization of NP-modified diamond films is necessary to both confirm nanoparticle deposition and understand the fundamental surface chemistry of the electrode. The size and morphology of deposited nanoparticles is best studied using

atomic force microscopy (AFM), scanning electron microscopy (SEM), and transmission electron microscopy (TEM). Notably, in situ studies of nanoparticle nucleation and growth are possible using electrochemical AFM (EC-AFM) [14, 79]. The surface chemistry of the deposited nanoparticles can be effectively determined using X-ray photoelectron spectroscopy (XPS), time-of-flight secondary ion mass spectroscopy (ToF-SIMS), and Raman spectroscopy. Crystal structure of both the substrate and the nanoparticles can be determined using X-ray diffraction (XRD). Finally, the electrochemical properties and mass loading of nanoparticles is usually determined by cyclic voltammetry and stripping voltammetry.

6.2.3.2 Nanoparticle Distribution

The distribution of nanoparticles across an electrode can be modified to achieve a given electrochemical or electroanalytic purpose. Higher current densities, higher signal to noise ratios, and higher faradaic to non-faradaic current ratios, occur at surfaces comprising widely-spaced and uniformly distributed nanoparticles [80, 81]. In this case, mass transport of reactants to the nanoparticles occur via fast, three-dimensional, diffusion, as opposed to linear diffusion [76, 80]. These characteristics are known to improve electroanalysis and electrocatalysis at nanoparticle-based electrodes. In cases where macroelectrode performance must be realised at reduced cost, one might distribute nanoparticles more densely (e.g. 50–100 nm particle to particle spacing), to ensure that electron transfer is limited by mass transport (i.e. planar diffusion) of the reactant to the surface, thereby lowering electrode sensitivity [76, 80, 81]. In some cases, the kinetics of electrochemical reactions are paramount; the location and distribution of reactive nanoparticles can control or exploit the interplay between reactant mobility and adsorption [81]. Nanoparticle deposition near active sites, defects, and grain boundaries could be of benefit if such sites are important to the electrochemical system. Finally, the promotion of certain nanoparticle shapes requires preferential growth on certain grain boundaries of diamond [39]. The degree to which particles distributed uniformly can be determined by comparing experimental data to theoretical models [81, 82].

Non-uniform nanoparticle distribution on BDE is promoted by inhomogeneous distributions of boron-centres, grain boundaries, high number of surface defects, and high levels of sp^2 contamination. These surface features are highly electroactive, with nanoparticles nucleating and growing on these sites during electrodeposition [31]. This explains the difficulty of depositing homogeneous distributions of NP by electrodeposition. More uniform distributions are obtained by reducing the number of defects or grain boundaries (cf. Fig. 6.5c, d), and by making the surface less electroactive by increasing the surface density of sp^3 carbon [83]. Some reports do suggest that electrodeposition of nanoparticles can occur grain-independently [43, 83].

Uniform nanoparticle distribution is produced, generally, by non-electrochemical methods of deposition [75]. An alternative is to functionalise the diamond and/or nanoparticle surface prior to deposition, in order to promote uniform nanoparticle

distribution. For example, two dimensional arrays of Au nanoparticles have been created by covalent attachment of citrate-coated Au NPs to an amine terminated diamond surface [84]. More simply, the pre-roughening of the diamond substrates has been shown to promote uniform nanoparticle distribution [32].

6.2.3.3 Nanoparticle Adhesion and Stability

The dissolution of nanoparticles from a diamond support is not desirable, as it leads to instable electrochemical performance and increases the cost of any electrical or catalytical device. Moreover, the introduction of metal ions into biological systems may have toxic effects. Therefore, the question of particle adhesion and stability is crucial.

Better adhesion and stability may be realised by using alternative materials to an initial choice. For instance, in acidic environments, metal nanoparticles can dissolve, therefore metal oxides should be considered for their stability in these environments. Examples of successful replacements include: use of RuO_2 instead of Ti, Ta, Ti-Pd by RuO_2 for chlorine evolution [33]; use of bimetallic or metal oxide nanoparticles instead of Pt nanoparticles [32, 34, 41]. A consultation of Table 6.1 may inspire the search for alternative materials for a given application.

Sandwiching nanoparticles between layers of CVD diamond seems to be the best method for retaining nanoparticles. The classic example is that of Swain et al. [40] who sputtered Pt onto CVD diamond, followed by a period of further diamond growth. The high stability of Pt nanoparticles was due to their being partially buried by diamond overlayers or anchored to the surface by diamond growth around the base of individual nanoparticles. Ion implantation achieves a similar level of stability as high energy metal ions are partially buried into the diamond substrate, as demonstrated for Ni [65], Cu [65], Pt [63], and Ir [64] implantation into BDE. Ion implantation offers 5 month stability, in the best case scenario [65, 85].

Other methods of deposition improve particle adhesion, as noted throughout this chapter. Multi-step potentiostatic methods may be superior to single step potentiostatic methods [3, 14, 76]. Potential pulsing leads to better IrO_x adhesion and is highly recommended for the deposition of metal oxides, compared to galvanostatic or potential cycling methods [58, 86]. Novel wet chemical routes (discussed in Sect. 6.5) also offer the potential for improved particle adhesion and stability [35].

Substrate pre-treatment can also improve particle adhesion and electrode stability. Increasing the surface density of oxygen moieties can improve nanoparticle adhesion [39]. This can be accomplished by pre-treatment in acid, anodic electrochemical treatment, or O_2 plasma [33, 43, 77, 78]. Sol-gel deposited metal oxide nanoparticles and sputter deposited Au nanoparticles have improved adhesion after a heat treatment [60, 62]. Thermal heat treatment can make BDE more hydrophilic, which may be the cause of improved adhesion [87]. Deliberate hydrophilic treatment of diamond lead to improved FeO_x adhesion [58, 88] Ultrasonic pre-treatment

of diamond in suspensions of diamond powders improves the adhesion of Pt nanoparticles [32]. Finally, the careful choice of the type of diamond improves particle adhesion. For instance, Pt nanoparticle modified micro-crystalline diamond outperforms its macro counterpart, providing electroanalytical performance in polluted tap and river water for 150 detection runs [76].

Poorly adhered nanoparticles do not necessarily leave the electrode, but can agglomerate along grain boundaries during an electrochemical experiment. For instance, Pt nanoparticles are stable on the (111) facet of BDD for a few hours during methanol oxidation, but on the (110) facet, particles agglomerate [39]. Agglomeration causes particle size to increase, with the consequence of reduced electrochemical selectivity and sensitivity to analytes, as nanoparticle diffusion layers overlap [14]. It is thought that functional groups on the (111) surface, such as sp^2 carbon and oxygen functionality help to stabilize attached particles [39].

6.2.3.4 Nucleation

The nucleation of materials using electrochemical techniques is still poorly understood and there is much controversy in the field. Hyde and Compton [89] have reviewed some of this debate and recent progress in this area. Due to existing controversy in the field, recent research is discussed in some detail.

Two types of nucleation processes are used throughout the literature on electrodeposition: instantaneous and progressive. The former assumes that nuclei grow slowly on a small number of active sites, simultaneously; the latter assumes that nuclei grow quickly on many active sites, which become activated as the electrodeposition proceeds [89–91]. There exist two methods of determining the nucleation type. The first involves analysing current-time transient curves obtained by chronoamperometry [31, 92]. The second involves the use of in situ EC-AFM [93]. In both cases, the results are most commonly compared to models by Scharifker and Mostany [94]. These models assume a constant nucleation rate and that particle growth is diffusion controlled; depending on the model chosen this can be planar or hemispherical [31, 92, 93].

Diamond is a low energy surface and nucleation is most commonly instantaneous, as exemplified by the electrodeposition of Cu [37], Bi [95], Pt [31, 36, 92] on non-polished, polycrystalline diamond. Instantaneous deposition is driven by high overpotentials and the extent of such nucleation can be controlled by varying the potential [92]. Also, instantaneous nucleation is prevalent on diamond with smaller grain sizes [31, 57]. This can be seen in Fig. 6.5d. Characteristics of instantaneous deposition include: the observation that the number of nucleation sites is controlled by the applied potential [96]; an monotonically broader size distribution during deposition [37], small particle size [37], small particle distribution [41], and the formation of dendritic microstructures on grain boundaries and surface defects [34]. These characteristics helped identify the nucleation type in the

case of Pt and Pt-Ru deposition by sequential potentiostatic methods, compared to deposition of Pt-Ru by simultaneous potentiostatic methods [34].

Progressive nucleation does occur on BDE as well. Platinum deposits onto smooth, polished diamond by a progressive nucleation process, as shown in Fig. 6.5a [31]. These particular nanoparticles are characterised by smooth, spherical morphology with decrease electroactive surface area. By contrast, in the same study, instantaneously nucleated Pt on small and large grain BDE had dendritic structure and higher electroactive surface area (cf. Fig 6.5d). Others characteristics of progressive nucleation include large particle sizes, clustering, and wide size distribution [41, 53, 79]. Some deposition methods may only be capable of progressive nucleation, such as the potential sweep method, in the case of simultaneous or sequential deposition of Pt-Ru onto polycrystalline diamond [34]. Progressive nucleation should be avoided if electrochemical performance is of utmost importance, as instantaneously nucleated particles are more favourable for this application [14].

It is commonly accepted that nucleation occurs most readily at grain boundaries, surface defects, and electroactive sites on the diamond surface, as in the case of Ni and Co [79, 97], Pt [26, 31, 32, 34, 36, 92], Pt-Ru [34], as well as other metal and metal oxides [14]. This phenomenon can be seen in Figs. 6.1, 6.4, and 6.5. The position of nucleation depends on the substrate, particularly the local electroactivity of the surface [31, 32]. On smooth, polished BDE nucleation of Pt may be promoted on the most electroactive facets of diamond [31]. For example, Pt is known to deposit on the (111) facet of polycrystalline diamond (see Fig. 6.4). The size and distribution of grains within the diamond substrate can affect nucleation. Pt nanoparticles are more homogeneously distributed on small grain BDE, compared to large grain BDE (see Fig. 6.5) [31]. The authors attribute this to the higher density of electroactive sites on small grain BDE. Higher boron doping levels make the BDE more electrochemically active [73], and one surmises this would promote instantaneous nucleation; however, to our knowledge this has not been systematically studied yet. Increasing the electroactivity of the BDE substrate is an effective strategy to promote nanoparticle nucleation.

6.2.3.5 Size and Morphology

There is much evidence showing that the best electrochemical performance results from the deposition of small particle sizes (5–10 nm) at low loading rates, with small size distributions [1, 14, 57]. These characteristics ensure a high electroactive surface area, hemispherical diffusion controlled electrochemistry, catalytically active quantum size effects, and the availability of low co-ordinated facets at the surfaces of small particles [14, 75, 98–100]. The above characteristics help ensure the resultant electrode is effective.

Sizes reported in the literature range from 5 nm to 5 μm, with size being controlled in a number of ways. The deposition method can affect the size.

Microemulsion routes [101, 102], wet chemical deposition [57], and the various electrodeposition techniques mentioned in Table 6.1 are capable of depositing nano-sized particles on the order of 2–10 nm. Some PVD methods are capable of depositing similarly sized particles [103]. The use of sol gel methods to deposit metal oxides tends towards large particle sizes, on the order of 0.5–5 μm [67–69]. However, this technique does trend towards low loading rates, on the order of 10^{13} mol^{-1} cm^2, [87] thereby minimizing diffusion zone overlap of particles [14].

Many electrodeposition methods have been evaluated for their ability to control particle size, as noted by Hu et al. [31], including: chronoamperometry [43], cyclic voltammetry [38, 54], galvanostatic [104], pulsed galvanostatic [44], potentiostatic step [105], and potentiostatic cooulometry [38]. These methods were used to control the size of various metal systems, including: Cu [38, 49], Pd [50], Ag [49], Au [49, 77], Ir [52, 106], and Pb [107]; other systems of interest can be found from Table 1.1 and in other reports [14].

Potentiostatic methods are better able to fine-tune the growth of metal nanoparticles [31, 32, 108]. For example, for the deposition of Cu^{2+}, Ag^{2+}, and $Pb^{2+,}$ potentiostatic coolumetry is a superior method to cyclic voltammetry [38]. The latter is known to incompletely strip metal sites, thus promoting uncontrolled growth of metal nanoparticles on pre-existing metal on the surface. Metal is a more energetically favourable deposition site than BDE [38, 109]. In potentiostatic coolumetry, only nanoparticles on non-electroactive sites are incompletely stripped, thus ensuring that particle growth is controlled by the electrochemistry of the diamond substrate, alone [38].

Multi-step electrodeposition can be a useful means to achieve better size control, by minimizing the disadvantages of any single method. For example, to adjust size more quickly, the Foord group utilizes a two stage process. In the first stage, nano-sized Pt nuclei are created by the slow increase of negative potential, followed by the application of a fixed potential to enlarge the nuclei to the desired size [3]. The size of metal oxides can be controlled in a third electrodeposition step, in which the oxide is precipitated at the metal nuclei, as done for the case of Pt-PrO_x [3].

Many deposition parameters are reportedly able to change the size of deposited particles, including: overpotential [3, 31, 38, 76, 97], metal ion concentration in the electrolyte [53, 57, 76, 110], deposition time [3, 31, 38, 76, 110], grain size of diamond substrate [43], solution acidity [57] and number of electrodeposition steps [76]. Of these parameters, the most important is overpotential, due to its influence on the energetics of the electrodeposition process, nucleation, and mass transport to electroactive sites on the substrate [14, 34]. Adjustment of the scan rates can homogenize size distribution after initial deposition [37]. Those deposition parameters which lead to instantaneous nucleation are typically those that create the smallest particle sizes, as described earlier. Progressive nucleation leads to the largest particle sizes [110].

There are several other parameters used to control size in the case of non-electrochemical methods. Heat treatment is capable of changing the size of metals,

such as Au, post-deposition [75]. Also, the facet to which the metal nanoparticle adheres may influence size. For example, it has been shown that Pt nanoparticles on (110) facets have larger particle diameter, while those on the (111) facet are smaller in size (see Fig. 6.4) [39]. In this same study it was shown that merely changing the sweep rate during deposition by cyclic voltammetry is sufficient to change the preferred facet of deposition, and thus the particle size [39]. Figure 6.4 shows the result of using the highest scan rate in that study.

6.2.3.6 Shape

Performance can be further enhanced by changing the morphology of deposited nanoparticles. A number of different shapes and particle morphologies have been made on diamond, including: convex polyhedron (see Fig. 6.3c), flower-like or dendritic (see Fig. 6.3a), spheres (see Fig. 6.3b), clusters, and agglomerations. The size of these features varies from the nano-scale to the micro-scale, depending on the system studied. Shape can be controlled in a number of ways, including: deposition type, nucleation type, overpotential, metal ion concentration, and linear sweep rates. The shape can expose favourable facets of the nanoparticle to the solution and increase the exposed surface area, both of which are desirable features for a modified BDE [55].

There are several reports showing that deposition type can control particle shape. Deposition from sol gels and microemulsion tend to form clusters and agglomerates of metal oxides and metals at BDE [57, 67, 111]. Dendritic and smooth particles result from potentiostatic and linear potential sweep methods, respectively [31, 54]. In multi-step methods, one might consider the effect of simultaneous versus sequential deposition. For example, they lead to spherical and dendritic structure, respectively, in the case of Pt-Ru deposition [34].

Other deposition parameters can be optimized to favour certain shapes. Flower and dendritic growth is promoted by instantaneous nucleation, while spheres, clusters and agglomerations are more prevalent during progressive nucleation [18, 34, 55, 75, 95]. The parameters which favour one or the other type of nucleation have been discussed earlier. Dendrite formation requires prismatic growth in the early stages of deposition and is related to overpotential [57, 112]. This may be due to the fact that higher overpotentials cause near maximum mass transport limits [113]. For example, at constant metal ion concentration, a simple change in overpotential is capable of changing Au deposition shape from flower-like to a convex polyhedron (cf. Fig. 6.3a, c) [55]. Also, heat treatment has been used to change the shape of Au nanoclusters and does so by exposing the nanoparticles to the very electroactive Au(111) plane, which promotes dendritic-like growth [75].

During the spontaneous deposition of Ag, Cu, Au, Pd, Hg, and Pt onto Si supported BDE, it was found that metal ion concentration is key to particle shape [57]. The authors note that dendritic, small spheres, and large spheres were related

to high, low, and dilute concentrations, respectively. In the case of dilute concentrations it is more favourable for metals to deposit onto metal rather than the underlying BDE electrode, thereby increasing particle size [57]. High and low concentrations of $HAuCl_4$ were found to lead to 'flower-like and spherical nanoparticle shapes on BDE (cf. Fig 6.3a, b) [55].

6.3 Diamond Nanoparticles as an Electrode Material

Detonation nanodiamond (DND) is of emerging interest, with research finding it to have a diverse set of applications, including biomedicine, catalysis, quantum computing, nano-composites, and for the seeding of CVD diamond growth [5]. It has a number of attractive features, including optical transparency, large surface area, and a bio-compatible sp^3 core structure. These characteristics make DND a material of choice for use in bio-medical implants, nano-scale electrochemistry, drug delivery, cell imaging technologies, and as a substrate for cellular growth [5, 20, 114–117]. The myriad of applications of nano-scale diamond has been reviewed by Holt [5] and Schrand [20].

6.3.1 Background on Detonation Nanodiamond

Lewis et al. [118] first found diamond nanoparticles in interstellar dust and meteorites. Since then, efforts have been made to create nano-scale diamond particles, synthetically by the controlled combustion of explosives. Nanoparticles of diamond are synthesized by the controlled combustion of explosives in high oxygen conditions [20, 116, 119]. These particles undergo cleaning processes (i.e. acid treatment, oxidation by Osswald method [120] to remove metal impurities and to reduce their size to primary particles, they must undergo deaggregation [20].

The resultant material is comprised inner, sp^3 diamond core of 4–5 nm and an outer shell of non-diamond character, with complex surface chemistry [121]. This outer shell of purified DND contains a mixture of sp^2 and sp^3 carbon [122] and oxygen based functional groups (i.e. carboxylic acids, esters, lactones) [20]. If desired, this surface chemistry can be changed by fluorination [123], hydrogenation [124], and the attachment of alkyl, amino, and amino acid groups [123, 125]. The physical and chemical properties of DND depend strongly on the size of the nanoparticles [124], with size control of the DND required for the stabilization of their colloidal suspensions [126] or to ensure specific reactivity [127, 128]. The surface area of primary sized DND is approximately 270–280 $m^2\ g^{-1}$ [129], thus providing greater surface area for nanoparticle attachment than conventional diamond films.

6.3.2 Electrochemistry of Detonation Nanodiamond

DND is an undoped form of diamond. One normally associates undoped diamond as being an insulator and impractical for use in an electronic device. Unlike the bulk material, DND is electrochemically active in its undoped form. Like many materials, the nano-sized version exhibits different chemical properties than its bulk form. This is due to its high surface area, multi-faceted nature, and its outer shell, which contains reactive sp^2 carbon and oxygenated functionality [126].

Commercial DND particles of primary particle size are redox active, but not in a classical sense. The classical picture considers that H-terminated diamond is redox active, if chemical potentials are below the valance band maximum [130, 131]. Also, it considers that p-type conductivity at the surface exists due to electron transfer between H-termination and dissolved oxygen in aqueous environments [132]. This is not true of DND, as determined by Holt and her colleagues in 2008 and 2009.

Our understanding of DND redox behaviour has been advanced by the Holt Group who have conducted extensive electrochemical studies of commercial DND (5 nm) [19, 133]. They found DND to have 'molecule-like' redox behaviour [19]. That is to say that the particles themselves undergo oxidation and reduction via surface states at specific potentials [19]. It is easier to reduce DND particles than to oxidise them [133]; this process is spontaneous and slow in the presence of certain redox species without an applied potential [19, 133]. The electrochemical behaviour may also be due to the presence of sp^2 carbon, delocalised electrons due to oxidation, and unsaturated bonding of surface atoms; all this gives DND surfaces a semiconductor/metallic character [133]. Although doping of DND particles is possible [134, 135], it is not required for the vast majority of its electrochemical applications, due to its intrinsic redox behaviour.

6.3.3 Methods of Deposition/Incorporation into Electrode Form

There are several methods available to make DND particles into a useful electrode. DND particles have been placed on Au electrodes by drop coating from ethanol suspensions [19] and on glassy carbon electrode by smearing a DND-mineral oil paste on its surface [19, 136, 137]. The former method leads to non-uniform coverage and DND agglomeration, while the latter method formed a thin uniform layer on the electrode [19]. Thin coatings are particularly important, in order to avoid electrochemical blocking effects by the DND particles on the glassy carbon electrode [19]. A DND electrode can be manufactured by grinding DND powder into the tip of a Pt wire sealed in a small pipette [136].

More sophisticated electrodes are in existence. For instance, DND has been electrophoretically deposited as thin uniform layers [138]. As well, DND-polyaniline

composites have been made by sequential and simultaneous deposition processes [139–142]. Interestingly, these methods lead to the nanostructuring of PANI in one-dimension, as the PANI oligimers aggregate under the influence of pi-pi stacking [142]. This result hints that DND co-deposited with other materials can lead to novel materials with interesting chemical properties. Non-contact microprinting [143] and layer-by-layer self-assembly by a high pressure/high-temperature methodology [144]. It has been theorised the DND can be electrodeposited onto electrodes [145], but to our knowledge this has not been evaluated in practice.

One example of co-deposition is the modification of diamond with metal or metal oxide nanoparticles, as discussed in this review. DND has also been modified with nanoparticles in a similar way, for similar applications (see also Table 6.1). Supporting catalysts on nanodiamond will benefit from the high surface area and increased reactivity of nanodiamond, compared to its bulk form. Thus, lower loading rates are required to make a practical electroanalytical or catalytical device, based on nanodiamond powders. This promises to reduce device costs.

Ni [146, 147], Sn/Pb alloys [148], TiO_2 [149], Pt [150], metal oxides [67], Pt/Ru [34, 151, 152] have been supported on nanodiamond powder based electrodes. Fruitful research can continue in this area, inspired by the work done on bulk diamond. In addition, further optimisation of particle loading, stability, and electroactivity of nanodiamond supported catalysts is necessary.

6.3.4 Characterization of Diamond Nanoparticle-Based Electrodes

Nanodiamond powder films on surfaces have been characterized by SEM and AFM [152, 153]. Nanoparticle layers form porous sub-micron structures, which enhances its electroactivity compared to bulk films [152]. Holt et al. have characterized DND films by FTIR, XPS, TEM, and Raman spectroscopy [19]. Graphite G and D bands in Raman spectroscopy indicate the presence of surface sp^2 carbon [19]. XPS shows the oxygenated character of the nanodiamond surface [19]. Nanodiamond has also been characterized by scanning electrochemical microscopy (SECM) [133]. Redox behaviour at diamond nanoparticles has also be evaluated by in situ infrared spectroscopy [154].

6.4 Interactions at the Metal-Diamond Interface

Interactions between diamond, in its various forms, and the nano-materials discussed in this review are key to the understanding of the stability and electronic performance of these composite systems. Diamond has no native oxide, and therefore the electronic behaviour of its surface is highly dependent on any surface modification. Doping of diamond films with impurities which induce p or n-type

doping transforms an otherwise insulating material into a semi-conductor. Redox active species at diamond surfaces (i.e. COOH, C–O-C, lactones, ketones) are known to facilitate electron transfer between the diamond interface, an electrolyte, and metal ions [155]. The above are all well-known phenomenon; however, there is a lack of systematic and fundamental research concerning other, more complex phenomena at the metal-diamond interface [25, 156]. A review of some progress in this area is presented here.

The manufacturing process, polishing, cleaning, and exposure to ambient environments can introduce impurities to the diamond surface. In the case of DND particles, the level of impurities can reach 10–12 % of the total surface area [157]. Examples of these impurities include sp^2 carbon, organic-based functionality (O, N, S, B), metal salts, and defects, among others [157]. Some impurities can lead to favourable interactions. For example, metals with a preference for the +2 oxidation state (e.g. Ni, Ti, Cu, Co, Fe, Al) are thought to be stabilized by interactions with oxygen groups, such as carboxyls and hydroxyls [14, 97, 157–159]. These functional groups, in close proximity to each other on DND particle surfaces have been found to participate in ion exchange with metals in the +2 state, as determined by ^{1}H and ^{13}C NMR [159, 160]. This is evidence for non-covalent bonding between oxygen-based impurities and metal nanoparticles. Covalent bonding is also possible, as in the case of Al bonding to DND nanocrystals via carboxyl terminations, thereby leading to aggregation of DND in solution [157]. Carbide bonding, such as that between diamond surfaces and Au/Ti, Al, and Ti are known to improve contact resistance and mechanical properties, as determined by the circular transmission line method (c-TLM) [161]. However, not all impurity-metal bonding has a purpose or is favourable. For instance, metal bonding to sp^2 carbon is known to interfere with the electrical properties of the diamond electrode and it reduces the strength of metal-diamond adhesion [162].

Electrostatic effects are thought to play a role in governing metal deposition and stability on diamond-based electrodes. O-terminated and H-terminated DND particles have negative and positive zeta potential over a large pH range (up to pH 12) [128, 157], and this may govern the dynamics of electropositive or negative metal ions to their surfaces. Facet dependent deposition of metal and alloy nanoparticles onto diamond thin films has been observed for a variety of systems (Au, Pt, and their alloys) [39, 156]. The reason for this behaviour seems to lie in the differing electrostatic properties of the various facets [39, 156]. This is supported by the finding that for DND particles sp^3 carbon (i.e. 100 orientation) is electropositive, while sp^2 carbon (i.e. 111 orientation) is electronegative [135].

Electronic interactions between diamond and metal nanoparticles have been observed. For example, the electrical potential of DND nanoparticles are affected by the substrate, size, height, and surface termination [163]. Stehilk et al. [163] observe that the work function diamond interfaces are altered when an electric dipoles (i.e. added metal nanoparticles) is added, thus changing the energy electrons require to reach the vacuum level.

Metallization is a useful change in the electronic properties of conductive diamond, as it improves charge transfer between diamond and any surface modifier [155].

Calculations based on Density Functional Theory (DFT) and experimentation have shown that the band gap is removed if modified by metals, O-terminated diamond, and/or sp^2 functionality [157, 164]. Also, the type of electrical contact improves charge transfer. Ohmic contacts between metals and diamond have been associated with better particle adhesion, higher bond strengths, and shorter bond lengths [164, 165]. This is possible for Ti, V, and Ta deposition, but not for Au or Pd deposition [115, 161]. Likely, charge density on carbon is facilitating backbonding to some metals [164, 165], with metals having more unpaired d orbitals (i.e. V, Ta, Ti) and filled d orbitals (Au, Pd) having stronger and weaker electronic interactions with diamond, respectively [164, 165].

There are other lesser known, or studied, electronic interactions between metals and diamond. These include: negative electron affinity [165–167], conductive surface protrusions [168], non-diamond sp^2 [167], conductive diamond to metal backbonding [165], intrinsic structural effects [167, 169], charge trapping/transfer [155, 163], and interpretations based on energy level confinement within quantum dots for particles <7 nm in size [163]. Plana et al. [155] note that many of these same reasons are applicable to the metal-diamond interface, in addition to electrochemical (e.g. electrolyte, double layer) and nanostructural effects. Other subtle effects are possible, such as quantum effects and metal-vacuum properties, as noted by Tyler et al. [166] in their study on electron emission from diamond nanoparticles on metal tips. The size of the metal or diamond nanoparticle is an important parameter to consider when studying any of the above effects [163]. Quantum-based and crystallinity-based arguments may have greater explanatory weight for metal-diamond interactions involving sub-5 nm nanoparticle sizes [81, 127, 163]. More research in this sub-field is necessary to truly isolate the electronic effects at the metal-diamond interface.

Some metal-diamond interactions have physical consequences. The catalytic etching of nano-sized features in diamond surfaces occurs in H_2 environments at elevated temperatures (>700 °C) [170]. Annealing diamond thin films after it has been modified with metal nanoparticles by ion bombardment can lead to the diffusion of metal nanoparticles from the bulk to the surface [14]. Metal adatoms could have preferred deposition sites, as suggested by DFT calculations of Ti on diamond (100), whereby Ti prefers pedestal sites on top of carbon dimer rows [162]. Annealing of surfaces leads to metal-diamond aggregates involving DND particles, which may be the result of covalent bonding between DND particles with metal ions acting as linkers [157].

6.5 Modern State-of-the-Art and Outlook

Research on the modification of diamond electrodes with metal and metal oxides, continues apace. Research in the past three years has been motivated by interest in fuel cell technologies, photocatalysis and water-splitting, and biological applications.

To our knowledge, two understudied areas of research concern the nanoparticle-diamond interface: the effect of doping levels and the use of epitaxial diamond. Most researchers use commercial BDE and do not investigate how doping levels, doping elements, or type of doping affect nanoparticle deposition. Secondly, studies of nanoparticle deposition on epitaxial diamond could prove fruitful. It is known that the diamond (111) facet is preferred for nanoparticle deposition and such deposition leads to enhanced electrochemistry. The fundamental chemistry of that interface is important, but little understood. One group has attempted to study the role of doping on epitaxial grown diamond [171]. However, more systematic studies, such as that done by Holt et al. [73] on the effect of doping levels for unmodified (i.e. H-terminated diamond) need to be made for the case of diamond electrodes modified with nanoparticles.

Renewable energy technologies are of high interest in the 21st century and new materials are sought to address challenges in environmental and energy technologies. The use of organo-metallic ligands to either aid in the deposition process or to support nanoparticles at the surface, has led to novel electrodes. Porphyrin rings stabilize the deposition of various metals, including Co and Ru, known to be effective in dye-sensitized solar cells and CO_2 reduction fuel cells [172–174]. The deposition of TiO_2 nanoparticles on BDE and DND is considered a promising approach for photocatalysis, water-splitting, and water treatment based on solar energy [149, 175–177]. Bimetallic nanoparticles deposition remains important for alcohol oxidation in fuel cells (Pt-Ru [34, 151, 152]) and nitrate reduction (Cu-Sn [178], Cu-Pd [178]). Nanoparticles which equal the effectiveness of Pt nanoparticles, with better stability, have yet to be discovered. Therefore, much recent effort has been expended in realizing the increased stability and reduction of fouling on Pt nanoparticles for electrocatalytic applications [3, 31, 32, 34, 35, 39, 41, 92, 151, 152, 171, 179, 180].

Recently, there has been a resurgence of interest in wet-chemical routes towards depositing metal nanoparticles on carbon-based materials. In particular, the reduction of metal precursors to metal nanoparticles at a reducing agent attached to an underlying carbon-based surface has emerged as a promising deposition route [151, 181–183]. This method was first attempted at diamond thin films by the Nebel group who seeded the substrate with Pt by reducing H_2PtCl_6 at diamond modified by $NaBH_4$ [35]. Surface coverage and size can be controlled by the number of repetitions of the above process. Further control of size was possible via electrochemical growth processes [35]. The advantage of this approach is the realisation of homogenous distribution of nanoparticles on diamond, which is difficult using non-physical deposition techniques. This approach is likely to have wider application, as exemplified by the modification of nanodiamond with nano-sized (2–5 nm), and homogenously distributed, Pt and Pt-Ru particles [182]. Wet-chemical assisted deposition of nanoparticles could be easily developed further, considering the existing literature on wet-chemical routes for modifying diamond [184–186].

In the past ten years, many have recognized the potential for diamond-based devices to be integrated into biological systems. This might be imagined as a direct-connection (i.e. neurological stimulation [187, 188]), stimulation of bio-molecules

(e.g. redox of proteins [189, 190]) or for biosensing [56, 179, 191–194]. Zirconia has been used to modify diamond for DNA detection by the Foord group [195]. Several reports exist showing the effectiveness of nickel and nickel hydroxide nanoparticles for glucose oxidase sensing [56, 196]. An array of self-assembled Au nanoparticles has been able to engage in direct electrochemistry with a microbe, thus suggesting more exotic use of diamond within microbial fuel cells [197]. Many reviews exist on this topic, and a selection is provided here [4, 12, 15, 20, 72, 198].

The principle of introducing nano-scale materials to diamond is also applied when proteins [189, 190, 199, 200], enzymes [191] or aptamers [201–203] are attached to the surface. This aids the detection of redox events and molecules at the diamond surface. Particularly exciting is the creation of a diamond FET-based device for HIV For example, the attachment of cytochrome c on BDE enables cyanide and arsenic to be detected [204]. The applicability of bio-modified diamond-based electrodes to clinical HIV detection was recently shown by Rahim Ruslinda et al. [201]. Diamond is poised to be a material of choice for the integration of solid-state and biological phenomena.

Nanoparticles of metals, metal oxides, or diamond can be easily damaged by physical means. Moreover, their preparation time can be lengthy. Various attempts are being made to address one or both of these issues by the following approaches: nano-structuring diamond [205–208], synthesizing new diamond-based nanoparticles (e.g. nanowires [209–211], nanograss [212]), grafting diamond nanoparticles [213, 214], micro-contact printing of diamond nanoparticles to surfaces [143], and the self-assembly of nanoparticles [197, 215–217]. The stabilization of nanoparticles with electropolymers continues to be a fruitful area of research, particularly for bio-applications [139–142, 193].

This chapter reviewed the methods used to construct boron-doped diamond electrodes. The methods and principles discussed here are applicable to the realisation of practical diamond-based electrodes which exploit the nano-scale, either via the deposition of nanoparticles or by having nanoparticle form. By understanding the chemical and physical consequences of any given methodology, one should be able better optimise diamond electrodes to address the biological, environmental, and industrial challenges of the 21st century.

References

1. R.G. Compton, J.S. Foord, F. Marken, Electroanalysis at diamond-like and doped-diamond electrodes. Electroanalysis **15**(17), 1349–1363 (2003). doi:10.1002/elan.200302830
2. J. Rubio-Retama, J. Hernando, B. Lopez-Ruiz, A. Hartl, D. Steinmuller, M. Stutzmann, E. Lopez-Cabarcos, J.A. Garrido, Synthetic nanocrystalline diamond as a third-generation biosensor support. Langmuir **22**(13), 5837–5842 (2006). doi:10.1021/la060167r
3. L. Chen, J. Hu, J.S. Foord, Electrodeposition of a Pt-PrO2-x electrocatalyst on diamond electrodes for the oxidation of methanol. Phys. Status Solidi (a) **209**(9), 1792–1796 (2012). doi:10.1002/pssa.201200049

4. A. Kraft, Doped diamond electrodes. New trends and developments. Jahrb. Oberflaechentech. **63**, 85–95 (2007)
5. K.B. Holt, Diamond at the nanoscale: applications of diamond nanoparticles from cellular biomarkers to quantum computing. Philos. Trans. Roy. Soc. A **365**(1861), 2845–2861 (2007). doi:10.1098/rsta.2007.0005
6. J. Wolters, G. Kewes, A.W. Schell, N. Nuesse, M. Schoengen, B. Loechel, T. Hanke, R. Bratschitsch, A. Leitenstorfer, T. Aichele, O. Benson, Coupling of single nitrogen-vacancy defect centers in diamond nanocrystals to optical antennas and photonic crystal cavities. Phys. Status Solidi (b) **249**(5), 918–924 (2012). doi:10.1002/pssb.201100156
7. M. Amanda, Schrand, A. Suzanne, Ciftan Hens, O.A. Shenderovab, Nanodiamond particles: properties and perspectives for bioapplications. CRC Cr. Rev. Sol. State **34**(1–2), 18–74 (2009). doi:10.1080/10408430902831987
8. V.Y. Dolmatov, Detonation synthesis ultradispersed diamonds: properties and applications. Russ. Chem. Rev. **70**, 607–626 (2001). doi:10.1070/RC2001v070n07ABEH000665
9. A. Kraft, Conductive diamond layers. Production, properties, and possible uses of new electrode materials. Jahrb. Oberflaechentech. **61**, 109–120 (2005)
10. K.I.B. Eguiluz, J.M. Peralta-Hernandez, A. Hernandez-Ramirez, J.L. Guzman-Mar, L. Hinojosa-Reyes, C.A. Martinez-Huitle, G.R. Salazar-Banda, The use of diamond for energy conversion system applications: a review. Int. J. Electrochem. **675124**, 675120 pp. (2012). doi:10.1155/2012/675124
11. J-b Zang, L. Dong, Y-h Wang, Review on electrochemical property and surface modifications of nanodiamond powders. Yanshan Daxue Xuebao **36**(2), 95–102 (2012)
12. H. Yuen Yung, C. Chia-Liang, C. Huan-Cheng, Nanodiamonds for optical bioimaging. J. Phys. D Appl. Phys. **43**(37), 374021 (2010). doi:10.1088/0022-3727/43/37/374021
13. N. Fujimori, T. Imai, A. Doi, Characterization of conducting diamond films. Vacuum **36** (1–3), 99–102 (1986). doi:http://dx.doi.org/10.1016/0042-207X(86)90279-4
14. K.E. Toghill, R.G. Compton, Metal nanoparticle modified boron doped diamond electrodes for use in electroanalysis. Electroanalysis **22**(17–18), 1947–1956 (2010). doi:10.1002/elan.201000072
15. Y. Zhou, J. Zhi, The application of boron-doped diamond electrodes in amperometric biosensors. Talanta **79**(5), 1189–1196 (2009). doi:10.1016/j.talanta.2009.05.026
16. I.A. Novolelova, E.N. Fedorishena, E.V. Panov, Electrodes from diamond and diamond-like materials for electrochemical use. Sverkhtverd. Mater. **1**, 32–50 (2007)
17. S. Szunerits, R. Boukherroub, Investigation of the electrocatalytic activity of boron-doped diamond electrodes modified with palladium or gold nanoparticles for oxygen reduction reaction in basic medium. C.R. Chim. **11**(9), 1004–1009 (2008). doi:10.1016/j.crci.2008.01.015
18. S.R. Belding, F.W. Campbell, E.J.F. Dickinson, R.G. Compton, Nanoparticle-modified electrodes. Phys. Chem. Chem. Phys. **12**(37), 11208–11221 (2010). doi:10.1039/c0cp00233j
19. K.B. Holt, C. Ziegler, D.J. Caruana, J. Zang, E.J. Millan-Barrios, J. Hu, J.S. Foord, Redox properties of undoped 5 nm diamond nanoparticles. Phys. Chem. Chem. Phys. **10**(2), 303–310 (2008). doi:10.1039/b711049a
20. A.M. Schrand, S.A.C. Hens, O.A. Shenderova, Nanodiamond Particles: Properties and Perspectives for Bioapplications. CRC Cr. Rev. Sol. State **34**(1–2), 18–74 (2009). doi:10.1080/10408430902831987
21. I. Duo, C. Comninellis, S. Ferro, B.A. De, Conductive metal-oxide nanoparticles on synthetic boron-doped diamond surfaces, in *Catalysis and Electrocatalysis at Nanoparticle Surfaces* (Marcel Dekker, New York, 2003), pp. 877–906
22. B. El Roustom, G. Siné, G. Fóti, C. Comninellis, A novel method for the preparation of bi-metallic (Pt–Au) nanoparticles on boron doped diamond (BDD) substrate: application to the oxygen reduction reaction. J. Appl. Electrochem. **37**(11), 1227–1236 (2007). doi:10.1007/s10800-007-9359-4
23. M. Watanabe, S. Motoo, Electrocatalysis by ad-atoms: Part II. Enhancement of the oxidation of methanol on platinum by ruthenium ad-atoms. J. Electroanal. Chem. Interf. Electrochem. **60**(3), 267–273 (1975). doi:http://dx.doi.org/10.1016/S0022-0728(75)80261-0

24. K.-W. Park, J.-H. Choi, B.-K. Kwon, S.-A. Lee, Y.-E. Sung, H.-Y. Ha, S.-A. Hong, H. Kim, A. Wieckowski, Chemical and electronic effects of Ni in Pt/Ni and Pt/Ru/Ni alloy nanoparticles in methanol electrooxidation. J. Phys. Chem. B **106**(8), 1869–1877 (2002). doi:10.1021/jp013168v
25. T. Kondo, K. Hirata, T. Kawai, M. Yuasa, Crystal-face-selective supporting of metal nanoparticles on polycrystalline diamond thin film. Pacific Chem. Conf. (ANYL-616. American Chemical Society) (2010)
26. I. Gonzalez-Gonzalez, E.R. Fachini, M.A. Scibioh, D.A. Tryk, M. Tague, H.D. Abruna, C.R. Cabrera, Facet-selective platinum electrodeposition at free-standing polycrystalline boron-doped diamond films. Langmuir **25**(17), 10329–10336 (2009). doi:10.1021/la8035055
27. R.-H. Tian, T.N. Rao, Y. Einaga, J.-F. Zhi, Construction of two-dimensional arrays gold nanoparticles monolayer onto boron-doped diamond electrode surfaces. Chem. Mater. **18**(4), 939–945 (2006). doi:10.1021/cm0519481
28. M.-J. Song, J.H. Kim, S.K. Lee, J.-H. Lee, D.S. Lim, S.W. Hwang, D. Whang, Pt-polyaniline nanocomposite on boron-doped diamond electrode for amperometric biosensor with low detection limit. Microchim. Acta **171**(3–4), 249–255 (2010). doi:10.1007/s00604-010-0432-z
29. M. Wei, Z. Xie, L. Sun, Z.-Z. Gu, Electrochemical properties of a boron-doped diamond electrode modified with gold/polyelectrolyte hollow spheres. Electroanalysis **21**(2), 138–143 (2009). doi:10.1002/elan.200804411
30. M. Wei, L.-G. Sun, Z.-Y. Xie, J.-F. Zhi, A. Fujishima, Y. Einaga, D.-G. Fu, X.-M. Wang, Z.-Z. Gu, Selective determination of dopamine on a boron-doped diamond electrode modified with gold nanoparticle/polyelectrolyte-coated polystyrene colloids. Adv. Funct. Mater. **18**(9), 1414–1421 (2008). doi:10.1002/adfm.200701099
31. J. Hu, X. Lu, J.S. Foord, Q. Wang, Electrochemical deposition of Pt nanoparticles on diamond substrates. Phys. Status Solidi (a) **206**(9), 2057–2062 (2009). doi:10.1002/pssa.200982226
32. J. Hu, X. Lu, J.S. Foord, Nanodiamond pretreatment for the modification of diamond electrodes by platinum nanoparticles. Electrochem. Commun. **12**(5), 676–679 (2010). doi:10.1016/j.elecom.2010.03.004
33. S. Ferro, B.A. De, Electrocatalysis and chlorine evolution reaction at ruthenium dioxide deposited on conductive diamond. J. Phys. Chem. B **106**(9), 2249–2254 (2002). doi:10.1021/jp012195i
34. X. Lu, J.-P. Hu, J.S. Foord, Q. Wang, Electrochemical deposition of Pt-Ru on diamond electrodes for the electrooxidation of methanol. J. Electroanal. Chem. **654**(1–2), 38–43 (2011). doi:10.1016/j.jelechem.2011.01.034
35. F. Gao, N. Yang, W. Smirnov, H. Obloh, C.E. Nebel, Size-controllable and homogeneous platinum nanoparticles on diamond using wet chemically assisted electrodeposition. Electrochim. Acta **90**, 445–451 (2013). doi:10.1016/j.electacta.2012.12.050
36. O. Enea, B. Riedo, G. Dietler, AFM study of Pt clusters electrochemically deposited onto boron-doped diamond films. Nano Lett. **2**(3), 241–244 (2002). doi:10.1021/nl015666l
37. C.M. Welch, M.E. Hyde, C.E. Banks, R.G. Compton, The detection of nitrate using in-situ copper nanoparticle deposition at a boron doped diamond electrode. Anal. Sci. **21**(12), 1421–1430 (2005). doi:10.2116/analsci.21.1421
38. C.M. Welch, A.O. Simm, R.G. Compton, Oxidation of electrodeposited copper on boron doped diamond in acidic solution: manipulating the size of copper nanoparticles using voltammetry. Electroanalysis **18**(10), 965–970 (2006). doi:10.1002/elan.200603493
39. I. Gonzalez-Gonzalez, F.E. Rosim, M.A. Scibioh, D.A. Tryk, M. Tague, H.D. Abruna, C.R. Cabrera, Facet-selective platinum electrodeposition at free-standing polycrystalline boron-doped diamond films. Langmuir **25**(17), 10329–10336 (2009). doi:10.1021/la8035055
40. J. Wang, G.M. Swain, T. Tachibana, K. Kobashi, The incorporation of Pt nanoparticles into boron-doped diamond thin-films: dimensionally stable catalytic electrodes. J. New Mater. Electrochem. Syst. **3**(1), 75–82 (2000)

41. J.P. Hu, X. Lu, J.S. Foord, Q. Wang, Electrochemical deposition of Pt nanoparticles on diamond substrates. Phys. Status Solidi (a) **206**(9), 2057–2062 (2009). doi:10.1002/pssa.200982226
42. J. Wang, G.M. Swain, T. Tachibana, K. Kobashi, Electrocatalytic diamond thin film electrodes with incorporated Pt. Proc. Electrochem. Soc. **2001-2025**(Diamond Materials VII), 157–167 (2002)
43. L. Hutton, M.E. Newton, P.R. Unwin, J.V. Macpherson, Amperometric oxygen sensor based on a platinum nanoparticle-modified polycrystalline boron doped diamond disk electrode. Anal. Chem. (Washington, DC, U. S.) **81**(3), 1023–1032 (2009). doi:10.1021/ac8020906
44. J.A. Bennett, Y. Show, S. Wang, G.M. Swain, Pulsed galvanostatic deposition of Pt particles on microcrystalline and nanocrystalline diamond thin-film electrodes: I. characterization of as-deposited metal/diamond surfaces. J. Electrochem. Soc. **152**(5), E184–E192 (2005). doi:10.1149/1.1890745
45. N.R. Wilson, S.L. Clewes, M.E. Newton, P.R. Unwin, J.V. Macpherson, Impact of grain-dependent boron uptake on the electrochemical and electrical properties of polycrystalline boron doped diamond electrodes. J. Phys. Chem. B **110**(11), 5639–5646 (2006). doi:10.1021/jp0547616
46. K.P. Loh, S. Liang Zhao, W. De Zhang, Diamond and carbon nanotube glucose sensors based on electropolymerization. Diam. Relat. Mater. **13**(4–8), 1075–1079 (2004). doi:10.1016/j.diamond.2003.11.009
47. P.R. Roy, M.S. Saha, T. Okajima, S.-G. Park, A. Fujishima, T. Ohsaka, Selective detection of dopamine and its metabolite, DOPAC, in the presence of ascorbic acid using diamond electrode modified by the polymer film. Electroanalysis **16**(21), 1777–1784 (2004). doi:10.1002/elan.200303026
48. C.A. Martínez-Huitle, N. Suely Fernandes, S. Ferro, A. De Battisti, M.A. Quiroz, Fabrication and application of Nafion-modified boron-doped diamond electrode as sensor for detecting caffeine. Diam. Relat. Mater. **19**(10), 1188–1193 (2010). doi:10.1016/j.diamond.2010.05.004
49. A.O. Simm, C.E. Banks, S. Ward-Jones, T.J. Davies, N.S. Lawrence, T.G.J. Jones, L. Jiang, R.G. Compton, Boron-doped diamond microdisc arrays: electrochemical characterisation and their use as a substrate for the production of microelectrode arrays of diverse metals (Ag, Au, Cu) via electrodeposition. Analyst **130**(9), 1303–1311 (2005). doi:10.1039/b506956d
50. C. Batchelor-McAuley, C.E. Banks, A.O. Simm, T.G.J. Jones, R.G. Compton, The electroanalytical detection of hydrazine: a comparison of the use of palladium nanoparticles supported on boron-doped diamond and palladium plated BDD microdisc array. Analyst (Cambridge, UK) **131**(1), 106–110 (2006). doi:10.1039/b513751a
51. C. Batchelor-McAuley, C.E. Banks, A.O. Simm, T.G.J. Jones, R.G. Compton, Nano-electrochemical detection of hydrogen or protons using palladium nanoparticles: distinguishing surface and bulk hydrogen. ChemPhysChem **7**(5), 1081–1085 (2006). doi:10.1002/cphc.200500571
52. A. Salimi, M.E. Hyde, C.E. Banks, R.G. Compton, Boron doped diamond electrode modified with iridium oxide for amperometic detection of ultra trace amounts of arsenic(III). Analyst **129**(1), 9–14 (2004). doi:10.1039/b312285a
53. N. Vinokur, B. Miller, Y. Avyigal, R. Kalish, Cathodic and anodic deposition of mercury and silver at boron-doped diamond electrodes. J. Electrochem. Soc. **146**(1), 125–130 (1999). doi:10.1149/1.1391574
54. I. Gonzalez-Gonzalez, D.A. Tryk, C.R. Cabrera, Polycrystalline boron-doped diamond films as supports for methanol oxidation electrocatalysts. Diam. Relat. Mater. **15**(2–3), 275–278 (2006). doi:10.1016/j.diamond.2005.08.037
55. M. Li, G. Zhao, R. Geng, H. Hu, Facile electrocatalytic redox of hemoglobin by flower-like gold nanoparticles on boron-doped diamond surface. Bioelectrochemical **74**(1), 217–221 (2008). doi:10.1016/j.bioelechem.2008.08.004

56. L.A. Hutton, M. Vidotti, A.N. Patel, M.E. Newton, P.R. Unwin, J.V. MacPherson, Electrodeposition of nickel hydroxide nanoparticles on boron-doped diamond electrodes for oxidative electrocatalysis. J. Phys. Chem. C **115**(5), 1649–1658 (2011). doi:10.1021/jp109526b
57. J.-S. Gao, T. Arunagiri, J.-J. Chen, P. Goodwill, O. Chyan, J. Perez, D. Golden, Preparation and characterization of metal nanoparticles on a diamond surface. Chem. Mater. **12**(11), 3495–3500 (2000). doi:10.1021/cm000465o
58. C. Terashima, T.N. Rao, B.V. Sarada, N. Spataru, A. Fujishima, Electrodeposition of hydrous iridium oxide on conductive diamond electrodes for catalytic sensor applications. J. Electroanal. Chem. **544**, 65–74 (2003). doi:10.1016/S0022-0728(03)00066-4
59. H. Terashima, T. Tsuji, Adsorption of bovine serum albumin onto mica surfaces studied by a direct weighing technique. Colloid Surf. B **27**(2–3), 115–122 (2003). doi:10.1016/s0927-7765(02)00044-9
60. R.B. El, G. Sine, G. Foti, C. Comninellis, A novel method for the preparation of bi-metallic (Pt-Au) nanoparticles on boron doped diamond (BDD) substrate: application to the oxygen reduction reaction. J. Appl. Electrochem. **37**(11), 1227–1236 (2007). doi:10.1007/s10800-007-9359-4
61. R.B. El, G. Foti, C. Comninellis, Preparation of gold nanoparticles by heat treatment of sputter deposited gold on boron-doped diamond film electrode. Electrochem. Commun. **7**(4), 398–405 (2005). doi:10.1016/j.elecom.2005.02.014
62. M. Limat, R.B. El, H. Jotterand, G. Foti, C. Comninellis, Electrochemical and morphological characterization of gold nanoparticles deposited on boron-doped diamond electrode. Electrochim. Acta **54**(9), 2410–2416 (2009). doi:10.1016/j.electacta.2008.02.050
63. T.A. Ivandini, R. Sato, Y. Makide, A. Fujishima, Y. Einaga, Pt-implanted boron-doped diamond electrodes and the application for electrochemical detection of hydrogen peroxide. Diam. Relat. Mater. **14**(11–12), 2133–2138 (2005). doi:10.1016/j.diamond.2005.08.022
64. T.A. Ivandini, R. Sato, Y. Makide, A. Fujishima, Y. Einaga, Electrochemical detection of arsenic(III) using iridium-implanted boron-doped diamond electrodes. Anal. Chem. **78**(18), 6291–6298 (2006). doi:10.1021/ac0519514
65. T.A. Ivandini, R. Sato, Y. Makide, A. Fujishima, Y. Einaga, Electroanalytical application of modified diamond electrodes. Diam. Relat. Mater. **13**(11–12), 2003–2008 (2004). doi:10.1016/j.diamond.2004.07.004
66. S. Treetepvijit, A. Preechaworapun, N. Praphairaksit, U. Chuanuwatanakul, Y. Einaga, O. Chailapakul, Use of nickel implanted boron-doped diamond thin film electrode coupled to HPLC system for the determination of tetracyclines. Talanta **68**(4), 1329–1335 (2006). doi:10.1016/j.talanta.2005.07.047
67. G.R. Salazar-Banda, K.I.B. Eguiluz, L.A. Avaca, Boron-doped diamond powder as catalyst support for fuel cell applications. Electrochem. Commun. **9**(1), 59–64 (2006). doi:10.1016/j.elecom.2006.08.038
68. G.R. Salazar-Banda, H.B. Suffredini, L.A. Avaca, Improved stability of PtOx sol-gel-modified diamond electrodes covered with a Nafion® film. J. Braz. Chem. Soc. **16**(5), 903−905 (2005). doi:10.1590/S0103-50532005000600003
69. H.B. Suffredini, G.R. Salazar-Banda, S.T. Tanimoto, M.L. Calegaro, S.A.S. Machado, L.A. Avaca, AFM studies and electrochemical characterization of boron-doped diamond surfaces modified with metal oxides by the sol-gel method. J. Braz. Chem. Soc. **17**(2), 257−264 (2006). doi:10.1590/S0103-50532006000200007
70. C. Zhang, L. Gu, Y. Lin, Y. Wang, D. Fu, Z. Gu, Degradation of X-3B dye by immobilized TiO_2 photocatalysis coupling anodic oxidation on BDD electrode. J. Photochem. Photobiol. A **207**(1), 66–72 (2009). doi:10.1016/j.jphotochem.2009.01.014
71. F.G. Celii, J.E. Butler, Diamond chemical vapor deposition. Annu. Rev. Phys. Chem. **42**, 643–684 (1991). doi:10.1146/annurev.pc.42.100191.003235
72. J.H.T. Luong, K.B. Male, J.D. Glennon, Boron-doped diamond electrode: synthesis, characterization, functionalization and analytical applications. Analyst (Cambridge, UK) **134**(10), 1965–1979 (2009). doi:10.1039/b910206j

73. K.B. Holt, A.J. Bard, Y. Show, G.M. Swain, Scanning electrochemical microscopy and conductive probe atomic force microscopy studies of hydrogen-terminated boron-doped diamond electrodes with different doping levels. J. Phys. Chem. B **108**(39), 15117–15127 (2004). doi:10.1021/jp048222x
74. G. Sine, G. Foti, C. Comninellis, Boron-doped diamond (BDD)-supported Pt/Sn nanoparticles synthesized in microemulsion systems as electrocatalysts of ethanol oxidation. J. Electroanal. Chem. **595**(2), 115–124 (2006). doi:10.1016/j.jelechem.2006.07.012
75. I. Yagi, T. Ishida, K. Uosaki, Electrocatalytic reduction of oxygen to water at Au nanoclusters vacuum-evaporated on boron-doped diamond in acidic solution. Electrochem. Commun. **6**(8), 773–779 (2004). doi:10.1016/j.elecom.2004.05.025
76. S. Hrapovic, Y. Liu, J.H.T. Luong, Reusable platinum nanoparticle modified boron doped diamond microelectrodes for oxidative determination of arsenite. Anal. Chem. **79**(2), 500–507 (2007). doi:10.1021/ac061528a
77. Y. Zhang, V. Suryanarayanan, I. Nakazawa, S. Yoshihara, T. Shirakashi, Electrochemical behavior of Au nanoparticle deposited on as-grown and O-terminated diamond electrodes for oxygen reduction in alkaline solution. Electrochim. Acta **49**(28), 5235–5240 (2004). doi:10.1016/j.electacta.2004.07.005
78. H. Notsu, I. Yagi, T. Tatsuma, D.A. Tryk, A. Fujishima, Introduction of oxygen-containing functional groups onto diamond electrode surfaces by oxygen plasma and anodic polarization. Electrochem. Solid State Lett. **2**(10), 522–524 (1999). doi:10.1149/1.1390890
79. A.O. Simm, X. Ji, C.E. Banks, M.E. Hyde, R.G. Compton, AFM studies of metal deposition: instantaneous nucleation and the growth of cobalt nanoparticles on boron-doped diamond electrodes. ChemPhysChem **7**(3), 704–709 (2006). doi:10.1002/cphc.200500557
80. D.W.M. Arrigan, Nanoelectrodes, nanoelectrode arrays, and their applications. Analyst **129**, 1157–1165 (2004). doi:10.1039/B415395M
81. F. Maillard, M. Eikerling, O.V. Cherstiouk, S. Schreier, E. Savinova, U. Stimming, Size effects on reactivity of Pt nanoparticles in CO monolayer oxidation: the role of surface mobility. Faraday Discuss. **125**, 357–377 (2004). doi:10.1039/B303911K
82. S.R. Belding, E.J.F. Dickinson, R.G. Compton, Diffusional cyclic voltammetry at electrodes modified with random distributions of electrocatalytic nanoparticles: theory. J. Phys. Chem. C **113**(25), 11149–11156 (2009). doi:10.1021/jp901664p
83. L.A. Hutton, M.E. Newton, P.R. Unwin, J.V. MacPherson, Factors controlling stripping voltammetry of lead at polycrystalline boron doped diamond electrodes: new insights from high-resolution microscopy. Anal. Chem. **83**(3), 735–745 (2011). doi:10.1021/ac101626s
84. S.H. Brewer, W.R. Glomm, M.C. Johnson, M.K. Knag, S. Franzen, Probing BSA binding to citrate-coated gold nanoparticles and surfaces. Langmuir **21**(20), 9303–9307 (2005). doi:10.1021/la050588t
85. U. Griesbach, D. Zollinger, H. Putter, C. Comninellis, Evaluation of boron doped diamond electrodes for organic electrosynthesis on a preparative scale. J. Appl. Electrochem. **35**(12), 1265–1270 (2005). doi:10.1007/s10800-005-9038-2
86. C. Terashima, T.N. Rao, B.V. Sarada, A. Fujishima, Electrochemical characteristics of electrodeposited iridium oxide on conductive diamond electrodes. Chem. Sens. **18**(Suppl. B), 106–108 (2002)
87. D.V. Bavykin, E.V. Milsom, F. Marken, D.H. Kim, D.H. Marsh, D.J. Riley, F.C. Walsh, K.H. El-Abiary, A.A. Lapkin, A novel cation-binding TiO_2 nanotube substrate for electro- and bioelectrocatalysis. Electrochem. Commun. **7**(10), 1050–1058 (2005). doi:10.1016/j.elecom.2005.07.010
88. K.J. McKenzie, F. Marken, Electrochemical characterization of hydrous ruthenium oxide nanoparticle decorated boron-doped diamond electrodes. ECS Solid State Lett. **5**(9), E47–E50 (2002). doi:10.1149/1.1497515
89. M.E. Hyde, R.G. Compton, A review of the analysis of multiple nucleation with diffusion controlled growth. J. Electroanal. Chem. **549**(0), 1–12 (2003). doi:http://dx.doi.org/10.1016/S0022-0728(03)00250-X

90. D. Grujicic, B. Pesic, Iron nucleation mechanisms on vitreous carbon during electrodeposition from sulfate and chloride solutions. Electrochim. Acta **50**(22), 4405–4418 (2005). doi:http://dx.doi.org/10.1016/j.electacta.2005.02.013
91. D. Grujicic, B. Pesic, Reaction and nucleation mechanisms of copper electrodeposition from ammoniacal solutions on vitreous carbon. Electrochim. Acta **50**(22), 4426–4443 (2005). doi:http://dx.doi.org/10.1016/j.electacta.2005.02.012
92. S. Jones, K. Tedsree, M. Sawangphruk, J.S. Foord, J. Fisher, D. Thompsett, S.C.E. Tsang, Promotion of direct methanol electro-oxidation by Ru terraces on Pt by using a reversed spillover mechanism. ChemCatChem **2**(9), 1089–1095 (2010). doi:10.1002/cctc.201000106
93. M.E. Hyde, R. Jacobs, R.G. Compton, In situ AFM studies of metal deposition. J. Phys. Chem. B **106**(43), 11075–11080 (2002). doi:10.1021/jp0213607
94. B.R. Scharifker, J. Mostany, Three-dimensional nucleation with diffusion controlled growth: Part I. Number density of active sites and nucleation rates per site. J. Electroanal. Chem. Interf. Electrochem. **177**(1–2), 13–23 (1984). doi:http://dx.doi.org/10.1016/0022-0728(84)80207-7
95. K.E. Toghill, G.G. Wildgoose, A. Moshar, C. Mulcahy, R.G. Compton, The fabrication and characterization of a bismuth nanoparticle modified boron doped diamond electrode and its application to the simultaneous determination of cadmium(II) and lead(II). Electroanalysis **20**(16), 1731–1737 (2008). doi:10.1002/elan.200804277
96. Z.D. Wei, S.H. Chan, Electrochemical deposition of PtRu on an uncatalyzed carbon electrode for methanol electrooxidation. J. Electroanal. Chem. **569**(1), 23–33 (2004). doi:10.1016/j.jelechem.2004.01.034
97. N.R. Stradiotto, K.E. Toghill, L. Xiao, A. Moshar, R.G. Compton, The fabrication and characterization of a nickel nanoparticle modified boron doped diamond electrode for electrocatalysis of primary alcohol oxidation. Electroanalysis **21**(24), 2627–2633 (2009). doi:10.1002/elan.200900325
98. M. Valden, X. Lai, D.W. Goodman, Onset of catalytic activity of gold clusters on titania with the appearance of nonmetallic properties. Science **281**(5383), 1647–1650 (1998). doi:10.1126/science.281.5383.1647
99. A. Sanchez, S. Abbet, U. Heiz, W.D. Schneider, H. Häkkinen, R.N. Barnett, U. Landman, When gold is not noble: nanoscale gold catalysts. J. Phys. Chem. A **103**(48), 9573–9578 (1999). doi:10.1021/jp9935992
100. M. Mavrikakis, P. Stoltze, J.K. Nørskov, Making gold less noble. Catal. Lett. **64**(2–4), 101–106 (2000). doi:10.1023/A:1019028229377
101. G. Sine, D. Smida, M. Limat, G. Foti, C. Comninellis, Microemulsion synthesized Pt/Ru/Sn nanoparticles on BDD for alcohol electro-oxidation. J. Electrochem. Soc. **154**(2), B170–B174 (2007). doi:10.1149/1.2400602
102. G. Sine, C. Comninellis, Nafion-assisted deposition of microemulsion-synthesized platinum nanoparticles on BDD. Electrochim. Acta **50**(11), 2249–2254 (2005). doi:10.1016/j.electacta.2004.10.008
103. O. Niwa, Electroanalytical chemistry with carbon film electrodes and micro and nano-structured carbon film-based electrodes. Bull. Chem. Soc. Jpn. **78**(4), 555–571 (2005). doi:10.1246/bcsj.78.555
104. J. Wang, G.M. Swain, Fabrication and evaluation of platinum/diamond composite electrodes for electrocatalysis—preliminary studies of the oxygen-reduction reaction. J. Electrochem. Soc. **150**(1), E24–E32 (2003). doi:10.1149/1.1524612
105. F. Montilla, E. Morallon, I. Duo, C. Comninellis, J.L. Vazquez, Platinum particles deposited on synthetic boron-doped diamond surfaces. Application to methanol oxidation. Electrochim. Acta **48**(25–26), 3891–3897 (2003). doi:10.1016/s0013-4686(03)00526-7
106. I. Duo, C. Comninellis, W. Haenni, A. Perret, Deposition of nanoparticles of iridium dioxide on a synthetic boron-doped diamond surface. Proc. Electrochem. Soc. **2001–2025** (Diamond Materials VII), 147–156 (2002)
107. A.J. Saterlay, S.J. Wilkins, K.B. Holt, J.S. Foord, R.G. Compton, F. Marken, Lead dioxide deposition and electrocatalysis at highly boron-doped diamond electrodes in the presence of ultrasound. J. Electrochem. Soc. **148**(2), E66–E72 (2001). doi:10.1149/1.339874

108. X.A. Lu, J.P. Hu, J.S. Foord, Q.A. Wang, Electrochemical deposition of Pt-Ru on diamond electrodes for the electrooxidation of methanol. J. Electroanal. Chem. **654**(1–2), 38–43. doi:10.1016/j.jelechem.2011.01.034
109. M.E. Hyde, C.E. Banks, R.G. Compton, Anodic stripping voltammetry: an AFM study of some problems and limitations. Electroanalysis **16**(5), 345–354 (2004). doi:10.1002/elan.200302863
110. N.R. Stradiotto, K.E. Toghill, L. Xiao, A. Moshar, R.G. Compton, The fabrication and characterization of a nickel nanoparticle modified boron-doped diamond electrode for electrocatalysis of primary alcohol oxidation. Electroanalysis **21**(24), 2627–2633 (2009). doi:10.1002/elan.200900325
111. F. Marken, A.S. Bhambra, D.-H. Kim, R.J. Mortimer, S.J. Stott, Electrochemical reactivity of TiO2 nanoparticles adsorbed onto boron-doped diamond surfaces. Electrochem. Commun. **6**(11), 1153–1158 (2004). doi:10.1016/j.elecom.2004.09.006
112. J.L. Barton, J.O.M. Bockris, The electrolytic growth of dendrites from ionic solutions. Proc. R. Soc. A **268**, 485–505 (1962). doi:10.1098/rspa.1962.0154
113. P. Milan, S. Mordechay, Kinetics and mechanism of electrodeposition, in *Fundamentals of Electrochemical Deposition* (Wiley, New York, 2006)
114. A. Thalhammer, R.J. Edgington, L.A. Cingolani, R. Schoepfer, R.B. Jackman, The use of nanodiamond monolayer coatings to promote the formation of functional neuronal networks. Biomater. **31**(8), 2097–2104 (2010). doi:http://dx.doi.org/10.1016/j.biomaterials.2009.11.109
115. R. Lam, M. Chen, E. Pierstorff, H. Huang, E. Osawa, D. Ho, Nanodiamond-embedded microfilm devices for localized chemotherapeutic elution. ACS Nano **2**(10), 2095–2102 (2008). doi:10.1021/nn800465x
116. Y. Wang, J. Zhi, Y. Liu, J. Zhang, Electrochemical detection of surfactant cetylpyridinium bromide using boron-doped diamond as electrode. Electrochem. Commun. **13**(1), 82–85 (2011). doi:10.1016/j.elecom.2010.11.019
117. B. Guan, J. Zhi, Nanodiamond as pH-responsive vehicle for an anti-cancer drug. Small **6**(14), 1514−1519 (2010). doi:10.1002/smll.200902305
118. R.S. Lewis, T. Ming, J.F. Wacker, E. Anders, E. Steel, Interstellar diamonds in meteorites. Nature **326**(6109) (1987). doi:10.1038/326160a0
119. V. Danilenko, Shock-wave sintering of nanodiamonds. Phys. Solid State **46**(4), 711–715 (2004). doi:10.1134/1.1711456
120. S. Osswald, G. Yushin, V. Mochalin, S.O. Kucheyev, Y. Gogotsi, Control of sp^2/sp^3 carbon ratio and surface chemistry of nanodiamond powders by selective oxidation in air. J. Am. Chem. Soc. **128**(35), 11635–11642 (2006). doi:10.1021/ja063303n
121. A. Krueger, M. Ozawa, G. Jarre, Y. Liang, J. Stegk, L. Lu, Deagglomeration and functionalisation of detonation diamond. Phy. Status Solidi (a) **204**(9), 2881–2887 (2007). doi:10.1002/pssa.200776330
122. B. Palosz, C. Pantea, E. Grzanka, S. Stelmakh, T. Proffen, T.W. Zerda, W. Palosz, Investigation of relaxation of nanodiamond surface in real and reciprocal spaces. Diam. Relat. Mater. **15**(11–12), 1813–1817 (2006). doi:10.1016/j.diamond.2006.09.001
123. Y. Liu, Z.N. Gu, J.L. Margrave, V.N. Khabashesku, Functionalization of nanoscale diamond powder: fluoro-, alkyl-, amino-, and amino acid-nanodiamond derivatives. Chem. Mater. **16**(20), 3924–3930 (2004). doi:10.1021/cm048875q
124. I. Kulakova, Surface chemistry of nanodiamonds. Phys. Solid. State **46**(4), 636–643 (2004)
125. A. Hartl, E. Schmich, J.A. Garrido, J. Hernando, S.C.R. Catharino, S. Walter, P. Feulner, A. Kromka, D. Steinmuller, M. Stutzmann, Protein-modified nanocrystalline diamond thin films for biosensor applications. Nat. Mater. **3**(10), 736–742 (2004). doi:http://www.nature.com/nmat/journal/v3/n10/suppinfo/nmat1204_S1.html
126. F. Neugart, A. Zappe, F. Jelezko, C. Tietz, J.P. Boudou, A. Krueger, J. Wrachtrup, Dynamics of diamond nanoparticles in solution and cells. Nano Lett. **7**(12), 3588–3591 (2007). doi:10.1021/nl0716303
127. P.H. Chung, E. Perevedentseva, C.L. Cheng, The particle size-dependent photoluminescence of nanodiamonds. Surf. Sci. **601**(18), 3866–3870 (2007). doi:10.1016/j.susc.2007.04.150

128. O.A. Williams, J. Hees, C. Dieker, W. Jager, L. Kirste, C.E. Nebel, Size-dependent reactivity of diamond nanoparticles. ACS Nano **4**(8), 4824–4830 (2010). doi:10.1021/nn100748k
129. V.S. Bondar, I.O. Pozdnyakova, A.P. Puzyr, Applications of nanodiamonds for separation and purification of proteins. Phys. Solid State **46**(4), 758–760 (2004). doi:10.1134/1.1711468
130. D. Shin, H. Watanabe, C.E. Nebel, Insulator–metal transition of intrinsic diamond. J. Am. Chem. Soc. **127**(32), 11236–11237 (2005). doi:10.1021/ja052834t
131. C.E. Nebel, H. Kato, B. Rezek, D. Shin, D. Takeuchi, H. Watanabe, T. Yamamoto, Electrochemical properties of undoped hydrogen terminated CVD diamond. Diam. Relat. Mater. **15**(2–3), 264–268 (2006). doi:http://dx.doi.org/10.1016/j.diamond.2005.08.012
132. V. Chakrapani, J.C. Angus, A.B. Anderson, S.D. Wolter, B.R. Stoner, G.U. Sumanasekera, Charge transfer equilibria between diamond and an aqueous oxygen electrochemical redox couple. Science **318**(5855), 1424–1430 (2007). doi:10.1126/science.1148841
133. K.B. Holt, D.J. Caruana, E.J. Millan-Barrios, Electrochemistry of undoped diamond nanoparticles: accessing surface redox states. J. Am. Chem. Soc. **131**(32), 11272–11273 (2009). doi:10.1021/ja902216n
134. T. Bruelle, A. Denisenko, H. Sternschulte, U. Stimming, Catalytic activity of platinum nanoparticles on highly boron-doped and 100-oriented epitaxial diamond towards HER and HOR. Phys. Chem. Chem. Phys. **13**(28), 12883–12891 (2011). doi:10.1039/c1cp20852g
135. A.S. Barnard, M. Sternberg, Crystallinity and surface electrostatics of diamond nanocrystals. J. Mater. Chem. **17**(45), 4811–4819 (2007). doi:10.1039/b710189a
136. J. Zang, Y. Wang, L. Bian, J. Zhang, F. Meng, Y. Zhao, S. Ren, X. Qu, Surface modification and electrochemical behaviour of undoped nanodiamonds. Electrochim. Acta **72**, 68–73 (2012). doi:10.1016/j.electacta.2012.03.169
137. L. Wang, Y.Gao, Q. Xue, H. Liu, T. Xu, Effects of nano-diamond particles on the structure and tribological property of Ni-matrix nanocomposite coatings. Mater. Sci. Eng. A **A390** (1–2), 313–318 (2005). doi:10.1016/j.msea.2004.08.033
138. L. La-Torre-Riveros, K. Soto, M.A. Scibioh, C.R. Cabrera, Electrophoretically fabricated diamond nanoparticle-based electrodes. J. Electrochem. Soc. **157**(6), B831–B836 (2010). doi:10.1149/1.3374403
139. X.Y. Zhao, J.B. Zang, Y.H. Wang, L.Y. Bian, J.K. Yu, Electropolymerizing polyaniline on undoped 100 nm diamond powder and its electrochemical characteristics. Electrochem. Commun. **11**(6), 1297–1300 (2009). doi:10.1016/j.elecom.2009.04.029
140. J. Zang, Y. Wang, X. Zhao, G. Xin, S. Sun, X. Qu, S. Ren, Electrochemical synthesis of polyaniline on nanodiamond powder. Int. J. Electrochem. Sci. **7**(2), 1677–1687 (2012)
141. E. Tamburri, S. Orlanducci, V. Guglielmotti, G. Reina, M. Rossi, M.L. Terranova, Engineering detonation nanodiamond—polyaniline composites by electrochemical routes: structural features and functional characterizations. Polymer **52**(22), 5001–5008 (2011). doi:10.1016/j.polymer.2011.09.003
142. E. Tamburri, V. Guglielmotti, S. Orlanducci, M.L. Terranova, D. Sordi, D. Passeri, R. Matassa, M. Rossi, Nanodiamond-mediated crystallization in fibers of PANI nanocomposites produced by template-free polymerization: conductive and thermal properties of the fibrillar networks. Polymer **53**(19), 4045–4053 (2012). doi:10.1016/j.polymer.2012.07.014
143. H. Zhuang, B. Song, T. Staedler, X. Jiang, Microcontact printing of monodiamond nanoparticles: an effective route to patterned diamond structure fabrication. Langmuir **27**(19), 11981–11989 (2011). doi:10.1021/la2024428
144. W. Hongthani, D.J. Fermin, Layer-by-layer assembly and redox properties of undoped HPHT diamond particles. Diam. Relat. Mater. **19**(7–9), 680–684 (2010). doi:10.1016/j.diamond.2010.01.039
145. G.L. Bilbro, Theory of electrodeposition of diamond nanoparticles. Diam. Relat. Mater. **11** (8), 1572–1577 (2002). doi:10.1016/S0925-9635(02)00104-8
146. L.-N. Tsai, G.-R. Shen, Y.-T. Cheng, W. Hsu, Performance improvement of an electrothermal microactuator fabricated using Ni-diamond nanocomposite. J. Microelectromech. Syst. **15**(1), 149–158 (2006). doi:10.1109/JMEMS.2005.863737

147. E.A. Levashov, P.V. Vakaev, E.I. Zamulaeva, A.E. Kudryashov, V.V. Kurbatkina, D.V. Shtansky, A.A. Voevodin, A. Sanz, Disperse-strengthening by nanoparticles advanced tribological coatings and electrode materials for their deposition. Surf. Coat. Technol. **201** (13), 6176–6181 (2007). doi:10.1016/j.surfcoat.2006.08.134
148. T. Fujimura, V.Y. Dolmatov, G.K. Burkat, E.A. Orlova, M.V. Veretennikova, Electrochemical codeposition of Sn-Pb-metal alloy along with detonation synthesis nanodiamonds. Diam. Relat. Mater. **13**(11–12), 2226–2229 (2004). doi:10.1016/j.diamond.2004.06.009
149. L.Y. Bian, Y.H. Wang, J. Lu, J.B. Zang, Synthesis and electrochemical properties of TiO2/nanodiamond nanocomposite. Diam. Relat. Mater. **19**(10), 1178–1182 (2010). doi:10.1016/j.diamond.2010.05.007
150. L.Y. Bian, Y.H. Wang, J.B. Zang, F.W. Meng, Y.L. Zhao, Detonation-synthesized nanodiamond as a stable support of Pt electrocatalyst for methanol electrooxidation. Int. J. Electrochem. Sci. **7**(8), 7295–7303 (2012)
151. L. La-Torre-Riveros, R. Guzman-Blas, A.E. Mendez-Torres, M. Prelas, D.A. Tryk, C.R. Cabrera, Diamond nanoparticles as a support for Pt and Pt-Ru catalysts for direct methanol fuel cells. ACS Appl. Mater. Interfaces **4**(2), 1134–1147 (2012). doi:10.1021/am2018628
152. L. La-Torre-Riveros, E. Abel-Tatis, A.E. Mendez-Torres, D.A. Tryk, M. Prelas, C.R. Cabrera, Synthesis of platinum and platinum-ruthenium-modified diamond nanoparticles. J. Nanopart. Res. **13**(7), 2997–3009 (2011). doi:10.1007/s11051-010-0196-8
153. L. Cunci, C.R. Cabrera, Preparation and electrochemistry of boron-doped diamond nanoparticles on glassy carbon electrodes. Electrochem. Solid State Lett. **14**(3), K17–K19 (2011). doi:10.1149/1.3532943
154. J. Scholz, A.J. McQuillan, K.B. Holt, Redox transformations at nanodiamond surfaces revealed by in situ infrared spectroscopy. Chem. Commun. **47**(44), 12140–12142 (2011). doi:10.1039/C1CC14961J
155. D. Plana, J.J.L. Humphrey, K.A. Bradley, V. Celorrio, D.J. Fermín, Charge transport across high surface area metal/diamond nanostructured composites. ACS Appl. Mater. Interf. **5**(8), 2985–2990 (2013). doi:10.1021/am302397p
156. T. Kondo, K. Hirata, T. Kawai, M. Yuasa, Self-assembled fabrication of a polycrystalline boron-doped diamond surface supporting Pt (or Pd)/Au-shell/core nanoparticles on the (111) facets and Au nanoparticles on the (100) facets. Diam. Relat. Mater. **20**(8), 1171–1178 (2011). doi:http://dx.doi.org/10.1016/j.diamond.2011.06.033
157. V.A. Plotnikov, B.F. Dem'yanov, S.V. Makarov, Effects of aluminum on the interaction of detonation diamond nanocrystals during high-temperature annealing. Tech. Phys. Lett. **35**(5), 473–475 (2009). doi:10.1134/S1063785009050265
158. K.E. Toghill, L. Xiao, N.R. Stradiotto, R.G. Compton, The determination of methanol using an electrolytically fabricated nickel microparticle modified boron doped diamond electrode. Electroanalysis **22**(5), 491–500 (2010). doi:10.1002/elan.200900523
159. A.M. Panich, A. Altman, A.I. Shames, V.Y. Osipov, A.E. Aleksenskiy, A.Y. Vul, Proton magnetic resonance study of diamond nanoparticles decorated by transition metal ions. J. Phys. D Appl. Phys. **44**(12), 125303 (2011). doi:10.1088/0022-3727/44/12/125303
160. A.M. Panich, A.I. Shames, O. Medvedev, V.Y. Osipov, A.E. Aleksenskiy, A.Y. Vul', Magnetic resonance study of detonation nanodiamonds with surface chemically modified by transition metal ions. Appl. Magn. Reson. **36**(2–4), 317–329 (2009). doi:10.1007/s00723-009-0028-0
161. H.J. Looi, L.Y.S. Pang, M.D. Whitfield, J.S. Foord, R.B. Jackman, Engineering low resistance contacts on p-type hydrogenated diamond surfaces. Diam. Relat. Mater. **9**(3–6), 975–981 (2000). doi:http://dx.doi.org/10.1016/S0925-9635(00)00240-5
162. Y. Jia, W. Zhu, E.G. Wang, Y. Huo, Z. Zhang, Initial stages of Ti growth on eiamond (100) surfaces: from single adatom diffusion to quantum wire formation. Phys. Rev. Lett. **94**(8), 086101 (2005). doi:10.1103/PhysRevLett.94.086101

163. S. Stehlik, T. Petit, H.A. Girard, J.-C. Arnault, A. Kromka, B. Rezek, Nanoparticles assume electrical potential according to substrate, size, and surface termination. Langmuir **29**(5), 1634–1641 (2013). doi:10.1021/la304472w
164. I. Motochi, N.W. Makau, G.O. Amolo, Metal–semiconductor ohmic contacts: an ab initio density functional theory study of the structural and electronic properties of metal–diamond (111)-(1x1) interfaces. Diam. Relat. Mater. **23** 10–17 (2012). doi:http://dx.doi.org/10.1016/j.diamond.2011.12.021
165. M.W. Geis, J.C. Twichell, T.M. Lyszczarz, Diamond emitters fabrication and theory. J. Vac. Sci. Technol. B **14**(3), 2060–2067 (1996). doi:10.1116/1.588986
166. T. Tyler, V.V. Zhirnov, A.V. Kvit, D. Kang, J.J. Hren, Electron emission from diamond nanoparticles on metal tips. Appl. Phys. Lett. **82**(17), 2904–2906 (2003). doi:10.1063/1.1570498
167. N.S. Xu, Y. Tzeng, R.V. Latham, Similarities in the 'cold' electron emission characteristics of diamond coated molybdenum electrodes and polished bulk graphite surfaces. J. Phys. D Appl. Phys. **26**(10), 1776 (1993). doi:10.1088/0022-3727/26/10/035
168. V.V. Zhirnov, E.I. Givargizov, P.S. Plekhanov, Field emission from silicon spikes with diamond coatings. J. Vac. Sci. Technol. B **13**(2), 418–421 (1995). doi:10.1116/1.587960
169. A.V. Karabutov, V.D. Frolov, V.I. Konov, Diamond/sp^2-bonded carbon structures: quantum well field electron emission? Diam. Relat. Mater. **10**(3–7), 840–846 (2001). doi:http://dx.doi.org/10.1016/S0925-9635(00)00569-0
170. Y. Takasu, S. Konishi, W. Sugimoto, Y. Murakami, Catalytic formation of nanochannels in the surface layers of diamonds by metal nanoparticles. Electrochem. Solid State Lett. **9**(7), C114–C117 (2006). doi:10.1149/1.2201995
171. T. Brulle, A. Denisenko, H. Sternschulte, U. Stimming, Catalytic activity of platinum nanoparticles on highly boron-doped and 100-oriented epitaxial diamond towards HER and HOR. Phys. Chem. Chem. Phys. **13**(28), 12883–12891 (2011). doi:10.1039/C1CP20852G
172. I. Casella, M. Contursi, Cobalt oxide electrodeposition on various electrode substrates from alkaline medium containing Co–gluconate complexes: a comparative voltammetric study. J Solid State Electrochem. **16**(12), 3739–3746 (2012). doi:10.1007/s10008-012-1794-4
173. S.A. Yao, R.E. Ruther, L. Zhang, R.A. Franking, R.J. Hamers, J.F. Berry, Covalent attachment of catalyst molecules to conductive diamond: CO_2 reduction using "smart" electrodes. J. Am. Chem. Soc. **134**(38), 15632–15635 (2012). doi:10.1021/ja304783j
174. I. Zegkinoglou, P.L. Cook, P.S. Johnson, W. Yang, J. Guo, D. Pickup, R. González-Moreno, C. Rogero, R.E. Ruther, M.L. Rigsby, J.E. Ortega, R.J. Hamers, F.J. Himpsel, Electronic structure of diamond surfaces functionalized by $Ru(tpy)_2$. J. Phys. Chem. C **116**(26), 13877–13883 (2012). doi:10.1021/jp304016t
175. P. Wang, M. Cao, Y. Ao, C. Wang, J. Hou, J. Qian, Investigation on Ce-doped TiO_2-coated BDD composite electrode with high photoelectrocatalytic activity under visible light irradiation. Electrochem. Commun. **13**(12), 1423–1426 (2011). doi:10.1016/j.elecom.2011.09.009
176. T. Ochiai, K. Nakata, T. Murakami, A. Fujishima, Y. Yao, D.A. Tryk, Y. Kubota, Development of solar-driven electrochemical and photocatalytic water treatment system using a boron-doped diamond electrode and TiO_2 photocatalyst. Water Res. **44**(3), 904–910 (2010). doi:10.1016/j.watres.2009.09.060
177. T. Zhao, J. Wang, L. Jiang, T. Cheng, Method for manufacturing titania and boron-doped diamond (BDD) composite photoelectrocatalytic synergistic electrode. CN101875007A
178. J.T. Matsushima, A.B. Couto, N.G. Ferreira, M.R. Baldan, Study of the electrochemical deposition of Cu/Sn alloy nanoparticles on boron doped diamond films for electrocatalytic nitrate reduction. MRS Online Proc. Libr. **1511** (Diamond Electronics and Biotechnology), opl.2013.2016, 2016 pp. (2012). doi:10.1557/opl.2013.16
179. M.-J. Song, J.-H. Kim, S.-K. Lee, D.-S. Lim, Fabrication of Pt nanoparticles-decorated CVD diamond electrode for biosensor applications. Anal. Sci. **27**(10), 985–989 (2011). doi:10.2116/analsci.27.985

180. L.Y. Bian, Y.H. Wang, J.B. Zang, J.K. Yu, H. Huang, Electrodeposition of Pt nanoparticles on undoped nanodiamond powder for methanol oxidation electrocatalysts. J. Electroanal. Chem. **644**(1), 85–88 (2010). doi:10.1016/j.jelechem.2010.04.001
181. N. Yang, F. Gao, C.E. Nebel, Diamond decorated with copper nanoparticles for electrochemical reduction of carbon dioxide. Anal. Chem. **85**(12), 5764–5769 (2013). doi:10.1021/ac400377y
182. L. La-Torre-Riveros, E. Abel-Tatis, A.E. Méndez-Torres, D.A. Tryk, M. Prelas, C.R. Cabrera, Synthesis of platinum and platinum-ruthenium-modified diamond nanoparticles. J. Nanopart. Res. **13**(7), 2997–3009 (2011). doi:10.1007/s11051-010-0196-8
183. P. Kim, J.B. Joo, W. Kim, J. Kim, I.K. Song, J. Yi, $NaBH_4$-assisted ethylene glycol reduction for preparation of carbon-supported Pt catalyst for methanol electro-oxidation. J. Power Sources **160**(2), 987–990 (2006). doi:10.1016/j.jpowsour.2006.02.050
184. Y. Liu, Z. Gu, J.L. Margrave, V.N. Khabashesku, Functionalization of nanoscale diamond powder: fluoro-, alkyl-, amino-, and amino acid-nanodiamond derivatives. Chem. Mater. **16** (20), 3924–3930 (2004). doi:10.1021/cm048875q
185. A. Barras, S. Szunerits, L. Marcon, N. Monfilliette-Dupont, R. Boukherroub, Functionalization of diamond nanoparticles using "click" chemistry. Langmuir **26**(16), 13168–13172 (2010). doi:10.1021/la101709q
186. A. Krueger, D. Lang, Functionality is key: recent progress in the surface modification of nanodiamond. Adv. Func. Mater. **22**(5), 890–906 (2012). doi:10.1002/adfm.201102670
187. C.-M. Sung, Diamond neural devices and associated methods. US20110282421A1
188. A. Thalhammer, R.J. Edgington, L.A. Cingolani, R. Schoepfer, R.B. Jackman, The use of nanodiamond monolayer coatings to promote the formation of functional neuronal networks. Biomaterials. **31**(8), 2097–2104 (2010). doi:10.1016/j.biomaterials.2009.11.109
189. N. Yang, R. Hoffmann, W. Smirnov, C.E. Nebel, Interface properties of cytochrome c on a nano-textured diamond surface. Diam. Relat. Mater. **20**(2), 269–273 (2011). doi:10.1016/j.diamond.2010.12.012
190. N. Yang, W. Smirnov, A. Kriele, R. Hoffmann, C.E. Nebel, Diamond nanotextured surfaces for enhanced protein redox activity. Phys. Status Solidi (a) **207**(9), 2069–2072 (2010). doi:10.1002/pssa.201000085
191. B.C. Janegitz, R.A. Medeiros, R.C. Rocha-Filho, O. Fatibello-Filho, Direct electrochemistry of tyrosinase and biosensing for phenol based on gold nanoparticles electrodeposited on a boron-doped diamond electrode. Diam. Relat. Mater. **25**, 128–133 (2012). doi:10.1016/j.diamond.2012.02.023
192. A. Liu, Q. Ren, T. Xu, M. Yuan, W. Tang, Morphology-controllable gold nanostructures on phosphorus doped diamond-like carbon surfaces and their electrocatalysis for glucose oxidation. Sens. Actuators B **162**(1), 135–142 (2012). doi:10.1016/j.snb.2011.12.050
193. M.-J. Song, S.-K. Lee, J.-H. Kim, D.-S. Lim, Dopamine sensor based on a boron-doped diamond electrode modified with a polyaniline/Au nanocomposites in the presence of ascorbic acid. Anal. Sci. **28**(6), 583–587 (2012). doi:10.2116/analsci.28.583
194. Y. Yu, Y. Zhou, L. Wu, J. Zhi, Electrochemical biosensor based on boron-doped diamond electrodes with modified surfaces. Int. J. Electrochem. **2012**, (2012). doi:10.1155/2012/567171
195. B. Liu, J. Hu, J.S. Foord, Electrochemical detection of DNA hybridization by a zirconia modified diamond electrode. Electrochem. Commun. **19**, 46–49 (2012). doi:10.1016/j.elecom.2012.03.007
196. A. Zeng, C. Jin, S.-J. Cho, H.O. Seo, Y.D. Kim, D.C. Lim, D.H. Kim, B. Hong, J.-H. Boo, Nickel nano-particle modified nitrogen-doped amorphous hydrogenated diamond-like carbon film for glucose sensing. Mater. Res. Bull. **47**(10), 2713–2716 (2012). doi:10.1016/j.materresbull.2012.04.041
197. W. Wu, R. Xie, L. Bai, Z. Tang, Z. Gu, Direct electrochemistry of Shewanella loihica PV-4 on gold nanoparticles-modified boron-doped diamond electrodes fabricated by layer-by-layer technique. J. Nanosci. Nanotechnol. **12**(5), 3903–3908 (2012). doi:10.1166/jnn.2012.6175

198. C.-C. Wu, C.-C. Han, H.-C. Chang, Applications of surface-functionalized diamond nanoparticles for mass-spectrometry-based proteomics. J. Chin. Chem. Soc. **57**(3B), 583–594 (2010). doi:10.1002/jccs.201000082
199. X. Fuku, F. Iftikar, E. Hess, E. Iwuoha, P. Baker, Cytochrome c biosensor for determination of trace levels of cyanide and arsenic compounds. Anal. Chim. Acta **730**, 49–59 (2012). doi:10.1016/j.aca.2012.02.025
200. R. Hoffmann, A. Kriele, S. Kopta, W. Smirnov, N. Yang, C.E. Nebel, Adsorption of cytochrome c on diamond. Physica Status Solidi (a) **207**(9), 2073–2077 (2010). doi:10.1002/pssa.201000043
201. A. Rahim Ruslinda, K. Tanabe, S. Ibori, X. Wang, H. Kawarada, Effects of diamond-FET-based RNA aptamer sensing for detection of real sample of HIV-1 Tat protein. Biosens. Bioelectron. **40**(1), 277–282 (2013). doi:http://dx.doi.org/10.1016/j.bios.2012.07.048
202. M.-J. Song, S.-K. Lee, J.-Y. Lee, J.-H. Kim, D.-S. Lim, Electrochemical sensor based on Au nanoparticles decorated boron-doped diamond electrode using ferrocene-tagged aptamer for proton detection. J. Electroanal. Chem. **677–680**, 139–144 (2012). doi:10.1016/j.jelechem.2012.05.019
203. D.T. Tran, V. Vermeeren, L. Grieten, S. Wenmackers, P. Wagner, J. Pollet, K.P.F. Janssen, L. Michiels, J. Lammertyn, Nanocrystalline diamond impedimetric aptasensor for the label-free detection of human IgE. Biosens. Bioelectron. **26**(6), 2987–2993 (2011). doi:10.1016/j.bios.2010.11.053
204. X. Fuku, F. Iftikar, E. Hess, E. Iwuoha, P. Baker, Cytochrome c biosensor for determination of trace levels of cyanide and arsenic compounds. Anal. Chim. Acta **730**(0), 49–59 (2012). doi:http://dx.doi.org/10.1016/j.aca.2012.02.025
205. A. Kriele, O.A. Williams, M. Wolfer, J.J. Hees, W. Smirnov, C.E. Nebel, Formation of nano-pores in nano-crystalline diamond films. Chem. Phys. Lett. **507**(4–6), 253–259 (2011). doi:10.1016/j.cplett.2011.03.089
206. F. Weigl, S. Fricker, H.-G. Boyen, C. Dietrich, B. Koslowski, A. Plettl, O. Pursche, P. Ziemann, P. Walther, C. Hartmann, M. Ott, M. Moeller, From self-organized masks to nanotips: a new concept for the preparation of densely packed arrays of diamond field emitters. Diam. Relat. Mater. **15**(10), 1689–1694 (2006). doi:10.1016/j.diamond.2006.02.007
207. K. Honda, M. Yoshimura, T.N. Rao, D.A. Tryk, A. Fujishima, K. Yasui, Y. Sakamoto, K. Nishio, H. Masuda, Electrochemical properties of Pt-modified nano-honeycomb diamond electrodes. J. Electroanal. Chem. **514**(1–2), 35–50 (2001). doi:10.1016/S0022-0728(01)00614-3
208. O. Babchenko, E. Verveniotis, K. Hruska, M. Ledinsky, A. Kromka, B. Rezek, Direct growth of sub-micron diamond structures. Vacuum **86**(6), 693–695 (2012). doi:10.1016/j.vacuum.2011.08.011
209. N. Yang, W. Smirnov, C.E. Nebel, Three-dimensional electrochemical reactions on tip-coated diamond nanowires with nickel nanoparticles. Electrochem. Commun. **27**, 89–91 (2013). doi:10.1016/j.elecom.2012.10.044
210. C.E. Nebel, N. Yang, H. Uetsuka, E. Osawa, N. Tokuda, O. Williams, Diamond nano-wires, a new approach towards next generation electrochemical gene sensor platforms. Diam. Relat. Mater. **18**(5–8), 910–917 (2009). doi:10.1016/j.diamond.2008.11.024
211. P. Subramanian, Y. Coffinier, D. Steinmuller-Nethl, J. Foord, R. Boukherroub, S. Szunerits, Diamond nanowires decorated with metallic nanoparticles: a novel electrical interface for the immobilization of histidinylated biomolecuels. Electrochim. Acta, Ahead of Print (2012). doi:10.1016/j.electacta.2012.11.010
212. M. Wei, C. Terashima, M. Lv, A. Fujishima, Z.-Z. Gu, Boron-doped diamond nanograss array for electrochemical sensors. Chem. Commun. **24**, 3624–3626 (2009). doi:10.1039/B903284C
213. D.H. Wang, L.-S. Tan, H. Huang, L. Dai, E. Osawa, In-situ nanocomposite synthesis: arylcarbonylation and grafting of primary diamond nanoparticles with a poly(ether-ketone) in polyphosphoric acid. Macromolecules **42**(1), 114–124 (2009). doi:10.1021/ma8019078

214. H.A. Girard, S. Perruchas, C. Gesset, M. Chaigneau, L. Vieille, J.-C. Arnault, P. Bergonzo, J.-P. Boilot, T. Gacoin, Electrostatic grafting of diamond nanoparticles: a versatile route to nanocrystalline diamond thin films. ACS Appl. Mater. Interf. **1**(12), 2738–2746 (2009). doi:10.1021/am900458g
215. O. Babchenko, A. Kromka, K. Hruska, M. Michalka, J. Potmesil, M. Vanecek, Nanostructuring of diamond films using self-assembled nanoparticles. Cent. Eur. J. Phys. **7**(2), 310–314 (2009). doi:10.2478/s11534-009-0026-8
216. G.A. Powch, A.R. Jain, Directed self assembly: a novel, high speed method of nanocoating ultra-thin films and monolayers of particles. NSTI Nanotechnology Conference and Expo, NSTI-Nanotech 2012 (Santa Clara, CA, USA), pp. 474–477 (2012). CRC Press. ISBN: 978-1-4665-6275-2
217. H. Sim, S.-I. Hong, S.-K. Lee, D.-S. Lim, J.-E. Jin, S.-W. Hwang, Fabrication of boron-doped nanocrystalline diamond nanoflowers based on 3D $Cu(OH)_2$ dendritic architectures. J. Korean Phys. Soc. **60**(5), 836–841 (2012). doi:10.3938/jkps.60.836
218. D. Yamada, T.A. Ivandini, M. Komatsu, A. Fujishima, Y. Einaga, Anodic stripping voltammetry of inorganic species of As^{3+} and As^{5+} at gold-modified boron doped diamond electrodes. J. Electroanal. Chem. **615**(2), 145–153 (2008). doi:10.1016/j.jelechem.2007.12.004
219. G. Sine, I. Duo, R.B. El, G. Foti, C. Comninellis, Deposition of clusters and nanoparticles onto boron-doped diamond electrodes for electrocatalysis. J. Appl. Electrochem. **36**(8), 847–862 (2006). doi:10.1007/s10800-006-9159-2
220. K.E. Toghill, L. Xiao, G.G. Wildgoose, R.G. Compton, Electroanalytical determination of cadmium(II) and lead(II) using an antimony nanoparticle modified boron-doped diamond electrode. Electroanalysis **21**(10), 1113–1118 (2009). doi:10.1002/elan.200904547
221. T.-L. Wee, B.D. Sherman, D. Gust, A.L. Moore, T.A. Moore, Y. Liu, J.C. Scaiano, Photochemical synthesis of a water oxidation catalyst based on cobalt nanostructures. J. Am. Chem. Soc. **133**(42), 16742–16745 (2011). doi:10.1021/ja206280g
222. V. Saez, J. Gonzalez-Garcia, F. Marken, Active catalysts of sonoelectrochemically prepared iron metal nanoparticles for the electroreduction of chloroacetates. Phys. Procedia **3**(1), 105–109 (2010). doi:10.1016/j.phpro.2010.01.015
223. L. Rassaei, M. Sillanpaa, R.W. French, R.G. Compton, F. Marken, Arsenite determination in phosphate media at electroaggregated gold nanoparticle deposits. Electroanalysis **20**(12), 1286–1292 (2008). doi:10.1002/elan.200804226
224. F. Shang, J.D. Glennon, J.H.T. Luong, Glucose oxidase entrapment in an electropolymerized poly(tyramine) film with sulfobutylether-β-cyclodextrin on platinum nanoparticle modified boron-doped diamond electrode. J. Phys. Chem. C **112**(51), 20258–20263 (2008). doi:10.1021/jp807482a

Chapter 7
Modified Diamond Electrodes for Electrochemical Systems for Energy Conversion and Storage

Patricia Rachel Fernandes da Costa, Elisama Vieira dos Santos, Juan M. Peralta-Hernández, Giancarlo R. Salazar-Banda, Djalma Ribeiro da Silva and Carlos A. Martínez-Huitle

Abstract The aim of this chapter was to summarize the techniques used for surface modification of BDD materials, improving their catalytic efficiency as supported catalysts for PEM fuel cells (methanol and ethanol oxidation) as well as the studies concerning to the production of electrochemical capacitors using BDD materials. Also, the recent advances on the use of modified BDD materials for fuel cells will be discussed.

7.1 Introduction

Petroleum is considered the main source of energy, but it has also caused considerable amount of damages such as atmospheric pollution and global warming. Nevertheless, the copious uses of petroleum as well as the demand of petrol in the near future have motivated scientists around the world to develop new clean and renewable energy sources. In this frame, the development of fuel technology has received great attention because this technology consists in directly converting

P.R.F. da Costa · E.V. dos Santos · D.R. da Silva · C.A. Martínez-Huitle (✉)
Instituto de Química, Universidade Federal do Rio Grande do Norte, Lagoa Nova CEP, Natal, RN 59078-970, Brazil
e-mail: carlosmh@quimica.ufrn.br

J.M. Peralta-Hernández
Departamento de Investigación Ambiental Omega-201, Centro de Inovación Aplicada en Tecnologías Competitivas (CIATEC), Fraccionamiento Industrial Delta, 37545 Leon, Guanajuato, Mexico

G.R. Salazar-Banda
Instituto de Tecnologia e Pesquisa e Programa de Pos-Graduacao em Engenharia de Processos, Universidade Tiradentes, Aracaju, SE 49032-490, Brazil

N. Yang (ed.), *Novel Aspects of Diamond*, Topics in Applied Physics 121,
DOI 10.1007/978-3-319-09834-0_7

chemical energy into electricity. Direct Alcohol Fuel Cell (DAFC), fed by ethanol and air (oxygen), is a very interesting option for such kind of energy production.

Several catalysts supported materials for energy storage and conversion have been carried out in order to improve of kinetic of the anode and cathode reactions, enhancing the activity for oxygen reduction, alcohols oxidation, avoiding mainly the CO and intermediates poisoning on electrode surfaces [1]. The use of Pt-Ru catalyst is considered the most promising approach as anode material. However, owing to its recognized proprieties (wide potential window, low background current, a high chemical and dimensional stability) the conductive films of boron-doped diamond (BDD) have gained a renewed attention for many researches as an outstanding electrode material for many electrochemical processes [2–10]. In the case of fuel cells, Shao et al. [11] has indicated that BDD materials can be used as a potential support in the Polymer Electrolyte Membrane (PEM) due to the mechanical and chemical stability of BDD to be modified. The aim of this chapter was to summarize the techniques used for surface modification of BDD materials, improving their catalytic efficiency as supported catalysts for PEM fuel cells (methanol and ethanol oxidation) as well as the studies concerning to the production of electrochemical capacitors using BDD materials. Also, the recent advances on the use of modified BDD materials for fuel cells will be discussed.

7.2 Modification of BDD Surface

The deposition of metal or metal oxide clusters on BDD surface, as nanoparticles, has been used to improve the catalytic activity of such nanoparticles using very small amounts compared to the conventional bulk material [12]. Therefore, a significant effort, to improve particles adherence and dispersion, has been performed by investigating several deposition techniques. These methods are well known to be efficient ways to prepare particles and nanoparticles; however, the synthesis technique influences strongly the shape and size distribution of particles. The choice of the material deposited depends on the intended application of the electrode and its required stability under harsh working conditions.

Microemulsion synthesis A microemulsion is defined as a thermodynamically stable isotropic dispersion of two immiscible liquids consisting of microdomains of one or both liquids stabilized by an interfacial film of surface active molecules. The microemulsion system is characterized by transparency (optical isotropic), droplet size (from 6 to 80 mm) and thermodynamic stability [13, 14]. The synthesis of inorganic nanoparticles is usually carried out in water/oil microemulsions (W/O). The microemulsion method has been used as microreactors to produce nanoparticles with narrow size distribution, since the first work described by Boutonnet et al. [15]. Water-in-oil microemulsion is the coexistence of an excess water phase and the surfactant molecules which aggregate in the oil phase in the form of reverse micelle. The water core of these aggregates is surrounded by surfactant molecules

Table 7.1 Survey of recent publications on metal/metaloxide particles from microemulsions deposited onto boron-doped diamond (BDD) thin film electrodes with applications in fuel cells

Catalyst	Microemulsion system	Metal precursor	Reducing/ precipitating agent	Particle diameter (nm)	Catalytic reaction	References
Pt	Brij-30[a]/ n-heptane	H_2PtCl_6	NH_2NH_2	2–3	Methanol oxidation	[16]
Pt/Sn	Brij-30[1]/ n-heptane	H_2PtCl_6, $SnCl_2$	$NaBH_4$	2–5	Ethanol oxidation	[17]
Pt/Ru	Brij-30[1]/ n-heptane	H_2PtCl_6, $RuCl_3$,	$NaBH_4$	2–5	Methanol and ethanol oxidation	[18]
Pt/Ru/ Sn	Brij-30[1]/ n-heptane	H_2PtCl_6, $RuCl_3$, $SnCl_2$	$NaBH_4$	2–5	Methanol and ethanol oxidation	[19]

[a] Brij-30: Polyoxiethylene (4) lauryl ether (non ionic surfactant)

which have the non-polar part of their molecule towards the oil phase. In the water core of this aggregate, electrolytes may be solubilized for instance metal salts. These metals will be then transformed into inorganic precipitates by using an appropriate reducing or precipitating agent. There are two main ways of preparation in order to obtain nanoparticles from microemulsions: (i) by mixing two microemulsions, one is containing the precursor and the other the precipitating agent and (ii) by adding the precipitating agent directly into the microemulsion containing the metal precursor.

Some publications have been presented in which the technique of microemulsion has been conducted for the synthesis of metallic nanoparticles (Pt [16], Pt–Ru [17], Pt–Sn [18], and Pt–Ru–Sn [19]) where the catalyst has been supported on BDD surfaces (see Table 7.1). The choice of Pt and Pt-based particles was motivated by its useful potential application in alcohol (methanol or ethanol) electrooxidation.

Siné et al. [16] obtained Pt-nanoparticles by reduction of chloroplatinic acid (H_2PtCl_6) with hydrazine at room temperature in a water-in-oil (w/o) microemulsion of tetraethyleneglycolmonododecylether (BRIJ-30)/n-heptane using two microemulsion steps method. After microemulsion step, Transmission Electron Microscopy (TEM) was used to characterize nanoparticle sizes (2–5 nm). TEM micrograph of Pt-nanoparticles synthesized by the microemulsion method is presented in Fig. 7.1, where Pt-nanoparticles were deposited onto the BDD substrate and in order to avoid detachment nanoparticles, Nafion® films were used to mechanically stabilize the electrode. BDD-Pt-Nafion® was more active than BDD-Pt for methanol oxidation.

Other bimetallic binary nanoparticles of Pt–Ru and Pt–Sn, and ternary Pt–Ru–Sn nanoparticles supported on BDD substrates by mixing the microemulsion with solid sodium borohydride as reducing agent, were synthesized by Sine et al. [17–19]. They also used TEM and X-ray Photoelectron Spectroscopy (XPS) techniques to characterize particle sizes and morphology, and to determine the effective particle

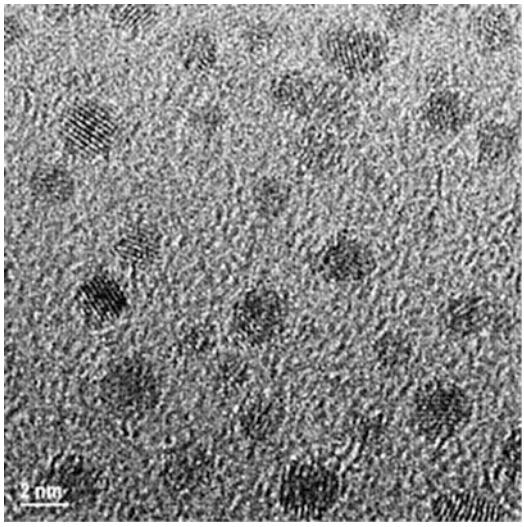

Fig. 7.1 TEM micrograph of platinum nanoparticles synthesized by the microemulsion method. Reprinted with permission from [16]

compositions and the identification of oxidation states of metals in the different samples, respectively. Pt/Ru nanoparticles of different compositions were synthesized by mixing appropriate ratios of Pt and Ru precursors in the aqueous phase of the microemulsion; and the size distributions obtained by them were similar for all the samples and the size domain of the particles was approximately 2–3 nm of diameter.

As showed in Fig. 7.2, cyclic voltammetry (CV) of Pt, $Pt_{50}Ru_{50}$, and Ru nanoparticles deposited on BDD in pure supporting electrolyte (1 M $HClO_4$) achieved substantial decrements in the quality of the H adsorption–desorption characteristic and increase in the background current in the double-layer region when the Ru content in the particles was increased. Other syntheses were carried out by the same authors in order to understand the effect of particles size and morphology on the efficiency. Therefore, bimetallic Pt/Sn particles of several compositions with theoretical atomic contents $Pt_{80}Sn_{20}$, $Pt_{60}Sn_{40}$, $Pt_{50}Sn_{50}$, $Pt_{40}Sn_{60}$, and $Pt_{20}Sn_{80}$ were synthesized via the microemulsion method [18]. TEM micrographs of Pt (A), $Pt_{60}Sn_{40}$ (B), and $Pt_{20}Sn_{80}$ nanoparticles (C) are presented in Fig. 7.3. As can be seen, small isolated and well-spherical units of diameter in the 2–5 nm range were obtained by this method.

For Pt–Ru–Sn nanoparticles [19], the particle size measured by TEM ranging from 2 to 5 nm. While the relative atomic amounts of Pt, Ru, and Sn in the nanoparticles of $Pt_{80}Ru_{10}Sn_{10}$ were determined by XPS analyses, were obtained values of 90, 3, and 7 %, respectively. XPS Pt4f spectra for Pt/Ru, PtSn, and Pt/Ru/Sn alloy nanoparticles are shown in Fig. 7.4. As can be seen, Pt4f binding energies for the Pt/Ru and Pt/Sn alloy nanoparticles were lower than those for clean Pt nanoparticles. This phenomenon was more marked in the case of $Pt_{80}Sn_{20}$ particles,

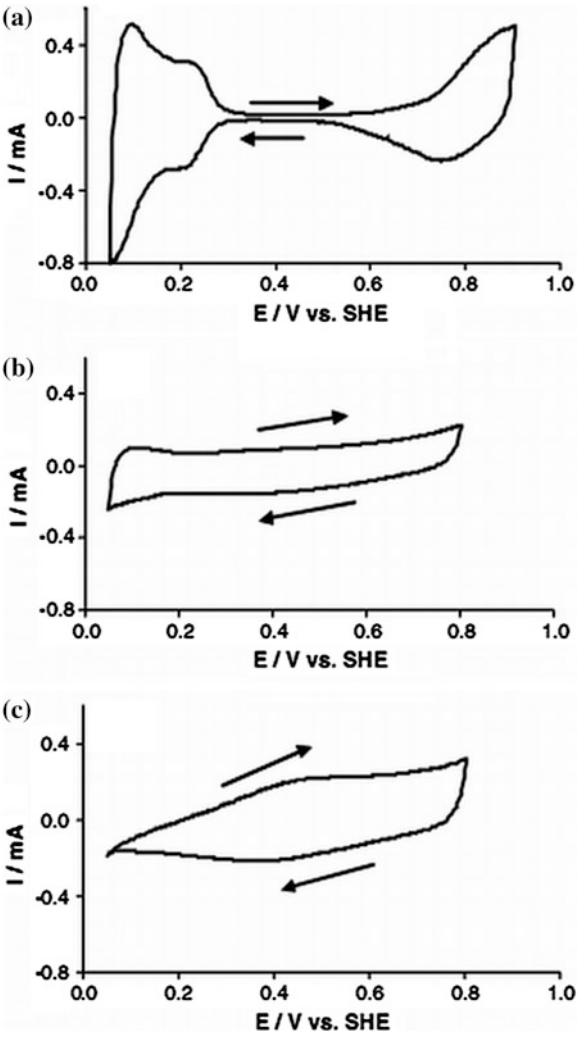

Fig. 7.2 CV of microemulsion-synthesized Pt (**a**), $Pt_{50}Ru_{50}$ (**b**) and Ru nanoparticles (**c**) deposited on BDD. Recorded in N_2-saturated 1 M $HClO_4$ solution at 50 mV s^{-1} and 25 °C. Reprinted with permission from [17]

in which the Pt4f contribution appeared at lower binding energy than in $Pt_{80}Ru_{20}$. The change in the electronic structure of the Pt component in the alloys (Pt/Sn and Pt/Ru) could modify the Pt work function and thus weakens bonding of adsorbed intermediates Pt-CO that could produce an enhancement in rates of methanol oxidation.

Thermal deposition Appropriate precursors are dissolved in suitable solvents and spread on a metallic support [20] before thermal decomposition. This method has been used to deposit iridium oxide [17, 21], gold [17, 22] and platinum nanoparticles [23] on BDD surfaces. The particle size, nonstoichiometry, and morphology of the oxide layer depends on the nature of the precursor and the decomposition

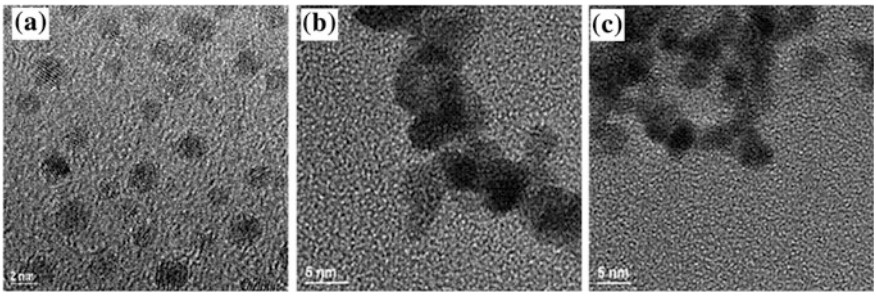

Fig. 7.3 TEM micrographs of Pt (**a**), $Pt_{60}Sn_{40}$ (**b**), and $Pt_{20}Sn_{80}$ (**c**) nanoparticles synthesized via the microemulsion method. Reprinted with permission from [17]

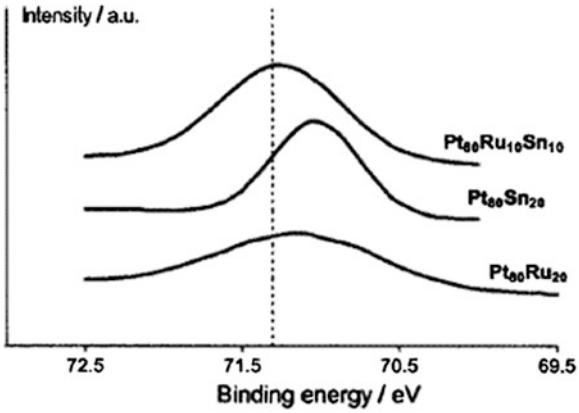

Fig. 7.4 XPS chemical shift of the Pt 4f7/2 line of Pt0 in Pt-rich ternary and binary nanoparticles supported on Au. The *dashed vertical line* represents the position of the signal in pure Pt nanoparticles. Reprinted with permission from [19]

temperature, therefore, these must be controlled during the procedure. Using only lower amounts of Ir, Au and Pt, are produce modified BDD electrodes with the well known properties of IrO_2, Au, or Pt nanoparticles. However, long term stability is not sufficient at the current state of development.

Deposition of IrO_2 particles onto BDD mild hydrophilic surface by thermal decomposition technique was studied by Duo et al. [21], observing that the oxygen evolution reaction (OER) was dramatically enhanced with the surface modification. Solutions of H_2IrCl_6 in 2-propanol was applied to the BDD surface (1 cm^2). After solvent evaporation at 80 °C, calcination was performed at 350 °C to oxidize the precursor acid to IrO_2. Different precursor concentrations of IrO_2 were deposited on BDD surface in order to vary the amount of deposited IrO_2 [17]. From these results, isolated IrO_2 particles had a size of about 2–3 nm, being concentrated at the grain boundaries of the diamond crystals; when low IrO_2 loading were employed.

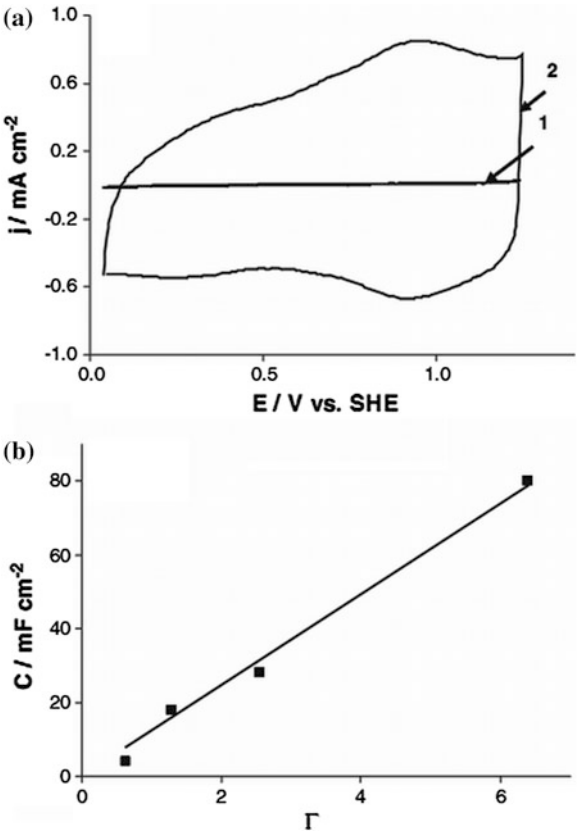

Fig. 7.5 **a** Cyclic voltammograms: *1* BDD mild electrode and *2* BDD–IrO_2 electrode with G = 6.4 prepared at 450 °C. Electrolyte: 0.5 M H_2SO_4. Scan rate 2,000 mV s^{-1}, T = 25 °C. G = 1 corresponds to 1,015 molecules IrO_2 cm^{-2}. **b** Capacitance values (E = 0.64, scan rate 20 mV s^{-1}) as a function of IrO_2 loading on BDD electrodes. Reprinted with permission from [18]

Conversely, the particles were larger (10 nm) and their concentration at the grain boundaries of the diamond crystals was significantly higher, when higher IrO_2 loading were used. The CV curves obtained with BDD–IrO_2 electrodes provided a fingerprint of electrode surface transitions occurring during the potential scan of 2 V s^{-1} (Fig. 7.5a, curve 2). The high capacitive current is related to changes in the oxidation state of the IrO_2 surface during the potential scan. The two pairs of peaks, seen at 0.40 and 0.95 V, can be related to the surface redox couples Ir(III)/Ir(II) and Ir(IV)/Ir(III), respectively. The very low currents recorded at a BDD electrode were certainly related to the absence of electroactive surface functionalities on the electrode surfaces. Whereas, Fig. 7.5b shows that the voltametric charge increased linearly with the IrO_2 loading.

On the other hand, Au-nanoparticles deposited on BDD surface by using a sputter deposition method with a heat treatment at 400–600 °C [17, 22]; exhibited an extraordinary electrocatalytic activity to CO oxidation, catalytic hydrogenation of unsaturated alcohols and aldehydes and O_2 reduction [22]. The Au-nanoparticles size depends on the amount of deposited gold, with an average size of 5–35 nm.

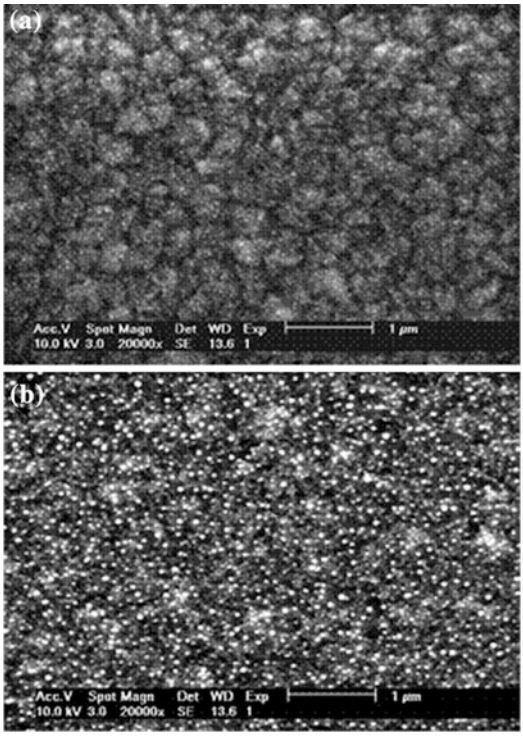

Fig. 7.6 SEM pictures of gold deposits on polycrystalline BDD substrate heated at 600 °C as a function of the deposited amount of gold: **a** 9.6×10^{15}, and **b** 1.9×10^{16} gold atom per cm^2 geometrical surface area, obtained with sputtering times of 6 and 12 s, respectively. Reprinted with permission from [18]

Figure 7.6 shows typical SEM images of Au-nanoparticles/BDD electrodes using this technique.

Alternatively, Pt particles were deposited on p-Si/BDD substrate by thermal decomposition procedure [23]. The application of 5 μL of 0.2–3 mM H_2PtCl_6 in 2-propanol on the BDD surface; evaporation of the solvent at 60 °C during 5 min, and finally, thermal decomposition of the precursor by treatment in an oven at 350 °C during 1 h, was the procedure of production of Pt-nanoparticles. The agglomeration of these platinum particles was related to the inhomogeneity of the interfacial surface tension of the BDD support. The reaction of methanol oxidation in acidic medium was used as reaction test of the prepared p-Si/BDD/Pt electrode, obtaining poor efficiencies.

Electrodeposition The electrodeposition is one of the most widely used methods for the preparation and deposition of particles on BDD. The modification of a BDD electrode surface has been reported for a limited range of metal nanoparticles, including Ag, Au, Pt, Pd, Cu, Bi, Ni, Hg, Pb, Co, Ir, Ru, Te, Ti, and Fe [24–28].

The advantages of electrodeposition include the fact that most compound semiconductor is obtained at or near room temperature, which is considered low temperature deposition. Electrodeposition also promotes controlled growth and it is

generally a low cost methodology when compared to the dry methods. The deposition and co-deposition of the different metals on BDD have been the most studied systems due to their high interest in electrocatalysis. Deposits in BDD received great attention due to their applicability in fuel cell systems, being the methanol oxidation the preferred test reaction [29]. The electrodeposition of Pt particles on a BDD electrode is generally performed by applying a potential step to a deaerated 2 mM H_2PtCl_6 solution in 1 M $HClO_4$. The potential is shifted from an equilibrium potential (1 V, where no reduction of platinic ions takes place) to a potential at which the reduction of Pt^{4+} to metallic Pt occurs (0.02–0.15 V). Several techniques for characterization of electrodeposits on BDD are used. Figure 7.7 shows SEM micrographs of a BDD–Pt electrode prepared by performing a potential step from 1 to 0.02 V in a 2 mM H_2PtCl_6 + 1 M $HClO_4$ solution for 5 s. Spherical and isolated particles are observed with a quite large size variation that covers the 40–700 nm range. This is indicative of continuous formation of new nuclei during deposition and it is in agreement with the progressive mechanism of nucleation of Pt on BDD.

A typical cyclic voltammogram for electrodeposited Pt particles on BDD is shown in Fig. 7.8. This voltammogram exhibits the characteristic feature of Pt, i.e. two distinctive H adsorption–desorption peaks between 0.05 and 0.35 V, followed by a fine double layer region corresponding to metallic Pt. Although electrodeposited Pt particles on BDD are efficient for methanol electrooxidation, their size domain is so broad that they cannot be strictly classified as nanoparticles. The literature attributes this heterodispersity to the inhomogeneous nature of the BDD substrates [30], mainly to the presence of non-diamond sp^2 impurities that act as preferential deposition sites. Therefore, a "size-effect" cannot be reasonably expected in this case, and some alternative synthesis techniques have to be employed to deposit real Pt nanoparticles on BDD.

The best electrocatalyst for methanol oxidation is Pt–Ru binary metallic, being oxidize according to a bifunctional mechanism [31]. Surface-sited Pt atoms oxidatively dehydrogenate the chemisorbed methyl moiety in consecutive steps to yield a residual Pt–CO fragment that cannot be oxidized to CO_2 at DMFC potentials, Pt adsorbed CO is removed via an oxygen-transfer step from electrogenerated Ru–OH. Ru transfers oxygen more effectively than Pt due to its ability to oxidatively absorb water at less positive potentials [32].

In this sense, polycrystalline BDD films were proposed by Gonzalez-Gonzalez et al. [33] as the alternative material to obtain high-area carbon supports using electrodeposition, with potential application for direct methanol fuel cell electrocatalysts. The electrocatalytical behavior of Pt/BDD, Pt-Ru/BDD and BDD electrodes towards the oxidation of methanol in acidic media was evaluated by CV in Fig. 7.9. Thus, the maximum current densities obtained for methanol oxidation were about 0.73 mA cm^{-2} for Pt and 0.94 mA cm^{-2} for Pt-Ru deposited on BDD. However, as indicated by the authors, the fact that Pt-Ru exhibited lower potentials than Pt may be expected in the basis of previous studies [34]; nevertheless, more investigation is necessary to completely understand the composition and particle size effects. The electrodeposition of Pt-Ru electrocatalytic particles was recently studied by comparing simultaneous and sequential deposition on BDD supports

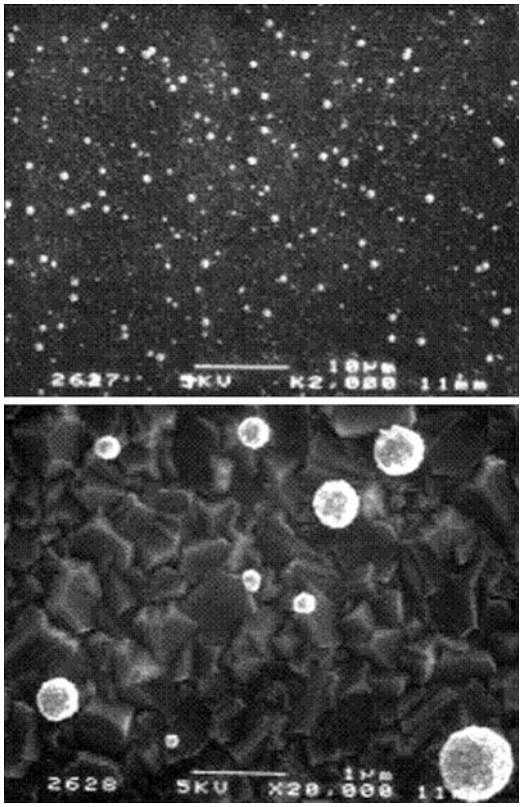

Fig. 7.7 SEM pictures at two different magnification scales of a BDD–Pt electrode prepared by electrodeposition with a single potential step (60 s) from 1 to 0.02 V in a N_2-saturated 2 mM H_2PtCl_6 + 1 M $HClO_4$ solution. Reprinted with permission from [23]

using a potentiostatic method [35]. Smooth cluster morphologies were observed for simultaneous deposition and a dendritic structure was observed for sequential deposition from SEM studies (Fig. 7.10). The morphology of sequential deposition was dominated by Pt deposition in the first step, while a change of aggregate morphology due to the presence of Ru was observed for simultaneous deposition. This different morphology and microstructure contributed to different electrochemical performance.

Sol-gel modification Surface modifications of BDD electrodes have been carried out with several metal oxides and some mixed composites using the sol-gel method [36, 37]. This technique is used for coating substrates to be applied for energy storage materials and electrochemical devices; in either case, there are many interfaces between components and many components that have to perform reliably and safely. In some cases, the interfaces are the location of failure in an operating fuel cell and problems due to chemical reactions and increased contact resistance can occur. Also, elevated temperatures lead to microstructure changes, crystallization, thermal expansion mismatch and delamination. In these complicated

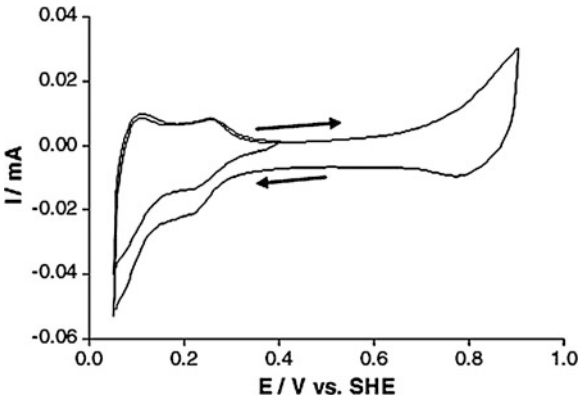

Fig. 7.8 Cyclic voltammograms of electrodeposited Pt particles on BDD electrode. Recorded in a N_2-saturated 1 M $HClO_4$ solution at 50 mV s^{-1} and 25 °C. Conditions of electrodeposition: single potential step (5 s) from 1 to 0.02 V in a N_2-saturated 2 mM H_2PtCl_6 + 1 M $HClO_4$ solution. Reprinted with permission from [18]

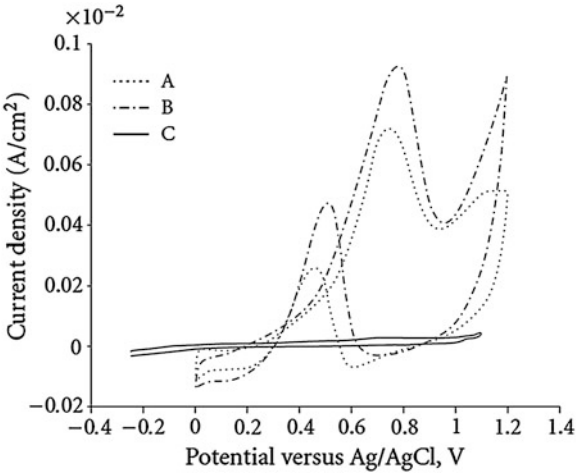

Fig. 7.9 Study of cyclic voltammetry of diamond films with electrocatalyst deposition on 0.1MeOH/ 0.5 m H_2SO_4 at 50mVs^{-1}: **a** Pt/BDD, **b** Pt-Ru/BDD, and **c** BDD

materials systems, the use of sol-gel processing is well suited to the need for accurate placement of critical materials [38].

The sol-gel method starts with a solution consisting of metal compounds, such as metal alkoxides, and acetylacetonates as source of oxides, water as hydrolysis agent, alcohol as solvent and acid or base catalyst. Metal compounds undergo hydrolysis and polycondensation at room temperature, giving rise to sol, in which polymers or fine particles are dispersed. Further reaction connects the particles, solidifying the sol into wet gel, which still contains water and solvents. Vaporization of water and solvents produces a dry gel (xerogel), an aerogel results from a

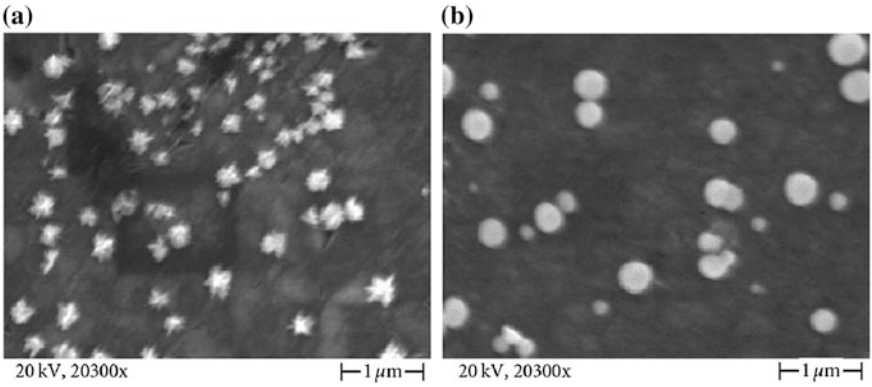

Fig. 7.10 SEM images of Pt-Ru deposited on BDD electrode at −0.2 V for 10 min, **a** sequential deposition, and **b** simultaneous deposition

supercritical drying process. Heating gels to several hundred degrees produces dense oxides as products. Coating films can be made by dip coating or spin coating of the sol. Unsupported films can be made by synthesizing the film at the interface between alkoxide solution and water. Membranes are prepared by pouring the sol on the porous oxide with coarse pores. Particles with sharp size distribution can be precipitated and grown in the sol [39].

The preparation of Pt–RuO_2 deposits on a carbon black substrate using the sol-gel method was reported by Suffredini et al. [36] and their activity toward methanol electrooxidation was investigated. Good performances were achieved at Pt–RuO_2/C anodes prepared by sol–gel than those prepared by alternative methods [40]. Deposition of platinum oxide particles PtOx on BDD electrodes by this method and testing several pre-and post-treatments of the surface for electrochemical experiments was investigated by Salazar-Banda et al. [41]. Electrochemical stability of the catalytic coatings showed that the electrodes retained 91.6 % of the coated material after 1,000 voltammetric cycles conducted in the water decomposition.

On the other hand, Pt, Pt–RuO_2, and Pt–RuO_2–RhO_2 modified BDD electrodes were prepared by the sol-gel process to oxidize methanol and ethanol [42]. The XRD patterns registered for each prepared electrode indicated that only pure Pt was deposited instead PtO_x, while Ru and Rh were deposited as RuO_2 and RhO_2 obtaining randomly and homogeneously nanometric catalytic deposits (EDX analysis). The AFM topological images for the BDD surface and for Pt/BDD, Pt–RuO_2/BDD and Pt–RuO_2–RhO_2/BDD electrodes showed the regular pyramidal structures without holes or cracks; however, the modified BDD electrodes exhibit as well small islands corresponding to the catalytic coatings, for all BDD modified samples some agglomerations of the catalytic coating were observed which indicate the presence of heterogeneous sites containing some clusters with small size (1–5 μm) [42] (Fig. 7.11).

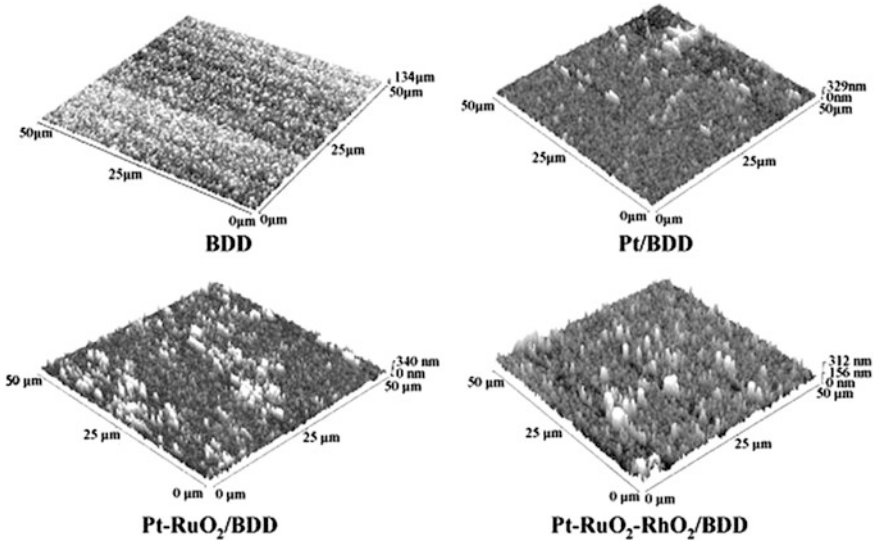

Fig. 7.11 AFM images for BDD, Pt/BDD, Pt–RuO_2/BDD, and Pt–RuO_2–RhO_2/BDD electrode surfaces. Reprinted with permission from [42]

The modification of the BDD electrode with other Pt-metal oxide catalysts prepared by sol-gel has been investigated with the aim to improve its electrocatalytic response to be used as a fuel cell anode. In this context, BDD electrodes with IrO_2, PbO_2, SnO_2, Ta_2O_5, and some mixed composites prepared by sol-gel have been investigated by electrochemical techniques to establish their catalytic activity towards methanol and/or ethanol oxidation reactions [36, 43–46]. Table 7.2 summarizes the most important examples of coating catalyst on BDD support synthesized by sol-gel technique.

Platinum-ruthenium oxide carbon powder composite (Pt–RuO_2/C) deposited on BDD surface, was studied on the oxidation of methanol and ethanol in H_2SO_4 solutions [37]. Alternatively, the composite catalysts Pt–PbO_x/C, Pt–IrO_2/C, Pt–(RuO_2–IrO_2)/C, Pt–(RuO_2–PbO_x)/C, and Pt–(IrO_2–PbO_x)/C were also fixed on BDD substrate to be used in direct ethanol fuel cells (DEFC). The sol-gel method favored the formation of the nanometric crystallite dimensions of the composites which can be responsible for the enhanced catalytic activity toward ethanol oxidation, in all cases [45]. On the other hand, Pt–SnO_2 and Pt–Ta_2O_5 catalysts have been incorporated on BDD surface in order to study the methanol and ethanol electrooxidation [46]. In this study, the authors estimated the mean crystallite size for Pt, Pt–SnO_2, and Pt–Ta_2O_5 coatings, achieving values of 4.6, 5.0, and 9.1 nm, respectively. Although all these catalysts showed high catalytic activities toward ethanol and methanol oxidation, Pt-SnO_2catalysts exhibited better performance than Pt–Ta_2O_5 for the oxidation of ethanol; whereas, Ta_2O_5 decreases the poisoning effect caused by the adsorbed CO generated in the methanol oxidation [46].

Table 7.2 The most important examples of coating catalyst on BDD support synthesized by sol-gel technique

Fuel cell system	Catalyst deposited on BDD electrode	Characterization technique	Average size crystallite (nm)	Precursors
Methanol and ethanol	Pt, Pt–RuO_2, Pt–RuO_2–RhO_2	XRD, EDX, AFM, SEM,	4.3–6.5	Acetylacetonates of Pt (II), Ru (III), and Rh; in a mixture of isopropyl alcohol in acetic acid
Ethanol	PtO_x, PtO_x–RuO_2, RuO_2, IrO_2, PbO_2	AFM	–	Acetylacetonates of Pt (II), Ru (III), Pb(II) and Ir(III); in a mixture of isopropyl alcohol in acetic acid
Methanol and ethanol	Pt–RuO_2/C	XRD, EDX	7.2	Acetylacetonates of Pt (II), Ru (III); in a mixture of isopropyl alcohol in acetic acid/carbon black powder (Vulcan® XC72R)
Methanol	Pt–RuO_x	SEM, DRX	500	Acetylacetonates of Pt (II), and Ru (III); in a mixture of isopropyl alcohol in acetic acid
Ethanol	Pt–RuO_2/C	XRD, EDX	5.0	Acetylacetonates of Pt (II), Ru (III), Pb(II) and Ir(III); in a mixture of ethanol in acetic acid/carbon black powder (Vulcan® XC72R)
	Pt–PbO_x/C			
	Pt–IrO_2/C			
	Pt–(RuO_2–IrO_2)/C			
	Pt–(RuO_2–PbO_x)/C			
	Pt–(IrO_2–PbO_x)/C			
Methanol and ethanol	Pt, Pt–SnO_2	XRD, EDX, SEM, AFM	4.6–9.1	Acetylacetonate of Pt (II), Sn(IV) bis acetylacetonate dibromide, Ta (V) ethoxide; in a mixture of isopropyl alcohol in acetic acid
	Pt–Ta_2O_5			

7.3 Application of Modified BDD Films as Electrocatalytic Surfaces for Fuel Cells

Salazar-Banda et al. [42] studied the oxidation of methanol and ethanol by using different modified BBD surfaces such as Pt, alloys Pt–RuO_2, and Pt–RuO_2–RhO_2 by sol-gel method. Voltammetric assays showed that BDD modified surfaces

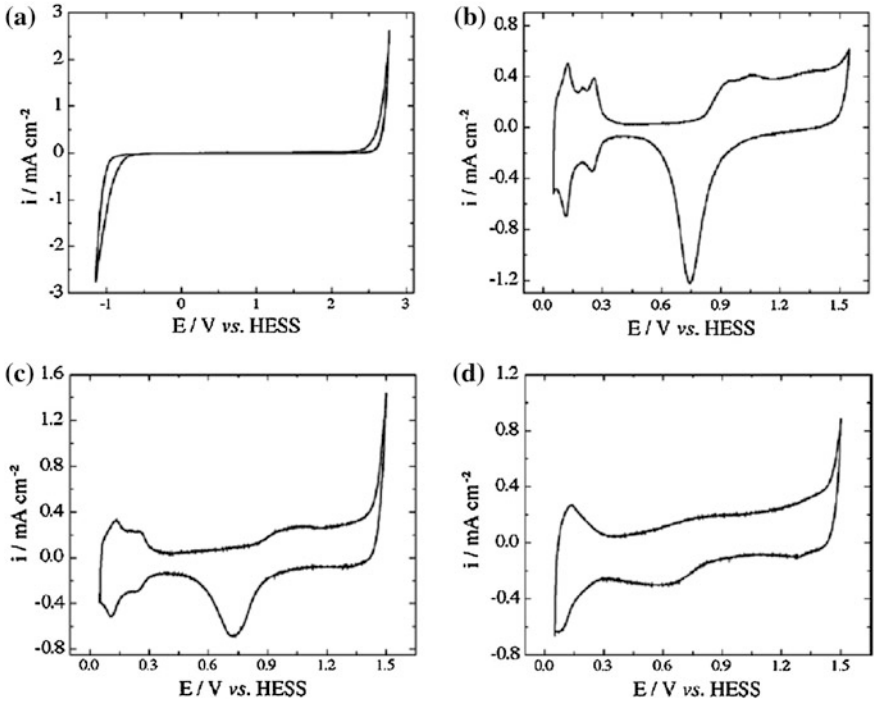

Fig. 7.12 Cyclic voltammetric studies in a 0.5 M of H_2SO_4 aqueous medium for **a** BDD, **b** Pt/BDD, **c** Pt–RuO_2/BDD, and **d** Pt–RuO_2–RhO_2/BDD. Reprinted with permission from [42]

improved the electroactive area in approximately five times with respect to original BDD surface and BDD/Pt, BDD/Pt–RuO_2, BDD/Pt–RuO_2–RhO_2 electrodes promoted that the oxygen reduction (OER) and the hydrogen evolution (HER) reactions were shifted toward low potentials due to the catalytic effect of the deposited metals after modification. The curve in Fig. 7.12 displays the typical electrochemical behavior of a polycrystalline Pt surface, such as hydrogen absorption/desorption and the oxide formation, evidencing that the Pt particles have a adequate contact with the BDD surface, high purity and homogeneous distribution. Methanol and ethanol oxidation in acidic conditions, by cyclic voltammetric assays, using modified BDD surfaces revealed that the CO poisoning effect for both alcohols oxidation reaction was mainly inhibited at ternary alloy BDD/Pt–RuO_2–RhO_2 electrode (solid lines in Fig. 7.13) due to the Rh presence, which promotes a better catalytic effect for these reactions by either prompting the oxidation of the adsorbed intermediate species to CO_2 or diminishing the absorption of CO and the others intermediates over Pt surface.

Catalytic properties of Pt–RuO_2/C supported on BDD surface was also evaluated by means of cyclic voltammetric technique [37] presented a higher current density than the composite supported on GC electrode. Voltammograms of Fig. 7.14 indicate that the forward and backward lines of BDD substrate were almost coincident

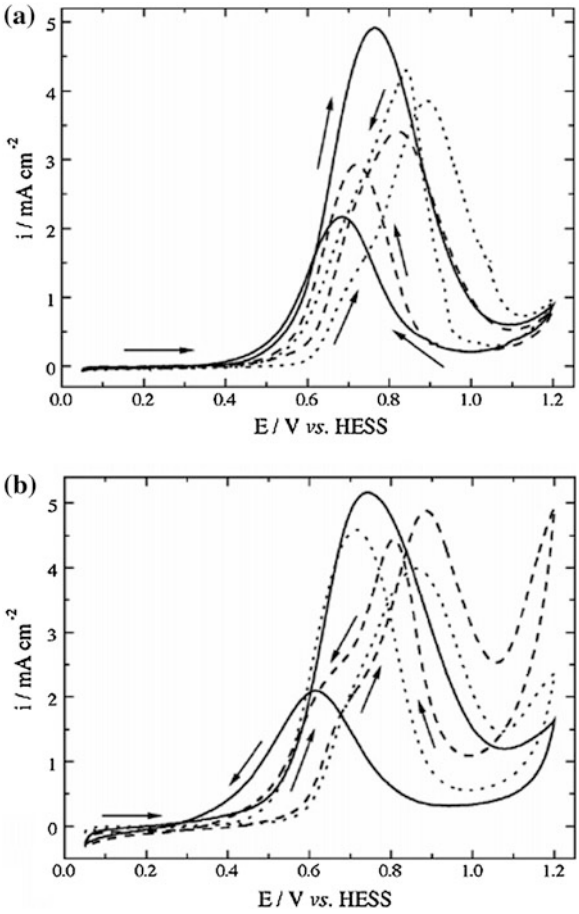

Fig. 7.13 Cyclic voltammetric study (*second cycle*) for electrochemistry oxidation of 0.5 M of **a** methanol, and **b** ethanol. *Dotted line* corresponds to Pt/BDD, *dashed line* to Pt–RuO_2/BDD, and *solid line* to Pt–RuO_2–RhO_2/BDD electrodes materials ($v = 0.005$ V s^{-1}). Reprinted with permission from [42]

while a large difference was observed for GC electrode. However, other tests using the same Pt–RuO_2/C material showed that the differences are attributed to the substrate evidencing the great capacitive effect of the GC. Conversely, the use of BDD surfaces practically avoids the substrate contribution and thus, the response of electrode was only dependent on the catalyst. Figures 7.15a and b show methanol and ethanol oxidation responses, respectively, for Pt–RuO_2/C catalyst on BDD surface, indicating that the oxidation of methanol stared at 380 mV vs HESS, in agreement with the data reported by He et al. [32] where Pt–Ru nanoparticles were electrodeposited on carbon nanotubes. For the case of ethanol oxidation (Fig. 7.15b), the electrochemical responses were extremely different for both cases, showing the presence of a re-activation process on the catalyst surface, but in the case of Pt–RuO_2/C material, the oxidation ethanol potential was much lower than for the Pt/C. However, the response in current density for Pt–RuO_2/C material was fairly large for an extended potential window, indicating a multistep processes during methanol oxidation.

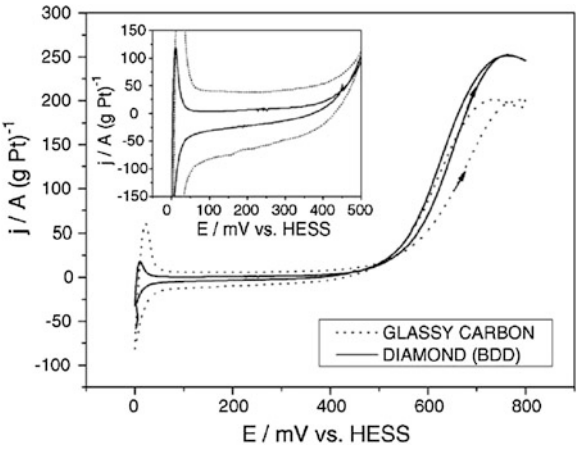

Fig. 7.14 Cyclic voltammetric response of the Pt–RuO_2/C composite fixed on BDD (*full line*) and on glassy carbon (*dotted line*) for the oxidation of 1.0 M methanol in 0.5 M H_2SO_4. The *insert* shows the region of capacitive responses for both electrode configurations, $\nu = 10$ mV s^{-1}. Reprinted with permission from [44]

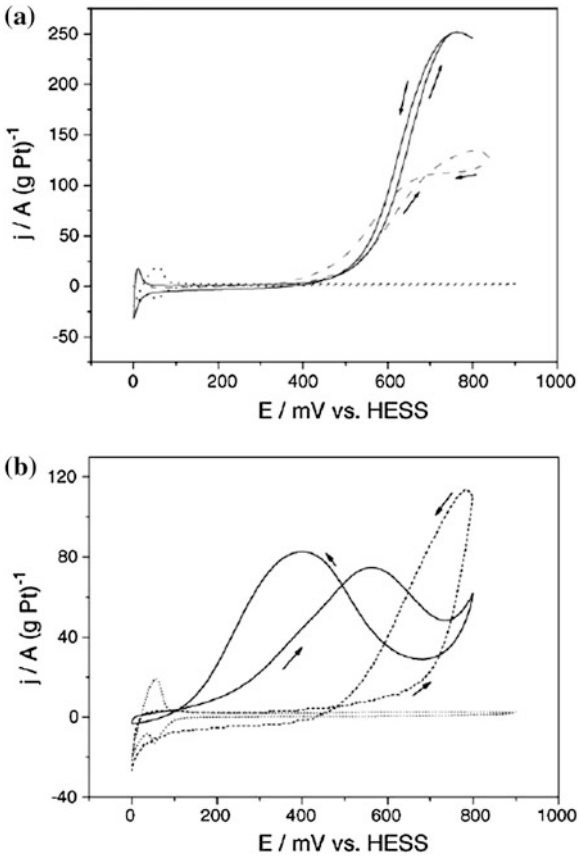

Fig. 7.15 Voltammetric oxidation of 1.0 M of methanol (**a**) and ethanol (**b**) in 0.5 M H_2SO_4 on Pt–RuO_2/C (*full lines*) and Pt/C (*traced lines*) composites fixed on BDD surfaces. Baselines (*dotted lines*) were included as a comparison. Scan rate 10 mV s^{-1}. Reprinted with permission from [44]

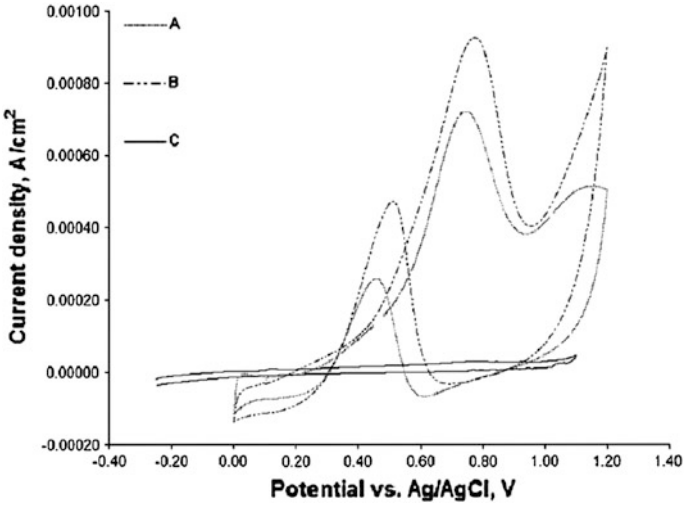

Fig. 7.16 Study of cyclic voltammetry of diamond films with electrocatalyst deposition on 0.1 MeOH/0.5 m H_2SO_4 at 50 mV s^{-1}. **a** Pt/BDD, **b** Pt–Ru/BDD, and **c** BDD. Reprinted with permission from [47]

Polycristalline boron-doped diamond films modified with different electrocatalysts (Pt/BDD and Pt–Ru/BDD) were studied by González-González et al. [47] for the oxidation of methanol in acid media by using cyclic voltammetry in Fig. 7.16. Thus, the maximum currents densities for methanol oxidation were obtained about 0.73 mA cm^{-2} for Pt and 0.94 mA cm^{-2} for Pt–Ru deposited on BDD, repsectively. However, as indicated by the authors, the fact that Pt–Ru exhibited lower potentials than Pt may be expected in the basis of previous studies [30] and hence, more investigation is necessary to completely understand the composition and particle size effects.

Salazar-Banda et al. [43] investigated the oxidation of methanol by using Pt-RuO_x/BDD powder electrode, and its comparison with a commercial catalyst (Pt–Ru/C); obtaining that the incorporation of ruthenium presents the inhibition of the hydrogen adsorption/desorption signals. Additionally, good capacitive currents were achieved (Fig. 7.17), then, methanol oxidation displayed close values on both electrodes (≈ 0.40 V vs. HESS). Furthermore, the magnitude of the current densities in the common fuel cell operation was approximately from 0.4 to 0.8 V vs HESS. As a consequence, the BDD powder modification presented an important enhancement of the catalytic activity to methanol oxidation with respect to other materials such as carbon modified composites. At the same time, analogous idea was recently proposed by Swope et al. [48], where they have prepared conductive diamond powders as a new catalyst for fuel cells. They have reported the development of higher surface area, approximately 100 m^2 g^{-1}, and good corrosion

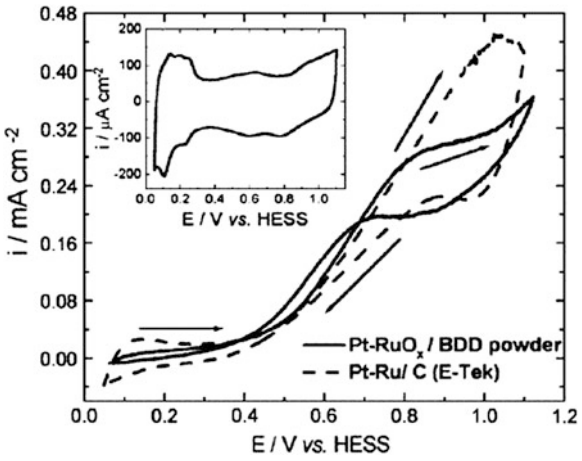

Fig. 7.17 Cyclic voltammograms for the electrochemical oxidation of 0.5 M of methanol in 0.5 M H_2SO_4 aqueous solution carry out on the Pt–RuOx/BDD powder/BDD (*solid line*) and on the Pt–Ru/C/BDD (*dashed line*) electrodes at $\nu = 10$ mV s^{-1}. Insert correspond to the cyclic voltammogram recorded on the Pt-RuO_x/BDD powder/BDD electrode in 0.5 M H_2SO_4 aqueous solution at $\nu = 50$ mV s^{-1}. Reprinted with permission from [43]

resistance by conductive diamond powders for application as the electrocatalyst support, using electrodeposition. In other study, Salazar-Banda et al. [46] modified BDD film surfaces with Pt, Pt–SnO_2, and Pt–Ta_2O_5 nanocrystalline deposits to evaluate the methanol and ethanol oxidation. Results for BDD before (thin solid line) and after modification with Pt (thick-solid line), Pt–SnO_2 (dashed line), and Pt–Ta_2O_5 (dotted line) showed the increase in the current for each material (Fig. 7.18); but the presence of tantalum oxides produced an enhance in defective surface sites, that increases the interfacial capacitance and also raises the ability of charge accumulation. Voltammograms carried out on BDD surface electrode without and in the presence of 0.5 M of methanol, and ethanol, respectively; showed that the oxidation of ethanol starts at approximately 0.39, 0.35, and 0.61 V on the same materials, clearly indicating the enhancement of the catalytic activity of the Pt coatings in the presence of Sn or Ta oxide, was mainly for the Sn-containing coating. In addition, Pt–SnO_2/BDD electrode exhibited a faster kinetic for ethanol oxidation avoiding the production of unwanted intermediates on the surface. However, other complementary techniques are necessary and emerging methods that can provide measurements or preparation to include other metals on BDD surface. Future developments will rely upon the close collaboration of analytical chemists, engineers and electrochemists to ensure effective application and exploitation of new catalysts to increase the efficiency of fuel cells using BDD anodes.

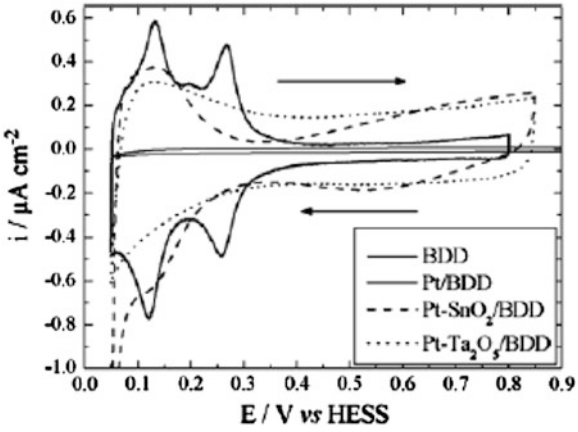

Fig. 7.18 Cyclic voltammograms recorded in 0.5 M H_2SO_4 for the BDD (*thin solid-line*), Pt/BDD (*thick-solid line*), Pt–SnO_2/BDD (*dashed line*), and Pt–Ta_2O_5/BDD (*dotted line*) surfaces, $\nu = 50$ mV s^{-1}. Reprinted with permission from [46]

7.4 BDD-Electrochemical Capacitors

Electrochemical capacitors (ECs) are an alternative as energy storage devices in many fields [49, 50]. ECs can charge and discharge much faster than a battery, and can have potentially much longer life than batteries. Typically they exhibit 20–200 times larger capacitance per unit volume or mass than conventional capacitors [51]. Therefore, a number of applications now use ECs or are strongly considering them for use [52, 53].

New types of carbon materials, such as carbon nanotubes and nanofibers, have been studied as possible EC electrode materials and these materials are attractive due to their high surface area and good matrix conductivity. However, it is desirable to have an electrode material with high capacitance and a wide working potential range in highly conductive aqueous electrolytes. Considering purely material properties, synthetic high-area BDD materials are very attractive candidates.

Honda and coworkers demonstrated the suitability of BDD nanoporous honeycomb electrodes for the development of aqueous electrochemical capacitors [54]. Nanoporous honeycomb diamond films were fabricated from microwave plasma chemical vapor deposited diamond films by oxygen plasma etching through an alumina mask. These films exhibited a wide working potential range (ca. 2.5 V) in the aqueous electrolytes, just as in the case of unetched as-deposited diamond electrodes. The capacitance of the honeycomb diamond electrode was found to be 1.97×10^{-3} F cm^{-2} (geometric area), which was 200 times greater than the unetched counterpart (as-deposited surface). The capacitance values obtained from

galvanostatic measurements, although somewhat higher, were consistent with this value, thus indicating that honeycomb diamond electrodes are some promise for electrochemical capacitor applications.

Afterward, the oxygen plasma-etched nanohoneycomb diamond thin film electrodes were examined for electrochemical capacitor applications in non-aqueous electrolytes [55], since, BDD films used in non-aqueous electrolytes exhibited 1.5–2.5 times wider potential windows (7.3 V) than those in aqueous electrolytes. For pore type 400 nm × 1.8 μm in non-aqueous electrolyte, the power and energy densities could reach only similar values as those in aqueous electrolytes. However, the impedance behavior observed in non-aqueous electrolytes was significantly different from that in aqueous electrolyte and indicated that the ac signal cannot penetrate to the bottom of the honeycomb pores in the non-aqueous electrolytes due to their low conductivity, and that not all the surface may contribute to the double-layer capacitance. Therefore, the authors concluded that the combination of pore type 400 nm × 1.8 μm and aqueous electrolyte could be best for examined thus far.

Later, nanoporous BDD films with various pore diameters (30–400 nm) and pore depths (50 nm to 3 μm) were fabricated by etching polished polycrystalline diamond films through porous alumina masks with oxygen plasma [56]. The capacitance values increased with increasing roughness factor, based on the pore dimensions. The honeycomb diamond electrode with pore dimensions 400 nm × 3 μm exhibited a 400-fold increase in the capacitance (3.91×10^{-3} μF cm^{-2}, geometric area) in comparison to the as-deposited surface, and this value was 80 and 500 times greater than that for GC and HOPG, respectively. For the porous film with 30 nm diameter pores, there was only a very small effect of the pore structure on the capacitance due to the high pore impedance.

Almeida and co-workers [57] developed nanocrystalline diamond (NCD) grown on carbon fibers (CF) substrate to be used as electric double-layer capacitor. A high specific capacitance (2.6 mF cm^{-2}) and rectangular-shaped CV curves were obtained up to a high potential scan rate (100 mV s^{-1}) in 0.5 mol L^{-1} H_2SO_4 aqueous solution for NCD/CF-1300 (CF-1300 consist of felt disks with 0.15-cm thickness diameter). These results showed that the NCD/CF electrodes could be an excellent candidate for electrochemical double-layer capacitors by controlling deposition parameters and CF substrate microstructures.

Later, these authors carried out the morphologic and electrochemical characterization of carbon fibers (CF) and their hybrid material formed by BDD films grown on CF [58]. Figure 7.19 shows the composition of CF surfaces, treated at 1,000 and 2,000 °C, associated with their respective SEM micrographs. SEM images obtained for the BDD/CF-1000 (A, A1 and A2) and BDD/CF-2000 electrodes (B, B1 and B2), exhibited in Fig. 7.20, demonstrate that the CF substrates were completely covered by a polycrystalline diamond coating. These micrographs also showed that the grain size of BDD/CF-2000 electrode was larger than that for BDD/CF-1000 electrode, supporting the strong influence of CF structural parameters on diamond

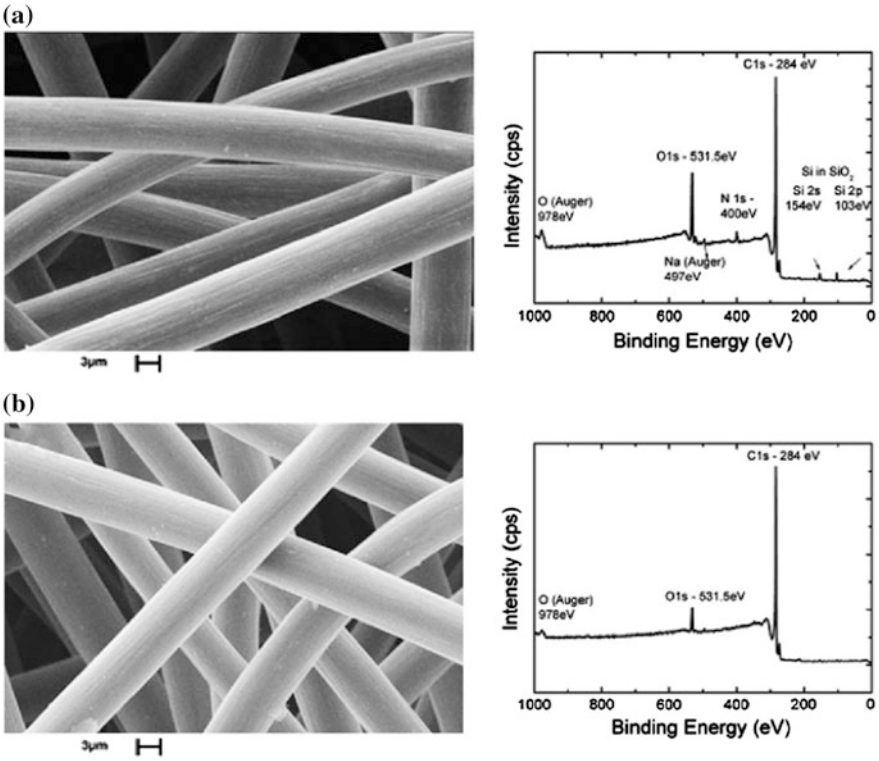

Fig. 7.19 Scanning electron microscopy images and X-ray photoelectron spectroscopy spectra of CF-1000 (**a**) and CF-2000 (**b**). Reprinted with permission from [58]

growth. Cyclic voltammetric curves demonstrated that BDD films grown on CF carbonized at 2,000 °C presented the highest capacitance value when compared with that for BDD/CF-1000 or those for CF electrodes, without diamond films. In addition, in electrochemical impedance experiments the BDD/CF-2000 electrode displayed almost an ideal capacitive behavior. The capacitance value for the BDD/CF-2000 was 1940 μF cm^{-2} (geometric area) that was approximately nine times larger than that for CF-2000 (Table 7.3). The best BDD/CF-2000 electrode capacitive behavior was attributed to its surface area increase as a result of the singular diamond film morphology formed on such carbon fiber.

Similar to batteries there are a few quantity of reports available in the literature about the use of BDD materials as ECs, thus, it is clear the necessity of studies with emphasis on the development of high-area BDD materials with both wide electrochemical windows and high capacitance. As a consequence, this is an open research area and an important challenge for future investigations.

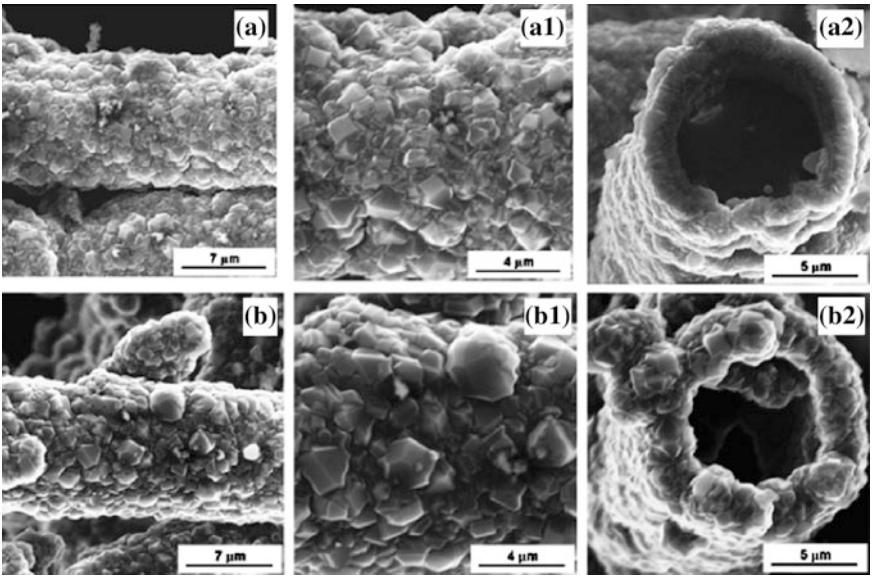

Fig. 7.20 Scanning electron microscopy images of the BDD films growth on carbon fibers: BDD/CF-1000 (A, A1 and A2) and BDD/CF-2000 (B, B1 and B2). A, A1, B, and B1 images show the surface film morphology, while images A2 and B2 show the film thickness around each fiber. Reprinted with permission from [58]

Table 7.3 BET area, capacitance and parameters used for fitting the impedance results in both the Nyquist and Bode plots

Electrode	BET ($m^2\ g^{-1}$)	C ($\mu F\ cm^{-2}$)	R_1 (Ω)	R_2 ($10^3\ \Omega$)	CPE_1 ($10^{-4}\ \Omega^{-1}\ s^n$)	n_1
CF-1000	1.51	266	142.6	0.474	0.06639	0.8427
CF-2000	0.33	245	16.26	1.338	0.1717	0.8493
BDD/CF-1000	4.05	459	305.4	4.41	0.1936	0.9004
BDD/CF-2000	14	1940	38.6	0.82	1.213	0.9086

7.5 Recent Applications of BBD for Electrochemical Energy Storage and Conversion

In recent years, new advances have been reported and we have summarized the most important contributions.

The electrosynthesis of uniformly dispersed nickel hydroxide nanoparticles (NPs) with narrow size distributions on pBDD electrodes was demonstrated for the first time by Hutton and co-workers [59]. This was achieved by electrogenerating OH^- in the presence of Ni^{2+} to create highly supersaturated ($S > 105$) nickel

hydroxide solutions close to the electrode for short periods of time (approximately seconds). This resulted in the electrodeposition of nickel hydroxide via precipitation directly on the electrode surface was confirmed by XPS, FE-SEM, and AFM. The size of the NPs could be tuned by controlling the reaction conditions, particularly the [OH^-] electrogeneration time. After 1 s, NPs with dimensions of 12 nm were produced with a surface coverage of 25 NPs μm^{-1}, increasing in size and surface coverage to ~39 nm and 87 NPs μm^{-2}, respectively, after 15 s. Longer times resulted in larger particles, which ultimately formed aggregates. After 100 s, the surface was dominated by such structures which were a few micrometers in height. The nickel hydroxide surface coverage was calculated by considering the charge passed during direct oxidation of nickel hydroxide. This value was in good agreement with that calculated on the basis of AFM images of the surface coverage, assuming spherical NPs. The close correlation of the two results suggests that during this solid-state electrooxidation process, the entire volume of nickel hydroxide was oxidized, not just the surface of the NP. The electrocatalytic oxidation of this electrode toward methanol and ethanol was found to be very efficient, achieving very high density currents of ~1,010 A g^{-1} for 0.5 Methanol and 990 A g^{-1} for 0.47 M methanol.

Gonzalez-Gonzalez and co-workers examined the possibility of the use of boron-doped diamond as the support for electrocatalyst particles in a fuel cell. The electrochemical behaviour of oxidized boron-doped diamond (BDD) films in 0.5 M H_2SO_4 using cyclic voltammetry showed a very wide electrochemical window. Platinum particles deposited a different platinum concentrations did not showed a different particle size; although they showed that exist a difference in the particle distribution. Pt and Pt-Ru particles deposited on BDD film substrate were characterized by SEM/EDS, XPS, and Auger, demonstrating that the BDD films were oxidized with C–O, C–OH, and C–O–C. Auger electron spectroscopy mapping showed that a complete oxidized surface of diamond and that ruthenium does not deposit on the oxidized diamond surface of the boron-doped diamond. Particles with 5–10 % of ruthenium with respect to platinum exhibited better performance for methanol oxidation in terms of methanol oxidation peak current and current stability. Subsequent deposit of ruthenium covers the platinum, and the catalytic property of the particle is lost. In the case of cyclic voltammogram for methanol oxidation, a current for the reverse peak was higher than what it is usually observed on carbon supports, may be due to the participation of electrogenerated hydroxyl radical on BDD that interact with Pt surface, oxidizing methanol.

Steam activation of boron doped diamond electrodes was conducted in an attempt to prepare porous BDD for fuel cell applications by Ohashi et al. [60]. Triangular pits and islands, most likely reflecting the atomic arrangement of the {111} plane, were formed by steam-activation at 700 °C. Higher activation temperatures lead to rigorous corrosion of the BDD surface forming a highly porous structure with a columnar texture. The electrochemically active surface area of the steam-activated BDD was up to 20 times larger than the pristine BDD electrode owing to the porous texture. In addition, a widening of the potential window was observed after steam activation, suggesting that the quality of BDD was enhanced due to oxidative removal of graphitic impurities during the activation process

allowing to fabricate high quality porous BDD electrodes with high surface area and a wide potential window for a durable electrocatalyst support for energy conversion applications.

Pt and Pt–Ru nanoparticle sizes obtained ranged from 2 to 5 nm and deposited on BDD surfaces (BDDNPs) by La-Torre-Riveros and co-workers [61]. These results indicated that this fast reaction was convenient to obtain small nanoparticles that are desirable to increase the surface area of a catalyst system. The undoped DNPs and BDDNPs surfaces were successfully used as support systems for metallic catalyst particulates obtained by chemical reduction. The platinum and ruthenium compounds mainly deposit on the –OH sites were confirmed by XPS and FTIR analysis. The spectroscopic and surface characterization showed the viability of obtaining a catalytic system based on undoped DNPs and BDDNPs supports, and platinum and ruthenium nanoparticles, which can be used in applications such as direct methanol fuel cells. Same research group [62] investigated BDD in nanosize particles and they were used as a support for noble metal-based nanoparticles. Nanosize platinum oxide was deposited on diamond nanoparticles as well as on boron-doped diamond nanoparticles by the sol-gel method. Cyclic voltammetric results showed an improvement in conductivity as well as in surface capacitance when diamond nanoparticles were doped with boron. The X-ray photoelectron spectroscopy boron binding energy peak showed B 0, which is consistent with the electrochemical characterization. Platinum oxide deposition was studied by cyclic voltammetry with an improvement when BDD nanoparticles were used as a support.

The route used to prepare the suspensions (inks) of DNPs and BDDNPs for the electrochemical studies performed by La-Torre-Riveros and co-workers [63] shown to be well suitable to obtain useful electrochemical information on these nanoparticle diamond supported systems. The cyclic voltammetry results showed that there were significant differences between the undoped DNP and BDDNPs samples, with the latter exhibiting superior characteristics in terms of various electrochemical applications, including that of catalyst support. For the latter application, perhaps the most important consequence of the observed low capacitance and wide potential window. Chemical reduction of metal nanoparticles at the nanometer scale was successfully performed using DNPs and BDDNPs as support materials by using an excess of a mild reducing agent ($NaBH_4$) and a surfactant (SDBS). X-ray diffraction peaks for the metallic nanoparticles were clearly demonstrated by them. The XPS and DRIFTS results provided important information about the type of surface functional groups on the diamond involved in the metal deposition. These techniques indicated that platinum ions interact, become reduced, and are deposited as metal on sites containing mainly –OH and CH_2 (or $–CH_3$) groups. TEM micrographs showed that the nanosize metals were crystals of less than 5 nm, which exhibited lattice fringes for the atomic planes of metal material, indicating good crystallinity, as well as of those of diamond. Anodic polarization results for methanol oxidation demonstrated that respectable current densities, in the range of mA cm^{-2}, could be obtained with both undoped DNPs and BDDNPs decorated with Pt and Pt–Ru catalysts prepared using excess reducing agent and surfactant. The power densities obtained from the best catalytic system (ca. 55 mW cm^{-2} for Pt–Ru/BDDNP) were comparable to those

obtained with amorphous carbon-supported catalytic systems, which are typically around 60 and 70 mW cm^{-2} at the same temperature. On the basis of the single fuel cell testing, it can be concluded that undoped DNPs and BDDNPs can be used as practical electrocatalyst supports for Pt and Pt–Ru in direct methanol fuel cells or hydrogen-fueled polymer electrolyte fuel cells.

The preparation of Pt-PrO_{2-x} electrocatalyst structures on diamond electrodes using electrodeposition techniques was explored by Chen et al. [64]. Pt was first electrodeposited on the diamond surface using a two-stage process involving PSD followed by a potentiostatic stage. Physically, the Pt deposited in this way consists of nanocrystals of the order of 5–30 nm diameter, depending on the Pt loading, aggregated into clusters of 200 nm diameter. XPS and electrochemical methods were then employed to demonstrate that thin porous PrO_{2-x} preferentially deposited on these crystals, thus modifying their electrochemical properties, as assessed through a range of redox couples. Electrochemical measurements confirmed that these modified Pt catalytic particles performed more efficiently than the unmodified Pt with regard to the oxidation of methanol. The data suggested that the main role of the PrO_{2-x} is to improve the tolerance to surface poisoning of the Pt structure.

The unsupported electrodeposition of Pt on carbon nano-onions (CNOs) produced from nanodiamond was investigated by Santiago et al. [65], using the rotating disk–slurry electrode (RoDSE) technique, obtaining mass production of platinum atoms and cluster-carbon-supported catalysts for fuel cell applications. CNOs were synthesized by annealing nanodiamond powder and subjected to acid treatment to increase their surface oxygen functionalities in order to facilitate platinum electrodeposition. The electrodeposition process behaves similarly to that for Vulcan as a carbon support. The quantity of Pt electrodeposited (i.e., metal loading) on Pt/CNOs is similar to that for samples prepared using Vulcan (i.e., 11.5 wt%). Although both Pt/CNOs and Pt/VXC have the same metal loading, the CNO samples exhibited enhanced thermal stability. The electrochemical analysis showed active platinum electrodeposited on CNOs with defined hydrogen adsorption–desorption peaks, showing enhanced onset potentials for methanol electrooxidation. Theoretical calculations showed the possibility of incorporating Pt atoms into carbon nano-onion systems. According to 3Pt/CNO geometric parameters obtained from the experimental study, they believe that Pt atoms are bonded to a hexagonal ring. Not surprisingly, as additional Pt atoms are added to the CNOs, the system becomes more metallic. These structural motifs obtained explain the improved thermal stability and lower methanol oxidation onset potentials. Optimizing the RoDSE technique using CNOs may pave the way to preparing bulk quantities of highly active supported metal atom and cluster catalysts for fuel cell applications.

Polytyramine (PTy) and cobalt oxide (Co_3O_4) were used as substrates for platinum electrodeposition by Spătaru et al. [66], in order to obtain electrode systems with electrocatalytic properties. PTy and Co_3O_4 were previously electrochemically deposited on graphite and boron-doped diamond (BDD) supports, respectively. Anodic oxidation of methanol was used as a test-reaction for assessing possible functional effects of the substrate on the electrochemical behaviour of the Pt particles. They found that, when deposited on PTy or cobalt oxide, the electrocatalyst

exhibited higher activity and it was less susceptible to fouling, via strong adsorption of reaction intermediates. X-ray photoelectron spectroscopy (XPS) measurements suggested that these features can be ascribed to the presence of −OH functional groups at the surface of the Pt particles. Electrodeposition of platinum on BDD resulted only in metallic Pt and $Pt(OH)_2$, whereas when graphite was used as substrate the presence of platinum oxides was also evident. During prolonged anodic oxidation of methanol, a higher stability of the −OH groups from the platinum surface was observed for graphite-supported Pt particles, compared to the case when bare BDD was used as support.

Although at first sight attractive, existing electro- and electroless routes for the deposition of Pt nanoparticles on diamond supports for fuel cell applications are problematic since they lead to very non-uniform deposits (electrodeposition) or require an activating coating (electroless deposition). Lyu et al. [67] demonstrated that a combined process, which involves simultaneous electroless and galvanic processes. The approach solves the uniformity problem associated with electrodeposition on heterogeneous substrates like BDD, and eliminates the requirement of a preactivation process used for conventional electroless deposition. A range of differing reaction conditions were explored using differing reducing agents to drive the electroless reaction, reaction temperature, addition of a surfactant and the use of ultrasonic pre-treatment. Optimal deposition conditions involve reaction at 0 °C, and the use of ascorbic acid as the reducing agent along with an ultrasonic pre-treatment. After optimising the deposition conditions, the Pt deposits were found to exhibit a uniform distribution of particles, and small particle size; they showed a high electrochemical activity in terms of a large electroactive area measured from hydrogen desorption, a low onset potential, and a high mass activity and surface activity for methanol oxidisation. The method therefore represented a significant improvement in current electrochemical and electroless approaches for the deposition of Pt nanoparticles on diamond and other inert substrates for electrocatalysis applications.

7.6 Conclusions

The modification of BDD surfaces with micro- and nanometric metallic and/or metallic oxide deposits using different methods like electrodeposition, sol-gel, thermal deposition, microemulsion methods, among others, was broadly investigated in the last two decades. The deposition of metal or metal oxide clusters onto the BDD film electrodes have been used to exploit the much higher catalytic activity of such nanoparticles using only very small catalyst amounts compared to the conventional bulk material. It has been widely related the use of these hybrid systems containing BDD as new anode catalysts formulations for future fuel cell applications. However, further developments should be carried out upon the close collaboration of analytical chemists, engineers and electrochemists to ensure effective application and exploitation of new catalysts to increase the efficiency of fuel cells using BDD anodes tested in real fuel cell operating conditions.

On the other hand, several efforts should be carried out for the application of BDD materials on electrochemical capacitors systems, due to the limited amount of reports available in the literature, which demonstrate that these subjects are in the beginning of development and the study of electrochemical behaviors is still needed for a significant advance in the application BDD for electrochemical energy storage and energy conversion systems.

References

1. E. Antolini, Platinum-based ternary catalysts for low temperature fuel cells Part II. Electrochemical properties. Appl. Cat. B: Environ. **74**(3–4), 337–350 (2007). doi:10.1016/j.apcatb.2007.03.001
2. U. Griesbach, D. Zollinger, H. Pütter, Ch. Comninellis, Evaluation of boron doped diamond electrodes for organic electrosynthesis on a preparative scale. J. Appl. Electrochem. **35**(12), 1265–1270 (2005). doi:10.1007/s10800-005-9038-2
3. M. Panizza, E. Brillas, Ch. Comninellis, Application of boron-doped diamond electrodes for wastewater treatment. J. Environ. Eng. Manage. **18**(3), 139–153 (2008)
4. P. Canizares, A. Gadri, J. Lobato, B. Nasr, R. Paz, M.A. Rodrigo, C. Saez, Comparison of the aluminum speciation in chemical and electrochemical dosing processes. Ind. Eng. Chem. Res. **45**(26), 3468–3473 (2006). doi:10.1021/ie060824a
5. J. Iniesta, P.A. Michaud, M. Panizza, G. Cerisola, A. Aldaz, Ch. Comninellis, Electrochemical oxidation of phenol at boron-doped diamond electrode. Electrochim. Acta **46**(23), 3573–3578 (2001). doi:10.1016/S0013-4686(01)00630-2
6. M.A. Rodrigo, P.A. Michaud, I. Duo, M. Panizza, G. Cerisola, Ch. Comninellis, Oxidation of 4-chlorophenol at boron-doped diamond electrode for wastewater treatment. J. Electrochem. Soc. **148**, D60–D64 (2001). doi:10.1149/1.1362545
7. B. Boye, P.A. Michaud, B. Marselli, M.M. Dieng, E. Brillas, Ch. Comninellis, Anodic oxidation of 4-chlorophenoxyacetic acid on synthetic boron doped diamond electrodes. New Diam. Front. C. Technol. **12**, 63–72 (2002)
8. I. Sirés, N. Oturan, M.A. Oturan, R.M. Rodríguez, J.A. Garrido, E. Brillas, Electro-Fenton degradation of antimicrobials triclosan and triclocarban. Electrochim. Acta **52**(17), 5493–5503 (2007). doi:10.1016/j.electacta.2007.03.011
9. C. Flox, J.A. Garrido, R.M. Rodríguez, P.L. Cabot, F. Centellas, C. Arias, E. Brillas, Mineralization of herbicide mecoprop by photoelectro-Fenton with UVA and solar light. Catal. Today **129**(1–2), 29–36 (2007). doi:10.1016/j.cattod.2007.06.049
10. I. Sirés, F. Centellas, J.A. Garrido, R.M. Rodríguez, C. Arias, P.L. Cabot, E. Brillas, Mineralization of clofibric acid by electrochemical advanced oxidation processes using a boron-doped diamond anode and Fe^{2+} and UVA light as catalysts. Appl. Catal. B-Environ. **72**(3–4), 373–381 (2007). doi:10.1016/j.apcatb.2006.12.002
11. Y. Shao, J. Liu, Y. Wang, Y. Lin, Novel catalyst support materials for PEM fuel cells: current status and future prospects. J. Mater. Chem. **19**(1), 46–59 (2009). doi:10.1039/B808370C
12. A. Kraft, Doped diamond: a compact review on a new, versatile electrode material. Int. J. Electrochem. Sci. **2**, 355–385 (2007)
13. M. Boutonnet, S. Lögdberg, E.E. Svensson, Recent developments in the application of nanoparticles prepared from w/o microemulsions in heterogeneous catalysis. Curr. Opin. Colloid Interface Sci. **13**(4), 270–286 (2008). doi:10.1016/j.cocis.2007.10.001
14. S. Eriksson, U. Nylén, S. Rojas, M. Boutonnet, Preparation of catalysts from microemulsions and their applications in heterogeneous catalysis. Appl. Catal. A Gen. **265**(2), 207–219 (2004). doi:10.1016/j.apcata.2004.01.014

15. M. Boutonnet, J. Kizling, P. Stenius, G. Maire, The preparation of monodisperse colloidal metal particles from microemulsions. Colloids Surf. **5**(3), 209–225 (1982). doi:10.1016/0166-6622(82)80079-6
16. G. Siné, Ch. Comninellis, Nafion®-assisted deposition of microemulsion-synthesized platinum nanoparticles on BDD: activation by electrogenerated OH radicals. Electrochim. Acta **50**(11), 2249–2254 (2005). doi:10.1016/j.electacta.2004.10.008
17. G. Siné, G. Fóti, Ch. Comninellis, Boron-doped diamond (BDD)-supported Pt/Sn nanoparticles synthesized in microemulsion systems as electrocatalysts of ethanol oxidation. J. Electroanal. Chem. **595**(2), 115–124 (2006). doi:10.1016/j.jelechem.2006.07.012
18. G. Siné, I. Duo, B. El Roustom, G. Fóti, Ch. Comninellis, Deposition of clusters and nanoparticles onto boron-doped diamond electrodes for electrocatalysis. J. Appl. Electrochem. **36**(8), 847–862 (2006). doi:10.1007/s10800-006-9159-2
19. G. Siné, D. Smida, M. Limat, G. Fóti, Ch. Comninellis, Microemulsion synthesized Pt/Ru/Sn nanoparticles on BDD for alcohol electro-oxidation. J. Electrochem. Soc. **154**(2), B170–B174 (2007). doi:10.1149/1.2400602
20. F. Cardarelli, P. Taxil, A. Savall, Ch. Comninellis, G. Manoli, O. Leclerc, Preparation of oxygen evolving electrodes with long service life under extreme conditions. J. Appl. Electrochem. **28**(3), 245–250 (1998). doi:10.1023/A:1003251329958
21. I. Duo, P.A. Michaud, W. Haenni, A. Perret, Ch. Comninellis, Activation of boron-doped diamond with IrO_2 clusters. Electrochem. Solid-State Lett. **3**(7), 325–334 (2000). doi:10.1149/1.1391137
22. B.E. Roustom, G. Fóti, C. Comninellis, Preparation of gold nanoparticles by heat treatment of sputter deposited gold on boron-doped diamond film electrode. Electrochem. Commun. **7**(4), 398–405 (2005). doi:10.1016/j.elecom.2005.02.014
23. F. Montilla, E. Morallón, I. Duo, Ch. Comninellis, J.L. Vázquez, Platinum particles deposited on synthetic boron-doped diamond surfaces. Application to methanol oxidation. Electrochim. Acta **48**(25–26), 3891–3897 (2003). doi:10.1016/S0013-4686(03)00526-7
24. A. De Battisti, S. Ferro, M. Dal Colle, Electrocatalysis at conductive diamond modified by noble-metal oxides. J. Phys. Chem. B **105**(9), 1679–1689 (2001). doi:10.1021/jp003216w
25. J.S. Gao, T. Arunagiri, J.J. Chen, P. Goodwill, O. Chyan, J. Perez, D. Golden, Preparation and characterization of metal nanoparticles on a diamond surface. Chem. Mater. **12**(11), 3495–3504 (2000). doi:10.1021/cm000465o
26. M. Li, G. Zhao, R. Geng, H. Hu, Facile electrocatalytic redox of hemoglobin by flower-like gold nanoparticles on boron-doped diamond surface. Bioelectrochemistry **74**(1), 217–224 (2008). doi:10.1016/j.bioelechem.2008.08.004
27. V. Saez, J. Gonzalez-Garcia, M.A. Kulandainathan, F. Marken, Electro-deposition and stripping of catalytically active iron metal nanoparticles at boron-doped diamond electrodes. Electrochem. Commun. **9**(5), 1127–1133 (2007). doi:10.1016/j.elecom.2007.01.018
28. K.E. Toghill, G.G. Wildgoose, A. Moshar, C. Mulcahy, R.G. Compton, The fabrication and characterization of a bismuth nanoparticle modified boron doped diamond electrode and its application to the simultaneous determination of cadmium (II) and lead (II). Electroanalysis **20** (16), 1731–1739 (2008). doi:10.1002/elan.200804277
29. J. Wang, G.M. Swain, Fabrication and evaluation of platinum/diamond composite electrodes for electrocatalysis preliminary studies of the oxygen-reduction reaction. J. Electrochem. Soc. **150**(1), E24–E32 (2003). doi:10.1149/1.1524612
30. O. Enea, B. Riedo, G. Dietler, AFM study of Pt clusters electrochemically deposited onto boron-doped diamond films. Nano Lett. **2**(83), 241–244 (2002). doi:10.1021/nl015666l
31. H.A. Gasteiger, N. Markovic, P.N. Ross, E.J. Cairns, Methanol electrooxidation on well-characterized platinum-ruthenium bulk alloys. J. Phys. Chem. **97**(46), 12020–12029 (1993). doi:10.1021/j100148a030
32. Z. He, J. Chen, D. Lui, H. Zhou, Y. Kuang, Electrodeposition of Pt–Ru nanoparticles on carbon nanotubes and their electrocatalytic properties for methanol electrooxidation. Diam. Relat. Mater. **13**(10), 1764–1770 (2004). doi:10.1016/j.diamond.2004.03.004

33. I. Gonzalez-Gonzalez, D.A. Tryk, C.R. Cabrera, Polycrystalline boron-doped diamond films as supports for methanol oxidation electrocatalysts. Diam. Relat. Mater. **15**(2–3), 275–278 (2006). doi:10.1016/j.diamond.2005.08.037
34. H.A. Gasteiger, N. Markovi´c, P.N. Ross, E.J. Cairns, Methanol electrooxidation on well-characterized platinum-ruthenium bulk alloys. J. Phys. Chem. **97**(46), 12020–12029 (1993). doi:10.1021/j100148a030
35. X. Lu, J. Hu, J.S. Foord, Q. Wang, Electrochemical deposition of Pt–Ru on diamond electrodes for the electrooxidation of methanol. J. Electroanal. Chem. **654**(1–2), 38–43 (2011). doi:10.1016/j.jelechem.2011.01.034
36. H.B. Suffredini, G.R. Salazar-Banda, S.T. Tanimoto, M.L. Calegaro, S.A.S. Machado, L.A. Avaca, AFM studies and electrochemical characterization of boron-doped diamond surfaces modified with metal oxides by the Sol-Gel method. J. Braz. Chem. Soc. **17**(2), 257–264 (2006). http://dx.doi.org/10.1590/S0103-50532006000200007
37. H.B. Suffredini, V. Tricoli, N. Vatistas, L.A. Avaca, Electro-oxidation of methanol and ethanol using a Pt–RuO_2/C composite prepared by the sol–gel technique and supported on boron-doped diamond. J. Power Sources **158**(1), 124–128 (2006). doi:10.1016/j.jpowsour.2005.09.040
38. L.C. Klein, M. Aparicio, F. Damay, Sol-gel processing for battery and fuel cell applications, in *Applications of Sol-Gel Technology*, vol. 3, ed. by S. Sakka (Kluwer Academic Publisher, New York, 2004), p. 311
39. S. Sakka (ed.), *Applications of Sol-Gel Technology* (Kluwer Academic Publisher, New York, 2004), p. 3
40. H.B. Suffredini, V. Tricoli, L.A. Avaca, N. Vatistas, Sol-gel method to prepare active Pt–RuO2 coatings on carbon powder for methanol oxidation. Electrochem. Commun. **6**, 1025–1028 (2004). doi:10.1016/j.elecom.2004.08.008
41. G.R. Salazar-Banda, H.B. Suffredini, L.A. Avaca, Improved stability of PtOx sol-gelmodified diamond electrodes covered with a Nafion® film. J. Braz. Chem. Soc. **16**(5), 903–906 (2005). http://dx.doi.org/10.1590/S0103-50532005000600003
42. G.R. Salazar-Banda, H.B. Suffredini, M.L. Calegaro, S.T. Tanimoto, L.A. Avaca, Sol–gel-modified boron-doped diamond surfaces for methanol and ethanol electro-oxidation in acid medium. J. Power Sources **162**(1), 9–20 (2006). doi:10.1016/j.jpowsour.2006.06.045
43. G.R. Salazar-Banda, K.I.B. Eguiluz, L.A. Avaca, Boron-doped diamond powder as catalyst support for fuel cell applications. Electrochem. Commun. **9**(1), 59–64 (2007). doi:10.1016/j.elecom.2006.08.038
44. H.B. Suffredini, V. Tricoli, N. Vatistas, L.A. Avaca, Electro-oxidation of methanol and ethanol using a Pt–RuO_2/C composite prepared by the sol–gel technique and supported on boron-doped diamond. J. Power Sources **15**(1), 124–128 (2006). doi:10.1016/j.jpowsour.2005.09.040
45. H.B. Suffredini, G.R. Salazar-Banda, L.A. Avaca, Enhanced ethanol oxidation on PbOx/-containing electrode materials for fuel cell applications. J. Power Sources **171**(2), 355–362 (2007). doi:10.1016/j.jpowsour.2007.06.048
46. G.R. Salazar-Banda, H.B. Suffredini, L.A. Avaca, S.A.S. Machado, Methanol and ethanol electro-oxidation on Pt–SnO_2 and Pt–Ta_2O_5 sol–gel-modified boron-doped diamond surfaces. Mater. Chem. Phys. **117**(2–3), 434–442 (2009). doi:10.1016/j.matchemphys.2009.06.027
47. I. González-González, D.A. Tryk, C.R. Cabrera, Polycrystalline boron-doped diamond films as supports for methanol oxidation electrocatalysts. Diam. Relat. Mater. **15**(2–3), 275–278 (2006). doi:10.1016/j.diamond.2005.08.037
48. V.M. Swope, I. Sasaki, A. Ay, G. M. Swain, Conductive diamond powder: a new catalyst support for the polymer electrolyte membrane fuel cell. ECS Trans. **3**(28), 27–36 (2007). doi:10.1149/1.2753281
49. A. Lewandowski, M. Galinski, Practical and theoretical limits for electrochemical double-layer capacitors. J. Power Sources **173**(2), 822–828 (2007). doi:10.1016/j.jpowsour.2007.05.062
50. H.D. Abruña, Y. Kiya, J.C. Henderson, Batteries and electrochemical capacitors. Phys. Today **61**(12), 43–47 (2008). http://dx.doi.org/10.1063/1.3047681

51. Y. Zhang, Y. Gui, X. Wu, H. Feng, A. Zhang, L. Wang, T.C. Xia, Preparation of nanostructures NiO and their electrochemical capacitive behaviors. Int. J. Hydrogen Energy **34** (5), 2467–2470 (2009). doi:10.1016/j.ijhydene.2008.12.078
52. J.R. Miller, Electrochemical capacitor thermal management issues at high-rate cycling. Electrochim. Acta **52**(4), 1703–1708 (2006). doi:10.1016/j.electacta.2006.02.056
53. C.-Z. Yuan, B. Gao, X.-G. Zhang, Electrochemical capacitance of NiO/Ru0.35/V0.65/O_2/ asymmetric electrochemical capacitor. J. Power Sources **173**(1), 606–612 (2007). doi:10.1016/j.jpowsour.2007.04.034
54. K. Honda, T.N. Rao, D.A. Tryk, A. Fujishima, M. Watanabe, K. Yasui, H. Masuda, Electrochemical characterization of the nanoporous honeycomb diamond electrode as an electrical double-layer capacitor. J. Electrochem. Soc. **147**(2), 659–644 (2000). doi:10.1149/1.1393249
55. M. Yoshimura, K. Honda, R. Uchikado, T. Kondo, T.N. Rao, D.A. Tryk, A. Fujishima, Y. Sakamoto, K. Yasui, H. Masuda, Electrochemical characterization of nanoporous honeycomb diamond electrodes in non-aqueous electrolytes. Diam. Relat. Mater. **10**(3–7), 620–626 (2001). doi:10.1016/S0925-9635(00)00381-2
56. K. Honda, T.N. Rao, D.A. Tryk, A. Fujishima, M. Watanabe, K. Yasui, H. Masuda, Impendance characteristics of the nanoporous honeycomb diamond electrodes for electrical double-layer capacitor applications. J. Electrochem. Soc. **148**(7), A668–A679 (2001). doi:10.1149/1.1373450
57. E.C. Almeida, A.F. Azevedo, M.R. Baldan, N.A. Braga, J.M. Rosolen, N.G. Ferreira, Nanocrystalline diamond/carbon felt as a novel composite for electrochemical storage energy in capacitor. Chem. Phys. Lett. **438**(1–3), 47–52 (2007). doi:10.1016/j.cplett.2007.02.040
58. E.C. Almeida, M.R. Baldan, J.M. Rosolen, N.G. Ferreira, Impedance characteristics of the diamond/carbon fiber electrodes for electrical double-layer capacitor. Diam. Relat. Mater. **17** (7–10), 1529–1533 (2008). doi:10.1016/j.diamond.2008.03.006
59. L.A. Hutton, M. Vidotti, A.N. Patel, M.E. Newton, P.R. Unwin, J.V. Macpherson, Electrodeposition of nickel hydroxide nanoparticles on boron-doped diamond electrodes for oxidative electrocatalysis. J. Phys. Chem. C **115**(5), 1649–1658 (2011). doi:10.1021/jp109526b
60. I. Gonzalez-Gonzalez, C. Lorenzo-Medrano, C.R. Cabrera, Sequential electrodeposition of platinum-ruthenium at boron-doped diamond electrodes for methanol oxidation. Adv. Phy. Chem. **2011**, Article ID 679246 (2011). doi:10.1155/2011/679246
61. E. Abel-Tatis, A.E. Mendez-Torres, D.A. Tryk, M. Prelas, C.R. Cabrera, Synthesis of platinum and platinum–ruthenium-modified diamond nanoparticles. J. Nanopart Res. **13**(7), 2997–3009 (2011). doi:10.1007/s11051-010-0196-8
62. L. Cunci, C.R. Cabrera, Preparation and electrochemistry of boron-doped diamond nanoparticles on glassy carbon electrodes. Electrochem. Solid-State Lett. **14**(3), K17–K19 (2011). doi:10.1149/1.3532943
63. L. La-Torre-Riveros, R. Guzman-Blas, A.E. Méndez-Torres, M. Prelas, D.A. Tryk, C.R. Cabrera, Diamond nanoparticles as a support for Pt and PtRu catalysts for direct methanol fuel cells. ACS Appl. Mater. Interfaces **4**(2), 1134–1147 (2012). doi:10.1021/am2018628
64. L. Chen, J. Hu, J.S. Foord, Electrodeposition of a Pt–PrO_2−x electrocatalyst on diamond electrodes for the oxidation of methanol. Phys. Status Solidi A **209**(9), 1792–1796 (2012). doi:10.1002/pssa.201200049
65. D. Santiago, G.G. Rodríguez-Calero, A. Palkar, D. Barraza-Jimenez, D.H. Galvan, G. Casillas, A. Mayoral, M. Jose-Yacamán, L. Echegoyen, C.R. Cabrera, Platinum electrodeposition on unsupported carbon nano-onions. Langmuir **28**(49), 17202–17210 (2012). doi:10.1021/la3031396
66. T. Spătaru, P. Osiceanu, M. Marcu, C. Lete, C. Munteanu, N. Spătaru, Functional effects of the deposition substrate on the electrochemical behavior of platinum particles. Jpn. J. Appl. Phys. **51**(9), 090119 (2012). doi:10.1143/JJAP.51.090119
67. X. Lyu, J. Hua, J.S. Foord, Q. Wang, A novel electroless method to prepare a platinum electrocatalyst on diamond for fuel cell applications. J. Power Sources **242**, 631–637 (2013). doi:10.1016/j.jpowsour.2013.05.057

Chapter 8
Diamond PN/PIN Diode Type Electron Emitter with Negative Electron Affinity and Its Potential for the High Voltage Vacuum Power Switch

Daisuke Takeuchi and Satoshi Koizumi

Abstract This chapter reviews the electron emission properties of hydrogen terminated diamond surfaces with a "true" negative electron affinity (NEA), and presents the recent development of electron emitters based on diamond *PN* and *PIN* junctions, that could apply to a high voltage vacuum power switch. The background to this topic, including the emission mechanism with free excitons, and carrier injection with a hopping conduction, is also introduced.

8.1 Electron Emission Mechanism of Diamond Surfaces with True NEA

8.1.1 Introduction

Basic device concepts and physics of negative electron affinity (NEA) cathodes have been developed by means of heavily doped *P*-type III–V compound semiconductors such as GaAs, GaN, and so on [1]. These device surfaces have strong downward band bending due to ionization of heavily doped acceptors with amount of surface states. In addition, alkali-halide oxides such as cesium oxides reduce the electron affinity. Both properties enable to make lowering of the vacuum level relative to the conduction band minimum in the bulk as shown in Fig. 8.1b, whereas the ordinal surface case with "positive" electron affinity is also shown in Fig. 8.1a. The case of Fig. 8.1b is called as "effective negative electron affinity (NEA)" [2].

D. Takeuchi (✉)
Energy Technology Research Institute, National Institute of Advanced Industrial Science and Technology (AIST), 1-1-1 Umezono, Tsukuba, Ibaraki 305-8568, Japan
e-mail: d.takeuchi@aist.go.jp

S. Koizumi
Environment and Energy Materials Division, National Institute for Materials Science (NIMS), 1-1 Namiki, Tsukuba, Ibaraki 305-0044 Japan

N. Yang (ed.), *Novel Aspects of Diamond*, Topics in Applied Physics 121,
DOI 10.1007/978-3-319-09834-0_8

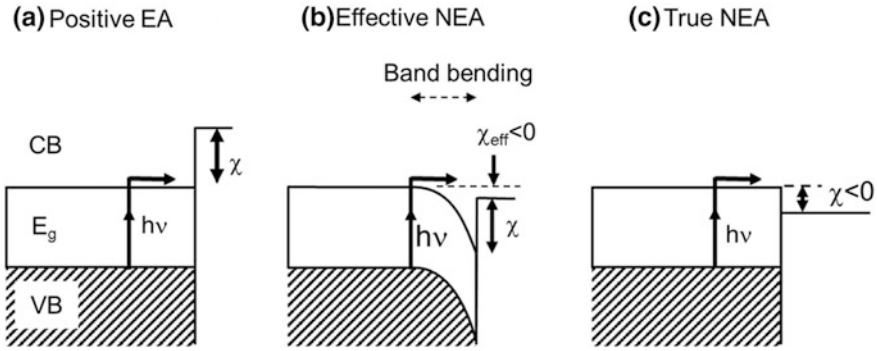

Fig. 8.1 Schematic energy band diagram in the surface; **a** an ordinal case of semiconductors with positive electron affinity (EA), where the vacuum level is higher than the conduction band (CB) minimum, **b** a case of heavily *P*-type semiconductors with surface treatment with cesium oxides, where the vacuum level is lower than the CB minimum in the bulk, **c** a case of "true" negative EA, where the vacuum level is lower than the CB minimum in the surface. E_g represents energy band gap, VB the valence band, χ the EA, χ_{eff} the effective EA, hν the photon energy for the photo-excitation model

The effective NEA devices have been well developed as photocathodes in high energy accelerator research fields [3]. GaAs/GaAsP super-lattice with effective NEA photocathodes were also developed for spin-polarized electron source applications [4].

On the other hand, diamond has been attracts a lot of researchers because of its superior semiconductor properties such as high thermal conductivity, high break-down field, high mobility, and true negative electron affinity (NEA), where the conduction band minimum is higher than the vacuum level even in the surface as shown in Fig. 8.1c.

The idea of NEA on natural diamond (111) was introduced by Himpsel et al. with a result of quantum photoelectron emission yield experiments [5]. They found that the yield raised from the absorption edge of diamond. In addition, they observed a sharp photoelectron emission count peak in the lowest cut-off kinetic energy region in ultraviolet-light induced photoelectron emission spectroscopy (UPS). These indicated that there was no potential barrier for the electrons in the conduction band minimum of diamond. In short, there is a large contribution of bulk-derived electron emission to the yield.

Baumann et al. found the same effect in the X-ray (XPS) or UPS using hydrogen plasma treated (100), (111), and (110) natural diamond, where there was sharp count peak in the lowest cut-off kinetic energy region [6]. Diedrich et al. indicated the unoccupied extended surface states below the conduction band minimum in the bulk for the hydrogen-terminated natural type-IIb (boron doped) (100) and (111) diamond by precise XPS experiments [7]. They indicated variation of NEA values, and a question about (111) case, where the lowest cut-off kinetic energy peak was not clearly appeared. Cui et al. also investigated natural IIb-type (111) diamond

which was exposed to hydrogen plasma. They clearly showed large amount change of electron affinity with more than 3 eV, and discuss the change from NEA to PEA by dehydrogenation with isothermal and isochronal annealing in ultra-high vacuum (UHV) [8]. They also found yields from the occupied states in the gap by total photoelectron emission yield spectroscopy (TPYS).

Ristein et al. also investigated the IIb-type (111) diamond with using high sensitive TPYS [9]. They revealed the bulk-derived yield above the band-gap energy excitations, which corresponded to the lowest cut-off kinetic energy peak in XPS and UPS as mentioned above. In addition, they found yields from the occupied states below the band-gap energy excitations.

Bandis and Pate also found the same effect by TPYS. They pointed that oscillatory yield spectrum was found, whose threshold energy was the same as the indirect free-exciton absorption edge with transverse optical (TO) phonon emission [2, 10]. In addition, they found that the period of oscillation was almost the same as a TO phonon energy of 160 meV, which is twice of the free-exciton binding energy of 80 meV [11, 12]. Moreover, they noticed that the oscillation was banished by annealing at 300 °C in vacuum.

Ristein and Cui were also revealed that the yield at around the indirect absorption edge showed threshold energies of free-exciton absorption edge with transverse acoustic (TA) and TO phonon emission [9]. Combining XPS results to check the work function change, they evaluated the value of NEA as −1.3 eV [13]. They used the annealed samples, and they did not report on the oscillatory yield pointed by Bandis et al.

As introduced these early works, the bulk-derived electron emission, which looked plausible as NEA, was confirmed. However, the detailed mechanism including surface states, free-excitons, and *P*-type surface conductivity related with hydrogen-terminated diamond surfaces, has not yet been totally discussed [14–23].

8.1.2 NEA Properties Investigated with TPYS System

In photoelectron yield spectroscopy (PYS) measurement, it is possible to measure the quantum efficiency of photoelectron emission as a function of photon energy. The dynamical range in these measurements was about three orders of magnitude in the yield. The sensitivity was limited by the fact that the number of photoelectrons emitted was measured as the (hole) current through the sample.

However, a large dynamic range is necessary as described by Schaefer et al. as follows: “It (the dynamic range) determines the sensitivity with which small numbers of occupied states can be detected in semiconductors where the photoemission threshold is ideally determined by a vanishing density of states at the valence band maximum. The sensitivity of the yield method determines thus the minimum density of gap states which can be detected. Low concentrations of gap states, for example, exist as a result of volume or surface defects, impurities or adsorbate” [24].

In total photoelectron yield spectroscopy (TPYS), the introduction of electron multipliers is able to detect single electrons, and then the sensitivity of yield measurements is greatly enhanced [24]. It allows very low excitation level, and then TPYS could be applied even for the high resistive case such as oxidized intrinsic IIa- or Ib-type diamond [25] (Fig. 8.2).

The electron affinity is determined from the onset and strong rise of photoelectron emission, taking the band gap of the semiconductors under investigation into account. For diamond, it is reasonable that TPYS is carried out with Xe and D_2 lamps, because they cover a photoexcitation range from 2 to 7.75 eV, means excitation in and above the band gap energy level. As TPYS measures the energy gap between occupied states and the vacuum level, the surface Fermi-level does not affect the results in principle.

According to these characteristics, the properties of electron affinity on diamond investigated with TPYS system are introduced in this section (Fig. 8.2). In TPYS system, the light was dispersed by a double monochromator with a resolution of 15 meV at 248 nm ($h\nu = 5$ eV) using 200 μm input/output slits. The samples were mounted on a molybdenum (Mo) sample holder with a tantalum (Ta) cover, and introduced into an ultra-high vacuum (UHV) system with a base pressure of 1×10^{-7} Pa. TPYS was carried out at RT.

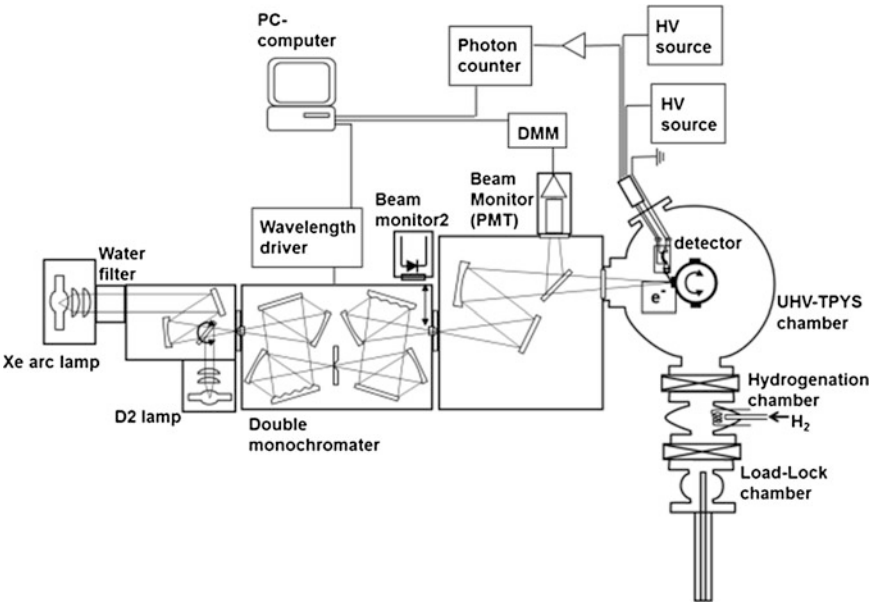

Fig. 8.2 TPYS system for diamond

8.1.2.1 Conduction Type and NEA

The measurements were performed on a B-doped *P*-type (001) chemical vapor deposited homoepitaxial film (CVD-B), and a P-doped *N*-type (001) CVD homoepitaxial film (CVD-P) grown on synthetic type Ib (001) diamond. Both were single crystals. The thickness of each film was about 2 μm. The doping concentration was 10^{17} cm^{-3} in the CVD-B film and 10^{18} cm^{-3} in the CVD-P film. The detailed growth conditions were reported in the literature [26, 27].

Hall-effect measurements confirmed that the CVD-B film was *P*-type and the CVD-P film was *N*-type. The samples were cleaned by boiling in a mixture of H_2SO_4 and HNO_3 at 230 °C to remove non-diamond carbon and to oxidize the surfaces. Next, the samples were H-terminated in a microwave hydrogen plasma at 800 °C.

Figure 8.3 shows the results for the TPYS of the CVD-B and CVD-P films. The CVD-B film exhibits a clear onset of exciton derived photoelectron emission near a band-gap energy (E_g) of 5.5 eV and a free exciton ground state (E_{gx}) of 5.4 eV. The CVD-P film do not perform as the CVD-B film, and exhibit a yield even below 4.5 eV [28].

Because TPYS is an integrating spectroscopy (no energy discrimination of the electrons) and photoelectrons are excited into a continuum of states, different excitation processes show up as characteristic thresholds resulting in a power-law increase in the TPY spectra. Hence, three distinct excitation channels can be identified in Fig. 8.3.

Channel I, corresponds to the excitation of electrons from the valence band. The fact that the threshold energy of around 5.5 eV coincides with the band gap of diamond indicates the NEA of the hydrogenated surface. The electrons excited into the conduction band thermalized immediately to the conduction band minimum [9], and a part of the electrons diffused to the surface could contribute to the yield of

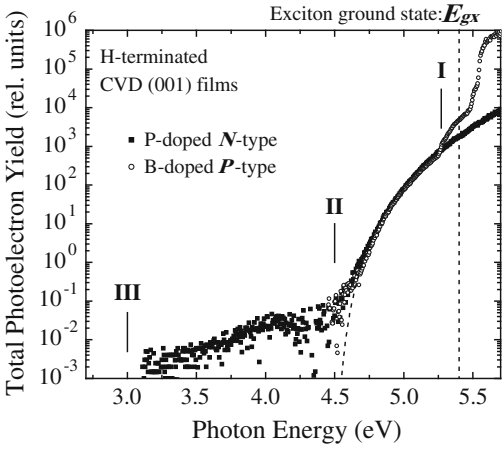

Fig. 8.3 TPYS results for H-terminated B-doped (CVD-B) and P-doped (CVD-P) CVD films

Channel I. Therefore, Fig. 8.3 indicates that there is an energy barrier such as upward band bending in the surface of an *N*-type CVD-P film.

In the literature, Sque et al. calculated that the upward band bending originates extended surface unoccupied states [29]. In addition, the bending seems to be too large for excitons to contribute electron emission as was discussed in our report [30]. The influence of the free excitons is discussed in more detail later.

Channel II, starting at a threshold energy of about 4.4–4.6 eV, can be interpreted as the direct excitation of electrons from occupied surface extended states (surface valence band) to the vacuum level through unoccupied surface extended states (surface conduction band) [29], without any transport inside the diamond crystal. Consequently, this is expected to be independent of carrier conduction type such as *P*- or *N*-type of the diamond films, film thickness, and crystalline quality [25, 28, 31]. In fact, the spectra from both the CVD-B and CVD-P samples are coincident with each other in this regime.

Channel III at a threshold of about 3.0 eV, then, corresponds to photoelectrons excited from surface defects situated at around 1.6 eV above the valence band maximum (VBM) into surface unoccupied extended states (surface conduction band) [30].

Note that Channel III was previously interpreted as photoelectrons excited from bulk defects situated at around 2.4 eV below the conduction band minimum (CBM) into the conduction band [9, 32]. Although this indicates that the sample is *N*-type which should inhibit electron emission from the bulk due to upward band bending as discussed above, a TPY from channel III was observed in the literatures even with intrinsic diamond [32].

Moreover, the dehydrogenated experiments with hydrogen thermal desorption indicated that the electronic states concerning channel III corresponded to occupied dangling bond states due to hydrogen desorption [33]. In the case of surface gap states, the energy level is well explained even for intrinsic diamond, and it is no longer necessary to discuss about the electron emission from the bulk of *N*-type diamond.

According to these results, photoexcitation paths could be summarized as shown in Fig. 8.4, where electron affinities are shown in terms of the photexcitation paths. In the case of a NEA, path I is the photoexcitation path from the valence band to the conduction band, path II is from the valence band on or in the vicinity of the surface to the vacuum level, and path III is from the occupied gap states in the surface. In the case of a PEA, path II' is from the valence band to the conduction band on or in the vicinity of the surface.

8.1.2.2 H-Terminated and H-Free (001) Diamond Surfaces

For the measurements high pressure and high temperature (HPHT) synthesized single crystalline type IIa (intrinsic) diamond with a (001) crystal orientation was used. The thickness of the IIa diamond was 300 μm. The electron affinities of samples with different H-terminations, ranging from fully H-terminated to dehydrogenated

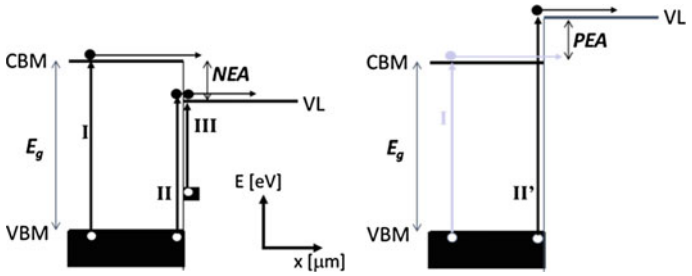

Fig. 8.4 Electron affinities shown in terms of the photoexcitation paths. In the case of a NEA, path I is the photoexcitation path from the valence band to the conduction band, path II is from the valence band on or in the vicinity of the surface to the vacuum level, and path III is from the occupied gap states in the surface. In the case of a PEA, path II' is from the valence band to the conduction band on or in the vicinity of the surface. Both paths II and III are allowed with unoccupied extended states in the gap [29]

surfaces, were characterized. The first sample was H-terminated in a microwave hydrogen plasma at 800 °C for 5 min, and after the first TPYS experiment at RT, it was annealed in an ultrahigh vacuum at 900 °C for 10 min [34].

In the case of a fully H-terminated (001) surface, the threshold energy of the sub-band yield was 4.4 eV as shown in Fig. 8.5, which corresponds to path II in Fig. 8.4, and a NEA of about −1.1 eV. H-termination related unoccupied surface extended states in the energy band gap (E_g) of diamond were reported by Sque et al., which supports our experimental findings [29].

Remarkable rises around the band gap energy E_g can be seen in the spectrum, which indicates the negative electron affinity in the photoemission from H-terminated

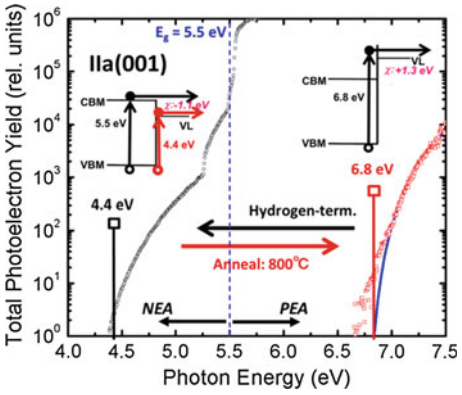

Fig. 8.5 TPY spectra from a fully hydrogenated (*open circles*) and dehydrogenated (*open squares*) diamond sample measured at RT. The *insets* show energy band diagrams for the photoelectron emission processes in the cases of negative (NEA) and positive electron affinity (PEA) surfaces

diamond. This feature is known as the NEA peak in XPS or UPS experiments as mentioned above, and corresponds to path I in Fig. 8.4.

The total photoelectron yield (TPY) for path I is proportional to the diffusion length of free electrons within the sample, which is at least a few micrometers in high quality intrinsic diamond samples [35]. Comparison of the TPY from path I and path II shows the onset of electron emission from the bulk into the vacuum as illustrated in Fig. 8.5 [2, 13, 25, 36].

The detailed structure of these parts of the spectra originates from exciton generation, which involves phonon absorption and emission in the diamond sample [8, 25–28]. These excitons partly diffuse to the surface where they recombine. The electrons can access the vacuum level as there is no energy barrier at the surface. Detailed mechanisms are discussed in Sect. 8.1.3.

On the other hand, on the fully-dehydrogenated (001) surface, the threshold energy is about 6.8 eV. Applying an established data fitting technique shows a positive electron affinity of +1.3 eV [34, 37–39]. In this case, the photoexcitation corresponds to path II' in Fig. 8.4.

8.1.2.3 Surface Conductivity and NEA

H-terminated diamond surfaces that absorb molecules such as C_{60} or materials from the air so called adsorbates, exhibit a *P*-type high surface conductivity (SC). To discuss electron emission from H-terminated diamond surfaces with NEA, it is necessary to understand the influence of the SC.

For the measurements a synthetic type IIa (001) single-crystal diamond was used. The samples were boiled in a mixture of H_2SO_4 and HNO_3 at 200 °C to remove contaminants and non-diamond carbon. It was hydrogenated in a microwave hydrogen plasma at 750 °C. The samples were introduced into a UHV system and annealing was carried out. Each annealing step lasted 10 min. Conductance measurements using two Au tips as contacts were performed at RT either under high vacuum conditions in a load lock attached directly to the UHV chamber or in air. These experiments were carried out with a TPYS system in Erlangen University in Germany [32].

Figure 8.6 shows the TPY spectra of the IIa (001) diamond. The first spectrum was obtained using the freshly hydrogenated sample with annealing at 200 °C (open circles) in the UHV. The sheet conductance, measured in a high vacuum after the TPYS, was 25 pS, indicating that the sample was in the low-SC state. Samples showing the spectral signature exhibited by the low-SC sample shall be termed as being in state A.

After re-establishing a high SC through exposure to the air, where the sheet conductance increased to 0.18 μS, the formation of the hole layer was confirmed. In this state, the sample was reintroduced into the UHV and characterized again by TPYS (filled triangles). At the same time, the electron yield is suppressed by more than one order of magnitude as shown by state B. Note that the change from A to B, or vice versa, is reproducible.

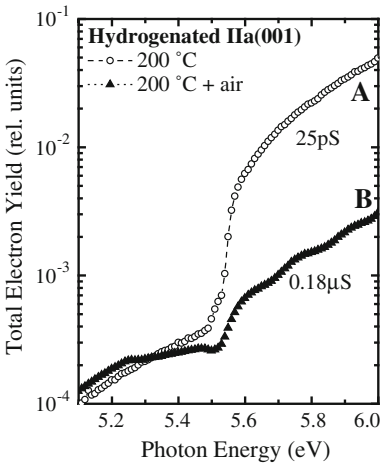

Fig. 8.6 TPY spectra of the H-terminated IIa (001) diamond measured at RT. Different excitation mechanisms for path I in Fig. 8.4 can be observed

Figure 8.6 shows that there are different emission mechanisms for A and B through path I of Fig. 8.4. The low SC of state A indicates flat band case in the surface energy band diagram as a nature of intrinsic semiconductors. In these cases, there are no energy barriers for free electrons in the conduction band, which results in electron emission through NEA surfaces through path I of Fig. 8.4.

On the other hand, the high SC of state B indicates *P*-type semiconductor characteristics [32], which leads to upward band bending in the surface region to align the Fermi-leve because the bulk IIa diamond is intrinsic type, that likely prevents free electrons from being emitted through the NEA surfaces [23, 32]. Note that even the bulk is lightly doped *P*-type semiconductor cases, there must be upward band bending with high SC because of very high concentration of holes in the SC layer at least with more than 10^{18} cm^{-3} [16, 17, 22, 23], which leads the Fermi-level closed to the top of valence band edge, while the lightly doped *P*-type diamond shows the Fermi-level about 0.3 eV above the valence band edge.

However, in Fig. 8.6, a small onset at around the band gap excitation region and slight oscillations appear in the TPY spectrum. Bandis and Pate suggested that this was due to free exciton derived electron emission [2, 10, 32].

According to their discussion, the binding energy of free excitons is 80 meV, and the transverse optical phonon energies from Γ position to the conduction band minimum in *k*-space are at around from 160 to 140 meV, which is almost double the binding energy of the free excitons. Then, stable and unstable conditions of free excitons occur while sweeping the photoexcitation energy in the TPYS experiments, which gives the oscillatory yield shown in Fig. 8.6. In short, the oscillation results from life time modulation of free excitons due to the excess internal energy at each photoexcitation energy.

As a result, free electrons and excitons determine the electron emission mechanism from H-terminated diamond NEA surfaces. Electronic states in diamond with free excitons will be discussed in the next session.

8.1.3 Electronic States of Diamond with Free Excitons

As discussed in Sect. 8.1.2, the mechanism of electron emission from NEA diamond surfaces is influenced by free exciton generation because free excitons looks stable in diamond even at RT since the binding energy of the free excitons in diamond is 80 meV, which is more than three times the thermal energy at RT. Okushi and Kanno have already discussed the mass action law among free excitons, electrons and holes in diamond [40, 41].

$$n_{ex} \rightleftharpoons n + p \tag{8.1}$$

Based on the Bose-Einstein statistics for free excitons, and the Fermi-Dirac statistics for free electrons and holes, the following equation was derived.

$$np = \left(\frac{\pi k_B T}{h^2}\frac{m_e^* m_h^*}{m_e^* + m_h^*}\right)^{\frac{3}{2}} \exp\left(-\frac{E_{ex}}{k_B T}\right) n_{ex} = A n_{ex}, \tag{8.2}$$

where n_{ex} is the density of free excitons, n is the density of free electrons, p is the density of free holes, k_B is the Boltzmann constant, h is the Planck constant, T is the absolute temperature, m_e^* and m_h^* are the effective masses of free electrons and free holes, respectively, and E_{ex} is the binding energy of free excitons.

In the case of photoexcitation, or high enough current injection into the intrinsic layer as a bipolar action, the charge neutrality requires $n \sim p$, and then (8.2) yields [42],

$$\frac{n}{n_{ex}} = A^{\frac{1}{2}} \frac{1}{\sqrt{n_{ex}}}, \tag{8.3}$$

Figure 8.7 illustrates results for the equation above. Here, the effective masses of electrons and holes were 0.57 and 0.69, respectively [43]. When n_{ex} is constant along the plotted line, the graph essentially indicates temperature dependence on the electron density n. However, the ratio of n/n_{ex} was plotted to consider the physics behind.

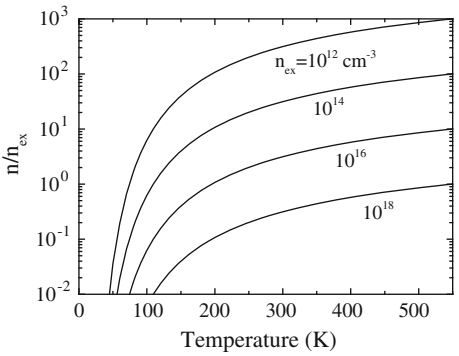

Fig. 8.7 Temperature dependence of the ratio of the density of free electrons (n) to that of free excitons (n_{ex}) in diamond for different values of n_{ex}

Of course, when the n_{ex} increases, the n also increases. For example, when the n_{ex} increases 100 times, the n also increase ten times. Note that then the ratio of n/n_{ex} is decreased with increasing the n_{ex} as shown in Fig. 8.7.

Figure 8.7 shows items as follows:

- The degree of excitation, resulting from impinging photons or an injection current, determines n_{ex}.
- The lower n_{ex}, the higher the n/n_{ex}.
- The lower T, the lower n/n_{ex}.

TPYS experiments are using the electron counting method, where the excitation by photons is very weak [24], hence the excitation at RT favors free electrons and holes, not the formation of free excitons.

Therefore, it is natural that in case of H-terminated *N*-type diamond, there was no bulk-derived electron emission as shown in Fig. 8.3 even with taking into account the free excitons due to the upward band-bending for the electrons dominant in the surface. This description outlines a further simple model for electron emission through NEA diamond surfaces as observed by TPYS.

In previous work, one to two orders of magnitude increase of the photoemission yield signal intensities of exciton-derived electron emission were observed when the sample temperature rose from RT to 550 K [34]. The scenario mentioned above with Fig. 8.7 indicated that these phenomena did not directly mean the electron emission from free excitons. Free excitons must generate at the certain photoexcitation energy levels, but then they were preferentially distributed as free electrons, since the higher the sample temperature, the further the distribution to free electrons from free excitons as shown in Fig. 8.7.

On the other hand, Bandis and Pate showed the opposite temperature dependence for the TPY before annealing after the hydrogenation process [2]. However, they also found an oscillatory TPY spectrum, as shown by the B state in Fig. 8.6. According to Bandis and Pate, such spectra can be expressed by

$$\mathrm{TPY} = C(h\nu - E_{th})^{\frac{1}{2}}, \tag{8.4}$$

where C is a constant, and E_{th} is the threshold energy [2].

The power index of 1/2, which is mainly contributed by the photo absorption coefficient, indicates that the emission actually follows photo-absorption on the free exciton generation, and $E_{th} = 5.54\,\mathrm{eV}$, which is indirect exciton generation assisted by an optical phonon in diamond [2, 9, 11, 13, 37]. In addition, this oscillatory yield is observed only in the case of the B state in Fig. 8.6, where the *P*-type surface conductivity was high [32]. As discussed in Sect. 8.1.2.3, upward band bending must be influenced.

Bandis and Pate did not describe the surface conductivity issues, but they showed indeed that the oscillatory character vanished after in situ rehydrogenation, as is also seen in Fig. 8.6 [2].

According to these results, it is plausible that the oscillatory TPY originates from exciton-derived electron emission, while the high intensity TPY without the oscillatory feature dominantly originates from electron-derived emission.

With increasing temperature, the exciton-derived electron emission decreases, as observed by Bandis and Pate with a sample that might have a high SC. Furthermore, using a sample with a low SC, the electron-derived electron emission yield was increased with temperature [34]. These tendencies are in good agreement with the trends in Fig. 8.7.

8.1.4 (111) and (110)

Features of photoelectron emission from diamond with NEA were introduced mainly with (100) face samples, but (111) and (110) also present NEA with hydrogen termination [2, 6, 8, 28]. (111) face samples are very important because electronic devices could be frequently realized with (111) due to the possibility to grow both high quality *N*-type diamond films, and heavily doped N^+-type diamond films, which will be introduced in Sect. 8.2 [26]. Thus, there are enough rooms to investigate TPY spectra for (111) and (110) samples. Detailed experiments with TPYS should be progressed.

8.1.5 Summary

H-terminated diamond surfaces have a NEA of −1.1 eV. There are two types of electron emission from the bulk of the sample: exciton-derived and electron-derived emissions. According to a simple argument based on the mass-action law, lower excitation results in electron-derived electron emission, while higher excitation results in exciton-derived electron emission during operation at RT.

Based on these understanding, performances of *PN* and *PIN* junction electron emitters with H-terminated diamond surfaces are discussed in the next section. In particular, diamond *PIN* junctions showing the exciton-derived electron emission features are introduced. The summary suggests that these are well suited for NEA electron emitters.

8.2 *PN* and *PIN* Junction Electron Emitters with NEA

8.2.1 Introduction

There have been many reports on the development of uniquely structured diamond electron emission devices that achieved high electron emission efficiency [44–48]. These gave superior performances as electron emitters. However, the majority of

these reports described field emission electron emitters, which did not fully extract gains of NEA [49]. Further development featuring NEA materials, that can operate with a high net current (or high current density) is required.

As discussed in Sect. 8.1.2.2, *N*-type diamond can have NEA, but strong upward band bending inhibits electron emission from the surface [30]. On the other hand, a *P*-type layer with NEA achieved through H-termination opens a channel for electron emission; however, there are few electrons at the CBM. Therefore, using electron injection from an *N*-type to a *P*-type layer, realizing an "excited" state as well as photoexcitation, can make use of the features of NEA.

8.2.2 *High Electron Emission Efficiency from* PN *Junction Electron Emitters*

Diamond *PN* junction was successfully formed in 2001 to show clear diode characteristics and ultraviolet light emission at 235 nm [50]. The 235 nm light emission has been attributed to the recombination of free exciton with phonon assists and this is a clear evidence that electrons and holes are injected from *N*-type to *P*-type and vice versa. This led to a possibility to fabricate an efficient electron emitter using electron injection into *P*-type diamond.

NEA cold cathodes have already been designed and reported to exhibit high electron emission efficiencies in 1970s which utilized cesium oxide absorption on *P*-type semiconductor surface of *PN* junction to induce strong downward band bending at the surface [51]. Due to the nature of cesium oxide, there were several problems to spoil the stability and robustness of the cathodes. Compared to this, hydrogen terminated diamond surface is naturally showing NEA characteristics in vacuum with very high thermal and chemical stability due to strong covalent bonding of C–H. The surface is stable even after exposure to the air or even heated over 400 °C. Based on this nature, there are some early researches aiming to have *PN* junction cold cathode of diamond, but the electron efficiencies were lower than 0.01 % which will be due to pour nature of junction formation mostly related to the difficulties to obtain *N*-type diamond before 1997 [45, 46]. After establishing *N*-type diamond growth technique [52] and successful formation of *PN* junction [50], the efficient *PN* junction cold cathode study was first reported in Japan in 2006 [53].

Diamond *PN* junction was formed on {111} single crystalline diamond surface because high quality *N*-type diamond had been feasible only on {111} growth orientation at that time. Growth of phosphorus (P) doped *N*-type diamond layer was performed on the diamond substrate by microwave plasma CVD using methane and hydrogen as source gases with phosphine (PH_3) as a dopant. The gas flow ratios were, PH_3/CH_4: 2,000 ppm, CH_4/H_2: 0.05 %. Growth temperature was 900 °C at microwave power of about 500 W and total gas pressure of 100 Torr. P-doped diamond film with 5 μm thick and 1×10^{19} cm^{-3} of doping concentration has been grown under this growth condition with the growth rate of 500 nm/h. On the surface

of *N*-type diamond, boron doped *P*-type diamond layer was formed using diborane as doping source at the same condition of *N*-type layer with the thickness of 500 nm and the doping concentration of 1×10^{18} cm^{-3}. After the *PN* stacking film formation, the sample was processed by reactive ion etching to build mesa structures for *PN* junction diode.

The electron emission measurements were performed in an ultra-high vacuum probe station. The sample was placed on the stage heated at 200 °C to get better conductivity in *N*-type layer that has large activation energy of donor, 0.57 eV and a collector electrode bias at 100 V was placed above a *PN* junction mesa with about 0.1 mm separation. A schematic drawing of diamond *PN* junction sample and the measurement circuits are shown in Fig. 8.8.

For the *PN* junction that show diode rectifying characteristics, the electron emission was observed in forward bias regime along with the diode turns on. The electron emission efficiency (electron emission current/diode current) was 0.64 % for the initially obtained sample in 2006 [53]. By the improvements of crystalline quality of semiconducting diamond layers, the emission efficiency was improved to 1.4 % as reported in 2009 [54].

Figure 8.9 shows the current–voltage characteristics of representative diamond *PN* junction cathode with the electron emission efficiency plots. It is clear that the electron emission occurs with forward diode current increase. Although the leakage current obviously observed, electron emission does not appear in the reverse bias regime. From these results, it is confirmed that the electron emission is driven by electron injection at the *PN* junction interface.

The emission area and the energy of emitted electron have been carefully analyzed using photoelectron emission microscopy setup without external photo excitation during the measurements [55]. The electron emission image clearly showed that the emission comes up from *P*-type diamond surface on the top of mesa structure. The energy of emitted electron was about 4 eV over the Fermi level of *P*-type diamond (0.37 eV from valence band maximum) with the energy spread of about 1 eV. It is considered that the electron injected from *N*-type layer drifted on the conduction band of *P*-type diamond occupy the empty surface states on

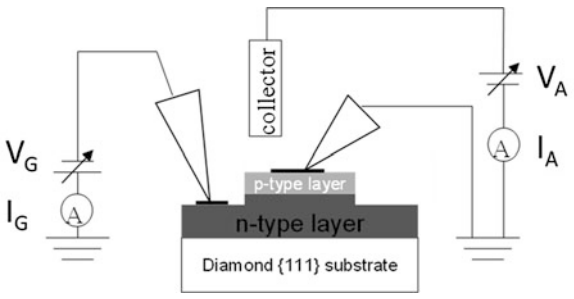

Fig. 8.8 Schematic drawing of diamond *PN* junction sample and the electron emission measurement diagram

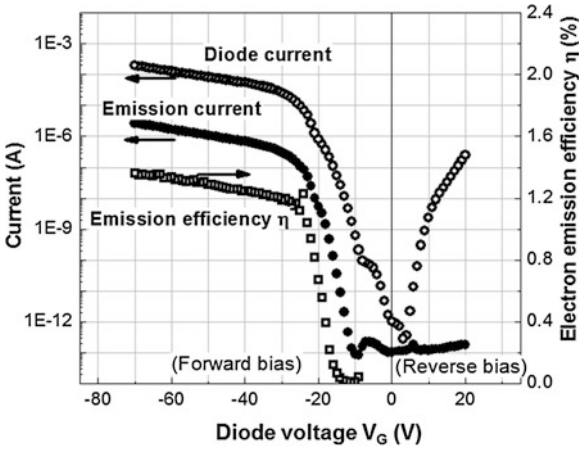

Fig. 8.9 Electron emission characteristics of a diamond *PN* junction cathode

hydrogen terminated surface and part of those electrons with the energy over vacuum level escape to vacuum as emission current measured with collector electrode.

8.2.3 PIN *Junction Electron Emitters*

The performance of the *PN* junction emitter was mainly reported at temperatures of 200–300 °C, which are required in order to activate the deep donor levels of phosphorous atoms in *N*-type diamond [26, 52]. Achieving a high electron emission current at RT is a major issue with diamond as to be an advanced electron emitters.

In addition, the higher the current, the higher the exciton-derived electron emission as discussed in Sect. 8.1.3. *PIN* junctions are more suitable than *PN* junctions for enhancing the excitonic properties because of the potential for high density free exciton states as well as 10^{18} cm^{-3} in the *I*-layer with taking into account the strong binding energy and small Bohr radius of free excitons in diamond [40, 41]. *PIN* diodes have also been developed for free exciton recombination based DUV-LEDs [57].

Based on the advanced techniques used in the diamond DUV-LEDs to obtain a high number (or high density) of free excitons, high current operation at RT of diamond-based *PIN* junction electron emitters were attempted to realize with NEA.

8.2.3.1 *PIN*$^+$ Junction Electron Emitters with a N^+ Top Layer

According to Oyama and Kato et al., heavily P-doped N^+-layers with a phosphorous concentration of around 10^{20} cm^{-3} shows the resistivity of about 100 Ω cm, while that of a conventional *N*-layer with a phosphorous concentration of around

10^{18} cm^{-3} is from 10^5 to 10^6 Ω cm at RT [58, 59]. Note that "heavily P-doped" does not imply a degenerate semiconductor; moreover, the conduction in such layers is no longer band conduction but hopping conduction.

In addition, the contact resistance of metal/N^+ junction is less than 10^{-2} Ω cm^2, while that of conventional metal/*N*-layer contact is 10^{3-5} Ω cm^2 at RT [58, 59].

Thus, it was expected that an additional heavily P-doped N^+ top layer on the *PN* diode structure would achieve a lower series resistance and a higher net diode current. Here the top layer faces a collector anode. Makino et al. developed DUV-LEDs with *PIN* diodes, which had *I*-layers of more than 1 μm in thickness, and achieved strong free exciton recombination radiation. The thicker *I*-layer provided a larger volume which allowed for a higher number of free excitons [60–62].

According to these findings, a diamond (111) *PIN* diode with an N^+ top layer was fabricated with thick high-quality *I*-layer to measure not only the electron emission properties but also electroluminescence from the diode, with the aim of determining the relationship between free exciton generation and electron emission in the diode. From the experimental results, an electron emission mechanism was proposed for the diamond *PIN* junction with NEA [63].

A *P*-type HPHT IIb (111) substrate of 2 mm × 2 mm × 0.5 mm with a mis-orientation angle of 2.7° was used for the *P*-layer. The *I*-layer, the *N*-layer, and the heavily phosphorous doped N^+-layer were grown on the substrate by microwave-assisted plasma CVD. The growth conditions for these films are summarized in Table 8.1. For the homoepitaxial *I*-layer, a thickness *t* was chosen to be more than 1 μm as a thick *I*-layer.

Figure 8.10 shows secondary ion mass spectrometry (SIMS) results for the sample. A N^+-layer heavily doped with phosphorous ([P] = 8×10^{19} cm^{-3}) with $t = 0.4$ μm was successfully grown on a *N*-layer ([P] = 5×10^{17} cm^{-3}) with $t = 0.2$ μm, forming the top layer. The nitrogen and boron abundance was under the detection limit in these layers. In the N^+-layer, however, incorporated hydrogen atoms were detected, but the concentration of phosphorous was so much higher than the concentration of hydrogen that this layer was electrically unchanged [26].

Mesa structures were fabricated by dry etching with an etching depth of 1.9 μm to expose the *PIN* junction interface. Circular shaped mesa structures were fabricated with typical diameters of 70, 120 and 170 μm, and rectangular structures with dimensions of 130 μm × 260 μm.

Figure 8.11 shows a schematic diagram of the *PIN* diode. After fabrication of the mesa structures, Ti electrodes with Pt caps were patterned with photolithography and lift-off processes. In order to obtain good adhesion and ohmic properties for the contact electrodes, the sample was annealed at 420 °C for 30 min in ambient Ar. To measure the current–voltage characteristics, the sample was electrically isolated from the sample stage. A grounded probe was attached to the N^+ top layer, and another probe was attached to the Au film. Thus, the positive biases corresponded to forward bias conditions. Electron emission measurements were performed in vacuum with anode probes of tungsten needle, which was set 100 μm above each diode. The radius of curvature at the needle tips was 25 μm. The anode voltage was fixed at 100 V. This setup is also depicted in Fig. 8.11.

Table 8.1 Growth conditions for each layer of the fabricated diode

	I-layer	*N*-layer	N^+-layer
Dopant	–	PH_3	PH_3
C/H_2 (%)	1	0.02	0.05
(Impurity atom)/C	–	(unintentional)	50
Temperature (°C)	800	900	900
Microwave Power (W)	3,500	750	750
Total Gas Flow (sccm)	400	400	400
Pressure (Torr)	150	75	75

The misorientation angle was 2.7°. A CVD system for heavy phosphorous doping was used. Light phosphorous doping for *N*-layer growth was achieved by unintentional doping

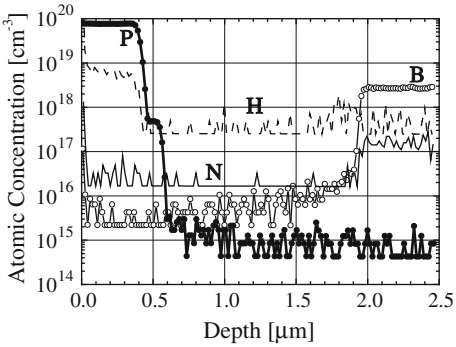

Fig. 8.10 Secondary ion mass spectrometry (SIMS) of the sample

Measurements of the diode current–voltage (I_G–V) and emission current–voltage (I_A–V) characteristics in vacuum were performed before and after hydrogenation of the whole sample. The hydrogenation process was used, which previously succeeded to produce NEA on various diamond surfaces as confirmed by TPYS experiments [34].

To evaluate the quality of these diodes, their electroluminescence was observed before hydrogenation. The dependence of the integrated intensity of free excitons and deep-level luminescence on the forward diode current was measured.

Figure 8.12 shows the dependence of the integrated intensity of (a) free exciton recombination luminescence and (b) deep-level luminescence on the forward diode current I_G. The range of wavelengths that contributed to the plots for the exciton emission and deep level emission were 220–246 nm and 300–734 nm, respectively, where the upper limits were imposed by the measurement system. In the literature, it is noted that the absolute intensity values could not be used to compare (a) and (b) in their simple setup, but the dependencies on I_G could be compared [63].

As shown in Fig. 8.12, a nonlinear increase was observed in (a), but a fairly linear increase was in (b). These phenomena were the same as observed by Makino et al. in our previous DUV-LED experiments. These results directly indicate that the

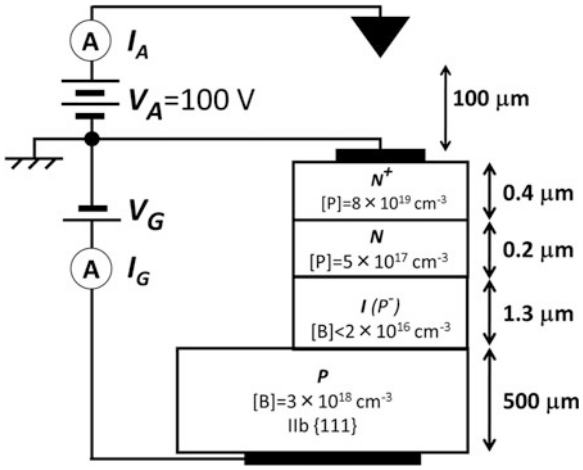

Fig. 8.11 Schematic diagram of the *PIN* diode with the heavily doped N^+ top layer. The electrode setup and circuit is also illustrated

free exciton life time is longer with a higher I_G, with overcoming a short life time by recombination at deep levels in indirect semiconductor natures [61].

Figure 8.13 shows the I_G–V and I_A–V characteristics of a diode in a vacuum operating at RT. The mesa area of this diode was 3.4 × 10^{-4} cm^2. The electron emission efficiency $\eta = I_A/I_G$ is also shown in Fig. 8.13. I_G shows the electron emission onset just below $V_G = 4.5$ V, which is the built-in potential expected

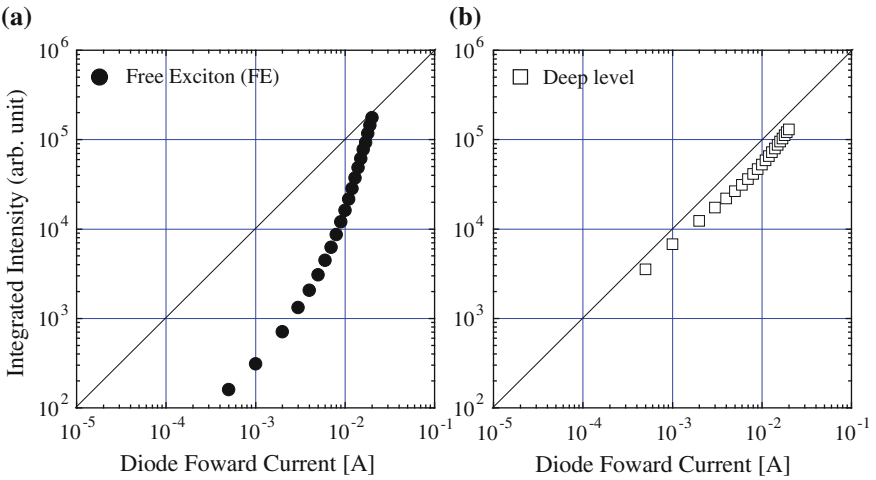

Fig. 8.12 Dependence of the integrated intensity of free exciton recombination luminescence and deep level luminescence on the forward diode current. The *solid lines* have a gradient of unity and serve as eye-guides only

in diamond *PN* junctions with boron acceptors and phosphorous donors. Here, $\eta = 0.2$ % was obtained at RT operation.

Electron emission was not observed before hydrogenation. Measurements for previous diodes prior to hydrogenation always yielded the same results [63, 64]. Hence, these results show the electron emission that is a result of the NEA of the diamond surface. In addition, the I_A was not observed in the reverse bias region, as this measurement also always yielded the same results for all previous diodes, including the case of *PN* cathodes [63, 64]. Clearly "excited" states of the diamond diode with forward current actually triggered electron emission as well as photo-electron excitation.

Figure 8.14 shows the dependence of η on I_G obtained from Fig. 8.13 on a double-logarithmic scale. That of a previous (001) *PIN* diode without the heavily P-doped N^+ top layer is also plotted [63]. η settled in the high current injection region as shown in the right hand of the figure; the settling values for both the current diode and a previous (001) *PIN* diode are given.

The η values for I_G above 30 mA were relatively similar, whereas below 30 mA there was a considerable difference between the two diodes.

Increasing the measurement temperature resulted in an increase of η. Figure 8.15 shows η as a function of V_G around the built-in potential, at 473, 523 and 573 K. The diode exhibited $\eta > 1$ % at 573 K with V_G around 4.2–4.4 V. The V_G's that yielded the highest values of η are marked with filled circles. The optimum voltage shifted by 0.1 V from 473 to 573 K as shown in Fig. 8.15.

The built-in potential V_{bi} was calculated using the following equation:

$$V_{bi} = \frac{kT}{q} \ln\left(\frac{n_{n0} p_{p0}}{n_i^2}\right), \tag{8.5}$$

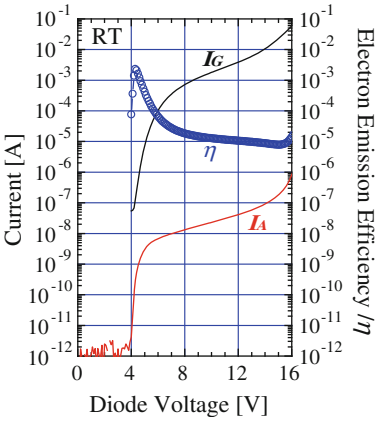

Fig. 8.13 Diode current–diode voltage, I_G–V (*black solid line*) and emission current–diode voltage, I_A–V (*red solid line*) characteristics of a diode in a vacuum at RT. The electron emission efficiency $\eta = I_A/I_G$ is also shown

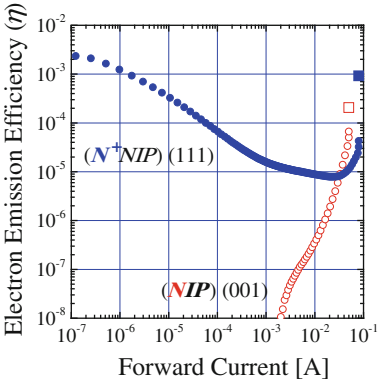

Fig. 8.14 Electron emission efficiency η obtained from Fig. 8.13, which is plotted with *filled circles* in double-logarithmic graph. That of a previous (001) *PIN* diode, which did not have a heavily P-doped top layer, is also plotted with *open circles*. The *filled* and *open squares* represent the η values when settled at the limited forward current level as shown in the right hand of Fig. 8.13

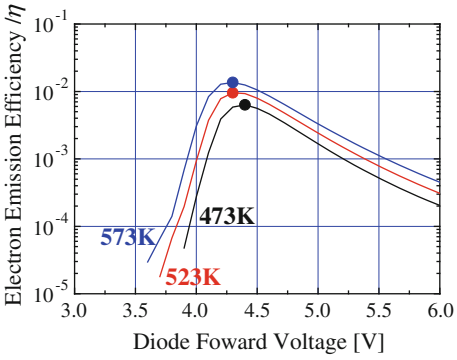

Fig. 8.15 Electron emission efficiency η with forward diode voltages around the built-in potential at 473, 523 and 573 K. The voltage yielding the highest η at each temperature is marked with a *filled circle*

where k is the Boltzmann constant, T is the absolute temperature, q is the elementary charge, n_{n0} is the free electron density in the N-layer at thermal equilibrium, p_{p0} is the free hole density in the P-layer at thermal equilibrium, and n_i is the intrinsic carrier density. The calculation of n_i took into account the effective masses of electrons (0.57) and holes (0.69) and the temperature dependence of the band-gap energy and carrier densities [35, 44, 65]. n_{n0} and p_{p0} were calculated using a donor density of 5×10^{17} cm^{-3} and an acceptor density of 5×10^{15} cm^{-3} (which treats the I-layer as a P-layer), respectively, based on the SIMS result shown in Fig. 8.10 [26].

The calculated values of V_{bi} for $T = 473$ K and $T = 573$ K were 4.44 V and 4.36 V, respectively. Hence, the optimum voltage shift calculated by (8.5) was about 0.08 V from $T = 473$ K to $T = 573$ K, which was almost the same as the value observed. Even if the highest value of [B] $= 2 \times 10^{16}$ cm^{-3} from the SIMS results was used for the *I*-layer, the shift was almost the same as above.

According to Figs. 8.13 and 8.14, η took maximum at $V_G \sim V_{bi}$, decreased when $V_G > V_{bi}$, and increased again in the high current injection region $I_G > 30$ mA. This indicates the presence of two electron emission mechanisms.

In the low current injection region, significant improvement of η, from below 10^{-6} % to over 10^{-1} %, was obtained using an N^+ top layer as shown in Fig. 8.14. Kato et al. reported that the contact resistance of a metal/N^+ (111) contact is less than 10^{-2} [Ω cm^2], while that of a metal/*N* (001) contact is over 10^5 [Ω cm^2] [58, 59]. The *N*-type side electrodes for each diode shown in Fig. 8.14 had an area of 1.4×10^{-4} cm^2. Then the resistance at the metal/N^+ (111) contact was 71 [Ω], while that at the metal/*N* (001) contact was 710 [MΩ]. In contrast, the evaluated series resistance for the N^+/N layers of the N^+NIP (111) diode was 60 [kΩ], and that for the *N* layer of the previous *NIP*(001) diode was 100 [kΩ].

The results above indicate that a reduction in the contact resistance, achieved through the use of a N^+ top layer, significantly improved the electron injection efficiency in the low current injection region. At around $V_G = V_{bi}$, flat-band conditions were expected in the *PIN* junction because I_G increased exponentially, which was likely caused by a diffusion current.

Under flat-band conditions, there are three candidates for the electron emission source: (1) free electrons in the *N*-layer, (2) free electrons injected from the *N*-layer to the *I*-layer without recombination with holes, and (3) free excitons generated in the *I*-layer by the electrons from (2) recombining with holes. The above argument is not changed by the fact that the *I*-layer is a P^--layer.

Based on the photoelectron emission experiments in Sect. 8.1.2.2, it was revealed that the hydrogenated *N*-type diamond surfaces with NEA, did not emit electrons from within the bulk of the material because of the intrinsic surface upward band bending, eliminating (1) as a possible candidate [29, 34].

According to the model suggested by Makino et al., higher I_G results in a longer free exciton life time in the *I*-layer [61]. Hence, the free exciton life time in the low current injection region is short, due to recombination at deep levels.

In practice, Fig. 8.12 indicated that the ratio I_{FE}/I_{deep} decreases with decreasing I_G, where the integrated electroluminescence intensity of the free excitons is I_{FE}, and that of deep levels is I_{deep}. On the other hand, the values of η at $V_G \sim V_{bi}$ and in the high current injection region were of almost the same order. This suggests that free excitons do not influence electron emission in the low current injection region. Thus, process (2) is more plausible than (3) in the low current injection region.

The discussion in Sect. 8.1.3 suggests that in the case of a *PIN* diode with a N^+ top layer, the low density electron injection into the *I*-layer with NEA results in a high value of η, because low density electrons and holes favor conduction and valence band states rather than free exciton states, and the metal/N^+ contact allows smooth electron injection. The NEA surface opens a channel for free electrons at

the CBM, yielding high efficiency electron emission. This might be the same in the case of *PN* diode. On the other hand, based on the results shown in Fig. 8.14 for the case of a *PIN* diode without a N^+ top layer operating in the low current region, electrons are not well injected.

Figures 8.13 and 8.15 show that the diode with the N^+ top layer exhibited the highest η when $V_G \sim V_{bi}$. Operating at RT, η reached 0.2 %, and at 573 K, η exceeded 1 %. The value at 573 K was close to that reported for *PN* junctions with a *P* top structure as described in Sect. 8.2.2 [54, 63]. This indicates that *PIN* junctions with N^+ top layers have the capability for practical use after further optimization of the device structure.

As mentioned above, η once dropped by two orders of magnitude just above $V_G = V_{bi}$. According to previous results reported, such a significant drop in η just above $V_G = V_{bi}$ was not observed with diodes using *P* top layer structures [53–55, 63]. In this region, the excess forward voltage V_G–V_{bi} induced an electric field in some parts of the diodes, which resulted in a drop of η in the low current injection region with the present diodes using N^+/N top layer structures. Further quantitative investigations into the dependence of η on the diode structure are necessary.

Furthermore, if process (2) is only considered to be the electron emission process, the rise of η in the high current injection region cannot be explained.

Figure 8.12 shows that this diode exhibited free exciton luminescence, which increased nonlinearly with increasing I_G above 0.5 mA. The second rise of η is shown in Fig. 8.13. According to the model used by Makino et al., it could be speculated that the higher the I_G, the longer the free exciton life time.

This speculation allows for a higher net number of free excitons in the *I* layer, and the production of an exciton-derived electron emission current I_A. Hence, process (3) starts to contribute to the electron emission in the high current injection region, which agrees with the discussion in Sect. 8.1.3. Comparing with the *PN* cathodes, this might be a feature of the *PIN* cathodes.

However, operation in the high current injection region may exhibit additional phenomena such as heating effects, further electron injection at the metal/N^+ contact with an excess forward bias accompanying effective free exciton generation, and electron "leakage" from the diode via electron emission as shown in Figs. 8.12 and 8.13. All of these effects might induce a carrier re-distribution in the diode. These complex phenomena are likely the reason that it takes a relatively long time of about 2 min for I_A to settle at the value of $I_A = 78$ μA with an efficiency of $\eta = 0.1$ % operating at RT in the DC mode [63]. Further experiments are required to understand the carrier re-distribution in the high current injection region.

Due to these complex issues, small differences in η in the high current injection region in Fig. 8.14 between the two diodes could not be simply explained. However, the electron emission mechanism in the high current injection region in both diodes seems to be the same, since the *PIN* (001) diode showed free exciton luminescence with nonlinear phenomena when $I_G > 20$ mA as shown in Fig. 8.12 [67].

A comparison of performances between (001) and (111) orientations has not yet been completed. Crystal quality of (001) seems to be better than (111) since

incorporation efficiency of impurity atoms for (001) during the CVD growth is less than that for (111) [68], but heavily doping for *N*-type films could be obtained only the (111) face [26].

Now these devices make use of not only band conduction but also hopping conduction in transport mechanism, and then this discussion seems to be further complicated with issues on the surface quality. Further investigations must be progressed.

8.3 High Voltage Vacuum Power Switch

8.3.1 Background

Compact high voltage power switches are highly desirable for intelligent power grids with renewable energy sources, which contribute to the global suppression of CO_2 emissions. As this infrastructure develops, the requirement for such electronics will increase drastically. In particular, there will be a high demand for reliable, compact high voltage switches that can operate at over 100 kV.

A compact high voltage vacuum power switch using electron emitters, which cannot be realized with conventional semiconductor devices, has been proposed, utilizing the insulation capability of a vacuum [69]. The most critical requirements for a vacuum switch are high current density, scalability and current uniformity in the on-state. However, the performance of conventional field emitters for use in power switches is still insufficiently low due to low uniformity and low stability by current concentration.

Spontaneous electron emission as well as thermionic emission at room temperature (RT) can meet the above requirements. Hydrogen (H-) terminated diamond has attracted the attention of many researchers because it has a low or negative electron affinity (NEA). For this reason, diamond can be used as a superior cold cathode that yields not only a high efficiency but also a high net current (or high current density) with spontaneous electron emission.

In this section, the results of 10 kV switching experiments was presented with using a diamond *PIN* junction diode electron emitter with an appropriate resistance load. The load should account for the vast majority of the voltage drop if the spontaneous electron emission from the diamond *PIN* junction electron emitter provides a sufficient current in the on-state [70, 71].

8.3.2 Capability of the Vacuum Power Switch

A vacuum switch consists of an electron emitter and an anode separated by a vacuum gap. A schematic diagram of the proposed vacuum power switch and the electric circuit are shown in Fig. 8.16.

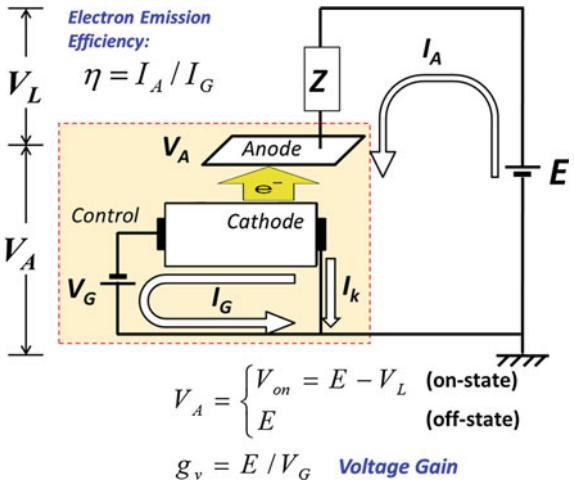

Fig. 8.16 Schematic diagram of the proposed vacuum switch and the electric circuit. A voltage gain $g_v = E/V_G$. E is the high voltage power supply, I_A is the anode current, or the current in the high voltage region, Z is the load, V_A is the anode voltage, V_L is the voltage drop at the load, V_G is the control voltage of the electron emitter, and I_G is the control current of the electron emitter. $I_A = I_G + I_K$. In the on-state, $V_A = V_{on}$, which is the on-voltage of the switch, and in the off state, $V_A = E$

As shown by the electric circuit model in Fig. 8.16, there are three sources of power loss in this system:

(1) The power consumption of the load.
(2) The power loss at the anode, which is due to the residual on-voltage (V_{on}) between the cathode and the anode. In the on-state, electrons accelerate across the vacuum to the anode, forming the emission current I_A. As they bombard the anode their kinetic energy is dissipated as heat, resulting in a voltage drop.
(3) The power lost by turning on the cathode.

Hence, the power transmission efficiency ξ of the vacuum power switch is given by:

$$\begin{aligned} \xi &= \frac{(1)}{(1)+(2)+(3)} \\ &= \frac{I_A(E - V_{on})}{I_A(E - V_{on}) + I_A V_{on} + I_G V_G} \\ &= \frac{I_A E - I_A V_{on}}{I_A E + I_G V_G} \\ &= \frac{1 - \frac{V_{on}}{E}}{1 + \frac{1}{\frac{E}{V_G}\frac{I_A}{I_G}}} \\ &= \frac{1 - R_{loss}^{Anode}}{1 + \frac{1}{g_v \eta}}, \end{aligned} \tag{8.6}$$

where $R_{loss}^{Anode} = V_{on}/E$ is the anode loss, $g_V = E/V_G$ is the voltage gain, and $\eta = I_A/I_G$ is the electron emission efficiency. η is a parameter similar to that of α for a bipolar transistor, which is the ratio ($\alpha = I_C/I_E$) of the collector (I_C) and emitter (I_E) currents.

It is apparent that larger g_V and η, and smaller R_{loss}^{Anode}, result in a larger ξ. Note that ξ increases not only with increasing η but with increasing the product $g_V\eta$. Hence ξ is maximized by a value of η which is as close to unity as possible, and a large g_V, which can easily exceed 10,000 when $E > 100$ kV and $V_G < 10$ V, demonstrating the vacuum power switch's potential for high efficiency.

By utilizing the insulating properties of a vacuum, it is possible to achieve a value of g_V larger than that in solid state devices, yielding a higher overall efficiency, despite η being further low from unity.

In addition, through spontaneous electron emission, V_{on} could theoretically reach zero. In short, the on-resistance R_{on} could reach zero as a switch. This is not the case for solid state devices because R_{on} is limited by the drift resistance for high voltage devices. This is because there is a trade-off between the breakdown voltage and R_{on} as a higher breakdown voltage requires a thicker drift layer, which results in a larger R_{on}.

In a vacuum power switch, the electrons encounter no resistance, meaning there is no such trade-off between the breakdown voltage and R_{on}.

However, high density electrons in vacuum are scattered by the space charge effect. Thus, a small on-voltage might be necessary, which is represented by R_{on} in the circuit. This effect can be partly reduced through the design of a suitable cathode and anode, and consideration of the operation current density.

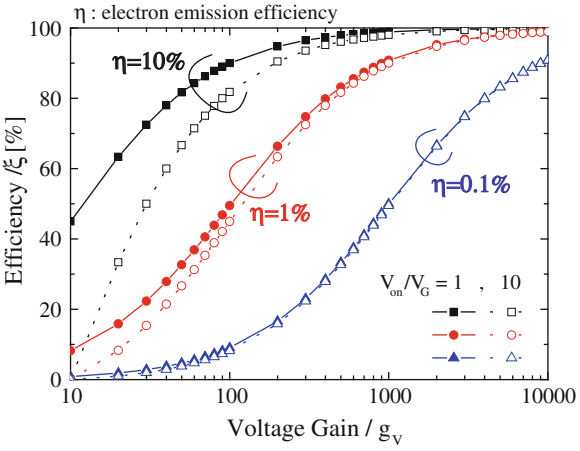

Fig. 8.17 Relationship between ξ and g_V for different values of η. The *solid lines* with *filled symbols* were obtained in the case of $V_{on} = V_G$, and the *dotted lines* with *open symbols* were obtained in the case of $V_{on} = 10$ V_G. The *lines* with *square*, *circle* and *triangle symbols* were obtained with η = 10, 1 and 0.1 %, respectively

Figure 8.17 shows the relationship between ξ and g_V for different values of η. Equation (8.6) can be written as follows:

$$\xi = \frac{g_V - \frac{V_{on}}{V_G}}{g_V + \frac{1}{\eta}} \tag{8.7}$$

The range of each parameter used in Fig. 8.17 was based on practical values as described in Sects. 8.2.3 and 8.3.3.

For example, when $E = 10$ kV, $V_G = 10$ V and $V_{on} = 100$ V, g_V becomes 1,000 and V_{on}/V_G becomes 10, then $\xi = 90$ % when $\eta = 1$ %. In addition, when $E = 100$ kV, g_V becomes 10,000, and ξ becomes 98.9 %.

As shown in Fig. 8.17, values of g_V larger than 1,000 yield efficiencies close to or larger than 90 % when $\eta > 1$ %, which is possible with diamond *PN* or *PIN* junction electron emitters as described in Sects. 8.2.3 and 8.3.3.

However, when $\eta < 0.1$ %, it is difficult to attain a sufficient value of ξ. This is the reason why conventional vacuum tubes with a filament, for which η is normally less than 0.01 %, cannot be used for high voltage switches.

8.3.3 10 kV Vacuum Switch Using a Diamond PIN^+ Electron Emitter with Negative Electron Affinity

As described in Sect. 8.2.1, spontaneous electron emission like thermionic emission at RT is a phenomenon that can be utilized in vacuum power switches. According to our results in Sect. 8.2.1, diamond *PN* and *PIN* electron emitters with NEA H-terminated surfaces show a potential for such an application.

To obtain experimental results at RT, diamond *PIN* diode emitters were fabricated through CVD film growth as shown in Fig. 8.18. A heavily phosphorus doped N^+-layer ($[P] = 7 \times 10^{19}$ cm^{-3}) with a thickness of 200 nm was grown on the *I*-layer to achieve high electron injection operation at RT with hopping conduction as described in Sect. 8.2.3.

The boron acceptor and the phosphorous donor impurity levels are 0.36 eV above the VBM and 0.57 eV below the CBM, respectively [66]. Thus, the carrier densities at RT are too low for use in power devices. However, according to our results, the junction between the intrinsic layer and the heavily doped layer with hopping conduction behaved as a normal semiconductor junction [57, 58].

In short, high current density by the hopping conduction leads the high carrier density in the band conduction layer even though there seems to be an energy barrier between the hopping level at around the donor level and the CBM at the junction. This advanced configuration from Sect. 8.2.3 utilizes one of the unique properties of diamond.

The impurity levels in the *I*-layer were below the detection limit of SIMS. Ti (30 nm)/Pt (100 nm) electrodes were deposited on the top and back sides of the diodes after fabricating the mesa structures with dry-etching. Finally, hydrogenation

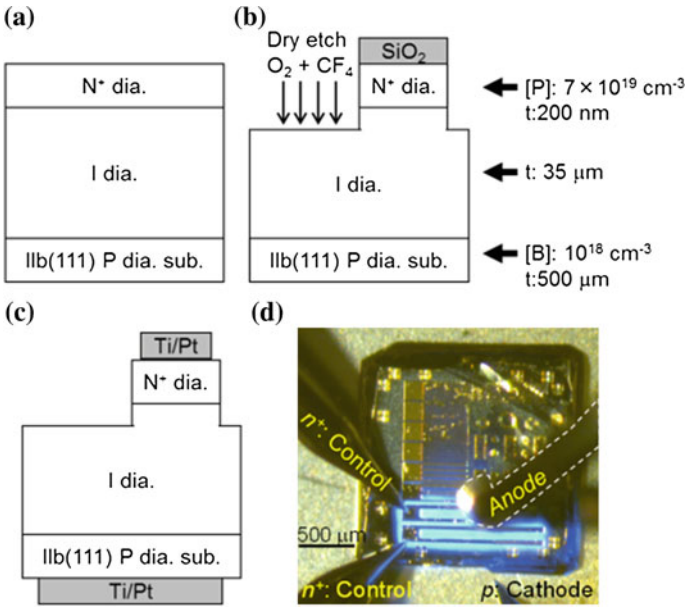

Fig. 8.18 Fabrication processes of diamond *PIN* diode emitter through CVD diamond film growth: **a** Deposition of homoepitaxial *I*- and N^+-layers on a *P*-type HPHT type IIb (111) diamond substrate. **b** Mesa structure fabrication. **c** Ohmic electrode fabrication was followed by exposing to a hydrogen radical shower to obtain NEA. **d** Image of fabricated diode (on-state) and measurement probes. Electroluminescence from defects was observed with forward biases only

of the diamond surfaces produced the NEA. The electric properties were measured in a vacuum, whose setup was shown in Fig. 8.18d. One grounded probe tip made contact with the back of the *P*-type substrate, and another probe tip with a negative bias during forward operation made contact with the top of the N^+-type layer. An additional probe tip was set 200 μm above the mesa diode as the anode.

As shown in Fig. 8.19, the electron emission efficiency (η) and the emission current (I_A) increased with increasing diode current (I_G), and η was as high as 0.9 % at $I_G = 40$ mA during operation at RT. An I_A value of 345 μA was obtained. The emission current density, which was elucidated with the mesa area, was 0.18 A/cm^2, which was as high as that for field emission arrays even though there was no field enhancement structure. No electron emission was observed in reverse operation or without H-termination, i.e., without NEA [63].

Note that the detection limit for the current measurement setup was limited by the lowest value of I_A, which also masked the behavior of η in the low forward voltage region. Thus, the behavior of η between this diode and the diodes in Sect. 8.2.3 could not be simply compared.

Static I_A–V_A characteristics with an anode voltage of V_A are shown in Fig. 8.20. A 10 kV off-mode was safely maintained in a vacuum with the diode voltage (V_G) turned off. The diode was turned on by V_G, which produced a current of I_G.

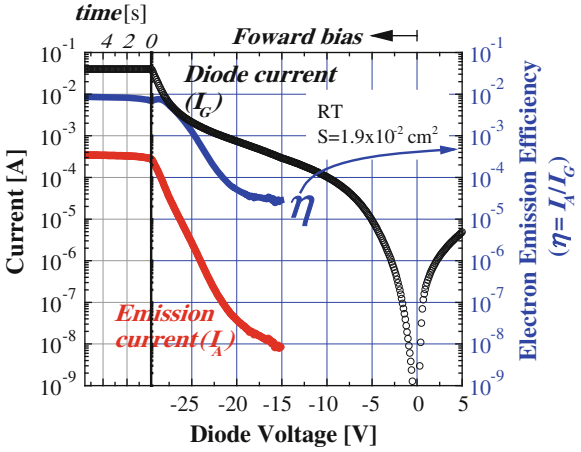

Fig. 8.19 *I–V* characteristics of the diamond *PIN* electron emitter with an anode voltage of V_A = 100 V. The *open circles* are the diode current values (I_G), the *red filled circles* are the electron emission current values (I_A), and the *blue line* shows the electron emission efficiency (η)

High voltage (E = 10 kV) switching experiments were carried out with a 200 MΩ load (Z) as shown in Fig. 8.21, as well as Fig. 8.16. V_A was monitored by a high voltage divider. When an emission current of 50 μA is obtained, the expected voltage drop at the load by a simple calculation must be 10 kV. An aim of this experiment was to investigate how low V_A becomes while maintaining a certain I_A.

Figure 8.22 shows the result of 10 kV switching at RT using the *PIN* junction electron emitter. In this experiment, V_G and I_G are the voltage and current input to the diode, respectively. When the input power was on with V_G = 23.6 V and I_G = 7.0 mA (pulse duty was 0.5), a current was induced in the anode I_A, and V_A immediately dropped from 9.8 kV to 160 V. This voltage difference was applied to the load, and the residual V_A of 160 V was termed the on-voltage (V_{on}) of the vacuum switch. Such on and off switching of a 10 kV voltage was performed without any instability. Noted that the slow rise of V_A (or drop of I_A) in the off-state was mainly due to the voltage divider of 10 GΩ and the large load resistance of 200 MΩ.

According to the model in Sect. 8.3.2, each parameter for the experimental results could be determined as follows: η = 0.69 %, g_V = 410, and R_{loss}^{anode} = 1.6 % when E = 9.8 kV, which is less than 10 kV due to probing of V_A with the voltage divider. Finally, ξ = 73 % between the output power (P_{out}) to the load and the input power (P_{in}) to the diode.

The performance evaluation of the proposed vacuum switch was carried out by calculating (8.7), and it was shown in Fig. 8.23. Note that the exact relation between V_{on} and V_g in the 10 kV switching experiment above was $V_{on} \sim 7\ V_G$ (160/24 V_G), but in fact the difference in the calculation results was negligible as shown in Fig. 8.17. Thus, discussion below is almost the same whether with Fig. 8.17 or 8.23.

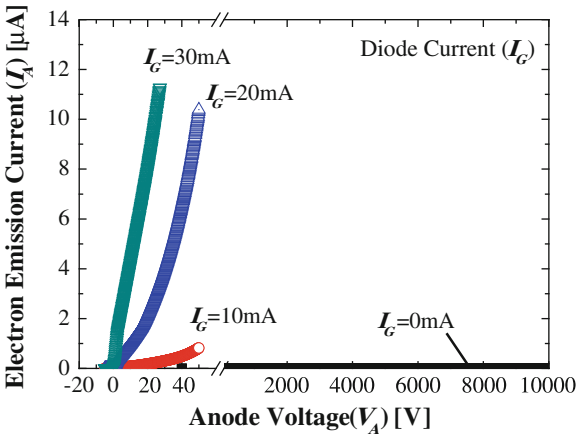

Fig. 8.20 An example of the anode current (I_A) (electron emission current)–anode voltage (V_A) curves at different diode currents (I_G). Vacuum was easily maintained 10 kV, and I_A rose almost from $V_A = 0$ V

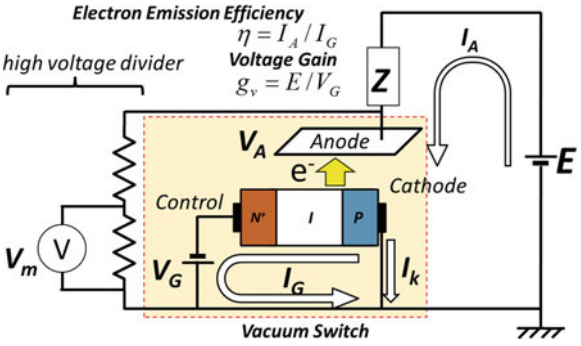

Fig. 8.21 A schematic diagram of the vacuum switch and electric circuit used in this experiment. V_A was monitored though V_m. The voltage gain $g_V = E/V_G$

It could be seen in Fig. 8.17 as that the power transmission efficiencies (ξ's) of two red lines, one is for $V_{on} = V_G$, the other for $V_{on} = 10\ V_G$ in the case of η = 1 %, at around $g_V = 410$ are much closed to each other.

In Fig. 8.23, the result using the data of Fig. 8.22 was plotted by a green circle. The case with η = 0.69 % as well as the case of Fig. 8.22 was also drawn by a green line. With assuming a system voltage of 100 kV, the voltage gain g_V increases by one order of magnitude from the case of 10 kV. As a result, the open circle shifts toward to the right along with the green line in Fig. 8.23, and then ξ reaches the filled yellow star with over 90 %, even with the same electron emitter.

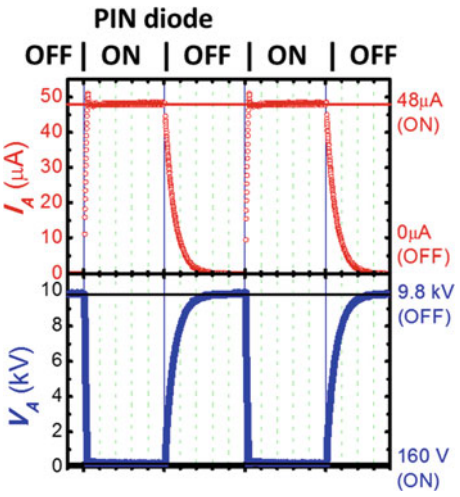

Fig. 8.22 Switching of 10 kV at RT using the *PIN* junction electron emitter

When the optimal values of each parameter was used, i.e., $\eta = 10$ % and $V_G = 8$ V with $E = 100$ kV, $\xi = 99.92$ % is obtained. Note that the parameters has been obtained independently in the experiments up to now. Hence, the vacuum switches are confirmed to be promising, compact (ultra) high voltage switches.

This chapter has been focused on the H-terminated surfaces of diamond. Recently, other functionalized diamond surfaces were reported as stable NEA

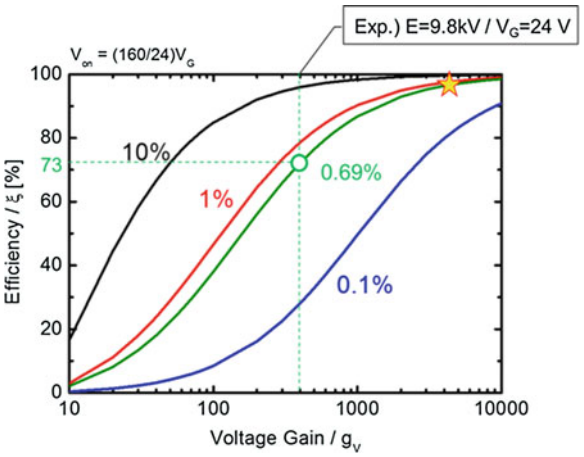

Fig. 8.23 Performance evaluation of the proposed vacuum switch as determined by (8.7) with $V_{on} = (160/24)V_G$. The result using the data of Fig. 8.22 was plotted by a *green circle*. The case with $\eta = 0.69$ % as well as the case of Fig. 8.22 was also drawn by a *green line*. With assuming a system voltage of 100 kV, the *open circle* shifts toward to the right along with the *green line*, and then ξ reaches *filled yellow star* with over 90 %, even with the same electron emitter

surfaces, such as a cycloaddition reaction of 1,3-butadiene on the bare diamond surface [72], and a lithium coated O-terminated diamond surface [73].

The latter case in particular may be relevant to the vacuum power switch applications since it is robust in air and high temperatures. These new results strengthened the capabilities of diamond-based NEA devices.

8.4 Conclusion

The electron emission efficiency of the *PN* diode was close to 10 % of the forward current. In addition, a 10 kV vacuum power switch using a NEA diamond *PIN* electron emitter exhibited a breakthrough power transmission efficiency of 73 % at 9.8 kV during operation at RT. This result was attributed to a combination of the NEA of the diamond surface, a high level of electron injection with a hopping conduction-type N^+-layer, and the insulation provided by the vacuum. Based on the principles validated by this result, vacuum power switches operating at over 100 kV with an efficiency of more than 99.9 % are possible principally.

Under these advanced results on electron emission from diamond, the electron emission properties of hydrogen terminated diamond surfaces with "true" negative electron affinity (NEA) were reviewed. Three areas are discussed to clarify the background physics of the high voltage vacuum switches:

(1) Electron emission mechanism through NEA.
(2) Electronic states in diamond with free excitons.
(3) Free carrier injection from a heavily doped layer with hopping conduction to a high purity intrinsic layer with band conduction.

The results of photoelectron emission experiments were used to elucidate (1) and (2), which led to a comparison of diamond *PN* and *PIN* junction diode electron emitters with NEA. Results of research on deep ultraviolet-light emitting diodes with diamond *PIN* junctions was introduced to develop a new structural scheme (3) to overcome the low carrier density at room temperature that results from the deep donor/acceptor levels of diamond, which have never previously been considered in conventional semiconductors.

Based on these summaries, continued progress is necessary to realize high voltage vacuum switches. Total solution with not only electronics, but also vacuum technologies, and power electronics must be merged by much population of researchers. Note that these are not simply based on Si semiconductor physics, but unique diamond semiconductor physics, means there are enough rooms to be developed in both science and technology.

Acknowledgments We extremely grateful to Prof. Dr. Yamasaki, Prof. Dr. Okushi, and Prof. Dr. Ohashi from AIST for their perceptive comments and helpful suggestions through this research. We also gratefully acknowledge Dr. Nishizawa, Dr. Makino, Dr. Kato, Dr. Ogura, Dr. Nakajima, Mr. Matsumoto, Mr. Kudo, Mr. Kuwabara, and Mr. Shirota from AIST for fruitful supports,

discussions and advices on experiments. We also thank Dr. Miyazaki and Dr. Miyamoto from AIST, Dr. Mizuochi from Osaka University, Dr. Tokuda from Kanazawa University, Dr. Oyama from Denso Co., Dr. Ri from Commet Inc., Prof. Nebel from the Fraunhofer institute, and Dr. Rezek from the Czech Academy of Science for fruitful discussions and encouragement.

We also express our gratitude to Prof. Ley, Dr. Ristein, and Dr. Riedel from Erlangen University, for their kind experimental support and fruitful discussion on TPYS results. Lastly we thank Prof. Pate in Naval Research Laboratory for his helpful discussion on TPYS and NEA with excitons.

This research was partly supported by Advanced Low CAbon technology research and development program (ALCA) from the Japan Science and Technology (JST), by Core Research for Evolutional Science and Technology (CREST) from JST, by the Industrial Technology Research Grant Program in 2008 from the New Energy and Industrial Technology Development Organization (NEDO) of Japan and Grants-in-Aid for Scientific Research 21360174 of JSPS. Part of this work was conducted at the Nano-Processing Facility, supported by IBEC Innovation Platform, AIST.

References

1. J.S. Escher, NEA semiconductor photoemitters, in *Semiconductors and Semimetals*, vol. 15, ed. by R.K. Willandson, A.C. Beer (Academic Press, New York, 1981), p. 196 (Chap. 3)
2. C. Bandis, B.B. Pate, Photoelectric emission from negative-electron-affinty diamond (111) surfaces: exciton breakup versus conduction-band emission. Phys. Rev. B **52**(16), 12056–12071 (1995). doi:10.1103/PhysRevB.52.12056
3. K. Togawa, T. Nakanishi, T. Baba, F. Furuta, H. Horinaka, T. Ida, Y. Kurihara, H. Matsumoto, T. Matsuyama, M. Mizuta, S. Okumi, T. Omori, C. Suzuki, Y. Takeuchi, K. Wada, K. Wada, M. Yoshioka, Surface charge limit in NEA superlattice photocathodes of polarized electron source. Nucl. Instr. Meth. A **414**(2−3), 431–445 (1998). doi:10.1016/S0168-9002(98)00552-X
4. M. Suzuki, M. Hashimoto, T. Yasue, T. Koshikawa, Y. Nakagawa, T. Konomi, A. Mano, N. Yamamoto, M. Kuwahara, M. Yamamoto, S. Okumi, T. Nakanishi, X. Jin, T. Ujihara, Y. Takeda, T. Kohashi, T. Ohshima, T. Saka, T. Kato, H. Horinaka, Real time magnetic imaging by spin-polarized low energy electron microscopy with highly spin-polarized and high brightness electron gun. Appl. Phys. Express **3**(2), 026601-1–026601-3 (2010). doi:10.1143/APEX.3.026601
5. F.J. Himpsel, J.A. Knapp, J.A. VanVechten, D.E. Eastman, Quantum photoyield of diamond (111)—stable negative-affinity emitter. Phys. Rev. B **20**(2), 624–627 (1979). doi:10.1103/PhysRevB.20.624
6. P.K. Baumann, R.J. Nemanich, Surface cleaning, electronic states and electron affinity of diamond (100), (111) and (110) surfaces. Surf. Sci. **409**(2), 320–335 (1998). doi:10.1016/S0039-6028(98)00259-3
7. L. Diederich, O.M. Kuettel, P. Aebi, L. Schlapbach, Electron affinity and work function of differently oriented and doped diamond surfaces determined by photoelectron spectroscopy. Surf. Sci. **418**(1), 219–239 (1998). doi:10.1016/S0039-6028(98)00718-3
8. J.B. Cui, J. Ristein, L. Ley, Dehydrogenation and the surface phase transition on diamond (111): Kinetics and electronic structure. Phys. Rev. B **59**(8), 5847–5856 (1999). doi:10.1103/PhysRevB.59.5847
9. J. Ristein, W. Stein, L. Ley, Defect spectroscopy and determination of the electron diffusion length in single crystal diamond by total photoelectron yield spectroscopy. Phys. Rev. Lett. **78**(9), 1803–1806 (1997). doi:10.1103/PhysRevLett.78.1803
10. C. Bandis, B.B. Pate, Electron-emission due to exciton breakup from negative electron-affinity diamond. Phys. Rev. Lett. **74**(5), 777–780 (1995). doi:10.1103/PhysRevLett.74.777

11. C.D. Clark, P.J. Dean, P.V. Harris, Intrinsic edge absorption in diamond. Proc. R. Soc. Lond. A **277**(1370), 312–329 (1964). doi:10.1098/rspa.1964.0025
12. P.J. Dean, E.C. Lightowlers, D.R. Wight, Intrinsic and extrinsic recombination radiation from natural and synthetic aluminum-doped diamond. Phys. Rev. **140**(1A), A352–A368 (1965). doi:10.1103/PhysRev.140.A352
13. J.B. Cui, J. Ristein, L. Ley, Low-threshold electron emission from diamond. Phys. Rev. B **60** (23), 16135–16142 (1999). doi:10.1103/PhysRevB.60.16135
14. M.I. Landstrass, K.V. Ravi, Resistivity of chemical vapor-deposited diamond films. Appl. Phys. Lett. **55**(10), 975–977 (1989). doi:10.1063/1.101694
15. H. Kawarada, Hydrogen-terminated diamond surfaces and interfaces. Surf. Sci. Rep. **26**(7), 205–259 (1996). doi:10.1016/S0167-5729(97)80002-7
16. T. Maki, S. Shikama, M. Komori, Hydrogenating effect of single-crystal diamond surface. Jpn. J. Appl. Phys. **31**(10A, Part 2), L1446–L1449 (1992). doi:10.1143/JJAP.31.L1446
17. K. Hayashi, S. Yamanaka, H. Watanabe, T. Sekiguchi, H. Okushi, K. Kajimura, Investigation of the effect of hydrogen on electrical and optical properties in chemical vapor deposited on homoepitaxial diamond films. J. Appl. Phys. **81**(2), 744–753 (1997). doi:10.1063/1.364299
18. F. Maier, M. Riedel, B. Mantel, J. Ristein, L. Ley, Origin of surface conductivity in diamond. Phys. Rev. Lett. **85**(16), 3472–3475 (2000). doi:10.1103/PhysRevLett.85.3472
19. P. Strobel, M. Riedel, J. Ristein, L. Ley, Surface transfer doping of diamond. Nature **430** (6998), 439–441 (2004). doi:10.1038/nature02751
20. S. Yamanaka, D. Takeuchi, H. Watanabe, H. Okushi, K. Kajimura, Electrical conduction of high-conductivity layers near the surfaces in hydrogenated homoepitaxial diamond films. Appl. Surf. Sci. **159–160**(12), 567–571 (2000). doi:10.1016/S0169-4332(00)00104-5
21. M. Riedel, J. Ristein, L. Ley, Recovery of surface conductivity of H-terminated diamond after thermal annealing in vacuum. Phys. Rev. B **69**(12), 125338-1–125338-8 (2004). doi:10.1103/PhysRevB.69.125338
22. S. Yamanaka, H. Watanabe, S. Masai, D. Takeuchi, H. Okushi, K. Kajimura, High-quality B-doped homoepitaxial diamond films using trimethylboron. Jpn. J. Appl. Phys. **37**(10A, Part 2), L1129–L1131 (1998). doi:10.1143/JJAP.37.L1129
23. J. Ristein, M. Riedel, L. Ley, D. Takeuchi, H. Okushi, Band diagrams of intrinsic and p-type diamond with hydrogenated surfaces. Phys. Status Solidi (A) **199**(1), 64–70 (2003). doi:10.1002/pssa.200303814
24. J. Schaefer, J. Ristein, L. Ley, H. Ibach, High-sensitivity photoelectron yield spectroscopy with computer-calculated electron optics. Rev. Sci. Instrum. **64**(3), 653–658 (1993). doi:10.1063/1.1144192
25. D. Takeuchi, Total photoyield spectroscopy experiments on hydrogen- and oxygen-terminated diamond films. New Diam. Front. Carbon Technol. **15**, 297–310 (2005). http://myukk.xsrv.jp/free_journal/download.php?fn=NDFCT495_full.pdf
26. H. Kato, T. Makino, S. Yamasaki, H. Okushi, N-type diamond growth by phosphorus doping on (001)-oriented surface. J. Phys. D **40**(20), 6189–6200 (2007). doi:10.1088/0022-3727/40/20/S05
27. S. Yamanaka, H. Watanabe, S. Masai, S. Kawata, K. Hayashi, D. Takeuchi, H. Okushi, K. Kajimura, Junction properties of homoepitaxial diamond films grown by step-flow mode. J. Appl. Phys. **84**(11), 6095–6099 (1998). doi:10.1063/1.368922
28. D. Takeuchi, H. Kato, G.S. Ri, T. Yamada, P.R. Vinod, D. Hwang, C.E. Nebel, H. Okushi, S. Yamasaki, Direct observation of negative electron affinity in hydrogen-terminated diamond surfaces. Appl. Phys. Lett. **86**(15), 152103-1–152103-3 (2005). doi:10.1063/1.1900925
29. S.J. Sque, R. Jones, P.R. Briddon, Structure, electronics, and interaction of hydrogen and oxygen on diamond surfaces. Phys. Rev. B **73**(8), 085313-1–085313-15 (2006). doi:10.1103/PhysRevB.73.085313
30. D. Takeuchi, M. Ogura, S.-G. Ri, H. Kato, H. Okushi, S. Yamasaki, Electron emission suppression from hydrogen-terminated n-type diamond. Diam. Relat. Mater. **17**(6), 986–988 (2008). doi:10.1016/j.diamond.2008.02.036

31. D. Takeuchi, K. Saeki, C.E. Nebel, S. Yamasaki, O.A. Williams, Photoelectron emission mechanism from hydrogen terminated nano-crystalline diamond. Mater. Res. Soc. Symp. Proc. **956**, 209–214 (2006). doi:10.1557/PROC-0956-J11-05
32. D. Takeuchi, M. Riedel, J. Ristein, Surface defect states analysis on diamond by photoelectron emission yield experiments. L. Ley, Surface band bending and surface conductivity of hydrogenated diamond. Phys. Rev. B **68**, 041304(R)-1–041304(R)-4 (2003). doi:10.1103/PhysRevB.68.041304
33. D. Takeuchi, C.E. Nebel, S. Yamasaki, Surface defect states analysis on diamond by photoelectron emission yield experiments. Diam. Relat. Mater. **16**, 823–825 (2007). doi:10.1016/j.diamond.2007.01.015
34. D. Takeuchi, C.E. Nebel, S. Yamasaki, Photoelectron emission from diamond. Phys. Status Solidi (a) **203**, 3100–3106 (2006). doi:10.1002/pssa.200671126
35. T. Teraji, S. Yoshizaki, S. Mitani, T. Watanabe, T. Ito, Transport properties of electron-beam and photo excited carriers in high-quality single-crystalline chemical-vapor-deposition diamond films. J. Appl. Phys. **96**, 7300–7305 (2004). doi:10.1063/1.1805723
36. D. Takeuchi, C.E. Nebel, S. Yamasaki, Photoelectron emission properties of hydrogen terminated intrinsic diamond. J. Appl. Phys. **99**, 086102-1–086102-3 (2006). doi:10.1063/1.2188070
37. E.O. Kane, Theory of photoelectric emission from semiconductors. Phys. Rev. **127**, 131–141 (1962). doi:10.1103/PhysRev.127.131
38. J.M. Ballantyne, Effect of phonon energy loss on photoemissive yield near threshold. Phys. Rev. B **6**, 1436–1455 (1972). doi:10.1103/PhysRevB.6.1436
39. F. Maier, J. Ristein, L. Ley, Electron affinity of plasma-hydrogenated and chemically oxidized diamond (100) surfaces. Phys. Rev. B **64**, 165411-1–165411-7 (2001). doi:10.1103/PhysRevB.64.165411
40. H. Okushi, H. Watanabe, S. Kanno, Characteristics of excitonic emission in diamond. Phys. Status Solidi (A) **202**, 2051–2058 (2005). doi:10.1002/pssa.200561922
41. H. Okushi, H. Watanabe, S. Yamasaki, S. Kanno, Emission properties from dense exciton gases in diamond. Phys. Status Solidi (A) **203**, 3226–3244 (2006). doi:10.1002/pssa.200671410
42. S.M. Sze, *Physics of Semiconductor Devices*, 2nd edn, vol. 2.7.7 (Wiley Inter-Science, New York, 1981)
43. L.S. Pan, D.R. Kania, *Diamond: Electronic Properties and Applications*, vol. 1.31 (Kluwer, Boston, 1995). *Note that the effective mass of holes (m_{dh}) was obtained with $m_{dh} = (m_h^{(3/2)} + m_l^{(3/2)})^{(2/3)}$, where m_h and m_l are the effective masses of heavy and light holes. These values are shown in Table. 1.4 in this book. The effective mass of electrons (m_{de}) was obtained with $m_{dh} = (m_{lc}\, m_{tc}^2)^{(1/3)}$, where m_{lc} and m_{tc} are the electron longitudinal and transverse effective masses. These values are based on the experimental values from Nava *et al.* as shown in Table. 1.6 in this book
44. J.L. Davidson, W.P. Kang, A. Wisitsora-At, Diamond field emission devices. Diam. Relat. Mater. **12**, 429–433 (2003). doi:10.1016/S0925-9635(03)00041-4
45. M.W. Geis, N.N. Efremow, J.D. Woodhouse, M.D. McAleese, M. Marchywka, D.G. Socker, J.F. Hochedez, Diamond cold-cathode. Electr. Dev. Lett. **12**, 456–459 (1991). doi:10.1109/55.119164
46. G.R. Brandes, C.P. Beetz, C.A. Feger, R.L. Wright, Diamond junction cold-cathode. Diam. Relat. Mater. **4**, 586–590 (1995). doi:10.1016/0925-9635(94)05267-0
47. K. Okano, T. Yamada, A. Sawabe, S. Koizumi, J. Itoh, G.A.J. Amaratunga, Metal-insulator-vacuum type electron emission from N-containing chemical vapor deposited diamond. Appl. Phys. Lett. **79**, 275–277 (2001). doi:10.1063/1.1385341
48. T. Ito, M. Nishimura, A. Hatta, Highly efficient electron emission from diode-type plane emitters using chemical-vapor-deposited single-crystalline diamond. Appl. Phys. Lett. **73**, 3739–3741 (1998). doi:10.1063/1.122879
49. C. Bandis, B.B. Pate, Simultaneous field emission and photoemission from diamond. Appl. Phys. Lett. **69**, 366–368 (1996). doi:10.1063/1.118062
50. S. Koizumi, K. Watanabe, M. Hasegawa, H. Kanda, Ultraviolet emission from a diamond pn junction. Science **292**(5523), 1899–1901 (2001). doi:10.1126/science.1060258

51. H. Schade, H. Nelson, H. Kressel, Novel gaas-(alga)as cold-cathode structure and factors affecting extended operation. Appl. Phys. Lett. **20**(10), 385–387 (1972). doi:10.1063/1.1653986
52. S. Koizumi, M. Kamo, Y. Sato, H. Ozaki, T. Inuzuka, Growth and characterization of phosphorous doped {111} homoepitaxial diamond thin films. Appl. Phys. Lett. **71**(8), 1065–1067 (1997). doi:10.1063/1.119729
53. S. Koizumi, T. Ono, T. Sakai, in *Proceedings of 20th Diamond Symposium* (2006), p. 262 [in Japanese]
54. S. Koizumi, S. Kono, in *Proceedings of 16th International Display Workshops 1479* (2009)
55. S. Kono, S. Koizumi, Images and energy distributions of electrons emitted from a diamond pn-junction diode. e-J. Surf. Sci. Nanotech. **7**, 660–664 (2009). doi:10.1380/ejssnt.2009.660
56. D. Takeuchi, T. Makino, H. Kato, I. Hirabayashi, H. Okushi, S. Yamasaki, Electron emission by current injection from n-type diamond film surface with negative electron affinity. Phys. Status Solidi (A) **207**(9), 2093–2098 (2010). doi:10.1002/pssa.201000092
57. T. Makino, K. Yoshino, N. Sakai, K. Uchida, S. Koizumi, H. Kato, D. Takeuchi, M. Ogura, K. Oyama, T. Matsumoto, H. Okushi, S. Yamasaki, Enhancement in emission efficiency of diamond deep-ultraviolet light emitting diode. Appl. Phys. Lett. **99**(6), 061110-1–061110-3 (2011). doi:10.1063/1.3625943
58. K. Oyama, S.-G. Ri, H. Kato, M. Ogura, T. Makino, D. Takeuchi, N. Tokuda, H. Okushi, S. Yamasaki, High performance of diamond p(+)-i-n(+) junction diode fabricated using heavily doped p(+) and n(+) layers. Appl. Phys. Lett. **94**(15), 152109-1–152109-2 (2009). doi:10.1063/1.3120560
59. H. Kato, T. Makino, M. Ogura, N. Tokuda, H. Okushi, S. Yamasaki, Selective growth of buried n(+) diamond on (001) phosphorus-doped n-type diamond film. Appl. Phys. Express **2**(5), 055502-1–055502-3 (2009). doi:10.1143/APEX.2.055502
60. T. Makino, K. Yoshino, N. Sakai, K. Uchida, S. Koizumi, H. Kato, D. Takeuchi, M. Ogura, T. Matsumoto, H. Okushi, S. Yamasaki, in *Abstract of Diamond 2010: 21st European Conference on Diamond, Diamond-Like Materials, Carbon Nanotubes, and Nitrides*, 13-3 (Budapest, Hungary, 2010)
61. T. Makino, N. Tokuda, H. Kato, S. Kanno, S. Yamasaki, H. Okushi, Electrical and light-emitting properties of homoepitaxial diamond p-i-n junction. Phys. Status Solidi (A) **205**(9), 2200–2206 (2008). doi:10.1002/pssa.200879717
62. T. Makino, S.-G. Ri, N. Tokuda, H. Kato, S. Yamasaki, H. Okushi, Electrical and light-emitting properties from (111)-oriented homoepitaxial diamond p-i-n junctions. Diam. Relat. Mater. **18**(5-8), 764–767 (2009). doi:10.1016/j.diamond.2009.01.016
63. D. Takeuchi, T. Makino, H. Kato, H. Okushi, S. Yamasaki, Electron emission from diamond p-i-n junction diode with heavily P-doped n(+) top layer. Phys. Status Solidi (A) **208**(9), 2073–2078 (2011). doi:10.1002/pssa.201100140
64. D. Takeuchi, T. Makino, H. Kato, M. Ogura, N. Tokuda, K. Oyama, T. Matsumoto, M.H. Okushi, S. Yamasaki, Electron emission from CVD diamond p-i-n junctions with negative electron affinity during room temperature operation. Diam. Relat. Mater. **20**(7), 917–921 (2011). doi:10.1016/j.diamond.2011.05.009
65. Y.P. Varshni, Temperature dependence of energy gap in semiconductors. Physica **34**(1), 149–154 (1967). doi:10.1016/0031-8914(67)90062-6
66. H. Kato, H. Umezawa, N. Tokuda, D. Takeuchi, H. Okushi, S. Yamasaki, Low specific contact resistance of heavily phosphorus-doped diamond film. Appl. Phys. Lett. **93**(20), 202103-1–202103-3 (2008). doi:10.1063/1.3005639
67. T. Makino, N. Tokuda, H. Kato, M. Ogura, H. Watanabe, S.-G. Ri, S. Yamasaki, H. Okushi, High-efficiency excitonic emission with deep-ultraviolet light from (001)-oriented diamond p-i-n junction. Jpn. J. Appl. Phys. **45**(37-41, Part 2), L1042–L1044 (2006). doi:10.1143/JJAP.45.L1042
68. H. Kawarada, Y. Yokota, A. Hiraki, Intrinsic and extrinsic recombination radiation from undoped and boron-doped diamonds formed by plasma chemical vapor-deposition. Appl. Phys. Lett. **57**(18), 1889–1891 (1990). doi:10.1063/1.104002

69. T. Ono, T. Sakai, N. Sakuma, K. Nakayama, H. Ohashi, Field emitter triode for power switching-a new power device candidate. in *Proceedings of ISPSD'98*, 151–154 (1998). doi:10.1109/ISPSD.1998.702657
70. D. Takeuchi, S. Koizumi, T. Makino, H. Kato, M. Ogura, H. Okushi, H. Ohashi, S. Yamasaki, A 10kV vacuum switch with negative electron affinity of diamond p-i-n electron emitter. in *IEDM2012* (*International Electron Devices Meeting*, San Francisco (CA, USA)) Technical Digest **7**, 167–170 (7.6.1–7.6.4) (2012). doi:10.1109/IEDM.2012.6479000
71. D. Takeuchi, S. Koizumi, T. Makino, H. Kato, M. Ogura, H. Ohashi, H. Okushi, S. Yamasaki, Negative electron affinity of diamond and its application to high voltage vacuum power switches. Phys. Stat. Sol. (A) **210**(10), 1961–1975 (2013). doi:10.1002/pssa.201300385
72. D. Qi, L. Liu, X. Gao, T. Ouyang, S. Chen, K.P. Loh, A.T.S. Wee, Tuning the electron affinity and secondary electron emission of diamond (100) surfaces by Diels-Alder reaction. Langmuir **23**(19), 9722–9727 (2007). doi:10.1021/la701285h
73. K.M. O'Donnell, M.T. Edmonds, J. Ristein, A. Tadich, L. Thomsen, Q.-H. Wu, C.I. Pakes, L. Ley, Diamond surfaces with air-stable negative electron affinity and giant electron yield enhancement. Adv. Funct. Mater. **23**(45), 5608–5614 (2013). doi:10.1002/adfm.201301424

Chapter 9
Diamond Ultramicro- and Nano-electrode Arrays

Nianjun Yang, Jakob Hees and Christoph E. Nebel

Abstract Boron-doped diamond as one of the best electrode materials has been used for the fabrication of diamond ultramicro- and nano-electrode arrays. These arrays amplify the signal of individual micro-/nano-electrodes but do not lose the beneficial characteristics of individual micro-/nano-electrodes. In this chapter we summarize the fabrication, properties, and applications of diamond ultramicro- and nano-electrode arrays. The technologies for the fabrication of these arrays and the characterization methods applied at Fraunhofer IAF are explained in detail as examples.

9.1 Introduction

Diamond was introduced as an electrode material by Iwaki et al. in 1983 [1] and later by Pleskov et al. in 1987 [2]. Soon heavily boron-doped diamond was recognized as one of the best electrode materials [3–14]. Boron-doped diamond films show numerous unique physical and chemical properties [7, 8, 14–18], such as (i) high chemical stability in harsh environments and/or at high current densities as working electrodes; (ii) weak or no surface bio-fouling; (iii) biocompatibility; (iv) low and stable capacitive currents in aqueous and non-aqueous solutions; and (v) wide electrochemical potential window. For example, the capacitive current of a hydrogen terminated diamond electrode (boron concentration: 2×10^{20} cm^{-3}) in 0.1 M pH 7 phosphate buffer is 10 times lower than that of a gold electrode and about 100 times lower than that of a glassy carbon electrode. If defined with an absolution value of current density of 1.0 mA cm^{-2} as a threshold value, one can achieve a wider electrochemical potential window for diamond electrode than other electrodes

N. Yang (✉)
Institute of Materials Engineering, University of Siegen, 57076 Siegen, Germany
e-mail: nianjun.yang@uni-siegen.de

J. Hees · C.E. Nebel
Fraunhofer-Institute for Applied Solid State Physics (IAF), 79108 Freiburg, Germany

N. Yang (ed.), *Novel Aspects of Diamond*, Topics in Applied Physics 121,
DOI 10.1007/978-3-319-09834-0_9

although it is affected by the electrolyte and the diamond sample. Figure 9.1 shows the potential window of a heavily boron-doped single crystalline diamond sample (boron concentration: 5×10^{20} cm^{-3}) in different media. The potential window is about 3.2 V in aqueous solutions, 4.6 V in organic solutions, and 4.9 V in room temperature ionic liquids. Diamond is chemically inert, not swelling in electrolyte solutions, and does not show surface fouling, especially when hydrogen-terminated. Its surface can be terminated [18] with hydrogen, with oxygen, or with mixtures of both, which allow convenient optimization of electronic properties of the solid/electrolyte interfaces. These terminations can be achieved by a hydrogen or oxygen plasma treatment at high temperatures or by electrochemical reduction/oxidation at high current densities in acidic solutions [18]. It is biocompatible and can be biofunctionalized via carbon chemistry [12–14, 19, 20]. Furthermore, its surface can be textured with dimensions of typically a few nanometers [21–23] to nanowires with lengths of a few micrometers [24]. Up to now, planar macroscopic polycrystalline diamond electrodes have been frequently applied for electrochemistry, bio electrochemistry, sensor, environment, and related applications [3–14].

Due to the non-uniform doping in polycrystalline diamond, boundary effects, and the ratio graphite to diamond, electrochemical signals recorded on diamond electrodes are average signal detected over the full electrode. To solve this problem, one efficient way is to fabricate and investigate small-dimensional (micro and sub-micrometers) electrodes [25–30]. These electrodes offer various benefits over planar macroscopic electrodes [25–30] such as reduced Ohmic resistance, enhanced mass transport, decreased charging currents, decreased deleterious effects of solution resistance, and high possibility for fast voltammetric measurements. Classified with their dimensions (e.g. diameters of electrodes, *d*), they have been

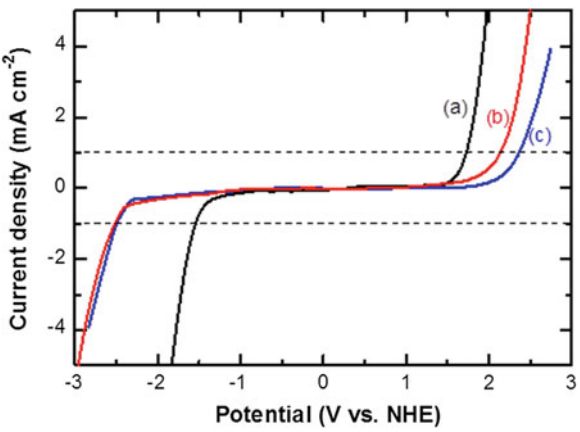

Fig. 9.1 Linear sweep voltammograms of a planar diamond electrode in 0.5 M $LiClO_4$ solution (**a**), 0.1 M $TBABF_6$/acetonitrile solution (**b**), and 1-Butyl-3-methylimidazolium hexafluorophosphate (BMIM-PF_6) (**c**) at a scan rate of 0.1 V s^{-1}. The boron concentration is 5×10^{20} cm^{-3}

divided into (i) microelectrode (25 μm < d < 100 μm), (ii) ultramicroelectrode (0.1 μm < d < 25 μm), and (iii) nanoelectrode (d < 100 nm) [25, 26]. Various diamond microelectrodes and ultramicroelectrodes have been produced [31–41]. However, single micro-, ultramicro-, or nano-electrode only generates small current that is relatively difficult to detect with conventional electrochemical setups. This has been circumvented by fabricating arrays or ensembles of these electrodes that operate in parallel. They amplify the signal of individual microelectrodes but do not lose the beneficial characteristics of individual small dimensional electrodes [1–4]. Several works have been conducted on the fabrication, characterization, and applications of diamond micro-, ultramicro-, and nano-electrode arrays/ensembles [42–57]. For example, they have been applied for sensor applications [49–55]. Their sensing performances with respect to the sensitivity, detection limit, life time, and reproducibility have been significantly improved. This is because boron-doped diamond is one of the most appropriate and optimized material for the fabrication of these arrays.

In this chapter, we first give a brief summary about the fabrication, properties and applications of diamond micro- and ultramicro-electrodes. In the second part, we summarize those for diamond micro-, ultramicro-, and nano-electrode arrays. Some arrays fabricated at Fraunhofer IAF are shown in detail. The last part is the summary and outlook.

9.2 Microelectrodes and Ultramicroelectrodes

In 1988 Cooper and his co-workers reported for the first time the fabrication of boron-doped diamond microelectrode [31]. For the fabrication of these microelectrodes, one frequently applied approach is to coat sharpened metal wires with a thin boron-doped diamond film. The used metals are mainly from tungsten [31–36] and platinum [37, 38]. Coating tungsten wires sealed in a quartz glass capillary with diamond is an alternative approach, which was developed by Martin and coworkers [39, 40]. These microelectrodes and ultramicroelectrodes have been characterized [31–40] with scanning electron microscope, optical microscope, and various electrochemical techniques (mainly voltammetry) [31–40]. They have been applied for electrochemical sensing applications in non-aqueous [31] and aqueous solutions [32–40]. For example, they have been used in biological media to detect dopamine in mouse brain [33], to monitor norepinephrine release in mesenteric artery [38], to investigate the role of adenosine in the modulation of breathing within animal tissue [39], and to inspect serotonin as a neuromodulator [40]. These microelectrodes and ultramicroelectrodes have shown lower detection limits towards analytes in solution and increased signal-to-noise ratios than those obtained on planar macroscopic diamond electrodes. In addition, they have shown high possibilities to conduct spatially and temporally resolved electrochemical measurements when they are adopted as the tip for scanning electrochemical microscope (SECM) [36, 41] as well as the sensor for in vivo detection of dopamine by fast scan voltammetry [33].

9.3 Diamond Electrode Arrays

9.3.1 Diamond Micro- and Ultramicro-electrode Arrays

In 2002 Fujishima and coworkers used structured silicon substrates and fabricated diamond microelectrode arrays [42]. The array consist of 200 micro-disks with the diameters between 25 and 30 μm and with electrode spacing of 250 μm. Rychen and coworkers [43] produced diamond ultramicroelectrode arrays by depositing a boron-doped diamond film onto patterned silicon nitrite (5 μm in thickness). The diameter of the microelectrodes is 5 μm, the distance between microelectrodes is 150 μm and the number of electrodes is 106. Kang, Swain and coworkers [44–48] realized diamond ultramicroelectrode arrays with different shapes, spacing, and number of electrodes. They utilized the "as-grown" diamond surface with randomly micro-structured topology as a planar diamond electrode. They also used a micro-patterning technique to produce a well-defined pyramidal tip-array with a controlled uniformity. Compton and coworkers [49–51] realized for the first time all-diamond ultramicroelectrode arrays in 2005. The diameters of electrodes are between 10 and 25 μm with a separation of 100–250 μm. Bergonzo et al. [52] and Carabelli et al. [53] utilized nano-crystalline diamond films to generate electrode arrays.

We recently demonstrated batch-production of integrated ultramicroelectrode arrays using polycrystalline diamond films [55, 56]. Insulting polycrystalline diamond films were grown on a silicon wafer in an ellipsoidal shaped, microwave plasma enhanced chemical vapor deposition system [56]. The growth temperature was in the range of 750–900 °C, the microwave power was 3 kW, the gas was 3 % methane in hydrogen, and the pressure was 60 mbar. Boron-doped polycrystalline diamond film was grown by adding 7,000 ppm trimethylboron to the gas phase. Prior to fabrication of electrodes, diamond films were cleaned wet-chemically in the mixture of concentrated sulfuric acid (98 %) and concentrated nitric acid (65 %) (V: V = 3:1) at 200 °C for 1.5 h. Figure 9.2 shows schematically the fabrication process of integrated ultramicroelectrode arrays [55, 56]. It includes three photolithography steps, two etching steps, one overgrowth step, one metal-deposition step, and one lift-off step. Figure 9.2a shows the first step where a boron-doped polycrystalline diamond film with a thickness 200–500 nm is deposited on a polished insulating diamond film (with a thickness of 8–10 μm). The second step (Fig. 9.2b) is the application of first photolithography treatment. After spin-coating of the wafer with the photoresist, a 350 nm SiO_2 layer is deposited. SiO_2 based patterns are generated by etching with SF_6 gas (Fig. 9.2c). To produce boron-doped diamond based structures, reactive ion etching of the wafer (Fig. 9.2d) is conducted in a gas mixture of oxygen and hydrogen [58]. Please note that these structures are protected. The conductivity of un-protected areas is checked frequently to make sure boron-doped diamond is etched away. For the overgrowth of insulating diamond, the second photolithography process is applied (Fig. 9.2e). The overgrowth (Fig. 9.2f) coats all area with insulating diamond except the parts of the counter, reference and ultramicroelectrodes which are protected by SiO_2. The third

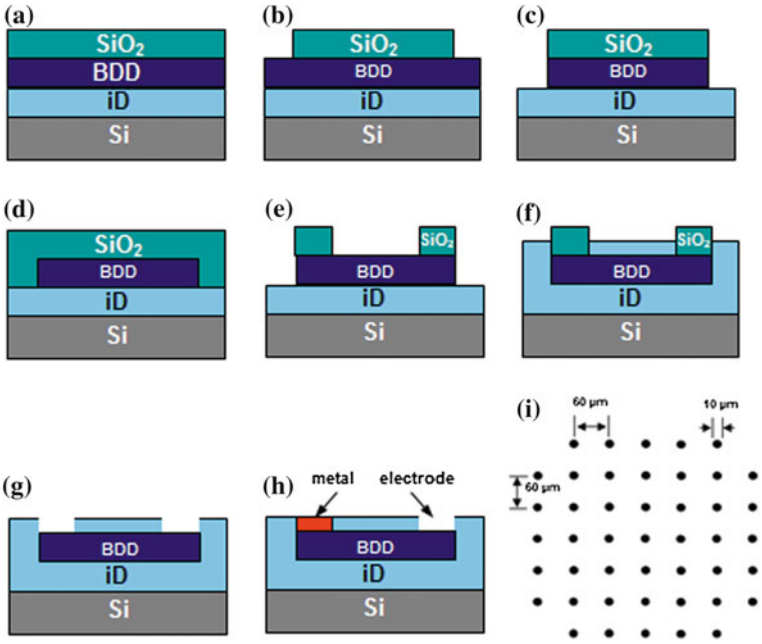

Fig. 9.2 Schematic plots (from **a** to **h**) of the fabrication of integrated all-diamond ultramicroelectrode arrays. Plot (**i**) is the arrangement of ultramicroelectrodes (d = 15 μm). BDD, iD and Si are denoted as boron-doped diamond, insulating diamond, and silicon substrate, respectively

photolithography step is finally applied (Fig. 9.2g) and the Ti/Pt/Au (20/60/200 nm) metal layers are deposited for electric connection. The last step is the application of the lift-off technique as shown in Fig. 9.2h. Figure 9.2i shows schematically the arrangement of one diamond array we fabricated. The diameter of ultramicroelectrode is 10 μm. The total number of ultramicroelectrodes is 45. The vertical and horizontal centre-to-centre spacing in between electrodes is 60 μm.

Depending on the design of the lithography masks, various diamond micro-, ultramicro-electrode arrays can be produced. Figure 9.3 shows one example [56]. The structure of the electrode with respect to the layers of diamond films is presented in Fig. 9.3a. The chip shown in Fig. 9.3b has a size of 5 × 5 mm^2. The counter and quasi-reference electrodes are oxidized boron-doped diamond films which are integrated on the chip. The size, arrangement and the distance of ultramicroelectrodes are shown in Fig. 9.2i. For one 2-inch wafer, more than 40 integrated chips were produced.

Electron and optical microscopes, Raman spectroscopy, and electrochemical techniques have been applied to investigate the properties of these arrays. Figure 9.4 shows the technique (a) we applied using scanning electrochemical microscope (SECM) and one resulted SECM image of these arrays (b). As shown in Fig. 9.4a, 3 μm Pt ultramicroelectrode (UME) was used as the tip and one diamond

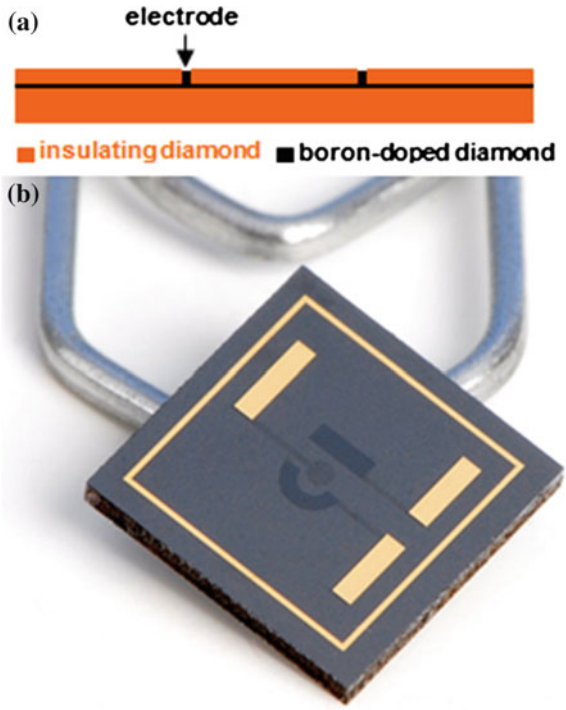

Fig. 9.3 **a** schematic plot of the structure of diamond electrode array, **b** Image of one integrated ultra-microelectrode array. The *yellow* parts are metal contacts. The *dark* part with a semi-circle is the counter electrode, the *dark rectangle* is the reference electrode and the center electrode is the working electrode

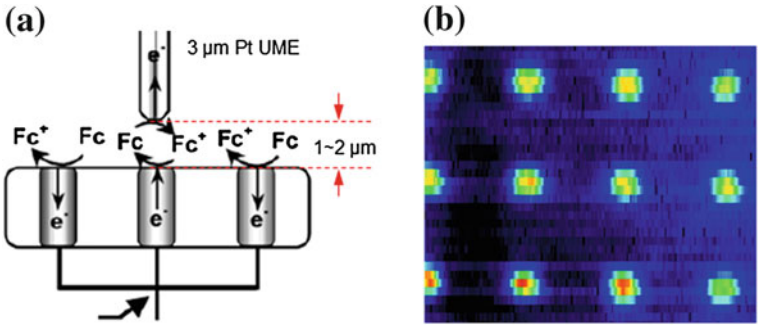

Fig. 9.4 **a** The setup for scanning electrochemical microscope (SECM) experiments, **b** one SECM image of diamond ultramicroelectrode arrays using tip-collection/substrate-generation mode

ultramicroelectrode array as the substrate. The solution was 5 mM Ferrocene dissolved in 0.1 M $TBAPF_6$/propylencarbonate. The distance between the tip and the substrate was about 1–2 μm. The tip-collection/substrate-generation mode was applied. From the image shown in Fig. 9.4b, the local reactivity of these individual ultramicroelectrodes is seen. From the diameter of each dot, the electroactive diameter of these ultramicroelectrodes is confirmed to be 10 μm. From the distance of two dots, the distance of two ultramicroelectrodes is approved to be 60 μm, the same as we designed.

These arrays are promising platforms for sensing applications. However to achieve sensitive detection of analytes in solutions with low detection limits by these arrays, one has to optimize the ratio of Faradaic current (signal, S) and capacitive current (background, B). Obviously the largest S/B ratio can be obtained when maximum Faradaic current is achieved with minimum capacitive current. The capacitive and Faradaic currents are known to be affected by the scan rates applied, the spacing between microelectrodes, and the concentration of supporting electrolyte. For diamond arrays, they are also affected by surface terminations and boron-doping densities of the transducer. Voltammetry was thus applied to investigate the effect of surface termination of diamond electrodes and boron doping densities on the Faradaic currents on diamond ultramicroelectrode arrays [55, 56]. The redox couple of $Fe(CN)_6^{3-/4-}$ were adopted as probes. Hydrogen-terminated diamond ultramicroelectrode arrays with boron-concentration of $4.2(\pm2) \times 10^{20}$ cm^{-3} show the highest Faradaic current, indicating the fastest electron transfer process. The variation of supporting electrolyte does not change much capacitive current but alter dramatically Faradaic current [25–30]. Figure 9.5 shows the effect of scan rate on Faradaic currents (solid lines) of 1.0 mM $Fe(CN)_6^{3-/4-}$ on a hydrogen-terminated diamond ultramicroelectrode array in 0.1 M KCl solution. The magnitude of the Faradaic currents increase and the shape of the voltammograms vary with increasing scan rate. At low scan rates ranging from 0.02 (a) to 0.2 (b) V s^{-1} and at fast scan rates of 20 V s^{-1} (d), peak-shaped voltammograms were obtained, indicating linear diffusion-limited transport of analytes. A sigmoidal-shaped voltammogram (c) was detected at a scan rate of 2 V s^{-1}, which is consistent with hemisphere diffusion to the ultra-microelectrodes on the array. To calculate the thickness of diffusion layer (δ), we applied the equation [25] $\delta = (2D\Delta E/v)^{1/2}$ (where v is the scan rate, $D = 7.6 \times 10^{-6}$ cm s^{-1} is the diffusion-coefficient of analytes, ΔE is the potential range over which electrolysis occurs). For example to estimate the size of the diffusion layer thickness at $E = 0.4$ V, we used the value $\Delta E = 0.8$ V since significant electrolysis current started at $E = -0.4$ V. The calculated values of δ at $E = 0.4$ V are summarized in Table 9.1. The center-to-center separation and the diameter of microelectrodes are 60 and 10 μm, respectively. Namely the separation between electrodes is 50 μm. At a scan rate of 0.02 V s^{-1}, $\delta = 250$ μm, which is much larger than the spacing between electrodes, indicating a complete overlap of redox molecule diffusion of individual electrodes and subsequently a linear diffusion profile. At a higher scan rate of 0.2 V s^{-1}, $\delta = 78$ μm, which is only slightly greater than the separation of electrodes, an overlap of adjacent diffusion profiles is still dominating. When δ becomes larger than the diameter of a microelectrode but

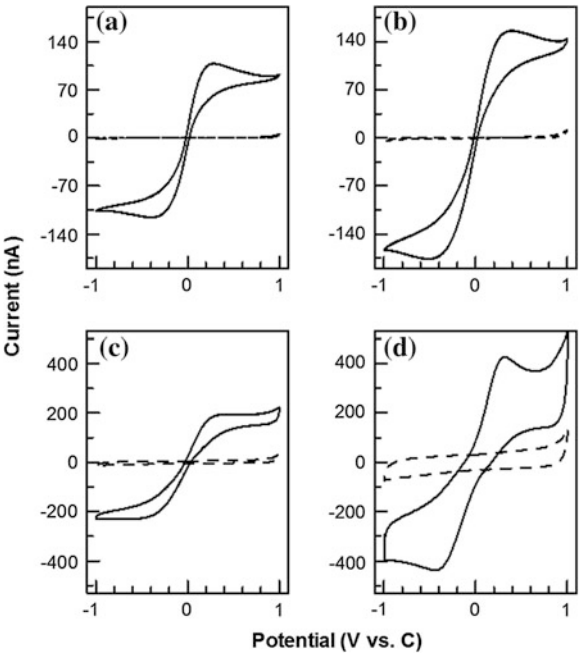

Fig. 9.5 Cyclic voltammograms of one diamond ultramicroelectrode array in 0.1 M KCl solution with (*solid lines*) and without (*dashed lines*) 1.0 mM Fe $(CN)_6^{3-/4-}$ at a scan rate of **a** 0.02, **b** 0.2, **c** 2, and **d** 20 V s^{-1}

Table 9.1 Summary of electrochemical response of 1.0 mM $Fe(CN)_6^{3-/4-}$ on hydrogen-terminated diamond ultramicroelectrode arrays

Scan rate/ V s^{-1}	Thickness of diffusion layer/ μm	Shape of Voltammogram	Diffusion profile
0.02	250	Peak-shaped	Linear
0.2	78	Peak-shaped	Linear
2	25	Sigmoidal-shaped	Hemi-sphere
20	7.8	Peak-shaped	Linear

diameter of ultramicroelectrode: 10 μm
center-to-center distance in between electrodes: 60 μm

is still smaller than the separation between electrodes, the voltammetric response is the response of an individual microelectrode (sigmoidal curve) multiplied by the total number of electrodes in the array. This can be detected for example at a scan rate of 2 V s^{-1}. However, further increase of the scan rate (e.g. to 20 V s^{-1}) leads to even smaller values of δ (e.g. to 7.8 μm) than the size of microelectrodes (10 μm). In this case the linear diffusion dominates the mass transport, resulting in peak-shaped voltammograms. On the other hand, the capacitive currents (dashed lines in Fig. 9.5) recorded in 0.1 M KCl increase linearly with scan rate. The S/B ratios (Faradaic current to capacitive current) for scan rate of 0.02, 0.2, 2 and 20 V s^{-1} were estimated to be 1,817 ± 40, 215 ± 18, 28 ± 6, 10 ± 1, respectively. The highest

S/B ratio was achieved at the slowest scan rate. In this case the diffusion profiles at neighboring microelectrodes overlapped and thus peak-shaped voltammograms were detected. The magnitude of the Faradaic current is thus proportional to the geometric area, which is comprised of all microelectrodes and the insulating parts. While the contribution of the capacitive current to the total current is small since the capacitive current is proportional to the scan rate and to the electrochemical active area, which is only the area for all microelectrodes. This gives rise to the enhanced ratios of S/B, leading to increased sensitivity for analytes. Since the geometric area of an ultramicroelectrode array is always 50–1,000 times larger than the electrochemical active area, a 50–1,000 times better sensitivity is expected for such electrode arrays [55, 56].

These diamond arrays have been applied for many different sensing applications, e.g. for the detection of environmental analytes (e.g. nitrate, 4-nitrophenol [49–51], Cr(VI) ions, Ag(I) ions, sulphate, peroxodisulfate [43], hydrogen peroxide [55]), for bio-detections (e.g. detection of dopamine [44–48], neuronal activity measurements [52, 53], quantal catecholamine secretion from chromaffine cells [54]), and for the generation and detection of peroxidisulfate with the aid of scanning electrochemical microscope (SECM) [59]. We have shown that dopamine can be sensitively and selectively detected on diamond ultramicroelectrode arrays in the presence of ascorbic acid [55]. Compared with the results shown on other diamond electrode (including macro-sized electrodes [60–65], microelectrode array [66], ultramicroelectrode arrays [47, 48], and diamond nanograss [67]), on diamond ultramicroelectrode arrays we achieved the lowest detection limit (1.0 nM) for dopamine detection, which is 50–100 times lower than that reported [55]. Diamond ultramicroelectrode arrays are thus promising for the detection of low concentrated dopamine (0.01–1 μM) in biological samples individually or in the presence of other similar compounds such as ascorbic acid.

9.3.2 Addressable Diamond Ultramicroelectrode Arrays

Several approaches have been applied to fabricate interconnected and individually addressable diamond micro- and ultramicro-electrode arrays, e.g. a 10-channel diamond array on polymer based microelectrode array by Hess et al. [68], a 4-channel nanocrystalliane diamond microelectrode array by Gao et al. to detect catecholamine [69], and a 64-channel diamond microelectrode arrays by Bergonzo et al. for biochemical and analytical applications [70]. Take the addressable array from Bergonzo et al. as an example, they fabricated an 8 × 8 multichannel diamond ultramicroelectrode array and then characterized it with optical and electrochemical methods, e.g. cyclic voltammetry and electrochemical impedance spectroscopy. A very fast electrode transfer rate up to 0.05 cm s^{-1} was achieved.

We have applied three diamond growth steps, three photolithography steps, and two-liftoff steps to fabricate addressable diamond ultramicroelectrode arrays. As shown in the SEM image of one array in Fig. 9.6a, three working electrodes have

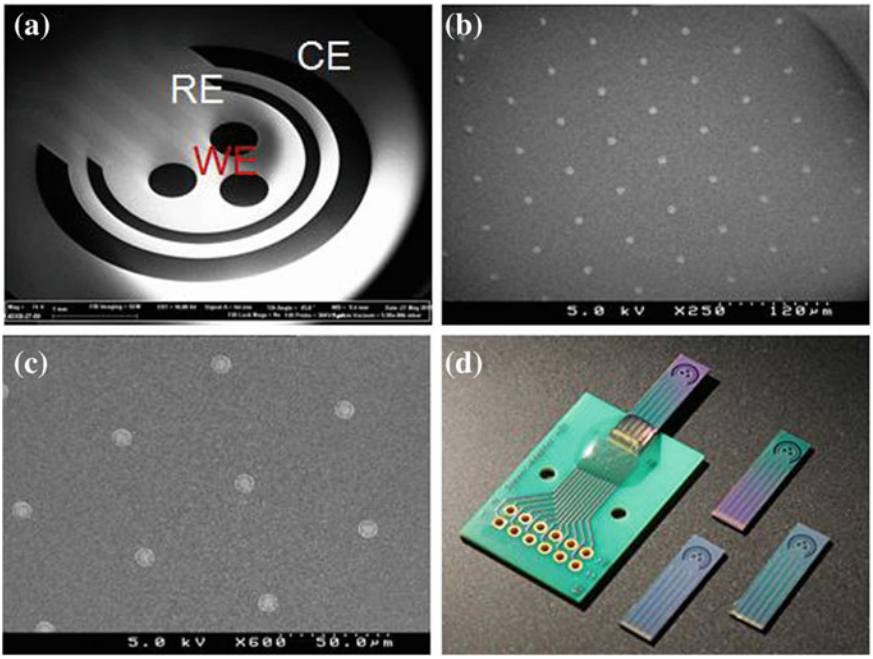

Fig. 9.6 **a** SEM image of an addressable diamond electrode array. WE, RE and CE are denoted for working electrode, reference electrode, and counter electrode, respectively; **b**, **c** SEM images of ultramicroelectrode arrays with 85 electrodes where the diameter of ultramicroelectrodes is 20 (**b**) and 10 (**c**) µm. **d** the layout of an addressable diamond electrode array after mounting the chips on a mother-board and wire-bonding

been addressed, including one 600-µm macro-sized electrode, two ultramicroelectrode arrays. The counter and reference electrodes made from boron-doped diamond have been integrated as well. As for the ultramicroelectrode arrays, these electrodes are arranged in a honeycomb structure. Their diameters are 20, 10, or 5 µm. Depending on the distance of these ultramicroelectrodes, the number of these electrodes is varied from 37 to 85. For example, for a center-to-center distance of 60 µm between electrodes, the number of electrodes is 85; for a distance of 120 µm, the number of electrodes is 37. More details are summarized in Table 9.2. Figure 9.6b, c show SEM images of one array having 85 ultramicroelectrodes with the diameter of 20 (b) and 10 (c) µm, respectively. In both case, the center-to-center distance between two ultramicroelectrodes is 60 µm. The layout of the electrochemical sensors after mounting the chips on a mother-board and wire-bonding them is illustrated in Fig. 9.6d.

We tested the voltammetric response of addressable electrochemical arrays using surface sensitive redox couple $Fe(CN)_6^{3-/4-}$. On a macro-sized electrode (600 µm) with an electrochemically hydrogen-terminated surface, the peak difference of the anodic peak potential from the cathodic peak is about 65 mV, measured at a scan

Table 9.2 Parameters of addressable diamond ultramicroelectrode arrays at Fraunhofer IAF

Electrode WEa-b[a]	Diameter/μm	Distance of two electrodes/μm	Number of electrodes
WE1-1	600	680	3
WE1-2	20	60	85
WE1-3	10	60	85
WE2-1	20	60	85
WE2-2	10	60	85
WE2-3	5	60	85
WE3-1	20	120	37
WE3-2	10	120	37
WE3-3	5	120	37

[a] a, b are denoted respectively as the chip number and the number of addressing electrode/electrode-arrays on the chip

rate of 100 mV s^{-1}. This indicates the good quality of the diamond electrode. Figure 9.7 shows voltammograms obtained on addressable ultramicroelectrode arrays shown in Table 9.2 at different scan rates. For voltammograms from (a) to (c), the number of electrodes is 37 and the center-to-center distance of the electrodes is 120 μm. While for voltammograms from (d) to (f), the number of electrodes is 85 and the center-to-center distance of the electrodes is 60 μm. The diamond of the electrodes is 20 (a, d), 10 (b, e), and 5 (c, f) μm, respectively. The shape of these voltammograms varies as a function of the diameter and scan rate. This is due to the changed thicknesses of diffusion layers at different scan rates as well as the distances in between the diamond electrodes. A peak-shaped voltammogram results from the overlapped diffusion domains of different ultra-micro electrodes; the sigmoidal curves arise from three dimensional diffusion properties toward the small electrodes. If the distance between electrodes is large, the diffusion properties of each electrode are not affected by the neighboring electrodes. Please note that by optimizing scan rates and the center-to-center distance of electrodes, the Faraday current can be maximized while at the same time with minimized capacitive current. In addition, the arrays has three working electrodes, indicating the possibility for simultaneous detection of at least three target compounds or the individual monitoring of different species on different working electrodes.

9.3.3 Nanoelectrode Arrays

As for nanoelectrode array (NEA), e-beam lithography [71], focused ion beam milling [72, 73] nanoimprint [71], and nanosphere lithography[74] have been applied in literature. For nanoelectrode ensembles (NEEs), different approaches have been developed such as the deposition of metals into pores of polycarbonate

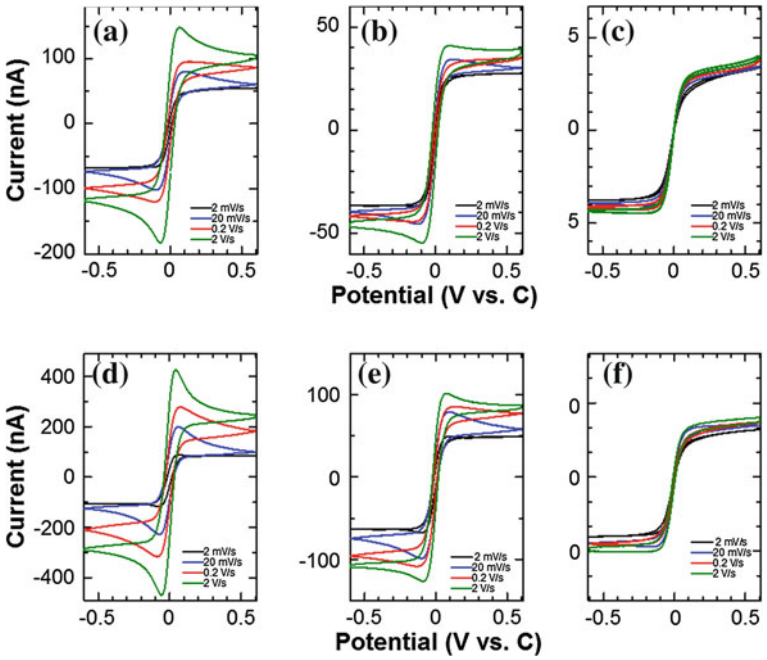

Fig. 9.7 Voltammograms of 1.0 mM $Fe(CN)_6^{3-/4-}$ on an addressable diamond electrode array at different scan rates. The diameter (*d*) of the electrodes is 20, 10 and 5 μm. The number (*N*) of electrodes is 85 or 37. The center-to-center distance (*l*) of the electrodes is 60 or 120 μm. **a** N = 37, l = 120 μm, d= 20 μm, **b** N = 37, l = 120 μm, d = 10 μm, **c** N = 37, l = 120 μm, d = 5 μm, **d** N = 85, l = 60 μm, d = 20 μm, **e** N = 85, l = 60 μm, d = 10 μm, **f** N = 85, l = 60 μm, d = 5 μm

nanoporous membranes [75–77], nanosphere lithography [78], or block copolymer self-assembly [79–81]. In addition, spatially separated carbon nanofibers and diamond nanograss as well as porous diamond film have been utilized as NEEs for electrochemical applications [82–91]. For the first time, we fabricated all-diamond NEAs and NEEs with nanocrystalline diamond (NCD) films [57]. As shown in Fig. 9.8, for NEA (a) nanoelectrodes are in a hexagonal order while for NEEs (b) nanoelectrodes are distributed randomly. The electrode in NEA has a radius of 250 nm and a distance of 10 μm next to another electrode. The density of electrodes for one NEA is 11×10^5 cm^{-2} and the number of electrodes is 18,000. The electrode in NEE has a radius of 175 nm and the density of electrodes is 8.5×10^5 cm^{-2}. The final electrode structure is schematically shown in Fig. 9.8c.

The use of NCD films has some features over polycrystalline diamond films. For example, the grain sizes of NCD films vary only from a few tens of nanometers up to hundreds of nanometer (e.g. 300 nm), resulting in better electrochemical activity than that obtained on polycrystalline diamond films which have grain sizes in the range of micrometers [92, 93]. The NCD films were grown on 3 inch silicon substrates in an ellipsoid reactor using microwave-assisted chemical vapor

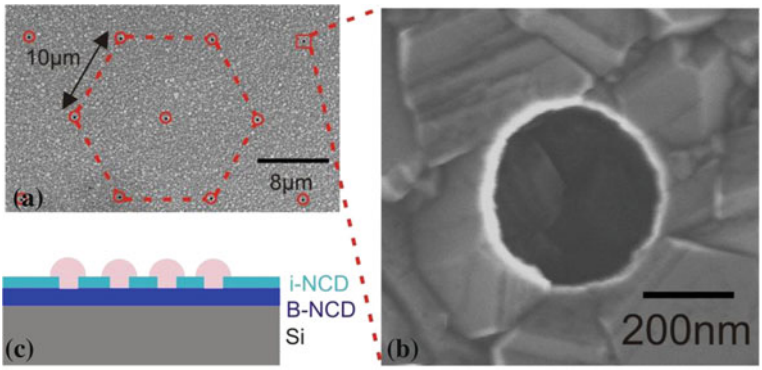

Fig. 9.8 SEM image of a NEA with an overview of distributed nanoelectrodes indicated by *red circles*, **b** SEM image of one nanoelectrode, **c** schematic plot of the electrode structure. I-NCD and B-NCD are denoted as insulting and boron-doped nanocrystalline diamond, respectively

deposition [56]. Seeding was conducted by immersing silicon wafers in nanodiamond suspension with average particle size of 5 nm [94]. The densities of diamond seeds are more than 10^{11} cm^{-2}. The growth of insulating NCD was performed using a H_2/CH_4 plasma with a methane admixture of 1 or 2 %. Boron-doping of NCD films was achieved by adding trimethylboron to the gas phase with B/C ratios of 6,000 ppm. The boron concentrations of doped NCD films were measured by secondary ion mass spectroscopy and in the range of 1 to 4 × 10^{21} cm^{-3}. E-beam lithography was applied to fabricate NEAs [57]. On a 200 nm thin boron-doped NCD film, a 200 nm thick SiO_2 is deposited. This oxide layer is structured using e-beam lithography with subsequent nickel deposition and SF_6 etching of SiO_2. In the next step, metal contacts are deposited using photolithography to allow electrical contact for electrochemical characterization. In the crucial step, a 140 nm thin insulating NCD film is grown on the part of the boron-doped NCD layer that is exposed to the CVD plasma and not protected by SiO_2 islands. With the removal of SiO_2 in hydrofluoric acid, arrays of recessed boron-doped NCD electrodes surrounded by insulating diamond are obtained. Nanosphere lithography is an approach we developed to fabricate NEEs [57]. Initially, a photolithography step is used to deposit metal contacts on NCD films. Thereafter, diamond samples are immersed in a solution of SiO_2 spheres with a radius of 500 nm. In an ultrasonic bath, an equilibrium occurs between spheres sticking to and leaving the sample surface. Thus the concentration of SiO_2 solution is directly correlated to the density of spheres on the diamond surface as well as to the average distance of neighboring spheres. The density of electrodes obtained from a SiO_2 sphere solution of the given concentration is derived from a large area scan of 50 µm × 50 µm. To obtain sigmoidal voltammograms, we chose a concentration of 9.55 × 10^8 cm^{-3}, corresponding to a surface density of 9.7 × 10^5 cm^{-2} and an average distance of neighboring spheres of ∼10 µm. The next step involves the growth of insulating

diamond around the abovementioned spheres. Insulating diamond selectively grows on the area exposed to the plasma. After removal of the SiO_2 spheres in hydrofluoric acid, we obtain electrodes of a concave shape.

Our NEEs were characterized with conductive atomic force microscopy [57]. The density determined by AFM is 8.5×10^5 cm^{-2}, which is in good agreement with the expected values from the sphere concentration in the solution. The size of electrodes is 175 nm in radius. The cross sections of the topography for two neighboring electrodes clarify that these conductive nanoelectrodes are surrounded by 140 nm thick insulating diamond. The NEA and NEE were characterized further with voltammetry in 1.0 mM $Fe(CN)_6^{3-/4-}$ in 0.1 M KCl. The scan rate varied from few mV s^{-1} up to 10 V s^{-1}. At slow scan rates (e.g. 20 mV s^{-1} for the NEA and 1 mV s^{-1} for the NEE), the voltammograms have mixed shapes, indicating partially overlapping diffusion hemispheres. Increasing the scan rate leads to typical steady-state sigmoidal voltammograms on both electrodes, indicating sphere-diffusion [95–99]. Additional to cyclic voltammetry, electrochemical impedance spectroscopy (EIS) was performed. The impedance spectra for them show similar characteristic features. Both graphs display a large semicircle in the high-frequency regime. At low frequencies, a transition to linear diffusion with unity slope occurs, particularly observable for the NEA. A semicircle at high frequency regime is due to a three-dimensional hemispherical diffusion on diamond NEA and NEE [95–97]. The transition at low frequency represents the regime of overlapping diffusion hemispheres. The change from typical three-dimensional diffusion to overlapping diffusion hemispheres is very distinct for the NEA.

Moreover, the voltammetric response of $Ru(NH_3)_6^{2+/3+}$ and $IrCl_6^{2-/3-}$ show the dependence of surface termination on the charge transfer rates of the analytes [57]. Please note that on planar macroscopic diamond electrodes both analytes show no dependence of electron transfer rate on the surface termination of diamond electrode [57, 100]. On diamond NEA, the voltammogram of the anion $IrCl_6^{2-/3-}$ shows a fast electron transfer process on the hydrogen-terminated surface, while at the oxygen-terminated surface, the steady-state current as well as the slope of the transition from reduction to oxidation decreases, indicative of a slower electron transfer rate. This tendency is similar as seen on another negatively charged redox couple of $Fe(CN)_6^{3-/4-}$. For the positively charged redox molecules $Ru(NH_3)_6^{2+/3+}$, the opposite effect is observed. On an oxygen-terminated diamond surface, the electron transfer rate for $Ru(NH_3)_6^{2+/3+}$ is faster than that on a hydrogen-terminated surface. This effect for $IrCl_6^{2-/3-}$ and $Ru(NH_3)_6^{2+/3+}$ is small compared to that for $Fe(CN)_6^{3-/4-}$. It is known that hydrogen-terminated surface has positive surface dipole layer ("positive" refers to the interface of diamond to the liquid) and the oxygen-terminated surface results in negative surface dipole layer. A macroscopic diamond electrode shows a higher degree of inhomogeneity with respect to boron-doping level and termination effects, due to its macroscopic dimensions. For the investigated NEA, one would expect a homogenized behavior due to the small grains of the NCD films as well as a more effective termination of the small electrochemical active area. Therefore the possible effects responsible for the decrease of electron transfer rate upon oxygenation of the electrode surface of NEAs are either an electrostatic or a site blocking effect.

Diamond nanoelectrode arrays (NEAs) have been thus applied to investigate surface-sensitive adsorption phenomena [100, 101]. The adsorption of neutral methyl viologen (MV^0) was used as a model system. The adsorption of MV^0 was examined with their different surface terminations, namely hydrogen- or oxygen-terminations. Diffusion-controlled processes manifest themselves as sigmoidal-shaped voltammograms on oxygen-terminated diamond NEAs, whereas adsorption-controlled processes result in peaks in the voltammogram for hydrogen-terminated diamond NEA. The change in the shapes of these voltammograms is due to the drastic changes that occur in the diffusion profiles during the transition. It alters from hemispherical diffusion on oxygen-terminated surface to thin layer electrochemistry upon adsorption on hydrogen-terminated surface. In this way the deconvolution of diffusion-controlled current from adsorption-controlled current was conducted. By further analysing anodic stripping process at high scan rates, the deposition of amorphous MV^0 was further approved on hydrogen-terminated diamond NEAs. The types and the concentration of the buffer solutions were then changed to alter the interaction of MV^0 with a hydrogen-terminated diamond nanoelectrode surface. Figure 9.9 shows the effect of guanidine, widely used for denaturation of proteins (which weakens hydrophobic interaction), on the stripping current of MV^0. The Voltammograms were recorded in 1 mM MV^{2+} and 0.1 M KCl with increasing concentrations of guanidine. Initially adsorption occurs, whereas the stripping peak continuously vanishes with increasing concentrations of guanidine up to 1.5 M. Measurements with increasing urea concentrations show the same impact on the adsorption of neutral MV as guanidine, which weakens hydrophobic interaction. Subsequently, the adsorption of MV^0 on a hydrogen-terminated diamond nanoelectrode is controlled by hydrophobic interaction. This effect of ions on the interaction of MV^0 and the hydrophobic diamond surface is correlated with the Hofmeister series. Therefore diamond NEA is ideal for the study of adsorption phenomena at the liquid-solid interface in voltammetry.

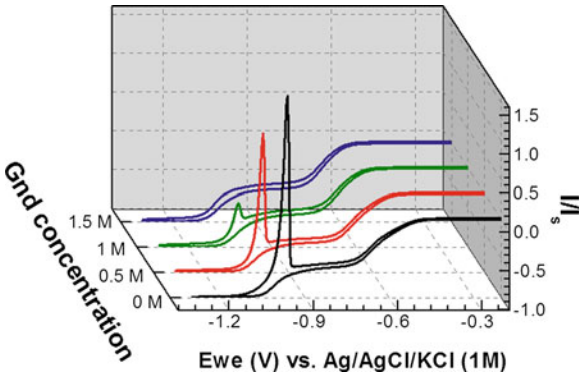

Fig. 9.9 Cyclic voltammograms of 1.0 mM MV^{2+} on a hydrogen-terminated diamond NEA in 0.1 M KCl at a scan rate of 5 V s^{-1} with increasing concentrations of guanidine. The currents were normalized to the steady state current of the reduction of MV^+ to MV^0

9.4 Summary and Outlook

Diamond micro-, ultramicro-, and nano- electrode arrays have been produced using technologies like photolithography, e-beam lithography, nanosphere lithographay, and etching processes. In particular, the NEE fabricated by nanosphere lithography offers a cheap and simple alternative to e-beam lithography. These small-dimensional electrode arrays have shown advantages over planar macro-sized diamond electrodes for sensor development, investigation of surface-sensitive reactions etc. For example, by optimizing of Faradaic and capacitive current on diamond ultramicroelectrode arrays, a 50–1,000 times better sensitivity than a planar macro-sized electrode has been achieved; by combining with the efficiency and suitability of the selective electrochemical surface termination of NEAs or NEEs, a new versatile system for electrochemical interface has been provided for the detection of surface-sensitive adsorption in a nanometer scales.

These diamond ultramicro- and nano-electrode arrays will trigger lots of new research topics centered on diamond nanoelectrochemistry. Future work should focus on in vivo applications of these arrays (e.g. fast and sensitive detection of biomolecules released from cells, in situ monitoring of cell/bacterial growth, etc.), surface treatment and properties in nanoscales, and formation of three-dimensional surface structures (nanotextures, nanowires, and porosity) on the arrays. Simplifying fabrication processes and marketing them in reasonable prices as well as their industrial applications are future research tendencies as well.

References

1. M. Iwaki, S. Sato, K. Takahashi, H. Sakairi, Electrical conductivity of nitrogen and argon implanted diamond. Nucl. Instrum. Methods Phys. Res. **209–210**(2), 1129–1133 (1983). doi:10.1016/0167-5087(83)90930-4
2. Y.V. Pleskov, A.Y. Sakharova, M.D. Krotova, L.L. Bouilov, B.V. Spitsyn, Photoelectrochemical properties of semiconductor diamond. J. Electroanal. Chem. **228** (1–2), 19–27 (1987). doi:10.1016/0022-0728(87)80093-1
3. R. Tenne, C. Levy-Clement, Diamond electrodes. Israel J. Chem. **38**(1–2), 57–73 (1998). doi:10.1002/ijch.199800007
4. G.M. Swain, A.B. Andreson, J.C. Angus, Applications of diamond thin films in electrochemistry. MRS Bull. **23**(9), 56–60 (1998). doi:10.1557/S0883769400029389
5. Y.V. Pleskov, Synthetic diamond in electrochemistry. Russ. Chem. Rev. **68**(5), 381–392 (1999). doi:10.1070/RC1999v068n05ABEH000494
6. C.E. Nebel, J. Ristein, *Thin Film Diamond II: Semiconductors and Semimetals*, vol. 77 (Elsevier Academic Press, New York, 2004)
7. A. Fujishima, Y. Einaga, T.N. Rao, D.A. Tryk, *Diamond Electrochemistry* (Elsevier Academic Press, Tokyo, 2005)
8. E. Brillas, C.A. Martinez-Huitle, *Synthetic Diamond Films: Preparation, Electrochemistry, Characterization, and Applications* (Wiley, New Jersey, 2011)
9. R.L. mcCreery, Advanced carbon electrode materials for molecular electrochemistry. Chem. Rev. **108**(7), 2646–2687 (2008). doi:10.1021/cr068076m
10. O. Chailapakul, W. Siangproh, D.A. Tryk, Boron-doped diamond-based sensors: a review. Sens. Lett. **4**(2), 99–119 (2006). doi:10.1166/sl.2006.008

11. Y.L. Zhou, J.F. Zhi, The application of boron-doped diamond electrodes in amperometric biosensors. Talanta **79**(5), 1189–1196 (2009). doi:10.1016/j.talanta.2009.05.026
12. C.E. Nebel, B. Rezek, D. Shin, H. Uetsuka, N. Yang, Diamond for bio-sensor applications. J. Phys. D Appl. Phys. **40**(20), 6443–6466 (2007). doi:10.1088/0022-3727/40/20/S21
13. R. Linares, P. Doering, B. Linares, Diamond bio electronics. Stud. Health Technol. Inform. **149**, 284–296 (2009). doi:10.3233/978-1-60750-050-6-284
14. V. Vermeeren, S. Wenmackers, P. Wagner, L. Michiels, DNA sensors with diamond as a promising alternative transducer material. Sensor **9**(7), 5600–5636 (2009). doi:10.3390/s90705600
15. A. Argoitia, H.B. Martin, E.J. Rozak, U. Landau, J.C. Angus, Electrochemical studies of boron-doped diamond electrodes. MRS. Proc. **416**, 349 (1995). doi:10.1557/PROC-416-349
16. G.M. Swain, R. Ramesham, The electrochemical activity of boron-doped polycrystalline diamond thin film electrodes. Anal. Chem. **65**(4), 345–351 (1993). doi:10.1021/ac00052a007
17. G.M. Swain, The use of CVD diamond thin films in electrochemical systems. Adv. Mater. **6** (5), 388–392 (1994). doi:10.1002/adma.19940060511
18. R. Hoffmann, A. Kriele, H. Obloh, J. Hees, M. Wolfer, W. Smirnov, N. Yang, C.E. Nebel, Electrochemical hydrogen termination of boron-doped diamond. Appl. Phys. Lett. **97**(5), 052103 (2010). doi:10.1063/1.3476346
19. W. Yang, O. Auciello, J.E. Butler, W. Cai, J.A. Carlisle, J.E. Gerbi, D.M. Gruen, T. Knickerbocker, T.L. Lasseter, J.N. Russell Jr., J.M. Smith, R.J. Hamers, DNA-modified nanocrystalline diamond thin-films as stable, biologically active substrates. Nat. Mater. **1**(4), 253–257 (2002). doi:10.1038/nmat779
20. A. Hartl, E. Schmich, J.A. Garrido, J. Hernando, S.C.R. Catharino, S. Walter, P. Feulner, A. Kromka, D. Steinmuller, M. Stutzmann, Protein-modified nanocrystalline diamond thin films for biosensor applications. Nat. Mater. **3**(10), 736–742 (2004). doi:10.1038/nmat1204
21. Y.S. Zou, Y. Yang, W.J. Zhang, Y.M. Chong, B. He, I. Bello, S.T. Lee, Fabrication of diamond nanopillars and their arrays. Appl. Phys. Lett. **92**(5), 053105 (2008). doi:10.1063/1.2841822
22. N. Yang, H. Uetsuka, E. Osawa, C.E. Nebel, Vertically aligned nanowires from boron-doped diamond. Nano Lett. **8**(11), 3572–3576 (2008). doi:10.1021/nl801136h
23. C.E. Nebel, N. Yang, H. Uetsuka, E. Osawa, N. Tokuda, O. William, Diamond nano-wires, a new approach towards next generation electrochemical gene sensor platforms. Diam. Relat. Mater. **18**(5–8), 910–917 (2009). doi:10.1016/j.diamond.2008.11.024
24. W. Smirnov, A. Kriele, N. Yang, C.E. Nebel, Aligned diamond nano-wires: fabrication and characterisation for advanced applications in bio- and electrochemistry. Diam. Relat. Mater. **19**(2–3), 186–189 (2010). doi:10.1016/j.diamond.2009.09.001
25. A.J. Bard, L.R. Faulkner, *Electrochemical Methods, Fundamentals and Applications*, 2nd edn. (Wiley-VCH, MA, 2001)
26. J. Wang, *Analytical Electrochemistry*, 2nd edn. (Wiley-VCH, MA, 2000)
27. X.J. Huang, A.M. O'Mahony, R.G. Compton, Microelectrode arrays for electrochemistry: approaches to fabrication. Small **5**(7), 776–788 (2009). doi:10.1002/smll.200801593
28. D.W.M. Arrigan, Nanoelectrodes, nanoelectrode arrays and their applications. Analyst **129** (12), 1157–1165 (2004). doi:10.1039/B415395M
29. R.G. Compton, G.G. Wildgoose, N.V. Rees, I. Streeter, R. Baron, Design, fabrication, characterisation and application of nanoelectrode arrays. Chem. Phys. Lett. **459**(1–6), 1–17 (2008). doi:10.1016/j.cplett.2008.03.095
30. O. Ordeig, J. del Campo, F.X. Munoz, C.E. Banks, R.G. Compton, Electroanalysis utilizing amperometric microdisk electrode arrays. Electroanalysis **19**(19–20), 73–1986(2007). doi:10.1002/elan.200703914
31. J.B. Cooper, S. Pang, S. Albin, J. Zheng, R.M. Johnson, Fabrication of boron-doped CVD diamond microelectrodes. Anal. Chem. **70**(3), 464–467 (1998). doi:10.1021/ac9707621
32. B.V. Sarada, T.N. Rao, D.A. Tryk, A. Fujishima, Electrochemical characterization of highly boron-doped diamond microelectrodes in aqueous electrolyte. J. Electrochem. Soc. **146**(4), 1469–1471 (1999). doi:10.1149/1.1391788

33. B. Duran, R.F. Brocenschi, M. France, J.J. Galligan, G.M. Swain, Electrochemical activation of diamond microelectrodes: implications for the in vitro measurement of serotonin in the bowel. Analyst 139(12), 3160–3166 (2014). doi:10.1039/c4an00506f
34. K.B. Holt, J.P. Hu, J.S. Foord, Fabrication of boron-doped diamond ultramicroelectrodes for use in scanning electrochemical microscopy experiments. Anal. Chem. **79**(6), 2556–2561 (2007). doi:10.1021/ac061995s
35. J.P. Hu, J.S. Foord, K.B. Holt, Hot filament chemical vapour deposition of diamond ultramicroelectrodes. Phys. Chem. Chem. Phys. **9**(40), 5469–5475 (2007). doi:10.1039/B710241K
36. J.P. Hu, K.B. Holt, J.S. Foord, Focused ion beam fabrication of boron-doped diamond ultramicroelectrodes. Anal. Chem. **81**(14), 5663–5670 (2009). doi:10.1021/ac9003908
37. J. Cvacka, V. Quaiserova, J.W. Park, Y. Show, A. Muck, G.M. Swain, Boron-doped diamond microelectrodes for use in capillary electrophoresis with electrochemical detection. Anal. Chem. **75**(11), 2678–2687 (2003). doi:10.1021/ac030024z
38. J. Park, Y. Show, V. Quaiserova, J.J. Galligan, G.D. Fink, G.M. Swain, Diamond microelectrodes for use in biological environments. J. Electroanal. Chem. **583**(1), 56–68 (2005). doi:10.1016/j.jelechem.2005.04.032
39. J.M. Halpern, S. Xie, G.P. Sutton, B.T. Higashikubo, C.A. Chestek, H. Lu, H.J. Chiel, H.B. Martin, Diamond electrodes for neurodynamic studies in aplysia californica. Diam. Relat. Mater. **15**(2–3), 183–187 (2006). doi:10.1016/j.diamond.2005.06.039
40. S. Xie, G. Shafer, C.G. Wilson, H.B. Martin, In vitro adenosine detection with a diamond-based sensor. Diam. Relat. Mater. **15**(2–3), 225–228 (2006). doi:10.1016/j.diamond.2005.08.018
41. A.L. Colley, C.G. Williams, U. D´Haenens Johnsson, M.E. Newton, P.R. Uniwin, N.R. Wilson, J.V. Macpherson, Examination of the spatially heterogeneous electroactivity of boron-doped diamond microarray electrodes. Anal. Chem. **78**(8), 2539–2548 (2006). doi:10.1021/ac0520994
42. K. Tsunozaki, Y. Einaga, T.N. Rao, A. Fujishima, Fabrication and electrochemical characterization of boron-doped diamond microdisc array electrodes. Chem. Lett. **31**(5), 502–503 (2002). doi:10.1246/cl.2002.502
43. C. Provent, W. Haenni, E. Santoli, P. Rychen, Boron-doped diamond electrodes and microelectrode-arrays for the measurement of sulfate and peroxodisulfate. Electrochim. Acta **49**(22–23), 3737–3744 (2004). doi:10.1016/j.electacta.2004.02.047
44. K.L. Soh, W.P. Kang, J.L. Davidson, Y.M. Wong, A. Wisisoraat, G. Swain, D.E. Cliffel, CVD diamond anisotropic film as electrode for electrochemical sensing. Sens. Actuators B **91**(1–3), 39–45 (2003). doi:10.1016/S0925-4005(03)00064-9
45. K.L. Soh, W.P. Kang, J.L. Davidson, S. Basu, Y.M. Wong, D.E. Cliffel, A.B. Bonds, G. Swain, Diamond-derived microelectrodes array for electrochemical analysis. Diam. Relat. Mater. **13**(11–12), 2009–2015 (2004). doi:10.1016/j.diamond.2004.07.025
46. K.L. Soh, W.P. Kang, J.L. Davidson, Y.M. Wong, D.E. Cliffel, G. Swain, Ordered array of diamond ultramicroband electrodes for electrochemical analysis. Diam. Relat. Mater. **17**(3), 240–246 (2008). doi:10.1016/j.diamond.2007.12.023
47. K.L. Soh, W.P. Kang, J.L. Davidson, Y.M. Wong, D.E. Cliffel, G. Swain, Diamond-derived ultramicroelectrodes designed for electrochemical analysis and bioanalyte sensing. Diam. Relat. Mater. **17**(4–5), 900–905 (2008). doi:10.1016/j.diamond.2007.12.041
48. S. Raina, W.P. Kang, J.L. Davidson, Fabrication of nitrogen-incorporated nanodiamond ultra-microelectrode array for Dopamine detection. Diam. Relat. Mater. **19**(2–3), 256–259 (2010). doi:10.1016/j.diamond.2009.10.013
49. M. Pagels, C.E. Hall, N.S. Lawrence, A. Meredith, T.G.L. Jones, H.P. Godfried, C.S.J. Pickles, J. Wilman, C.E. Banks, R.G. Compton, L. Jiang, All-diamond microelectrode array device. Anal. Chem. **77**(11), 3705–3708 (2005). doi:10.1021/ac0502100
50. A.O. Simm, C.E. Banks, S. Ward-Jones, T.J. Davies, N.S. Lawrence, T.G.J. Jones, L. Jiang, R.G. Compton, Boron-doped diamond microdisc arrays: electrochemical characterisation and their use as a substrate for the production of microelectrode arrays of diverse metals (Ag, Au, Cu) *via* electrodeposition. Analyst **130**(9), 1303–1311 (2005). doi:10.1039/B506956D

51. N.S. Lawrence, M. Pagels, A. Meredith, T.G.J. Jones, C.E. Hall, C.S. Pickles, H.P. Godfried, C.E. Banks, R.G. Compton, L. Jiang, Electroanalytical applications of boron-doped diamond microelectrode arrays. Talanta **69**(4), 829–834 (2006). doi:10.1016/j.talanta.2005.11.020
52. M. Bonnauron, S. Saada, L. Rousseau, G. Lissorgues, C. Mer, P. Bergonzo, High aspect ratio diamond microelectrode array for neuronal activity measurements. Diam. Relat. Mater. **17** (7–10), 1399–1404 (2008). doi:10.1016/j.diamond.2007.12.065
53. M. Bonnauron, S. Saada, C. Mer, C. Gesset, O.A. Williams, L. Rousseau, E. Scorsone, P. Mailley, Transparent diamond-on-glass micro-electrode arrays for ex-vivo neuronal study. Phys. Stat. Sol. (a) **205**(9), 2126–2129 (2008). doi:10.1002/pssa.200879733
54. V. Carabelli, S. Gosso, A. Marcantoni, Y. Xu, E. Colombo, Z. Gao, E. Vittone, E. Kohn, A. Pasquarelli, E. Carbone, Nanocrystalline diamond microelectrode arrays fabricated on sapphire technology for high-time resolution of quantal catecholamine secretion from chromaffin cells. Biosens. Bioelectron. **26**(1), 92–98 (2010). doi:10.1016/j.bios.2010.05.017
55. W. Smirnov, N. Yang, R. Hoffmann, J. Hees, H. Obloh, W. Muller-Sebert, C.E. Nebel, Integrated all-diamond ultramicroelectrode arrays: optimization of Faradaic and capacitive currents. Anal. Chem. **83**(19), 7438–7443 (2011). doi:10.1021/ac201595k
56. N. Yang, W. Smirnov, J. Hees, R. Hoffmann, A. Kriele, H. Obloh, W. Müller-Sebert, C.E. Nebel, Diamond ultra-microelectrode arrays for achieving maximum Faradaic current with minimum capacitive charging. Phys. Stat. Sol. (a) **208**(9), 2087–2092 (2011). doi:10.1002/pssa.201100016
57. J. Hees, R. Hoffmann, A. Kriele, W. Smirnov, H. Obloh, K. Glorer, B. Raynor, R. Driad, N. Yang, O.A. Williams, C.E. Nebel, Nanocrystalline diamond nanoelectrode arrays and ensembles. ACS Nano **5**(4), 3339–3346 (2011). doi:10.1021/nn2005409
58. W. Smirnov, J.J. Hees, D. Brink, W. Muller-Sebert, A. Kriele, O.A. Williams, C.E. Nebel, Anisotropic etching of diamond by molten Ni particles. Appl. Phys. Lett. **97**(7), 073117 (2010). doi:10.1063/1.3480602
59. D. Khamis, E. Mahe, F. Dardoize, D. Devilliers, Peroxodisulfate generation on boron-doped diamond microelectrodes array and detection by scanning electrochemical microscopy. J. Appl. Electrochem. **40**(10), 1829–1838 (2010). doi:10.1007/s10800-010-0114-x
60. E. Popa, H. Notsu, T. Miwa, D.A. Tryk, A. Fujishima, Selective electrochemical detection of dopamine in the presence of ascorbic acid at anodized diamond thin film electrodes. Electrochem. Sol. Stat. Lett. **2**(1), 49–51 (1999). doi:10.1149/1.1390730
61. A. Fujishima, T.N. Rao, E. Popa, B.V. Sarada, I. Yagi, D.A. Tryk, Electroanalysis of dopamine and NADH at conductive diamond electrodes. J. Electroanal. Chem. **473**(1–2), 179–185 (1999). doi:10.1016/S0022-0728(99)00106-0
62. D. Sopchak, B. Miller, R. Kalish, Y. Avyigal, X. Shi, Dopamine and ascorbate analysis at hydrodynamic electrodes of boron doped diamond and nitrogen incorporated tetrahedral amorphous carbon. Electroanalysis **14**(7–8), 473–478 (2002). doi:10.1002/1521-4109(200204)
63. W.C. Poh, K.P. Loh, W.D. Zhang, S. Triparthy, J.-S. Ye, F.-S. Sheu, Biosensing properties of diamond and carbon nanotubes. Langmuir **20**(13), 5484–5492 (2004). doi:10.1021/la0490947
64. P.S. Siew, K.P. Loh, W.C. Poh, H. Zhang, Biosensing properties of nanocrystalline diamond film grown on polycrystalline diamond electrodes. Diam. Relat. Mater. **14**(3–7), 426–431 (2005). doi:10.1016/j.diamond.2004.11.016
65. G.-H. Zhao, M.-F. Li, M.-L. Li, Differential pulse voltammetric determination of dopamine with the coexistence of ascorbic acid on boron-doped diamond surface. Cent. Eur. J. Chem. **5** (4), 1114–1123 (2007). doi:10.2478/s11532-007-0049-1
66. A. Suzuki, T.A. Ivandini, K. Yoshimi, A. Fujishima, G. Oyama, T. Nakazato, N. Hattori, S. Kitazawa, Y. Einaga, Fabrication, characterization, and application of boron-doped diamond microelectrodes for in vivo dopamine detection. Anal. Chem. **79**(22), 8608–8615 (2007). doi:10.1021/ac071519h
67. M. Wei, G. Terashima, M. Lv, A. Fijishima, Z.-Z. Gu, Boron-doped diamond nanograss array for electrochemical sensors. Chem. Comm. **45**(24), 3624–3629 (2009). doi:10.1039/b903284c

68. A.E. Hess, D.M. Sabens, H.B. Martin, C.A. Zorman, Diamond-on-polymer microelectrode arrays fabricated using a chemical release transfer process. J. Microelectromech. Syst. **20**(4), 867–875 (2011). doi:10.1109/JMEMS.2011.2159099
69. Z. Gao, V. Carabelli, E. Carbone, E. Colombo, M. Dipalo, C. Manfredotti, A. Pasquarelli, A. Feneberg, K. Thonke, E. Vittone, Transparent microelectrode array in diamond technology. J. Micro-Nano Mech. **6**(1–2), 33–37 (2011). doi:10.1007/s12213-010-0032-3
70. R. Kiran, L. Rousseau, G. Lissorgues, E. Scorsone, A. Bongrain, B. Yvert, S. Picaud, P. Mailley, P. Bergonzo, Multichannel boron doped nanocrystalline diamond ultramicroelectrode arrays: design, fabrication and characterization. Sensors **12**(6), 7669–7681 (2012). doi:10.3390/s120607669
71. M.E. Sandison, J.M. Cooper, Nanofabrication of electrode arrays by electron-beam and nanoimprint lithographies. Lab Chip **6**(8), 1020–1025 (2006). doi:10.1039/B516598A
72. Y.H. Lanyon, D.W.M. Arrigan, Recessed nanoband electrodes fabricated by focused ion beam milling. Sens. Actuators B **121**(1), 341–347 (2007). doi:10.1016/j.snb.2006.11.029
73. Y.H. Lanyon, G. De Marzi, Y.E. Watson, A.J. Quinn, J.P. Gleeson, G. Redmond, D.W.M. Arrigan, Fabrication of nanopore array electrodes by focused ion beam milling. Anal. Chem. **79**(8), 3048–3055 (2007). doi:10.1021/ac061878x
74. H. Li, N. Wu, A large-area nanoscale gold hemisphere pattern as a nanoelectrode array. Nanotechnology **19**(27), 275301 (2008). doi:10.1088/0957-4484/19/27/275301
75. R.M. Penner, C.R. Martin, Preparation and electrochemical characterization of ultramicroelectrodes ensembles. Anal. Chem. **59**(21), 2625–2630 (1987). doi:10.1021/ac00148a020
76. V.P. Menon, C.R. Martin, Fabrication and evaluation of nanoelectrode ensembles. Anal. Chem. **67**(13), 1920–1925 (1995). doi:10.1021/ac00109a003
77. M. Yang, F. Qu, Y. Lu, Y. He, G. Shen, R. Yu, Platinum nanowire nanoelectrode array for the fabrication of biosensors. Biomaterials **27**(35), 5944–5950 (2006). doi:10.1016/j.biomaterials.2006.08.014
78. T. Lohmuller, U. Muller, S. Breisch, W. Nisch, R. Rudorf, W. Schuhmann, S. Neugebauer, M. Kaczor, S. Linke, S. Lechner, J. Spatz, M. Stelzle, Nano-porous electrode systems by colloidal lithography for sensitive electrochemical detection: fabrication technology and properties. J. Micromech. Microeng. **18**(11), 115011 (2008). doi:10.1088/0960-1317/18/11/115011
79. E. Jeoung, T.H. Galow, J. Schotter, M. Bal, A. Ursache, M.T. Tuominen, C.M. Stafford, T.P. Russell, V.M. Rotello, Fabrication and characterization of nanoelectrode arrays formed via block copolymer self-assembly. Langmuir **17**(21), 6396–6398 (2001). doi:10.1021/la010531g
80. C. Wang, X. Shao, Q. Liu, Y. Mao, G. Yang, H. Xue, X. Hu, One step fabrication and characterization of platinum nanopore electrode ensembles formed via amphiphilic block copolymer self-assembly. Electrochim. Acta **52**(2), 704–709 (2006). doi:10.1016/j.electacta.2006.06.003
81. C. Wang, Q. Liu, X. Shao, G. Yang, H. Xue, X. Hu, One step fabrication of nanoelectrode ensembles formed via amphiphilic block copolymers self-assembly and selective voltammetric detection of uric acid in the presence of high ascorbic acid content. Talanta **71**(1), 178–185 (2007). doi:10.1016/j.talanta.2006.03.055
82. J. Li, J.E. Koehne, A.M. Cassell, H. Chen, H.T. Ng, Q. Ye, W. Fan, J. Han, M. Meyyappan, *Inlaid Multi-Walled Carbon Nanotube Nanoelectrode Arrays for Electroanalysis*, vol. 17 (Wiley-VCH, Weinheim, 2005), pp. 15–27. doi:10.1002/elan.200403114
83. J. Koehne, J. Li, A.M. Cassell, H. Chen, Q. Ye, H.T. Ng, J. Han, M. Meyyappan, The fabrication and electrochemical characterization of carbon nanotube nanoelectrode arrays. J. Mater. Chem. **14**(4), 676–684 (2004). doi:10.1039/B311728F
84. Y. Tu, Y. Lin, W. Yantasee, Z. Ren, *Carbon Nanotubes Based Nanoelectrode Arrays: Fabrication, Evaluation, and Application in Voltammetric Analysis, Electroanalysis*, vol. 17 (Wiley-VCH, Weinheim, 2005) , pp. 79-84. doi:10.1002/elan.200403122

85. S. Siddiqui, P.U. Arumugam, H. Chen, J. Li, M. Meyyappan, Characterization of carbon nanofiber electrode arrays using electrochemical impedance spectroscopy: effect of scaling down electrode size. ACS Nano **4**(2), 955–961 (2010). doi:10.1021/nn901583u
86. N. Yang, W. Waldemar, C.E. Nebel, Fabrication, properties and electrochemical applications of diamond nanostructures. MRS Proc. **1511**, mrsf12-1511-ee07-01 (2013). doi:10.1557/opl.2012.1661
87. D. Luo, L. Wu, J. Zhi, Fabrication of boron-doped diamond nanorod forest electrodes and their application in nonenzymatic amperometric glucose biosensing. ACS Nano **3**(8), 2121–2128 (2009). doi:10.1021/nn9003154
88. M. Lv, M. wei, F. Rong, C. Terashima, A. Fujishima, Z.-Z. Gu, Electrochemical detection of catechol based on as-grown and nanograss array boron-doped diamond electrodes. Electroanalysis **22**(2), 199–203 (2010). doi:10.1002/elan.200900296
89. W. Wu, L. Bai, X. Lin, Z. Tang, Z. Gu, Nanograss array boron-doped diamond electrode for enhanced electron transfer from *Shewanella loihica* PV-4. Electrochem. Commun. **13**(8), 872–874 (2011). doi:10.1016/j.elecom.2011.05.025
90. D. Luo, J. Zhi, Fabrication and electrochemical behaviour of vertically aligned boron-doped diamond nanorod forest electrodes. Electrochem. Commun. **11**(6), 1093–1096 (2009). doi:10.1016/j.elecom.2009.03.011
91. Y. Yang, J.-W. Oh, Y.-R. Kim, C. Terashima, A. Fujishima, J.S. Kim, H. Kim, Enhanced electrogenerated chemiluminescence of a ruthenium tris(2,2′)bipyridyl/tripropylamine system on a boron-doped diamond nanograss array. Chem. Commun. **46**(31), 5793–5795 (2010). doi:10.1039/c0cc00773k
92. M.C. Granger, G.M. Swain, The influence of surface interactions on the reversibility of ferri/ferrocyanide at boron-doped diamond thin-film electrodes. J. Electrochem. Soc. **146**(12), 4551–4558 (1999). doi:10.1149/1.1392673
93. W. Gajewski, P. Achatz, O.A. Williams, K. Haenen, E. Bustarret, M. Stutzmann, J.A. Garrido, Electronic and optical properties of boron-doped nanocrystalline diamond films. Phys. Rev. B **79**(4), 045206 (2009). doi:10.1103/PhysRevB.79.045206
94. O.A. Williams, O. Douheret, M. Daenen, K. Haenen, E. Osawa, M. Takahashi, Enhanced diamond nucleation on monodispersed nanocrystalline diamond. Chem. Phys. Lett. **445** (4–6), 255–258 (2007). doi:10.1016/j.cplett.2007.07.091
95. J. Guo, E. Lindner, Cyclic voltammograms at coplanar and shallow recessed microdisk electrode arrays: guidelines for design and experiment. Anal. Chem. **81**(1), 130–138 (2009). doi:10.1021/ac801592j
96. M. Fleischmann, S. Pons, J. Daschbach, The ac impedance of spherical, cylindrical, disk, and ring microelectrodes. J. Electroanal. Chem. **317**(1–2), 1–26 (1991). doi:10.1016/0022-0728(91)85001-6
97. M. Fleischmann, S. Pons, The behavior of microdisk and microring electrodes. Mass transport to the disk in the unsteady state: the ac response. J. Electroanal. Chem. **250**(2), 277–283 (1988). doi:10.1016/0022-0728(88)85169-6
98. L.M. Abrantes, M. Fleischmann, L.M. Peter, S. Pons, B.R. Scharifker, On the diffusional impedance of microdisc electrodes. J. Electroanal. Chem. **256**(1), 229–233 (1988). doi:10.1016/0022-0728(88)85023-X
99. O. Koster, W. Schuhmann, H. Vogt, W. Mokwa, Quality control of ultra-microelectrode arrays using cyclic voltammetry, electrochemical impedance spectroscopy and scanning electrochemical microscopy. Sens. Actuators B **76**(1–3), 573–581 (2001). doi:10.1016/S0925-4005(01)00637-2
100. J. Hees, R. Hoffmann, N. Yang, C.E. Nebel, Diamond nanoelectrode arrays for the detection of surface sensitive adsorption. Chem. Euro. J. **19**(34), 11287–11292 (2013). doi:10.1002/chem.201301763
101. J. Hees, *All-Diamond Nanoelectrode Arrays, Science for Systems*, vol. 10 (Fraunhofer-Verlag, Freiburg, 2012)

Chapter 10
Advances in Electrochemical Biosensing Using Boron Doped Diamond Microelectrode

Stéphane Fierro and Yasuaki Einaga

Abstract The development of boron doped diamond (BDD) as electrode material lead to significant improvement toward optimal sensitivity, reproducibility and stability during the in vivo monitoring of electroactive species. The most recent developments in the field of biosensing using BDD electrodes, namely the fabrication of the sensor and application in monitoring of dopamine and glutathione, are described in this chapter.

10.1 Introduction

Owing to its simplicity and accuracy electrochemical biosensors have recently been employed for in vivo monitoring of electroactive species. Since the first principles of electrochemical biosensing were presented at the New York Academy of Sciences symposium [1], electrodes have been used for many biological applications ranging from glucose assays to urease detection [2, 3]. Other applications are summarized in [4]. The monitoring of important biological targets can be performed using several electroanalytical techniques such as, for instance, amperometry or potentiometry. Furthermore, the miniaturization of electrodes used as biosensors have opened new and exciting research and application pathways due to the advantages bestowed by their micron-sized dimensions. In addition to several unique properties, such as non-linear diffusion, increased rate of mass transport, and reduced capacitance allowing a fast response, the very small size of microelectrodes have provided a major breakthrough in electrochemistry, because they have greatly improved the quality of the analysis and the range of experiments that can be

S. Fierro · Y. Einaga (✉)
Department of Chemistry, Faculty of Science and Technology, Keio University,
3-14-1, Hiyoshi, Yokohama 223-8522, Japan
e-mail: einaga@chem.keio.ac.jp

S. Fierro
e-mail: sfierro@chem.keio.ac.jp

N. Yang (ed.), *Novel Aspects of Diamond*, Topics in Applied Physics 121,
DOI 10.1007/978-3-319-09834-0_10

performed, for example, fast scan measurements and analysis in low conducting media [5–7]. In particular, the small size of the microelectrodes allows their utilization for in vivo detection, such as monitoring the brain via a neurotransmitter, which is usually performed in a very small sample volume [8]. Carbon fiber (CF) electrodes have already been established for some in vivo tests owing to (i) their good biocompatibility, (ii) relatively low cost and (iii) their wide availability [9–12]. Moreover, CF is thin enough to penetrate biological tissue with the minimum disruption [8]. CF has well-known disadvantages, however, such as brittleness and high adsorption behavior.

Recently, boron-doped diamond (BDD) as primary media within sensing electrode has attracted heightened attention due to their peculiar electrochemical properties, such as (i) their wide potential window, (ii) their very small charging current, (iii) their chemical inertness and (iv) their mechanical durability relative to other conventional electrode materials [13–16]. These properties have enabled the development of a new field of electrochemical analysis, especially the detection of trace amounts of environment-related or bio-related substances [13, 17–20]. BDD also has good biocompatibility [13–16]. For these reasons, BDD has progressively replaced other biocompatible electrode materials such as gold, which usually require time consuming pretreatments before being able to obtain reproducible results. Moreover, the use and preparation of gold tend to complicate the experimental procedure and, therefore, these methods have become more obsolete for in vivo analytical applications. Additionally, adsorption and subsequent fouling on these types of electrode materials often occurs during the oxidation of various organic compounds and, thus, it becomes increasingly difficult to use these electrode materials for in vivo biosensing.

For the aforementioned reasons, BDD has recently supplanted other methods for electrochemical in vivo analysis. The fabrication and characterization of BDD microelectrodes have been reported previously and the uniqueness of BDD microelectrodes for electrochemical analysis has been well established [21–29].

One of the primary targets to be analyzed in vivo by BDD microelectrode is the neurotransmitter dopamine. Recently, however, these electrodes have provided solutions for the in vivo monitoring of other targets such as the reduced form of glutathione (GSH) for cancer tumor assessment.

In this chapter, an exhaustive review of the most recent advances in biosensing via BDD electrode is presented through the examples of in vivo monitoring of dopamine and glutathione.

10.2 BDD Microelectrode Preparation and Structural Characterization

Tungsten wire was used as the substrate for BDD deposition. The wire was electrochemically etched in an aqueous solution of 2 M NaOH at +3.0 V (vs. Ag/AgCl) for 20 s. During this process, tungsten wire was gradually lifted up from the etching

solution. As a last step, the tip of the wire was conically shaped to leave a tip with a diameter of ~3 µm. The sharpened wire was then immersed into HF solution (46.0 %) for a few minutes to eliminate the tungsten oxide layer from the surface, which was then followed by a seeding process in an ultrasonic bath containing a 2-propanol suspension of diamond particles (0–500 nm particles, Kemet Co.) for 1 h. A thin film of BDD was deposited on the prepared tungsten wire using a microwave plasma assisted chemical vapor deposition (MPCVD) system (ASTeX Corp.) with a plasma power of 2,500 W. The deposition time was fixed at 3 h. Acetone was used as a carbon source, and $B(OCH_3)_3$ as a source of boron. The concentration of the latter was controlled as between 5.0 and 0.1 % w/w in the source. The surface morphology and crystalline structure of the BDD thin film was determined using scanning electron microscopy (SEM, JOEL JSM 5400) and Raman spectroscopy (Renishaw System 2000). The tungsten wire coated with the BDD thin film was then connected to the coated metal wire using silver paste and then dried. This BDD wire was then inserted into the capillary for insulation through a pre-pulled glass capillary (using capillary puller, Narishige, Tokyo, Japan) followed by resin infusion. Resin was soaked up by capillary action. After drying overnight, the fabrication of BDD microelectrode reached completion. The details are illustrated in Fig. 10.1.

CF electrodes were prepared via the same procedure as shown in Fig. 10.1. The electrode length can be easily controlled by adjusting its tip until it had the same length than the BDD microelectrode.

A SEM image of the fabricated BDD microelectrode shows that the tip diameter is distinctly small (about 5 µm) with the polycrystalline diamond grain size being approximately ~2 µm (Fig. 10.2a). The tip size was almost the same as the conventional CF electrode used in this experiment shown as example (Fig. 10.2b). Based on the experimental trial for in vivo measurement the average tip length was set at 250 µm (Fig. 10.2c). Use of similar length of CF for in vivo monitoring of dopamine was also reported by Gonon's group [30]. The Raman spectrum of the BDD microelectrode shows one clear peak at 1,333 cm^{-1} for sp^3 carbon bonds indicating that the BDD thin film has a fine quality with the absence of the peak at ~1,600 cm^{-1} generally attributed to non diamond carbon impurities (Fig. 10.2d).

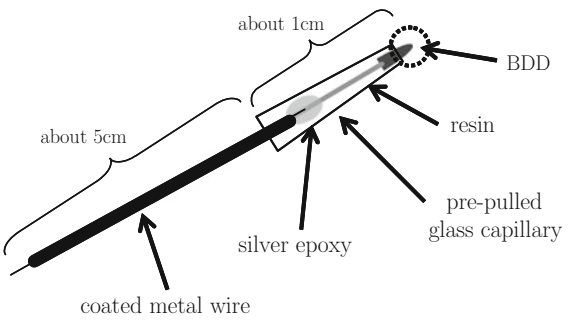

Fig. 10.1 Schematic drawing of a BDD microelectrode. Copyright (2007) American Chemical Society

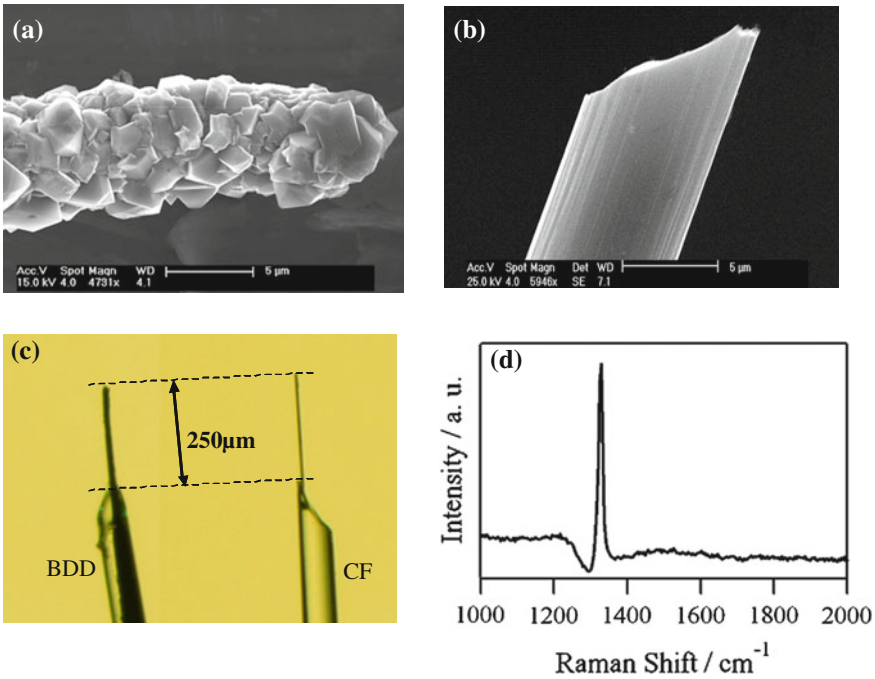

Fig. 10.2 SEM image of **a** BDD wire and **b** CF electrode. **c** Shows a comparison of the optical microscope image of the BDD microelectrode (*left side*) and a conventional CF microelectrode (*right side*). **d** Raman spectra of the BDD wire. Copyright (2007) American Chemical Society

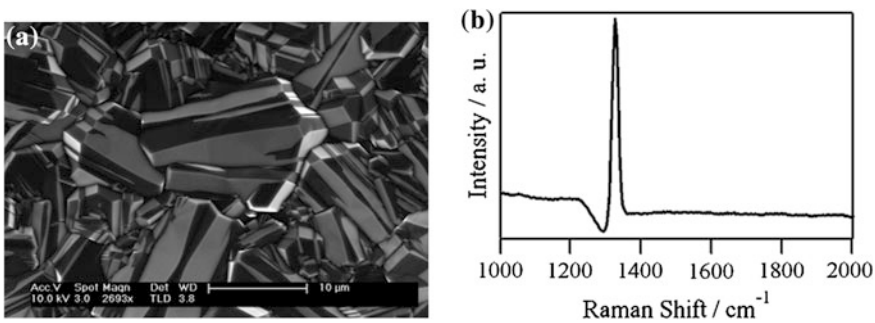

Fig. 10.3 BDD macroelectrode. **a** SEM image and **b** Raman spectra. Copyright (2007) American Chemical Society

The shoulder before the sp^3 carbon peak is attributed to the high boron doping concentration. The SEM image and Raman spectrum in this report are comparable with common BDD films on silicon wafers (Fig. 10.3). The results indicate that by optimizing the deposition conditions, similar BDD quality, in terms of the

morphology and crystalline structure, can be deposited on different types and sizes of substrate.

10.3 Dopamine Detection

Dopamine, which is a precursor of two other neurotransmitters: adrenaline and noradrenalin can be found in the nervous tissues and body fluids as organic cations This chemical substance is relevant topic of research because it is involved in memory or attention span disorders [31, 32]. In particular, low levels of dopamine can cause severe neurological disorders, such as Parkinson's disease [33, 34]. The dopamine concentration found usually within a living system can be below 26 nM [35, 36]. Therefore, the development of accurate electrochemical biosensors can make a great contribution to the early diagnosis of mental diseases. In recent years, much effort has been devoted toward improving the catalytic properties, sensitivity, and selectivity of electrochemical sensors, particularly via the application of nanomaterials [37–42]. Many of the electrochemical biosensors employed for dopamine detection use the enzyme tyrosinase as recognition element together with amperometry [43, 44]. The use of tyrosinase can eschew several issues such as the presence of electrochemical interferents or biofouling of the sensor. Biofouling refers to the formation of a polymeric film at the electrode surface, which, if severe, can lead to its deactivation [45, 46]. Recently, Compton et al. [47] provided a literature review on amperometric detection of DA in the presence of interferents (e.g., AA, UA, and serotonin) in which they describe polymers, carbon nanotubes, and other types of surface modifications.

In this section, the electrochemical behavior of the microelectrodes prior to in vivo analysis was investigated as a pathway to enable accurate monitoring of dopamine using BDD microelectrode. Figure 10.4 shows a comparison of the CVs of $Fe(CN)_6^{2-}/Fe(CN)_6^{3-}$ with CF and BDD microelectrodes in 0.1 M Na_2SO_4.

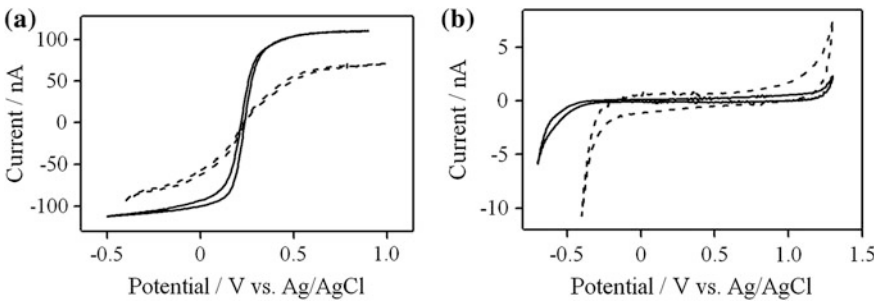

Fig. 10.4 Comparison of the CVs for 0.1 M Na_2SO_4 in the presence (**a**) and absence (**b**) of 1 mM each $Fe(CN)_6^{2-}/Fe(CN)_6^{3-}$ with a CF electrode (*dashed line*) and a BDD microelectrode (*solid line*) with a scan rate of 50 mV/s. Copyright (2007) American Chemical Society

Table 10.1 Comparison of the signal, background, and signal to background (S/B) ratio for oxidation of 1 mM $Fe(CN)_6^{2-}/Fe(CN)_6^{3-}$ in 0.1 M Na_2SO_4 at a CF electrode (extracted at a potential of 0.6 V vs. Ag/AgCl) and a BDD microelectrode (extracted at a potential of 0.8 V vs. Ag/AgCl)

	S/nA	B/nA	S/B
CF electrode	67.6	0.70	97
BDD microelectrode	108	0.25	428

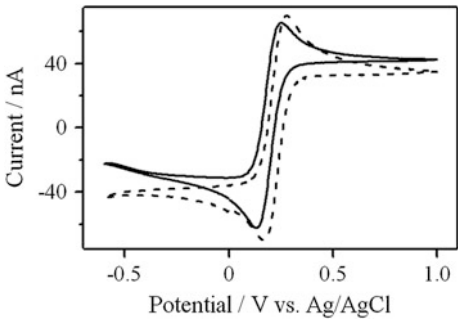

Fig. 10.5 CVs of $Fe(CN)_6^{2-}/Fe(CN)_6^{3-}$ in 0.1 M Na_2SO_4 (*dashed line*) and in double distilled ultrapure water (*solid line*) with BDD microelectrodes with a scan rate of 50 mV/s. Copyright (2007) American Chemical Society

A higher current is shown for the BDD microelectrode indicating a larger electroactive area than that of CF (Fig. 10.4a). In spite of this, a lower background current and wider potential is found for the BDD microelectrode (Fig. 10.4b). Table 10.1 shows a comparison of the signal, background, and signal to background ratio (S/B) of both CF and BDD microelectrodes extracted from the CVs in Fig. 10.4. The BDD electrode has the advantage of a higher S/B ratio (more than four times), which accounts for the very low detection limit.

An important characteristic of microelectrodes for in vivo detection, is their ability to endure high resistance media without the need to adjoin any supporting electrolyte [5]. This characteristic exists because of the small current response that arises from the limited electroactive area of microelectrodes. The IR drop problem encountered in the absence of added electrolyte is generally minimized owing to the small current range of the steady state measurement. Figure 10.5 shows the voltammetric response for the oxidation of $Fe(CN)_6^{2-}/Fe(CN)_6^{3-}$ in double-distilled ultrapure water and in 0.1 M Na_2SO_4 (behaving as a supporting electrolyte) at a BDD microelectrode. The supporting electrolyte is generally added for charged species to suppress the migration current. If the supporting electrolyte volume is not sufficient, the electrochemical reaction is difficult to initiate. In the case of the BDD microelectrode, deceleration was not observed, as comparison of the ferric-ferrous redox reactions at the BDD microelectrodes shows that the difference between the peaks in the presence or absence of an additional supporting electrolyte is very small. In contrast, greater peak separation was obtained in the CVs of BDD macroelectrodes measured in

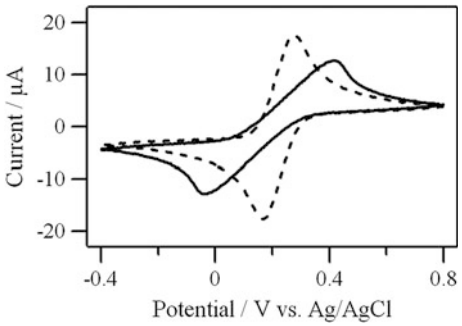

Fig. 10.6 CVs for $Fe(CN)_6^{2-}/Fe(CN)_6^{3-}$ in 0.1 M Na_2SO_4 (*dashed line*) and in double distilled ultrapure water (*solid line*) using a BDD macroelectrode at a scan rate of 50 mV/s. Copyright (2007) American Chemical Society

ultrapure water. This suggests that the BDD microelectrode can enlarge the surroundings for the electrochemical measurements (Fig. 10.6).

The effect of surface termination was also investigated as BDD electrodes are strongly influenced by this process. As-deposited BDD (ad-BDD) electrodes are initially hydrogen-terminated via deposition inside a hydrogen plasma CVD chamber [14]. It has been reported that the surface charge of BDD electrodes can switch from positive to negative polarity via the formation of surface carbon-oxygen functionalities by the following four processes: (i) an anodic treatment [48]; (ii) an oxygen plasma treatment [49]; (iii) boiling in strong acid [50] or (iv) long-time exposure to air [51]. Fujishima et al. have reported the effect of surface termination of BDD electrodes on the oxidation of some compounds [52–55], including the selective detection of DA and ascorbic acid (AA) [52]. In living organisms, AA is present in concentrations of 10–100 times higher than DA. AA was found to have almost the same oxidation potential as DA (∼+0.6 V vs. Ag/AgCl) in pH 2 buffer at ad-BDD, but the peaks were separated at an anodically oxidized BDD (ao-BDD) surface due to the electrostatic interaction between AA and the negative charge on the electrode surface [52, 53]. This behavior was also obtained for BDD microelectrodes, as shown in the comparison of the voltammetric responses for a mixture solution of DA and AA at ad- and ao-BDD microelectrodes (Fig. 10.7a). Moreover, because of the constant current response, which is a typical characteristic of microelectrodes, the peak separation was more evident than for the BDD macroelectrode (Fig. 10.8). The constant current response of the BDD microelectrode enabled us to analyze DA oxidation quantitatively with high precision. Good linearity (r^2 = 0.99) of the DA concentration in the range from 20 to 100 μM (n = 6) in mixture solutions with 1 mM AA in ultrapure water could be obtained by the I–V method (Fig. 10.7b). Furthermore, lower concentrations investigated by the chronoamperometric method (applied potential was ∼+0.8 V vs. Ag/AgCl) show that the calibration was continuously linear (r^2 = 0.99) for the concentration range of 0.5 nM–100 μM with an experimental detection limit of 50 nM (Fig. 10.7c) even without additional supporting electrolyte media.

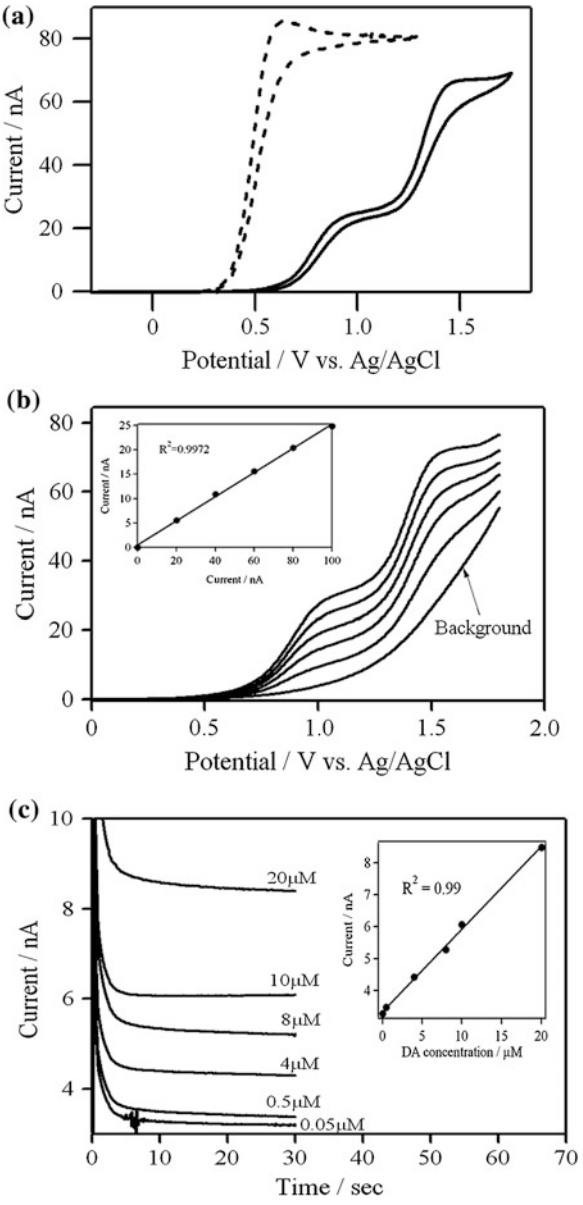

Fig. 10.7 DA measurements in double distilled ultrapure water. **a** CVs for a mixture of 0.1 mM DA and 1 mM AA at ad-BDD (*dashed line*) and ao-BDD (*solid line*) with a scan rate of 50 mV/s, **b** linear sweep voltammograms of various concentrations of DA (20–10 μM) in mixture solutions with 1 mM AA with a scan rate of 50 mV/s, and **c** chronoamperograms of various concentrations of DA (0.05–20 μM) in a mixture with 1 mM AA measured at an applied potential of 0.8 V (vs. Ag/AgCl). The insets in Figures **b** and **c** show linear calibration curves for current versus concentration. Copyright (2007) American Chemical Society

Selectivity of ao-BDD microelectrodes for DA oxidation in the presence of AA was also demonstrated by the different potential dependence between DA and AA in differential pulse voltammetry (DPV). Solutions of 1 μM DA and 100 mM AA, each in 0.1 M phosphate buffer solution (pH 7), were measured. Plots of the signal currents versus the applied potential are shown in Fig. 10.9. The potential dependence of DA shows a maximum peak at a potential of ∼0.8 V (vs. Ag/AgCl),

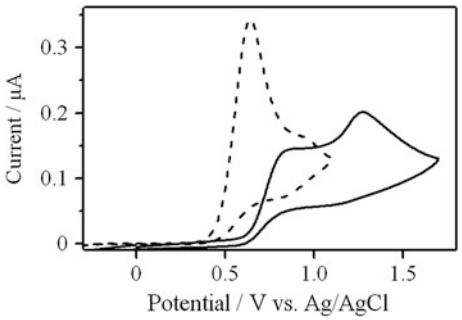

Fig. 10.8 CVs for 0.1 mM DA in a mixture of 0.1 M AA in double distilled ultrapure water with ad (*dashed line*) and ao (*solid line*) BDD macroelectrodes. The scan rate is 50 mV/s. Copyright (2007) American Chemical Society

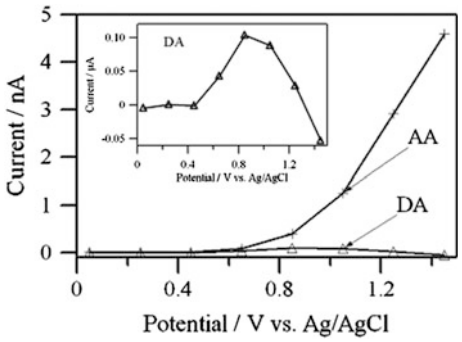

Fig. 10.9 Correlation diagrams for the signal current response versus applied potential for the oxidation of 1 μM DA (*triangle dots*) and 100 μM AA (*crossed dots*) in 0.1 M PBS measured by the DPV method. The inset shows a magnified view of the DA plot. DPV settings; frequency 50 Hz, potential step 200 mV, pulse amplitude 150 mV, starting potential 0.025 V versus Ag/AgCl. Copyright (2007) American Chemical Society

whereas that of AA exhibits a tendency to rise with increasing applied potential. These results are in good agreement with the I–V behavior illustrated in Fig. 10.7a which shows the optimum oxidation potential of DA to be at ~0.8 V (vs. Ag/AgCl). The maximum current in the AA measurements was not reached up to a potential of 1.3 V (vs. Ag/AgCl) but it should be found at a more positive potential (>1.4 V vs. Ag/AgCl). The shifting of the peak to a much higher potential can be explained as the result of electrostatic repulsion of negatively charged AA by the negative potential of the ao-BDD microelectrode surface. This behavior suggests that an unknown target (DA or AA) can be determined by observation of the potential dependence at ao-BDD microelectrodes. In the case of CF, this behavior could not be seen, as maxima of current at the same potential, ~0.2 V (vs. Ag/AgCl), were observed in the investigation of the potential dependence of DA and AA (data are not shown). This potential is even lower than the oxidation

potential of DA and AA at ad-BDD (~0.6 V vs. Ag/AgCl in Fig. 10.7a) because adsorption of DA and AA easily occurs at the CF electrode surface and accelerates the oxidation reactions [56, 57].

Due to its sp3 compact structure, BDD electrodes are known to have high stability for adsorption, including physisorption and chemisorption [14, 15]. This behavior strongly affects the stability of the current response produced by an electrochemical reaction. As per the above detailed experiment, the original termination of BDD, i.e. hydrogen termination, can be easily oxidized to become oxygen terminated. Once the BDD surface is oxidized, it remains difficult to recover the hydrogen-termination [54, 55]. The stability of oxygen-terminated BDD electrodes has already been reported [58, 59]. Anodic oxidation, however, has been reported as an effective method for recovering the BDD surface if the electrode loses sensitivity [59]. Therefore, oxygen-terminated BDD can be deemed more stable than hydrogen-terminated BDD. For instance, the stability of oxygen-terminated BDD microelectrodes was demonstrated via 10 independent measurements of a mixture of 1 mM dopamine and 100 μM ascorbic acid with an RSD of 0.6 % (not shown).

The above experiment showed that BDD microelectrodes were overall more stable, selective, sensitive and more performant in high resistance media than BDD macroelectrodes and CF electrodes.

Nevertheless, one of the reoccurring problems of biosensors is related to the reproducibility of the measurements. In fact, successive electrochemical measurements can lead to the formation of a polymeric film at the electrode surface, which deactivates it. This well-known phenomenon is called biofouling. This problem, however, can be avoided during cyclic voltammetry measurements by applying high scan rates: Fig. 10.10 shows the evolution of cyclic voltammetry measurements for 100 successive scans (only the 2nd, the 20th, the 50th and the 100th are displayed) recorded at (a) 1 V s^{-1} and (b) 100 V s^{-1} for 1 mM DA solution in 0.1 M PBS. On Fig. 10.10a, one oxidation peak (a) and two reduction peaks (c1 and c2) are observed whereas in Fig. 10.10b, only oxidation peak (a1) and reduction peak c1 can be distinguished. The broad peak a on Fig. 10.10a likely includes two electrochemical oxidations: dopamine is first oxidized to dopaquinone (DOQ) and after chemical transformation of DOQ to yield 5,6-dihydroxyindoline (DHI), the latter is further oxidized to aminochrome (AC) giving an ECE type mechanism. Consequently, the peaks c1 and c2 are most likely related to the reductions of DOQ to DA and of AC to DHI, respectively, as illustrated in Fig. 10.11. Two oxidation peaks should be distinguished on Fig. 10.10a but if the oxidation potentials of DA and DHI are not distinct, overlapping might occur to form a broader peak. On Fig. 10.10b, however, the oxidation peak a1 corresponds to the oxidation of DA to DOQ as the reduction peak c2 is not observed.

Moreover, on Fig. 10.10a, an important decrease in current related to the oxidation and reduction peaks can be seen after successive cycles. This decrease in current (and, hence gradual deactivation of the electrode) is caused by the formation of a polymer film through the electrochemical generation of AC [45, 46]. Similar deactivation, however, did not occur with higher scan rates (Fig. 10.10b). This is

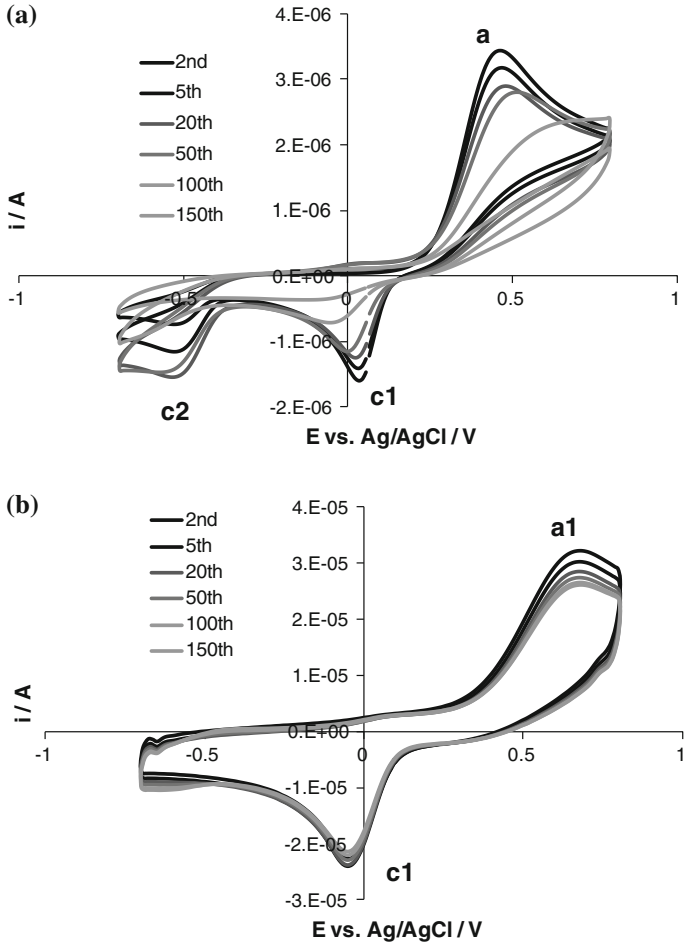

Fig. 10.10 Cyclic voltammograms (100 successive cycles) of 1 mM DA recorded on BDD microelectrode and at different scan rate: **a** 1 V s^{-1} and **b** 100 V s^{-1}. Potential window between −0.7 and 0.8 V versus Ag/AgCl. Support electrolyte: 0.1 M PBS. T = 23 °C. Copyright (2012) Chemical Society of Japan

because DOQ is not further transformed to DHI (and later AC) but is rather reduced to DA. Since DHI oxidation is the lead cause of the formation of a polymeric film at the electrode surface, deactivation can be avoided by using high scan rates for the cyclic voltammetry measurements.

In summary, reproducible electrochemical measurements can be obtained for the accurate detection of dopamine by applying a high scan rate during cyclic voltammetry measurements.

As a next step, the effect of dopamine detection on the activity of BDD and glassy carbon electrode was studied through cyclic voltammetry measurements

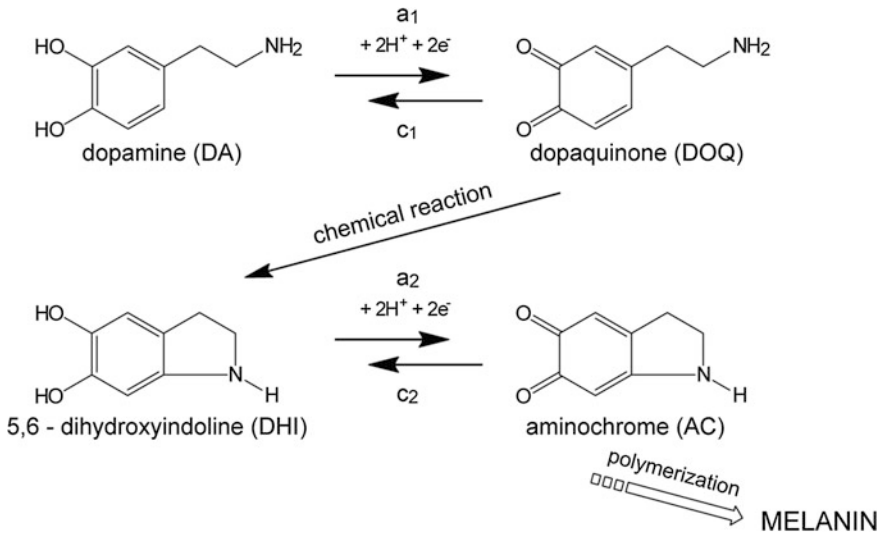

Fig. 10.11 Electrochemical reaction pathways of DA oxidation. Copyright (2012) Chemical Society of Japan

performed using the $[Fe(CN)_6]^{3-}/[Fe(CN)_6]^{4-}$ redox couple. Figure 10.12 shows cyclic voltammetry measurements of the $[Fe(CN)_6]^{3-}/[Fe(CN)_6]^{4-}$ couple (1 mM) performed on BDD electrode at (a) 1 V s^{-1} and (b) 100 V s^{-1}. In Fig. 10.12a, b, cyclic voltammetry measurements conducted before and after dopamine detection measurements are presented for: (i) 100 cycles at 1 V s^{-1} (Fig. 10.12a) and (ii) 1,165 cycles at 100 V s^{-1} (for Fig. 10.12b). The number of scans for DA detection performed in between the measurements of the $[Fe(CN)_6]^{3-}/[Fe(CN)_6]^{4-}$ couple were selected to obtain the same cumulative voltammetric charge corresponding to DA detection measurements at both scan rates (1 and 100 V s^{-1}). Figure 10.12a shows that the oxidation and reduction peaks related to the $[Fe(CN)_6]^{3-}/[Fe(CN)_6]^{4-}$ couple disappear entirely after performing DA detection measurements proving that the BDD electrode was deactivated due to the formation of a polymeric film at the electrode surface inherent to the low scan rate applied for DA detection. However, Fig. 10.12b shows that DA detection measurements have no influence on the electrochemical activity of the BDD electrode, which proves that the fouling of the electrode can be avoided if the scan rate applied during DA detection is high enough. The same experiment was performed using glassy carbon electrode and the results (Fig. 10.13a, b) demonstrate that the electrode is deactivated even when the DA detection measurements were recorded at 100 V s^{-1}.

Hence, in summary, electrode fouling can only be avoided by using BDD electrodes at high scan rates for DA measurements. It is also worthwhile to mention that microelectrodes are preferred for potential in vivo applications owing to the possibility of applying very high scan rates [60].

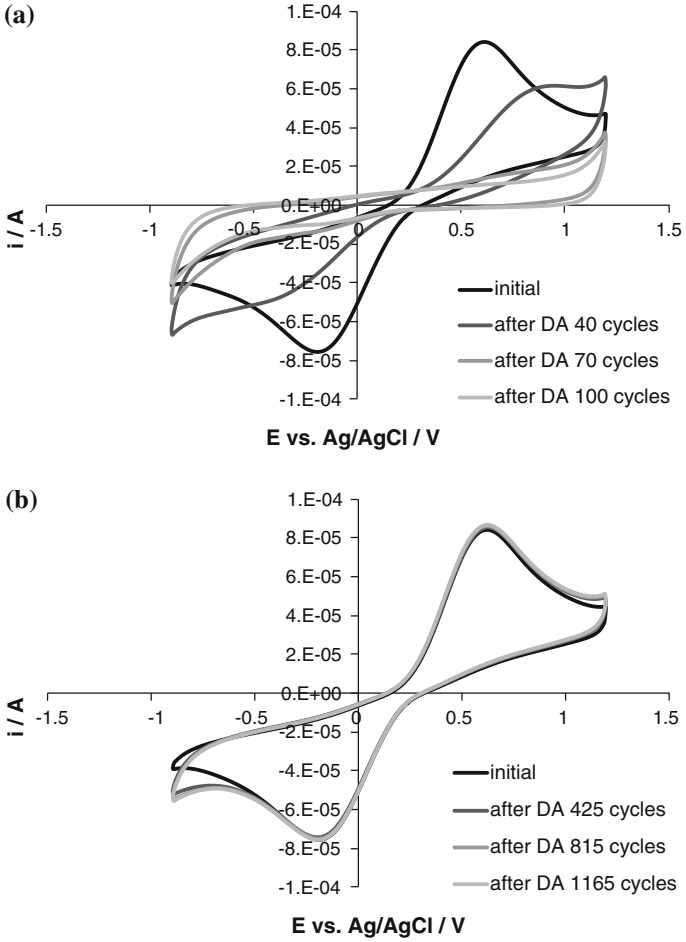

Fig. 10.12 Cyclic voltammograms of $[Fe(CN)_6]^{3-}/[Fe(CN)_6]^{4-}$ couple (1 mM) recorded on BDD electrode and at different scan rate: **a** 1 V s^{-1} and **b** 100 V s^{-1}. Potential window between −0.9 and 1.2 V versus Ag/AgCl. In Fig. 10.12a, measurements performed before and after 100 cycles recorded at 1 V s^{-1} for DA detection are presented and in Fig. 10.12b, measurements performed before and after 1,165 cycles recorded at 100 V s^{-1} for DA detection are presented. Support electrolyte: 0.1 M PBS. T = 23 °C. Copyright (2012) Chemical Society of Japan

To evaluate the ability of potential application of BDD microelectrodes for in vivo detection, MFB stimulation was employed. Stimulation of dopaminergic neurons in the MFB caused the selective release of DA into the corpus striatum, where the BDD microelectrode was applied. Therefore, monitoring the changes in DA concentration can be performed. The results herein, strongly suggest that the BDD microelectrodes will have sufficient capability for in vivo analysis, because the DA concentration measured after MFB stimulation is estimated to be up to several micromoles in the extracellular fluid [61].

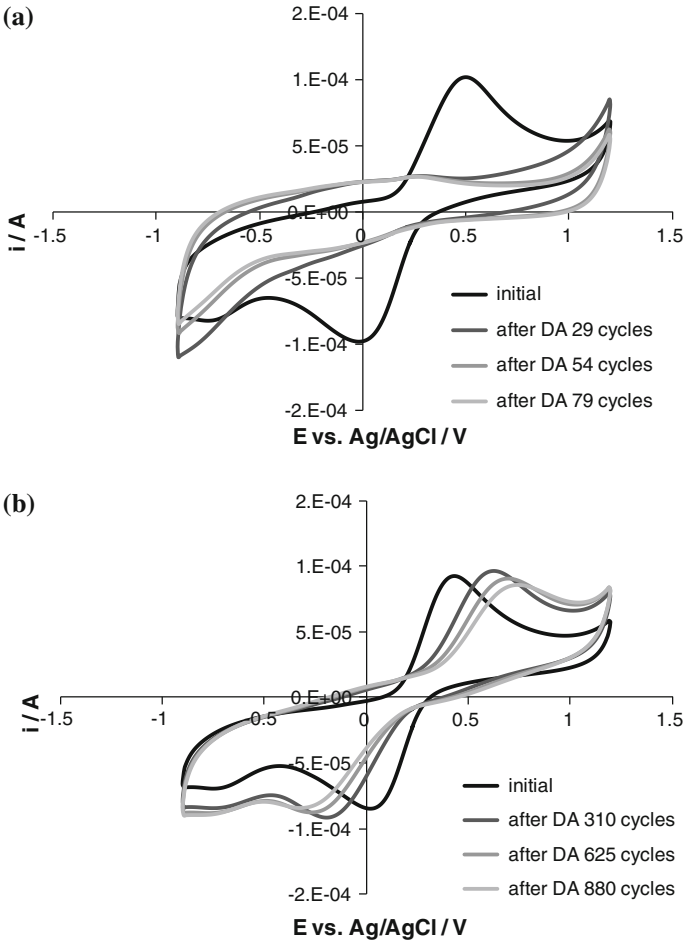

Fig. 10.13 Cyclic voltammograms of $[Fe(CN)_6]^{3-}/[Fe(CN)_6]^{4-}$ couple (1 mM) recorded on glassy carbon electrode and at different scan rate: **a** 1 V s^{-1} and **b** 100 V s^{-1}. Potential window between −0.9 and 1.2 V versus Ag/AgCl. In Fig. 10.13a, measurements performed before and after 79 cycles recorded at 1 V s^{-1} for DA detection are presented and in Fig. 10.13b, measurements performed before and after 880 cycles recorded at 100 V s^{-1} for DA detection are presented. Support electrolyte: 0.1 M PBS. T = 23 °C. Copyright (2012) Chemical Society of Japan

The stimulating electrode was carefully inserted into the brain cortex of a live mouse following the direction of the dopaminergic neurons. Electrical stimulation at a depth of 0.25 mm was applied. The position was then optimized by gradually increasing the depth in increments of 0.25 mm. The position of the electrode was fixed when the current response had reached its maximum value. In this report, a fixed depth of 4.875 mm was selected.

Fast scan CVs of the background for in vivo measurements are shown for BDD microelectrodes (Fig. 10.14a) and for a CF electrode (Fig. 10.14b). In this potential

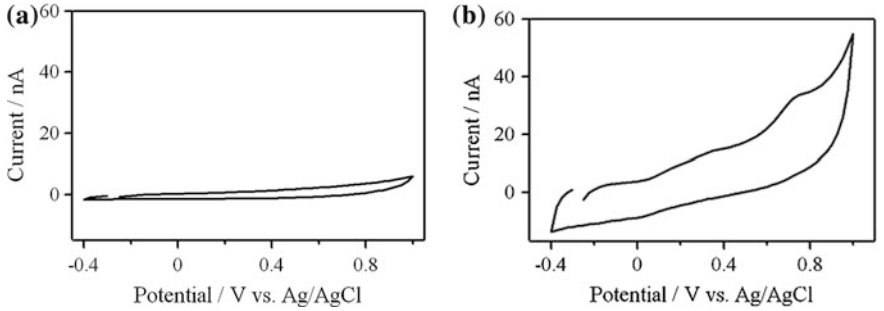

Fig. 10.14 Fast scan cyclic voltammograms of brain liquid without any stimulation at **a** an ao-BDD microelectrode and **b** CF electrode. Scan rate was 500 mV/s. Copyright (2007) American Chemical Society

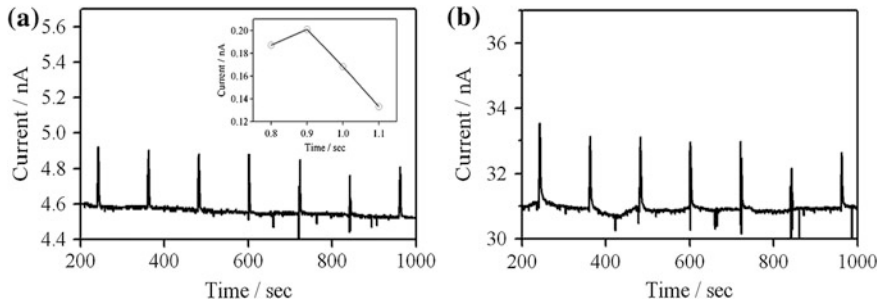

Fig. 10.15 DPV monitoring of current response following MFB stimulation (50 Hz, 100 pulses for 2 s) measured at an applied potential of 0.9 V (vs. Ag/AgCl) with **a** an ao-BDD microelectrode and **b** a CF electrode. The inset in Fig. 10.15a shows the dependence of the signal current on the applied potential. DPV setting; frequency 50 Hz, potential step 100 mV, pulse amplitude 150 mV, starting potential 0.65 V versus Ag/AgCl. Copyright (2007) American Chemical Society

range, no remarkable electroactive substance was recorded with the BDD microelectrode and the background current was almost 10 % lower than that of the CF electrode. The signal current response following MFB stimulation was monitored by the DPV method. The response for applied potentials between 0.8 and 1.1 V versus Ag/AgCl was monitored. Figure 10.15 shows that good response and stability could be obtained for a BDD microelectrode. The average signal current response following MFB stimulation was 0.33 nA with very low noise ($\sim$0.02 nA). An RSD of 0.88 % was observed for 7 measurements using the BDD microelectrode. The potential dependence for the signal current (inset of Fig. 10.15a) was found to have a maximum point at $\sim$0.9 V versus Ag/AgCl confirming the previously reported DA behavior in Fig. 10.7. The potential shift to the higher value was likely caused by the absence of electrolyte in brain liquid, which leads to deceleration of electron transfer in dopamine oxidation reaction. Simultaneous measurements at CF electrodes show an average signal current response, noise, and RSD of 1.99 nA, 0.2 nA and 1.2 %,

Table 10.2 Analytical performance of in vivo dopamine detection following MFB stimulation (50 Hz, 100 pulses for 2 s) for 7 measurements at a CF electrode and a BDD microelectrode measured by the DPV method with an applied potential of 0.9 V (vs. Ag/AgCl)

	S/nA	B/nA	N/nA	S–B	S/N	RSD/% n = 7
CF electrode	32.92	30.93	0.2	1.99	9.95	1.2
BDD microelectrode	4.88	4.56	0.02	0.33	16.50	0.9

DPV setting; frequency 50 Hz, potential step 100 mV, pulse amplitude 150 mV, starting potential 0.65 V (vs. Ag/AgCl)

respectively. Comparison of in vivo measurements of dopamine at a BDD microelectrode and a CF electrode are summarized in Table 10.2. The results suggest the superiority of BDD microelectrodes over CF electrodes in terms of S/N ratio and stability. If a regeneration of the BDD microelectrodes is needed, an oxidation treatment in 0.1 M PBS at +2.0 V (vs. Ag/AgCl) for 20 min will suffice to completely recover their surfaces. The effect of nomifensine administration was observed at the BDD microelectrode as experimental proof that DA oxidation was monitored in vivo. Nomifensine (1,2,3,4-tetrahydro-2-methyl-4-phenylisoquinolin-8-amine) is a medicine known to inhibit the DA uptake process. Nomifensine increases the amount of synaptic dopamine available to receptors by blocking the dopamine's re-uptake transporter [61–64]. Normally, the DA concentration in the extracellular fluid is very low because the rate of DA uptake into the synapses and that of DA diffusion are quite fast [45]. By nomifensine administration, the DA uptake rate can be inhibited, increasing the amount of DA in the extracellular fluid. Figure 10.16 shows the effect of nomifensine by using the DPV method. Before administration of nomifensine, small, but stable signal responses were observed following MFB

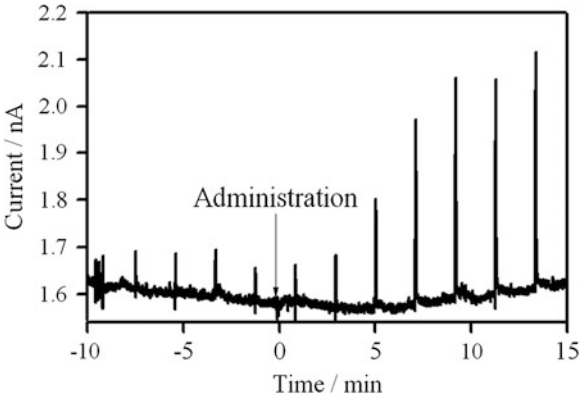

Fig. 10.16 DPV monitoring of current response following MFB stimulation before and after the administration of nomifensine (dose of 7 mg/kg) measured at an applied potential of 1.0 V (vs. Ag/AgCl). The time at which nomifensine was administered was adjusted to 0 min. The MFB stimulation conditions are the same as in Fig. 10.15. Copyright (2007) American Chemical Society

stimulation. At the time of 0 min, nomifensine (dose 7 mg/kg) was administered subcutaneously, and soon after, the signal current response rose remarkably. Therefore, there is no doubt that the DA was monitored precisely.

10.4 Glutathione Detection

Glutathione is a tripeptide found in high concentrations in many living cells and exists in reduced form (L-γ-glutamyl-L-cysteinyl-glycine, GSH) and oxidized form (disulfide form of GSH, GSSG) [65–67]. It is one of the strongest biological antioxidant, which signifies that under oxidative stress, GSH will be oxidized to GSSG and immediately reduced back to GSH by an enzyme (glutathione reductase) [65–68]. Because of this fast turnover, GSH concentrations in living cells are usually much higher compared to GSSG. Hence, the ratio of GSH to GSSG often serves as a sensitive indicator of oxidative stress and is a key marker for the redox status of cells [65–68]. Additionally, it was reported that GSH concentrations in cancerous cells are much higher when compared to healthy tissues [69]. It is thus believed that this high concentration of GSH is the chief reason of the high resistance of cancer stem cells against oxidative stress such as radiotherapy or chemotherapy [69, 70]. Therefore, the in vivo monitoring of GSH could be critical for the assessment of the biological features of cancer cells.

Several techniques devised at measuring GSH concentration have been recently put forth in the literature. The vast majority involves liquid chromatography with different detection methods such as fluorescence or UV [71–73]. Most of these methods, however, are based on column derivatization followed by fluorimetric detection or on the conversion to their phenyl or pyridine derivatives followed by UV detection [71–73]. Therefore, these methods require costly equipment and time-consuming procedures. Additionally, these techniques are not suited for in vivo GSH detection and thus require tissue samples obtained through biopsy, which is an invasive procedure for the patient. An in vivo glutathione concentration measurement technique involving labeling with monochlorobimane using HPLC prior to detection was reported [74]. This method, nonetheless, was exclusively tested on plants (*Arabidopsis*) and the concentration measured includes both the reduced and oxidized form of glutathione [74]. Another in vivo method for GSH detection in human brain by means of double quantum coherence filtering was also reported [75]. This analysis gave satisfactory results for in vivo GSH determination but this indirect detection method involves complicate spectra analysis and time consuming calibration procedures [75].

Electrochemical methods are a viable alternative due to their simplicity, speed and excellent sensitivity. Several electrochemical methods for glutathione detection have already been proposed using electrodes such as platinum, gold or gold/mercury [76–79]. These methods have shown to be quite efficient for in vitro glutathione determination. However, gold electrodes usually require time-consuming pretreatments in order to get reproducible results. Moreover, the use and preparation

of gold/mercury tend to complicate the experimental procedure and therefore, these methods are less suited for real analytical applications. Additionally, adsorption and subsequent fouling on these types of electrode materials often occurs during the oxidation of various organic compounds and, consequently, it becomes difficult to use these electrode materials for in vivo GSH detection.

The separate electrochemical detection of both the reduced and oxidized form of glutathione has been reported on boron doped diamond (BDD) electrode [79]. This electrode material was selected due to its outstanding properties relative to other conventional electrode materials. Such properties include; a wide electrochemical potential window, low background current and weak adsorption of polar molecules [13, 14]. Only macroelectrodes, however, were used in the latter study and the detection was performed in BRB buffer (pH 2). Therefore, only in vitro electrochemical detection of GSH is feasible using the method described in [79]. To the authors knowledge, the in vivo monitoring of GSH concentration for cancer tumor assessment via electrochemical methods has never been attempted.

In a recent study, BDD electrodes were used to evaluate the variation of GSH concentration inside a cancerous tumor. The measurements were performed in normal tissue and inside xenograft tumors derived from human squamous cell carcinoma cells (HSC-2 cell) that had been inoculated in three different mice for 2 weeks. Figure 10.17 shows that the anodic current recorded increases when the measurement was performed inside the tumor when compared to the healthy tissue. Preliminary in vitro calibration measurements carried out under conditions simulating a biological environment (pH 7.4 and 37 °C) showed that highly accurate calibration curves could be obtained using chronoamperometry measurements with BDD microelectrode.

Furthermore, it was shown that for an environment containing both GSH and GSSH, it would still be possible to separate the detection of GSH from GSSG if the

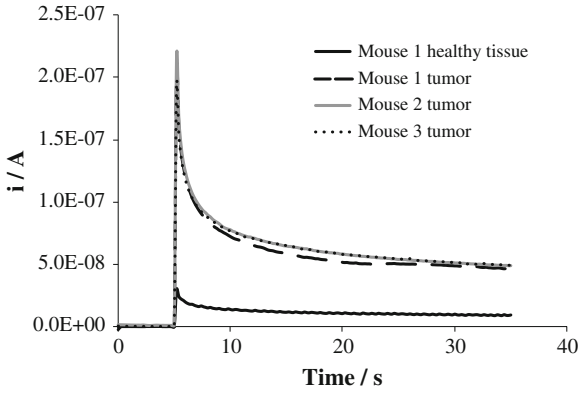

Fig. 10.17 Chronoamperometry measurements recorded on BDD microelectrode at 1.3 V versus Ag/AgCl: in normal tissue (flank) of mouse 1, in the HSC-2-derived xenograft tumor of mouse 1, in the HSC-2-derived xenograft tumor of mouse 2 and in the HSC-2-derived xenograft tumor of mouse 3. All tumors had been inoculated for 2 weeks. T = 37 °C

potential applied during the chronoamperometry measurement is carefully selected (i.e. before the on-set potential of GSSG oxidation). It would still not be possible, however, to separate the detection of GSSG from GSH. In fact, if the on-set potential of GSSG oxidation was selected for the chronoamperometry measurement, GSH oxidation would also occur and the current measured would be related to the oxidation of both GSH and GSSG.

Measurements performed in three distinct healthy mice gave similar results proving the reproducibility of the method. If one considers that the difference between the different currents recorded is almost exclusively due to the difference in GSH concentration inside the tissue (due to its affinity for oxidation), these measurement (Fig. 10.17) showed that it is possible to perform an in vivo assessment of the tumor using the proposed method.

It is worthwhile to mention, however, that biofouling of the BDD electrode did occur after one measurement, which induced a decrease in the current difference between the measurements performed in normal and tumorous tissues. For this reason, a cathodic treatment was performed (−3 V for 20 min) in 0.1 M PBS between each measurement. Also, for reliable results using this method, the in vivo current measurement should not last more than 5 s.

To attest if a decrease in GSH concentration inside the tumor can be detected; two mice (out of the three) were X-ray irradiated for 2 min but at different levels (2 and 6 Gy). X-ray irradiation has shown to considerably decrease the amount of GSH in living tissues as reported in [80].

After 3 h of X-ray irradiation, GSH detection measurements were carried out in the HSC-2-derived xenograft tumors of the three mice (among which only two were X-ray irradiated) and compared with the results presented in Fig. 10.18.

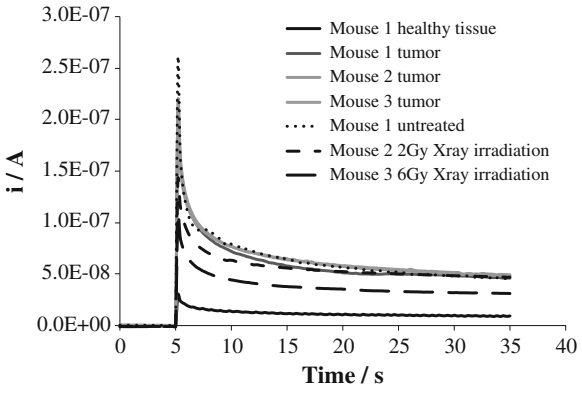

Fig. 10.18 The results presented in Fig. 10.17 are compared with chronoamperometry measurements recorded on BDD microelectrode at 1.3 V versus Ag/AgCl: in the HSC-2-derived xenograft tumor of mouse 1 (untreated; measurement performed 3 h after the results presented in Fig. 10.5), in the HSC-2-derived xenograft tumor of mouse 2 (3 h after the tumor had been X-ray irradiated for 2 min at 2 Gy) and in the HSC-2-derived xenograft tumor of mouse 3 (3 h after the tumor had been X-ray irradiated for 2 min at 6 Gy). T = 37 °C

Figure 10.18 displays this comparison and shows that the current density recorded in the tumor decreased significantly after irradiation whereas the current density measured in the tumor remained unchanged for the control mouse. Moreover, the decrease in current density increased with increasing intensity of the irradiation. This figure thus suggests that it is possible to detect the variation of GSH concentrations in cancerous tumors before and after a specific treatment using this technique.

10.5 Conclusions

The promising results obtained through a large breadth of experiments presented herein strongly suggest that boron-doped diamond (BDD) based electrochemical biosensors bear a great potential for early diagnosis or research. This technology owes its practical value from a combination of selective biochemical recognitions such as the high sensitivity of electrochemical detection and the outstanding electrochemical properties of BDD. These biosensors also profit from modern miniaturized electrochemical instrumentation and are thus very valuable for specific sophisticated applications simultaneously requiring portability, rapid accurate measurement and use with small sample volume. Numerous commercial applications have confirmed the attractiveness of BDD based electrochemical biosensors.

References

1. L. Clark, C. Lyons, Electrode system for continuous monitoring in cardiovascular surgery. Ann. N. Y. Acad. Sci. **102**, 29–45 (1962). doi:10.1111/j.1749-6632.1962.tb13623.x
2. H.B. Yildiz, L. Toppare, Biosensing approach for alcohol determination using immobilized alcohol oxidase. Biosens. Bioelectron. **21**(12), 2306–2310 (2006). doi:10.1016/j.bios.2005.11.006
3. H. Barhoumi, A. Maaref, M. Rammah, C. Martelet, N. Jaffrezic-Renault, C. Mousty, S. Cosnier, E. Perez, E. Rico-Lattes, Insulator semiconductor structures coated with biodegradable latexes as encapsulation matrix for urease. Biosens. Bioelectron. **20**(11), 2318–2323 (2005). doi:10.1016/j.bios.2004.10.010
4. K. Jackovska, P. Krysinski, New trends in the electrochemical sensing of dopamine. Anal. Bioanal. Chem. **405**(11), 3753–3771 (2013). doi:10.1007/s00216-012-6578-2
5. A.M. Bond, Past, present and future contributions of microelectrodes to analytical studies employing voltammetric detection, a review. Analyst **119**, R1–R21 (1994). doi:10.1039/AN994190001R
6. D.J. Wiedemann, T.K. Kawagoe, R.T. Kennedy, E.L. Ciolkowski, R.M. Wightman, Strategies for low detection limit measurements with cyclic voltammetry. Anal. Chem. **63**(24), 2965–2970 (1991). doi:10.1021/ac00024a030
7. A.M. Bond, M. Fleischmann, J. Robinson, Electrochemistry in organic solvents without supporting electrolyte using platinum microelectrodes. J. Electroanal. Chem. **168**(1–2), 299–312 (1984). doi:10.1016/0368-1874(84)87106-3

8. P.S. Cahill, Q.D. Qalker, J.M. Finnegan, G.E. Mickelson, E.R. Travis, R.M. Wightman, Microelectrodes for the measurement of catecholamines in biological systems. Anal. Chem. **68** (18), 3180–3186 (1996). doi:10.1021/ac960347d
9. C.D. Paras, R.T. Kenedy, Amperometry and cyclic voltammetry of tyrosine and tryptophan-containing oligopeptides at carbon fiber microelectrodes applied to single cell analysis. Electroanalysis **9**(3), 203–208 (1997). doi:10.1002/elan.1140090303
10. P.T. Kissinger, J.B. Hart, R.N. Adams, Voltammetry in brain tissue—a new neurophysiological measurement. Brain Res. **55**(1), 209–213 (1973). doi:10.1016/0006-8993(73)90503-9
11. J.L. Ponchon, R. Cespuglio, F. Gonon, M. Jouvet, J.-F. Pujol, Normal pulse polarography with carbon fiber electrodes for in vitro and in vivo determination of catecholamines. Anal. Chem. **51**(9), 1483–1486 (1979). doi:10.1021/ac50045a030
12. B.P. Jackson, S.M. Dietz, R.M. Wightman, Fast-scan cyclic voltammetry of 5-hydroxytryptamine. Anal. Chem. **67**(6), 1115–1120 (1995). doi:10.1021/ac00102a015
13. A. Fujishima, Y. Einaga, T.N. Rao, D.A. Tryk (ed.), *Diamond Electrochemistry* (Elsevier-BKC, Tokyo, 2005)
14. T. Yano, D.A. Tryk, K. Hashimoto, A. Fujishima, Electrochemical behavior of highly conductive boron-doped diamond electrodes for oxygen reduction in alkaline solution. J. Electrochem. Soc. **145**(6), 1870–1876 (1998). doi:10.1149/1.1838569
15. M.D. Koppang, M. Witek, J. Blau, G.M. Swain, Electrochemical oxidation of polyamines at diamond thin-film electrodes. Anal. Chem. **71**(6), 1188–1195 (1999). doi:10.1021/ac980697v
16. A. Hartl, E. Schmich, J.A. Garrido, J. Hernando, S.C.R. Catharino, S. Walter, P. Feulner, A. Kromka, D. Steinmuller, M. Stutzmann, Protein-modified nanocrystalline diamond thin films for biosensor applications. Nat. Mater. **3**, 736–742 (2004). doi:10.1038/nmat1204
17. A. Suzuki, T.A. Ivandini, A. Kamiya, S. Nomura, M. Yamanuki, K. Matsumoto, A. Fujishima, Y. Einaga, Direct electrochemical detection of sodium azide in physiological saline buffers using highly boron-doped diamond electrodes. Sens. Actuat. B **120**(2), 500–507 (2007). doi:10.1016/j.snb.2006.03.003
18. T. Ochiai, K. Arihara, C. Terashima, A. Fujishima, Electrochemical reduction of ozone dissolved in perchloric acid solutions at boron-doped diamond electrodes. Chem. Lett. **35**(9), 1018–1019 (2006). doi:10.1246/cl.2006.1018
19. T. Watanabe, T.A. Ivandini, Y. Makide, A. Fujishima, Y. Einaga, Selective detection method derived from a controlled diffusion process at metal-modified diamond electrodes. Anal. Chem. **78**(22), 7857–7860 (2006). doi:10.1021/ac060860j
20. T.A. Ivandini, T.N. Rao, A. Fujishima, Y. Einaga, Simultaneous detection of purine and pyrimidine at highly boron-doped diamond electrodes by using liquid chromatography. Talanta **71**(2), 648–655 (2007). doi:10.1016/j.talanta.2006.05.009
21. B.V. Sarada, T.N. Rao, D.A. Tryk, A. Fujishima, Electrochemical characterization of highly boron-doped diamond microelectrodes in aqueous electrolyte. J. Electrochem. Soc. **146**(84), 1469–1471 (1999). doi:10.1149/1.1391788
22. H. Olivia, B.V. Sarada, D. Shin, T.N. Rao, A. Fujishima, Selective amperometric detection of dopamine using OPPy-modified diamond microsensor system. Analyst **127**, 1572–1575 (2002). doi:10.1039/B208729D
23. H. Olivia, B.V. Sarada, K. Honda, A. Fujishima, Continuous glucose monitoring using enzyme-immobilized platinized diamond microfiber electrodes. Electrochim. Acta **48**(13), 2069–2076 (2004). doi:10.1016/j.electacta.2003.10.026
24. D.C. Shin, B.V. Sarada, D.A. Tryk, A. Fujishima, J. Wang, Application of diamond microelectrodes for end-column electrochemical detection in capillary electrophoresis. Anal. Chem. **75**(3), 530–534 (2003). doi:10.1021/ac020513j
25. G.W. Muna, V. Quaiserova-Mocko, G.M. Swain, The analysis of chlorinated phenol solutions by capillary electrophoresis coupled with direct and indirect amperometric detection using a boron-doped diamond microelectrode. Electroanalysis **17**(13), 1160–1170 (2005). doi:10.1002/elan.200403230
26. J. Park, V. Quaiserova-Mocko, K. Peckova, J.J. Galligan, G.D. Fink, G.M. Swain, Fabrication, characterization, and application of a diamond microelectrode for electrochemical

measurement of norepinephrine release from the sympathetic nervous system. Diam. Relat. Mater. **15**(4–8), 761–772 (2006). doi:10.1016/j.diamond.2005.11.008
27. J. Park, J.J. Galligan, G.D. Fink, G.M. Swain, In vitro continuous amperometry with a diamond microelectrode coupled with video microscopy for simultaneously monitoring endogenous norepinephrine and its effect on the contractile response of a rat mesenteric artery. Anal. Chem. **78**(19), 6756–6764 (2006). doi:10.1021/ac060440u
28. J. Park, Y. Show, V. Quaiserova-Mocko, J.J. Galligan, G.D. Fink, G.M. Swain, Diamond microelectrodes for use in biological environments. J. Electroanal. Chem. **583**(1), 56–68 (2005). doi:10.1016/j.jelechem.2005.04.032
29. S. Xie, G. Shafer, C.G. Wilson, H.B. Martin, In vitro adenosine detection with a diamond-based sensor. Diam. Relat. Mater. **15**(2–3), 225–228 (2006). doi:10.1016/j.diamond.2005.08.018
30. C. Dugast, M.F. Suaud-Chagny, F. Gonon, Continuous in vivo monitoring of evoked dopamine release in the rat nucleus accumbens by amperometry. Neuroscience **62**(3), 647–654 (1994). doi:10.1016/0306-4522(94)90466-9
31. F. Mora, G. Segovia, A. del Arco, M. de Blas, P. Garrido, Stress, neurotransmitters, corticosterone and body-brain integration. Brain Res. **1476**, 71–85 (2012). doi:10.1016/j.brainres.2011.12.049
32. V. Hefco, K. Yamada, A. Hefco, L. Hrticu, A. Tiron, T. Nabeshima, Role of the mesotelencephalic dopamine system in learning and memory processes in the rat. Eur. J. Pharmacol. **475**(1–3), 55–60 (2003). doi:10.1016/S0014-2999(03)02115-0
33. A. Galvan, T. Wichmann, Pathophysiology of parkinsonism. Clin. Neurophysiol. **119**(7), 1459–1474 (2008). doi:10.1016/j.clinph.2008.03.017
34. S.H. Kollins, J.S. March, Advances in the pharmacotherapy of attention-deficit/hyperactivity disorder. Biological Psychiatry. Biol. Psychiatry **62**(9), 951–953 (2007). doi:10.1016/j.biopsych.2007.08.009
35. M. Shou, C.R. Ferrario, K.N. Schultz, T.E. Robinson, R.T. Kennedy, Monitoring dopamine in vivo by microdialysis sampling and on-line CE-laser-induced fluorescence. Anal. Chem. **78**(19), 6717–6725 (2006). doi:10.1021/ac0608218
36. D. Wang, W. Zhu, Y. An, J. Zheng, W. Zhang, L. Jin, H. Gao, L. Lin, LC with novel electrochemical detection for analysis of monoamine neurotransmitters in rat brain after administration of (R)-salsolinol and (R)-N-methylsalsolinol. Chromatographia **67**(5–6), 369–374 (2008). doi:10.1365/s10337-008-0532-7
37. M. Pumera, S. Sanchez, I. Ichinose, J. Tang, Electrochemical nanobiosensors. Sens. Actuat. B **123**(2), 1195–1205 (2007). doi:10.1016/j.snb.2006.11.016
38. U. Yogeswaran, S.-M. Chen, A review on the electrochemical sensors and biosensors composed of nanowires as sensing material. Sensors **8**(1), 290–313 (2008). doi:10.3390/s8010290
39. J. Wang, Y. Lin, Functionalized carbon nanotubes and nanofibers for biosensing applications. Trend Anal. Chem. **27**(7), 619–626 (2008). doi:10.1016/j.trac.2008.05.009
40. K. Balasubramanian, M. Burghard, Biosensors based on carbon nanotubes. Anal. Bioanal. Chem. **385**(3), 452–468 (2006). doi:10.1007/s00216-006-0314-8
41. Y. Lu, M. Yang, F. Qu, G. Shen, R. Yu, Enzyme-functionalized gold nanowires for the fabrication of biosensors. Bioelectrochemistry **71**(2), 211–216 (2007). doi:10.1016/j.bioelechem.2007.05.003
42. J.M. Pingarron, P. Yanez-Sadeno, A. Gonzalez-Cortes, Gold nanoparticle-based electrochemical biosensors. Electrochim. Acta **53**(19), 5848–5866 (2008). doi:10.1016/j.electacta.2008.03.005
43. E.I. Solomon, U.M. Sundaram, T.E. Machonkin, Multicopper oxidases and oxygenases. Chem. Rev. **96**(7), 2563–2606 (1996). doi:10.1021/cr950046o
44. S.S. Shleev, J. Tkac, A. Christenson, T. Ruzgas, A.I. Yaropolov, J.W. Whittaker, L. Gorton, Direct electron transfer between copper-containing proteins and electrodes. Biosens. Bioelectron. **20**(12), 2517–2554 (2005). doi:10.1016/j.bios.2004.10.003

45. U.E. Majewska, K. Chmurski, K. Biesada, A.R. Olszyna, R. Bilewicz, Dopamine oxidation at per(6-deoxy-6-thio)-α-cyclodextrin monolayer modified gold electrodes. Electroanalysis **18**(15), 1463–1470 (2006). doi:10.1002/elan.200603556
46. A. Ciszewski, G. Milczarek, Polyeugenol-modified platinum electrode for selective detection of dopamine in the presence of ascorbic acid. Anal. Chem. **71**(5), 1055–1061 (1999). doi:10.1021/ac9808223
47. M.C. Henstridge, E.J.F. Dickinson, M. Aslanoglu, C. Batchelor-McAuley, R.G. Compton, Voltammetric selectivity conferred by the modification of electrodes using conductive porous layers or films: The oxidation of dopamine on glassy carbon electrodes modified with multiwalled carbon nanotubes. Sens. Actuat. B Chem. **145**(1), 417–427 (2010). doi:10.1016/j.snb.2009.12.046
48. H. Notsu, I. Yagi, T. Tatsuma, D.A. Tryk, A. Fujishima,Introduction of oxygen-containing functional groups onto diamond electrode surfaces by oxygen plasma and anodic polarization. Electrochem. Solid-State Lett. **2**(2), 522–524 (1999). doi:10.1149/1.1390890
49. I. Yagi, H. Notsu, T. Kondo, D.A. Tryk, A. Fujishima, Electrochemical selectivity for redox systems at oxygen-terminated diamond electrodes. J. Electroanal. Chem. **473**(1–2), 173–178 (1999). doi:10.1016/S0022-0728(99)00027-3
50. K. Hayashi, S. Yamanaka, H. Watanabe, T. Sekiguchi, H. Okushi, K. Kajimura, Investigation of the effect of hydrogen on electrical and optical properties in chemical vapor deposited on homoepitaxial diamond films. J. Appl. Phys. **81**(2), 744 (1997). doi:10.1063/1.364299
51. H.B. Martin, A. Argoitia, U. Landau, A.B. Andersin, J.C. Angus, Hydrogen and oxygen evolution on boron-doped diamond electrodes. J. Electrochem. Soc. **143**(6), L133–L136 (1996). doi:10.1149/1.1836901
52. E. Popa, H. Notsu, T. Miwa, D.A. Tryk, A. Fujishima, Selective electrochemical detection of dopamine in the presence of ascorbic acid at anodized diamond thin film electrodes. Electrochem. Solid-State Lett. **2**(1), 49–51 (1999). doi:10.1149/1.1390730
53. E. Popa, Y. Kubota, D.A. Tryk, A. Fujishima, Selective voltammetric and amperometric detection of uric acid with oxidized diamond film electrodes. Anal. Chem. **72**(7), 1724–1727 (2000). doi:10.1021/ac990862m
54. T.A. Ivandini, B.V. Sarada, T.N. Rao, A. Fujishima, Electrochemical oxidation of underivatized-nucleic acids at highly boron-doped diamond electrodes. Analyst **128**(7), 924–929 (2003). doi:10.1039/B301483E
55. T.A. Ivandini, T.N. Rao, A. Fujishima, Y. Einaga, Electrochemical oxidation of oxalic acid at highly boron-doped diamond electrodes. Anal. Chem. **78**(10), 3467–3471 (2006). doi:10.1021/ac052029x
56. M. Benoit-Marand, E. Borelli, F. Gonon, Inhibition of dopamine release via presynaptic D2 receptors: time course and functional characteristics in vivo. J. Neurosci. **21**(23), 9134–9141 (2001)
57. C. Terashima, T.N. Rao, B.V. Sarada, D.A. Tryk, A. Fujishima, Electrochemical oxidation of chlorophenols at a boron-doped diamond electrode and their determination by high-performance liquid chromatography with amperometric detection. Anal. Chem. **74**(4), 895–902 (2002). doi:10.1021/ac010681w
58. T.N. Rao, B.H. Loo, B.V. Sarada, C. Terashima, A. Fujishima, Electrochemical detection of carbamate pesticides at conductive diamond electrodes. Anal. Chem. **74**(7), 1578–1583 (2002). doi:10.1021/ac010935d
59. C.D. Allred, R.L. McCreery, Adsorption of catechols on fractured glassy carbon electrode surfaces. Anal. Chem. **64**(4), 444–448 (1992). doi:10.1021/ac00028a020
60. L.R.F. Allen, J. Bard, *Electrochemical Methods: Fundamentals and Applications* (Wiley, New York, 1980)
61. P.A. Garris, E.A. Budygin, P.E.M. Phillips, B.J. Venton, D.L. Robinson, B.P. Bergstrom, G.V. Rebec, R.M. Wightman, A role for presynaptic mechanisms in the actions of nomifensine and haloperidol. Neuroscience **118**(3), 819–829 (2003). doi:10.1016/S0306-4522(03)00005-8
62. L. Vidal, M. Alfonso, L.F. Faro, F. Campos, R. Cervantes, R. Duran, Evaluation of the effects and mechanisms of action of mercuric chloride on striatal dopamine release by using in vivo

microdialysis in freely moving rats. Toxicology **236**(1–2), 42–49 (2007). doi:10.1016/j.tox.2007.03.023
63. M.J. Hansard, L.A. Smith, M.J. Jackson, S.C. Cheetham, P. Jenner, Dopamine, but not norepinephrine or serotonin, reuptake inhibition reverses motor deficits in 1-methyl-4-phenyl-1,2,3,6-tetrahydropyridine-treated primates. Pharmacol. Exp. Ther. **303**(3), 952–958 (2002). doi:10.1124/jpet.102.039743
64. R.M. Wightman, C. Amatore, R.C. Engstrom, P.D. Hale, E.W. Kristensen, W.G. Kuhr, L. May, Real-time characterization of dopamine overflow and uptake in the rat striatum. Neuroscience **25**(2), 513–523 (1988). doi:10.1016/0306-4522(88)90255-2
65. A. Pompella, A. Visvikis, A. Paolicchi, V. De Tata, A.F. Casini, The changing faces of glutathione, a cellular protagonist. Biochem. Pharmacol. **66**(8), 1499–1503 (2003). doi:10.1016/S0006-2952(03)00504-5
66. Y. Morel, R. Barouki, Repression of gene expression by oxidative stress. Biochem. J. **342**(3), 481–496 (1999)
67. A. Pastore, F. Piemonte, M. Locatelli, A. Lo Russo, L.M. Gaeta, G. Tozzi, G. Federici, Determination of blood total, reduced, and oxidized glutathione in pediatric subjects. Clin. Chem. **47**(8), 1467–1469 (2001)
68. M. Asensi, J. Sastre, F.V. Pallardo, A. Lloret, M. Lehner, J. Garcia-de-la Asuncion, J. Viña, Ratio of reduced to oxidized glutathione as indicator of oxidative stress status and DNA damage. Meth. Enzym. **299**, 267–276 (1999). doi:10.1016/S0076-6879(99)99026-2
69. G.K. Balendiran, R. Dabur, D. Fraser, The role of glutathione in cancer. Cell Biochem. Funct. **22**(6), 343–352 (2004). doi:10.1002/cbf.1149
70. T. Ishimoto, O. Nagano, T. Yae, M. Tamada, T. Motohara, H. Oshima, M. Oshima, T. Ikeda, R. Asaba, H. Yagi, T. Masuko, T. Shimizu, T. Ishikawa, K. Kai, E. Takahashi, Y. Imamura, Y. Baba, M. Ohmura, M. Suematsu, H. Baba, H. Saya, CD44 variant regulates redox status in cancer cells by stabilizing the xCT subunit of system xc(-) and thereby promotes tumor growth. Cancer Cell **19**(3), 387–400 (2011). doi:10.1016/j.ccr.2011.01.038
71. R. Gotti, V. Andrisano, V. Cavrini, A. Bongini, Determination of glutathione in pharmaceuticals and cosmetics by HPLC with UV and fluorescence detection. Chromatographia **39**(1–2), 23–28 (1994). doi:10.1007/BF02320453
72. R.C. Fahey, G.L. Newton, Determination of low-molecular-weight thiols using monobromobimane fluorescent labeling and high-performance liquid chromatography. Meth. Enzym. **143**, 85–96 (1987). doi:10.1016/0076-6879(87)43016-4
73. D. Tsikas, G. Brunner, High-performance liquid chromatography of glutathione conjugates. Fresenius J. Anal. Chem. **343**(3), 326–329 (1992). doi:10.1007/BF00322384
74. A.J. Meyer, M.J. May, M. Fricker, Quantitative in vivo measurement of glutathione in Arabidopsis cells. Plant J. **27**(1), 67–78 (2001). doi:10.1046/j.1365-313x.2001.01071.x
75. A.H. Trabesinger, O.M. Weber, C.O. Duc, P. Boesiger, Detection of glutathione in the human brain in vivo by means of double quantum coherence filtering. Magnet. Reson. Med. **42**(2), 283–289 (1999). doi:10.1002/(SICI)1522-2594(199908)42:2<283::AID-MRM10>3.0.CO;2-Q
76. L.A. Allison, R.E. Shoup, Dual electrode liquid chromatography detector for thiols and disulfides. Anal. Chem. **55**(1), 8–12 (1983). doi:10.1021/ac00252a006
77. P. Vandeberg, D.C. Johnson, Pulsed electrochemical detection of cysteine, cystine, methionine, and glutathione at gold electrodes following their separation by liquid chromatography. Anal. Chem. **65**(20), 2713–2718 (1993). doi:10.1021/ac00068a002
78. J.C. Hoekestra, D.C. Johnson, Comparison of potential−time waveforms for the detection of biogenic amines in complex mixtures following their separation by liquid chromatography. Anal. Chem. **70**(1), 83–88 (1998). doi:10.1021/ac970806q
79. C. Terashima, T.N. Rao, B.V. Sarada, Y. Kubota, A. Fujishima, Direct electrochemical oxidation of disulfides at anodically pretreated boron-doped diamond electrodes. Anal. Chem. **75**(7), 1564–1572 (2003). doi:10.1021/ac020583q
80. M.J. Ashwood-Smith, The effect of whole-body X-irradiation on the glutathione content of rat thymus. Int. J. Rad. Biol. **3**(2), 125–132 (1961). doi:10.1080/09553006114550141

Index

N. Yang (ed.), *Novel Aspects of Diamond*, Topics in Applied Physics 121,
DOI 10.1007/978-3-319-09834-0